SHOCK DIFFRACTION PHENOMENA AND THEIR MEASUREMENT

A thesis submitted to the University of Manchester for the degree of Doctor of Philosophy in the Faculty of Engineering and Physical Sciences

2013

By
Mark Kenneth Quinn
Mechanical, Aerospace and Civil Engineering

Contents

List of Tables

List of Figures

List of Publications

1. **M. K. Quinn**, N. Gongora-Orozco, K. Kontis, P. Ireland. Application of Pressure-Sensitive Paint to Low-speed Flow Around a U-Bend of Strong Curvature. *Experimental Thermal Fluid Science* 18:58-66, **2013**

2. **M. K. Quinn**, K. Kontis. Pressure-Sensitive Paint Measurements of Transient Shock Phenomena. *Sensors* 13(4):4404-4427, **2013**

3. **M. K. Quinn**, K. Kontis. A Combined Study on Shock Diffraction. *5th Symposium on Integrating CFD and Experiments in Aerodynamics*, Tokyo, Japan, **2012**

4. **M. K. Quinn**, K. Kontis. Experiments and Simulations of Weak Shock Wave Diffraction Phenomena. *20th International Shock Interaction Symposium*, Stockholm, Sweden, **2012**

5. **M. K. Quinn**, L. Yang, K. Kontis. Pressure-Sensitive Paint: Effect of Substrate. *Sensors* 11(12):11649-11663, **2011**

6. **M. K. Quinn**, N. Gongora-Orozco, K. Kontis, P. Ireland. Application of Pressure-Sensitive Paint to Low-speed Flow Around a U-Bend of Strong Curvature. *8th Pacific Symposium on Flow Visualization and Image Processing*, Moscow, Russia, **2011**

7. **M. K. Quinn**, N. Gongora-Orozco, H. Zare-Behtash, R. Mariani, K. Kontis. Experimental Studies of Shock Diffraction. *28th International Symposium on Shock Waves*, Manchester, United Kingdom, **2011**

8. R. Mariani, **M. K. Quinn**, K. Kontis, L. Marraffa. Shock-Free Compressible Vortex Rings Impinging on a Stationary Surface: Effects of Surface Angle Variation. *Experimental Thermal Fluid Science*, **2013**

9. R. Mariani, **M. K. Quinn**, K. Kontis. A Note on the Generation of a Compressible Vortex Rings Using Helium as Driver Gas. *Proceedings of the Institution of Mechanical Engineers, Part G, Journal of Aerospace Engineering.*, **2012**

10. K. Kontis, H. Zare-Behtash, N. Gongora-Orozco, L. Yang, **M. K. Quinn**, R Efrani, E Erdem. Development of Non-Intrusive Flow Diagnostic Capabilities at The Aero-Physics Laboratory. *Symposium on Applied Aerodynamics and Design of Aerospace Vehicles*, Bangalore, India, **2011**

Nomenclature

a	=	Speed of sound $[m/s]$
$\mathbf{a}$	=	Acceleration $[m/s^2]$
A	=	Generic coefficient
B	=	Generic coefficient
c	=	Circle of confusion $[m]$
$\bar{c}$	=	Molecular speed $[m/s]$
c_0	=	Speed of light $[m/s]$
c_p	=	Specific heat capacity $[J/KgK]$
C	=	Generic coefficient, Contrast
C_u	=	Cunningham compressibility correction
d	=	Diameter of particle
D	=	Diffusivity
e	=	Internal energy $[kJ/Kg]$
E	=	Illuminance $[m^2/J]$
E_{A_x}	=	Activation energy of x
f	=	Focal length $[m]$
$f_\#$	=	f number
g	=	Acceleration due to gravity $[m/s^2]$
h	=	Enthalpy $[kJ/Kg]$
H	=	Hyperfocal distance $[m]$
I	=	Luminescent intensity
K	=	Rate constant, Chisnell function
Kn	=	Knudsen number
k	=	Gladstone-Dale coefficient $[m^3/kg]$
L	=	Characteristic length $[m]$, Luminophore molecule
n	=	Refractive index
N_0	=	Avogadro's number 6.02×10^{23}
M	=	Mach number, Molecular mass
M_C	=	Convective Mach number
M_R	=	Relative Mach number
m	=	Magnification factor
P	=	Pressure $[Pa]$
Q	=	Quencher molecule
r	=	Velocity ratio
R	=	Specific gas constant $[J/kgK]$
Re	=	Reynolds number $[\rho VL/\mu]$ or $[VL/\nu]$
t	=	Time $[s]$
T	=	Temperature $[K]$

s	=	Density ratio, Distance to focal plane $[m]$
St	=	Strouhal number $[fL/V]$
Stk	=	Stokes number $\tau U/L$
U	=	Velocity in x direction $[m/s]$
u_p	=	Induced velocity $[m/s]$
V	=	Velocity in y direction $[m/s]$, Velocity $[m/s]$
W	=	Velocity in z direction $[m/s]$, Wave speed $[m/s]$

Symbols

α	=	Wave number, Image scale $[px/mm]$
δ	=	Generic angle
δ_w	=	Vorticity thickness
γ	=	Ratio of specific heat capacity
ϵ	=	Refraction angle
θ	=	Deflection angle
Θ	=	Adsorption fraction
μ	=	Molecular mass $[kg/mol]$, Dynamic viscosity $[kg/ms]$
ν	=	Kinematic viscosity $[m^2/s]$
ρ	=	Density $[kg/m^3]$
σ	=	Uncertainty component
τ	=	Time constant, Luminescent lifetime
ϕ	=	Quantum yield, Incidence angle to shock, velocity potential
χ	=	Triple point trajectory
χ_x	=	Molar fraction of x
Ψ	=	Total uncertainty
ω	=	Angular velocity $[1/s]$
$\Re$	=	Universal gas constant $[8.314J/Kmol]$

Subscripts

i	=	Inlet/incident quantity
ie	=	Experimental incident quantity
it	=	Theoretical incident quantity
$\mathbf{i}$	=	Unit vector
nr	=	Non-radiative process
p	=	Tracer particle
q	=	Quenching process
r	=	Radiative process
ref	=	Reference value
t	=	Theoretical Value
0	=	Stagnation value, Vacuum value
1	=	Driven gas value
2	=	Gas ahead of contact surface
3	=	Gas behind contact surface
4	=	Driver gas value

Superscript

$*$	=	Excited state
$\bar{}$	=	Vector quantity
	=	Dimensionless coordinate

Abstract

The motion of shock waves is important in many fields of engineering and increasingly so with medical applications and applications to inertial confinement fusion technologies. The flow structures that moving shock waves create when they encounter a change in area is complex and can be difficult to understand. Previous researchers have carried out experimental studies and many numerical studies looking at this problem in more detail. There has been a discrepancy between numerical and experimental work which had remained unanswered. One of the aims of this project is to try and resolve the discrepancy between numerical and experimental work and try to investigate what experimental techniques are suitable for work of this type and the exact way in which they should be applied. Most previous work has focused on sharp changes in geometry which induce immediate flow separation. In this project rounded corners will also be investigated and the complex flow features will be analyzed.

Two geometries, namely a sharp 172° knife-edge and a 2.8 mm radius rounded corner will be investigated at three experimental pressure ratios of 4, 8 and 12 using air as the driver gas. This yields experimental shock Mach numbers of 1.28, 1.46 and 1.55. High-speed schlieren and shadowgraph photography with varying levels of sensitivity were used to qualitatively investigate the wave structures. Particle image velocimetry (PIV), pressure-sensitive paint (PSP) and traditional pressure transducers were used to quantify the flow field.

Numerical simulations were performed using the commercial package Fluent to investigate the effect of numerical schemes on the flow field produced and for comparison with the experimental results. The sharp geometry was simulated successfully using an inviscid simulation while the rounded geometry required the addition of laminar viscosity. Reynolds number effects will be only sparsely referred to in this project as the flows under investigation show largely inviscid characteristics. As the flow is developing in time rather than in space, quotation of a distance-based Reynolds number is not entirely appropriate; however, Reynolds number based on the same spatial location but varying in time will be mentioned.

The density-based diagnostics in this project were designed to have a depth of field appropriate to the test under consideration. This approach has been used relatively few times despite its easy setup and significant impact on the results. This project contains the first quantative use of PIV and PSP to shock wave diffraction. Previous studies have almost exclusively used density-based diagnostics which, although give the best impression of the flow field, do not allow for complete analysis and explanation of all of the flow features present. PIV measurements showed a maximum uncertainty of 5% while the PSP measurements showed an uncertainty of approximately 10%.

The shock wave diffraction process, vortex formation, shear layer structure, secondary and even tertiary expansions and the shock vortex interaction were investigate. The experimental results have shown that using one experimental technique in isolation can give misleading results. Only by using a combination of experimental techniques can we achieve a complete understanding of the flow field and draw conclusions on the validity of the numerical results.

Expanding the range of the experimental techniques currently in use is vital for experimental aerodynamic testing to remain relevant in an industry increasingly dominated by numerical research. To this end, significant research work has been carried out on extending the range of the PSP technique to allow for the capture of shock wave diffraction, one of the fastest transient fluid processes, and for applications to low-speed flow (< 20 ms^{-1}).

Declaration

No portion of the work referred to in this report has been submitted in support of an application for another degree or qualification of this or any other university or other institute of learning.

Copyright

Acknowledgements

I would like to thank my Mum and Dad for believing in me and not telling me to leave 'school' and get a job. Thanks to Nikki for giving me a reason to get up in the morning and smile. I would like to thank my good friends Dr Mark Mawson, Dr Nicholas *The Yorkshire Pelé* Johnson and all my other friends and fellow Whitby Wanderers in Manchester for keeping me going during my long periods of injury. A special thanks goes to 'The Gaffer' for allowing me to take time out of training to complete my PhD. Many thanks to the 'brain trust' for distracting me during the writing of this thesis, especially Dr David Roberts.

Thanks to Professor Kontis for giving me this opportunity. Many thanks to the MACE technicians, especially Dave Golding, Dr Hugh Frost and Lee Paul for helping me to become an engineer rather than a student. Finally I'd like to thank Dr Craig Hale, Dr Erinc Erdem, Dr Leichao Yang, Dr Hossein Zare-Behtash, and most of all Dr Nalleli Gongora-Orozco and Dr Raffaello Mariani for teaching me everything I know.

Chapter 1

Introduction

It is a miracle that curiosity survives formal education - Albert Einstein

1.1 Shock Waves

High-speed fluid dynamics are dominated by the effects of compressibility i.e. change in density. The effects of compressibility were strong enough to cause aileron reversal on the Supermarine Spitfire, causing pilots to lose control [5]. More modern aircraft often operate in the transonic regime and regularly encounter shock waves. The interaction of shockwaves influence the design of high-speed aircraft including space vehicles, projectiles, and the use of explosives.

The movement of shock waves around objects is crucial in understanding of unsteady processes such as weapons discharge and suppressors. Regular firearms are operated by detonating a small explosive charge which propels a small projectile at high speed. The explosive wave generated by the propellant is the largest source of noise from firearms. Silencers or suppressors, reduce the pressure behind the blast wave by allowing it to expand in the suppressor chamber. As the expanding shock wave is traveling down the barrel of the weapon, it is constrained to expand only in the direction of the barrel. The suppressor chamber is significantly larger than the barrel of the weapon allowing the gas to expand and therefore reducing the strength of the pressure wave that is ejected to the atmosphere. The design of suppressors frequently includes the use of baffles and vanes to slow the shock wave down.

The use of pulse-detonation engines has gathered significant interest over recent years and continues to be an active area of research. The potential increase in thermal efficiency over conventional turbofan or turbojet engines is well known but has proved difficult to exploit. The cycle performance and flow phenomena have been shown by Ma et al. [6] for a range of flight envelopes. The repetitive discharge of a pulse-detonation engine is very difficult to model using a conventional shock tube. Despite this, working with single-shot shock tubes allows us to investigate some of the fundamental flow phenomena involved and show the applicability various experimental techniques.

The book by Professor I. I. Glass [7] details mans endeavors with shock waves and how we are affected by them. Unfortunately almost all of the examples given in this book are destructive. The destructive power of shock waves has been utilized for hundreds of years, however over the past 20 years mankind has found more

constructive uses for them. Shock waves are commonly used to treat kidney stones [8] and are beginning to be used to treat sporting injuries and tendinitis [9].

The supply of energy is of the utmost concern to engineers and society in general, especially in times of economic hardship. One of the most tantalizing forms of energy that has, so far, evaded mankind is nuclear fusion. Fusion reactions are what power the sun and have led engineers and scientists to build several attempts to harness the same power source here on Earth. There two main methods of containing a fusion reaction; inertial confinement and magnetic confinement. One of the, as yet unresolved, issues with inertial confinement fusion (ICF) is the presence of hydrodynamic instabilities present when shock waves compress the fuel pellet. Some of these instabilities can be explored using conventional shock tubes [10].

1.2 Experiments versus CFD

Wind tunnels are expensive to run, equipment is expensive to buy and models are expensive to build. It is well known that experimental aerodynamics is an expensive business. After (often prohibitively) high initial costs, the running costs (depending on the wind tunnel) are often quite manageable. Experiments are expensive and often inflexible, but if conducted correctly can give fantastic results. Computational fluid dynamics (CFD) is beginning to take over from experimental aerodynamics in research institutions and industry alike due to its low initial cost and high flexibility.

As our knowledge of fluid dynamic problems evolves over time we understand more and more about *basic* large-scale phenomena. In order to advance our knowledge we need to look at smaller, finer phenomena which are often extremely difficult to capture. This lends itself to numerical simulations as grid sizes and time steps are at the users discretion whereas camera resolution and frame rate are finite values not under the control of the engineer. However, numerical results alone are not enough to give us a complete picture as there is no such thing as a perfect CFD code (not yet at least).

Although CFD has its place in examining simple phenomena, its results when applied to complex geometries are still limited. A recent proof that CFD cannot be used exclusively for complex designs can be seen in Formula One. In 2010 a new team entered the Formula One arena, the Virgin Racing team. Lead by Nick Wirth, a well-renowned engineer, the team designed their first car, the VR-01, using a only CFD [11]. After a predictably difficult rookie season in F-1, the team designed their second car, the VR-02, in the same fashion [12]. The performance of this car did not (ironically for CFD) improve on the previous iteration and lead to a running joke that CFD stood for *can't find downforce* [13]. It was in the middle of the 2011 F-1 season that Virgin racing abandoned their CFD only design ethos in favor of a more conventional approach [14].

Great advances have been made in CFD since the original panel methods up to modern large-eddy simulations and this trend will surely continue as long as Moore's law holds. However, until the computational power available allows for an unsteady, molecular-scale Lagragian simulation of fluid flow, CFD will never be completely reliable. To this end, it is the aim of the author to investigate unsteady, small-scale, high-speed phenomena using the latest experimental equipment in order to show that experimental studies are as important today as they ever were and how CFD

results can be misleading without them.

1.3 Aims of the Project

The main aims of this project are as follows:

1. To investigate shock wave shock wave diffraction around sharp and round geometries using modern diagnostic techniques (schlieren, shadowgraph, particle image velocimetry and pressure-sensitive paint) and compare with simulations using commercial numerical codes (Fluent)

2. To show the applicability of these experimental techniques and highlight the differences in results between the different techniques

3. To apply pressure-sensitive paint to measure transient shock wave phenomena at very high speed

4. To prove the relevance of experiments in todays computationally dominated engineering society

5. To attempt to answer the question of the existence of instabilities on shock generated shear layers and to explain why this has not been solved in the past

1.4 Thesis Structure

This thesis contains the following sections:

- Chapter 2 - Literature Review
- Chapter 3 - Experimental Techniques Review
- Chapter 4 - Apparatus
- Chapter 5 - Results
  - Density-Based Results
  - Particle-Based Results
  - Pressure Measurements
  - Pressure-Sensitive Paint Results
- Chapter 6 - Conclusions
- Chapter 7 - Future Work

Chapter 2

Literature Review

I would rather have my ignorance than another mans knowledge, because I have so much more of it. - Mark Twain

This chapter contains a review of literature relevant to flow physics involved in this project. A comprehensive discussion of the experimental techniques used will be given in Chapter 3.

2.1 Shock Waves

In order to address the nature of shock waves, it is helpful to initially consider a sound wave. Sound waves are molecular collisions between gas particles that transmit disturbances. The speed of these disturbances (Equation 2.1) can be derived by applying the perfect gas equations to a weak adiabatic compression and is closely linked to the molecular (kinetic) speed (see Equation 2.2).

$$a = \sqrt{\gamma RT} \tag{2.1}$$

$$\bar{c} = \sqrt{\frac{8RT}{\pi M}} \tag{2.2}$$

Any disturbance which travels faster than the speed of sound acts differently to a normal pressure wave and no longer exhibits continuous properties on either side of the wavefront. These are known as shock waves and they act as a discontinuous jump in fluid properties. Shock waves are almost always treated as adiabatic unless there is some form of external heat transfer to the system.

Shock waves can be considered in different frames of reference depending on the desired application. If the shock is stationary then the choice of frame of reference is largely academic. However, if the shock is propagating, then the choice of frame of reference allows the analysis to be greatly simplified. The frame of reference can either be attached to the shock, as shown in Fig.2.1a, or attached to the lab, as per Fig.2.1b, where U is the velocity, U_p is the induced velocity and W is the shock velocity. If the frame of reference is attached to the shock, then the system can often be considered pseudo-stationary; this will become more important as we progress to the study of different shock interactions.

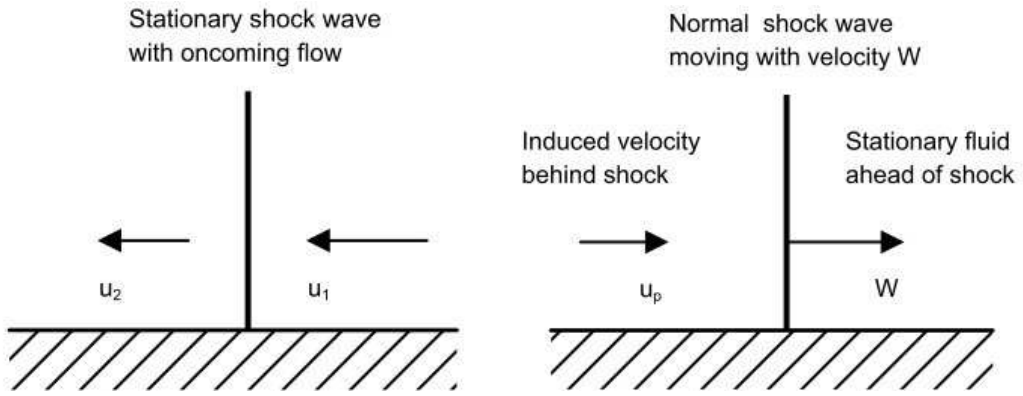

(a) Frame of reference attached to the shock (b) Frame of reference attached to the lab

Figure 2.1: Schematic of shockwave frame of reference

2.2 Shock Tube

The shock tube is a simple yet very cost-effective device for delivering high-speed, high-temperature flow. It is comprised of a *driver* and a *driven* section. The driver section contains high-pressure gas and is separated from the driven section by means of a non-permeable diaphragm. The type of diaphragm used here is acetate, although at extremely high pressures the thickness of acetylene required to separate the two gases becomes very significant and can interfere with the flow physics and cause deviations from simple theory. This problem can be overcome by using a multiple-stage shock tube, where the diaphragms do not have to withstand extremely large pressure differences.

The driven section can either be a tube of open air (i.e. open at one end and atmospheric pressure) or it can be closed off and evacuated, allowing for a greater pressure differential across the diaphragm. Once the diaphragm has been ruptured, compression waves begin to propagate into the driven section. The compression wave causes an increase in temperature and pressure, meaning that the compression wave immediately behind it travels at a slightly higher velocity. These compression waves eventually coalesce into a discontinuous shockwave. In contrast to this, an expansion wave propagates into the driver section. As the expansion wave lowers the temperature and the pressure in the gas, each expansion wave propagates slower than the one preceeding it, causing expansion fans to spread rather than coalesce.

Shock tubes can have either one or two diaphragms. Single-diaphragm shock tubes are commonplace and can be ruptured either by mechanical means (a plunger), electrical means (vaporising the diaphragm) or by using a combustible mixture in the driver section and igniting it. The use of two diaphragms can create stronger shockwaves by causing reflection of the incident shockwaves, creating an effective driver section of higher pressure and temperature. There are various methods of triggering multiple-diaphragm shock tubes. They are commonly triggered using mechanical means, as mentioned previously. Conversely, they can be triggered using a stepped pressure differential and evacuating the intermediate chamber. The reader is directed to Wright [15] for more information on multiple-diaphragm shock tubes.

2.2.1 Basic Theory

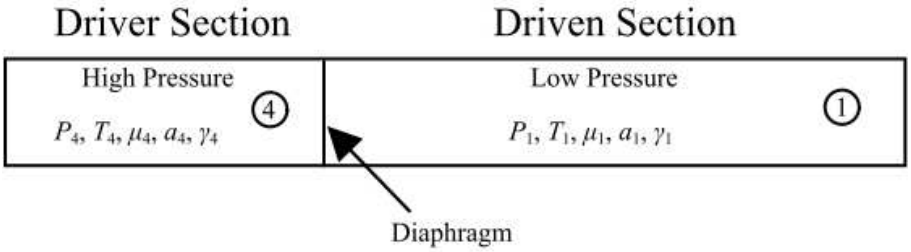

Figure 2.2: Basic layout of a shock tube

Shock tubes can be modelled using one-dimensional flow theory with a great degree of success. As the dimensions of shock tubes differ, viscous effects can be more or less important. The larger the shock tube diameter, the more negligible viscous effects are. However, even in the 1-inch diameter shock tubes present at the University of Manchester, viscous effects are almost insignificant. Deviations from this one-dimensional theory will be discussed in Section 2.2.3.

Fig.2.2 shows a simple diagram of a shock tube prior to rupturing of the diaphragm. By convention the driver section is usually referred to as *region 4* and the driven section is referred to as *region 1*. The two sections may be filled with the same or different gases, which will alter the values of γ and μ.

Once the diaphragm has been ruptured, the picture becomes more complicated as waves begin to travel into the two sections (see Fig.2.3).

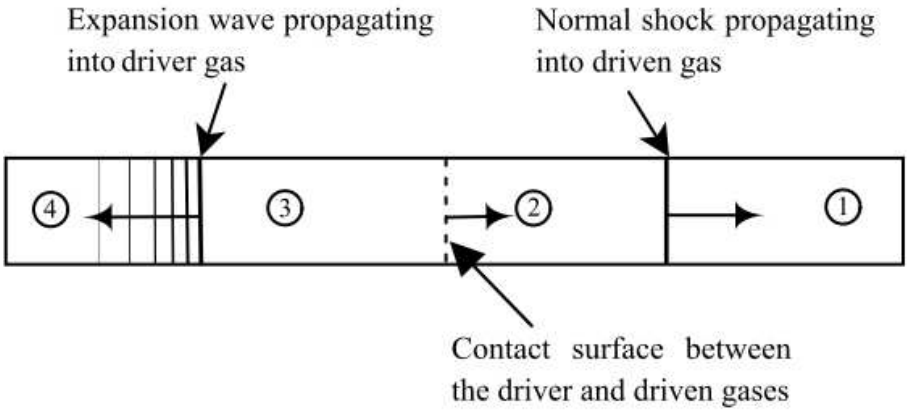

Figure 2.3: Shock tube flow after the diaphragm is ruptured

The analysis of a moving shock wave is more straightforwards than the analysis of an expansion fan and as such will be discussed first. In order to treat the one-dimensional movement of a shock wave analytically, we must state the continuity, momentum and energy equations:

$$\rho_1 u_1 = \rho_2 u_2 \tag{2.3}$$

$$P_1 + \rho_1 u_1^2 = P_2 + \rho_2 u_2^2 \tag{2.4}$$

$$h_1 + \frac{u_1^2}{2} = h_2 + \frac{u_2^2}{2} \tag{2.5}$$

where the subscripts 1 and 2 represent the flow ahead and behind the shock wave respectively. These equations can be stated in the lab frame of reference rather than the shock frame of reference (see Fig.2.1) to give:

$$\rho_1 W = \rho_2 (W - u_p) \tag{2.6}$$

$$P_1 + \rho_1 W^2 = P_2 + \rho_2 (W - u_p)^2 \tag{2.7}$$

$$h_1 + \frac{W^2}{2} = h_2 + \frac{(W - u_p)^2}{2} \tag{2.8}$$

We now aim to eliminate any wave or particle velocities from the above equations. Equation 2.6 can be substituted into 2.7 to give:

$$W^2 = \frac{P_2 - P_1}{\rho_2 - \rho_1} \frac{\rho_2}{\rho_1} \tag{2.9}$$

If Eq.2.6 is rearranged for W ,it can be substituted into 2.9 to give:

$$(W - u_p)^2 = \frac{P_2 - P_1}{\rho_2 - \rho_1} \frac{\rho_1}{\rho_2} \tag{2.10}$$

We can now substitute Eqs. 2.9 & 2.10 into the energy equation (Eq.2.8). If we then include the definition of enthalpy ($h = e + P/\rho$), we arrive at:

$$e_1 + \frac{P_1}{\rho_1} + \frac{1}{2}\left[\frac{P_2 - P_1}{\rho_2 - \rho_1}\frac{\rho_2}{\rho_1}\right] = e_2 + \frac{P_2}{\rho_2} + \frac{1}{2}\left[\frac{P_2 - P_1}{\rho_2 - \rho_1}\frac{\rho_1}{\rho_2}\right] \tag{2.11}$$

which reduces to the well-known Rankine-Hugoniot equation:

$$e_2 - e_1 = \frac{P_1 + P_2}{2}\left(\frac{1}{\rho_1 - \rho_2}\right) \tag{2.12}$$

If we assume that we have a perfect gas (this is a valid assumption for the shock waves under investigation here), we can use $e = c_v T$ and $\rho = P/RT$ to state Eq.2.12 as the ratio of thermodynamic variables across the moving shock wave:

$$\frac{T_2}{T_1} = \frac{P_2}{P_1}\left[\frac{\frac{\gamma_1+1}{\gamma_1-1} + \frac{P_2}{P_1}}{1 + \frac{\gamma_1+1}{\gamma_1-1}\left(\frac{P_2}{P_1}\right)}\right] \tag{2.13}$$

$$\frac{\rho_2}{\rho_1} = \left[\frac{1 + \frac{\gamma_1+1}{\gamma_1-1}\left(\frac{P_2}{P_1}\right)}{\frac{\gamma_1+1}{\gamma_1-1} + \frac{P_2}{P_1}}\right] \tag{2.14}$$

If we define the Mach number of the moving shock as the ratio of the wave speed, W, to the sound speed ahead of the wave, a_1, we can use the normal shock relations to give us the Mach number of the moving shock wave as a function of the pressure ratio across it:

$$M_i = \sqrt{\frac{\gamma_1 + 1}{2\gamma_1}\left(\frac{P_2}{P_1} - 1\right) + 1} \tag{2.15}$$

Multiplying by the sound speed, we get the wave speed:

$$W = a_1\sqrt{\frac{\gamma_1 + 1}{2\gamma_1}\left(\frac{P_2}{P_1} - 1\right) + 1} \tag{2.16}$$

If we return to Eq.2.6 and solve for W, we can introduce Eqs. 2.14 & 2.16. With some rather tedious simplification we arrive at a relationship for the induced particle velocity:

$$u_p = \frac{a_1}{\gamma_1}\left(\frac{P_2}{P_1} - 1\right)\sqrt{\left(\frac{\frac{2\gamma_1}{\gamma_1+1}}{\frac{P_2}{P_1} + \frac{\gamma_1+1}{\gamma_1-1}}\right)} \tag{2.17}$$

The above equations have allowed us to look at the flow induced by a moving shock wave created after the burst of a diaphragm in a shock tube. In order to understand the flow completely, we must now look at the expansion wave travelling in the opposite direction. To do this, we need to consider the movement of a finite wave as set out by Anderson [16]. Expansion waves tend to spread out rather than coalesce as each individual finite wave lowers the temperature meaning that the sonic velocity is lower for the subsequent wave. Using the method of characteristics, we can reduce the partial differential equations of momentum and continuity to an ordinary differential equation (the compatibility equation) which we can solve along a specific curve (characteristic line). We have two characteristic lines and compatibility equations: one relating to left-moving waves and one relating to right-moving waves. If we integrate the compatibility equation along a characteristic line, we acquire functions known as Riemann invariants. Riemann invariants are constant along a given line (in our case, the characteristic line) and are given in Eqs. 2.18, 2.19.

$$J_+ = u + \frac{2a}{\gamma - 1} = \text{constant} \qquad \text{along a } C_+\text{characteristic line} \tag{2.18}$$

$$J_- = u - \frac{2a}{\gamma - 1} = \text{constant} \qquad \text{along a } C_-\text{characteristic line} \tag{2.19}$$

If we assume that this problem is completely one-dimensional and that the wave is propagating into a uniform region, then we can assume that one family of characteristics is made up of straight lines. This is known as a simple wave and is applicable for this problem before the expansion wave reaches the end of the shock tube. The J_+ Riemann invariant is constant throughout a centred expansion wave, which leaves us with:

$$u + \frac{2a}{\gamma - 1} = \text{constant through the wave} \tag{2.20}$$

In region 4 of the shock tube the flow is initially at rest, meaning $u_4 = 0$. We can now evaluate Equation 2.20 in region 4 and at a generic location inside the expansion wave to give us:

$$\frac{a}{a_4} = 1 - \frac{\gamma - 1}{2}\frac{u}{u_4} \tag{2.21}$$

We can now use the sonic speed definition to introduce temperature and then isentropic flow relations to introduce the other thermodynamic variables:

$$\frac{T}{T_4} = \left[1 - \frac{\gamma - 1}{2}\frac{u}{u_4}\right]^2 \tag{2.22}$$

$$\frac{P}{P_4} = \left[1 - \frac{\gamma - 1}{2}\frac{u}{u_4}\right]^{\frac{2\gamma}{\gamma-1}} \tag{2.23}$$

$$\frac{\rho}{\rho_4} = \left[1 - \frac{\gamma - 1}{2}\frac{u}{u_4}\right]^{\frac{2}{\gamma-1}} \tag{2.24}$$

We can now apply Eq.2.23 across an expansion fan, remembering that $P_3 = P_2$ and $u_3 = u_2 = u_p$, to give us:

$$\frac{P_2}{P_4} = \left[1 - \frac{\gamma - 1}{2}\frac{u_p}{u_4}\right]^{\frac{2\gamma}{\gamma-1}} \tag{2.25}$$

which can be solved for u_p and equated to Eq.2.17:

$$\frac{a_1}{\gamma_1}\left(\frac{P_2}{P_1} - 1\right)\left(\frac{\frac{2\gamma_1}{\gamma_1+1}}{\frac{P_2}{P_1} + \frac{\gamma_1+1}{\gamma_1-1}}\right)^{\frac{1}{2}} = \frac{2a_4}{\gamma_4 - 1}\left[1 - \left(\frac{P_2}{P_4}\right)^{\frac{\gamma_4-1}{2\gamma_4}}\right] \tag{2.26}$$

After some further tedious algebraic manipulation, this can be rearranged to give:

$$\frac{P_4}{P_1} = \frac{P_2}{P_1}\left\{1 - \frac{(\gamma_4 - 1)(\frac{a_1}{a_4})(\frac{P_2}{P_1})}{2\gamma_1\sqrt{2\gamma_1 + (\gamma_1 + 1)\left(\frac{P_2}{P_1} - 1\right)}}\right\}^{\frac{-2\gamma_4}{\gamma_4-1}} \tag{2.27}$$

Once the diaphragm pressure ratio, P_4/P_1, has been prescribed and the incident shock strength has been calculated from Equation 2.27, the remaining flow parameters can be calculated using equations 2.13, 2.14, 2.16 and 2.17. Using the simple relationship:

$$\frac{P_3}{P_4} = \left(\frac{P_3}{P_1}\right)\left(\frac{P_1}{P_4}\right) = \left(\frac{P_2}{P_1}\right)\left(\frac{P_1}{P_4}\right)$$

allows us to calculate the strength of the expansion wave travelling into the driver gas. Now we have enough information to calculate the flow properties anywhere in the domain.

Despite the removal of the diaphragm, the interface between the driven and driver gas is preserved. This surface is called the contact surface, for obvious reasons. The pressures and velocities either side of this surface are equal. This greatly simplifies the analysis of the shock tube.

This analysis facilitates the construction of a so-called *x-t diagram*. This diagram shows the wave patterns inside a shock tube and also shows the complex regions

of interaction. It is extremely useful for predicting the location of waves a given time after the diaphragm rupture. Diagrams relevant to this work will be shown in Section 4.1.

As is evident from Eq.2.27, the shock strength is dependent on the properties of the gases in the driven and driver sections. In order to increase the shock strength and therefore the velocity of the shockwave and the induced flow behind it, a lighter gas must be used in the driver section. Lighter gases have a larger specific gas constant and therefore a faster speed of sound. A brief illustration of this can be found in Fig.2.4. This will not be attempted in this research however, as density effects can play an important role in the development of shear layers.

2.2.2 Applications

Shock tubes can be used to examine a wide variety of flows and to investigate many different areas of the flow physics; the list given here is by no means exhaustive. The normal shock wave that travels in a shock tube can be increased in strength by increasing the initial diaphragm pressure ratio. If this pressure ratio is high enough then the shockwave will become so strong that the temperature rise across it can be enough to cause dissociation in the gases. This dissociation results in ionised flow, allowing for the study of real gas effects; a good example is given by Lin [17].

Shock tubes are commonly used to investigate compressible vortex rings, as they are an almost ideal way to generate them. This type of testing has been performed extensively at the University of Manchester with a great deal of success [18], [19]. Shock tubes have also been used to characterise the response time of pressure-sensitive paint (PSP), as they give a predictable and discrete pressure jump.

Shock tubes can be modified by attaching a convergent divergent nozzle to the driven end. This variant is known as a shock tunnel and can generate extremely high-speed flows. The initial shock wave generated by the diaphragm rupture is reflected from the throat of the nozzle, causing a second compression and almost decelerating the flow to a stand still. This highly compressed region now acts as a reservoir for the nozzle.

2.2.3 Deviations from Theory

The one-dimensional theory presented in Section 2.2.1 is adequate, providing that the shock strength is not too great and that the length of the shock tube is not too big. As the pressure ratio and the length (especially of the driven section) increase, viscous effects come to play a more important role in the flow physics. As the shock strength increases, the boundary layer inside the shock tube thickens. This causes blockage of the flow and can cause pressure gradients in *regions 2 & 3*, whereas the theory assumes that the flow in this region is isobaric. As the boundary layer thickens, it reduces the effective area that is open to the flow. This blockage reduces the mass flow rate which in turn slows the shock and the induced velocity. This process is commonly called attenuation.

Glass [20] showed that strong shock waves experience two major deviations from the theoretical values that weaker counterparts do not.[1] Glass called these two

[1] Glass classified strong shocks as those with $P_2/P_1 > 3$

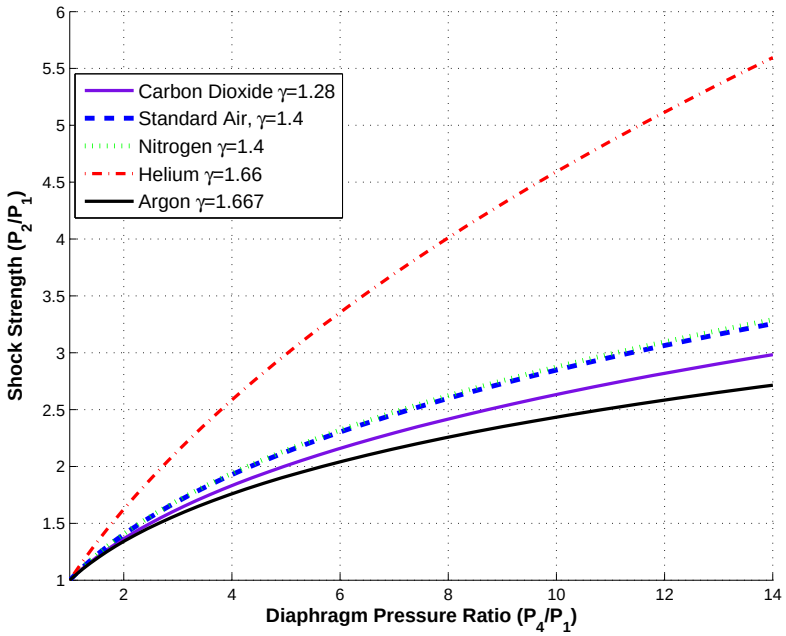

(a) Shock strength vs. pressure ratio

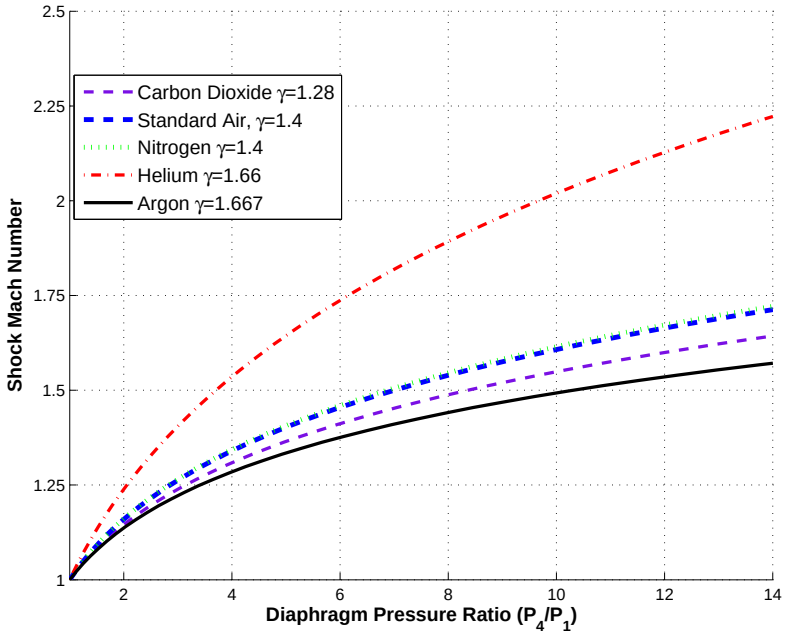

(b) Shock Mach number vs. pressure ratio

Figure 2.4: Dependency of flow on the diaphragm pressure ratio

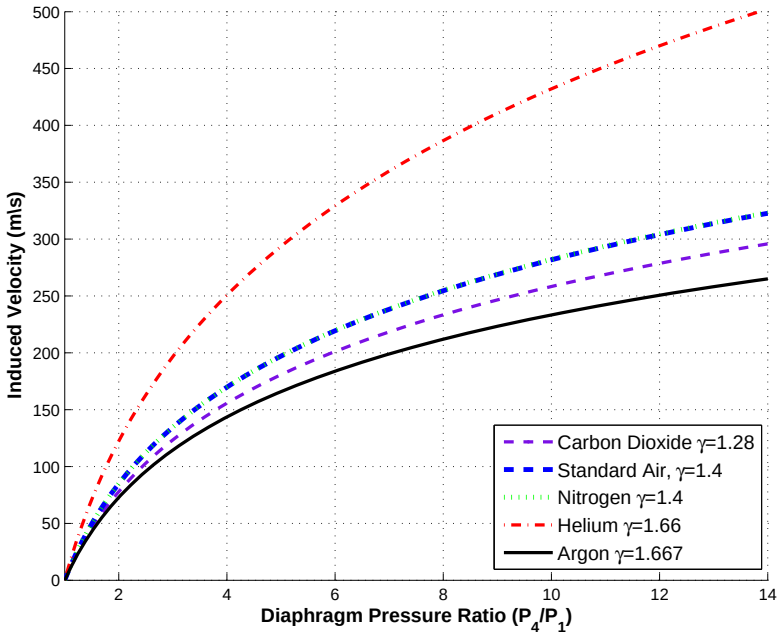

(c) Induced velocity vs. pressure ratio

Figure 2.4: Dependency of flow on the diaphragm pressure ratio

phenomena *formation decrement* and *distance attenuation*.

Formation decrement is the deficit of wave velocity from its maximum value to its theoretical value. Distance attenuation is the tendency for strong shocks to slow down as they pass further down the tube. From the results presented by Glass, it is clear that formation decrement is mainly significant for pressure ratios higher than 20. If the pressure ratios are significantly higher than 50, the assumption of the shock to be adiabatic and travelling through a calirocally perfect gas becomes questionable. In this case, real gas effects may need to be taken into account, as the ratio of specific heats of the gasses is not longer constant.

When the diaphragm of a shock tube is ruptured, it is assumed that the compression waves are instantly planar and normal to the axis of the shock tube. However, prior to the rupture of the diaphragm there is a large pressure gradient across it and it is stressed almost to breaking point. This leads to the conclusion that the diaphragm is curved when it is ruptured, giving rise to curved compression waves. These curved compression waves quickly coalesce into a normal moving shock; however, the effects of initial curvature are not modelled at all by the one-dimensional theory. Surplus to curvature effects, the diaphragm rupture process can have several other impacts on the resulting flow field. When the diaphragm is ruptured, pieces often break off into the flow. These pieces absorb energy from the flow and can attenuate the shock strength. Therefore, in order to reduce the impact of this source of error, the diaphragm material must be as light as possible. This reduces the energy needed to accelerate the fragments of the shattered diaphragm to the speed of the induced flow.

2.3 Unsteady Shock Wave Motion

2.3.1 Shock Wave Reflection

When shock waves impinge on a solid boundary they are reflected back from it. There are many types of shock wave reflection; the type generated will depend on the flow conditions and the surface inclination. Reflections can broadly be broken down into two different categories: *regular reflection* (RR) and *irregular reflection* (IR). There are many different types of irregular reflection. Fig.2.5 shows the tree of possible reflections and their abbreviations. This diagram by Prof. G. Ben Dor [21] has received one update since its first publication [22] and it would not be unexpected if further revisions and additions were to appear in the future.

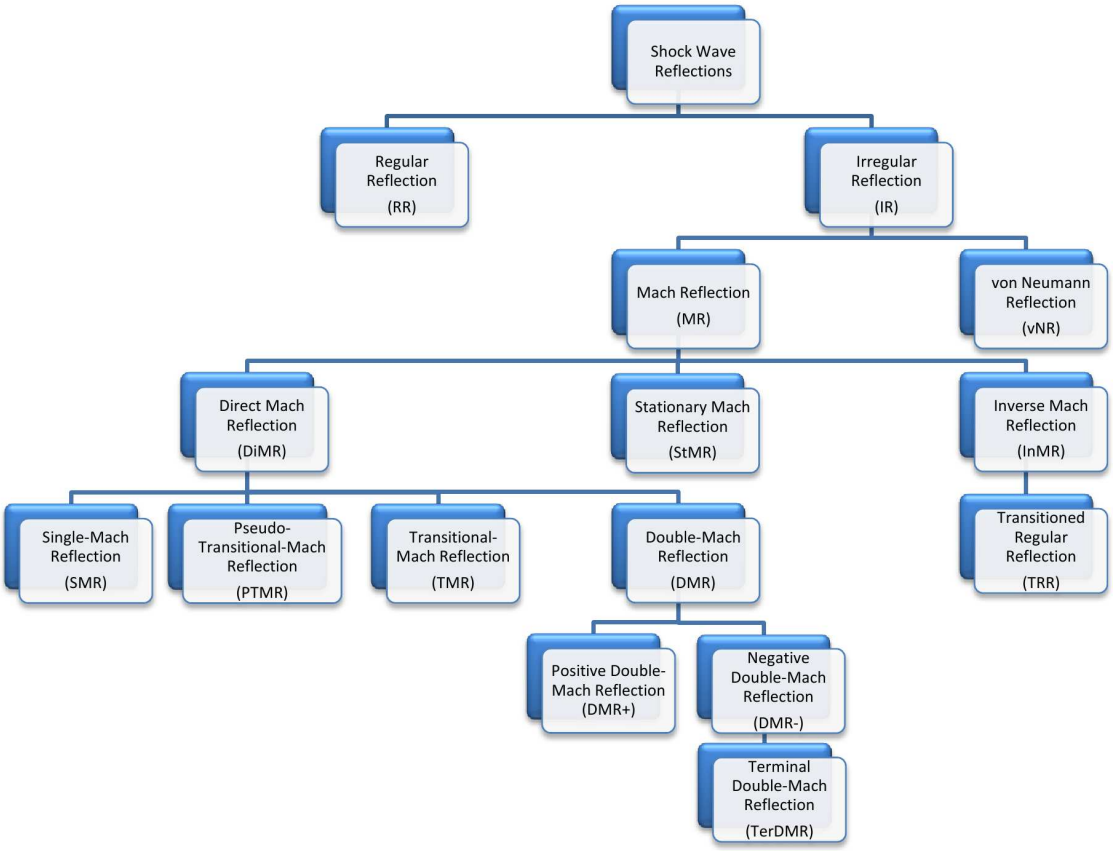

Figure 2.5: Different types of shock wave reflection

2.3.1.1 Regular Reflection

Regular reflections are the simplest to analyse as they only contain two waves: an incident and a reflected one. Fig.2.6a contains a schematic of the motion of a regular reflection in a moving frame of reference. Fig.2.6b shows the analytical treatment of such a system using inviscid two-shock theory. The region (0) corresponds to the flow ahead of the incident shock **I**, (1) corresponds to the region immediately after the incident shock and region (2) is after the reflected shock **R**. The point **CP** is the point of contact with the surface.

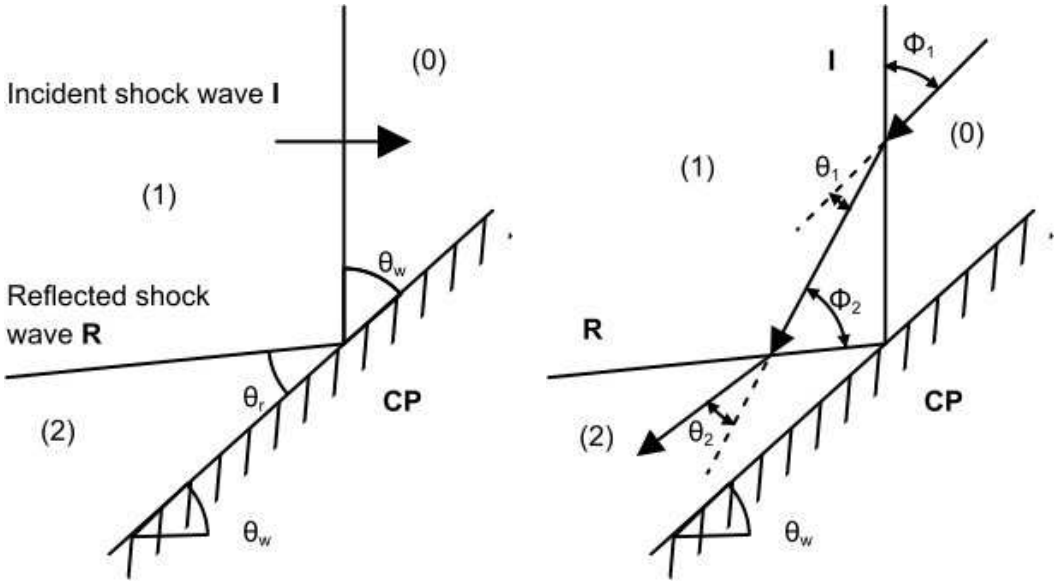

(a) Regular shock wave reflection (b) Two-shock theory

Figure 2.6: Analysis of regular reflection: (a) lab frame of reference and (b) showing two-shock theory

In the moving frame of reference the flow in region (0) is inclined to the incident shock at an angle Φ_1. Once the flow has passed through this shock it is deflected towards the wall by an angle of θ_1. The flow then encounters the reflected shock with an angle of incidence of Φ_2 and is now deflected by an angle θ_2, causing it to fall parallel to the wall. When the reflected shock **R** cannot deflect the flow enough to make it parallel to the wall, transition to an irregular reflection occurs.

Shock polars are a graphical representation of the possibilities of shock wave reflections and can be useful when analysing reflection systems. Shock polars are a representation of flow deflection against pressure and show both weak and strong shock solutions. Fig.2.7 is a typical pressure-deflection shock polar for a regular reflection, as shown in Fig.2.6. This example has a wedge angle of $\theta_w = 9°$ and a Mach number ahead of the incident shock $M_0 = 2$. In this example, point a on the incident shock polar corresponds to a Mach wave (i.e. a wave with infinitesimal strength). As we have regular reflection in this example we will have a deflection angle that is equal to the wedge angle. At this point we can read off the shock strength from the y-axis. Moving then to the reflected shock polar, we reach the point where there is no net flow deflection (the point where the flow returns to being parallel with the wall). Clearly there are two solutions along the reflected polar which correspond to zero net deflection: the weak and the strong solution. The weak solution (2^w) corresponds to a supersonic flow in region 2. The strong solution (2^s) corresponds to a sub-sonic flow in region 2. Although both solutions are theoretically possible, it is an experimental fact that the weak shock solution almost always occurs [21]. Point s represents the deflection angle which will leave the flow in region 2 exactly sonic. Point m represents the point of maximum deflection that can be achieved by an oblique shock. From this it is clear to see that between points a and s the flow is supersonic, whereas between points s and b the flow is subsonic.[2]

[2]It should be noted that the positions of m and s in Fig.2.7 are only for illustration. They are

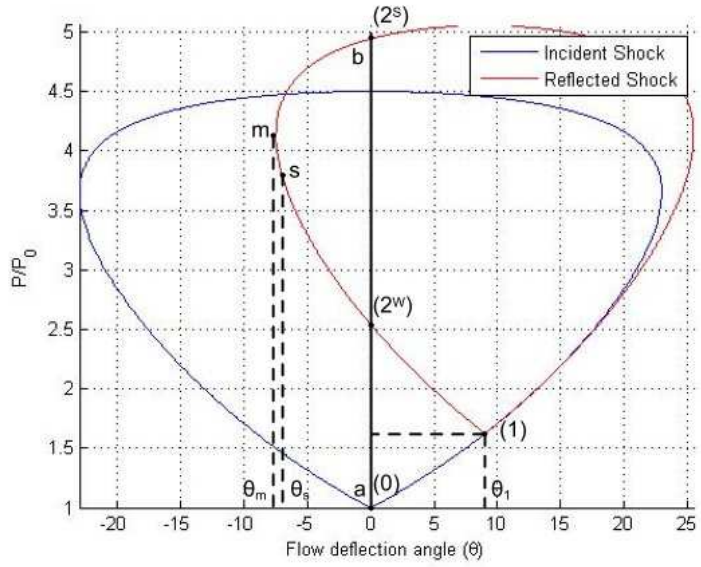

Figure 2.7: Shock polar with $\theta_w = 9°$ and $M_0 = 2$

2.3.1.2 Irregular Reflection

Irregular reflections of shock waves are more complex than regular reflections as there are many different specific types, as shown in Fig.2.5. The most common irregular reflection is the Single-Mach Reflection (SMR). Mach reflections are based around a three-shock theory, as they contain both the incident and reflected shocks (see Fig.2.8) and a third shock, known as the Mach stem (**M**). These three shocks meet at the triple point (**TP**). A contact discontinuity known as the slipstream (**S**) arises, as the gas in region 3 has passed through a different shock wave system from that in region 2 and therefore has a different velocity and the same pressure.

Irregular reflections form because the reflected shock wave cannot return the flow to its original direction. This can be seen in Fig.2.9, as the reflected shock polar does not touch the y-axis. Fig.2.9 is comparable to Fig.2.7 as the flow Mach numbers are similar; however, the wedge angle is significantly different.

Aside from the common Mach reflection, there are other forms of irregular reflection such as the von Neumann reflection which has localised supersonic flow behind the incident shock wave. This leads to an unusual wave configuration; however, it is extremely difficult to capture experimentally due to the very small length scales involved close to the triple point [23].

2.4 Shock Wave Diffraction

An overview of unsteady shock wave interactions is given in the excellent review by Bazhenova, Gvozdeva and Nettleton [24]. This review covers shock wave diffraction, types of reflection and the boundaries between them. This section will mainly focus on the wave profiles created during planar shock wave diffraction and the perturbed

usually found within a fraction of a degree of each other and as such are often treated as a single point.

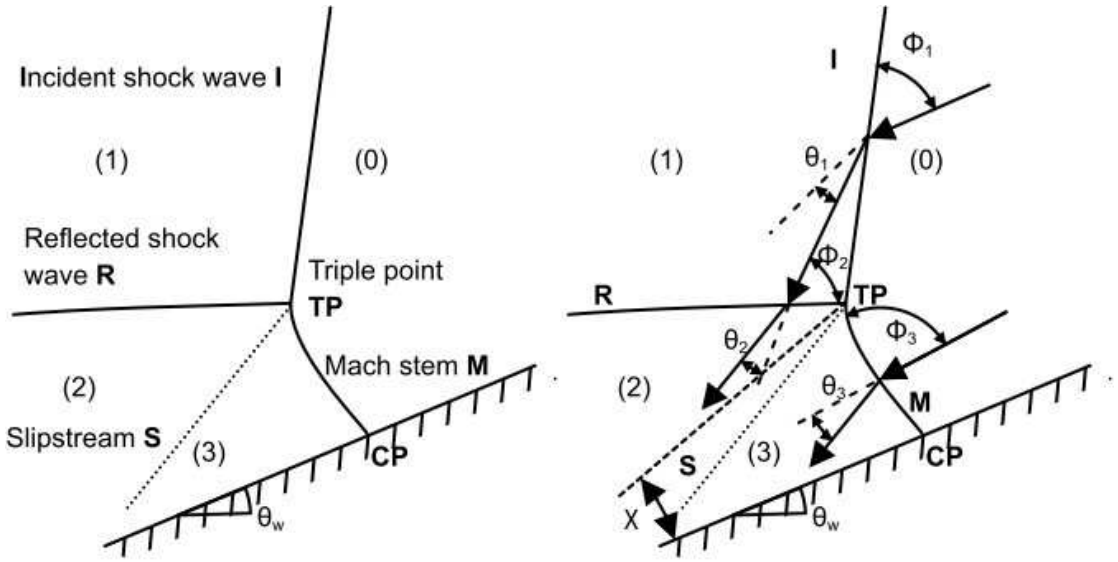

(a) Direct Mach wave reflection (b) Three-shock theory

Figure 2.8: Analysis of a pseudo-steady Mach reflection

region behind the shock wave. Experimental and analytical studies will be discussed here, with numerical simulations discussed in Section 2.7.

Diffraction of planar shock waves has been treated analytically by Whitham [25],[26] in the method now famously known as *Geometrical Shock Dynamics*. A full derivation of this method, although relatively algebraically simple, is rather long-winded, and the reader is directed to the excellent book on shock dynamics by Han & Yin [27]. The derivation of this method involves a change from dimensional to curvilinear coordinates along and orthogonal to the shock front at any given moment in time (see Fig.2.10). The area bounded by the shock position and *rays*, as they are known, is called a ray tube. The edges of this ray tube are assumed, for simplicity, to be solid walls. This is one of the most limiting assumptions of this theory, as the rays are not particle paths. This method was compared to experimental shock wave profiles by Skews [28], who found that the theory underpredicted weak shock wave propagation and overpredicted that of strong shock waves. The Mach number of diffracting weak shock waves were predicted to quickly vanish to $M = 1$ whereas, in reality, this takes significantly longer to occur.

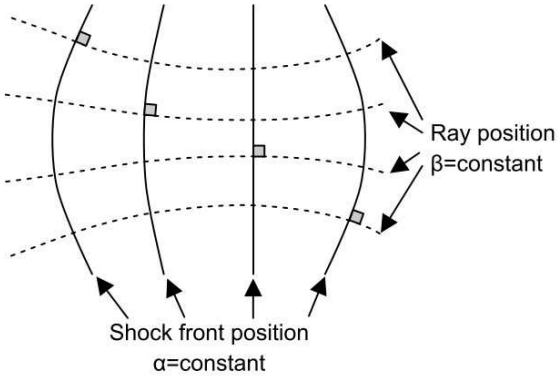

Figure 2.10: Position of curved shocks and rays

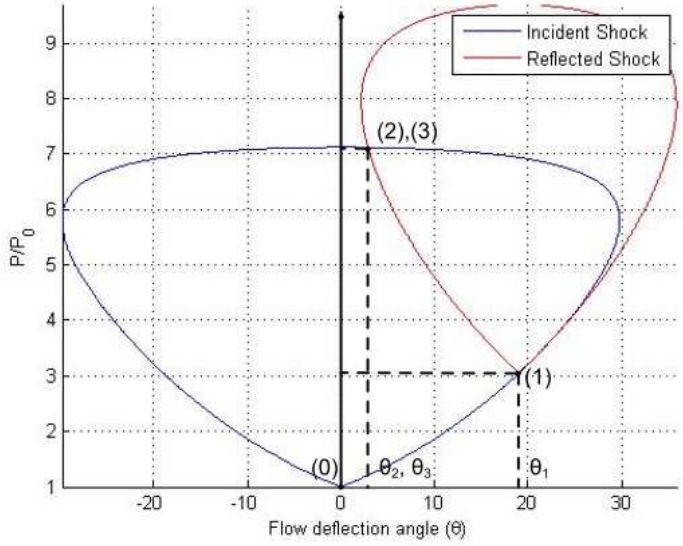

Figure 2.9: Shock polar with $\theta_w = 19°$ and $M_0 = 2.5$

This theory was expanded on by Oshima et al. [29], who used a more general version of the characteristic solution presented by Rosciszewski [30]. The shape of a diffracting shock front is then predicted by:

$$\tilde{x} = \frac{x}{M_0 a_0 t} = \cos\theta \cosh\left(\theta\sqrt{\frac{K}{2}}\right) - \theta\sqrt{\frac{K}{2}} \sin\theta \sinh\left(\theta\sqrt{\frac{K}{2}}\right) + \sqrt{1 - \frac{1}{M_0^2}} \left[\cos\theta \sinh\left(\theta\sqrt{\frac{K}{2}}\right) - \theta\sqrt{\frac{K}{2}} \sin\theta \cosh\left(\theta\sqrt{\frac{K}{2}}\right)\right] \tag{2.28}$$

$$\tilde{y} = \frac{y}{M_0 a_0 t} = \sin\theta \cosh\left(\theta\sqrt{\frac{K}{2}}\right) + \theta\sqrt{\frac{K}{2}} \cos\theta \sinh\left(\theta\sqrt{\frac{K}{2}}\right) + \sqrt{1 - \frac{1}{M_0^2}} \left[\sin\theta \sinh\left(\theta\sqrt{\frac{K}{2}}\right) + \theta\sqrt{\frac{K}{2}} \cos\theta \cosh\left(\theta\sqrt{\frac{K}{2}}\right)\right] \tag{2.29}$$

where K is a slowly varying function of Mach number given by Chisnell [31]. It is convenient to present these equations in terms of $\frac{x}{a_0 t}$, making it easy to see at which point theory predicts degeneration into a sound wave.

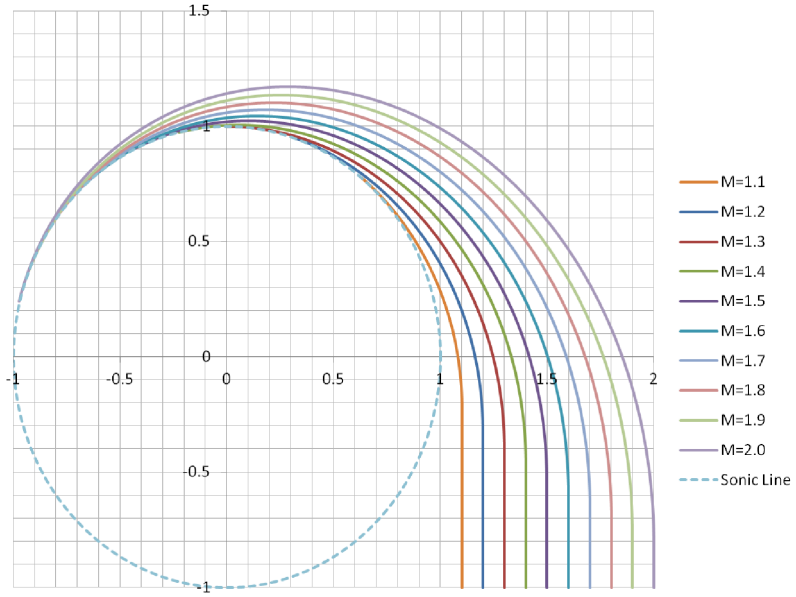

Figure 2.11: Shock front profile after a sharp corner

Figure 2.11 shows the predicted wave shape after diffracting around a sharp corner until they fall below the sonic speed (denoted by the dashed line). The variation can be accounted for by looking at the variation in K with Mach number. The growth of a shock front undergoing this kind of expansion is assumed to be self-similar in time; as such, Fig.2.11 can be representative of any wave.

Although the shape of a diffracted shock wave is interesting in its own right, in this project we are more concerned with the complex region behind the shock wave. It makes sense at this point to divide the discussion into the two geometries under investigation, namely a sharp and a round corner, to examine the flow features found in what Skews termed *the perturbed region* behind a diffracting shock wave [32]. If the flow has no associated length scale, it will grow self-similarly in time. However, if there is an associated length scale, then this assumption is no longer valid. Sharp and round corners will be discussed separately in subsequent sections.

2.4.1 Sharp Geometries

Sharp changes in geometry, i.e. changes of infinitesimal radius, create a self-similar flow structure that is only dependent on incident shock Mach number. This discussion will present the flow structure created by weak waves and then build upon this until strong waves are shown. The seminal work on this flow type was conducted by Prof. Beric Skews in 1967 [32], in which he showed experimentally the flow features present behind a diffracting shock wave. In this work he showed how complex flow features varied with differing corner angle and Mach number. The research highlighted that past a critical corner angle of $\theta > 75°$, the flow features are largely independent of corner angle for a given incident shock speed. Therefore, the flow past a corner angle greater than 75° is directly comparable. Past this value of $\theta > 75^o$ the flow becomes dependent only on incident shock Mach number. As we will discuss later, this may not necessarily be the case. Professor Skews himself has recently cast doubt on the self-similarity of the whole flow field [33]; reasons for this

will be discussed in Section 2.5.1. For now at least, we will assume that the flow is self-similar in time until there are any changes in geometry.

Many researchers have investigated the flow generated by a shock wave diffracting around a 90° corner. Notable experimental works were carried out by Skews ([28],[32], [34], [33]), Bazhenova et al. [35] and Sun & Takayama [36]. All of the experiments undertaken have used some form of density-based optical diagnostics. Possible weaknesses of these techniques will be discussed in Section 3.1. However, all of the experimental work performed does confirm the existence of the basic flow features that will be discussed in this section. Disagreements between the results of different researchers will be discussed later after simulations of this type of flow have been introduced in Section 2.7.

Fig.2.12 shows the wave diagrams for three differing incident Mach numbers. Figs. 2.12a, 2.12b & 2.12c all have subsonic flow behind the incident shock.

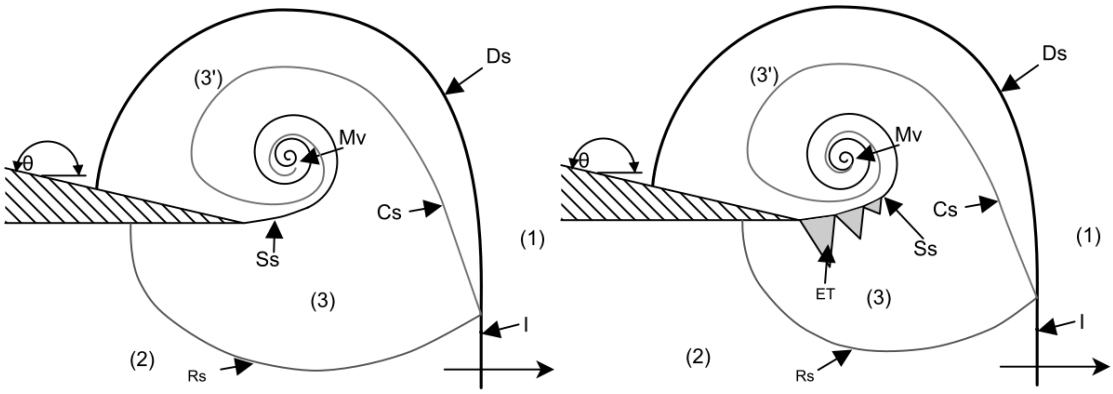

(a) $1 < M_i \leq 1.35$ incident shock wave (b) $1.35 < M_i \leq \approx 1.8$ incident shock wave

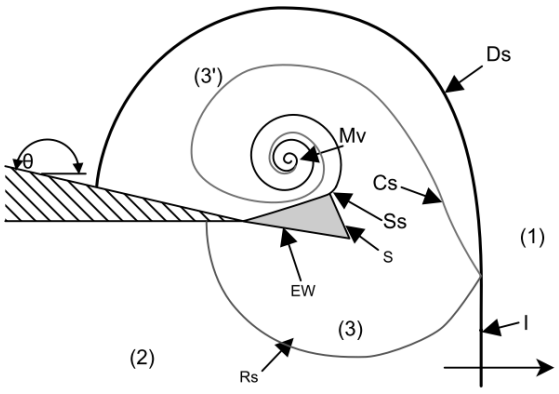

(c) $\approx 1.8 < M_i < 2.07$ incident shock wave

Figure 2.12: Basic flow structure behind a shock wave diffracting around a sharp corner

In Fig.2.12, **I** is the planar incident shock, **Ds** is the diffracted (curved) shock, **Rs** is the reflected expansion wave and can be thought of as the influence of the corner, **Cs** is the contact surface separating the gas shocked by **I** and **Ds**, **Ss** is the slipstream created by flow separating from the corner apex, **Mv** is the main vortex created, **ET** is a train of expansion waves, **EW** is the last running expansion wave and **S** is the terminating (secondary) shock. Localized pockets of supersonic flow

are shaded grey. Different regions of the flow are labeled according to the waves they have encountered. Region **(0)** is quiescent air ahead of any shock waves, **(1)** has passed through the planar shock wave **I** and is uniform, region **(2)** is the most complex region as it has been effected by **I** and **Rs** and includes the complex vortex roll-up process, **(2')** has been influenced by **Ds** only and has strong variations in all flow parameters. If the incident shock Mach number is increased to $M_i > 2.07$ the same flow patterns are seen as in Fig.2.12c, however induced flow is supersonic everywhere. For more information on this, see Section 2.2 and refer to Skews [32].

Region **(2)**, bounded by **Cs** and **Rs**, is what Skews termed the perturbed region and is one of the main focuses of this work. For very weak shock waves (Fig.2.12a) the perturbed region is relatively simple as it is subsonic throughout and only contains a shear layer that rolls up into a strong vortex. The shear layer is shed from the corner as the induced flow behind **I** is unable to navigate the sharp turn. The extreme velocity changes required for the flow to remain attached around such a sharp corner are clearly not possible, so the flow separates leading to the creation of a shear layer. The dynamics and stability of an impulsively started shear layer will be discussed in Section 2.5.1.

If $M_i > 2.07$ then the induced flow is supersonic everywhere and when flow reaches an area expansion it would be expected that an expansion fan is formed leading to the creation of a secondary shock as shown in Fig.2.12c. However, it has been noted that secondary shocks can appear in flow which is subsonic; clues were shown by Skews [32] but it was shown more conclusively by Kleine et al. [37]. In order to resolve this apparent confusion, Sun and Takayama [36] treated this problem in the same way as we treated the centered expansion wave in Section 2.2.1. The reflected sound wave, **Rs**, represents the head of a centered expansion wave traveling back upstream in the shock tube into region **(2)**. If we assume that gradients away from the wall are negligible, i.e. the flow is one-dimensional, we can use the same analysis we derived in the previous section. This is shown in Fig.2.13.

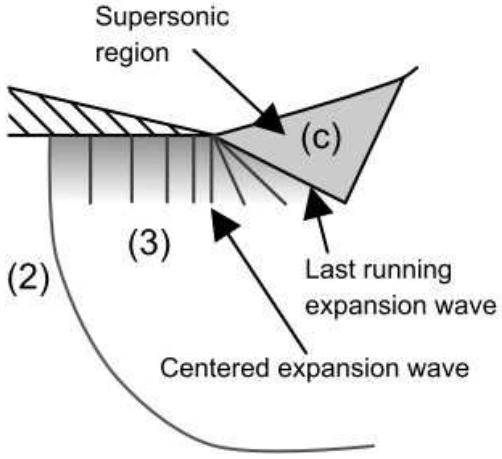

Figure 2.13: Close-up of the expansion wave

Equation 2.20 can be applied to across the expansion wave between the flow in **(2)** (Fig.2.13) and the shaded, supersonic region, **(c)**.

$$U_2 + \frac{2a_2}{\gamma - 1} = U_c + \frac{2a_c}{\gamma - 1} \tag{2.30}$$

Dividing by a_2 and then a_c and the rearranging for M_c gives us

$$M_c = \left(M_2 + \frac{2}{\gamma - 1}\right)\frac{a_2}{a_c} - \frac{2}{\gamma - 1} \tag{2.31}$$

Using the isentropic flow relation 2.32, the local speed of sound can be eliminated from 2.31 to give 2.33.

$$\frac{a_2}{a_c} = \left(\frac{P_2}{P_c}\right)^{\frac{\gamma-1}{2\gamma}} \tag{2.32}$$

$$M_c = \left(M_2 + \frac{2}{\gamma - 1}\right)\left(\frac{P_2}{P_c}\right)^{\frac{\gamma-1}{2\gamma}} - \frac{2}{\gamma - 1} \tag{2.33}$$

M_2 is the Mach number of the induced flow behind the incident shock wave which can be written as a combination of (2.13) and (2.17) to give

$$M_c = \frac{1}{\gamma}\left(\frac{P_2}{P_1} - 1\right)\left[\frac{\frac{2\gamma}{\gamma+1}}{\frac{P_2}{P_1} + \frac{\gamma+1}{\gamma-1}}\right]^{\frac{1}{2}}\left[\frac{1 + \frac{\gamma+1}{\gamma-1}\left(\frac{P_2}{P_1}\right)}{\frac{\gamma+1}{\gamma-1}\left(\frac{P_2}{P_1}\right) + \left(\frac{P_2}{P_1}\right)^2}\right]^{\frac{1}{2}} \tag{2.34}$$

Assuming we know the incident shock wave strength which can be calculated from Eq.2.27 we can estimate the Mach number induced by the expansion wave if we know the pressure ratio across the expansion wave. Skews [32] stated that the pressure in the region of the slipstream is almost equal to the pressure ahead of the incident shock. This has also been proved numerically by Sun & Takayama [36]. This allows us to assume that $P_c \approx P_1$. Substituting this and Eq.2.34 into Eq.2.33 gives us a relationship between the induced Mach number in region (c) and the incident shock strength. Given that for a secondary shock to exist the flow must be supersonic, we can set $M_c = 1$, giving us a minimum incident shock strength of 1.947. From Eq.2.27 the minimum diaphragm pressure ratio is ≈ 4 corresponding to an incident shock Mach number of $M_i = 1.346$.

This result means that any diffracting shock waves with $M_i > 1.346$ are expected to have pockets of supersonic flow in the expansion region below the shear layer. Fig.2.12b has several regions of supersonic flow bounded by expansion waves and shocks. This psuedo-shock train is similar to those seen in underexpanded nozzle flows as the flow is not correctly expanded to the correct pressure. The expansion wave grows in strength as M_i is increased leading to an increase in M_c. Eventually the supersonic regions grow in size until there is only one region. This is the strong shock wave diffraction pattern seen by Skews [32] and others. This shock wave is essentially required to match the pressure of the expanded flow to the post shock condition [38].

Although the 90° corner is a standard test case, there has been comparatively little experimental work done on much larger corner angles. Skews [32] showed some images of the flow, however, these were far from extensive. Bazhenova et al. [35] [39] showed visualization of the flow created by very strong shock waves diffracting around large corners. However, the strong shocks created such large density changes that they overranged the schlieren system (see Section 3.1.2.2) meaning that the perturbed region cannot be investigated in detail. Chang et al. [40] showed two

brief frames of the shock wave diffraction process of a $M_i = 1.4$ shock wave, however the main focus of this work was on shock vortex interaction, which will be mentioned later. More recent studies have been performed by Gongora-Orozco et al. [41] in which high-speed schlieren and PIV were used to evaluate the flow. The results of this study were inconclusive as the frame rate of the high-speed camera was too low and the PIV particle inertia was too high to acquire reliable quantitative measurements in such a transient flow.

2.4.2 Round Geometries

Compared to sharp geometries, there has been relatively little work on the diffraction process and perturbed region created by round geometries. Unlike sharp corners where there is no associated length scale, this flow contains a length scale (the corner radius) meaning that the flow is not self similar in time and is therefore significantly more challenging to investigate. The earliest work, to the authors knowledge, on the topic is a brief conference paper by Skews in 1968 [42]. In this paper, Professor Skews developed important conclusions based on his experimental results and comparisons with Whitham's theory. Similar to sharp geometries, Skews concluded that that the shock does not decay as fast as is predicted by Whitham's theory resulting in the theory over predicting the curvature of the diffracted shock. The shape of the incident and diffracted waves are similar to that of the previous section [43], however, the perturbed region is significantly different.

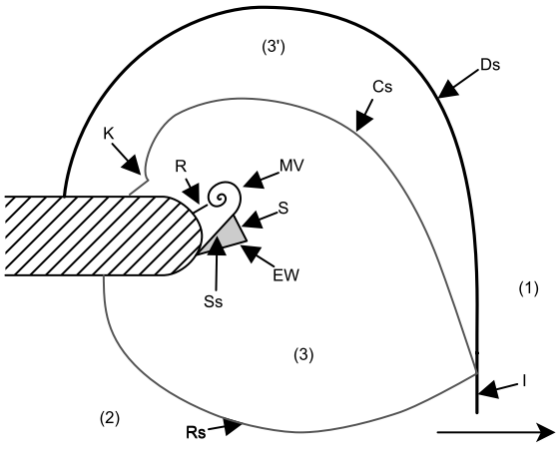

Figure 2.14: Flow structure created by a rounded corner

The perturbed region, as shown by Skews [42] is given in Fig.2.14. The main waves **I**, **Rs** and **Ds** are almost identical to Fig.2.12. Due to the distribution of curvature, the separation point has moved along the curved surface meaning that the expansion wave is no longer centered. The separation point is known to move along the radius of curvature with time [44]. This has the effect of delaying the creation of the slipstream, **Ss** as the pressure rise is moved downstream [24]. The main vortex, **MV**, is not as large as the sharp corner and is in much closer proximity to the corner. The lower level of vorticity produced was mentioned by Sun & Takayama [45]. There is a recompression shock, **R**, due to the proximity of the vortex to the wall. The recompression shock equalizes the pressure above and below the shear layer. This

is similar to the *vortex shock* seen during diffraction around a 90° sharp corner [38]. Skews also noted that the contact surface is no longer swept up into the main vortex [42]. Instead, it contains a sharp kink, **K**, after which it meets the wall at an oblique angle. The kink and the recompression shock were conveniently explained by Law et al. [44] as a function of the main vortex strength. The main vortex will entrain fluid towards the core; however, some of the entrained fluid will impinge on the surface leading to the creation of a stagnation point. This stagnation point will cause a jetting effect parallel to the surface, pushing the contact surface away at that point. The jet heading towards the main vortex can be heavily accelerated by the converging streamlines in that region. The low pressure created there must be balanced with the pressure on the other side of the slipstream, leading to the creation of a recompression shock.

Muritala et al. [46] showed experimental schlieren pictures of the perturbed region created and mentioned the importance of turbulence to the flow. No specific details are given about the experimental setup in this work such as the camera, light source and exposure time used. As a result of this it is difficult to interpret the mentioned patches of turbulence as they could be periodic structures. The lack of a recompression shock in the experimental images is ascribed to a patch of turbulence obscuring the shock wave seen in simulations. This is doubtful based on the appearance of the schlieren images.

2.5 Shear Layers

Shear layers have become increasingly important to a variety of engineering applications. Applications range from essentially incompressible low-speed shear flows, such as those found in automotive engineering, to high-speed compressible mixing layers such as those found in scramjets. The stability of shear layers has pervaded scientific and engineering literature over the past 150 years since Helmholtz originally posed the problem of shear layer instability in 1868 and Lord Kelvin solved it in 1871. The features of this kind of flow can be seen regardless of length scale. The same kind of instabilities are found in micro-fluidic devices up to atmospheric scale (Fig. 2.15[3]). The Kelvin-Helmholtz instability is even predicted at planetary scale between the solar wind and Earth's magnetosphere [47].

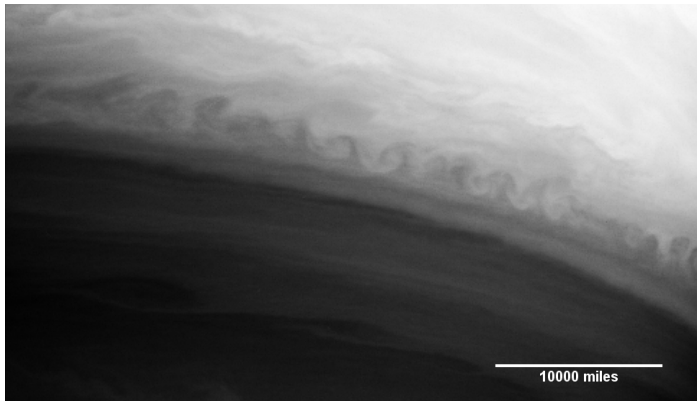

Figure 2.15: Kelvin-Helmholtz instability images on Saturn taken by the Cassini Orbiter

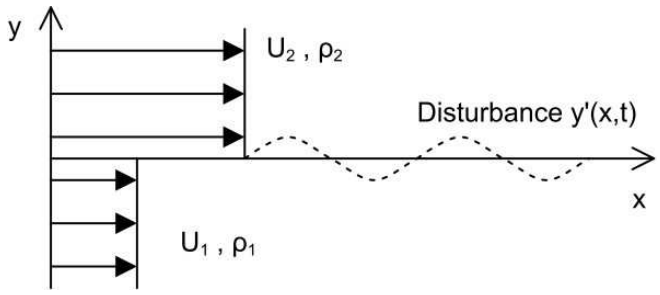

Figure 2.16: Schematic of the flow showing a discontinuity in the velocity profile and the assumed disturbance

The most basic shear layer, a step change in velocity at a perturbed interface between two inviscid fluids (as shown in Fig. 2.16), can be solved to give the stability criteria.

The basic flow can be set up as follows:

$$\mathbf{U} = \begin{cases} U_2\mathbf{i} \\ U_1\mathbf{i} \end{cases} \quad \rho = \begin{cases} \rho_2 \\ \rho_1 \end{cases} \quad P = \begin{cases} p_0 - g\rho_2 y & y > 0 \\ p_0 - g\rho_1 y & y < 0 \end{cases} \tag{2.35}$$

[3]Photo credit to NASA/JPL/Space Science Institute - http://photojournal.jpl.nasa.gov/catalog/PIA06502

We can then define velocity potentials $\mathbf{u} = \nabla\phi$ where

$$\phi = \begin{cases} \phi_2 & y > y' \\ \phi_1 & y < y' \end{cases} \tag{2.36}$$

where y' is the interface elevation

$$y = y'(x,t) \tag{2.37}$$

It is known from the continuity and incompressibility conditions that the Laplacian of velocity is equal to zero, meaning that the Laplacian of our velocity potentials is also equal to zero.

$$\Delta\phi_2 = 0 \qquad (y > y') \qquad \text{and} \qquad \Delta\phi_1 = 0 \qquad (y < y') \tag{2.38}$$

We can then set up the boundary conditions. We are assuming that any disturbances to the interface are only significant near the interface and that they are finite in amplitude:

$$y \to -\infty \qquad \nabla\phi_1 = U_1 \qquad \text{and} \qquad y \to +\infty \qquad \nabla\phi_2 = U_2 \tag{2.39}$$

The second boundary condition is that the fluid at the interface must have the same vertical velocity top and bottom, therefore leaving no cavities.

$$v = \frac{\partial\phi_2}{\partial y} = \frac{\partial y'}{\partial t} + U_2\frac{\partial y'}{\partial x} \tag{2.40}$$

$$v = \frac{\partial\phi_1}{\partial y} = \frac{\partial y'}{\partial t} + U_1\frac{\partial y'}{\partial x} \tag{2.41}$$

The final boundary condition is that the fluid must have the same pressure on either side of the interface. This can be formulated using the unsteady Bernoulli equation. Ignoring the buoyancy term, we have:

$$\frac{\partial\phi}{\partial t} + \frac{1}{2}(\nabla\phi)^2 + \frac{P}{\rho} = C(t) \tag{2.42}$$

Equating the pressures gives

$$\rho_1\left\{\frac{\partial\phi_1}{\partial t} + \frac{1}{2}(\nabla\phi_1)^2 - C_1(t)\right\} = \rho_2\left\{\frac{\partial\phi_2}{\partial t} + \frac{1}{2}(\nabla\phi_2)^2 - C_2(t)\right\} \tag{2.43}$$

Now we begin to introduce perturbations into the flow. To do this we need to start with the reference flow at the interface. The velocity potentials are

$$\phi_1 = U_1 x \qquad \text{and} \qquad \phi_2 = U_2 x \tag{2.44}$$

At $y = y'$ the constants C_1 & C_2 can be related

$$\rho_1\left(C_1 - \frac{1}{2}{U_1}^2\right) = \rho_2\left(C_2 - \frac{1}{2}{U_2}^2\right) \tag{2.45}$$

satisfying all the boundary conditions of the problem.

Equations 2.39-2.41, 2.43 and 2.45 now represent the nonlinear equations for instability of the basic flow (Eq.2.35). We now aim to introduce perturbations and linearise the equations by assuming that the interface initial displacements are very small. Our perturbations are given by

$$\phi_1 = U_1 x + \phi_1'(x, y, t) \qquad \text{and} \qquad \phi_2 = U_2 x + \phi_2'(x, y, t) \tag{2.46}$$

Substitution of this into equations 2.39-2.41, 2.43 and 2.45 leaves us with

$$\Delta\phi_2' = 0 \qquad \text{and} \qquad \Delta\phi_1' = 0 \tag{2.47}$$

with boundary conditions of

$$y \to -\infty \qquad \nabla\phi_1' = 0 \qquad \text{and} \qquad y \to +\infty \qquad \nabla\phi_2' = 0 \tag{2.48}$$

The interface conditions become

$$\frac{\partial\phi_1'}{\partial y} = \frac{\partial y'}{\partial t} + U_1\frac{\partial y'}{\partial x} \tag{2.49}$$

$$\frac{\partial\phi_2'}{\partial y} = \frac{\partial y'}{\partial t} + U_2\frac{\partial y'}{\partial x} \tag{2.50}$$

and the Bernoulli equation, when evaluated at the interface, becomes

$$\rho_1\left\{U_1\frac{\partial\phi_1'}{\partial x} + \frac{\partial\phi_1'}{\partial t}\right\} = \rho_2\left\{U_2\frac{\partial\phi_2'}{\partial x} + \frac{\partial\phi_2'}{\partial t}\right\} \tag{2.51}$$

Now we need to solve the Laplacians of Equation 2.47. This is achieved by separation of variables, followed by the realisation that the Laplace equation accepts solutions of the form:

$$y' = \hat{y}e^{i\alpha x + st} \tag{2.52}$$

$$\phi_1' = \hat{\phi}_1 e^{i\alpha x + st} \tag{2.53}$$

$$\phi_2' = \hat{\phi}_2 e^{i\alpha x + st} \tag{2.54}$$

After solving these equations and substituting back into the Bernoulli equation, we end up with a quadratic equation for the eigenvalues of the system.

$$s = -i\alpha\frac{\rho_1 U_1 + \rho_2 U_2}{\rho_1 + \rho_2} \pm \sqrt{\frac{\alpha^2\rho_1\rho_2(U_1 - U_2)^2}{(\rho_1 + \rho_2)^2}} \tag{2.55}$$

In this equation, the real part represents the amplification (growth) rate, the complex part represents the frequency and α represents the wavenumber. As it is clear to see, this equation will always have one positive real root and is therefore unstable in one mode and asymptotically stable in the other. This *saddle type* stability property means that the system is always unstable. This result is only true for inviscid flow with a discontinuous velocity profile [48]. Real flows have a length scale attached to them and as such can be stable to short wavelength oscillations [49] depending on the ratio between the disturbance wavelength and shear layer thickness [50].

Equation 2.55 does exhibit an interesting property regarding the sensitivity of the shear layer to density ratio and velocity ratio. The complex part of the eigenvalues represent a measure of frequency of oscillation based on the normal modes assumption used to solve Equation 2.47. This complex part is dependent on the inverse square root of the density ratio $\frac{\rho_1}{\rho_2}$ and weakly, linearly dependent on the velocity ratio $\frac{U_1}{U_2}$. This means that even small changes in density can be significant. This power of $-\frac{1}{2}$ is reduced to approximately -0.3 for shear layers of finite thickness [51]. Papamoschou & Roshko [52] showed that the growth rate of compressible shear layers is slower when the heavier gas is on the high-speed side. It was shown by Monkewitz & Huerre [53] that increasing the velocity ratio has the effect of decreasing the spreading rate of the shear layer. However, this has little influence on the complex root of the eigenvalue equation, as shown by Abraham & Magi [54]. They showed that the the slowing of spatial growth due to an increasing velocity ratio had actually increased the frequency of shed structures.

The Kelvin-Helmholtz instability will grow from its initial small perturbation into the well-known larger billowing structures. As the waves grow, the small-amplitude theory used here begins to break down. The billows will grow in size, forming *Kelvin's cat's eyes* until they reach a finite size and then begin to break down into turbulence.

As has been hinted at in the previous discussion, viscous effects play an important role in the development of shear layers. Only a completely inviscid flow can be considered in the way shown in Fig. 2.16. Real flows have a distributed velocity profile. This is commonly modelled using a hyperbolic tangent velocity profile or by adding together several piecewise linear gradients. The analysis of these types of velocity profiles is performed by solving the Orr-Sommerfeld equation (2.56).

$$(U-c)(v''-\alpha^2 v) - U''v + \frac{i\nu}{\alpha}(v''''-2\alpha^2 v''+\alpha^4 v) = 0 \tag{2.56}$$

The majority of the shear layers found in this work are almost completely inviscid; as such, only a qualitative description of viscous effects will be given. However, one interesting point to note is that if viscosity is neglected from Eq. 2.56, we are left with the Rayleigh equation. This leads on to Rayleigh's classical theory, stating that an inflection point in the velocity profile is a necessary condition for instability [55]. It has since been proved by many researchers that this is a necessary but insufficient criteria for instability.

As mentioned earlier, viscous shear layers (finite thickness) can be stable for short wavelength oscillations. However, if a free-shear layer is constructed of an extremely thin boundary layer shed from a knife-edge corner (as we will see later), it may still be unstable to extremely short wavelengths, despite the viscous characteristics of the flow.

The effect of supersonic disturbances and general compressibility on shear layers has been the focus of many studies. One of the earliest and most widely read works is by John Miles in 1958 [1]. In this work Miles describes the effect of supersonic disturbances on stability and derives a stability criteria based on the rather restrictive assumption that $\rho_1 a_1 = \rho_2 a_2$. His criteria does show that a flow of this type is stabilised as the Mach number ratio between the two streams is increased. Fig. 2.17 shows the stability boundary based on the Mach number of the two streams.

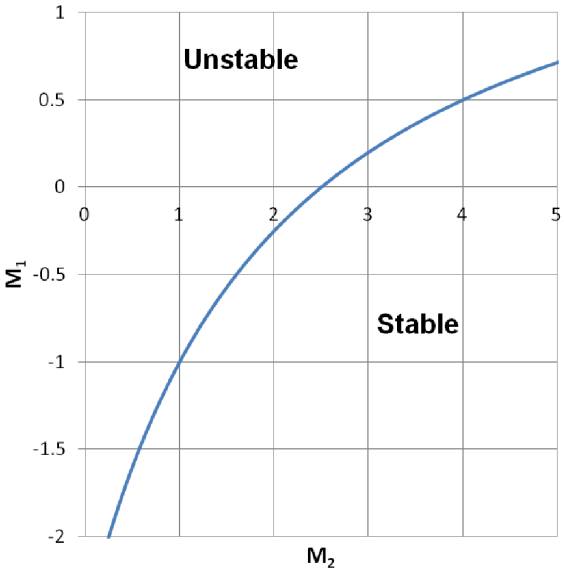

Figure 2.17: Stability contour as calculated by Miles [1]

His Mach number requirement for stability is significantly higher than anything we are likely to encounter in this research; nonetheless, it is useful for the purpose of understanding the trend.

In the mid-1980s, there was a dramatic increase in interest in turbulent mixing layer research which was initiated by work by Brown & Roshko [56] and Roshko [57]. Work on the structure of the compressible shear layer was presented by Bogdanoff [58]. Bogdanoff's paper lays the foundations for the derivation of a scaling parameter which is now commonplace: the convective Mach number (M_C). The definition of the convective Mach number is given in Eq. 2.57 and is derived by equating the static pressure on either side of a saddle point between moving large scale structures. The work on compressible shear layers by Papamoschou & Roshko [52] used normalised vorticity thickness (Eq. 2.60) as their definition of shear layer thickness and plotted this against convective Mach number. This showed a predictable and repeatable decline in growth rate with an increase in convective Mach number. Papamoschou & Roshko explained the difference between a vortex sheet and a finite thickness shear layer at supersonic speeds, showing how even a completely supersonic flow will have a portion of *convectively* subsonic flow, allowing for the growth of subsonic-type instabilities.

$$\left(1+\frac{\gamma_1-1}{2}M_{C1}\right)^{\frac{\gamma_1}{\gamma_1-1}}=\left(1+\frac{\gamma_2-1}{2}M_{C2}\right)^{\frac{\gamma_2}{\gamma_2-1}} \tag{2.57}$$

The effect of compressibility on the growth rate and turbulent fluctuations of the shear layer seems to become significant around a convective Mach number of $M_C \approx 0.5$. However, Elliott & Samimy [59] suggested that the effect on turbulent fluctuations begins at much lower values of M_C. Their study also showed that the effects of compressibility were much more pronounced at higher convective Mach numbers ($M_C = 0.86$).

$$\delta_w = \frac{U_1 - U_2}{\frac{dU}{dY}} \tag{2.58}$$

$$y^* = \frac{y - y_{0.5}}{\delta_w} \tag{2.59}$$

$y_{0.5}$ is where $$U = \frac{U_1 + U_2}{2} \tag{2.60}$$

All of the analysis that has been conducted so far has been limited to plane shear layers with no curvature. It is important to this work that we consider the effects of curvature on shear layers and their stability. There has been comparatively sparse literature on curved shear layers when compared to its planar counterpart, especially considering how often this phenomenon occurs in engineering flows. The linear stability of a curved shear layer has been considered by Liou [60]. He analysed a hyperbolic tangent profile with the high-speed stream on both the inside and the outside of curvature. This meant that the flow was not only subjected to a possible Kelvin-Helmholtz instability but also to a centrifugal instability (similar to Taylor vortices). However, if the high-speed stream is on the outside of the curvature (as we are likely to find in this work), the Rayleigh criterion (Eq. 2.62) states that the flow is stable.

$$\frac{d}{dr}\left|\Omega r^2\right| < 0 \tag{2.61}$$

$$\Omega_1 {r_2}^2 > \Omega_2 r_2^2 \tag{2.62}$$

This implies that Kelvin-Helmholtz should be the dominant mechanism for instability. Liou showed that the curvature of the shear layer has a stabilising effect by reducing the growth rate of Kelvin-Helmholtz instabilities over the entire frequency range [60].

2.5.1 Induced Shear Layers

In order to facilitate our discussion on shock wave-induced shear layers, it makes sense to initially consider the roll-up process of a shear layer into a starting vortex. The now famous experiment by Prandtl [61] showed the evolution of a starting vortex from an impulsively started airfoil. Mathematically speaking, this starting vortex creates a loop with the wingtip vortices and the bound vortex, fulfilling Kelvin's theorem that vortex lines never end in the fluid and satisfying the Kutta condition. Physically, this vortex is generated by a combination of pressure and viscous torques acting on the fluid.

Pullin & Perry [2] showed some interesting flow visualisation on starting vortices using dye injected into an impulsively started water tunnel. They showed the familiar vortex sheet rolling up into a strong vortex. The results also showed a perturbed shear layer (Fig. 2.18a); however, Pullin & Perry ascribed this to equipment vibration and not to an initial stage of shear layer instability. Nonetheless, they also showed some secondary and even tertiary vortices (Fig. 2.18b). The secondary vortex appears to be generated because of the comparatively shallow corner angle and

thus, the proximity of the main vortex to it. However, the *tertiary* vortex appeared to be contained entirely within the shear layer. Lian & Huang [62] showed similar flow structures albeit, with a much greater level of instability in the flow. Individual vortices can easily be seen in the shear layer roll-up process.

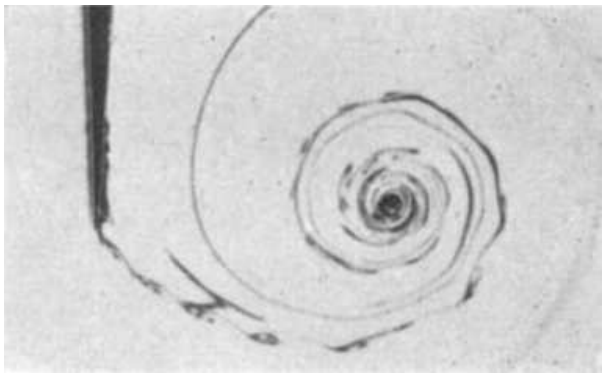

(a) Starting vortex around thin wedge

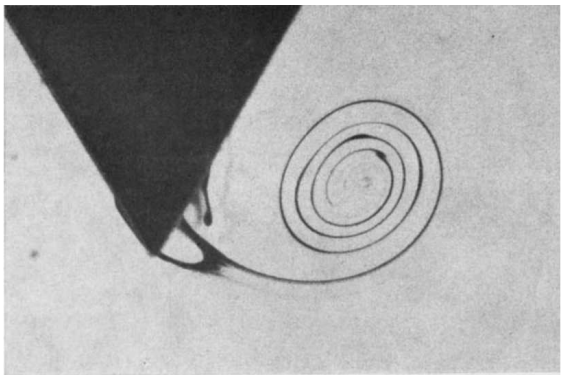

(b) Starting vortex around large wedge

Figure 2.18: Starting vortices generated by Pullin & Perry [2]

Moore [63] gave an interesting discussion on the appearance of Kelvin-Helmholtz instabilities on a curled up shear layer based on the classical analysis given by Kaden [64]. Kaden proposed that the local vorticity in a spiral vortex, as we have here, is a function of an ordinate along the spiral and is zero at the vortex core. This means that at some location there may be Kelvin-Helmholtz instabilities, but they may decay towards the vortex core.

Sun & Takayama [45] showed by way of iso-vorticity contours that the vorticity produced by shock wave-induced shear layers is largely created by the slipstream coming from the separated flow. The slipstream has a tangential velocity jump across it, meaning that it will be a source of vorticity in the flow. The analysis by Sun & Takayama showed that the effect of baroclinic torque is negligible when compared with the effect of singularities in the flow, such as the shear layer shed from a sharp corner. The shear layer connected to the corner apex feeds vorticity into the main vortex core until the shear layer breaks down and the vortex propagates as a free vortex.

As will be discussed in Section 2.7.4, there has been some debate about the structure of the shear layer produced during the shock diffraction process. To this end, recent experimental studies by Skews et al. [34][33] focused on the evolution of shear layers created by shock diffraction around a 90° corner. This work used

density-based diagnostics but unfortunately did not give many details on the exact experimental setup. The shock tube investigated was approximately 18 times larger than the one used in this project, which allowed for the perturbed region to grow without interference from returning waves. Skews noted the onset of a Kelvin-Helmholtz-style instability around 1ms after the passage of the incident shock which, although has little significane in a completely inviscid flow, will be significant as all real flows have some viscosity associated.

2.6 Shock-Vortex Interaction

Initial experimental work on the interaction of a shock wave with a vortex by Dosanjh & Weeks [65] has been expanded on significantly, primarily through numerical simulations. Experimental work on a problem of this type is extremely difficult to perform, primarily as density gradient-based optical techniques are easily overranged by strong interactions, which is often the case with shock-vortex interactions. Most numerical work has been focused on understanding the basics of shock-vortex interaction by considering a discrete vortex and a planar shock wave with varying strengths [66][67]. This situation, although a good basis for further study, is physically unrealistic.

Chang & Chang [68] showed that there are four main types of shock wave vortex interactions, which depend on the strength of both the shock and the vortex. These interactions were termed: *weak shock-weak vortex*, *strong shock-weak vortex*, *weak shock-strong vortex* and *strong shock-strong vortex*.

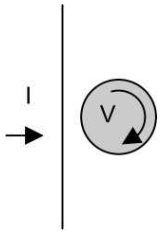

Figure 2.19: Planar shock **I** impacting on vortex **V**

Fig. 2.20 shows the four main types of shock-vortex interaction. As the incident shock wave I propagates toward the vortex V, it begins to deform. The region of the shock with oncoming flow is retarded, I_1, while the other side is accelerated, I_2. This causes the shock wave to take on a sinusoidal form in the vicinity of the shock while remaining planar at regions further away. The accelerated portion, I_2, causes a reflection to occur as it passes around the vortex, resulting in the generation of two new waves, I_1' and I_2'. This reflection can be either a regular or Mach type depending on the strength of the vortex and the shock [66]. As mentioned above, the structure of this reflection is dependent on the shock strength. Sufficiently strong vortices generate a transmitted wave, T, which appears upstream of the vortex. Numerical shadowgraphs presented by Chang et al. [69] show the four different interactions shown in Fig 2.20 very clearly. In this work the authors investigated the effects that a vortex with regions of associated supersonic flow would have on a planar incident shock. Rough boundaries between the different types of shock-vortex interactions were shown by Chang et al. [69].

The generation of waves by shock-vortex interaction has been numerically studied at length [66] [67] [68] [70]. All of these researchers showed that the interaction of a planar shock wave with a vortex generates, initially, a dipole source of sound, immediately followed by a quadrupole source emitting three distinct (out of phase) waves. This is extremely difficult to investigate experimentally.

Skews [71] investigated, both experimentally and numerically, the interaction of a curved shock wave with a spiral vortex at a single Mach number. His results showed that there is an associated pressure spike created by the focusing together of several

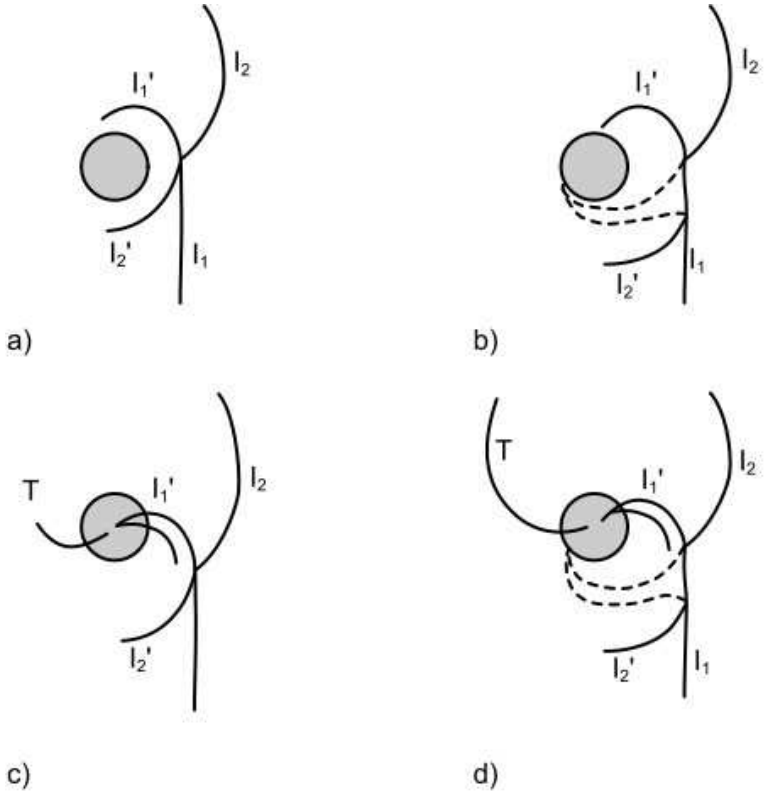

Figure 2.20: Types of shock vortex interaction: a) weak shock - weak vortex b) strong shock - weak vortex c) weak shock - strong vortex d) strong shock - strong vortex

shock waves as a result of the vortex curving them towards each other. Skews [71] and Chang & Chang [40] found that when investigating shock-vortex interaction using a shock tube generated spiral vortex, similar to those seen in Section 2.4, the returning shock wave has a strong impact on the shear layer connected to the corner. Immediately after the passage of the shock, two very strong vortices are created which propagate along the shear layer. These vortices are likely to be baroclinic in nature, due to the misalignment of pressure and density in the region. Leading on from this result, Chang & Chang [72] showed the interaction of a series of vortices with a shock wave. Their numerical results showed that the shock wave contained a set of diverging acoustic waves. To the author's knowledge, waves of this type have not been seen experimentally, as they are relatively small waves surrounded by much stronger interactions.

Barbosa & Skews [73] mentioned a spike in pressure caused by focusing the shock waves after transit through a vortex. It is a well-known phenomena that as a shock wave begins to exhibit a concave curvature, it will begin to focus in on itself, leading to a pressure spike in the focal region. [74]. However, Barbosa & Skews succeeded in showing, by careful experimentation, the magnitude of the pressure spike created.

2.7 Numerical Simulations

An extensive body of simulation work has been produced on shock wave diffraction. This is hardly surprising, as the Sod shock tube problem is one of the most well-known test cases for CFD codes. As has been previously shown in this literature review, the flow generated by sharp and round corners are fundamentally different and as such will be discussed in separate sections. However, initially we will discuss general simulations of shock tubes, their applicability and any associated problems.

2.7.1 Shock Tube Simulations

As was mentioned in Section 2.2, shock tubes can be modelled using one-dimensional, inviscid theory. This makes them ideal for testing out the response of numerical simulations to step impulses. This was originally suggested as a test case by G. A. Sod in 1978 [75], where he showed how some solvers overpredicted pressure peaks and responded like under-damped or over-damped systems. A thorough test matrix of simulation parameters is explored using the commercial code FLUENT as part of ANSYS 13 in Section 4.3.

2.7.2 Simulations of Sharp Geometries

At the 18$^{\text{th}}$ International Symposium on Shock Waves, Professor Kazuyoshi Takayama proposed a poster session for numerical codes from around the world to examine at the problem of shock wave diffraction over a 90° corner [76]. This work shows how many different types of schemes and solvers can produce largely identical results. The shape of the shock wave is almost exactly the same for all of the work presented. There appeared to be no difference between the work based on the Euler equations and Navier-Stokes equations, leading to the conclusion that all of the flow features present in the perturbed region are inviscid in nature. Just before the conference Professor Richard Hillier produced his well-known numerical work on shock wave diffraction around a sharp corner [38] (a brief portion of which was presented at ISSW 18). In this work he discusses the applicability of an Euler simulation to shock diffraction around a 90° sharp corner. He states that *sharp-edged* separation (i.e. separation from sharp edge where attached flow would create completely non-physical gradients in the flow) can be captured and resolved well by the Euler equations. To the author's knowledge, Hillier's work was the first to show what has now become known as the vortex shock.

Sun & Takayama [36] showed very similar wave structures to Hillier but seemed to struggle with the exact prediction of the expansion wave train, **ET**. They ascribed this to a mismatch between the artificial viscosity introduced in the simulation and the physical viscosity of the flow. Numerical viscosity is found in Euler simulations because large gradients are smeared over the finite grid size [77]. As the grid resolution is increased, the numerical viscosity is reduced and the flow tends towards the completely inviscid case. However, this can lead to fractal-esque patterns in flow features and overprediction of growth rates. As a result of this, the development time of unsteady flow features is a function of the solver and the grid size. This time, t_{ff}, is given in Equation 2.63, where Δx is the grid spacing and α is a non-physical constant and is a function of the scheme and solution method [78].

$$t_{ff} = \alpha \Delta x \tag{2.63}$$

Many other simulations have produced largely the same shock wave structure, regardless of the solver or scheme employed [79] [80] [81] [82]. The only apparent differences are in the prediction of the expansion wave train. This appears to be poorly resolved by simulations using adaptive grids and better resolved by simulations using uniform grids.

2.7.3 Simulations of Round Geometries

Similar to the experimental section (2.4.2), there is a lack of numerical simulations on the diffraction of shock waves around rounded corners. This could be down to the difficulty in predicting the location of the separation point, which has a dominant effect on the flow development. The only two studies known to the author are the combined experimental and simulation works produced by Law et al. [44] and Muritala et al. [46]. Of note in these studies are some of the waves found between the shear layer and the corner. These waves appear very clearly in the simulations (particularly in [46]); however, they are not discernible in the experimental results. A useful note to take away from these papers is the large density gradient present in the perturbed region of the flow. These gradients appear to be so large that they could well overrange any schlieren system.

2.7.4 Simulations of Shear Layers

The simulation of shock wave-induced shear layers has been a point of contention within the shock wave community, as different numerical codes, schemes and solvers appear to give contradictory results. In particular, the stability of the shear layer and the appearance of Kelvin-Helmholtz instabilities in simulations but not in experiments is difficult to explain. Of all the posters presented at the ISSW 18 session dedicated to this type of flow, there was only one simulation that showed K-H instabilities on the shear layer. Table 2.1 shows some of the other relevant numerical studies.

From Table 2.1 there does not appear to be any real clear pattern as to what causes some simulations to display K-H instabilities on the rolled-up shear layer. The inclusion of turbulence models appears to have the property of smoothing out the shear layer and suppressing the instability. Liang et al. [80] suggested that the instabilities on the shear layer, could be a function of the grid resolution only. We have already mentioned that the numerical diffusion present in Euler simulations due to the grid resolution could have a damping effect on the flow. This, combined with grid sizes too large to accurately resolve the instabilities, could account for disagreements between simulations. Sun & Takayama [78] suggested several reasons why their simulations could have spurious vortices on the shear layer; however, they failed to produce a complete reason, and the problem remains as yet unsolved. De and Thangadurai [82] showed instabilities present on the shear layer; however, they

[4]Two vortices were formed after a reflected shock hit the shear layer, this is not a result of the Kelvin-Helmholtz instability

[5]Can be suppressed by adding in numerical dissipation into the ASUM+ formulation

Table 2.1: Numerical Simulation of Shear Layer

Author	Formulation	Grid	M_i	θ	K-H Instabilities?
Hillier [38]	Euler	Uniform	1.65, 2	90	No
Uchiyama [83]	Euler	Adaptive $\frac{d\rho}{dx}$	1.3, 1.5, 1.7	90	Yes
Jiang [84]	Euler	Uniform	1.5	90	No[4]
Sun [36]	Euler	Adaptive	1.7	90	No
Sun [78]	Euler	Adaptive	1.5	90	Yes, on fine grid
Liang [80]	Euler	Uniform	1.2	180	Yes
Tseng [81]	Euler	Non-uniform	1.5	90	No
Sun [78]	N-S Laminar	Adaptive	1.5	90	Yes, on fine grid
Liang [80]	N-S Laminar	Uniform	1.2	180	No
Tseng [81]	N-S Laminar	Non-uniform	1.5	90	No
De [82]	N-S Laminar	Uniform	1.5	180	Yes[5]
Sun [78]	N-S K-ϵ	Adaptive	1.5	90	No
De [82]	N-S SST	Uniform	1.5	180	No
De [82]	N-S SST SAS	Uniform	1.5	180	Yes

appeared to be functions of the formulation used, namely the flux vector splitting scheme. Additional dissipation in the ASUM+ was found to suppress the instabilities and reduce non-physical oscillations. They also found that introducing turbulence models into the flow changed the rate of development of the shear layer.

2.8 Conclusion

Shock wave propagation and interaction is a highly transient and complex flow phenomenon that has applications ranging from the world of aerospace engineering to medical treatments. Understanding of the finest scale phenomena and features is more a pursuit of science than engineering, but the implications could be important on larger scales. This is especially true if the applicability of certain experimental techniques could be expanded into different regimes.

The diffraction of shock waves around different geometries is a complex process that is not fully understood, particularly around distributed geometries. Section 2.4.1 showed the major flow features that have been resolved by experiments using density-based techniques. The strong density gradients present can obscure some small-scale flow features, particularly if interferometry is not used. In areas where density gradient-based techniques have been overranged, no information can be gathered about the flow. Simulations have been shown to be effective in capturing most of the large-scale features, namely the shock waves, albeit with some difficulty when resolving the expansion wave train. The majority of simulations have been performed using an assumption of inviscid flow, as the flow is forced to separate at the sharp corner. Fine-scale features are still a source of discussion within the research community, as they appear to be a function of the scheme and solver used rather than a feature of the flow, especially as they have never been resolved experimentally at the same scales. Simulations also have the problem that any small-scale features may be smoothed out by numerical viscosity if the grid is not fine enough. However, the use of adaptive grids seems to inhibit the accurate resolution of some other features, such as the expansion wave train. The appearance of Kelvin-Helmholtz instabilities on the shear layer is to be expected in the limiting case of a vortex sheet, but may take longer to develop with the addition of viscosity and an associated length scale. This leads to the assumption that the flow is not self-similar and that viscosity has an important effect in this region, invalidating the inviscid assumption. To the author's knowledge, there have been no investigations into the effect of incident shock Mach number on the stability of the shear layer created. *The disagreement between experimental and simulation work on this topic is one that should be resolved; this is the main aim of this project. This is to be achieved by using different experimental techniques to look at the flow and see what state-of-the art diagnostics are capable of resolving.*

Diffraction of shock waves around sharp corners is a complex process; however, round corners produce even more complex flow structures that have not been sufficiently examined, either experimentally or computationally. The rounded corner has the effect of delaying the separation point and therefore the formation of the shear layer and the associated vortex. This is a viscous phenomenon and therefore the inviscid assumption used in the analysis of sharp corner flows is no longer valid (at least in the region of the separation point). The proximity of the vortex to the wall also has implications on the shape of the contact surface and the flow entrained by the vortex. The same problems of investigating sharp corners apply to rounded corners, namely the overranging of density gradient-based techniques obscuring flow features and the extremely high-speed nature of the flow. Careful setup of optical experiments, as well as other techniques such as PIV and PSP, will allow further insight into this flow.

The process of shock-vortex interaction in a confined geometry will be investigated in this study, using the same techniques. Simulations of isolated, discrete vortices and incident shock waves have been performed, but it is extremely difficult to investigate this situation in reality. Simulations of the whole shock diffraction process will be performed and compared to experimental results to see if there are any differences between experiments and simulations.

In order to investigate these two challenging flows effectively, a comprehensive literature review of the history, theory and application of the relevant experimental techniques will follow.

Chapter 3

Experimental Techniques

> *CFD is a fantasy, whereas getting the correct results from a supersonic wind tunnel is an art* - Professor Konstantinos Kontis in a lecture to undergraduate students

Experimental fluid dynamics is, like many areas of physics, an art of measuring without disturbing. In order to achieve this effectively there must be as little interference with the flow physics as possible. This is less of a problem in supersonic flow, as the *butterfly effect* is less prominent when measuring downstream quantities. Despite this, in order to gain credible results, all care must be taken to reduce measurement-induced errors. This consideration favours using optical measurement techniques and measuring quantities using transducers which are flush to the wall. Modern-day computing and the advancement of high-speed cameras have made this a reality. Some modern-day cameras, such as the *Shimadzu HPV-1*, are capable of recording at one million frames per second. Such high speeds allow the development of transient phenomena in unsteady high-speed flows to be examined in great detail. Using the *HPV-1* in conjunction with a shadowgraph or schlieren optical system (see Section 3.1) gives a fantastic insight into unsteady high-speed phenomena and will be used to great effect in this project.

The development over the last two decades of *particle image velocimetry* (PIV) and, more recently, *pressure-sensitive paints* (PSP) have unlocked new potential in non-intrusive measurement and has allowed phenomena to be experimentally quantified with an unprecedented accuracy. A review of flow measurement techniques is given by Jensen [85] highlighting the advantages of modern flow diagnostic techniques, while not forgetting the applications of traditional and far less expensive systems.

3.1 Schlieren and Shadowgraph

Schlieren and shadowgraph techniques are two of the three main density-based flow diagnostic techniques, the third one being interferometry. In this section, schlieren and shadowgraph will be discussed at length; however, interferometry will not. This is partially because of the complexity of the process, but also because interferometry has a finite sensitivity, which is a significant drawback when compared to the other

techniques.[1]

3.1.1 History and Development

If you look down a road on a hot sunny day you can often see a *heat haze*. This is caused by changes in density (and therefore changes in refractive index) brought on by temperature gradients in the air. This simple phenomenon, based on density change, is the basis for two of the most powerful and widely used imaging techniques in fluid dynamics. Schlieren and shadowgraph are simple (at least, in theory) techniques for imaging gradients in transparent media which have the power to make the invisible visible. Their ability to highlight gradients in transparent media has given scientists qualitative results leading to many breakthroughs and makes them the weapons of choice in qualitative flow analysis.

The *recorded* history of phenomena visualised by changes in refractive index dates back almost 350 years [87]. The refraction of light rays by changes in the properties of air was first mentioned by Robert Hooke in his prodigious 1667 work, Micrographia (specifically observation LVIII) [88]. Hooke used one candle as a light source to visualise the plume from a second candle. Hooke brought in a demonstration of this experiment to the Royal Society and described the plume from a candle as: *"several turnings, whirlings, or vortices in the ambient air"* [89].

As with many of the achievements of Hooke, they have been forgotten or are often accredited to others due to his argumentative personality and his battles with his peers [90]. Approximately a decade later, the well-known Dutch scientist Christiaan Huygens independently developed a similar technique for imaging the defects in lenses and mirrors [91]. Despite their important and independent contributions to the field, these men are seldom credited with their discovery which has become so fundamental to compressible aerodynamics.

The findings of Hooke and Huygens remained unheeded until a Swiss born physicist, Jean-Paul Marat developed what he called a *helioscope*. The *helioscope* is essentially a solar-powered, projecting microscope [92]. Marat used this device extensively in his research and published what is the first recorded shadowgraph sketch in his 1780 work, *Recherches physiques sur le feu* [3]. The original shadowgraphs, shown in Fig.3.1, show the plume rising from two hot objects and the plume from a candle. The transition to turbulence of the candle flame is clearly shown, over a century before Sir Osbourne Reynolds published his seminal paper on turbulent transition [93].

[1] The application of interferometry is not only difficult due to the number of optical components required, but also because in flows with discontinuities such as we have here, counting the number of fringes becomes almost impossible. Kleine et al. [86] compared the three density-based techniques and showed that the main disadvantage of interferometry is that the absolute sensitivity is finite. As we will see, this is not the case with schlieren or shadowgraph imaging, and as a result they are able to yield significantly better qualitative results.

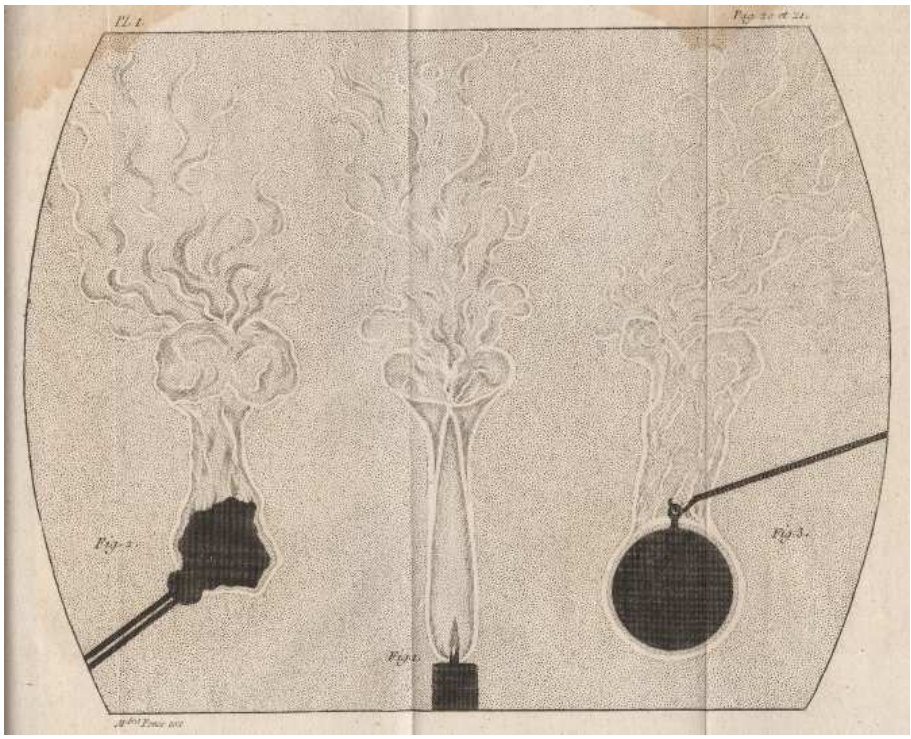

Figure 3.1: Original sketches of shadowgraphs seen by Marat [3]

All the preceding work was not acted upon until a French physicist, Léon Foucault, developed a test to measure the surface shape and imperfections in mirrors [94]. Foucault's *knife-edge test* is the first known use of a knife-edge, and therefore is the first recorded example of what we would recognise as a modern schlieren system [95]. Foucault never made any comments or records on disturbances in the air which he surely must have seen. Even though it was Foucault who first used a distinct knife-edge, it is the German physicist, August Töepler, who is often accredited with the invention of schlieren imaging, and it is he who had the distinction of naming the technique [96].

Töepler was the first person to use this method to image optical heterogeneities in *any* medium [97]. He named these *Schlieren*, meaning streak or striation in German. The accreditation of the modern schlieren technique to Töepler was still a point of contention in the early 20^{th} century. An article by Taylor & Waldram [98], noting methods of improving the technique, was met with an angry response by Smith of the National Physical Laboratory, who refused to acknowledge Töepler as the true father of the technique [99].

Töepler used his technique to visualise shock waves [96], leading to numerous publications. These articles proved to be both the starting point and inspiration for many researchers to follow, notably including: Ernst Mach, Peter Salcher, Ludwig Prandtl, Theodor Meyer, Carl Cranz and Hubert Schardin. Modern-day scientists and engineers who have become famous in the field for their work on schlieren optics include: Beric Skews, Anatol Roshko, Gary Settles and Harald Kleine. The latter has published many works on colour schlieren which more closely resemble art than science [86][100][101].

Development of quantitative schlieren was recently initiated by Meier and his colleagues at DLR, who championed a technique now known as background-oriented

schlieren (BOS) [102] [103] [104]. This technique, still relatively in its infancy, relies on measuring deformations of a background pattern and correlating them to a reference image. The mathematics of image correlation is closely related to PIV image cross-correlation, which will be briefly mentioned later (see Section 3.2.2). Recent additions to this technique include the addition of colour to the background image and using the different colour combinations to give more images to correlate between [105].

There are two methods of illuminating a schlieren imaging system: spark light source or continuous illumination. The setup of mirrors etc. is the same for both; the only differences are the light sources and imaging systems used. Spark schlieren uses a short-duration light pulse ($\approx 10^{-8}s$) and a high-resolution imaging device with the shutter left open. This has the advantage of high spatial resolution but is limited to a single image per run in most cases.[2] Historically, this has been the only method of visualising high-speed unsteady phenomena. Despite the single-shot nature of spark schlieren, it has been used to gain great insight into unsteady shock wave interactions. Continuous illumination schlieren uses a modern high-speed camera to image the flow and has excellent temporal resolution. However, at such high frame rates, spatial resolution is often compromised.

3.1.2 Theory

The working principles of schlieren and shadowgraph imaging will now be covered, but for a more extensive derivation and further information the reader is directed to the excellent book by Settles [107]. Light propagates in straight lines through homogeneous media. If there is any non-uniformity then the light experiences a change in refractive index. The refractive index of a medium, n, is a ratio of the speed of light in a vacuum to the speed of light in the medium $n = c_0/c$. The relationship between the refractive index and density is a simple linear one:

$$n - 1 = k\rho \tag{3.1}$$

Where k is the Gladstone-Dale coefficient and is dependent on the wavelength of light used, as well as the characteristics of the gas. For air, the Gladstone-Dale coefficient is weakly dependent on the wavelength of light [108]; however, it does mean that schlieren and shadowgraph optics are slightly more sensitive in infrared than they are in visible light. This can cause significant chromatic aberrations around strong schliere.

As light passes through regions of gas with a different refractive index, the wave front can be considered to be inclined.

[2] Papamoschou [106] developed a twin-spark schlieren system using two spark sources and one set of lenses.

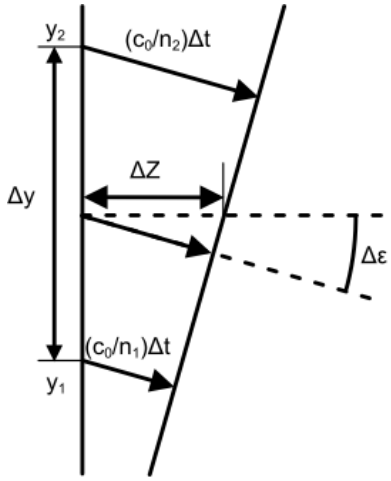

Figure 3.2: Diagram of refraction of light through a change in refractive index

From Fig.3.2 it can be seen that for small values of ε:

$$\sin \Delta\varepsilon = \frac{(c_0/n_2 - c_0/n_1)\,\Delta t}{\Delta y} \approx \Delta\varepsilon \tag{3.2}$$

with:

$$\Delta t = \Delta z \frac{n}{c_0} \tag{3.3}$$

replacing Δt yields:

$$\Delta\varepsilon = \frac{n}{n_1 n_2} \frac{n_1 - n_2}{\Delta y} \Delta z \tag{3.4}$$

As Δy tends to zero, Δn also tends to zero, therefore Equation 3.4 tends to:

$$\Delta y, \Delta n \to 0 \qquad \frac{d\varepsilon}{dz} = \frac{1}{n}\frac{dn}{dy} \tag{3.5}$$

For very small ε (ε is usually of the order of 10 arcseconds or lower), we can approximate $\varepsilon \approx \frac{dy}{dz}$, giving us:

$$\frac{\partial^2 y}{\partial z^2} = \frac{1}{n}\frac{\partial n}{\partial y} \tag{3.6}$$

Integrating once along the optical axis:

$$\varepsilon_y = \frac{1}{n}\int \frac{\partial n}{\partial y} dz \tag{3.7}$$

Similarly:

$$\varepsilon_x = \frac{1}{n}\int \frac{\partial n}{\partial x} dz \tag{3.8}$$

This can be evaluated along the optical length of the system to give:

$$\varepsilon_y = \frac{L}{n_0}\frac{\partial n}{\partial y} \tag{3.9}$$

$$\varepsilon_x = \frac{L}{n_0}\frac{\partial n}{\partial x} \tag{3.10}$$

These equations are the basis for schlieren and shadowgraph systems as they show the refraction of light with respect to change in refractive index normal to the optical axis.

3.1.2.1 Shadowgraph Specifics

Shadowgraph imaging, as the name suggests, is based on the imaging of shadows. The shadows are caused by the method shown in Fig.3.3. It shows that some light has been refracted by a disturbance. Light slows in regions of higher refractive index and speeds up in regions of lower refractive index. According to the induced curvature of the wavefront seen in Fig.3.2, this means that light bends towards regions of higher refractive index.

This explains the light pattern found in the shadowgraph of a flame seen by Hooke [88], reproduced by the author on a wall illuminated by light reflected from a nearby office block (Fig.3.4). The light is bent away from the flame as it has a lower refractive index than the air around it, causing the inside of the plume to be darker and the outside to be lighter.

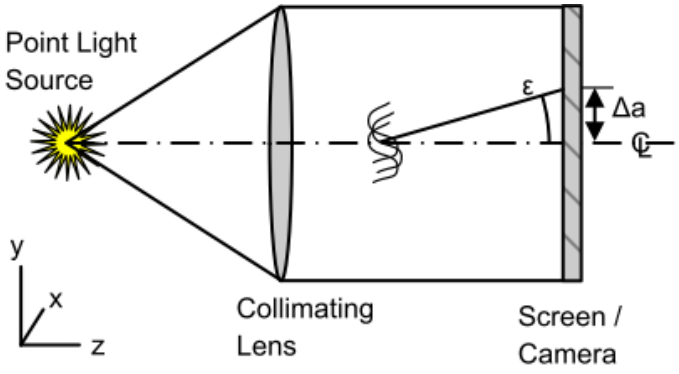

Figure 3.3: Principle of shadowgraphy

As can be seen in Fig.3.3, the variation of ε with x or y is what is measured on the screen. Differentiating Equations 3.9 and 3.10 gives:

$$\frac{d\varepsilon}{dy} = \frac{L}{n_0}\frac{\partial^2 n}{\partial y^2} \tag{3.11}$$

$$\frac{d\varepsilon}{dx} = \frac{L}{n_0}\frac{\partial^2 n}{\partial x^2} \tag{3.12}$$

This therefore shows that the shadowgraph technique is sensitive to the second spatial derivative of refractive index, i.e. ray displacement. The only way to increase the sensitivity of a shadowgraph system is to increase the distance between the disturbance and the imaging plane; therefore, increasing Δa. If this distance is too large, flow features can become obscured, as large changes in density, such as shocks or strong vortices, will appear as thick black shadows or become too blurred to give the required information. This can be overcome by using the *focused* shadowgraph technique, which is essentially the schlieren technique without a knife-edge.

Figure 3.4: Homemade shadowgraph of a lighter flame

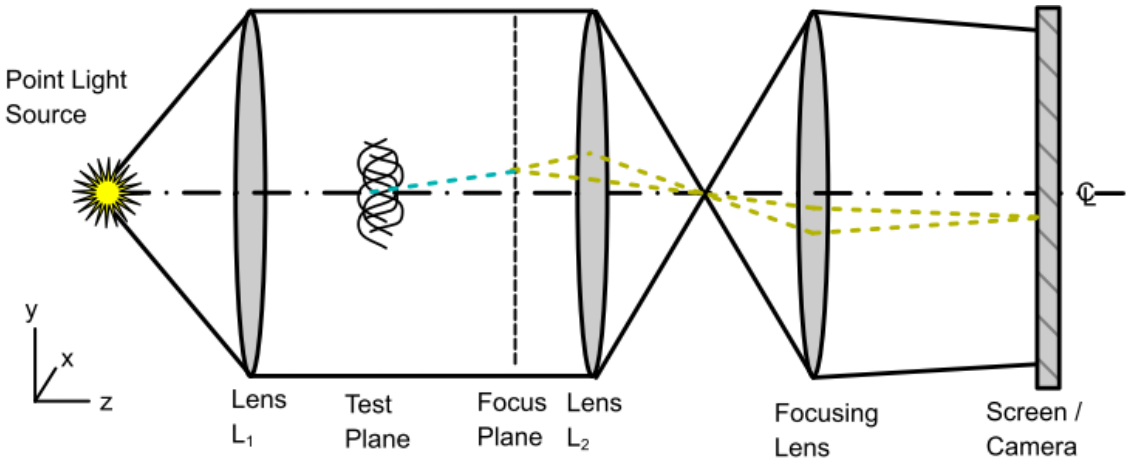

Figure 3.5: Principle of focused shadowgraphy

If a point light source is used and the shadowgraph image is focused onto an imaging plane (imagine Fig.3.6 without a knife-edge), then there will be no disturbances to image. Therefore, removing the knife-edge completely will produce what is known as a focused shadowgraph. This is depicted in Fig.3.5. However, as extended light sources are finite in size, they have an associated depth-of-field. This means that not all the field can be in focus at once. Biss et al. [109] showed that if the camera focal plane and the test plane are coincident, almost no phenomena are visible. However, as the distance between the focal plane and the test plane is increased, the sensitivity of the *focused* shadowgraph is increased, albeit at the cost of blurring the test plane. This increase in sensitivity can be introduced either by deliberately defocussing the test plane or having an optical system with a short depth-of-field. The trade-off between geometric blur and sensitivity yields the limit of what can be measured using the focused shadowgraph technique. Section 3.1.5 will cover this in more detail.

3.1.2.2 Schlieren Specifics

The schlieren schematic, shown in Fig.3.6, contains lenses; however, the same mathematical principles apply to systems that utilise mirrors. The wave pattern shows that a *bundle* of rays are deflected by a disturbance. When these rays are focused on the knife edge, some of the rays are blocked and some pass through. Whether or not the rays pass through is down to the deflection angle caused by the schliere. Therefore, schlieren systems are described by Equations 3.9 and 3.10.

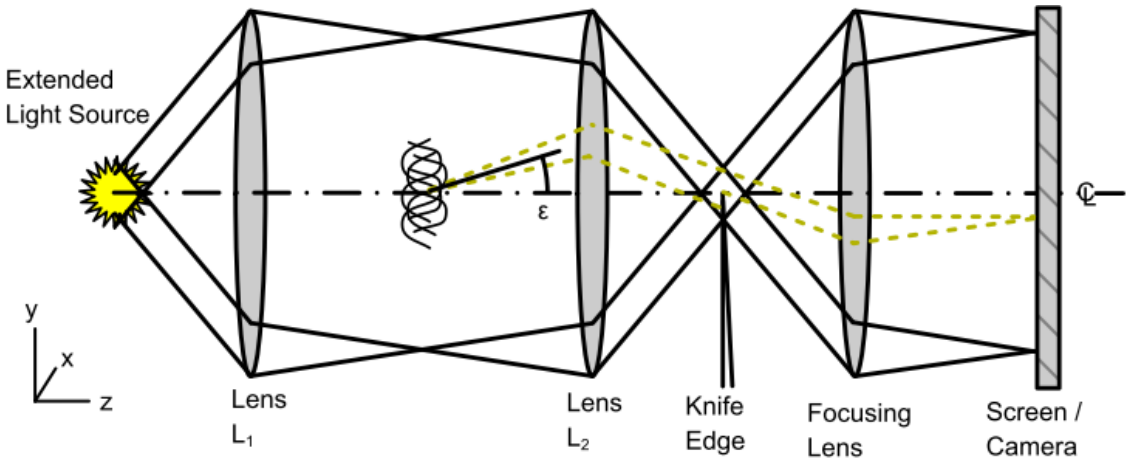

Figure 3.6: Principle of schieren imaging

The user can change the sensitivity of a schlieren system by changing the amount of light cut off at the knife-edge. The sensitivity of a schlieren system can be analysed by first considering the illuminance, E, that falls on the imaging plane without any knife-edge.

$$E_0 = \frac{Bbh}{m^2 {f_1}^2} \tag{3.13}$$

Where B is the illuminance from the light source, b is the width of the slit source, h is the height of the slit source, f_1 is the focal length of the first mirror and m is the magnification factor. The height of the source can be related to the unobstructed height of the light source by considering the image at the cut-off plane $h = af_1/f_2$, Fig.3.7.

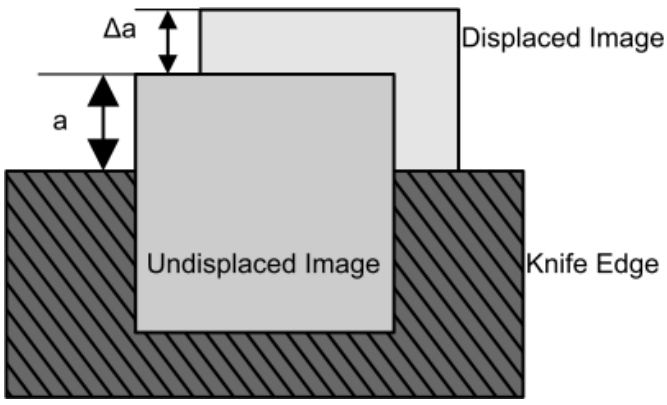

Figure 3.7: Diagram of knife-edge plane

$$E_0 = \frac{Bba}{m^2 f_1 f_2} \tag{3.14}$$

Assuming a disturbance causes a refraction angle, ε_y, the image at the cut-off plane will be displaced by $\Delta a = \varepsilon_y f_2$. Substituting Δa for a in Equation 3.14 gives the incremental change in illuminance on the imaging plane, ΔE.

$$\Delta E = \frac{Bb\varepsilon_y}{m^2 f_1} \tag{3.15}$$

Contrast is defined as the ratio of *luminance difference* to *average luminance*:

$$C \equiv \frac{\Delta E}{E} = \frac{f_2 \varepsilon_y}{a} \tag{3.16}$$

The sensitivity, S, of any system can be defined as the rate of change of output with respect to input [107]. In terms of schlieren imaging, this can be defined as the rate of change of contrast with respect to refraction angle:

$$S = \frac{dC}{d\varepsilon} = \frac{f_2}{a} \tag{3.17}$$

From Equation 3.17, we can see that the sensitivity of a schlieren system can be augmented either by reducing the unobscured image height (increasing the knife-edge cut-off) or by increasing the focal length of the second lens or mirror. However, as the knife-edge cut-off is increased ($a \to 0$) the overall measurement range decreases [110]. The more the knife-edge is moved away from the 50% cut-off point (i.e. $a = h/2$) the more nonuniform the measurement range becomes. As more light is cut out, the darkening measurement range narrows and the lightening measurement range widens. The system can then be described as over-ranged.

The ultimate limit on schlieren sensitivity is due to diffraction effects at the knife-edge [111]. As $a \to 0$, the knife-edge begins to act like a narrow slit and the well-known diffraction effect begins to smear the image. Although the sensitivity of the system is at its maximum, the resolving power is at its lowest. Therefore, a compromise between these conflicting requirements is needed.

3.1.3 Limitations

Despite the capabilities of the schlieren and shadowgraph techniques, they are far from the perfect diagnostic tool. The integration required to give Equations 3.9 & 3.10 assumes that changes along the optical axis are negligible. In three-dimensional phenomena, this is not the case. Therefore, the integrative nature of both schlieren and shadowgraph techniques mean that they are more applicable to two-dimensional rather than three-dimensional phenomena. This can also give erroneous results if there are any disturbances along the optical path apart from the test section. This can be especially apparent when using a high-intensity arc lamp, as the convection currents caused by the high temperatures involved can appear in the final schlieren image.

Schlieren and shadowgraph techniques are regarded as qualitative techniques rather than quantitative. It is true that it is extremely difficult to extract quantitative measurements of density from these techniques (interferometry is usually

required for that [112] [113]). However, other information can be gained, such as shear layer spreading, wave propagation speeds and shock wave angles.

3.1.4 Applications

Schlieren systems are applicable to almost any type of flow, provided optical access is available. This ranges from investigating shock waves, shear layers and turbulence to *seeing sound*, as they can often be sensitive enough to pick up acoustic waves [94] or even weaker phenomena [114]. They can also be used to see heat transfer patterns, combustion and even microscopy.

Colour filters can be used as source masks as a replacement for a knife-edge in a schlieren setup to produce colour images. Colour schlieren has the advantage that it can not only show variations in refractive index very clearly, but if a two-dimensional source mask is used, it can also give information about the direction of the gradient [115]. Howes describes this as *"the principle benefit of color is in labeling the refraction with respect to direction and magnitude"* [116].

If a fluid of different density can be introduced into the flow, it will be very visible using schlieren and shadowgraph. Several researchers have made great use of this fact (Pierce [117] and Roshko [57] are two excellent examples of this method).

Schlieren and shadowgraph systems can be used to create x-t diagrams (see Section 2.2.1) by extracting a line of pixels from a *stack* of schlieren images and superimposing them above each other. This can be completed quickly and easily and is known as image *re-slicing*. From x-t diagrams, shock propagation speeds can be calculated by measuring the gradient of the line present.

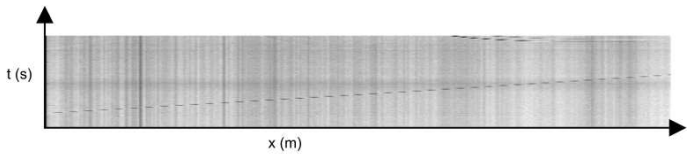

Figure 3.8: x-t diagram for a $M_i = 1.46$ shock

3.1.5 Setup

The schlieren and shadowgraph system used in this project is the ubiquitous Z-style system. Illumination comes from an in-house-built 300W Xenon arc lamp. The beam expands towards a hemispherical lens which condenses the beam to a slit placed at the focal distance from the first mirror. The two mirrors are 8 inches in diameter at $f_{\#} = 4.5$, giving a focal length of 3 feet. The imaging device is the Shimadzu HPV-1, capturing at 250 kfps with an exposure time of 2μs. The HPV-1 is a fast frame CCD camera with an 8-bit dynamic range. Despite the powerful light source, the full dynamic range of the HPV-1 could not be utilised with a 2μs exposure time. However, a longer exposure time would have blurred the moving shock waves, and so 2μs was found to be the best compromise between these requirements.

In order to eliminate the effect of coma and minimise astigmatism, the angles shown in Fig.3.9 are: $\delta_1 = \delta_2 = 3°$. Astigmatism is a smearing effect caused by having different optical lengths along the optical axis and the edge. This arises due to the tilting of the mirrors seen in Fig.3.9. It is not possible to eliminate the problem

of astigmatism in Z-style schlieren setups; however, it is possible to minimise them by having the smallest angle, δ, possible. The difference in optical path length is given by Equation 3.18.

$$\Delta f = f\frac{\sin^2\delta}{\cos\delta} = 2.77mm \tag{3.18}$$

This indicates that, for this system, astigmatism is not a significant problem [107].

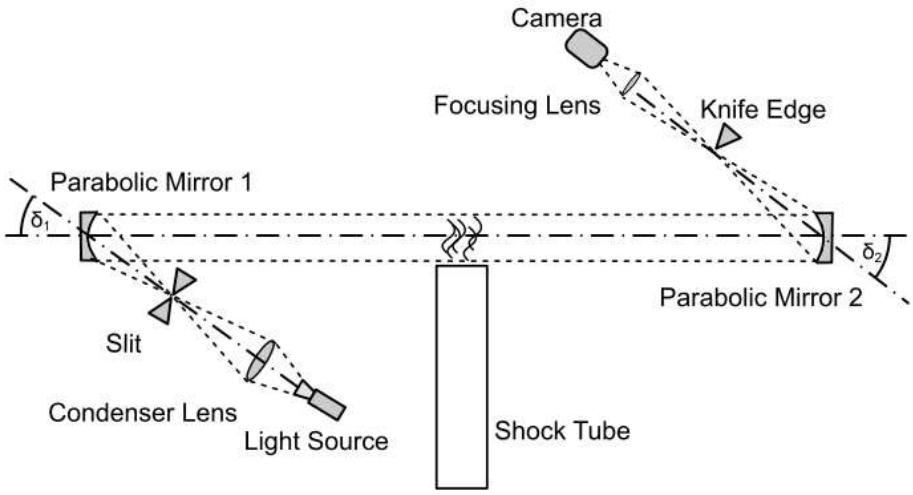

Figure 3.9: Schlieren setup

The beam is the passed through then test section to the second mirror and on to the knife-edge. Two optical zooms will be employed in this project, with careful attention paid to the depth-of-field in each case. The focusing lens for the full-field images is a combination of 55mm +1 and +2 diopter macro lenses. These lenses have an optical power of 3, giving them a focal length of 0.33m. For the close-up images, the beam was allowed to expand further from the knife-edge before passing through a +1 diopter lens to produce a sharp image. These lens combinations were deliberately chosen to have a shallow depth-of-field. The imaging device is the Shimadzu HPV-1. The sensor of this camera is 20.7 x 17.2 mm in size (pixel size 66.7μm). The circle of confusion of the optical system is set to be the pixel size of the HPV-1. This allows us to estimate the depth-of-field of the system once we calculate the hyperfocal distance, H (Eq.3.19) and eventually the depth-of-field [118].

$$H = \frac{f^2}{f_{\#}c} + f \tag{3.19}$$

Where f is the lens focal length, $f_{\#}$ is the f-number and c is the circle of confusion. Now we can calculate the near (D_n) and far (D_f) distances of acceptable sharpness

$$D_n = \frac{s(H-f)}{H+s-2f} \tag{3.20}$$

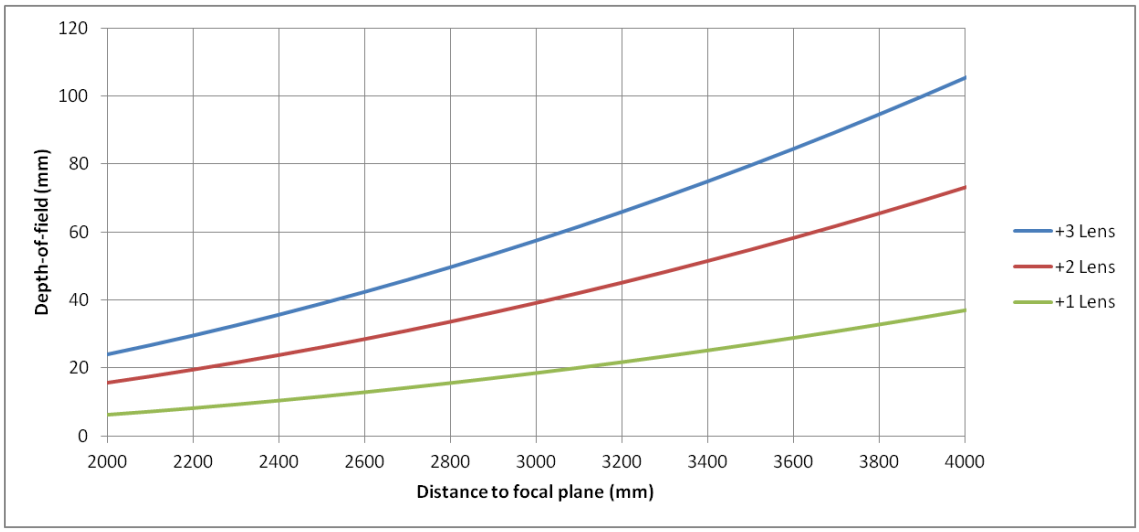

Figure 3.10: Depth of field of a shadowgraph system

Table 3.1: Depth of field

	Full-Field	Close-Up
f (mm)	330	1000
$f_{\#}$	6	23.6
s (mm)	3000	3200
H (mm)	279000	650000
D_n (mm)	2971	3189
D_f (mm)	3029	3210
DOF (mm)	57.5	21.7

$$D_f = \frac{s(H-f)}{H-s} \tag{3.21}$$

where s is the distance to the focal plane.

Fig.3.10 shows the dependency of the depth-of-field on the distance from the focal plane, which can be though of as a measure of the magnification. This shows us that for a larger magnification we need to use a longer lens in order to keep a shallow depth-of-field. With this in mind, Tab.3.1 shows the parameters used for the full-field and close-up shadowgraph images.

The scale of the images, α, is and 4.71 and 7.80 px/mm for the full-field and close-up images respectively. The field of view of the schlieren setup is shown in Fig.3.11. The finite exposure time of any image will lead to the blurring of moving objects. Based on the scale of the image in pixels per mm, we can calculate the expected blur from the shadowgraph and schlieren results for different incident shock Mach numbers. Tab.3.2 shows the blur in the full-field and close-up images.

When imaging of distributed density gradients was required, a knife-edge was introduced at the focal point of the second mirror.

The triggering of the image acquisition is performed using a Kulite XT190-M transducer connected to a Fylde 254 GA Mini Amp. This amplifier has a bandwidth

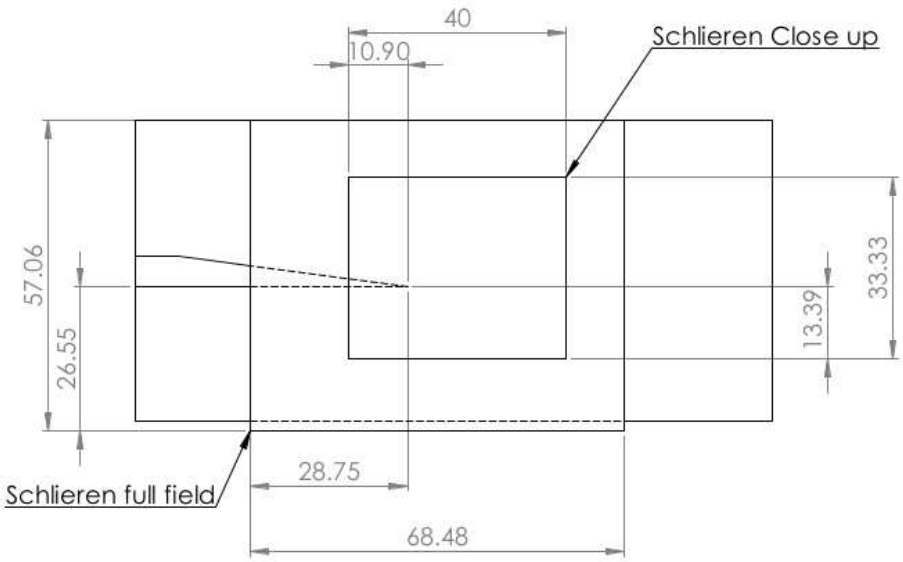

Figure 3.11: Field of view of the schlieren system (all dimensions in mm)

Table 3.2: Shock blur for full-scale images

M_{ie}	Geometric Blur (mm)	Full-field Blur (Pixels)	Close-up Blur (pixels)
1.28	0.87	3.96	6.79
1.46	0.99	4.51	7.74
1.55	1.05	4.79	8.22

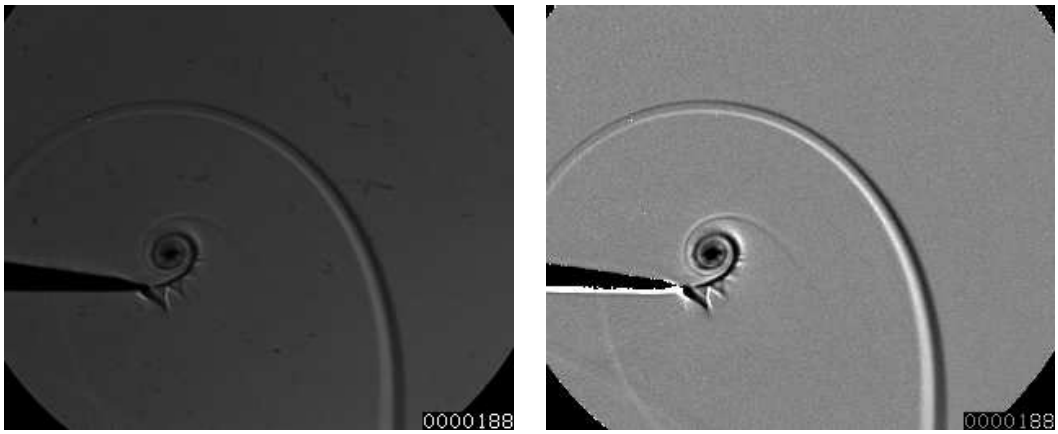

(a) Raw shadowgraph image (b) Processed shadowgraph image

Figure 3.12: Two identical shadowgraph images before and after processing

of 40kHz to 3dB. This signal is sent to a Photonics Four Pulse Sequencer (SEQ400) which creates a trigger pulse once a threshold level is detected from the transducer and allows the user to set a hardware delay before acquisition.

3.1.6 Post-Processing

Schlieren and shadowgraph images can often suffer from non-uniform illumination or excessive darkness when trying to reach a specific sensitivity. Artifacts such as scratches on windows can also be seen and make the images difficult to comprehend. Factors such as non-uniform illumination can be reduced by dividing the test images by a tare image with no flow. This is essentially the same processing technique as is used with intensity-based pressure-sensitive paint (see Section 3.4.2). Provided that these images are divided at 32-bit precision, the contrast and brightness can be scaled to make the image visible and can often show flow features that otherwise would have been missed. Fig.3.12 shows the effect of processing in this way. When dividing two images, areas of darkness can often have regions of brightness around them. These edges are regions where there is no light in the initial image. This means that, provided that there is a small amount of light there in subsequent images, large values will be calculated. This is an artifact of the processing technique, not optical misalignment.

The Shimadzu HPV-1 has sometimes exhibited an apparent difference in ISO over its recording time. This is sometimes periodic, although it is not predictable from test to test. Also, the first and last eight images recorded are often significantly brighter than the others. This can be seen in the x-t diagrams, as it appears as horizontal bands (Fig.3.15). This phenomenon does not detract from the measurements; however, it does make them slightly more difficult to present.

3.1.7 Uncertainty and Repeatability

The x-t diagrams created from the shadowgraph images allowed for the incident shock speed to be calculated and compared with theory. As the incident shock wave propagation speed is unaffected by the apex geometry used, both the sharp and round geometries can act as repeats to help with the uncertainty estimation. Fig.3.13

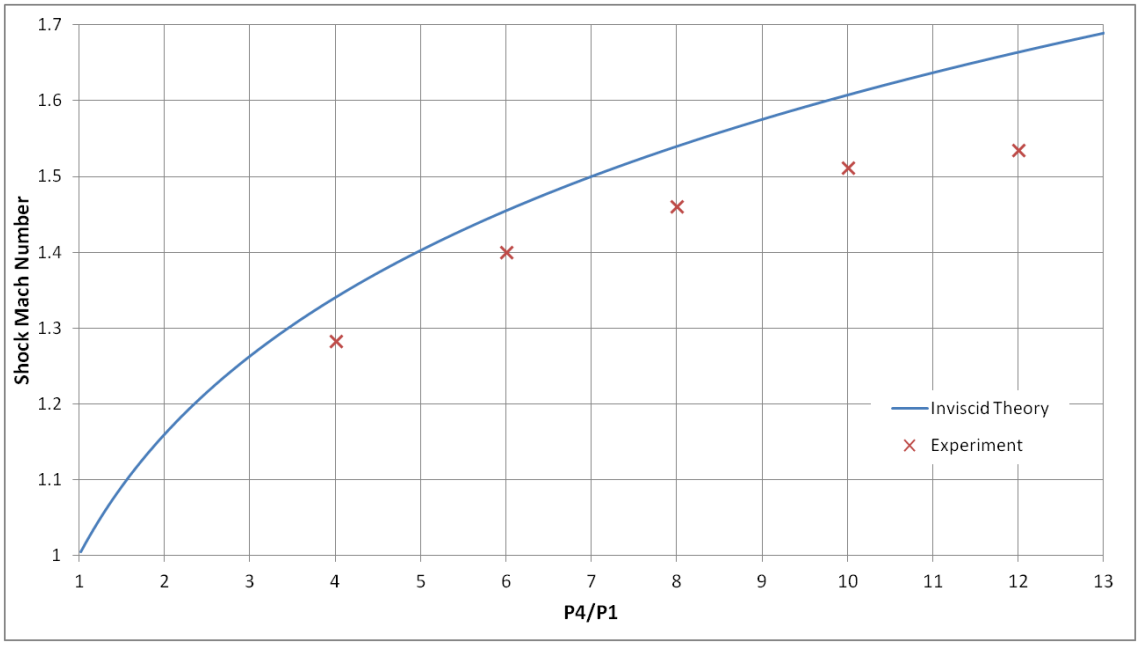

Figure 3.13: Experimental vs. theoretical incident shock Mach number

Table 3.3: Theoretical and experimental shock Mach numbers

P_4/P_1	Theoretical Mach number M_{it}	Experimental Mach number M_{ie}	Discrepancy
4	1.34	1.28	-0.06
6	1.45	1.40	-0.05
8	1.54	1.46	-0.08
10	1.61	1.51	-0.10
12	1.66	1.55	-0.11

shows the discrepancy between the experimental and theoretical shock Mach numbers for a range of pressure ratios. This is to be expected for the reasons discussed in Section 2.2.3. As these measurements are the most time accurate measurements of shock speed that are performed in this research, the shock strength (P_2/P_1) is assumed to be that of the experimental Mach number measured in the x-t diagram. As a result of this, the induced theoretical velocities and pressures that will be compared with the experimental values are those for an inviscid shock with the experimental shock Mach number. Inviscid simulations (to be introduced later) are performed at pressure ratios corresponding to the experimental Mach number, not to the experimental pressure ratio, P_4/P_1.

Based on the bandwidth of the amplifier and the fact that the XT190M has a rise time of the order of microseconds, the uncertainty in the exact triggering time is expected to be about $\pm 15\mu$s. This was found to be the case in the x-t diagrams produced from the shadowgraph images. An example of 3 x-t diagrams for $P_4/P_1 = 4$ is given in Fig.3.14. The gradient produced by the moving shock wave is extremely similar; however, the shocks arrival time can vary. This tells us that the shock strength is the same for these tests, even though the apparent delay

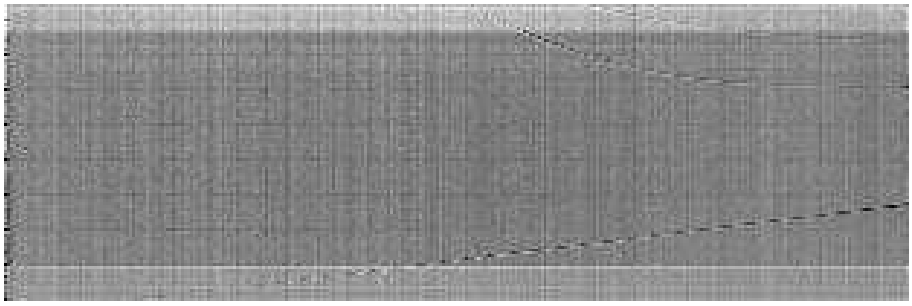

(a) Run 1 (Shadowgraph)

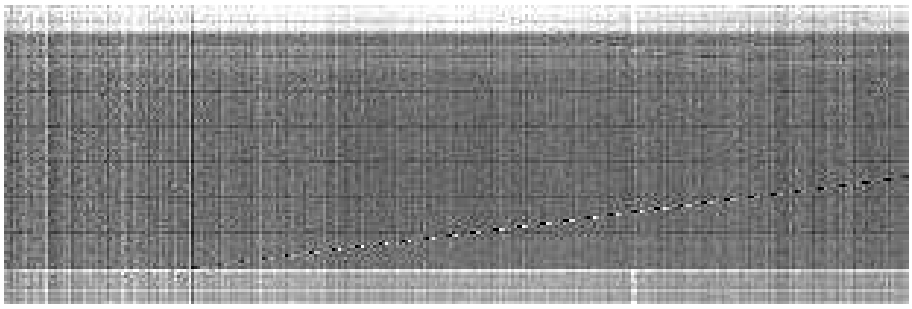

(b) Run 2 (Shadowgraph)

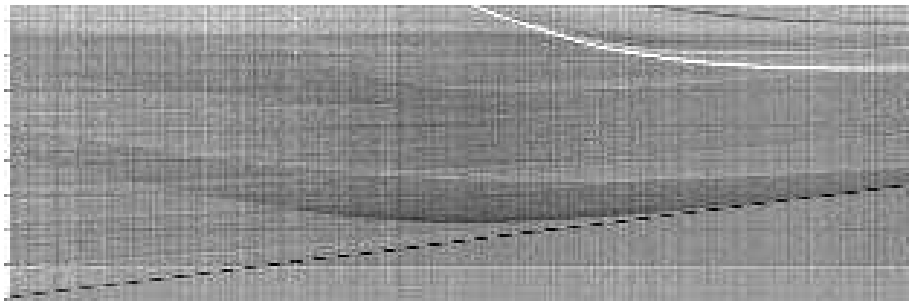

(c) Run 3 (Schlieren)

Figure 3.14: Experimental x-t diagrams resliced from 101 frames

is different. The curved waves appearing at the top of the x-t diagrams are reflected diffracted waves returning from the upper surface of the test section. The shock position is only measured until the reflected expansion wave has reached the reslice line (which is as low as it can be in the image). Abate & Shyy refer to this as when the shock becomes critical [79]. It physically means that the shock wave is no longer planar and will therefore have a different propagation velocity.

Fig.3.15 shows the shock position as a function of time for both full-field and close-up tests for all three pressure ratios tested. The gradients of these lines represent the propagation speed of the shock wave. For each pressure ratio, five shock speeds were analysed and the statistical uncertainty is presented in Tab.3.4. The bias error is a combination of incorrectly estimating the scale of the images by .5 mm and incorrectly estimating the shock wave position by 2 pixels. The random errors are calculated to 95% confidence (1.96σ).

Estimating the uncertainty in velocity estimations from schlieren measurements is relatively simple. The images are scaled so that $\frac{x_{image}}{\alpha} = x_{real}$, where α is the scale of the images in pixels per mm. Substituting this into the simple equation

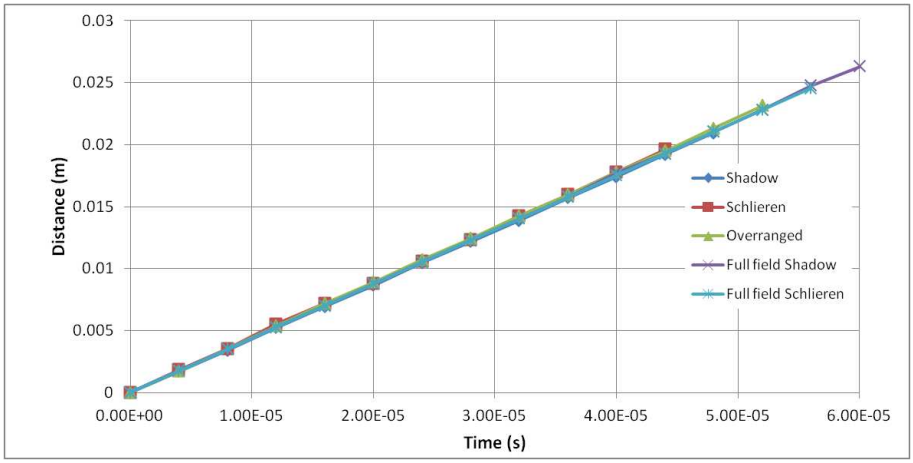

(a) $P_4/P_1 = 4$

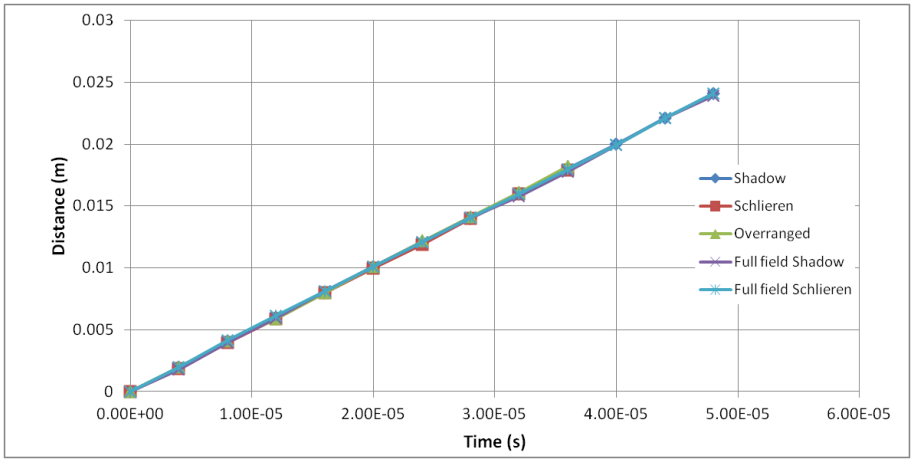

(b) $P_4/P_1 = 8$

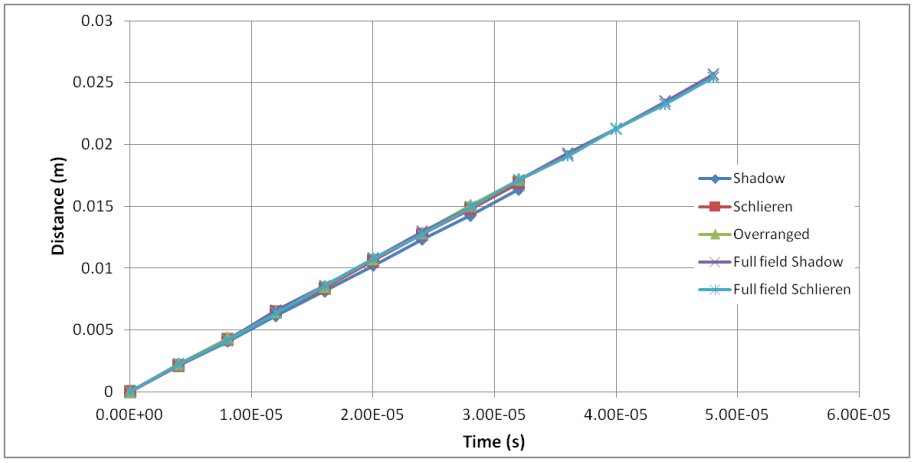

(c) $P_4/P_1 = 12$

Figure 3.15: Shock wave propagation measured from the x-t diagrams

Table 3.4: Incident shock Mach number uncertainty

P_4/P_1	Standard Deviation (m/s)	σ_{random} (m/s)	Total Velocity Uncertainty Ψ (m/s)	Mach Number Uncertainty
4	4.43	3.07	3.10	$\pm$0.009
8	2.33	1.72	6.84	$\pm$0.020
12	8.46	6.27	7.61	$\pm$0.023

for velocity and differentiating with respect to x gives us the sensitivity coefficient $\frac{\partial V}{\partial x_{image}} = \frac{1}{\alpha t}$, where t is the time over which the distance is estimated and has a minimum value of 32μs.

$$\sigma_{bias} = \sqrt{\left(\frac{\partial V}{\partial x_{image}} \times \sigma_{shockposition}\right)^2 + \left(\frac{\partial V}{\partial x_{image}} \times \sigma_{xscale}\right)^2} \tag{3.22}$$

This gives us a constant bias error of $\sigma_{bias} = 4.33$.

In order to characterise the random error between runs, the shock propagation velocity is measured in eight separate experiments and the random deviation is calculated. The overall uncertainty is then given by

$$\Psi = \sqrt{\sigma_{random}^2 + \sigma_{bias}^2} \tag{3.23}$$

3.2 Particle Image Velocimetry (PIV)

Particle Image Velocimetry (PIV) is an essentially non-intrusive method[3] of measuring the velocity components of a whole flow field in one test. This gives it a distinct advantage over more traditional methods of measuring point velocities, such as hot-wire anemometry (HWA), laser Doppler anemometry (LDA) and pitot measurements. PIV is capable of capturing phenomena which are almost impossible to capture with traditional point methods, such as the complex structures of shed vortices. This increase in spatial resolution compared to traditional techniques is a similar leap forward to the increased resolution of PSP over pressure tappings.

3.2.1 History and Development

The earliest recording of particle-based flow diagnostics can be traced back to the work of Ludwig Prandtl in 1904 [119]. In this early work, a suspension of mica particles in water was used to visualise the starting flow behind an airfoil. This led him to develop theories about the starting vortices and also to show the effects of flow separation and vortex streets.

Over the past 20 years PIV has become a powerful tool of scientists exploring fluid flows. Initial attempts to quantitatively measure the velocity of a fluid using seeder particles were performed using what is now known as laser speckle velocimetry. This technique involved measuring the interference fringes created by pairs of displaced speckles [120]. Laser speckle velocimetry requires the density of particles in the fluid to be extremely high. This can lead to two-phase flow effects, which is not usually the intention.

Modern PIV systems, previously called high-density PIV, have evolved from low-density PIV, also known as particle-tracking velocimetry (PTV). The distinction is based upon the concentration of seeding particles in the flow. PTV uses simpler image processing algorithms than PIV, as there are much fewer particles in the flow. The nature of PIV means that high-speed applications are more challenging than low-speed applications, due to the more complicated imaging systems involved and expensive, high-energy, double-pulsed lasers.

When compared with integrative diagnostic techniques such as schlieren imaging, PIV has the advantage that the flow can be imaged in a 2D plane, showing structures that could otherwise be missed. PIV is not only capable of measuring two velocity components, but it is also capable of capturing all three velocity components in a given plane by use of stereoscopic imaging. Recent advances in PIV technology have shown the development of tomographic PIV, which involves using four cameras to measure all three components of velocity in a given laser volume rather than a laser plane [121]. Tomographic measurements require an enormous amount of processing power and data storage and currently have not been applied to high-speed flow such as the ones investigated in this project. Despite tomographic PIV appearing to be the future of particle-based flow diagnostics, regular two-dimensional PIV will be used in this project due to its robustness and lower processing time.

[3]The use of large seeder particles can be intrusive, altering the flow; however, this can be avoided by a proper choice of seeding material.

3.2.2 Theory

PIV is based on the displacement of particles suspended in the flow between two images. Given a known delay between consecutive images and assuming that individual particles can be identified in both images, the velocity of each particle can be calculated. Assuming that the particles are small enough not to affect the flow, but to accurately follow it, the velocity of the flow can be calulated. The simplicity of the basic explanation above understates the complexity of the systems and mathematics involved in PIV experiments. A full derivation of the mathematics of PIV and the image processing involved is beyond the scope of this project; however, an error analysis and detailed discussion of seeder particle characteristics will follow.

The flow is illuminated by a high-power, double-pulse, typically ND:YAG laser with a pulse energy of approximately 400mJ. This laser is passed through a series of lenses to create a laser sheet. The flow is seeded with light-scattering particles. These particles scatter light towards the imaging device, usually a high-speed camera with a filter to cut out background noise. The imaging device records two images separated by a short time (Δt). These images are then broken down into smaller sections, called *interrogation regions*, to be analysed by the data acquisition system. The smaller the size of the interrogation region, the smaller the flow features that can be captured. However, if the interrogation region is too small then there is the possibility of the particle moving from one window to another, causing large errors. Some researchers [122] [123] have applied an iterative grid refinement technique based on the multi-grid method. This adaptive grid is crucial in high-speed applications of PIV, as the presence of sharp gradients (i.e. shock waves) tends to be smoothed out if large interrogation regions are used [124].

In order to ascertain the velocities of the particles in the flow, the two images must be compared. The process of determining which particle has travelled to where inside the interrogation region is called cross-correlation. This is a statistical analysis that shows the probability that the particles in each image have been correctly identified.

3.2.3 Seeder Particles

Seeder particles have two functions in PIV experiments:

- To follow the path of the flow as closely as possible
- To scatter light to the PIV imaging device

These two requirements are conflicting in that smaller particles follow the flow more closely but larger particles scatter more light. Some seeder particles such as TiO_2 perform both of these functions very well; however, they are difficult to seed into the flow reliably. Therefore, the selection of seeder particles is a compromise between these requirements and ease of use. Low-density particles are the best option for vortical flows, as centrifugal forces tend to eject heavy particles [125].

The analysis of the seed particles' performance as flow tracers is based upon Stokes' drag law and is shown by Raffel et al. [126]. Equation 3.24 shows the *slip velocity*, U_s, which is the difference between the seed particle velocity (U_p) and the flow velocity (U). The particle diameter is d_p and the particle density is ρ_p.

This equation is valid for particles bigger than 1 micron in diameter; however, below this size, the Knudsen number (based on the particle diameter $K_n = \lambda/d_p$) becomes sufficiently large that the assumption of continuum dynamics is no longer valid [127]. In this case, Stokes' drag law can be corrected using Cunninghams' slip correction factor, C_u, which is an empirical relationship (Equation 3.25) based on Knudsen number. If the seed particles are even smaller, i.e. smaller than the mean free path length, then Brownian motion should be taken into consideration [127]. The response of the seed particle to a step change in velocity, such as a shock wave, can be modelled by a single exponential, as in Equation 3.26, where τ_s is the relaxation time given by Equation 3.27.

$$U_s = U_p - U = {d_p}^2 \frac{(\rho_p - \rho)}{18\mu} C_u \tag{3.24}$$

where,

$$C_u = 1 + K_n \left[A + Be^{-\frac{C}{K_n}} \right] \tag{3.25}$$

where A, B and C are empirically derived constants. Jennings [128] showed values of these constants estimated by previous researchers and showed their effect on C_u. The values estimated by Jennings will be used in these calculations: $A = 1.252$, $B = 0.399$, $C = 1.10$.

$$U_p(t) = U\left(1 - e^{-\frac{t}{\tau_s}}\right) \tag{3.26}$$

$$\tau_s = {d_p}^2 \frac{\rho_p}{18\mu} C_u \tag{3.27}$$

Melling [129] shows similar results to those in Table 3.5, stating that for supersonic flows the particle diameter should be sub-micron, otherwise the velocity lag becomes prohibitively large. It was shown computationally by Samimy & Lele [130] that the size of the particles shown in Table 3.5 should faithfully follow the flow for the velocities of interest in compressible shear layer experiments. However, more recent studies by Ragni et al. [131] and Ghaemi et al. [132] have shown that, even when using nanoparticles, the relaxation time can still only be as low as $\approx 0.3\mu$s.

Clearly, it is advantageous to have a relaxation time which is as short as possible. However, smaller particles scatter less light, making it much harder to image them. This is the reason that applications of PIV in gas flows require more powerful and therefore more expensive lasers than liquid flows.

The values in Tab.3.5 are based on a normal shock in an isentropically expanded Mach 1.5 flow with an initial temperature of 300K. This gives a shock strength of 2.46, giving a velocity drop of 200 m/s. The relaxation distances shown in Tab.3.5 are for steady flow. Fig 3.16 shows the dependency of the response characteristics on particle diameter for various materials. If the flow is psuedo-steady, in that it is oscillatory but can be time-averaged, the response times above still apply. However, if the flow is transient, as in the case of shock wave diffraction, a slightly more involved approach must be used.

During the characteristic rise time shown above, the particle is accelerating towards the flow velocity. However, if the flow is induced by a moving shock wave, a

Table 3.5: Relaxation Characteristics of Seeder Particles

Particle	ρ_p $[Kgm^{-3}]$	d_p $[\mu m]$	τ_s $[\mu s]$
Al_2O_3	3970	2	51.6
		1	13.4
		0.5	3.55
		0.1	0.23
TiO_2	3500	2	45.5
		1	11.8
		0.5	3.19
		0.1	0.21
$CaCO_3$	2830	2	36.8
		1	9.57
		0.5	2.58
Glass Balls	2600	2	3.38
		1	8.79
		0.5	2.37
Olive Oil	970	2	12.6
		1	3.28
DEHS	912	2	11.9
		1	3.08

theoretically instantaneous velocity change, the shock wave has propagated further downstream during the rise time. In order to calculate the shock spreading distance (i.e. the distance over which an instantaneous velocity change is spread), first we must integrate Equation 3.26 with respect to time to attain the distance travelled in the relaxation time, x_r.

$$x_r = U\left[t + \tau_s\left[1 - e^{-\frac{t}{\tau_s}}\right]\right] \tag{3.28}$$

This distance should then be subtracted from the distance the shock has travelled in this time. Fig.3.16b shows the spreading of a shock wave by particles commonly used in PIV. The shock Mach number of this analysis is 1.34, giving an induced velocity of $\approx$ 170 m/s. It should be noted that some of the particles cannot be reliably generated at sizes smaller than those shown in Fig.3.16.

As shown in Table 3.5, olive oil is an excellent seeder material as it has very good relaxation characteristics. Olive oil can be atomised by numerous methods; however, a Laskin nozzle is the simplest and the most cost-effective. Olive oil is used as the seeder material in the majority of experiments at the University of Manchester, as it is reliable and simple to use. However, the *relatively large* particle size limits the application of liquid seeder materials in extremely high-speed or transient flows; as a result, solid particles are often used.

Generation of uniform seeder particles is often difficult to achieve when seeding with solid particles such as Al_2O_3. Although solid seeder material is generally bought in bulk from a supplier to sizes as small as $15nm$, when they are seeded into the

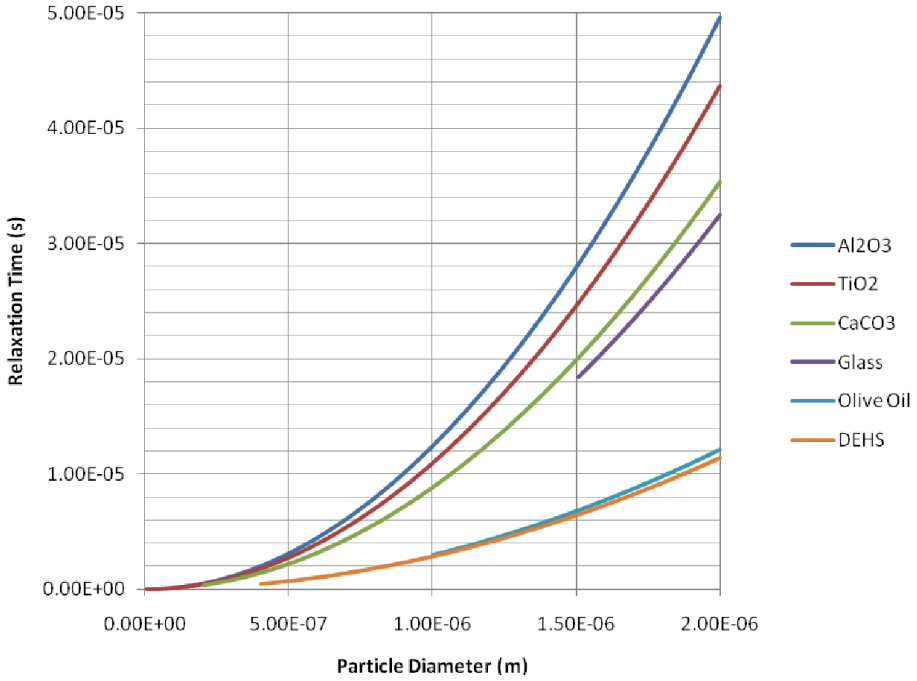

(a) PIV particle relaxation distance

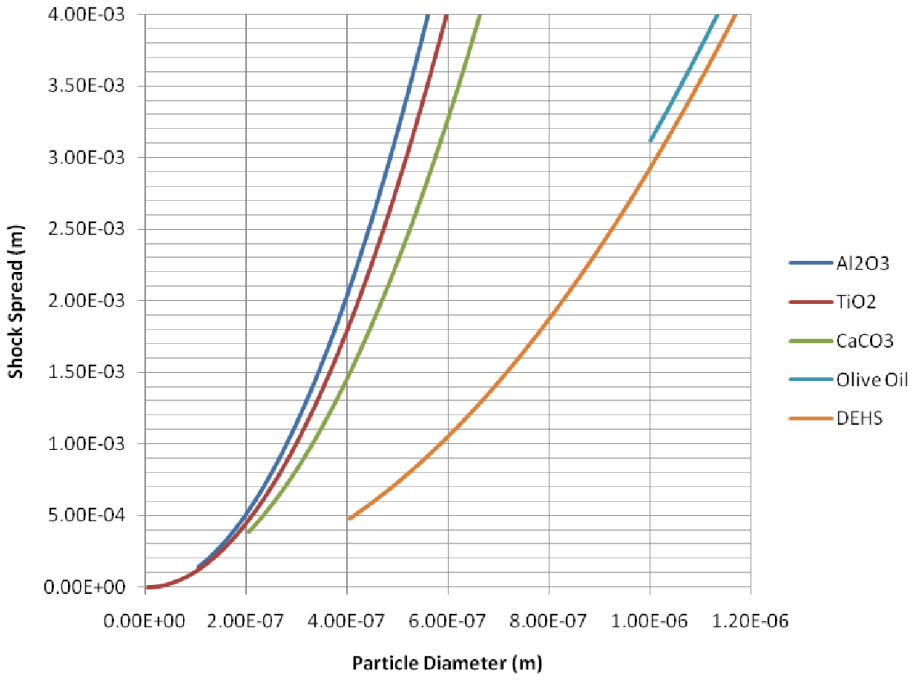

(b) Unsteady shock wave spreading

Figure 3.16: PIV particle relaxation characteristics

flow they can agglomerate due to their hydrophilic nature to form larger, irregular particles (see Fig.3.17). Ragni et al. [131] attempted to overcome this problem by baking the seeding material in an oven before testing, hoping to dry the material further. This proved successful in reducing the relaxation time of particles, with the curious exception of the smallest TiO_2 particles. Solid seeder material used in this study will be baked overnight at 350K before testing. Both Fig.3.17a and Fig.3.17b have been passed through the seeder described in Section 3.2.6; however, the particle drum had been baked for Fig.3.17b and was not for Fig.3.17a.

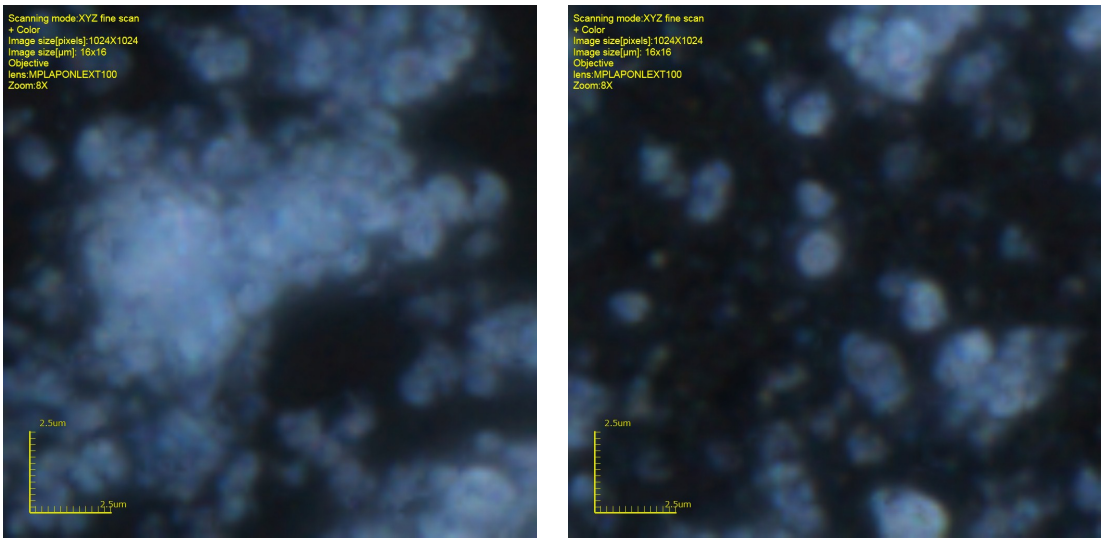

(a) Particles before baking

(b) Particles after baking

Figure 3.17: Laser confocal microscope images of Al_2O_3 particles with and without baking

According to Melling [129], the ideal concentration of seeder particles for high-speed measurements should be $\approx$ 15 particles per interrogation volume. Seeding open-ended, continuous high-speed wind tunnels with an adequate number of seeder particles is extremely challenging due to the flow rates of the atomisers involved. However, seeding shock tubes and variants thereof (Ludwieg tubes, shock tunnels etc.) is simpler as, the test section can be seeded before the test run [133].

3.2.4 Limitations

Despite the excellent data that can be captured with PIV systems, they do have some limitations. Laser repetition rate sets the ultimate capture limit for a system. Modern double-pulse lasers are capable of 10 kHz. The Δt between images is ultimately set by the imaging device. This sets the maximum velocity that can be measured in a given interrogation region. The resolution of the imaging system limits the number of vectors that can be produced. In high-speed flow, this is rarely a reachable limit as the limit is usually set by the density of seeder particles. Two-dimensional PIV is highly susceptible to out-of-plane velocity components, which often mean that the particles can pass out of the laser sheet between the frames.

3.2.5 Applications

Researchers have applied PIV across a wide range of speed regimes, from incompressible to hypersonic. Hale et al. [134] [135] applied PIV to a induced jet from a plasma actuator in quiescent air, capturing velocities ranging from $0 - 8$m/s. Ragni et al. [136] applied PIV to a transonic airfoil with localised supersonic regions. Using the isentropic relations, Ragni et al. were able to estimate the surface pressure on each side of the airfoil and as a result estimate the lift, drag and pitching moment.

Application of PIV to high-speed flow, more relevant to this project, has been performed despite the technical challenges involved. Gongora-Orozco et al. [41] successfully applied PIV to shock tube flows with and without co-flow jets, albeit using olive oil as the seeder material.

High-velocity shock tunnel flows have been investigated by Haertig et al. [137]. By their nature of compression by two normal shocks, shock tunnels have extremely high enthalpy flow conditions that resemble actual hypersonic flight conditions. The velocity of the flow after a convergent-divergent nozzle was ≈ 1500 m/s. The level of accuracy of the PIV measurements was extremely good (more than 99% accurate); however, the spatial resolution was limited. The improvement in laser and CCD technology since this research has led to research of similar velocities with significantly higher spatial resolution [124].

Schrijer et al. [122] applied PIV to hypersonic flow (Mach 7) over a double-ramp generated by a Ludwieg tube. This research used the adaptive grid method of interrogation (as mentioned in Section 3.2.2) and showed a freestream velocity discrepancy of 10% with isentropic theory. This is unsurprising given the high Mach number of the flow; however, the flow structures which were visible correlated well with schlieren images. Later research by Schrijer et al. [138] applied stereoscopic PIV to the same experimental rig and compared the results with CFD. Boundary/shock layer measurements of the flow showed highly complex structures such as Görtler type vortices and a large separation bubble.

Not only have freestream flow fields been investigated using PIV, but shock wave turbulent boundary layer interactions have also been investigated by Humble et al. [139] in a Mach 2.1 flow. The region of investigation in this research was 16mm high and 5mm wide. Despite this small area, the flow was well resolved and highlighted instantaneous regions of reversed flow and unsteady shock wave movement. Later work using a high-speed tomographic PIV system by Humble et al. [140] detailed highly complex three-dimensional vortical structures. The results were very promising; however, the author did highlight the technical difficulties associated with this technique, such as the prohibitively large data storage required.

In addition to yielding quantitative velocity data, PIV can also give excellent flow visualisation that is not readily available from other techniques. The particles seeded into the flow will tend to be ejected from vortex cores, no matter how low their inertia is. This means that we should expect the raw PIV images to highlight the edges of any vortices present in the flow (see Fig.3.22), although this means that it will not be possible to obtain any quantitative data in this region.

3.2.6 Setup

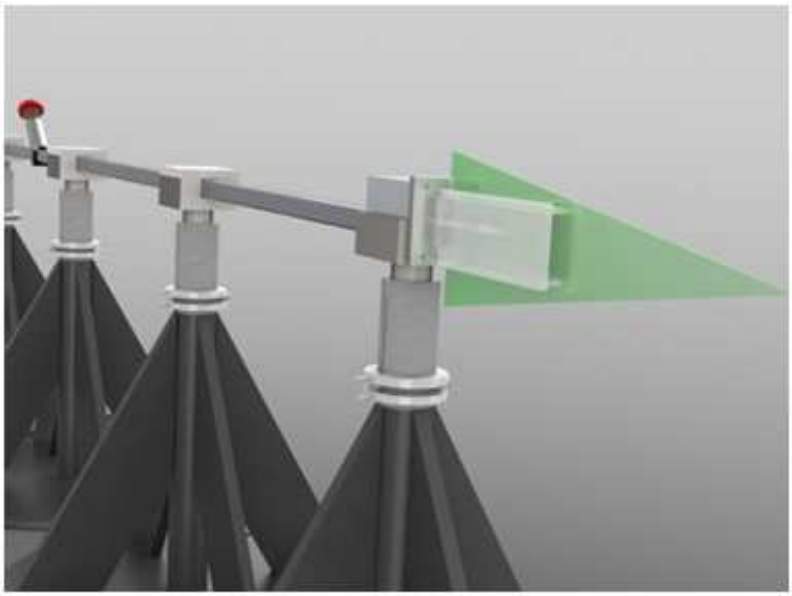

Figure 3.18: Position of laser sheet in shock tube

A light sheet was shone down the centre-line of the shock tube, as shown in Fig.3.18. This light sheet was created using two lenses, and a slit-like cut-off was used to produce a more top hat-like profile. The position of the second lens controlled the position of the *waist* of the sheet. The waist of the beam should not be within the measurement area of the experiment, as it is this area of the beam that exhibits the largest gradients in power [141]. In this setup, the waist of the beam was before the test section.

Several measurements were taken at different spanwise locations to ensure the two-dimensionality of the flow. The flow measurements were indistuingishable at all of the spanwise locations. This concurs with the conclusion at the start of Section 5.1 that two-dimensional simulations are suitable for investigating this flow.

The system often used at The University of Manchester is the TSI high-speed, high-resolution particle image velocimetry system. This system consists of the Pegasus double pulse laser with the Photron APX-RS as the imaging device, which has a resolution of 512 x 512 pixels. Initial tests were performed using this system with olive oil as the seed and it was found that $\Delta t_{min} = 2.5\mu$s. This minimum value was imposed by the interframe time of APS-RX. It was found from these initial tests that olive oil droplets do not respond quickly enough to accurately capture the flow, and that the spatial and temporal resolution of the APX-RS is not sufficient to give accurate enough results.

The only PIV system available with a small enough Δt was the LaVision FlowMaster with an Imager Pro X2M camera coupled with a Litron Nano-L-200-15 PIV Nd:YAG laser. This system allows $\Delta t_{min} = 110$ ns and has an image resolution of 1600 x 1200 pixels. The field of view of the PIV system is shown in Fig.3.19. Values of Δt were changed from 1μs for $P_4/P_1 = 4$ to 0.5μs for $P_4/P_1 = 8$ and 0.3μs for $P_4/P_1 = 12$. This kept the effective CFL number down to manageable values. Solid Al_2O_3 nanoparticles were passed through the SciTech Consultants PS-10 powder

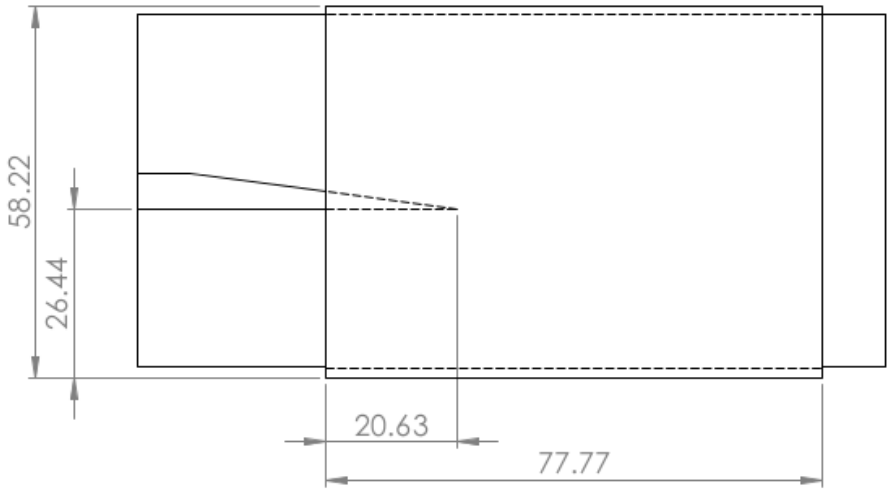

Figure 3.19: Field of view of the PIV system (all dimensions in mm)

seeder which has sonic jets to break up any agglomerates. This system is usually used for low-speed PIV measurements, as the laser has a repetition rate of 15 Hz. The low repetition rate meant that the PIV tests had to be conducted in a spark fashion, i.e. that only one pair of images was captured per run of the shock tube. In order to give time-accurate data, the delay must be stepped on after each test. As mentioned previously, the timing uncertainty on triggering measurements is $\pm 15\mu$s, meaning that it is impossible to gain completely time-accurate data. However, as the HPV-1 yields time accurate data, the position of the shock waves can be compared to give an estimate of the exact flow time ($\pm 2\mu$s).

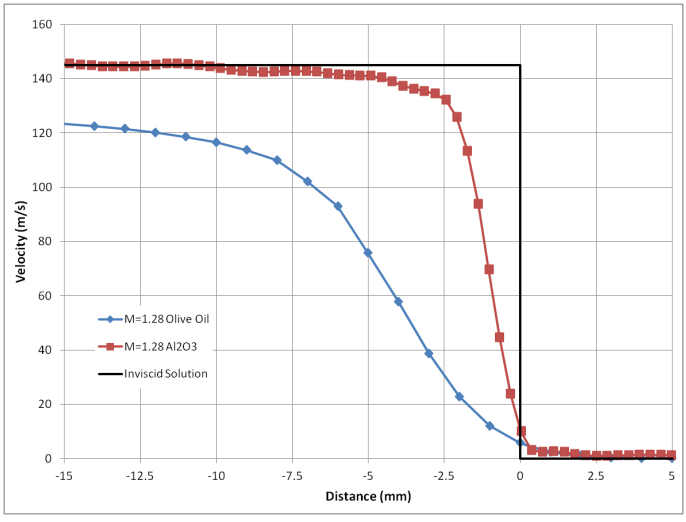

Figure 3.20: Comparison of two PIV setups to a $M_i = 1.28$ shock front

A comparison of the measured response of both the TSI system using olive oil and the LaVision system using Al_2O_3 is given in Fig.3.20. This clearly highlights the advantage of the LaVision system.

It is very difficult to attain uniform seeding using solid particles. Furthermore, these particles have a tendency to stick to the walls of the test section and, as they

are not transparent, block the signal from the laser sheet. This meant that after every five runs, the shock tube had to be cleaned using anti-static screen wipes and allowed to dry before testing could continue.

3.2.7 Post-Processing

The acquired raw PIV images were processed using LaVision's Davis 7 software. Initial coarse grids were refined using an iterative multi-grid method. The best interrogation window was found to be 32×32 pixels (1.56×1.56 mm). When combined with a 0.75 overlap factor between windows, this gives a vector plot of 150×200 vectors.

Post-processing of the velocity vectors was performed using Tecplot 2011. This software allowed for the calculation of streamlines and vorticity magnitude. It was found that the shock positions are most easily highlighted by calculating the ϵ_{xy} component of the strain tensor.

$$\epsilon_{xy} = \frac{1}{2}\left(\frac{dU}{dy} + \frac{dV}{dx}\right) \tag{3.29}$$

Statistical errors and the repeatability of the system were analysed using Tecplot by extracting sub-zones of the whole data set around the region of interest.

3.2.8 Sources of Uncertainty

Measurement uncertainty and errors in PIV can be split into three main categories:

1. Errors associated with the camera and optical setup (signal measurement)

2. Errors associated with the tracer particle

3. Image/post-processing errors (signal analysis)

3.2.8.1 Signal Measurement Errors

The detection system used for PIV is usually a CCD camera. As a result of this, most of the errors associated with CCD cameras apply to PIV, such as shot noise etc.; however, these are usually negligible. If one particular pixel well on the CCD is full, then a *bleeding* effect may occur, where the bloomed pixel spills over into the pixel below it. Two-dimensional PIV is highly susceptible to large out-of-plane velocity. The same is true of stereoscopic PIV if the laser sheet is not thick enough. Incorrect scale calibration, as mentioned for density-based techniques, is another possible source of error.

Errors caused by compressibility effects are harder to eliminate. The refractive index of air changes with its density. As a result, if there are large density gradients, such as in compressible flow for example, then optical aberrations can be caused which blur the recorded image [142].

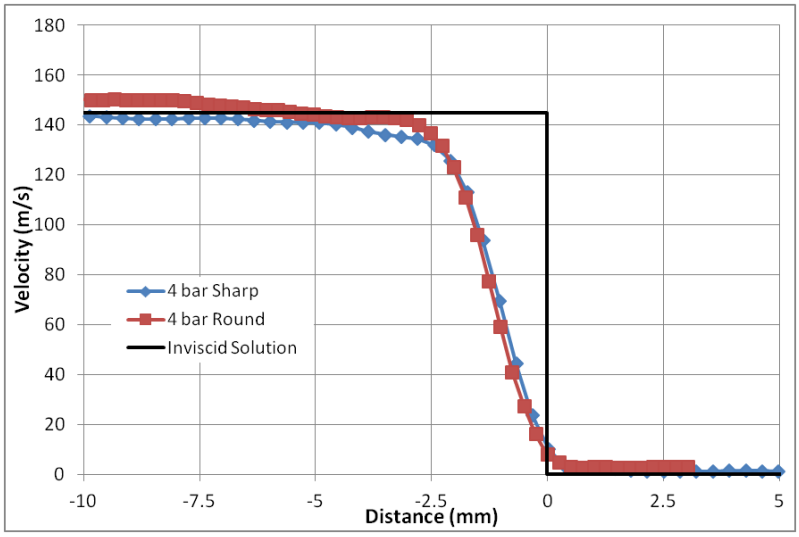

(a) $P_4/P_1 = 4$

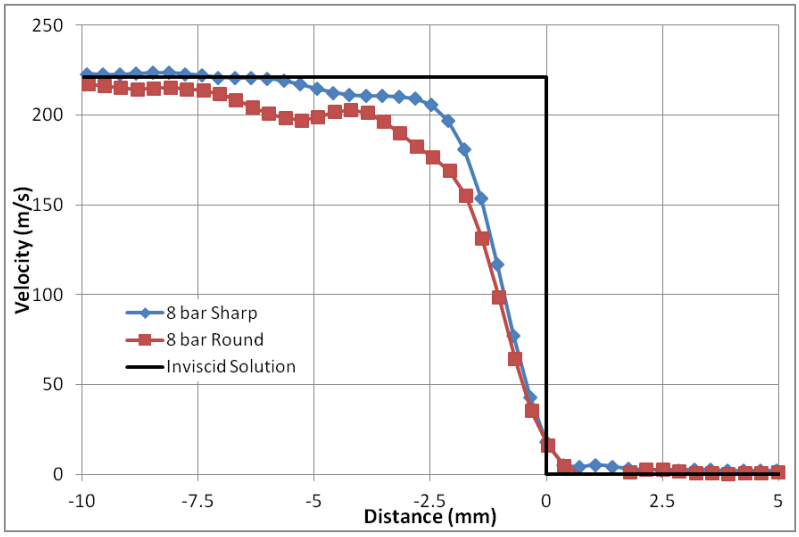

(b) $P_4/P_1 = 8$

Figure 3.21: Shock front profile as measured by Al_2O_3 particles

3.2.8.2 Tracer Particle-Induced Errors

As mentioned in Section 3.2.3, tracer particles do not follow the flow precisely. This can be a significant problem in compressible flow. The relaxation time causes velocity lag which in turn creates spreading of the shock, often to several mm, whereas in reality it is the same order as the mean free path length. A comparison of the three pressure ratios used in this project is given in Fig.3.21. From these figures it is clear that shock spread due to the tracer particle inertia is almost constant for all of the Mach numbers being tested. Havermann et al. [124] showed the curious phenomenon of a perceived velocity decrease upstream of a shockwave. He ascribed this to the finite width of the interrogation region and the finite value of Δt causing a predictive velocity drop. The effect of this can be reduced by altering the size of the interrogation region accordingly.

Many researchers have encountered problems with measurements near the wall.

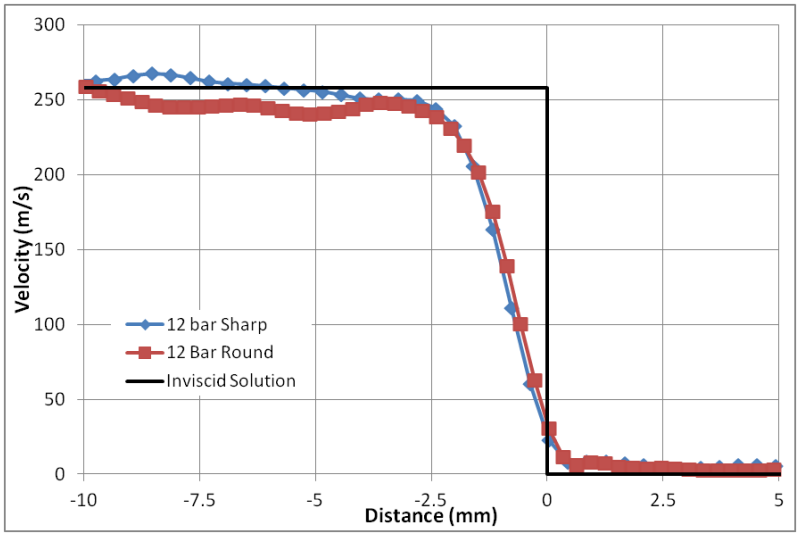

(c) $P_4/P_1 = 12$

Figure 3.21: Shock front profile as measured by Al_2O_3 particles

Schrijer et al. [122] cites direct light scattering from the solid wall, limited tracer response and limited spatial resolution as possible reasons. This is often a problem in thin boundary layers originating in high-speed flow, Mach 7 (1000m/s) in the case of Schrijer et al. In order to counter this, other researchers (Humble et al. [140]) allowed the boundary layer to develop over a 2m long plate, allowing it to become $\approx$ 20mm thick. This thicker layer has longer scales associated with it and is therefore easier to measure; however, this is not always possible due to length constraints of experimental apparatus.

Based on the spread of the shock fronts displayed in Fig.3.21, it is estimated that the nominal diameter of the tracer particles is approximately 0.5μm.

3.2.8.3 Signal Analysis Errors

Analysis of the images gained from PIV can contain errors associated with low particle density, giving rise to so-called *spurious vectors*. This is often the case in vortex cores where, as mentioned earlier (Section 3.2.3), particles tend to be ejected due to the centrifugal forces involved. Fig.3.22 shows a raw PIV image of a vortex ring emanating from a shock tube.[4] The low level of data in these areas can often give rise to large and clearly erroneous velocity vectors. Care must be taken not to over-seed the flow in an effort to cure this problem, as saturation can also lead to spurious vectors.

The most obvious factor that can be altered is the interrogation window size. This will not only have the effect of producing more vectors but also of reducing upstream velocity predictions [124]. This is only a valid option if there are enough seeder particles in the fluid to fill each interrogation window. In such a transient flow as this, it is virtually impossible to guarantee uniform seeding and, as such, shrinking the interrogation window did not have any positive impact on the results.

[4]Image reproduced with the permission of Dr. Raffaello Mariani

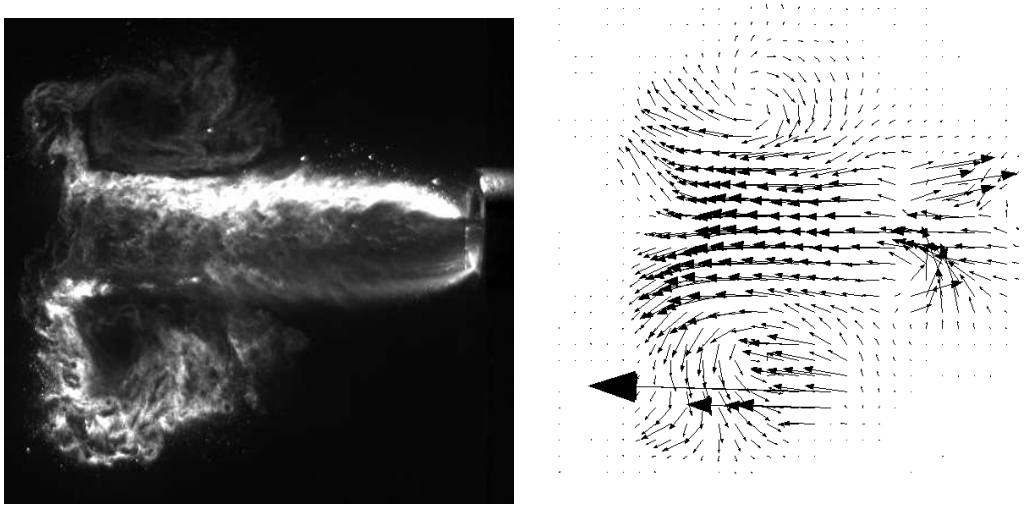

(a) Raw PIV image with low particle density in the vortex core

(b) PIV vector image showing spurious vectors

Figure 3.22: PIV of vortex ring emanating from a shock tube

3.2.9 Uncertainty and Repeatability

The triggering repeatability of the PIV measurements is the same as is discussed in Section 3.1.7 and as a result will not be discussed at length here. However, the uncertainty and repeatability of the velocity measurements behind the incident shock will be discussed.

Due to the unavoidable non-uniformity of seeding in the test section, some runs exhibited considerable holes in the processed vector field. These time steps, which clearly had to be repeated, gave an excellent example visual of the repeatability of measurements and shock position (assuming some seeding particles are present) and can be seen in Fig.3.23.

Fig.3.23 also shows that the most uniformly seeded region appears to be the region behind the incident shock, which should have uniform flow. This uniform region is the simplest way to reliably compare the measured and expected velocities induced by the incident shock wave. As before, the velocity induced behind the incident shock wave is unaffected by the corner geometry, meaning that both geometries can be used as repeats to characterise the random error more accurately. Velocity averages from across the inlet were taken at times up until the influence of the reflected expansion wave became significant. This is easily seen in the PIV measurements, as the reflected expansion wave induces a vertical velocity that was not present before. Tab.3.6 shows the expected and measured induced velocities. The induced velocities based on incident shock Mach number are calculated from the analysis given in Section 2.2.1. The measured induced velocities are closer to the calculated values based on M_{ie} from Section 3.1.7.

Estimating the uncertainty in PIV measurements is relatively simple. The images are scaled so that $\frac{x_{image}}{\alpha} = x_{real}$, where α is the scale of the images in pixels per mm. Substituting this into the simple equation for velocity and differentiating with respect to x gives us the sensitivity coefficient $\frac{\partial V}{\partial x_{image}} = \frac{1}{\alpha t}$, where t is the time between two PIV images. This coefficient can then be multiplied by error induced by incorrectly scaling the image by an assumed error of 0.2 mm and a component

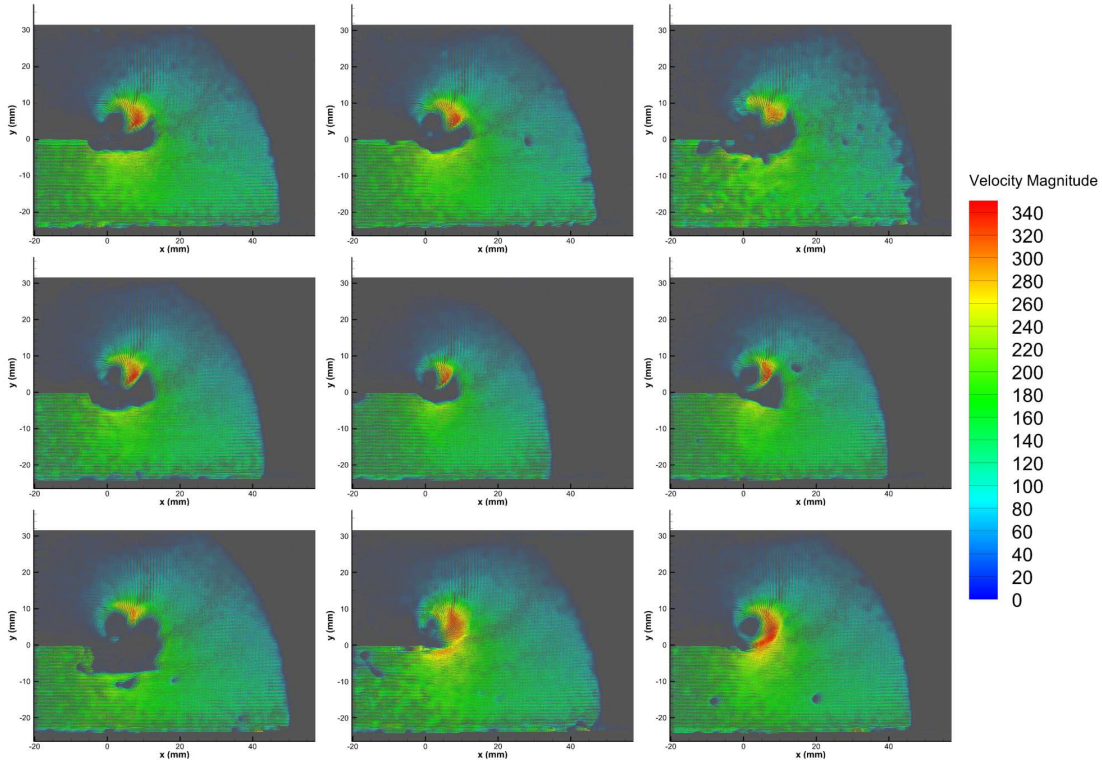

Figure 3.23: Nine repeats for $M_i = 1.28$ with the same delay in order to gain adequate seeding everywhere in the flow

Table 3.6: Theoretical and experimental induced velocity

P_4/P_1	Induced velocity based on M_{it}	Induced velocity based on M_{ie}	Measured induced velocity (m/s)
4	169.95	143.47	148.35
8	254.87	221.89	215.81
12	304.49	259.09	264.34

from the camera not being normal to the laser plane by 3°.

$$\sigma_{bias} = \sqrt{\left(\frac{\partial V}{\partial x_{image}} \times \sigma_{xplane}\right)^2 + \left(\frac{\partial V}{\partial x_{image}} \times \sigma_{xscale}\right)^2} \tag{3.30}$$

In order to characterise the random error between runs, the velocity measured in the uniform region behind the incident shock is compared to inviscid theory. The overall uncertainty is then given by

$$\Psi = \sqrt{\sigma_{random}^2 + \sigma_{bias}^2} \tag{3.31}$$

Table 3.7: PIV uncertainty

P_4/P_1	Standard Deviation (m/s)	σ_{random} (m/s)	σ_{bias} (m/s)	Total Velocity Uncertainty Ψ(m/s)
4	6.39	4.76	3.62	5.96
8	7.60	5.63	6.58	8.66
12	11.17	8.28	12.07	14.63

3.3 Pressure Measurements

The driver section pressure was measured using a Druck PDCR820-0800 connected to a Fylde 254 GA MINI AMP. High-speed pressure measurements were taken using three flush-mounted Kulite XT190-M transducers in the locations shown in Fig.3.24. The Kulites were connected to an in-house-built signal conditioner to amplify their millivolt outputs. The natural frequency of these transducers is 380kHz, which limited the safe acquisition speed to 100kHz at most. The amplifier, which was made up of a series of operational amplifier circuits, had a low-noise linear gain of 250 up to a frequency of 900kHz. To keep costs down, the amplifier had a fixed gain, but, the offset voltage could be adjusted using a potentiometer, maximizing the ±10V range of the DAQ. The amplified signals were recorded by a NI-USB6251 16-bit, 1.25 MS/s M Series Multifunction DAQ. The DAQ was connected to a HP Windows 7 Laptop running LabView 2011. The LabView code, written by the author, monitored the driver section pressure until the desired limit was reached. At this point the software sent the acquisition tasks to the hardware using low-level VI functions rather than the Express-VIs built into LabView, as they are restricted in their timing to the Windows clock speed of 2ms. The DAQ takes an analogue input as a trigger, meaning that a fourth XT190-M could be used at a distance (1m) from the end of the shock tube in order to trigger acquisition. The trigger signal was connected to a Photonics Four Pulse Sequencer (SEQ400), allowing the user to set a hardware delay.

Unfortunately, Wheatstone bridge-based pressure transducers, as we have here, are not ideal for measuring such transient flows as they have a tendency to ring when subjected to step function inputs. Piezoelectric transducers would be more suitable; however, these too suffer from some ringing.

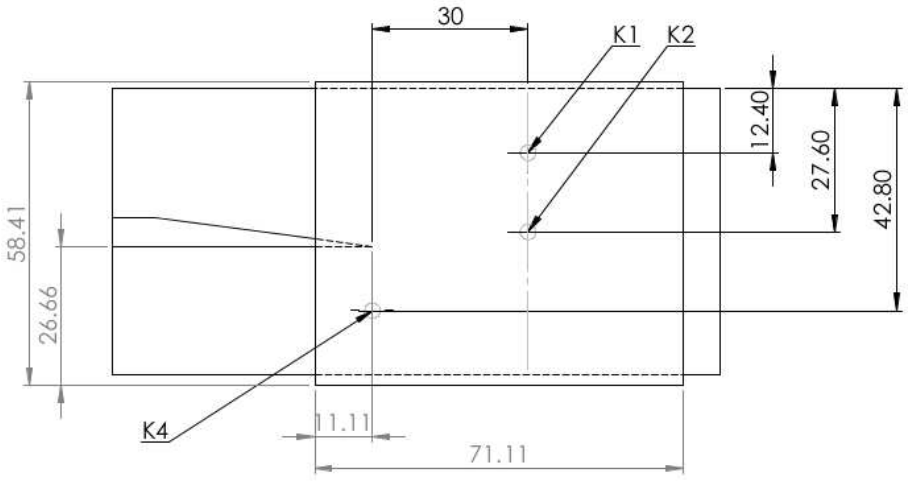

Figure 3.24: Location of the pressure taps in relation to the splitter edge and the PSP test field of view (all dimensions in mm)

3.3.1 Calibration

All of the pressure transducers were calibrated using a LabView calibration program written by the author. The pressure in the in-house-designed calibration chamber

Table 3.8: Transducer Calibrations

Transducer	Slope	Offset	R^2
Pressure Scanner	5.2176	0.8211	1
K1	2.7370	0.3376	1
K2	2.7323	0.3348	1
K4	2.7469	0.3384	1

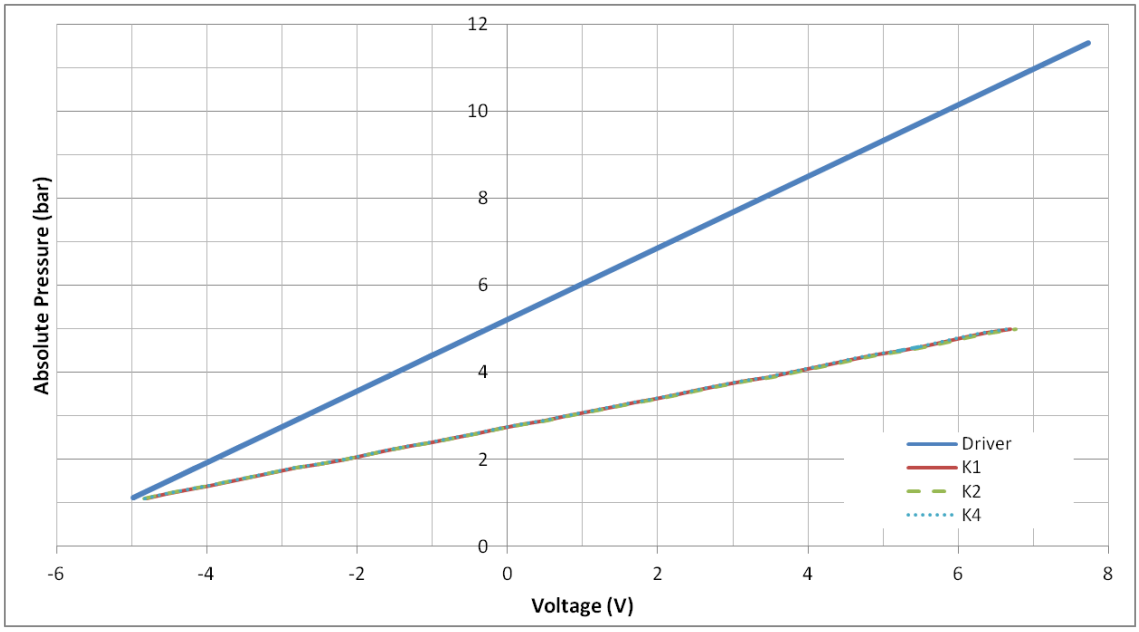

Figure 3.25: Transducer calibration curves

was automatically varied using a Druck DPI530 pressure controller. The LabView program used the analogue outputs from the DAQ mentioned previously to control the pressure in the chamber and wait for the relay signal to indicate that the correct pressure had been reached. The pressures were then recorded and stepped on up to the user-set maximum. The transducers used in the experiments showed excellent linearity; however, another transducer, **K3**, which had suffered mechanical damage which affected its linearity. As the response time of the transducer was unaffected, this transducer was used for triggering.

The calibration of all of the transducers used in this research is shown in Fig.3.25 and Tab.3.8.

3.3.2 Error Analysis

It is difficult to estimate the bias error of the high-speed pressure measurements, as they are being read at a frequency reasonably close to their natural frequency and they are exposed to a discontinuous pressure jump.

The random error of the pressure measurements is analysed by comparing the maximum pressure rise over a set of repeat tests. The pressures were measured four times for all Mach numbers and geometries. Given that the initial pressure rise for **K4** should be independent of the geometry used, 8 repeats were conducted for each

Table 3.9: Pressure measurement repeatability

$\frac{P_4}{P_1}$	Geometry	Average (bar)	Standard Deviation	Random Error (bar)	Total Uncertainty (bar)	$\frac{P_2}{P_1}$ based on M_{ie}
4	Sharp	1.84	0.0252	0.0247	0.0841	1.75
8	Sharp	2.38	0.1079	0.1057	0.1328	2.32
12	Sharp	2.62	0.1070	0.1048	0.1321	2.64
4	Round	1.78	0.0308	0.0302	0.0859	1.75
8	Round	2.38	0.0513	0.0502	0.0948	2.32
12	Round	2.67	0.0443	0.0435	0.0915	2.64

Mach number. Tab.3.9 shows that there appears to be quite a large standard deviation of the peak pressure measurements. The error induced by ringing is estimated by fitting a curve through the decrease in pressure after the initial shock, as seen in Fig.3.26. The residual sum of the squares of a curve fit through this region gives us an estimate due to the *ringing* of the transducer, $\sigma_{ringing} = 0.08037$. The measured values also seem slightly higher than the predicted values based on the shock wave propagation speed. Transducers of this type are known to overshoot instantaneous pressure jumps and act like an underdamped system. The signal noise from the transducers for a steady signal, σ_{noise}, is ± 0.0034. The total uncertainty can then be estimated using Eq.3.32.

$$\Psi = \sqrt{\sigma_{ringing}^2 + \sigma_{noise}^2 + \sigma_{random}^2} \tag{3.32}$$

Fig.3.26 shows the pressure history of all 8 of the $M_i = 1.28$ runs over the shock impact time. The arrival time of the shock wave appears to have deviated by up to 30μs. This is consistent with the estimate given by the density-based optical diagnostics presented previously.

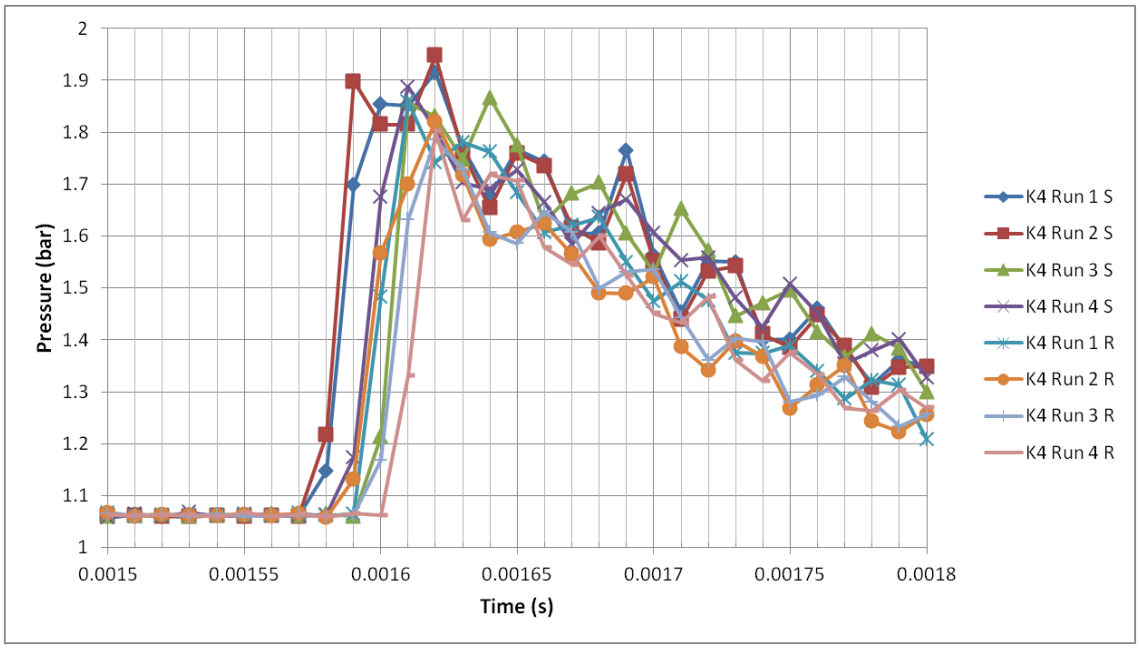

Figure 3.26: Pressure history repeatability

3.4 Pressure-Sensitive Paints (PSP)

Although relatively still in its infancy, pressure-sensitive paint (PSP) is a useful experimental tool for acquiring quantitative surface pressure measurements without the need for a large number of pressure transducers. This method significantly reduces the complexity of a model and can reduce the cost of creating a model too. Installing many pressure transducers in a model is not only expensive and labour-intensive but only gives discrete values of pressure, unlike PSP. Full surface pressure maps can be achieved with PSP, as every pixel of an image can be regarded as a pressure transducer. An excellent review of recent high-speed PSP (circa 2008) is given by Gregory et al. [143].

3.4.1 History & Development

The origins of pressure-sensitive paint go back to the early 20th century and a paper by Professor Max Volmer and Professor Otto Stern [144]. In this paper, the researchers noted that luminescence of iodine vapour under the excitation of sunlight was reduced by increasing pressure. This led them to a now famous relation bearing their name. However, it took a further 16 years for the phenomena to be properly understood. The German scientist Hans Kautsky discovered that the quenching of luminescence was due to the presence of oxygen [145]. Kautsky adsorbed luminescent compounds such as porphyrins onto silica gels and found a reciprocal relationship between oxygen concentration and luminescent output. Soon after this work was published, two independent streams of research on optical pressure sensors were carried out on either side of the iron curtain. The two systems were developed in Russia and the USA completely independently of each other, as is often the case with scientific discoveries. The two teams remained completely unaware of each other's activities until an advertisement for the Russian system was published in the February 12^{th} 1990 edition of *Aviation Weekly* and was spotted by the American team.

The American system evolved by chance from an idea by Dr. Martin Gouterman to use luminescent molecules to sense the concentration of oxygen in blood. One of Gouterman's future PhD students, Prof. Jim Callis, had continued the research on this topic and on the measurement of luminescent spectra. Prof. Jim Crowder, who worked in the same building as Callis but on aerodynamic research, looked at ways to improve the performance of the technique he championed, known as fluorescent minitufts [146]. The collaboration between these two researchers and Gouterman led them to apply luminescent coatings to the whole surface. This eventually led to a transonic test of pressure-sensitive paint at NASA Ames [147], which showed the feasibility of the technique and how it could be applied to whole surfaces. Kavandi et al. [148] expanded on this work, showing the applicability of PSP and how it could be used.

Meanwhile, Russian scientists at the the Central AeroHydrodynamic Institute (TsAGI) had built on their own research of luminescent oxygen sensors [149] and temperature-sensitive paints to design their own intensity-based pressure-sensitive paint system. Wind-on and wind-off images and calibration techniques were presented by Aradsheva et al. [150]. This work led to the creation of a new research team at TsAGI: the luminescent pressure sensor team. On this team was Prof.

Vladimir Mosharov, who was tasked with improving the system in use at TsAGI at the time. The luminophore commonly used was acridine orange; a strange choice, as it has an extremely low quantum yield ($\phi < 3\%$), requiring very high-power incident lights to achieve a measurable signal. The polymer coating also had a long response time (almost three minutes!). As this performance was improved over the following years, an Italian firm (INTECO) reached an agreement to market the Russian system to the West, leading to the aforementioned advertisement.

The Russian and American systems were very similar in specification and both required significant improvement before they could be used reliably in transonic tests and applied to different flow regimes. The vast majority of PSP tests have been performed in steady transonic flow. These conditions give the largest pressure rise to temperature rise and are therefore the easiest to measure. Low-speed measurements are more challenging as PSP is an absolute pressure sensor, meaning that the changes in absolute pressure can be very small. Unsteady PSP measurements have been performed in a variety of ways, such as taking phase-locked point measurements using photomultiplier tubes [151] or by introducing a different gas to change the local partial pressure of oxygen [152].

3.4.2 Theory of PSP

There are two methods of utilising PSP: the lifetime and the intensity methods. The intensity-based method will be discussed here, as it is in common use and is currently the only method of PSP used at the University of Manchester. Lifetime PSP systems involve significantly more complex and expensive setups. Despite this, there are certain applications of PSP that can only be made using the lifetime method (see Section 7.6).

Pressure-sensitive paints are based around the theory of oxygen quenching of luminescence. This is closely related to, and often used in conjunction with, the thermal quenching of luminescence, which is the basis of temperature-sensitive paint (TSP). The photoactive molecule in the paint is called the luminophore and the photophysics of this molecule is the basis for the PSP technique. Explained briefly, an electron of a photoactive molecule absorbs a particular wavelength of light and is excited from its ground state (S_0) to a higher energy (singlet) state (S_1 or S_2). The excited electron relaxes from higher vibrational states to the singlet level. The electron can then relax to lower energy states by various methods, as shown by the Jablonsky diagram (Fig.3.27). If the electron is in the S_2 state, then by a method called internal conversion, it can transfer to a vibrationally excited lower singlet state by releasing some heat. The state S_1 has many methods of returning to the ground state which can be either radiative or radiationless. Radiative methods involve fluorescence, i.e. the release of a photon. Radiationless methods include:

- Internal conversion: transfer to a vibrationally excited level of the ground state followed by vibrational relaxation
- Intersystem crossing: transfer to a triplet excited state T_1
- External conversion: contact with another molecule and transferring the energy to that molecule

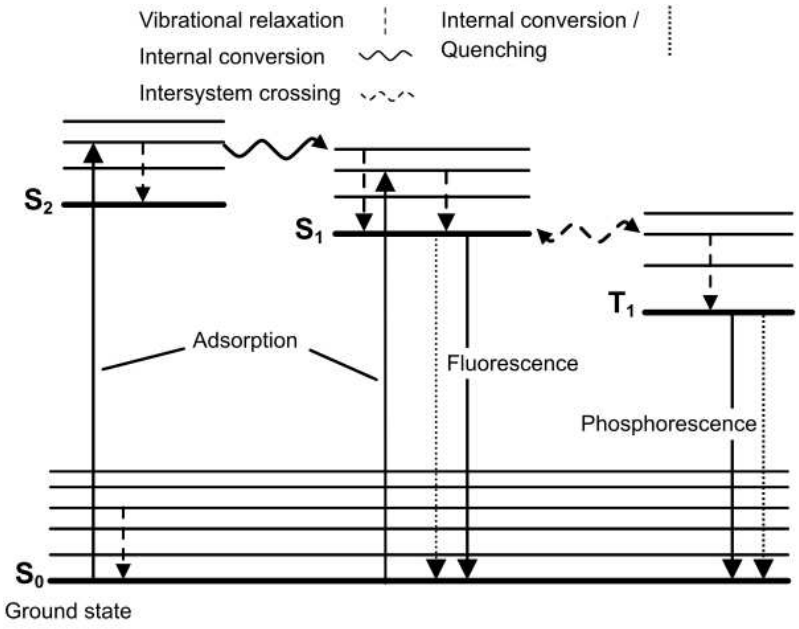

Figure 3.27: Jablonsky energy level diagram

The triplet excited state, T_1, can relax to the ground state by emitting a photon of different wavelength to that emitted by the singlet state; this process is called phosphorescence.[5] Alternatively, the triplet state can relax to the ground state by radiationless methods:

- Internal conversion: transfer to a vibrationally excited level of the ground state followed by vibrational relaxation
- Intersystem crossing: transferring back to the singlet state S_1, making all of the above events possible again
- External conversion: contact with another molecule and transferring the energy to that molecule

The processes of fluorescence and phosphorescence are grouped together as radiative processes and are usually referred to as luminescence [153]. As the processes of fluorescence and phosphorescence have different lifetimes, they account for different wavelengths of emission and cause spreading of the overall emission spectra (see Fig.3.31).

The process knwon as external conversion is the basis of the PSP experimental method as the oxygen molecules in air remove the extra energy from the luminophore, allowing it to return to its ground state. Oxygen molecules exhibit excellent qualities as a *quencher* due to their unusual electronic ground state. The oxygen molecules then return to their ground state by the methods presented above.[6] Moreover, it should be noted that these oxygen molecules actually contribute to the

[5]Fluorescence is the more useful form of radiation, as it takes place significantly faster ($10^{-10}s$) than phosphorescence ($10^{-3}s$)

[6]Oxygen does emit light but at a much higher wavelength, mid infra-red ($\lambda > 1240nm$)[154]

degradation of the paint. The excited oxygen molecule is highly reactive and can bind irreversibly with the paint surface, causing it to lose its photoactive properties.

Clearly, there are different ways in which an excited molecule can return to its ground state: radiative processes K_r, non-radiative processes K_{nr} or by quenching K_q. The *quantum yield* (ϕ) is the ratio of luminescence to excitation and is a measure of the efficiency of a paint.

$$\phi = \frac{luminescence}{excitation} = \frac{K_r\,[L^*]}{I_a} = \frac{K_r}{K_r + K_{nr} + K_q\,[Q]} \tag{3.33}$$

where L^* is an excited luminophore, I_a is the incident light absorbed, Q is the quencher and all brackets enclosed in square brackets [ ] denote concentration. If we now consider the response of the paint in a vacuum we arrive at the quantum yield without any quenching:

$$\phi_0 = \frac{K_r}{K_r + K_{nr}} = \frac{I_0}{I_a} \tag{3.34}$$

noting that I_0 is the emission in a vacuum and, in general, symbols with a subscript $_0$ denote vacuum conditions. Now taking the ratio of the quantum yields with and without quenching:

$$\frac{\phi_0}{\phi} = \frac{\left(\frac{K_r}{K_r+K_{nr}}\right)}{\left(\frac{K_r}{K_r+K_{nr}+K_q[Q]}\right)} = \frac{K_r + K_{nr} + K_q\,[Q]}{K_r + K_{nr}} = 1 + \frac{K_q}{K_r + K_{nr}}\,[Q] = 1 + K_q\tau_0\,[Q] \tag{3.35}$$

Equation (3.35) is the initial form of the widely recognised Stern-Volmer equation. This equation can reduce to give the luminescent lifetime τ with and without quenching depending on whether or not quenching is included:

$$\tau_0 = \frac{1}{K_r + K_{nr}} \tag{3.36}$$

$$\tau = \frac{1}{K_r + K_{nr} + K_q\,[Q]} \tag{3.37}$$

This means that the Stern-Volmer equation (3.35) can be written as:

$$\frac{\phi_0}{\phi} = \frac{I_0}{I} = 1 + K_q\tau_0\,[Q] = \frac{\tau_0}{\tau} \tag{3.38}$$

As mentioned above, oxygen is an excellent quencher and is the quencher that is of use here. With this in mind, we can replace $[Q]$ with $[O_2]$.

The rate constants K_{nr} and K_q are temperature-dependent. It is this temperature dependency that is the main flaw of almost all PSP measurements. Non-radiative processes can be modelled by the Arrhenius relationship and broken down into temperature-dependent and temperature-independent terms.

$$K_{nr} = K_{nr_0} + K_{nr_1} e^{-\left(\frac{E_{A_{nr}}}{\Re T}\right)} \tag{3.39}$$

where $E_{A_{nr}}$ is the activation energy of the reaction, $\Re$ is the universal gas constant, K_{nr_0} is the temperature-independent, non-radiative process and K_{nr_1} is the

temperature-dependent, non-radiative process.

From this point onwards in the derivation of PSP, the exact format of the models used is dependent on the substrate and the application method, whether polymer-based or porous. This will be covered in Section 3.4.3. However, for now we will treat polymer-based PSP first and then extend this to include porous-based PSP.

The temperature-dependency of the quenching rate is due to the diffusion of the quenching molecules through the polymer layer[7]. This can be modelled by the Smoluchowski relationship, where the rate of quenching can be expressed as:

$$K_q = 4\pi R_{AB} N_0 D \tag{3.40}$$

where R_{AB} is an interaction distance, N_0 is Avogadro's number and D is the diffusivity. The diffusivity is the term which is dependent on temperature; all of the others are constants for a given system. Kinetic theory dictates that the kinetic energy of a molecule is dependent on the cube of temperature. If the temperature increases then the increase in kinetic energy increases the frequency of collisions between the luminophores and O_2 molecules. This increased frequency of collisions makes it more likely that the excited luminophore will be deactivated by external conversion (quenched). The diffusivity of the quencher through the polymer can be modelled by the Arrhenius relationship.

$$D = D_0 e^{-\left(\frac{E_{A_D}}{\Re T}\right)} \tag{3.41}$$

where E_{A_D} is the activation energy required for diffusion. Equations 3.39, 3.40 and 3.41 can be substituted into equation 3.37 to give:

$$\frac{1}{\tau} = K_r + K_{nr} + K_q [Q] = K_r + K_{nr_0} + K_{nr_1} e^{-\left(\frac{E_{A_{nr}}}{\Re T}\right)} + 4\pi R_{AB} N_0 D_0 e^{-\left(\frac{E_{A_D}}{\Re T}\right)} [O_2]_{polymer} \tag{3.42}$$

Henry's Law states that, at constant temperature, the amount of gas dissolved in a solid is proportional to the gas pressure at the surface. This means that the amount of oxygen in the polymer layer is related to the partial pressure of oxygen by a solubility constant, S. From Dalton's law of partial pressures, the total pressure of the gas (P) multiplied by the molar fraction of oxygen (χ_{O_2}) gives us the partial pressure of oxygen. This means that Equation 3.42 can be written in the form:

$$\frac{1}{\tau} = K_r + K_{nr_0} + K_{nr_1} e^{-\left(\frac{E_{A_{nr}}}{\Re T}\right)} + 4\pi R_{AB} N_0 D_0 e^{-\left(\frac{E_{A_D}}{\Re T}\right)} S P \chi_{O_2} \tag{3.43}$$

Previously, the ratio of intensity with and without quenching was shown. As mentioned before, the only condition in which no quenching will occur is in a vacuum (or oxygen-free environment). In order to generate a more practical expression

[7]The increased temperature gives the molecules more kinetic energy, which increases the diffusion rate. Although a porous PSP setup involves no diffusion through a polymer layer, the same increase in quenching is observed. This is related to the increased kinetic activity of the quenching molecules and is accounted for in the equation, as many of the constants drop out leaving only temperature ratios.

(rather than referencing to a vacuum), Equation 3.43 is evaluated at any arbitrary condition and divided by Equation 3.43 at a reference condition.

$$\frac{\tau_{ref}}{\tau} = \frac{I_{ref}}{I} = \frac{K_r + K_{nr_0} + K_{nr_1} e^{-\left(\frac{E_{A_{nr}}}{\Re T}\right)}}{K_r + K_{nr_0} + K_{nr_1} e^{-\left(\frac{E_{A_{nr}}}{\Re T_{ref}}\right)}} + \frac{4\pi R_{AB} N_0 D_0 e^{-\left(\frac{E_{A_D}}{\Re T}\right)} SP\chi_{O_2}}{4\pi R_{AB} N_0 D_0 e^{-\left(\frac{E_{A_D}}{\Re T_{ref}}\right)} SP_{ref}\chi_{O_2 ref}} \tag{3.44}$$

Assuming that the only variables that change are pressure and temperature between the two conditions and assuming that the temperature change is not significant enough to cause species change in the gas and therefore a change in the molar fraction of diatomic oxygen, Equation (3.44) can be reduced to give:

$$\frac{I_{ref}}{I} = A(T) + B(T)\frac{P}{P_{ref}} \tag{3.45}$$

Equation 3.45 is a modified form of the Stern-Volmer relationship and has the advantage that, when practically applied to an image of a painted surface, any surface non-uniformities are *theoretically* eliminated. This can be extended by considering the method of contact between luminophore and quencher.

If we assume that the oxygen concentration adsorbed on to the surface can be modelled by a fraction of the coverage of the surface:

$$\Theta = \frac{[O_2]_{ads}}{[O_2]_{adsMax}} \tag{3.46}$$

where $[O_2]_{adsMax}$ is the maximum oxygen concentration on the surface, we can write Equation 3.35 as

$$\frac{I_0}{I} = 1 + K_q \tau_0 [O_2]_{adsMax} \Theta \tag{3.47}$$

leading to

$$\frac{I_{ref}}{I} = A(T) + B(T)\frac{\Theta}{\Theta_{ref}} \tag{3.48}$$

Sakaue [155] showed that the Freundlich isotherm (Equation 3.49) can be used as a model for the surface adsorption of oxygen onto the substrate, as it is a model of the amount of occupied adsorption sites compared to the total number of possible sites.

$$\Theta = b_f (P_{O_2})^{\gamma} \tag{3.49}$$

The constant b_f is a function of temperature and activation energy (also a function of temperature) and γ is an empirical constant to be experimentally determined for every system. Substituting Equation 3.49 into Equation 3.48 gives:

$$\frac{I_{ref}}{I} = A_{Freundlich}(T) + B_{Freundlich}(T)\frac{P_{O_2}}{P_{O_{2ref}}}^{\gamma} \tag{3.50}$$

If PSP measurements are required over very large pressure ranges, Equation 3.45

does not model the non-linear behavior of the PSP well and it is more useful to use Equation 3.50, as the constant, γ, accounts for the non-linearity. This was shown experimentally by the author [156].

The exact format of the constants $A_{Freundlich}$ & $B_{Freundlich}$ is not important as they are determined by proper calibration. Naturally, it would be more helpful if they were weak functions of temperature; however, this is not just dependent on the substrate but also a function of the combination of the substrate and luminophore.

3.4.3 PSP Substrates

The substrate of a PSP determines some of its most important characteristics, such as the response time and the sensitivity range. Temperature sensitivity, signal output and, occasionally, spectral performance, can also be affected. The choice of an appropriate substrate is one of the most important decisions in the design of any PSP experiment and was the subject of a recent study by the author [156].

There are two main types of PSP substrate and a variety of hybrids of the two. The main choice is between either a permeable or a porous substrate. Permeable substrates commonly consist of a polymer layer which is highly permeable to oxygen. The luminophore is suspended in this oxygen-permeable layer, allowing it to be deactivated by oxygen which has diffused into the layer. The application of a reflective basecoat increases the adhesive properties of the active layer but also reflects more light towards the imaging device, increasing the measurable signal (Fig.3.28a). The polymers used at the University of Manchester are known as sol-gels. The sol-gel method is relatively cheap and very easy to perform, requiring very little expensive equipment and has been shown to give excellent results [157]. B. J. Basu [158] showed that the sol-gel films have excellent optical and mechanical properties when applied properly and also showed that the porosity, as well as other properties, of the sol-gel matrix layer can be tailored to suit. MacCraith & McDonagh [159] showed the versatility of sol-gel layers and how their chemical composition has a large impact on the response of the luminophore (or flurophore, as they called it). The sol-gel layer can develop cracks after it has been cured, due to the sol-gel matrix reducing in volume as the solvent (ethanol in many cases) is evaporated off.

Tab 3.10 shows the typical response time of some polymer-based PSP tests. Clearly, for this project such a slow response time is unacceptable and faster alternatives must be considered. The limit on the response time of polymer-based PSP is the diffusion time through the polymer layer [153]. In order to remove this limit, several researchers have developed the use of porous substrates where the luminophore is adsorbed onto the surface, meaning that it is in direct contact with the test gas (Fig.3.28b).

Baron et al. [160] compared the response times between porous and polymer-based oxygen-sensing coatings. This study paved the way for porous substrates to be developed by other researchers, as it showed that the response time could easily be sub-millisecond.

There are two common porous substrates used in high-speed PSP testing: Thin Layer Chromatography (TLC) plates and anodised aluminium. TLC plates are highly adsorbent and have an excellent response time. The work by Baron et al. [160] illustrated that a porous TLC PSP setup could be used to give very fast response times (10s of microseconds). Sakamura et al. [161] showed that a TLC

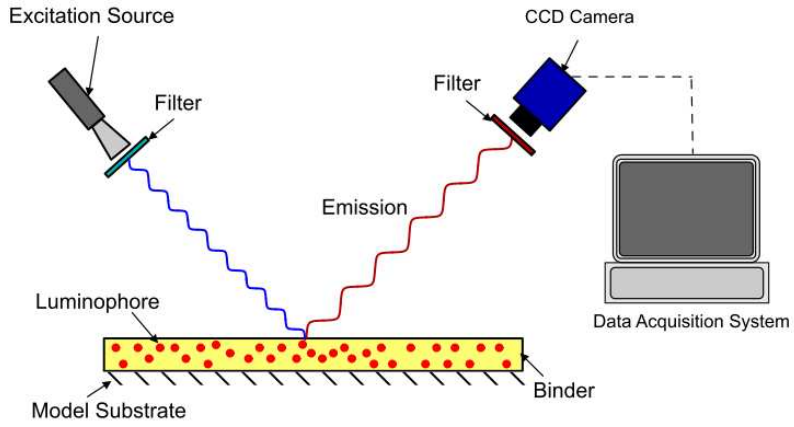

(a) Polymer-based PSP

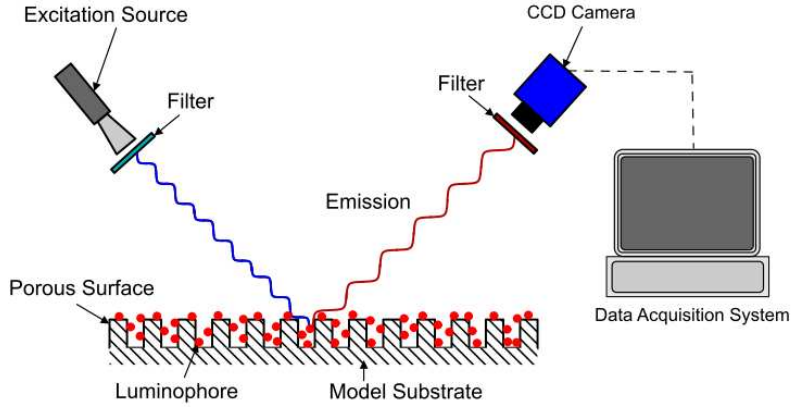

(b) Porous-based PSP

Figure 3.28: Different types of PSP configuration

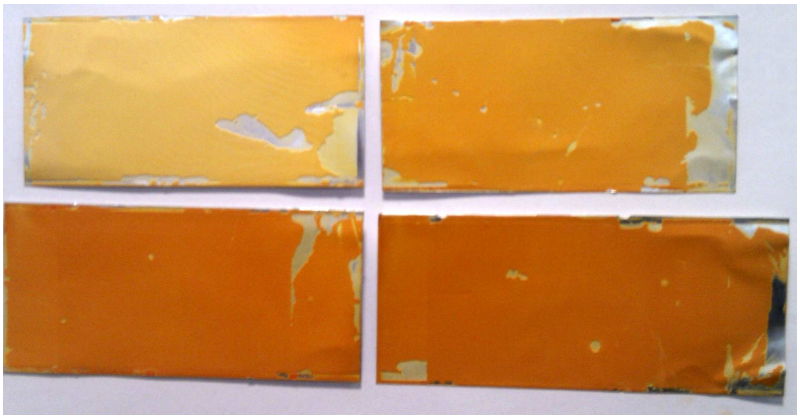

Figure 3.29: Mechanical damage to several initial TLC plates after 10 runs of the shock tube

plate could be used to show transient shock wave phenomena such as the movement of starting shocks in supersonic nozzles, almost impossible to achieve with a finite number of pressure transducers. TLC plates are cheap to buy and it is very easy to apply the luminophore to the surface. However, the plates themselves are extremely brittle and can easily be subject to mechanical damage. As a result of this, they are usually applied only to simple geometries [162] and often have to be replaced due to cracking or fracturing. An example of this can be seen in Fig.3.29.

Anodised aluminium was first suggested as a suitable porous matrix material by Mosharov et al. [163]. A comparison of various matrix materials and binding methods was performed by Sakaue & Sullivan [164], which showed that anodised aluminium gives response times that are fast enough to capture high-speed unsteady phenomenon such as moving shock waves. The speed of this response, as shown by Kameda et al. [165] and Hangai et al. [166], is determined by both the pore diameter and depth. It was shown that the anodisation process (voltages, electrolytes and length of time) has a large effect on the pore size and depth. The most effective combination appears to be the shallowest and widest pores, as these have the fastest response time. The author has shown [156] that the signal level given by luminophores adsorbed onto anodised aluminium is far too low to measure at high speed using a single shot approach.

So far we have encountered a porous substrate which can only be used on simple flat surfaces and one which can only be used on aluminium. There is a hybrid of these two types of substrates where a porous substrate can be sprayed on to any surface. This is known as the polymer ceramic method. Of the limited literature available on this method ([143],[167],[168],[169],[170]), it has been shown that the response time appears to be 25μs minimum. In a similar way to polymer-based PSP, this is dependent on the thickness of the coat [143] and the polymer content [170].

The response time of different PSP substrates is given in Tab.3.10. Many more researchers have shown similar response times; however, these cover the typical range. Several different values given in the research of Sakaue [164] [171] [172] show variation of solvents and of pore depth. A more detailed discussion on this topic is given in the review by Gregory et al. [143].

Table 3.10: Response time of PSP substrates

Substrate	Test type	90% response time $[ms]$	Author
Silica gel	Solenoid valve	10	Baron et al. [160]
Silica gel	Solenoid valve	1.5	Baron et al. [160]
Polymer	Solenoid valve	480-2500	Carroll et al. [173]
Polymer	Shock tube	3-6	Hubner et al. [174]
Polymer	Shock tube	172	Sakaue & Sullivan [164]
Sol-gel	Solenoid valve	5-540	McDonagh et al. [175]
Anodised aluminium	Shock tube	0.035-0.102	Sakaue & Sullivan [164]
Anodised aluminium	Shock tube	0.03-0.04	Sakaue [171]
Anodised aluminium	Shock tube	0.06	Kameda et al. [176]
Anodised aluminium	Shock tube	0.05-0.15	Sakaue et al. [172]
TLC	Solenoid valve	0.025	Baron et al. [160]
TLC	Shock tube	0.065	Sakaue & Sullivan [164]
TLC	Shock tube	0.04	Sakamura et al. [161]
TLC	Shock tube	0.15	Hayashi et al. [169]
Polymer ceramic	Shock tube	0.349	Sakaue & Sullivan [164]
Polymer ceramic	Shock tube	0.15	Hayashi et al. [169]

3.4.4 Luminescent Compounds

Optical pressure measurements are only possible using compounds which display sensitivity to the gas used (in our case oxygen). There are many luminophores that exhibit different properties, such as pressure and temperature sensitivity, quantum yield, luminescent lifetime and photodegradation. The review by Takeuchi & Amao [177] gives an excellent overview of the photoactive compounds which are currently in use. They are largely broken down into three categories: transition metal polypyridyl complexes, porphyrins and polyaromatic hydrocarbons. With the exception of polyaromatic hydrocarbons, these complexes are extremely difficult to synthesise and, as such, can be very expensive.

Only $Ru(dpp)_3^{2+}$ (or, to give it its full name, *tris-Bathophenanthroline Ruthenium II Perchlorate)* will be covered in detail in this review. The other two luminophores considered, PtTFPP and PBA, have problems associated with this kind of test which prohibited their use (namely, PtTFPP has too long of a luminescent lifetime to gain meaningful results; and PBA has very high photodegradation [178] and it is difficult to illuminate it with the required power in its absorption range).

$Ru(dpp)_3^{2+}$ (Fig.3.30) has excellent properties as a luminophore, such as a high quantum yield, excellent pressure sensitivity and acceptable temperature sensitivity [156]. The molecule has also been shown to be highly photostable, meaning that it can be used in repeat tests. It also exhibits a large Stokes shift [179], a desirable property of any photoactive molecule. This large Stokes shift can be seen in Fig.3.31 as the large gap between the excitation and emission signals. The luminescent lifetime of $Ru(dpp)_3^{2+}$ is approximately $5\mu s$ [180], which sets the ultimate limit on the luminophore response time. Other luminophores have much shorter lifetimes

(PBA, for example); however, $Ru(dpp)_3^{2+}$ is the best all-round luminophore, which explains why it is the most commonly used.

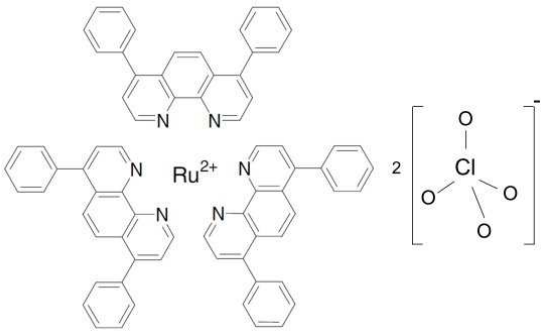

Figure 3.30: $Ru(dpp)_3^{2+}$ molecule

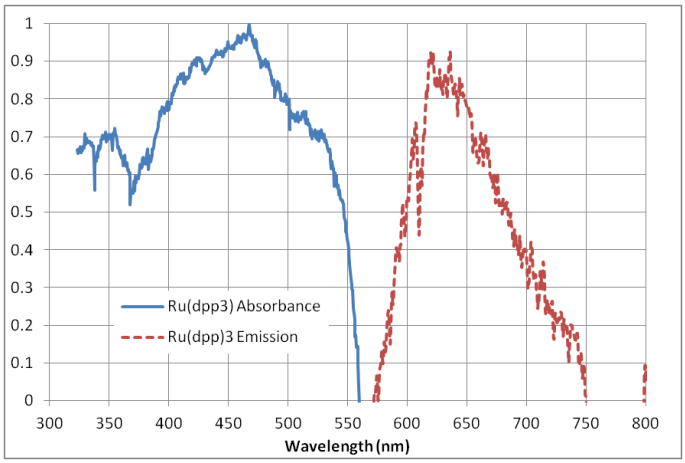

Figure 3.31: Excitation and emission spectra of Ru(II) and PtTFPP[4]

3.4.5 Limitations

There are several limitations of PSP which affect its application to all flow speeds. Low-speed limitations have been covered by the author in other works [156][181][182]. Consequently, only high-speed limitations will be covered in this section.

As with all PSP measurements, the temperature-induced error is often the largest source of error. This has been a major problem in the application of PSP to high-speed flow, as large changes in static temperature are expected. This has led some researchers to use different calibrations on either side of a shock wave to account for the temperature change [148][183]. The author has shown that the temperature dependency of the PSP formulations typically used at the University of Manchester [156] is typically $-0.9\%^{\circ}C^{-1}$. This is a significant problem for the measurement of steady and quasi-steady flows. However, the flow under investigation in this project is transient; as such, the temperature change over the model is expected to be negligible.[8]

[8]Estimates using the thermal conductivity properties of aluminium gave temperature changes of less than 0.01°C over 250μs.

Over time, and under illumination, PSP will photodegrade, become less sensitive to oxygen and give out a lower signal output. The mechanisms of this were the focus of a study by Egami & Asai [178]. The use of powerful light sources for excitation only exacerbates this problem. Photodegradation rates of 4.5% per hour are typical for low-level excitation [156]; however, for this research, the use of a much more powerful light source means that this value could be significantly higher. Despite this, the total acquisition time for this project is only of the order of milliseconds, meaning that photodegradation can be neglected (provided that in-situ calibration is used).

Gregory et al. [184] showed the difference in response between an increase and a decrease in pressure. Their results showed that decreases in pressure were displayed in the PSP results more quickly than increases in pressure. They showed the variation of these changes for different constant values of Equation (3.50). It was found that the response times became closer as the exponent, γ, decreased.

Porous substrates readily adsorb water from the test gas onto the surface. This can have a significant effect on the sensitivity and luminescent output of the samples [176] (up to a 10% change in intensity output from dry air to 50% relative humidity). To this end, Sakaue et al. [172] developed a hyrdophobic coating to apply to porous PSP in order to reduce its sensitivity to changes in humidity. Due to the sensitivity of the PSP to humidity, all of the TLC samples created were baked in an oven to reduce their local moisture content before testing.

Due to the extremely short exposure time required to accurately capture transient flows, acquiring a measurable signal can be a significant problem. One cannot simply increase the luminophore concentration, as this will affect the sensitivity and can actually reduce the signal output [185]. Therefore, the only viable alternatives are to use very powerful light sources and highly sensitive cameras. In some high-speed experiments [176][172], laser light sources have been used. This has the advantage of guaranteeing that there is no spectral leakage between excitation and emission, but also has the problem of not utilising the whole excitation spectrum of the luminophore. Therefore, broadband light sources can be used in conjunction with filters. Using high-power broadband light sources increases risks to safety, with high levels of UV radiation emitted.[9] The heat generated by these light sources needs to be removed, ideally by using a water filter; however, this is sometimes not enough to prevent damage to other components in the optical train. It is the recommendation of the author that any experimentalist wishing to conduct tests of this nature do so using filters based on reflectance rather than absorption. Despite taking every possible cooling precaution when using absorption-based filters, they are still likely to break due to the thermal stresses created by the beam (see Fig.3.32 for an example[10]).

[9]High-power light sources also give rise to the creation of O-zone, another potential health hazard.

[10]The same fate was met by other filters, including *heat-proof* glass used for IR absorbance.

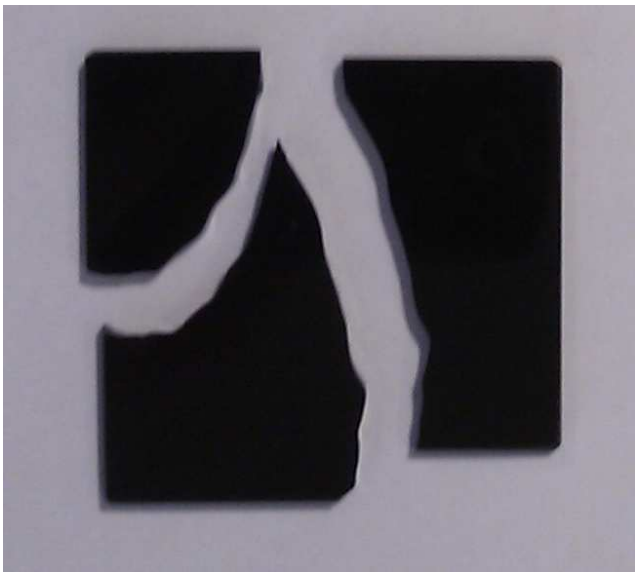

Figure 3.32: The fate of a UG5 400 nm short-pass filter after 20 seconds' exposure to a 1 kW beam after a water and blue dichroic filters

3.4.6 Applications

Pressure-sensitive paints have been used in wind tunnels of almost all speeds from low-speed automobile testing up to hypersonic vehicle design. The range of pressure changes that they can reliably detect is always on the increase and appears to be a function of the imaging system used. Engler et al. [186] captured a resolution of 500 Pa using a lifetime-based method and managed to successfully resolve leading-edge vortex roll-up on a delta wing at Mach 0.9 using an intensity-based system. It was shown by McGraw et al. [187] that pressure changes as low as 6 Pa can be detected in a resonant cylinder, allowing the PSP sample to effectively be used as a microphone. McGraw et al. [151] and Nakakita [188] both showed resolutions of $\approx$ 200 Pa for vortex shedding from two-dimensional objects at a frequency of $95 - 125$ and 2000 Hz respectively. Nakakita utilised a very interesting and novel data analysis technique based on the Fast Fourier Transform (FFT) which showed the importance of different parts of the frequency range of vortex shedding allowing for accurate calculation of the Strouhal number. Henne [189] showed a resolution of 150 Pa on measurements of an A400m half model at low speeds. This research incorporated active temperature correction by using an infra-red imaging device. The author has used PSP to capture the flow around a U-bend used to model the flow around the cooling passages found in turbine blades [181][182].

The advent of porous PSP has meant that it became possible to use PSP in cryogenic applications, as no oxygen diffusion is needed (it is usually hindered/prevented by a polymer layer at such low temperatures [190]).

Practical applications of PSP have been shown by numerous researchers: Klein et al. [191], Zare-Behtash et al. [192], Engler et al. [193] [186] and Sakamura & Suzuki [194], to name just a few. Klein et al. [191] showed that PSP can be used to calculate normal forces and moments on model aircraft in wind tunnel tests. Although force balances are an excellent way of measuring this and do not usually need to be replaced, the comparison shows that surface integration of PSP tests

can yield accurate results ±5%. Sakamura & Suzuki [194] showed that the starting shock of a de-Laval nozzle can be captured using a porous PSP setup and a high-speed CMOS camera. This body of research highlights the potential that PSP has for imaging transient phenomena, leading to almost limitless applications within the aerospace research or design sectors. Non-engineering applications of PSP, or rather oxygen sensitive luminophores, have also been demonstrated. Mills [195] and other researchers have used luminescent complexes to measure the oxygen levels of blood samples.

3.4.7 Setup

The high-speed PSP system used in this research is shown in Fig.3.33. Two blue dichroic filters purchased from Edmund optics, used in conjunction with heat absorbent glass, were placed in front of the excitation light source (consisting of 1000 W and 300 W xenon arc lamps, providing broadband excitation). Both xenon arc lamps were purchased from Newport Oriel. The 1000 W lamp requires a water filter, which was powered using an in-house-constructed water filter system. The emission signal was filtered using a 530 nm long-pass filter attached to a Vision Research Phantom 710 high-speed video camera. The spectra of the light source and the relevant filter transmissions were measured using the Princeton Instruments ICCD spectrometer and are given in Fig.3.34. The Phantom camera is well-suited to tests of this type due to its large pixel size and high quantum efficiency over a wide range of wavelengths. The capture rate is 100 kHz with an exposure time of 9.6μs. At such a high frame rate, the image resolution was limited to 224×184 pixels giving a pixel density of approximately 3.2 pixels per mm. The field of view of the PSP experiment is shown in Fig.3.24. The images were stored on a PC running Windows XP using Vision Research's proprietary software. Triggering of the capture as performed using the same Kulite transducer as the previous tests without the delay generator. The decision not to use a delay generator was taken so that the images taken before the arrival of the shock wave could be averaged and used as the reference, wind-off image.

3.4.7.1 Sample Preparation

In order to deposit some luminophore onto a surface, it first must be dissolved in solution. Sakaue [171] showed the difference between ten solvents with widely varying polarity. It was found that some non-polar solvents would not dissolve even a small amount of the luminophore (this is especially a problem for PBA). The two most promising solvents for dissolving $Ru(dpp)_3^{2+}$ are dichloromethane and acetone, as these deposited the most luminophore on the surface, therefore producing the highest signal level. Dichloromethane gave the highest pressure sensitivity over a large range; however, acetone gave the highest signal output.

It is known that the higher the concentration of luminophore in solution, the more will be deposited on the surface, until the surface is saturated. However, Sakaue & Ishii [185] showed that increasing the amount of luminophore deposited on the surface does not monotonically increase the signal output or the sensitivity; rather, it decreases past a critical value. They found that the optimum luminophore concentration is of the order of 0.1 mM. Sakaue & Ishii [196] also showed that the

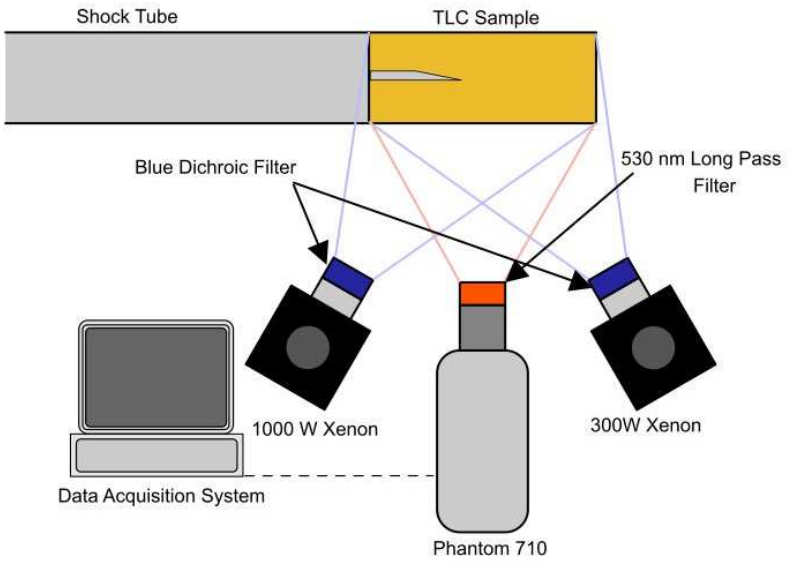

Figure 3.33: PSP setup

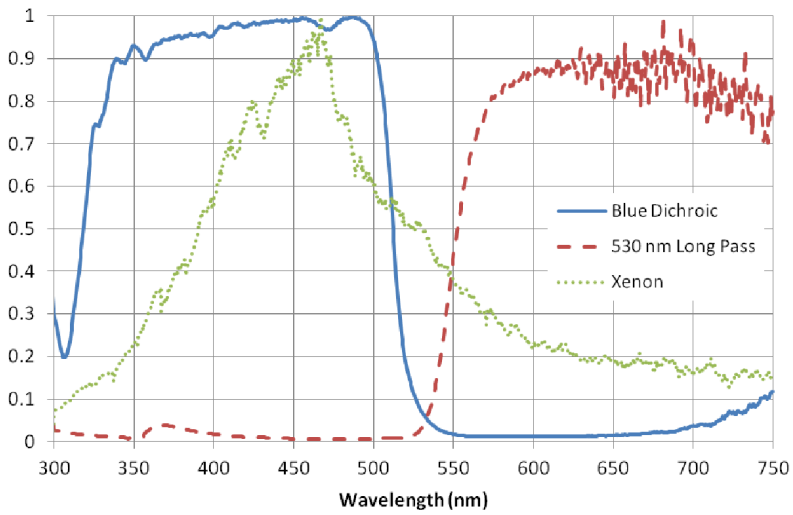

Figure 3.34: PSP filters used in this project

length of time for which the substrate is immersed in the luminophore solution has a strong effect on the signal output and the temperature sensitivity of the final sample. They found the optimum time to be approximately 17 minutes.

Using the two basic formulae related to molar concentrations allows for the calculation of the required mass of luminophore in a given volume of solvent for a specific concentration. 64.85 mg of $Ru(dpp)_3^{2+}$ (purchased from GFS chemicals) was dissolved in 100 ml of dichloromethane (purchased from Sigma Aldrich) at room temperature, giving a 0.5 mM solution.[11] The TLC plate (MERCK HPTLC Silica-Gel 60) has been used previously by Gongora-Orozco et al. [197], who showed the difficulties which can occur using the dipping method of application. If great care is taken, uniform application can be achieved using this method, as can be seen in Fig.3.29. The samples were placed in the solution for 17 minutes and then placed in an oven at 340 K to evaporate the solvent, leaving a uniform coat of luminophore molecules on the porous substrate.

Preparation of PSP samples in this way should be performed using safety apparatus such as high-grade filter masks in order to prevent inhalation of the dichloromethane fumes. Thick safety gloves should be worn when handling the samples, as the solution can easily pass into the bloodstream if it comes into contact with the skin.

3.4.8 Post-Processing

The data that is gained from performing PSP tests is in the form of intensity maps that can be converted to pressure maps if the correct factors are applied (Equations 3.48 or 3.50). However, before we begin to apply these factors, the images must be processed in order to make them more usable. The initial processing of this data is performed using ImageJ and then the data is finally presented in Tecplot.

Up to the arrival of the shock wave, approximately 150 images are captured by the Phantom 710. These images are averaged (z-projected) to create a wind-off reference image. The reference image is then divided by all the images captured after this, giving us the intensity ratio, I_{ref}/I. Three runs were repeated for each initial pressure ratio and model, meaning that they can be ensemble averaged to reduce the random shot noise. The images sequences are synchronised to the point where the incident shock wave reaches the apex of the model. This final sequence of images is smoothed using a 3×3 linear filter. The calibration curve is then applied in Tecplot to give the pressure map over the surface.

Other types of filters have been considered, such as bandpass FFT; however, these appear to have little advantage over the simple linear filter.

3.4.8.1 Calibration

There are two conventional methods of calibrating pressure-sensitive paints; *in situ* and *a priori*. *In situ* calibration involves using pressure taps and transducers on the actual test model in order to verify the response of the paint. This increases the cost and complexity of the model (the very thing PSP is designed to reduce). Only *in situ* calibration can realistically and reliably be used with low-speed flow. Recently, some researchers have applied *a priori* calibration to low-speed flow, with

[11] Initial attempts with lower concentrations gave an unsatisfactory signal output.

Table 3.11: PSP calibration constants

$\frac{P_4}{P_1}$	Geometry	A	B	γ	R^2
4	Sharp	-284.001	285.002	2.736 $\times 10^{-4}$	0.934
8	Sharp	-603.976	604.980	1.185 $\times 10^{-4}$	0.923
12	Sharp	-511.035	512.037	1.590 $\times 10^{-4}$	0.930
4	Round	-96.327	97.327	1.160 $\times 10^{-3}$	0.917
8	Round	-3605.311	3606.312	2.569 $\times 10^{-5}$	0.932
12	Round	-3405.599	3406.600	2.660 $\times 10^{-4}$	0.922

some success by Mori et al. [198]. However, Mori does not mention the possibility of photodegradation or the method of image processing used. It does mention temperature correction; however, the correction seems to be purely arbitrary to fit results obtained from pressure tappings. In general, *a priori* is used as it gives the Stern-Volmer coefficients prior to testing in a wind tunnel. The *a priori* method can also be used to evaluate potential paint formulations without the need for full-scale testing. This lower cost and simplicity is the reason that *a priori* calibration is more widely used. *A priori* calibration is more sensitive to temperature changes between the calibration and the test run and as such a complete temperature map is often required. *A priori* calibration is difficult to achieve if there are significant differences between the static calibration performed under controlled conditions and the physical test. It is important to ensure the same optical conditions between the static calibration and the test. Initial static calibrations of the TLC samples (with such powerful light sources) showed significant photodegradation over the calibration process, meaning that the calibration constants were not reliable. Also, as the humidity changes from day to day, the PSP test response will change; however, the calibration will not. Therefore, it was decided to use *in situ* calibration.

The pressure measurements taken using the Kulite transducers, shown in Section 3.3, are used to calibrate the intensity ratio at the tap location. This type of unsteady calibration means that instead of the usual 10 or so pressure taps used for *in situ* calibration, three taps over 50 images can be used, giving 150 discrete calibration points.

The intensity ratio from the PSP images is plotted against the pressure ratio measured by the Kulites in Figs. 3.35 & 3.36. The trend between the two follows the expected curve given by Equation 3.50 and is consistent with previous researchers' results. Using the signal processing package OriginPro, a curve fit for the data is estimated to give the calibration constants for each test (Tab.3.11).

3.4.9 Sources of Uncertainty

PSP offers a seemingly vast improvement in the field of pressure measurement; however, it is not without its limitations. There are specific limitations that affect high-speed flow, low-speed flow and PSP measurements in general. Uncertainty in PSP measurements can be categorised into three broad categories:

- Calibration errors
- Signal measurement errors

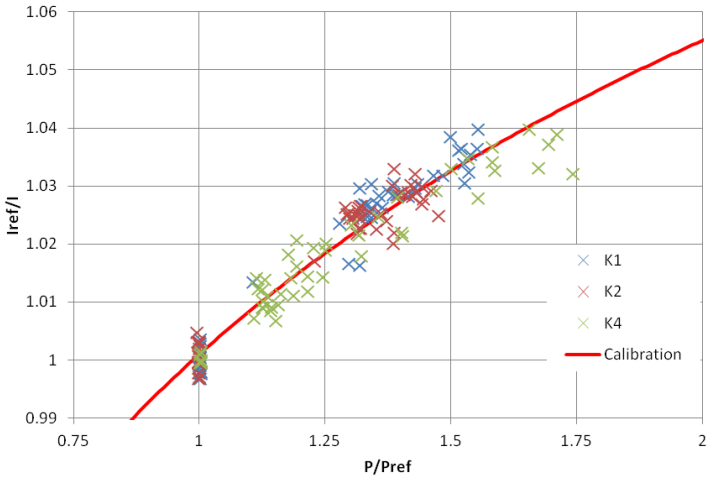

(a) $\frac{I_{ref}}{I}$ vs $\frac{P}{P_{ref}}$, $\frac{P_4}{P_1} = 4$ Sharp geometry

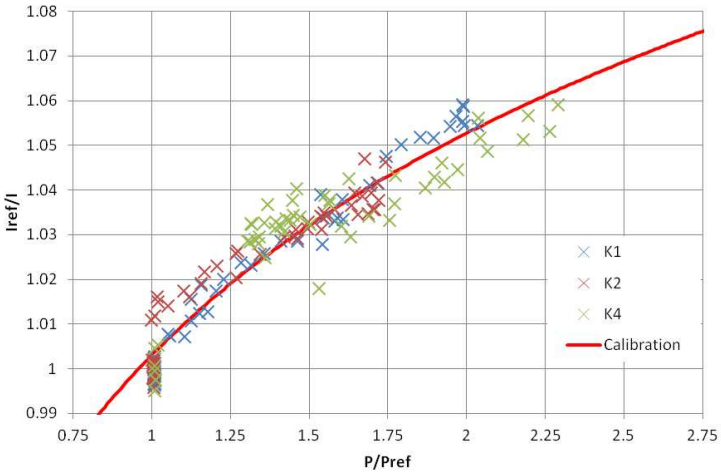

(b) $\frac{I_{ref}}{I}$ vs $\frac{P}{P_{ref}}$, $\frac{P_4}{P_1} = 8$ Sharp geometry

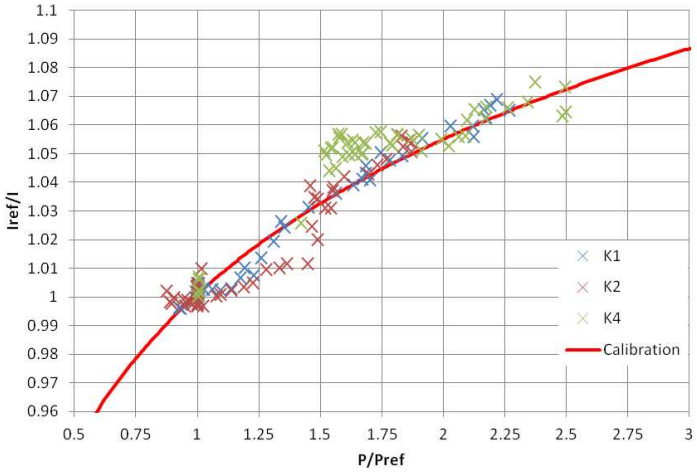

(c) $\frac{I_{ref}}{I}$ vs $\frac{P}{P_{ref}}$, $\frac{P_4}{P_1} = 12$ Sharp geometry

Figure 3.35: Dynamic calibration of PSP samples for sharp geometry

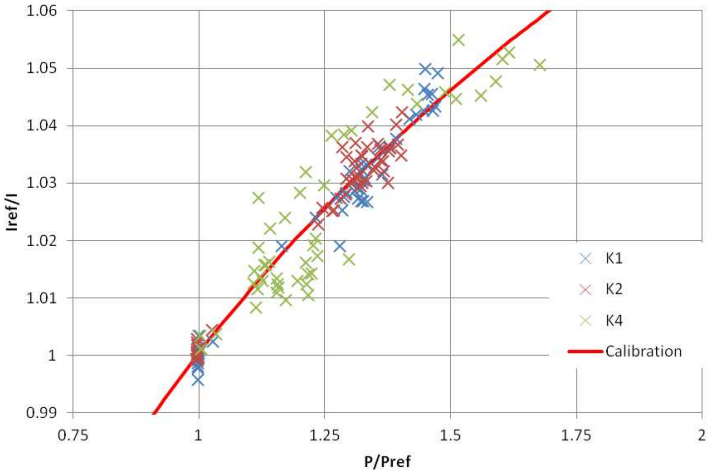

(a) $\frac{I_{ref}}{I}$ vs $\frac{P}{P_{ref}}$, $\frac{P_4}{P_1} = 4$ Round geometry

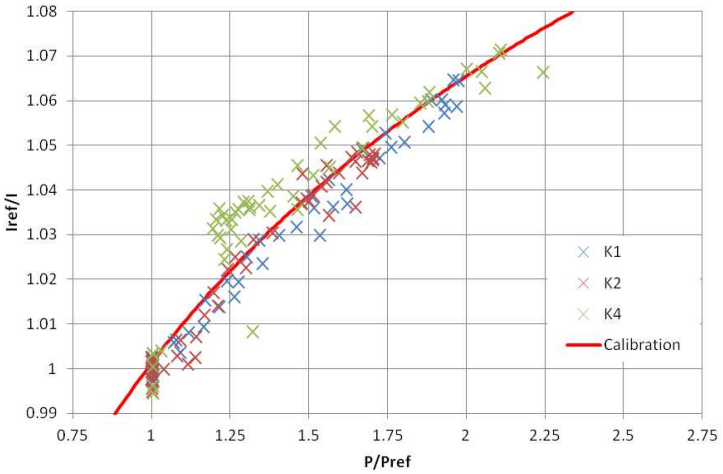

(b) $\frac{I_{ref}}{I}$vs $\frac{P}{P_{ref}}$, $\frac{P_4}{P_1} = 8$ Round geometry

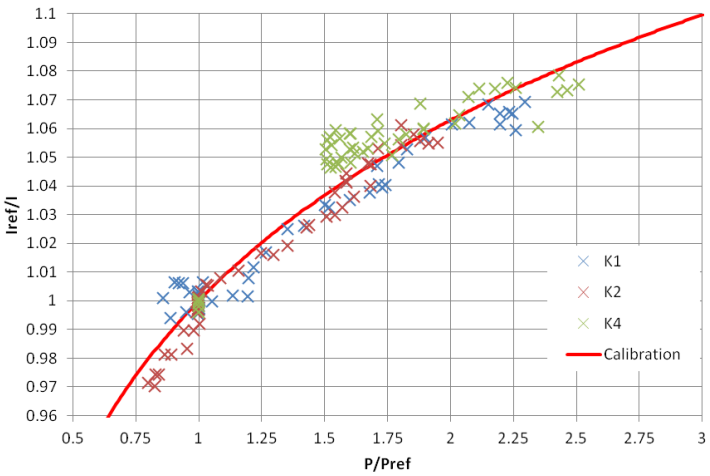

(c) $\frac{I_{ref}}{I}$ vs $\frac{P}{P_{ref}}$, $\frac{P_4}{P_1} = 12$ Round geometry

Figure 3.36: Dynamic calibration of PSP samples for round geometry

- Response time errors

Given that PSP measurements are only taken over very short time frames (250μs) and that silica-gel (the main component of the TLC substrate) is a very good thermal insulator, it is assumed that there are no temperature-induced errors.

3.4.9.1 Calibration Errors

Drift between calibration curves is a problem for systems using the *a priori* method, especially porous PSP. Changes between the test temperature and the calibration temperature cannot be accounted for, such as changes in the day-to-day temperature. This can lead to significant bias errors in the final results. *In situ* calibration suffers from these problems less, as the calibration curve is captured at the same time as the test. The major source of calibration error, at least in this experiment, is how well the calibration curve is fitted to the experimental data. It can be seen in Figs. 3.35 & 3.36 that there is some spread of the data around the curve fit. In order to quantify the extent of this error, the residual sum of squares (σ_{cal}) must be recorded. This value is given by the OriginPro and is recorded in Tab.3.12.

3.4.9.2 Signal Measurement Errors

The errors introduced by signal measurement are essentially concerned with the detector shot noise, which cannot be avoided. However, as this error is statistically random, summing a number of images reduces it by a factor of $N^{-1/2}$. Temporal fluctuations in the intensity emitted by the light source also cause errors. These temporal fluctuations are often caused by the cooling of light sources such as Xenon lamps. In order to minimise these errors, the light sources were left to settle for 5 minutes so that the cooling flow reached a steady state before any images were taken. It is important to make sure that the PSP sample is not exposed to the light during this time, as the high-intensity light causes significant photodegradation.

3.4.9.3 Response Time Errors

The finite response time of the luminophore and substrate combination will spread the shock wave over a finite distance. This, combined with the minimum exposure time of 9.6 μs, means that the blur of the shock wave is expected to be at least equal to its distance travelled over that time. Fig.3.37 shows the response of all of the cases tested. From this figure it is clear to see that the response of the PSP layer is independent of the shock speed. The constant response of the PSP implies that it is independent of any physical processes, or at least that the strength of the shock wave does not effect any physical processes involved. It is difficult to separate out the dependency of the lifetime of the luminophore from the finite time required to diffuse into the porous layer. Fig.3.37 is based on normalising the pressure output to its maximum value; this is slightly misleading due to the random noise on the signal (to be covered shortly), and as a result it is difficult to ascertain the 90% rise time. However, it does show that moving shock fronts can be captured using this experimental setup.

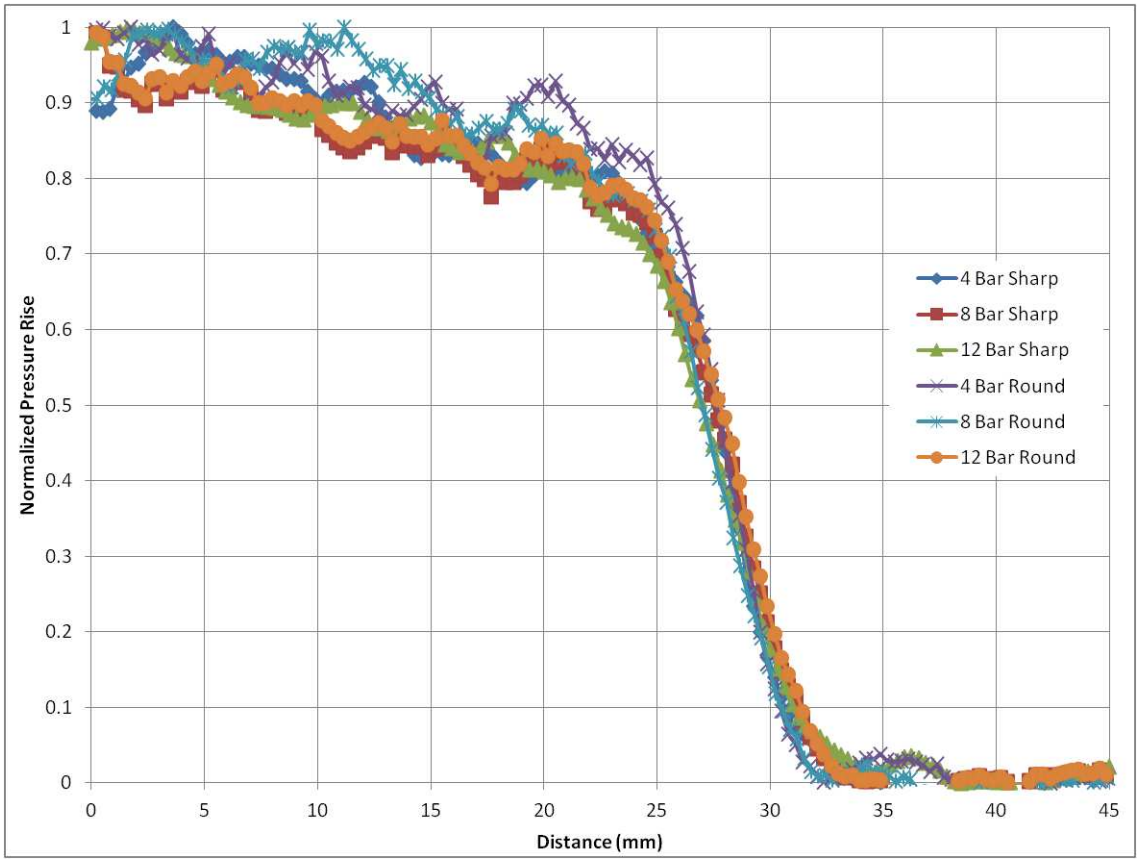

Figure 3.37: Shock fronts measured using PSP

3.4.10 Uncertainty and Repeatability

The triggering uncertainty, as mentioned previously, is the same for this experiment and as such will not be discussed. Despite the triggering uncertainty, the 10 μs exposure time means that shock fronts will be smeared. It is difficult to separate out the response time of the paint from the exposure time required to get a measurable signal. The PSP measurements appear to give the same intensity ratio for repeat tests and, as is shown in Fig.3.38, show good repeatability. As before, random error is estimated from the uniform region behind the incident shock wave for all three repeats of each test condition. There is a random component of the bias error which accounts for the shot noise and excitation light intensity changes. As three sequences of images are ensemble averaged to give the final results, this shot noise error is divided by $\sqrt{3}$. Bias error also consists of the average deviation between the calibration curve and the experimental data in Figs. 3.35 & 3.36.

The uncertainty calculation for the PSP results is rather involved. To calculate the sensitivity coefficient, we first rearrange Equation 3.50 for P/P_{ref}, giving:

$$\frac{\partial \frac{P}{P_{ref}}}{\partial \frac{I_{ref}}{I}} = \frac{1}{\gamma B}\left(\frac{\frac{I_{ref}}{I} - A}{B}\right)^{\frac{1}{\gamma}-1} \tag{3.51}$$

Equation 3.51 can then be multiplied by the shot noise estimation (σ_{shot}) and the calibration error (σ_{cal}) to give us a bias in P/P_{ref}. Multiplying by P_{ref} gives us the bias in P. The total uncertainty of the Kulites Equation 3.32 used for calibration

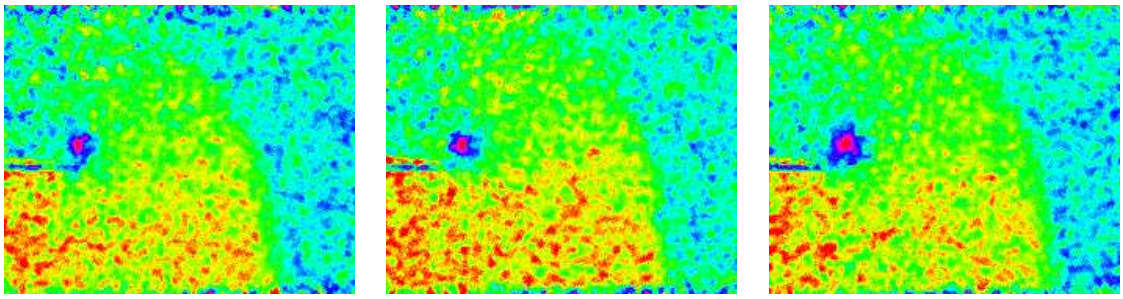

(a) $\frac{P_4}{P_1} = 4$ repeat 1 (b) $\frac{P_4}{P_1} = 4$ repeat 2 (c) $\frac{P_4}{P_1} = 4$ repeat 3

Figure 3.38: Three repeats of the same strength shock measured using PSP

Table 3.12: PSP uncertainty

$\frac{P_4}{P_1}$	Geometry	σ_{shot} I_{ref}/I	σ_{cal} I_{ref}/I	σ_{random} I_{ref}/I	Total Pressure Uncertainty Ψ (bar)
4	Sharp	0.0291	0.00156	0.0045	0.261
8	Sharp	0.0283	0.00394	0.0024	0.271
12	Sharp	0.0287	0.00684	0.0022	0.259
4	Round	0.0304	0.00294	0.0060	0.213
8	Round	0.0294	0.00510	0.0046	0.241
12	Round	0.0319	0.00962	0.0143	0.276

must also be considered in this analysis. The total uncertainty, Ψ, can then be estimated:

$$\Psi = \sqrt{\Psi_{kulites}^2 + \sigma_{random}^2 + \sigma_{bias}^2} \tag{3.52}$$

where

$$\sigma_{bias} = P_{ref}\sqrt{\left(\frac{\partial \frac{P}{P_{ref}}}{\partial \frac{I_{ref}}{I}} \times \sigma_{shot}\right)^2 + \left(\frac{\partial \frac{P}{P_{ref}}}{\partial \frac{I_{ref}}{I}} \times \sigma_{cal}\right)^2} \tag{3.53}$$

The total uncertainty appears to be relatively constant for all pressure ratios, implying that the bias error is dominant. This is to be expected given the repeatability of the shock tube from the other experiments. Increasing the pressure ratio of the shock tube (ideally by evacuating the test section) should lead to a reduction in the percentage of uncertainty.

Chapter 4

Apparatus

People like to imagine that because all our mechanical equipment moves so much faster, that we are thinking faster, too - Christopher Morley

This chapter shows the experimental apparatus used in the tests and the numerical procedure adopted.

4.1 Shock Tube

The shock tube is of square cross-section where the driver and driven sections are the same cross-sectional size. The internal width and height of the shock tube is 24.8 mm and the external height and width is 30 mm, giving a wall thickness of 2.6 mm. The driver section is 0.7 m long and the driven section is 1.7 m long and is open to the atmosphere. The plunger of the shock tube is pointed from the driver to the driven section and has a spring-loaded sharp tip to rupture the diaphragm. The diaphragm section comprises of two gaskets (one attached to the driver and one to the driven) which are bolted together before pressurisation. The diaphragms used are made of acetate and are of the minimum thickness required to stop premature rupturing while pressurising the driver section. The minimum thickness is used so that as little as possible of the energy of the shock wave is wasted, accelerating the fragments of the diaphragm to the induced velocity, as discussed in Section 2.2.3.

The supports of the facility were, previously, rather flimsy and caused repeatability issues [162]. New supports were manufactured in order to reduce vibrations and enhance repeatability.

The calculation of x-t diagrams from the theory given in Section 2.2.1 allows us to estimate the arrival time of the incident shock and run time of the shock tube, i.e. the time before the contact surface reaches the test section or if the reflected expansion head crosses the contact surface. This calculation is based on the experimental Mach number from Section 3.1.7. Fig.4.1 shows the x-t diagrams based on M_{ie} as calculated by a Matlab code written by the author. The test times and shock arrival times are given in Tab.4.1.

4.1.1 Test Section

The test section is made of perspex, with interchangeable side walls so that different experiments can be performed. Using the standard perspex walls, schlieren and

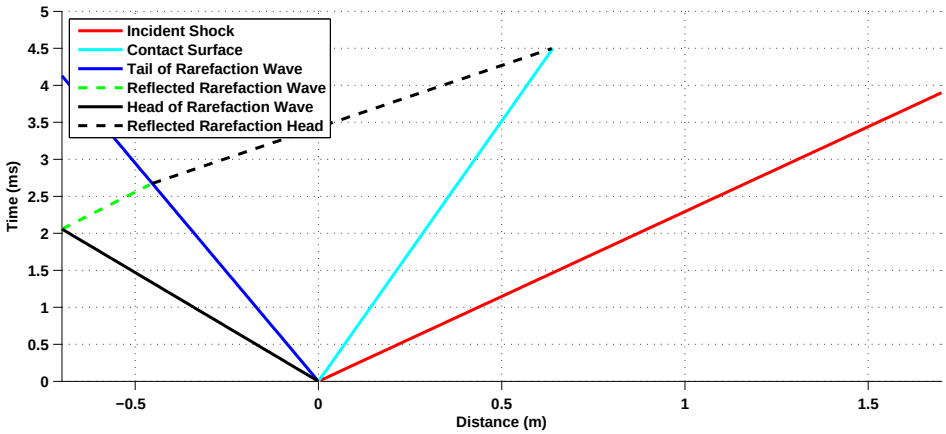

(a) $M_i = 1.28$

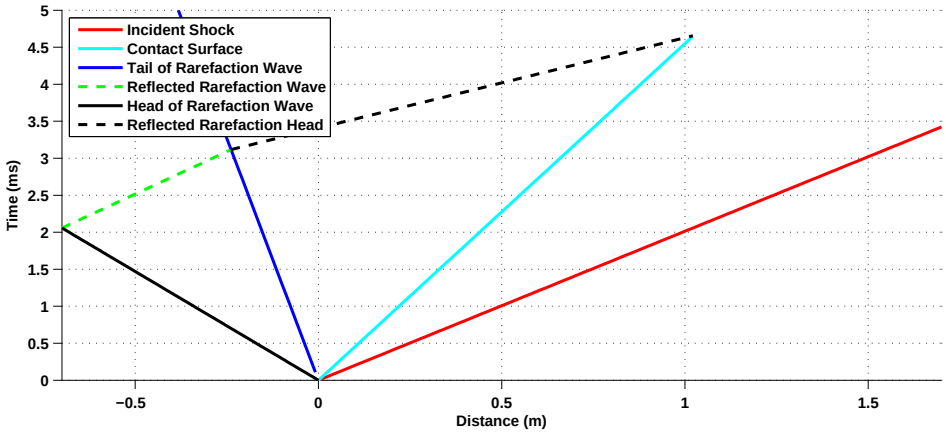

(b) $M_i = 1.46$

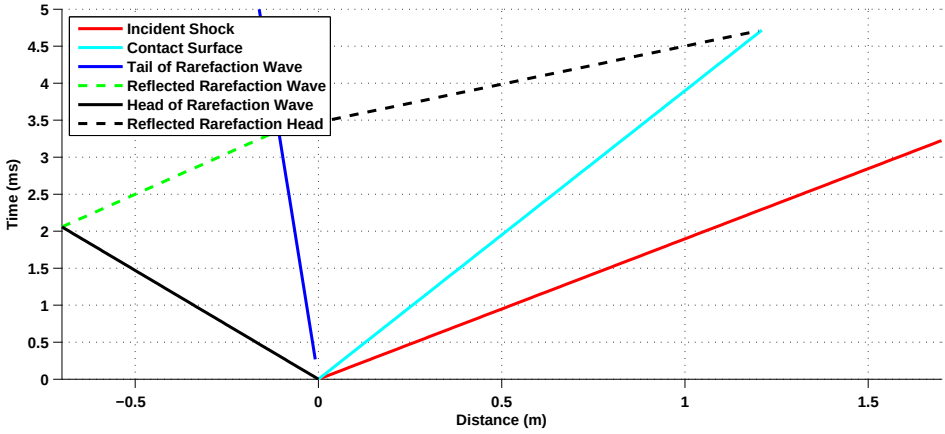

(c) $M_i = 1.55$

Figure 4.1: x-t diagrams for experimental Mach numbers

Table 4.1: Theoretical and experimental induced velocity

M_{ie}	Shock arrival time ms	Test time ms
1.28	3.91	1.89
1.46	3.42	1.69
1.55	3.23	1.60

PIV can be performed. A UV-transmitting perspex side wall is used for the PSP experiments and an aluminium side wall is used for the pressure measurements. All of the test section configurations are flush-mounted to the shock tube using a perspex flange.

The two models that will be tested are a 172° sharp corner and a rounded corner with a corner radius of 2.8 mm.

Figure 4.2: Diagram of test section and shock tube

4.2 Spanwise Variations

All of the analysis, experimentation and simulations in this project assume that the flow is completely two dimensional. To this end, some of the PIV experiments were repeated at different spanwise locations to demonstrate the lack of any meaningful three dimensionality. Fig 4.3 shows the same timestep of a M= 1.46 shock wave diffracting around the rounded geometry at four different spanwise locations. The variations in velocity are within experimental error, demonstrating that two-dimensional simulations and analysis are sufficient for this investigation.

Later results of side-wall pressure histories compared with two-dimensional simulations (see sections 5.3 and 5.4) also confirm this hypothesis.

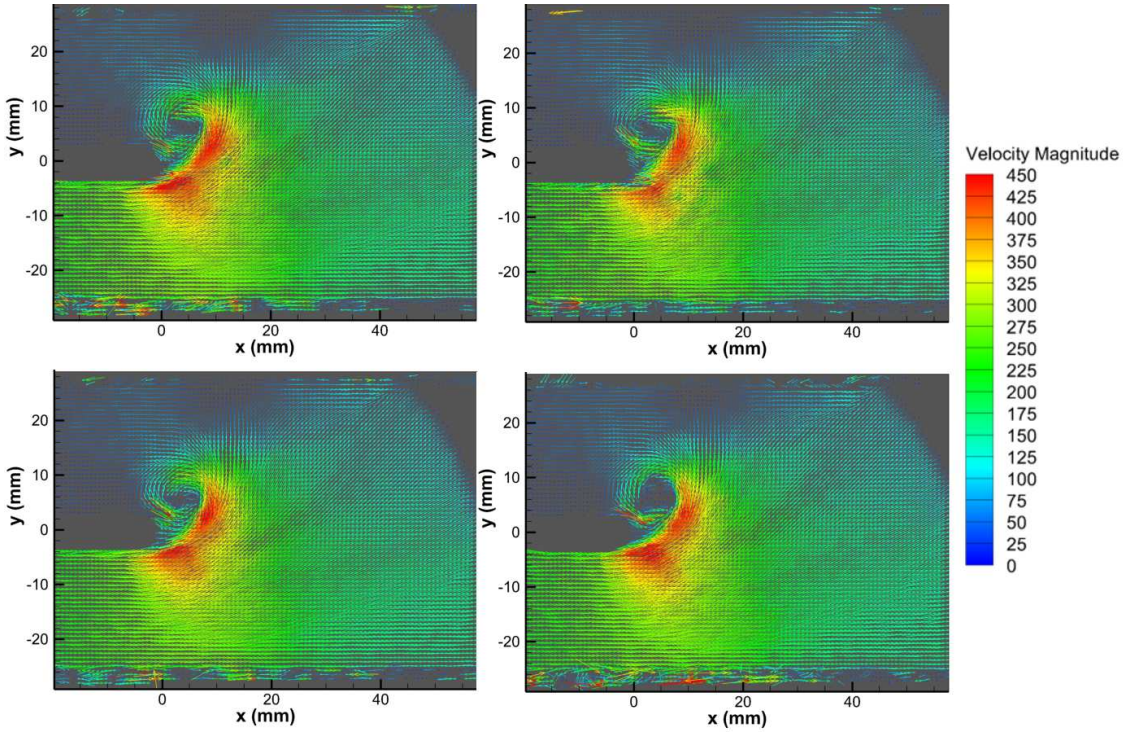

Figure 4.3: M= 1.46 shock at same time step and 4 different spanwise locations

4.3 Simulation Setup

When performing simulations, the choice of discretisation scheme in both space and time is crucial. This is especially a problem when simulating flows containing shock waves, as these discontinuities can give rise to Gibbs phenomenon[1] if higher-order discretisation schemes are used. A low-order scheme can give a severely over-damped solution, resulting in sharp gradients being spread out. This is not suitable for the computation of moving discontinuities. However, if a higher-order scheme is used, sharp gradients can be over-predicted. This can result in the system being under-damped, leading to non-physical oscillations. It is therefore necessary to perform the same simulation with different schemes to find which ones agree best with the analytical inviscid solution.

In this project, the commercial code FLUENT as part of Ansys 13 was used to simulate the shock tube and the shock wave diffraction process.

Initial inviscid, implicit simulations showed poor convergence and large non-physical oscillations at discontinuities in the flow. Despite lowering the CFL number, convergence was still poor. Very poor convergence characteristics and the lack of complete control over the time step led on to the use of an explicit discretisation scheme. Even with explicit discretisation and an extremely small time step was required as there were still some small non-physical oscillations. This indicated that FLUENT is a very non-diffusive code, usually a good property for a shock tube problem. This gave rise to a CFL criterion of CFL$\approx$ 0.2 to reduce non-physical oscillations; however, this did increase the computational cost significantly.

Initial inviscid simulations were performed with a coarse grid made up of 80k

[1]Gibbs phenomena is the term used to describe non-physical oscillations around discontinuities in CFD

quadrilateral cells (0.4×0.4 mm), with an 0.08 m driver section and a 0.12 m driven section, giving a shock tube length of 0.2 m. The boundary condition is a pressure outlet, with a gradual sponge layer to reduce waves reflected back by the *non-reflecting boundary*. The flow is initialised at atmospheric pressure everywhere, with the driver section patched to have a higher pressure. The shock tube diaphragm pressure ratio corresponds to the experimental Mach numbers discussed previously (Tab.3.3). The CFL number was 0.2 for all the schemes and the simulation was left to run for 148.5 μs before comparison with inviscid theory, computed using a MATLAB code written by the author.

Initially, we will look at the shock region. Fig.4.4 shows the pressure profile across the incident shock wave. One of the first things to notice is that the temporal discretisation of the solution appears to have a much less significant impact than the spatial discretisation. All of the discretisation schemes spread the shock across several cells; however, the first-order schemes spreads the shock over approximately 20 cells whereas the second- and third-order schemes spread the shock over only 7 cells. From this plot it appears that there is little to choose between second- and third-order spatial schemes.

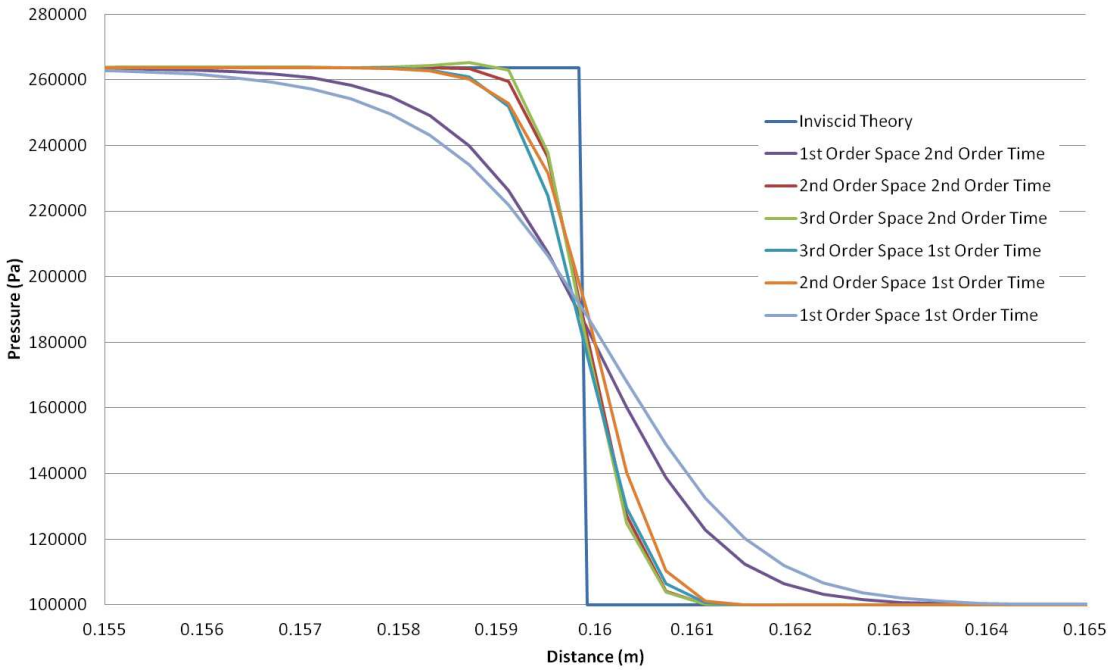

Figure 4.4: Pressure profile computed for different discretisation schemes

If we now consider the entire shock tube, we can see that the third-order discretisation schemes appear to have introduced some non-physical oscillations around the diaphragm and leading into the tail of the expansion wave (Fig.4.5). Given that the computation time was almost equal between the second- and third-order schemes, it was decided to use second-order discretisation in both space and time as this appeared to be more robust.

As mentioned earlier, these simulations were performed using a coarse, uniform grid. Due to the large localised gradients with adjacent regions of uniform flow, an adaptive mesh refinement scheme could yield significantly better results without a prohibitively high computational cost. To this end, a basic study in adaptive mesh

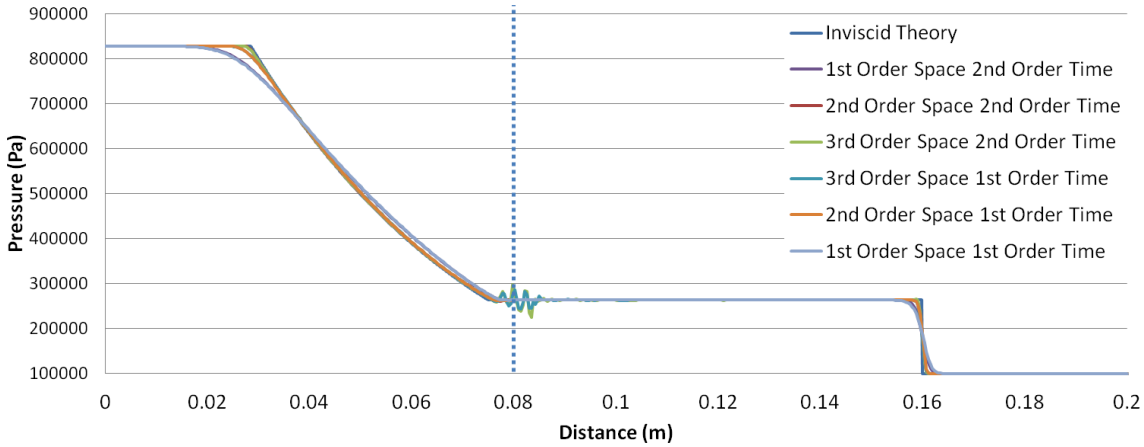

(a) Pressure distribution

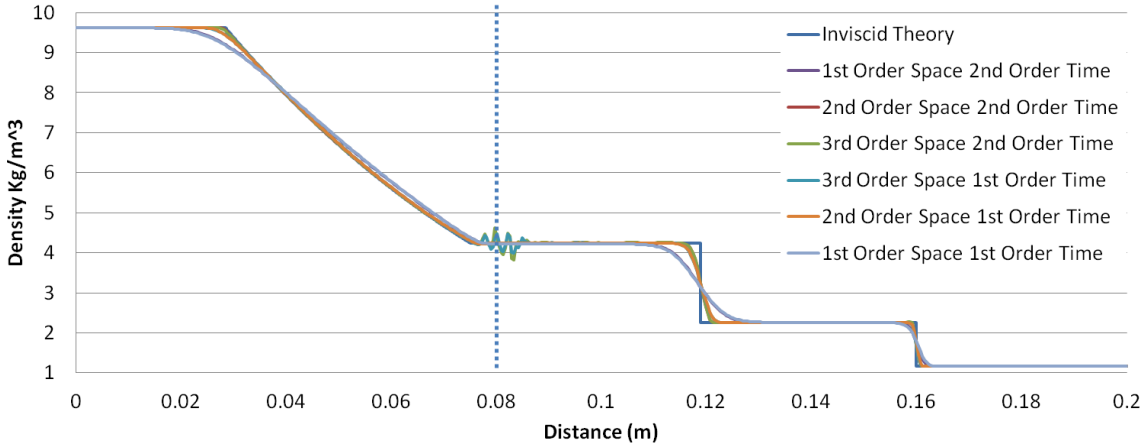

(b) Density distribution

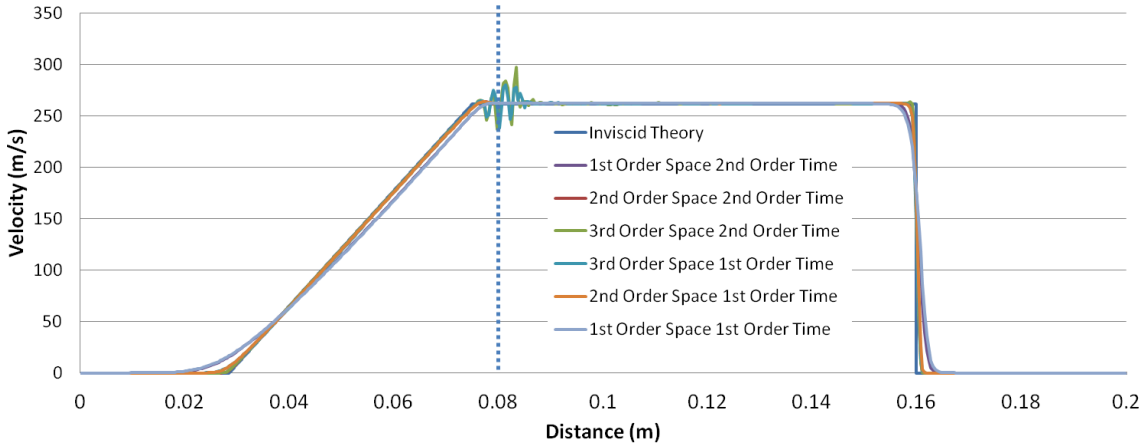

(c) Velocity distribution

Figure 4.5: Shock tube simulation

refinement was undertaken in an attempt to improve the accuracy of the results. The grid adaption is based on the pressure gradient in that cell and includes both refinement and coarsening every time step. Refining one cell involves halving both the horizontal and vertical grid size, leading to the creation of 4 new cells.

Despite the flow containing both shocks and shear layers (making it a likely candidate for density-gradient based adaption) a pressure-gradient based adaption scheme was chosen. Initial attempts density-based schemes resolved the shear layer and the surrounding area even more finely than is shown in Fig.4.6. This not only lowered the numerical viscosity present in the simulation (showing a departure from the experimental results) but also reached the cell limit of the software license much more quickly than the pressure-gradient based adaption. The software permits the user to select an upper and lower threshold for the spatial pressure gradient across a cell based on its neighbours. If the gradient is above the threshold then the grid is refined, conversely if the gradient is below the lower threshold, the grid is coarsened (up to its original coarseness).

Unfortunately, when calculating gradient-based properties (such as numerical schlieren), the hanging nodes present in the adaptively refined mesh introduce artifacts.

4.3.1 Sharp Geometry Grid Dependency

Fig.4.6 shows the grid dependency of an inviscid simulation of the complex region behind a $M_i = 1.28$ shock wave. Figs.4.6a through 4.6d suggest that the flow is grid independent; aside from the features becoming more sharply resolved, there are no significant changes in the flow features visible. If the grid is refined again, shear layer instabilities begin to develop in the simulations. Further refining the grid makes these instabilities grow more quickly. If the simulated flow is inviscid, and self-similar in time, this result seems counter-intuitive. However, as we refine the grid we reduce the numerical viscosity, which has the effect of damping and smoothing the flow (see Section 2.7.2). With that in mind and due to the extra computational time required, a four-pass adaption scheme was used for all of the inviscid simulations, giving a minimum grid size of 12.5×12.5 μm. Numerical schlieren is based on density gradient magnitude rather than either a horizontal or vertical gradient. This parameter was chosen as it was difficult to gain the required range of sensitivity for numerical shadowgraph due to the grid adaption. Moreover, horizontal and vertical density gradients failed to adequately resolve vertical and horizontal shockwaves respectively. In the real schlieren images, where a horizontal knife-edge was used, a vertical shock wave would still be captured due to the finite exposure time of the image, something which is not possible in numerical simulations.

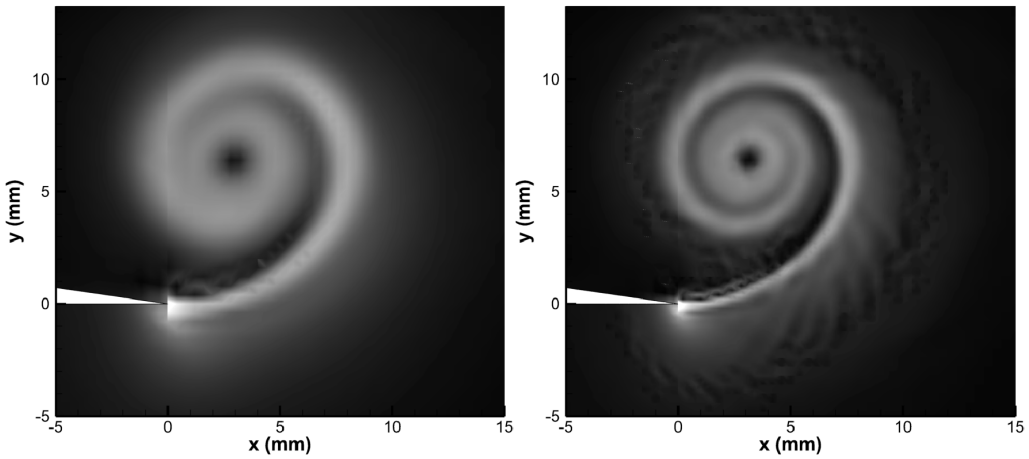

(a) No adaption $\Delta x = 0.4$mm (b) One-pass adaption $\Delta x = 0.2$mm

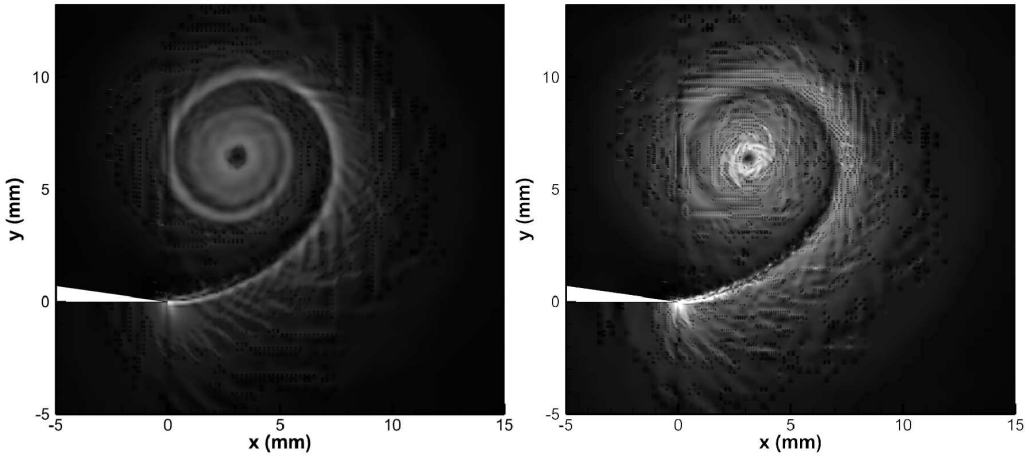

(c) Two-pass adaption $\Delta x = 0.1$mm (d) Three-pass adaption $\Delta x = 0.05$mm

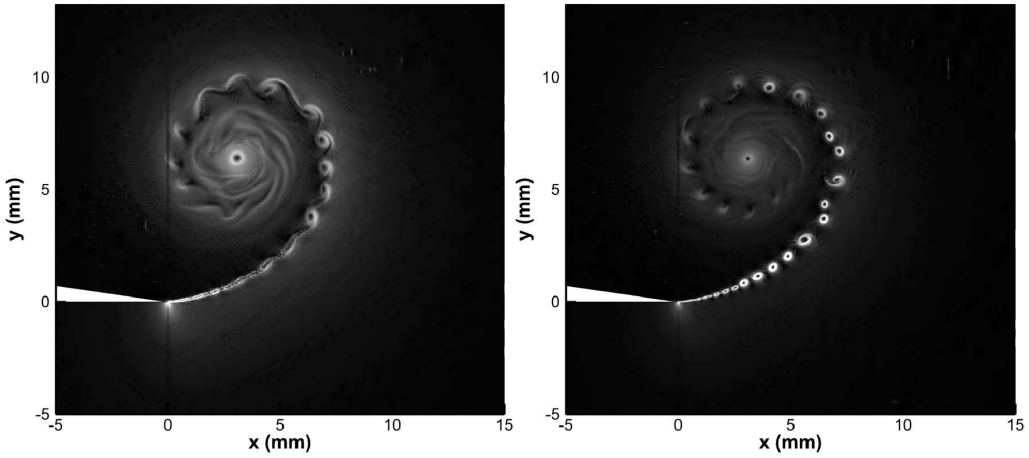

(e) Four-pass adaption $\Delta x = 0.025$mm (f) Five-pass adaption $\Delta x = 0.0125$mm

Figure 4.6: Numerical schlieren showing grid dependency of shear layer roll-up

The introduction of laminar viscosity was investigated on the sharp geometry; however, there was no discernible difference in comparison with the inviscid case. The shear layer vortices appeared at the same time step and were shed at the same frequency as the inviscid case. Numerical values of velocity and pressure were

marginally different, but the dominant shock structure was the same.

4.3.2 Round Geometry Grid Dependency

Based on the successes of the previous simulations, it was decided to attempt a similar simulation of the round geometry. Fig.4.7 shows the same time step using an inviscid solver at two different grid refinements. The initial coarse grid (Fig.4.7a) shows a shock wave at approximately 85° around the corner with no flow separation. The shocks are not very well captured, similarly to the coarse results seen previously. Refining the grid had the effect of resolving the shock waves; however, there was still no sign of flow separation. This is contrary to the experimental results (to be shown later) and previously published literature ([42],[44],[46]). This shows that an inviscid simulation is not capable of resolving all of the relevant flow features.

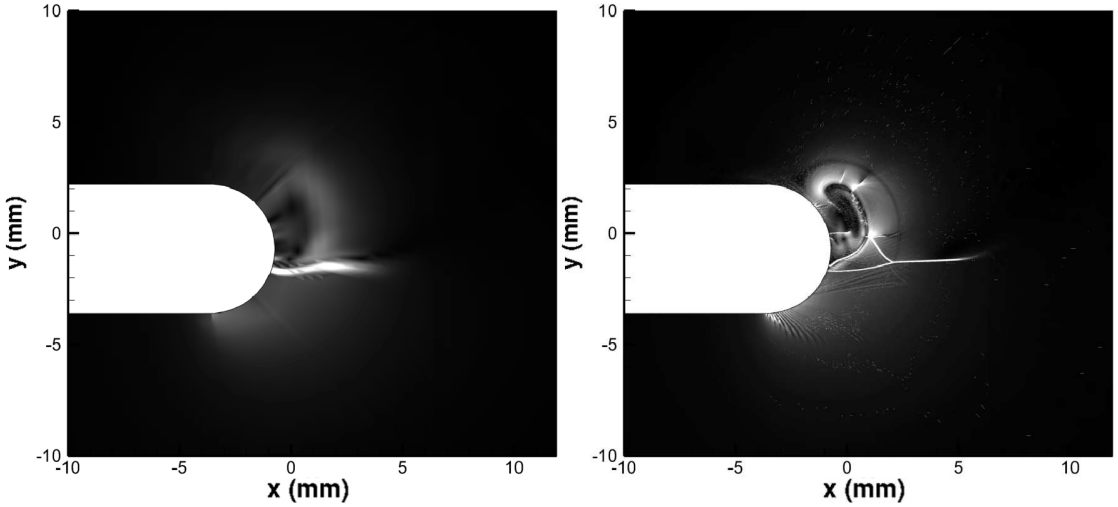

(a) Inviscid simulation, coarse grid (b) Inviscid simulation, Four-pass adaption

Figure 4.7: Numerical schlieren of inviscid simulation around round geometry

The associated length scale (radius of the corner) means that separation is not induced by a sharp point and the separation of the flow is a viscous effect. The introduction of laminar viscosity should be sufficient to model the separation of the flow around the corner [199]. Simulations performed using laminar viscosity with different levels of grid refinement are shown in Fig.4.9.

A new mesh was generated with the boundary layer resolved. The minimum cell size in the boundary layer was 13 μm and the boundary layer was wrapped around the corner as shown in Fig.4.8 as well as along the top and bottom walls of the shock tube and the test section. Unfortunately, due to the round geometry, it was necessary to include a portion of the mesh as tetrahedral rather than quadrilateral cells. These cells are, at most, half the size of the quadrilateral cells in the rest of the grid, and as such the minimum grid size in this region is lower than the $\Delta x = 0.025$ mm seen in the previous four-pass adaption cases. The computational cost of these simulations is significantly higher than the inviscid simulations, as the addition of viscosity led to localised convergence issues in some cells at the shock foot.

Simulations performed using turbulence models tended to incorrectly predict the boundary layer separation. A Reynolds stress model was also tried; however, the

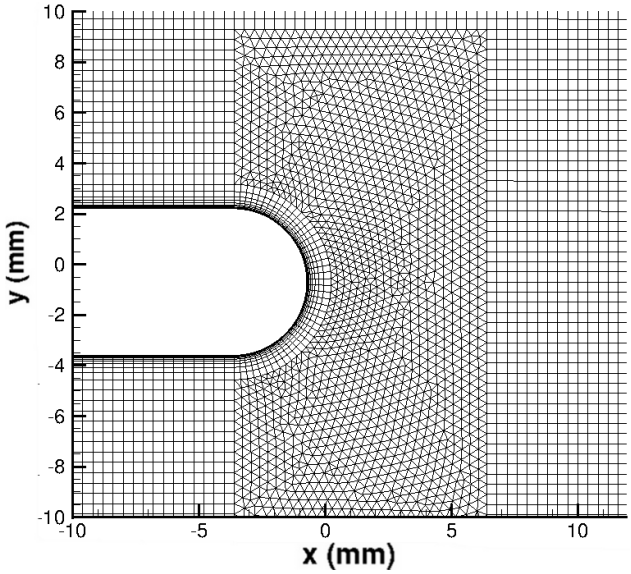

Figure 4.8: Initial grid of round geometry

simulation suffered from very slow convergence (approximately 4000 iterations per time step) making them unfeasible to use given the computational power available.

The shock waves present are not well-refined in Figs. 4.9a & 4.9b; however, the separation is captured. As the grid is further refined in Figs. 4.9c to 4.9e, more and more shock waves are captured and the flow becomes increasingly complex. In Fig.4.9e there are now fewer than 8 individual vortices between the separation point and the main vortex. Based on the fact that more and more vortices are found as the grid is refined, showing different orientations of circulation and that the computational cost of the three- & four-pass adaption simulations is prohibitively high, it was decided to proceed with the two-pass adaption scheme, as this appears to give the best correlation with experimental results.

4.3.3 Final Simulation Parameters

The initial simulation work presented above gives a good basis for the final simulation parameters. The sharp case will be investigated using an inviscid simulation with a four-pass adaption scheme based on pressure gradient. The round geometry will be investigated using laminar viscosity and a two-pass adaption scheme based on pressure gradient. The simulation results will be presented alongside the relevant experimental data in each section of the following chapter.

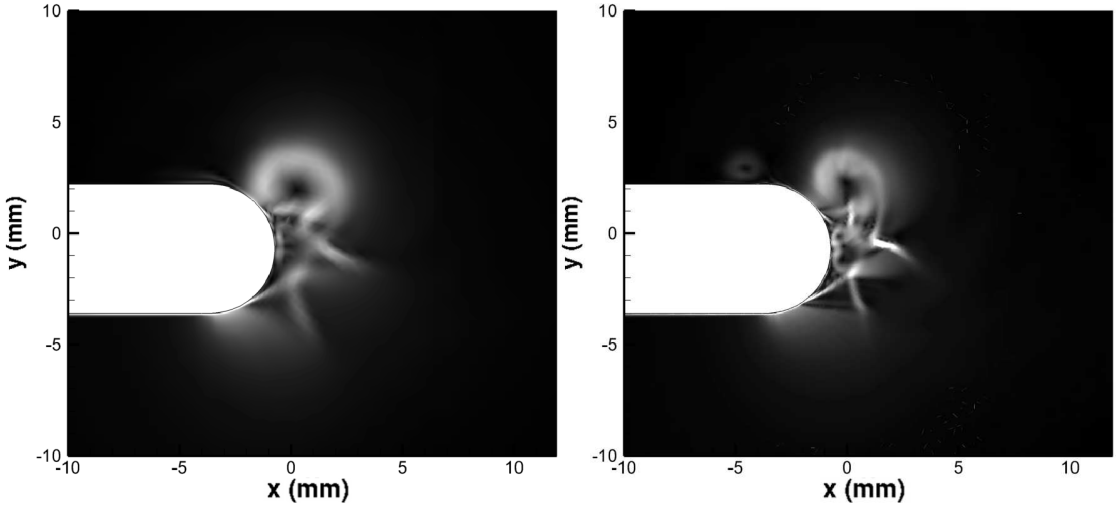

(a) Laminar simulation, coarse grid

(b) Laminar simulation, one-pass adaption

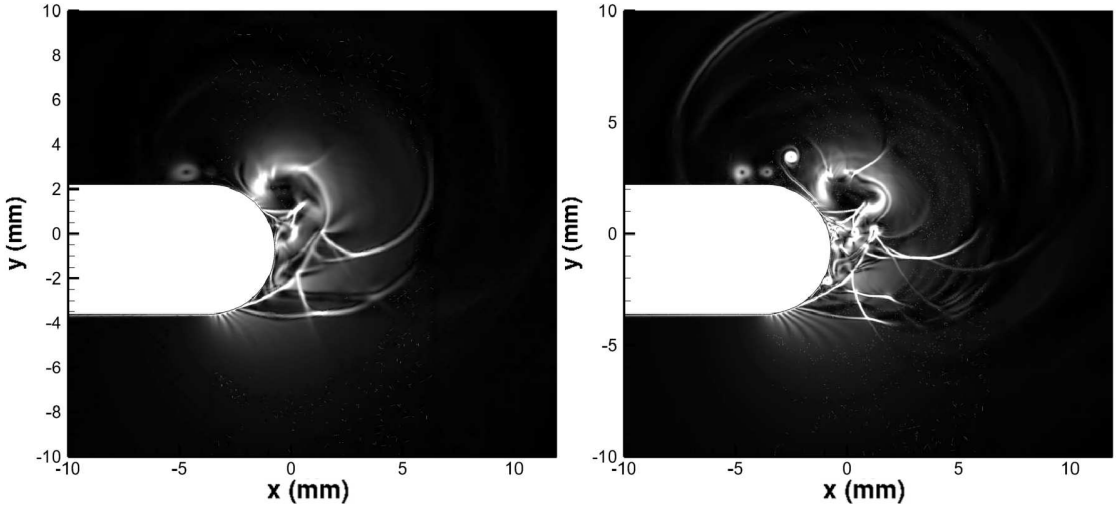

(c) Laminar simulation, two-pass adaption

(d) Laminar simulation, three-pass adaption

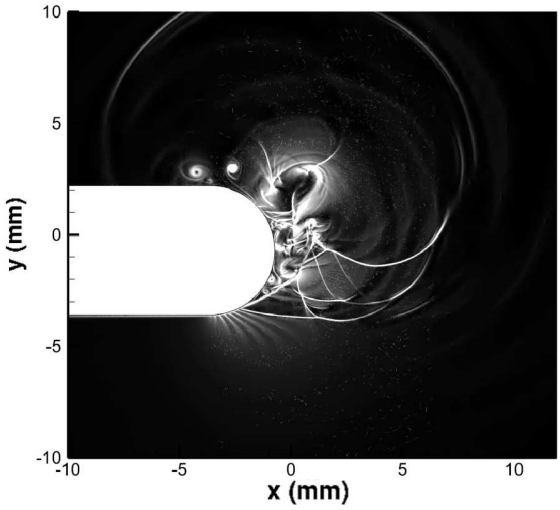

(e) Laminar simulation, four-pass adaption

Figure 4.9: Grid dependency of laminar simulations of round geometry

Chapter 5

Results and Discussion

> *That hat had been with the station for twenty years and was one day away from retirement* - Kent Brockman to Homer Simpson in The Simpsons episode *Bite Back*

5.1 Density-Based Results

This section contains the experimental and numerical density-based diagnostics of the six flow conditions under investigation. In the first case for the sharp geometry, all of the different experimental setups will be covered to show the differences between them in that they highlight certain flow features. For the sake of brevity, subsequent cases will only use conditions to present features of interest.

Due to the integrative nature of the density-based diagnostics used in this section, any three-dimensionality in the flow will be integrated into a flat image. However, the sharp shock waves show that the flow can be considered two-dimensional, making two-dimensional simulations suitable for comparison.

As in the previous discussions, all of the cases regarding the sharp geometry will be covered in separate sections from the round geometry.

5.1.1 Sharp Geometry

5.1.1.1 Mi = 1.28 Experimental Results

Fig.5.1 shows the shadowgraph results from the full test section. Initially (Figs.5.1a to 5.1d), the diffracting shock wave is expanding in the same way as expected from the published literature as discussed in Section 2.4.1. The contact surface and reflected expansion wave are not clearly seen. This is due to a combination of both waves being rather weak (due to the low Mach number of the incident shock) and the low sensitivity of the shadowgraph system in this setup. There are no clear shocks or expansions seen below the shear layer, again due to the low incident Mach number. This is to be expected based on the analysis presented in Section 2.4.1. The shear layer is tightly rolled up into the main vortex and shows no sign of any disturbances. From Fig 5.1e onwards, the diffracted shock has been reflected by the upper wall of the test section, forming a regular reflection initially and is returning towards the main vortex. Some distortion of the reflected diffracted shock wave can be seen in Fig.5.1g, as the flow around the right-hand side of the vortex opposes

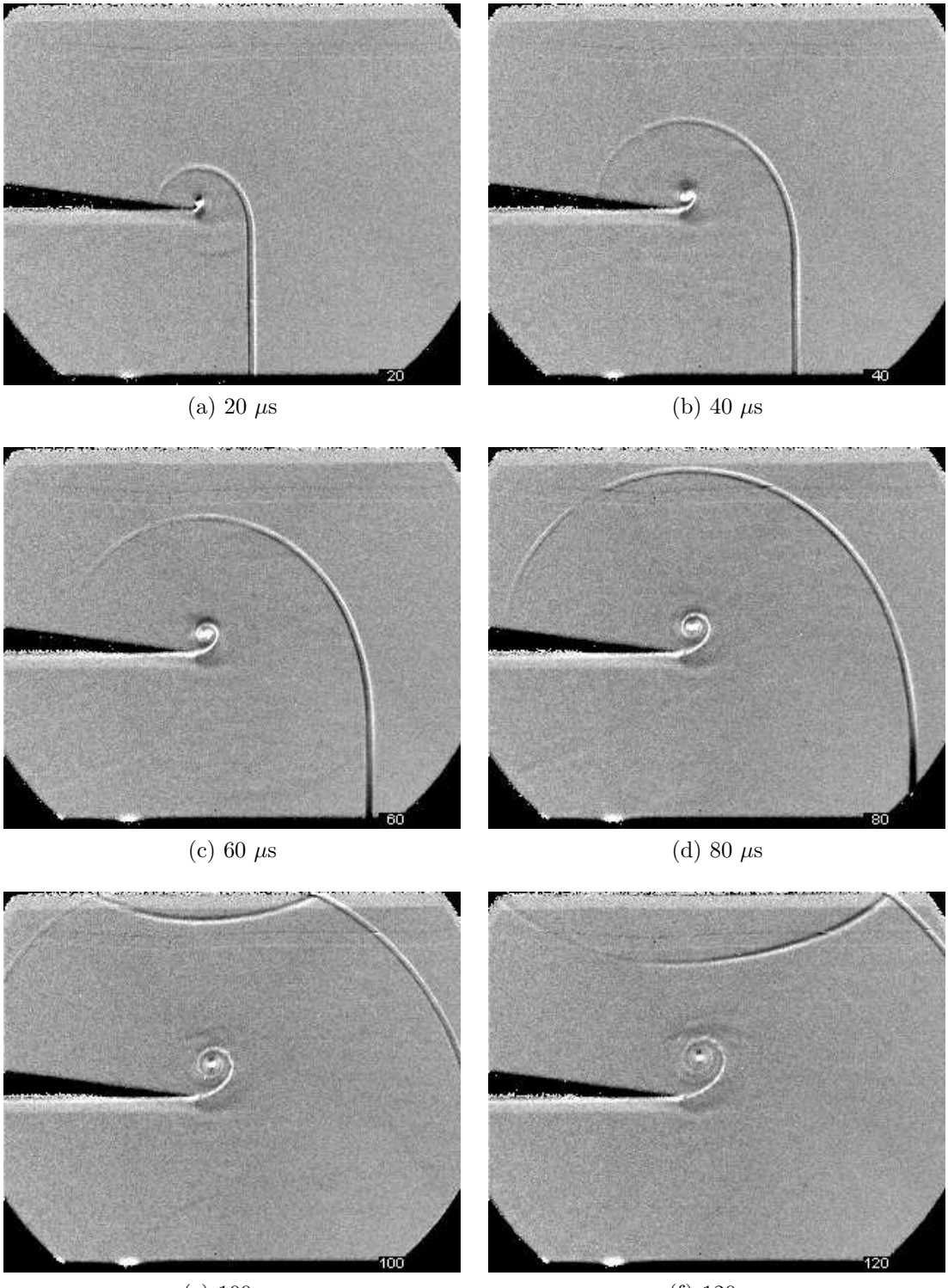

(a) 20 μs (b) 40 μs

(c) 60 μs (d) 80 μs

(e) 100 μs (f) 120 μs

Figure 5.1: Full-field shadowgraph of $M_i = 1.28$ shock diffraction process around a sharp geometry

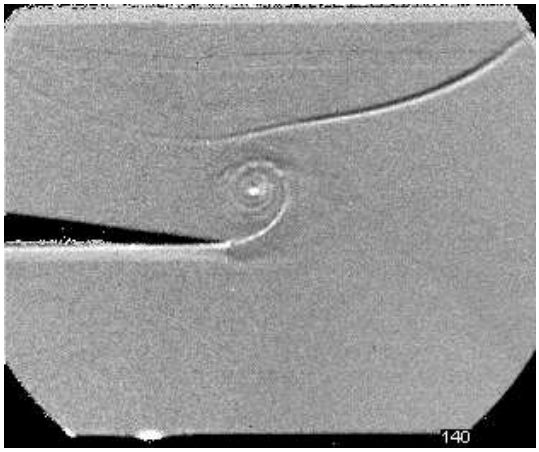

(g) 140 μs

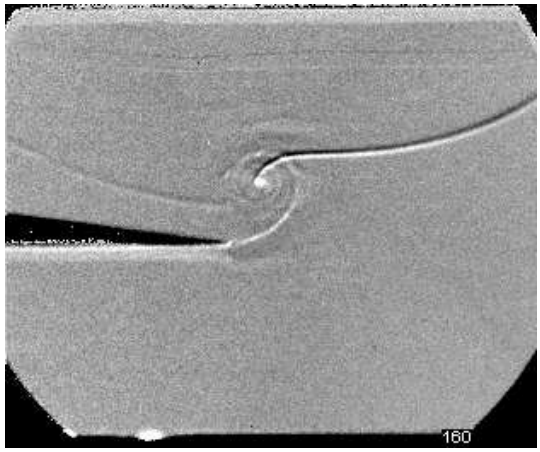

(h) 160 μs

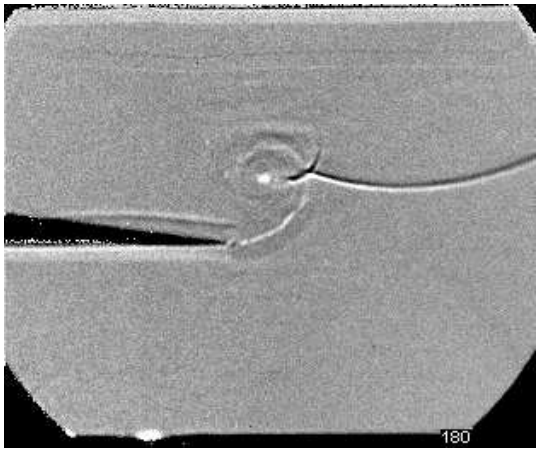

(i) 180 μs

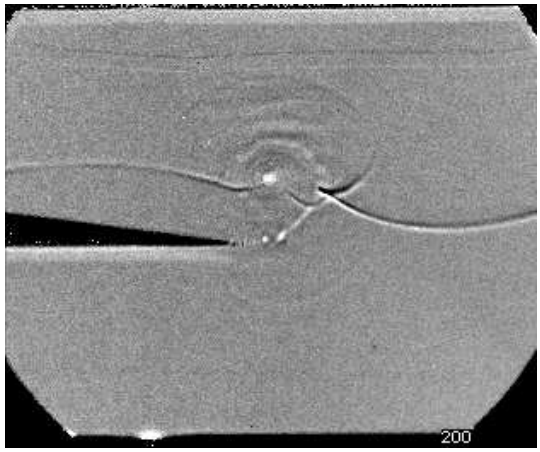

(j) 200 μs

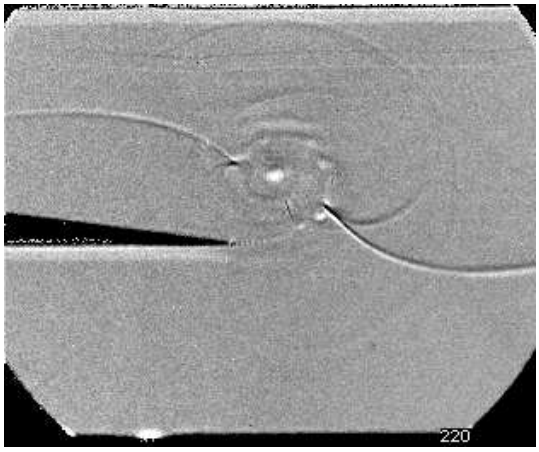

(k) 220 μs

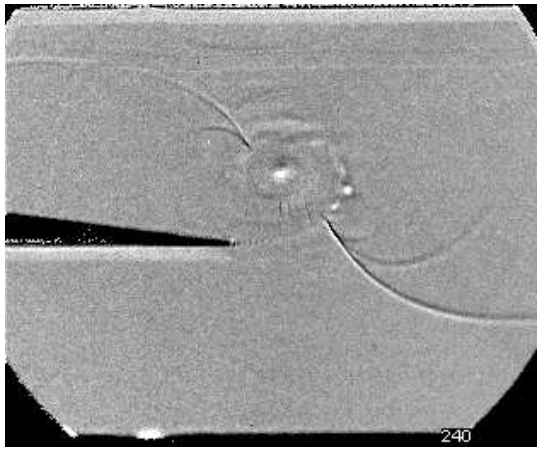

(l) 240 μs

Figure 5.1: Full-field shadowgraph of $M_i = 1.28$ shock diffraction process around a sharp geometry

the shock wave while the flow on the left does not. By Fig.5.1h it is clear that the returning shock wave is beginning to be split by the main vortex; the right-hand side forms a Mach reflection, with the Mach stem inside the shear layer appearing to be connected to the centre of the vortex. As the waves propagate further, the Mach stem appears to travel faster than the wave structure outside of the shear layer and begins to disperse into weaker waves. Meanwhile, the accelerated returning wave on the left of the vortex has impinged on the splitter plate. Figs.5.1i to 5.1l do not show much distortion to the shape of the shear layer; however, two strong vortices are formed, as was seen by Skews [71].

The full-field schlieren images in Fig.5.2 show some of the flow features more clearly than the shadowgraph images in Fig.5.1. The contact surface between the gas affected by the planar shock and the curved, diffracted shock is visible and the reflected expansion wave is propagating upstream. There is very limited information available in Figs. 5.2a to 5.2f about the vortex and the shear layer as the density changes in this region are strong enough to overrange the schlieren system. After 120 μs the vortex has grown in size to a level where the local gradients are no longer strong enough to overrange the system. From Fig.5.2g onwards, there appear to be several *bumps* serially arranged around the shear layer. These bumps are, as we will see shortly, the Kelvin-Helmholtz instability on the shear layer. In Fig.5.2j, the two strong vortices formed from the impact of the returning shock on the shear layer are clearly seen. There is little more to say about the shock-vortex interaction process further than what was shown in the previous figure; however, there is a region of flow which appears much darker in Figs.5.2j & 5.2k, indicating a strong interaction.

In the close-up shadowgraph images, as expected, the sensitivity of the system is higher, and as such more flow features are visible. Unlike in Fig.5.1, the reflected expansion wave can be seen in Figs.5.3a & 5.3b before it has passed out of view. The contact surface is also visible throughout the sequence and can be seen to be pulled into the centre of the vortex. Even as early as 80 μs we can begin to see changes in intensity along the shear layer, indicating the presence of disturbances. As the vortex grows, these disturbances become accordingly larger, allowing us to see individual vortices present on the shear layer. These individual vortices grow and are clearest at approximately 90° around the vortex (starting from the splitter tip)[1]. After this point the vortices begin to dissipate and become more diffuse until they are indistinguishable by approximately 300°.

Following the impact of the returning shock on the splitter plate (Fig.5.3i onwards), the shear layer again shows two large disturbances, followed by a region showing a repetitive alternating light and dark pattern. It is not possible to discern from these images what this exact structure is. In Fig.5.3j the returning shock wave on the right of the vortex is split into a complex structure involving a Mach reflection in close proximity to a regular reflection. This only appears outside the shear layer, which seems to act as a barrier. The final image, Fig.5.3l, shows a series of diverging waves that emanate from the shear layer and are connected to the returning shock wave. This is a series of diverging acoustic waves created by the interaction of the shock with the individual K-H vortices on the shear layer, similar to that investigated by Chang & Chang [72].

[1]All angles noted in descriptions of flow features around the vortex start from 6 o'clock and progress anticlockwise

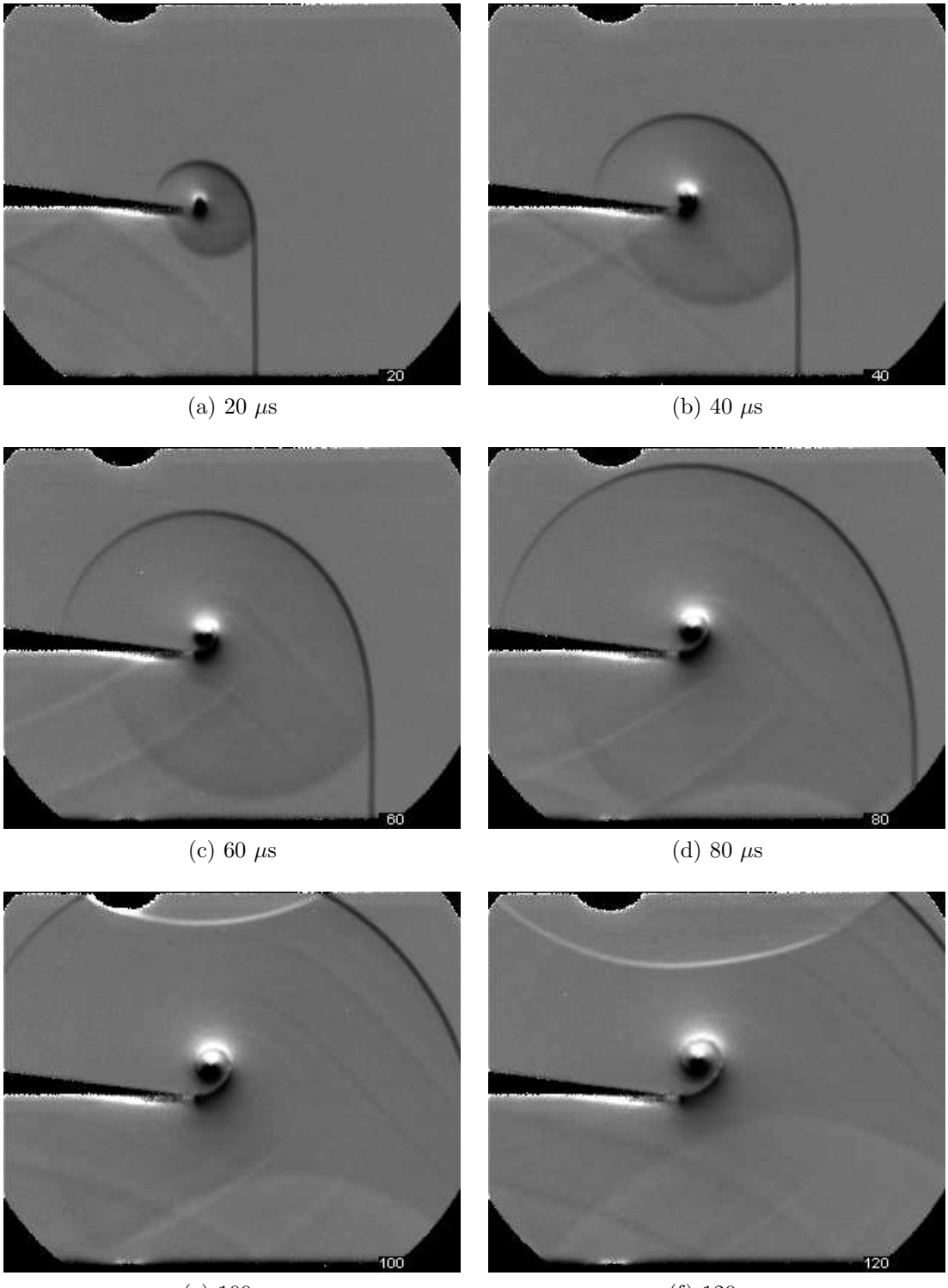

(a) 20 μs

(b) 40 μs

(c) 60 μs

(d) 80 μs

(e) 100 μs

(f) 120 μs

Figure 5.2: Full-field schlieren of $M_i = 1.28$ shock diffraction process around a sharp geometry

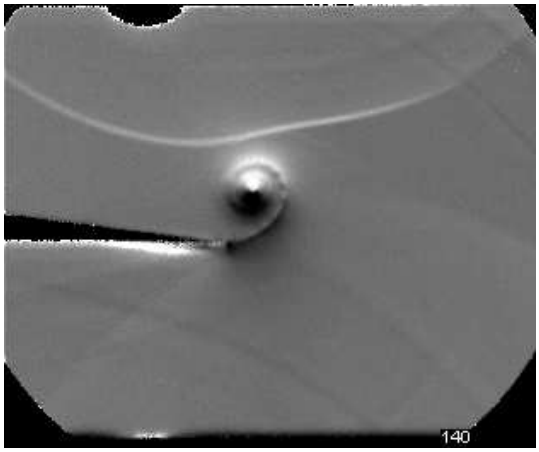

(g) 140 μs

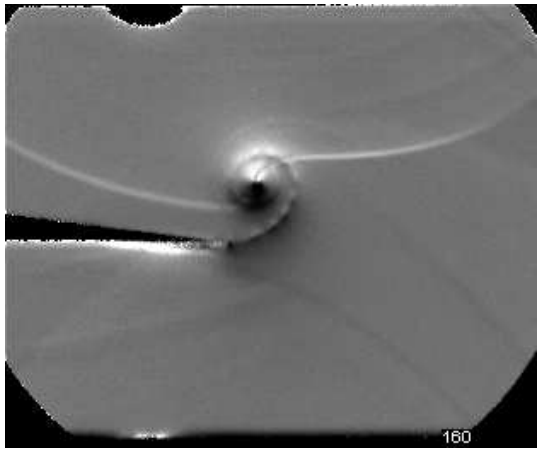

(h) 160 μs

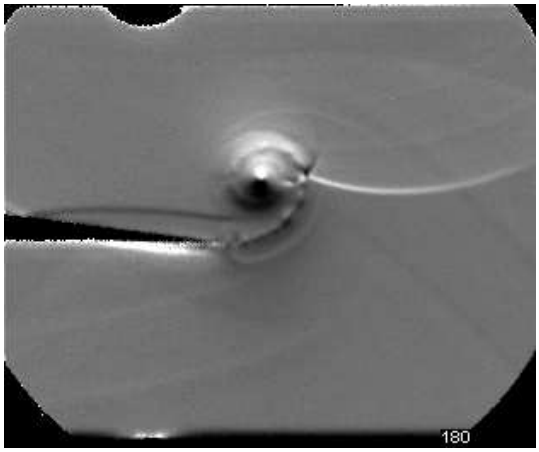

(i) 180 μs

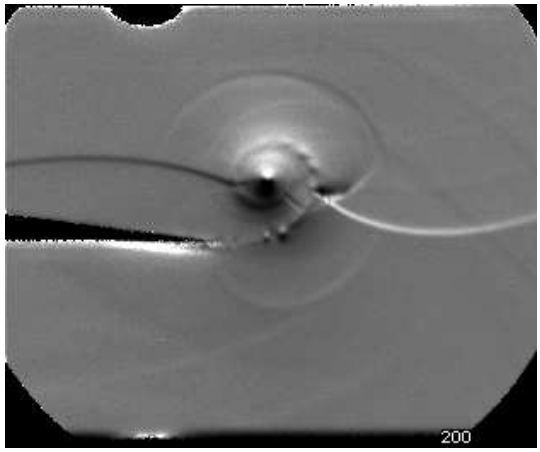

(j) 200 μs

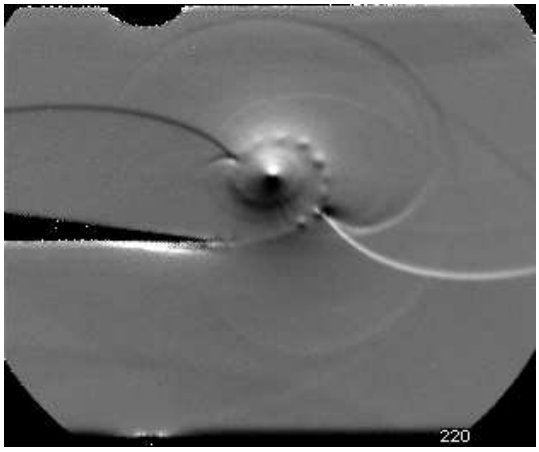

(k) 220 μs

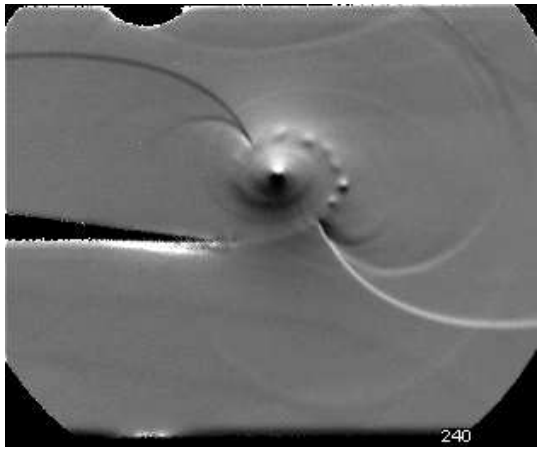

(l) 240 μs

Figure 5.2: Full-field schlieren of $M_i = 1.28$ shock diffraction process around a sharp geometry

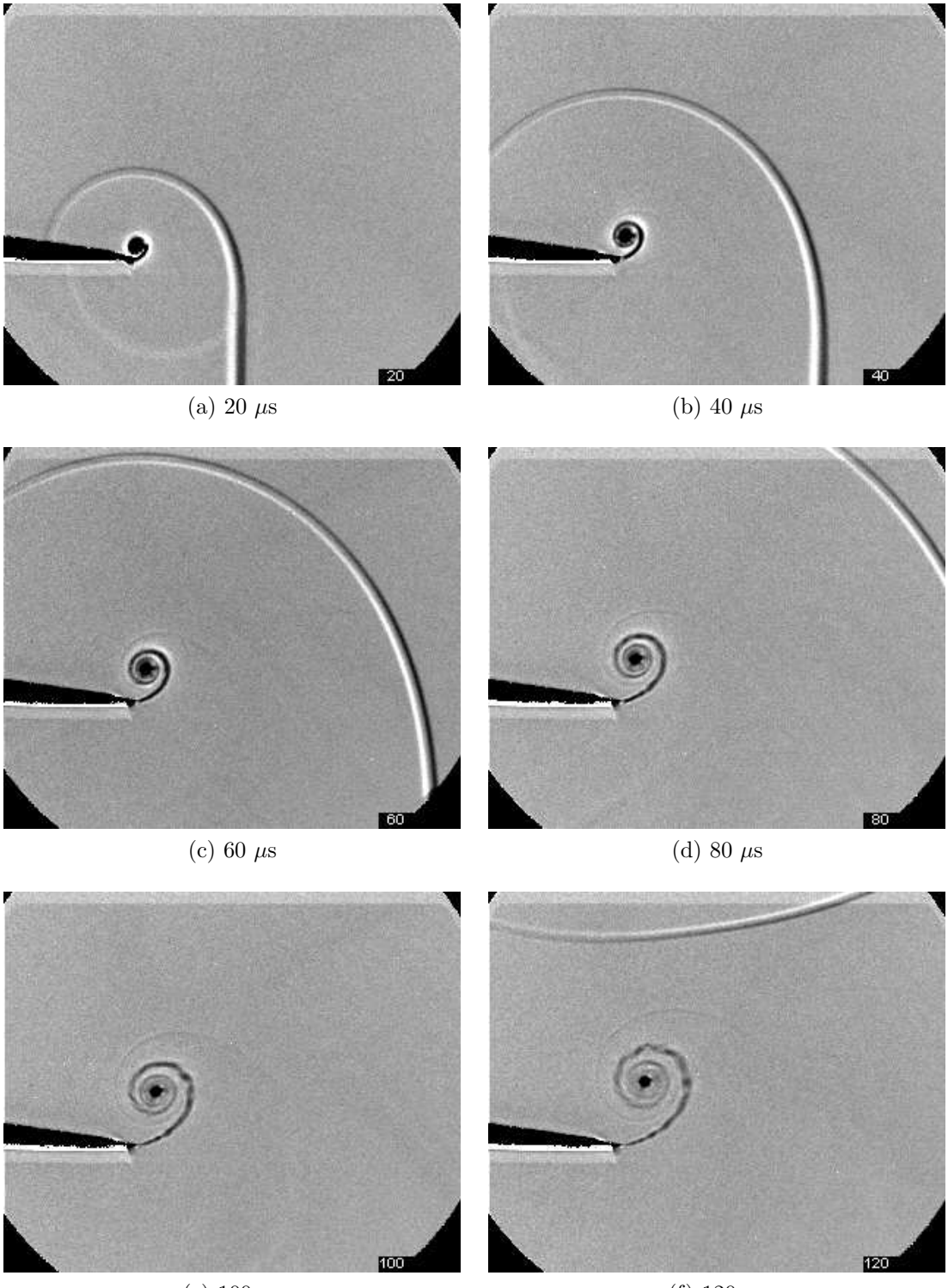

(a) 20 μs

(b) 40 μs

(c) 60 μs

(d) 80 μs

(e) 100 μs

(f) 120 μs

Figure 5.3: Close-up shadowgraph of $M_i = 1.28$ shock diffraction process around a sharp geometry

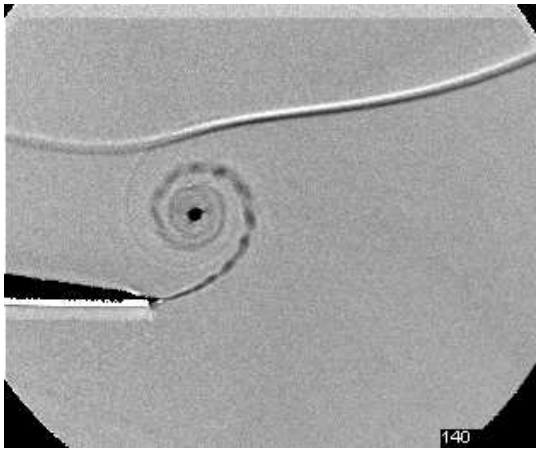

(g) 140 μs

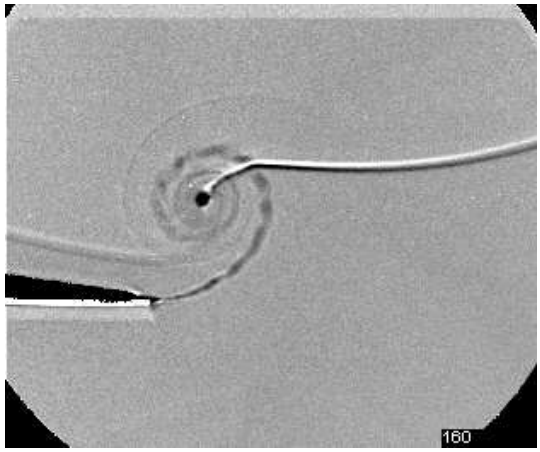

(h) 160 μs

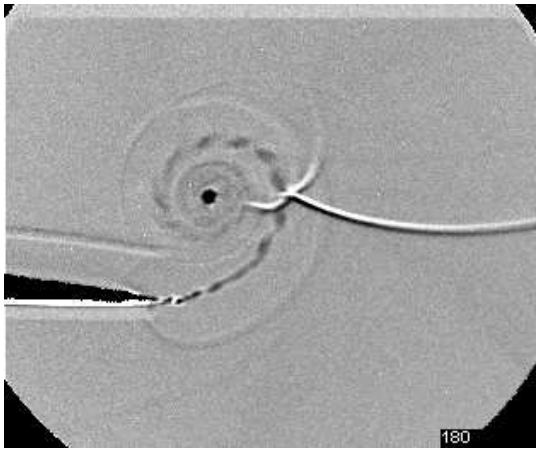

(i) 180 μs

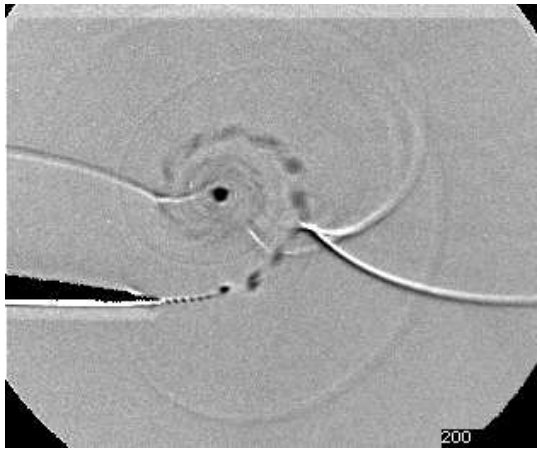

(j) 200 μs

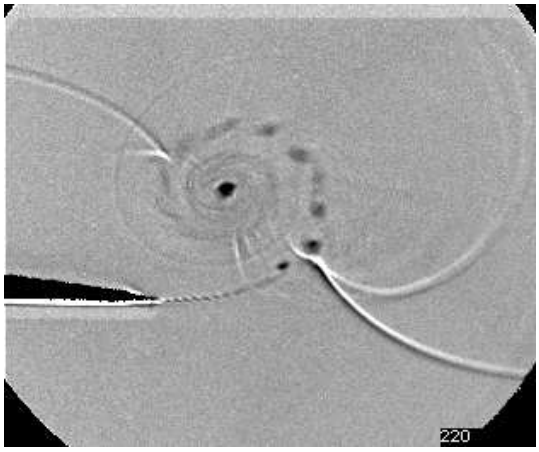

(k) 220 μs

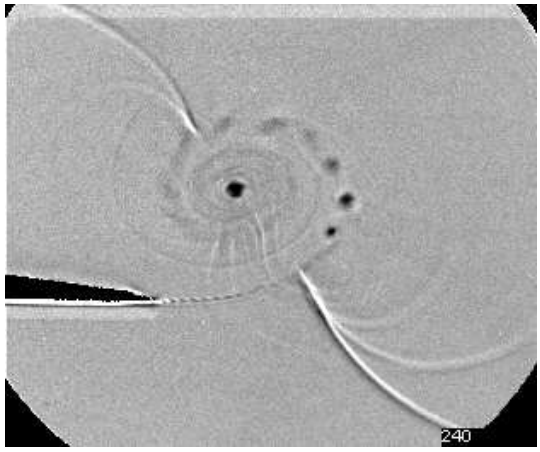

(l) 240 μs

Figure 5.3: Close-up shadowgraph of $M_i = 1.28$ shock diffraction process around a sharp geometry

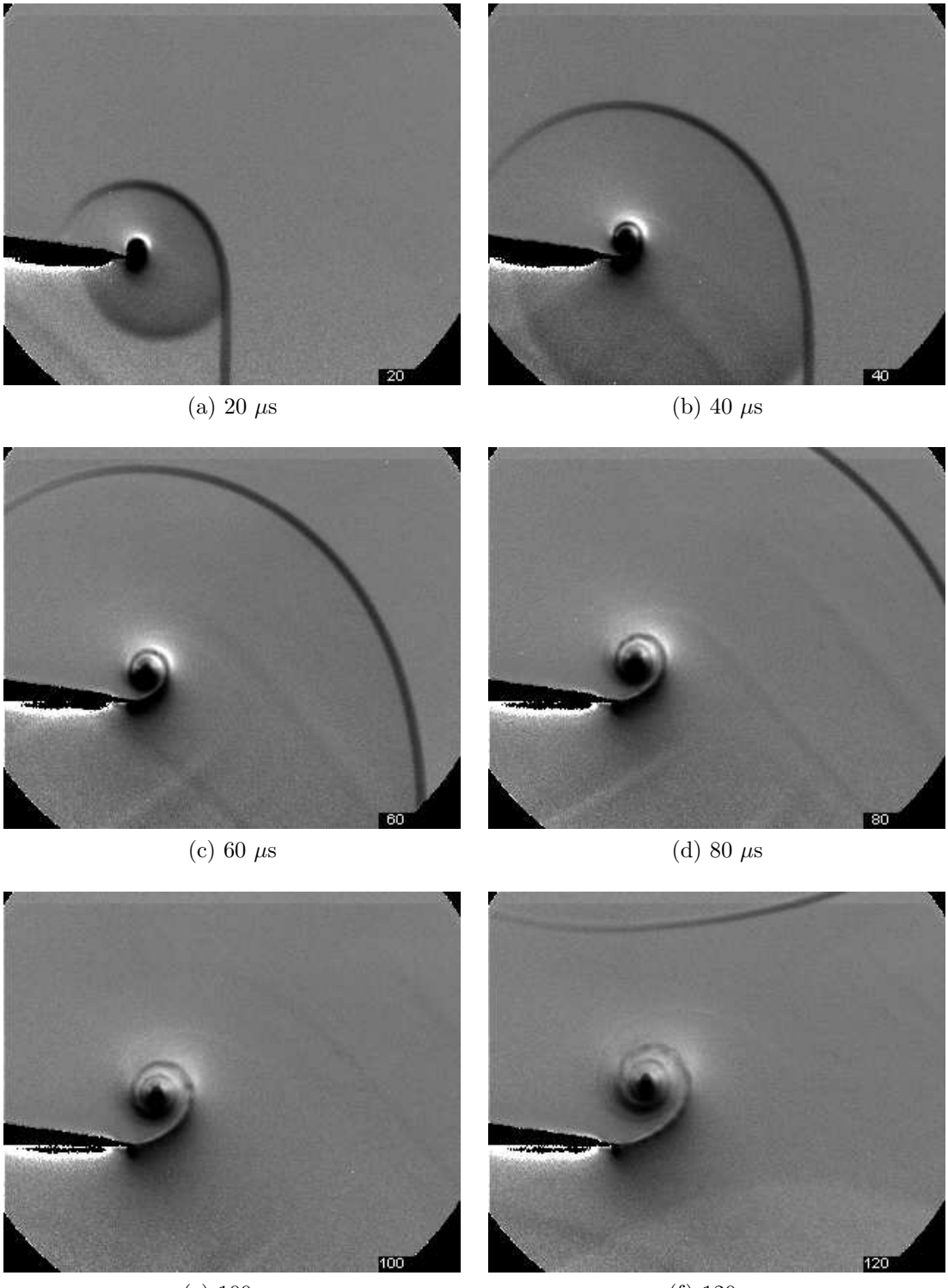

(a) 20 μs (b) 40 μs

(c) 60 μs (d) 80 μs

(e) 100 μs (f) 120 μs

Figure 5.4: Close-up schlieren of $M_i = 1.28$ shock diffraction process around a sharp geometry

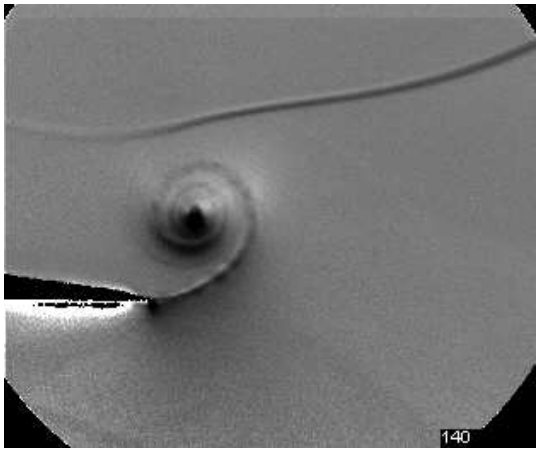

(g) 140 μs

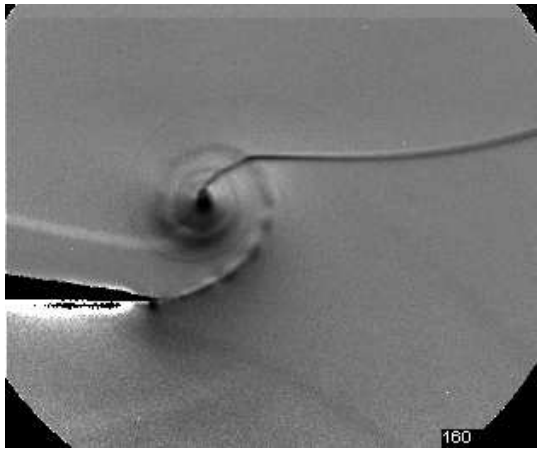

(h) 160 μs

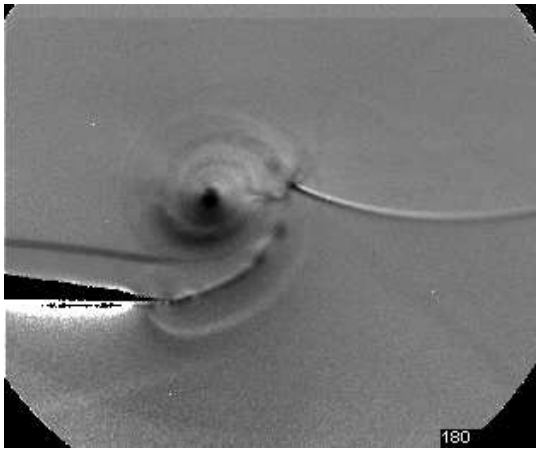

(i) 180 μs

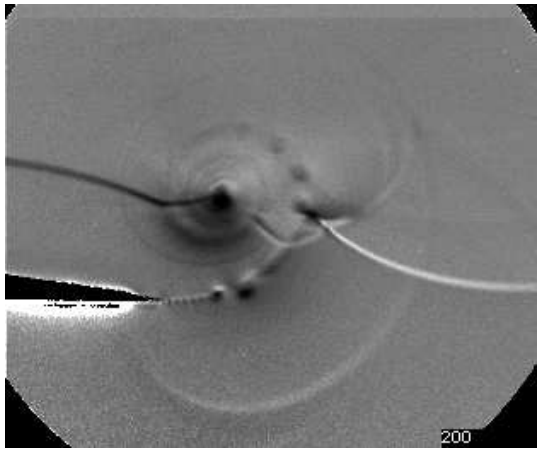

(j) 200 μs

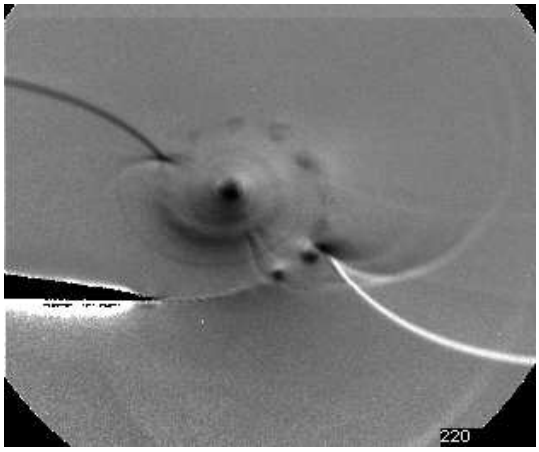

(k) 220 μs

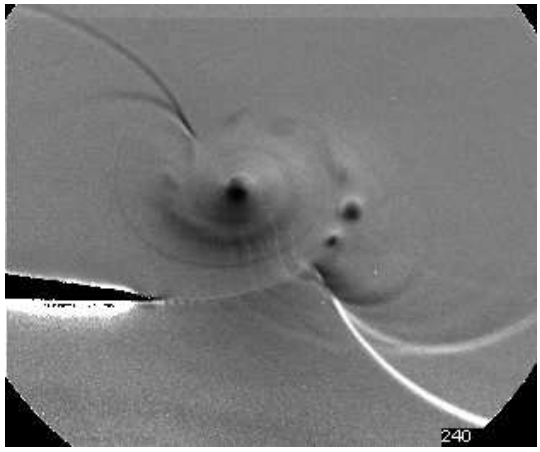

(l) 240 μs

Figure 5.4: Close-up schlieren of $M_i = 1.28$ shock diffraction process around a sharp geometry

The final set of images, close-up schlieren, do not show any more flow features than the close-up shadowgraph of Fig.5.3. The same flow features are present, highlighting the repeatability of the tests, but they are not as finely resolved. Diverging acoustic waves appear more strongly in the later images of Fig.5.4 than for Fig.5.3. However, as this is the lowest Mach number case (suggesting they would be the weakest in this test) and given that they are visible in Fig.5.3l, there is little to be gained from analysing these images in greater detail.

The returning diffracted shock wave is so weak that it causes very little distortion to the main vortex. Fig.5.1i shows that the shape of the vortex has not changed. Subsequent images show that there is a slight distortion, leading to the vortex being stretched in the horizontal direction and compressed in the vertical direction. As we will see later, this is a very negligible; distortion.

5.1.1.2 Mi = 1.28 Numerical Results

Numerical schlieren images are shown in Figs.5.5 & 5.6. Both zooms will be shown for this case only, as the basic wave structures (incident shock, diffracted shock, contact surface, reflected expansion wave and returning shock) are captured exactly as predicted in the experiments.

Fig.5.5 shows that the basic wave structure is captured well by the numerical simulations. The contact surface is difficult to resolve in the images due to the finite scale that can be presented; however, it is present in the simulations. The reason for this is that pressure on either side of the contact surface is reasonably constant (along the length of the contact surface) and the grid adaption technique is based on the gradient of pressure. Therefore, in regions where the grid adaption is higher, density gradient magnitude (used as numerical schlieren) is also significantly higher. The complex region behind the diffracting shock wave and the shock vortex interaction will be discussed in conjunction with the close-up numerical images in Fig.5.6.

The final numerical schlieren result, Fig.5.6, shows the complex region behind the incident shock wave and the shock vortex interaction. Fig.5.6d shows that the shear layer, which has rolled up into the main vortex, is already exhibiting some kind of disturbance along its length. With the passage of time, these disturbances begin to grow into individual vortices in the way expected for a Kelvin-Helmholtz instability. By comparing Figs.5.6g & 5.3g, we can see that the simulations overpredict the frequency at which these vortices are generated. This is to be reasonably expected given that the only viscosity in the simulation is present in the form of numerical diffusion and does not match the viscosity of the actual flow; rather it is a function of the grid spacing. The instabilities begin to decay by approximately 270° around the vortex, in a similar way to the experiments; however, they do seem to persist for longer. The shock-vortex interaction from Fig.5.6h onwards agrees very well with the experimental results. The complex structure seen at 200 μs is repeated in the numerical results, as are the two large vortices formed after the impact of the returning shock wave. The diverging acoustics appear clearly in Figs.5.6k & 5.6l.

It is interesting to note that the light-dark structure of the shear layer after the passage of the returning shock is also captured. A closer inspection of this is shown in Fig.5.7. The numerical schlieren shows that there are some disturbances present, but this is rather ambiguous. However, the vorticity plot yields much

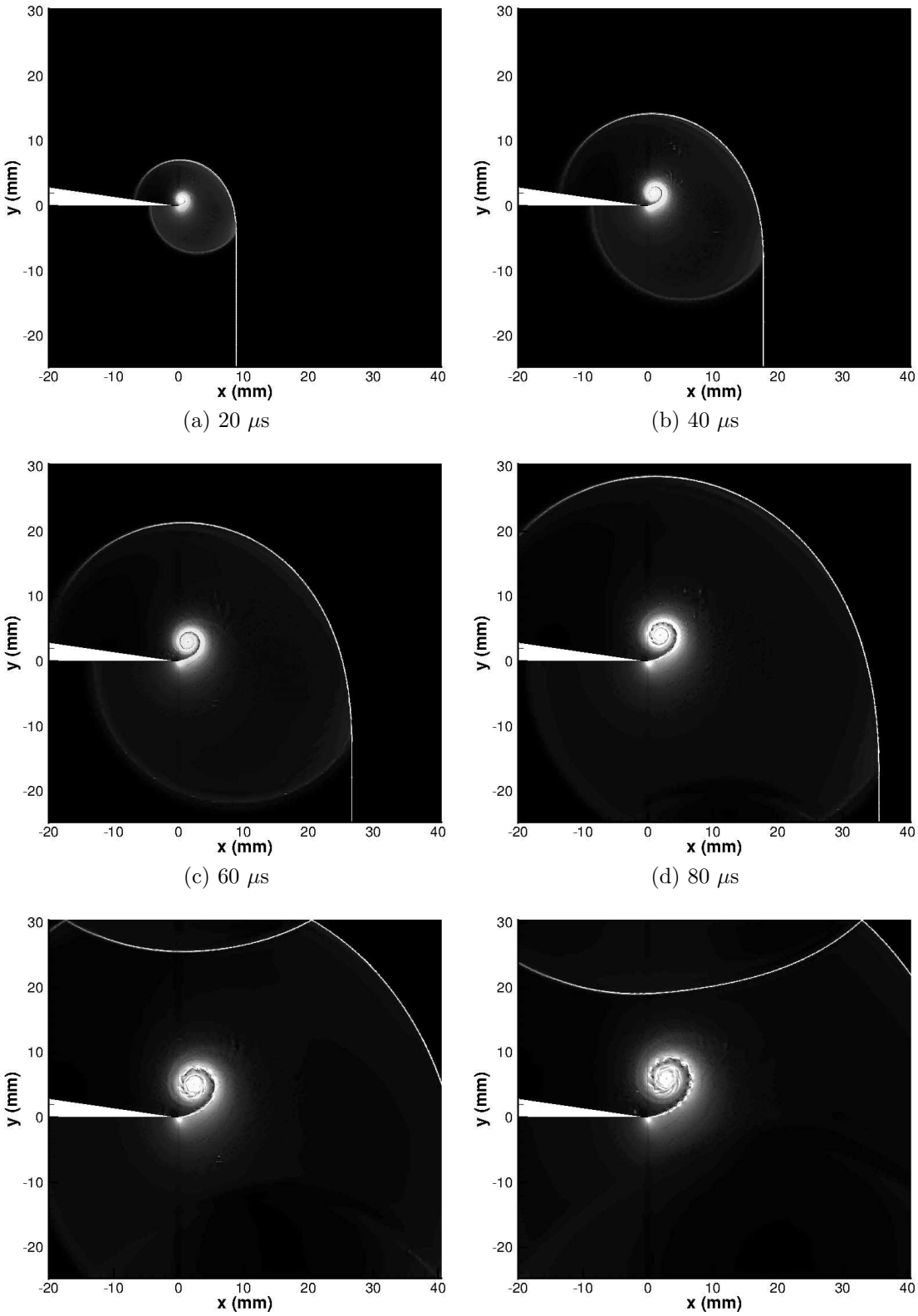

(a) 20 μs (b) 40 μs

(c) 60 μs (d) 80 μs

(e) 100 μs (f) 120 μs

Figure 5.5: Full-field numerical schlieren of $M_i = 1.28$ shock diffraction process around a sharp geometry

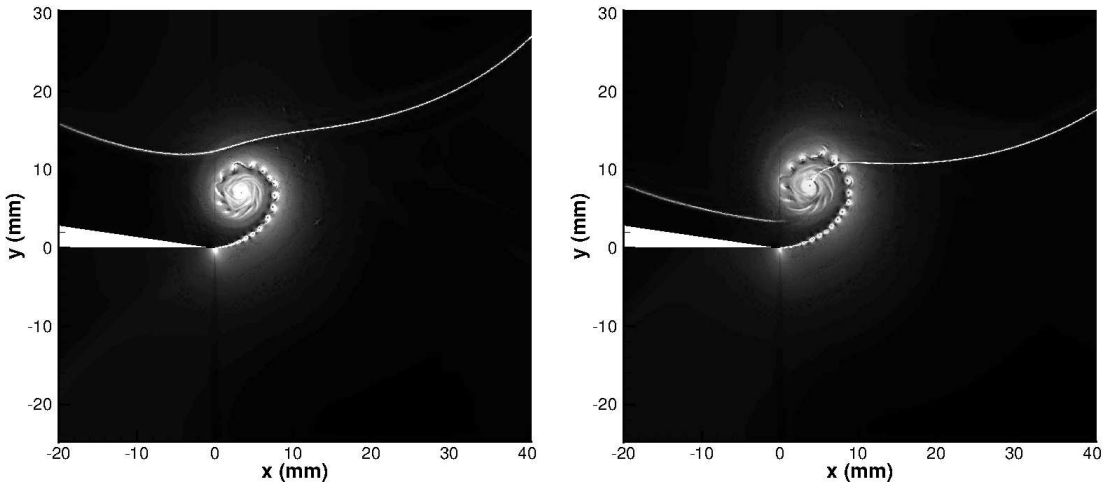

(g) 140 μs (h) 160 μs

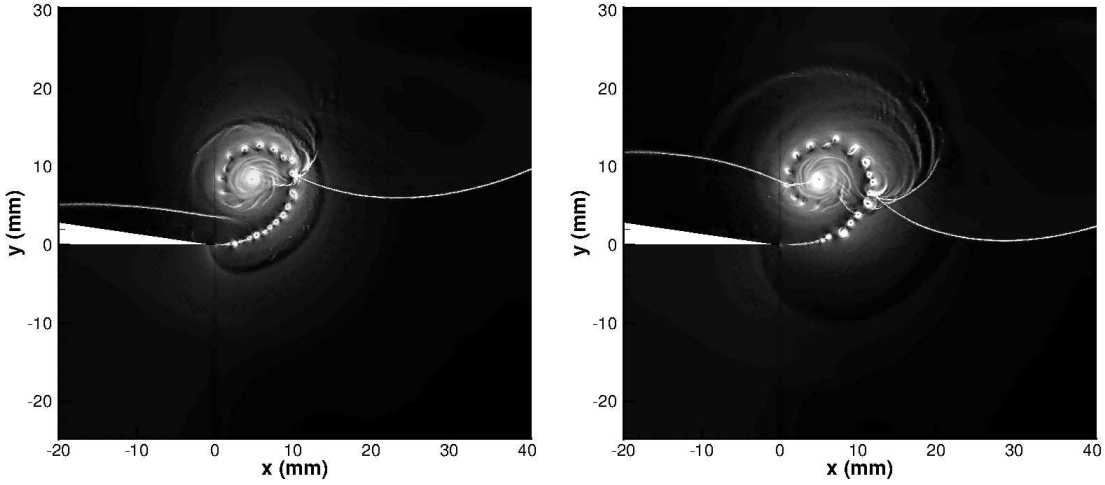

(i) 180 μs (j) 200 μs

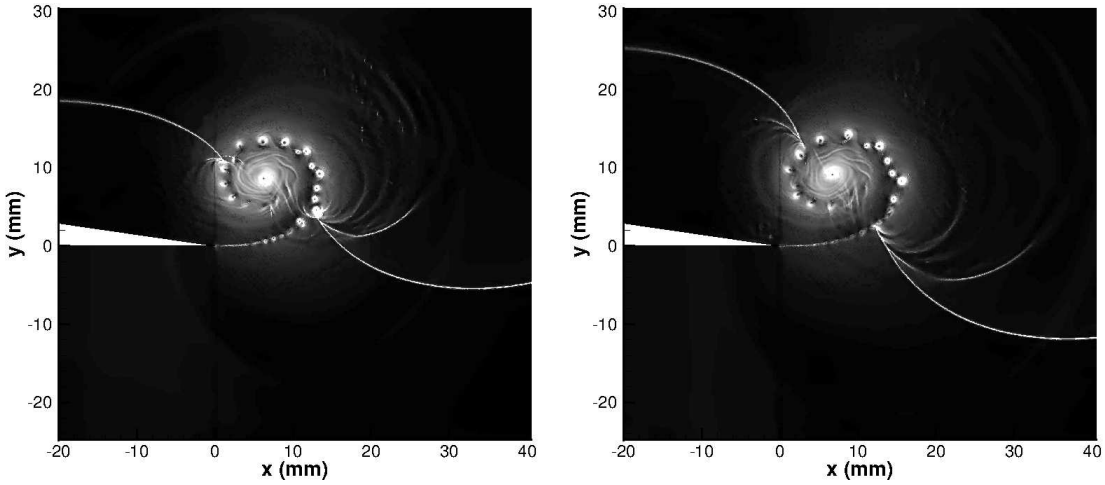

(k) 220 μs (l) 240 μs

Figure 5.5: Full-field numerical schlieren of $M_i = 1.28$ shock diffraction process around a sharp geometry

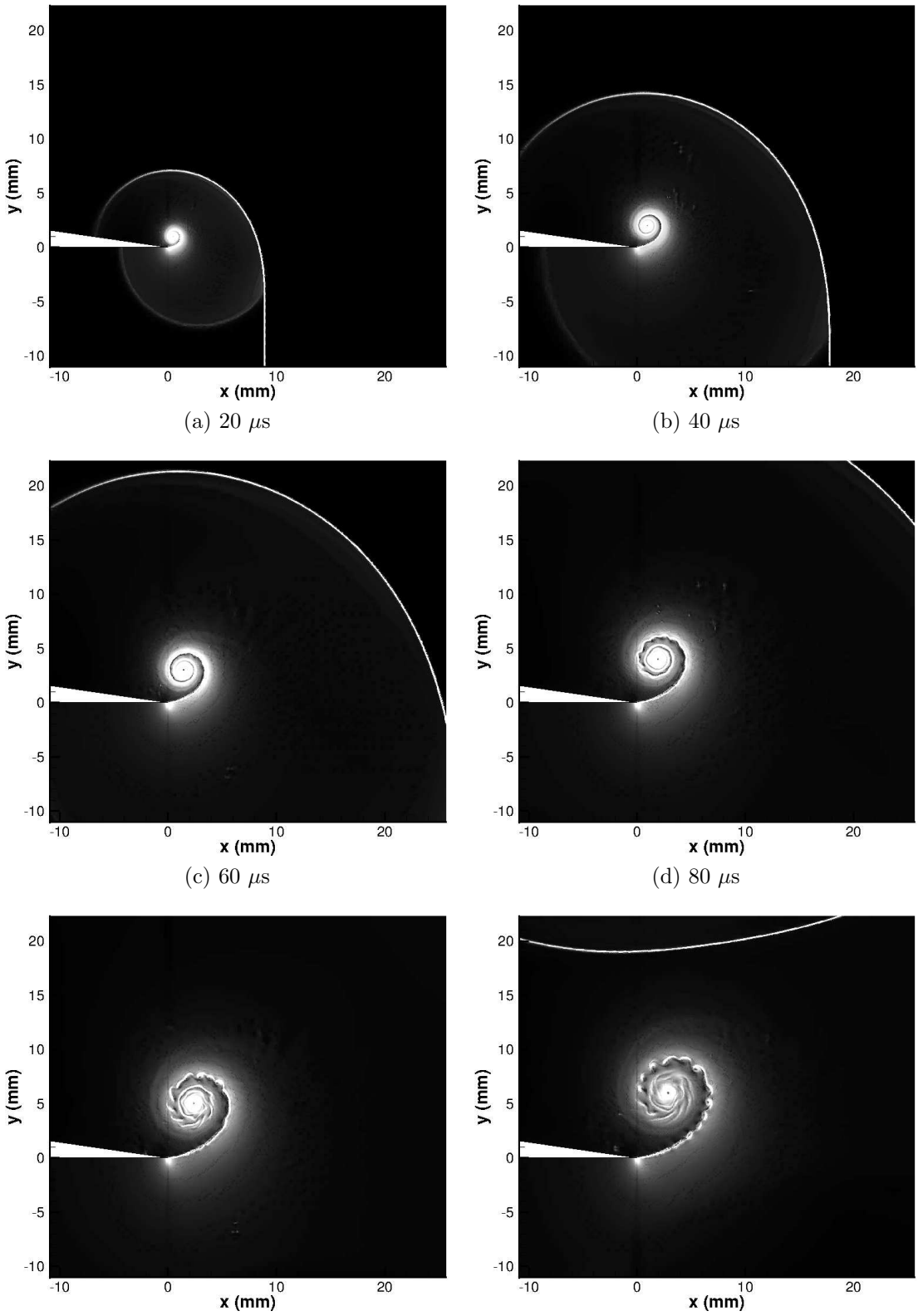

(a) 20 μs (b) 40 μs

(c) 60 μs (d) 80 μs

(e) 100 μs (f) 120 μs

Figure 5.6: Close-up numerical schlieren of $M_i = 1.28$ shock diffraction process around a sharp geometry

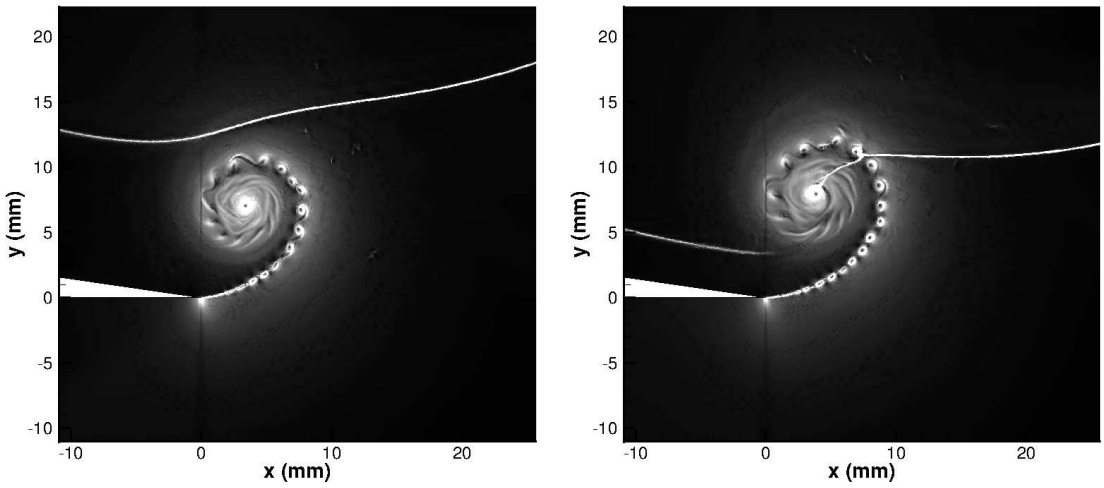

(g) 140 μs (h) 160 μs

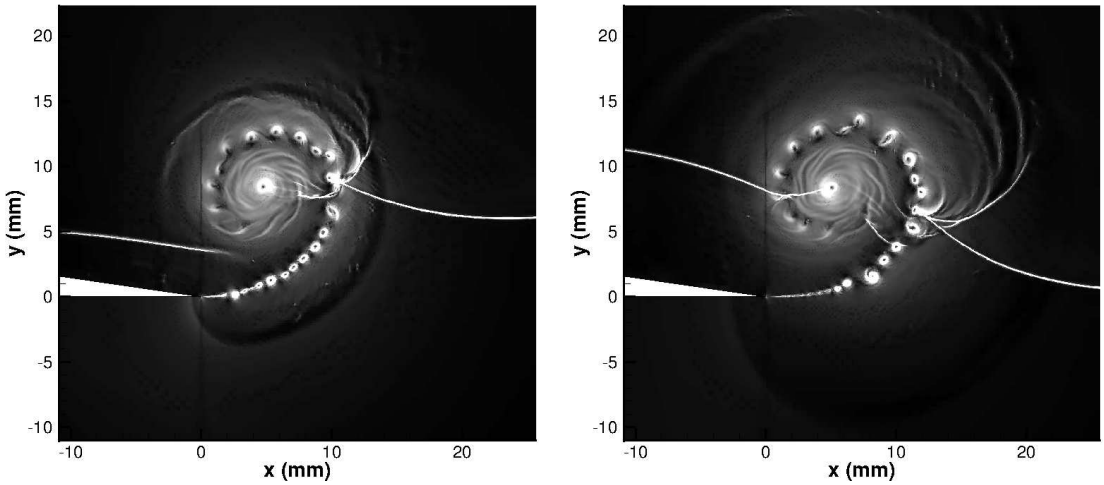

(i) 180 μs (j) 200 μs

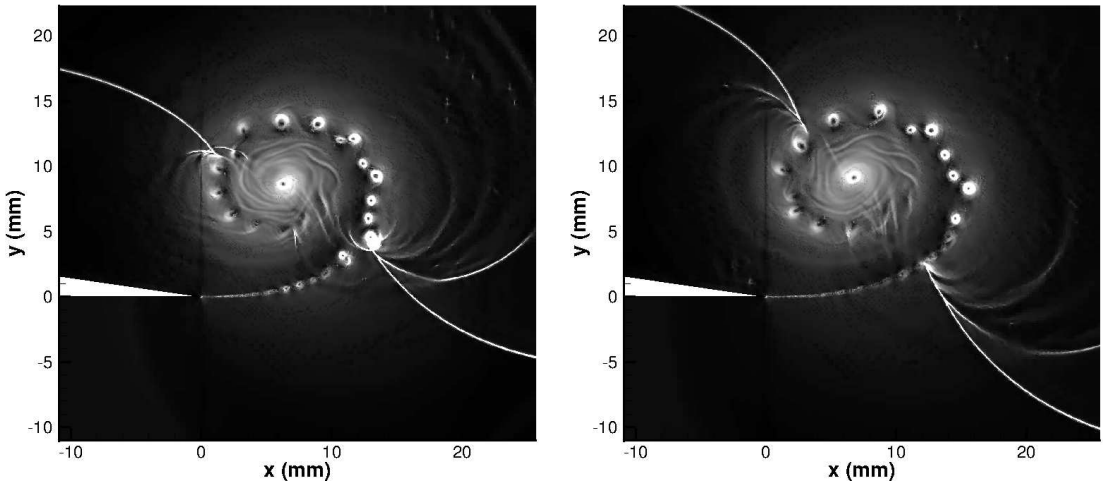

(k) 220 μs (l) 240 μs

Figure 5.6: Close-up numerical schlieren of $M_i = 1.28$ shock diffraction process around a sharp geometry

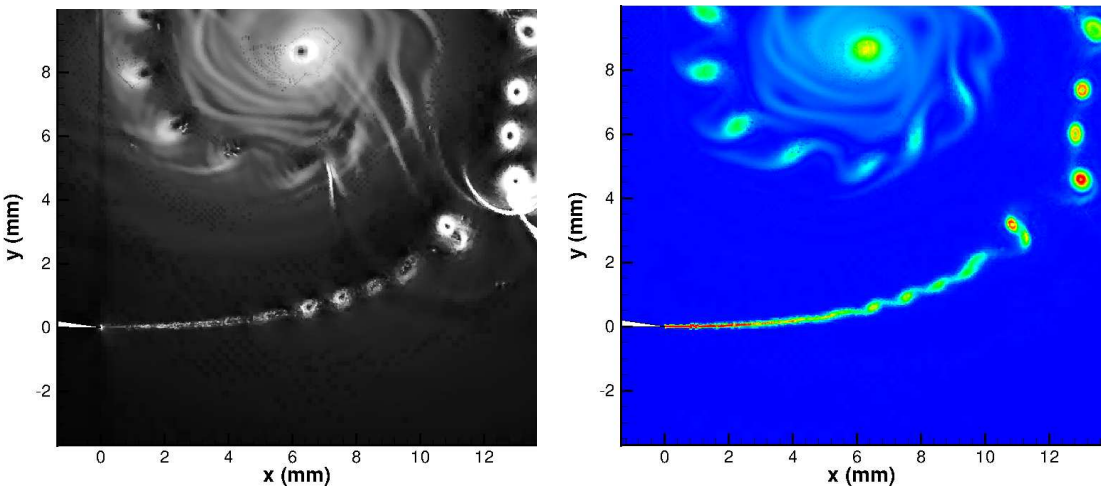

(a) Numerical schlieren 220 μs

(b) Vorticity magnitude 220 μs

Figure 5.7: Numerical schlieren and vorticity magnitude

more information about the structure, showing that it is another Kelvin-Helmholtz-style instability, albeit with a different spatial and temporal frequency from the previous one. Due to the lack of conclusive experimental evidence from the density-based techniques shown above, we cannot confirm the presence of this structure, as the numerical schemes discussed in Section 2.7.4 have proven to be unreliable in capturing phenomena such as this.

5.1.1.3 Mi = 1.46 Experimental Results

As discussed previously, only the images that best show the flow features will be shown from now on. Fig.5.8 shows the close-up shadowgraph images of the $M_i = 1.46$ shock diffracting around the sharp corner. There are two main differences between this flow and the one shown previously; namely that the reflected expansion wave has not propagated as far upstream due to the higher induced flow velocity, and there is now a shock wave structure on the underside of the shear layer which was not present at lower M_i. From as early as 20 μs (Fig.5.8a), there are some structures seen under the shear layer; however, it is not until the later images (Fig.5.8c) that the individual structures become discernible. The furthest upstream, and the largest, structure is triggered by the last running expansion wave, as shown in Fig.2.13. This region of incorrectly expanded supersonic flow is then decelerated by a shock wave, which leads into another expansion fan. This train of lambda shocks grows smaller as we progress along the shear layer until we reach approxaimtely 90° around the vortex. The lambda structures have become so small and frequent that we can no longer tell them apart. However, in Fig.5.8f it is possible to make out seven individual lambda shock structures.

The main vortex has propagated faster for this Mach number than in the previous case. The instabilities on the shear layer are still present but are more difficult to discern individually. Figs.5.8e & 5.8f show the instabilities most clearly before the interaction of the returning shock wave. The growth of the instabilities relative to the size of the shear layer seems to be reduced. This may indicate a stabilizing

effect as the velocity ratio across the shear layer increases. The diffracted shock wave slows down the motion of the shear layer instabilities, making them more visible in Figs.5.8i to 5.8l. This could indicate that, the motion and small scale of these vortices means that they are blurred together in the experimental images.

The diffracted shock wave does not return from the top wall of the test section any more quickly in this case than in the previous one, indicating that it is travelling at almost sonic speeds. However, the higher induced velocity (especially in the expansion region) and the stronger vortex generated means that the shock vortex interaction is much stronger in this case. Fig.5.8h shows the early signs of a transmitted wave that was not present at this time in the previous case. On the right hand side of the vortex, as before, the returning shock wave forms a regular reflection (Figs.5.8i & 5.8j); however, this has grown into a Mach reflection by Fig.5.8k. The shock connected to the centre of the vortex decayed away at lower Mach numbers; however, in this case, it persists (Fig.5.8l) and appears to be growing stronger. The two strong vortices generated after the shock wave impacts on the shear layer generate their own shock vortex interaction, generating diverging acoustic waves, as seen before. On the left-hand side of the vortex, there is a double shock structure with a kink in it.

At the centre of the vortex there is a large patch of turbulent flow with only a faint trace of the shear layer inside it. This patch of turbulence is similar to that seen by Skews [71].

It is difficult to estimate the strength of individual interactions using the shadowgraph technique. However, the schlieren technique affords a little more information in this respect. Fig.5.9 suggests that the strongest interaction is to be found on the right-hand side of the vortex, as the returning shock wave forms a Mach reflection.

As mentioned in Section 3.1, the schlieren system can be overranged to give a higher sensitivity, at the cost of not obtaining any information in regions where the image is total darkness or has saturated the CCD. Fig.5.10 shows the overranged schlieren images at 100, 120 & 140 μs. In these figures it is interesting to note the development of the structures on the right-hand side of the vortex, outside the shear layer. These lambda structures appear to have faint diverging acoustic level waves which propagate upstream. These structures are not visible in Fig.5.9, demonstrating how weak they are in comparison with the other waves in the flow.

Fig.5.9f shows that, when compared to the previous $M_i = 1.28$ case, it is clear that a returning shock wave causes much more distortion to the vortex, implying that it is a significantly stronger wave.

5.1.1.4 Mi = 1.46 Numerical Results

The numerical simulation results (Fig.5.11) show, in general, very good agreement with the experimental shadowgraphs presented previously. All of the main waves are captured, with the shock-vortex interaction captured in detail. The lambda shock structure is poorly resolved in this simulation. The last running expansion wave can be seen clearly up until the impact of the returning shock. Fig.5.11d shows a faint shock and further expansion fan but nothing more than this is resolved, even if the sensitivity of the image is increased. This is believed to be a function of the grid adaption technique. Individual Kelvin-Helmholtz vortices on the shear layer are very clearly resolved, possibly because there is no motion blur due to exposure

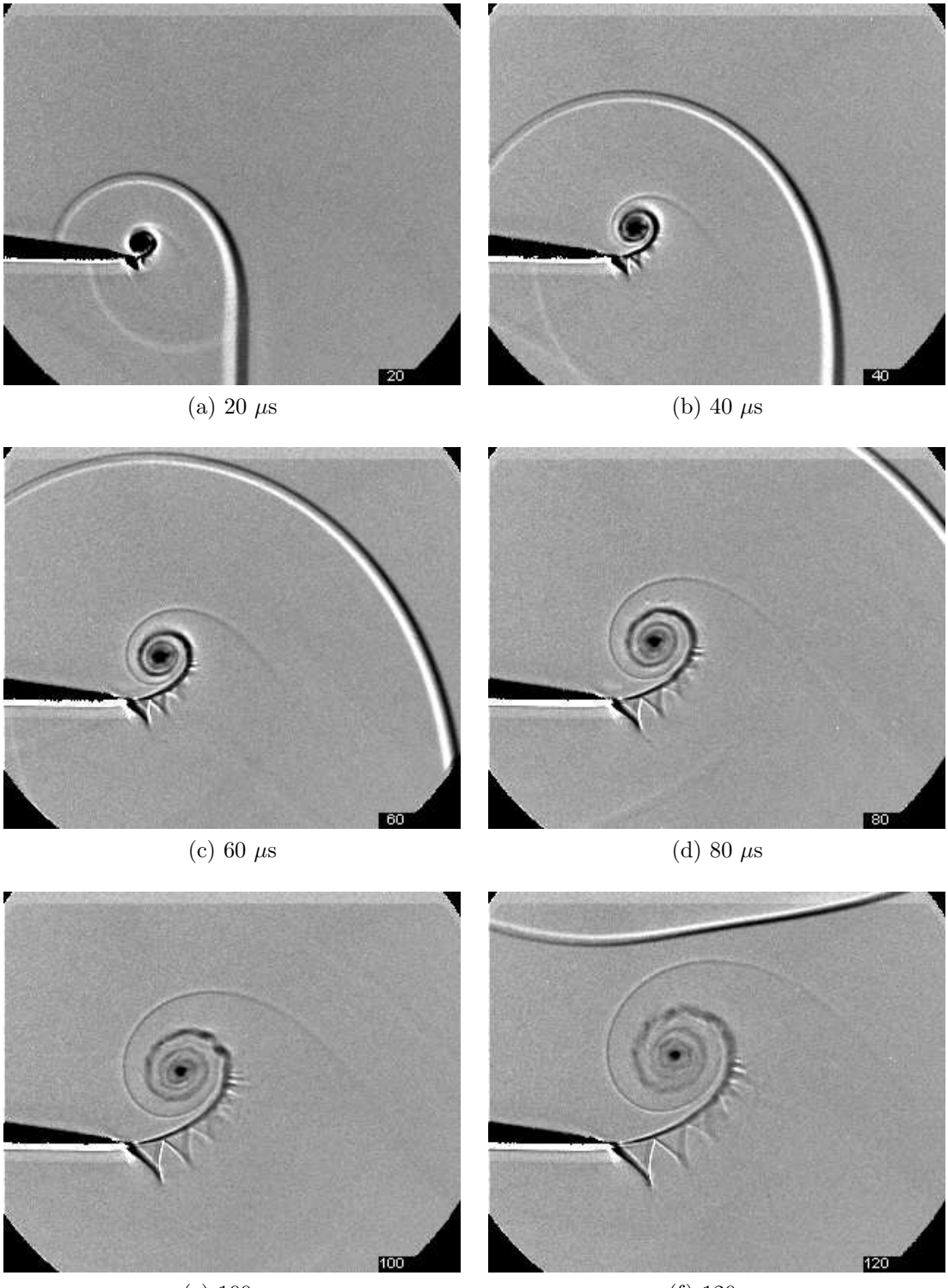

(a) 20 μs

(b) 40 μs

(c) 60 μs

(d) 80 μs

(e) 100 μs

(f) 120 μs

Figure 5.8: Close-up shadowgraph of $M_i = 1.46$ shock diffraction process around a sharp geometry

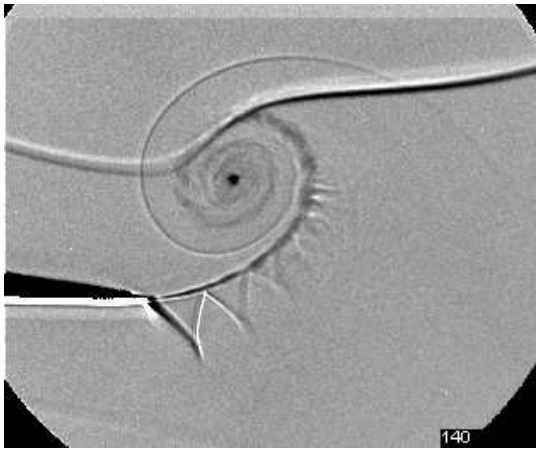

(g) 140 μs

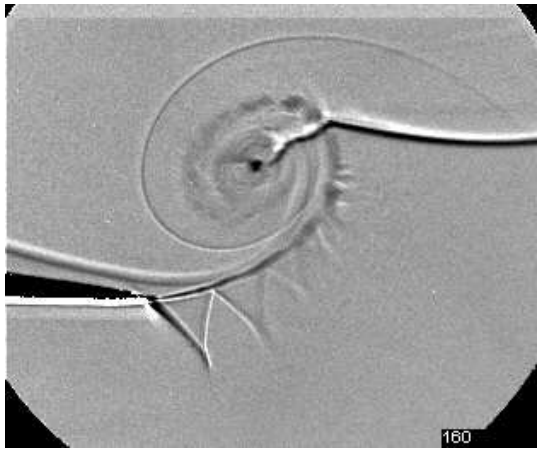

(h) 160 μs

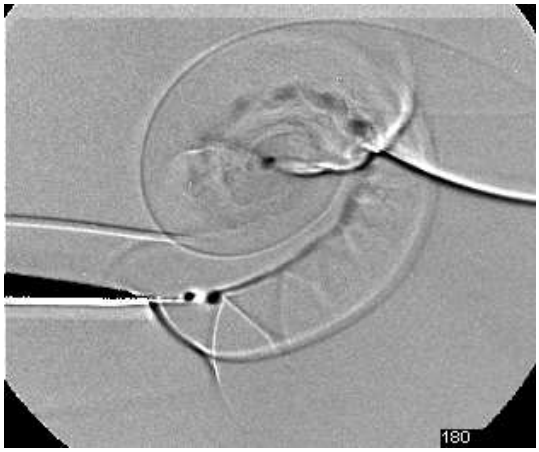

(i) 180 μs

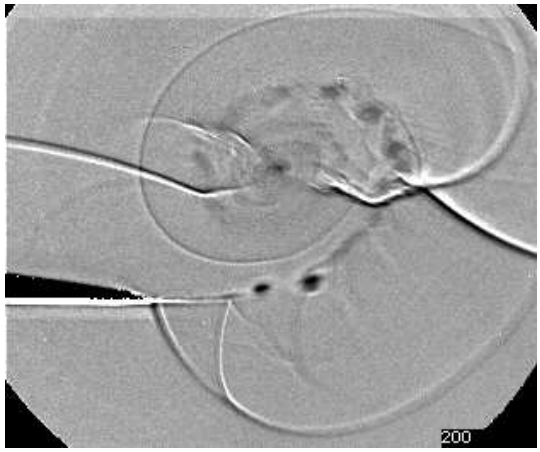

(j) 200 μs

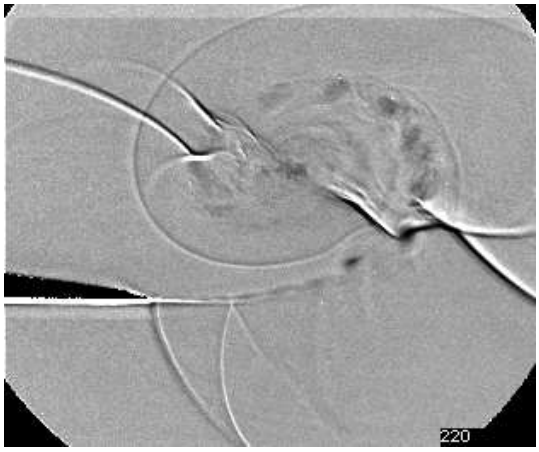

(k) 220 μs

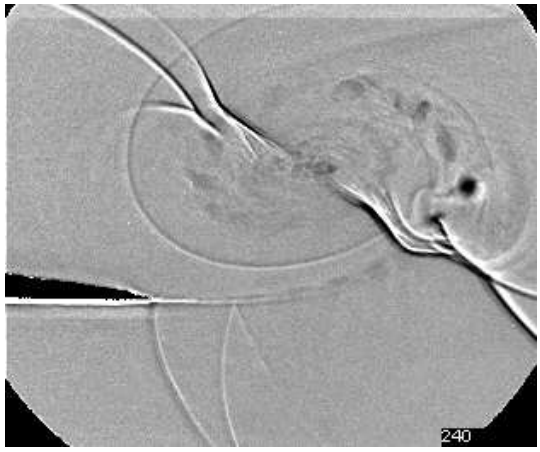

(l) 240 μs

Figure 5.8: Close-up shadowgraph of $M_i = 1.46$ shock diffraction process around a sharp geometry

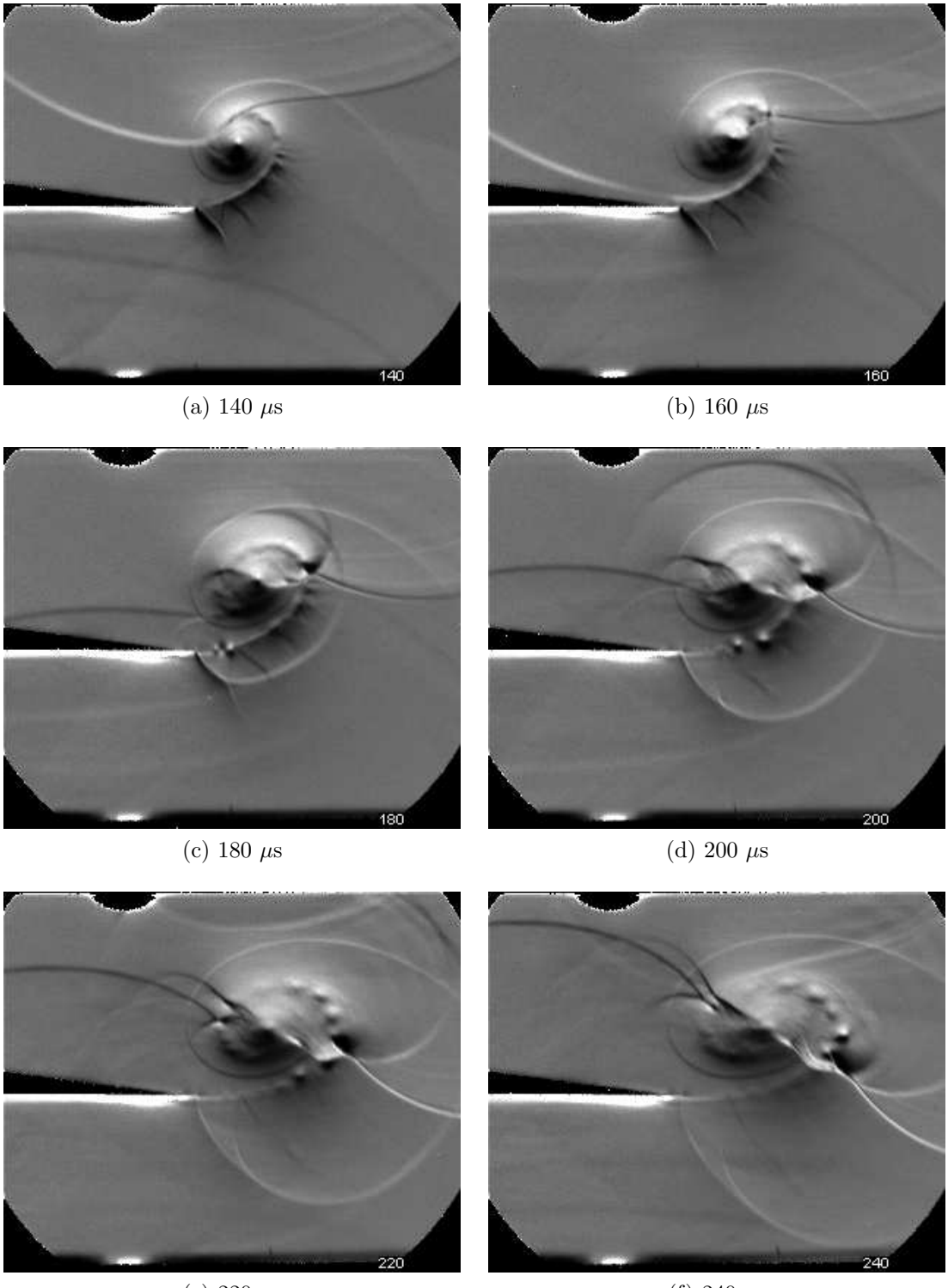

(a) 140 μs (b) 160 μs

(c) 180 μs (d) 200 μs

(e) 220 μs (f) 240 μs

Figure 5.9: Full-field schlieren of $M_i = 1.46$ shock diffraction process around a sharp geometry

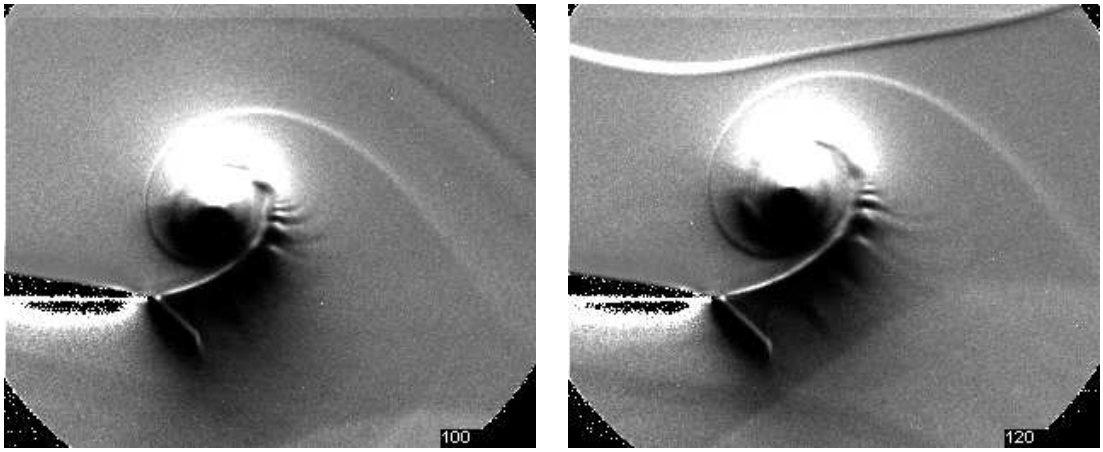

(a) 100 μs

(b) 120 μs

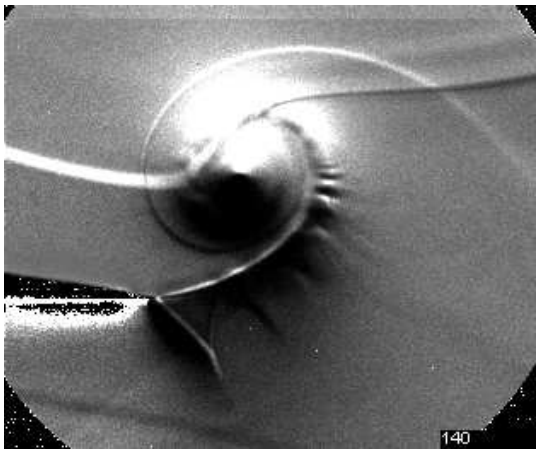

(c) 140 μs

Figure 5.10: Close-up schlieren of $M_i = 1.46$ shock diffraction process around a sharp geometry

of the image. Based on the results in Fig.5.8, they seem to be overpredicted.

Fig.5.11g is of particular interest, as it shows the disturbance of the returning shock wave as it passes through individual vortices on the shear layer. Each one of these vortices creates an acoustic level wave, which can be seen most clearly in Fig.5.11i, propagating away from the site of disturbance. It is interesting to note that after the impact of the returning shock on the shear layer, the K-H instability grows at a much faster rate, with individual vortices beginning to pair up and spin around each other. This is not seen in the experimental shadowgraphs or schlieren images, again hinting that the K-H growth rate is overpredicted.

5.1.1.5 Mi = 1.55 Experimental Results

In a manner befitting of an episode of *The Simpsons*, the Shimadzu HPV-1 irreparably broke just before the final test was to be completed (see the quote at the beginning of this chapter). This means that there is no *close-up shadowgraph* data available for this test case. However, a slightly more thorough combination of the other optical conditions should allow for complete understanding of the flow.

The basic shock wave structure shown in Fig.5.12 is largely similar to what has been shown for the previous case, with some exceptions. Firstly, as would be expected, the reflected expansion wave has not travelled as far upstream, due to the higher induced velocity. Secondly, there are a fewer lambda shaped structures below the shear layer (only 5 individual structures can be seen in Fig.5.12f; however, each lambda structure is larger than the previous case. Finally, from Fig.5.12d onwards, there is a faint shock wave inside the vortex connecting the vortex core to the shear layer. There are no noticeable instabilities on the shear layer in the far-field shadowgraph images.

The returning diffracted shock appears to be affected by the vortex slightly sooner than the previous case (Fig.5.12e), indicating that the vortex must be stronger as its influence can be felt further away. As before, the impact of the returning shock on the splitter generates two strong vortices, which propagate along the shear layer. On the right-hand side of the vortex the shock is again split up, initially forming a regular reflection in Fig.5.12h which transforms into a Mach reflection by Fig.5.12j.

The greater sensitivity in the schlieren images (Figs.5.13 & 5.14) gives us significantly more information about some of the weaker processes that occur, although this comes at the cost of knowing nothing about what is happening in the first 60 μs due to the system being overranged. It is more noticeable in the close-up images that the vortex has propagated further downstream in this case compared to the previous two. The right-hand side of the shock-vortex interaction happens out of the field of view of Fig.5.14.

Figs.5.13e to 5.13g and 5.14e & 5.14f show the structures on the outside of the shear layer most clearly. The structures in this region are clearly much stronger for this Mach number than for the previous ones, as the dark regions behind them are much more pronounced. These structures appear to have *tails* which stretch further into the flow field than would be expected. The *tails* propagate upstream in time, in a similar way to the diverging acoustics seen previously. The long tails of the lambda structure are shown even more clearly in the overranged schlieren images of Fig.5.15.

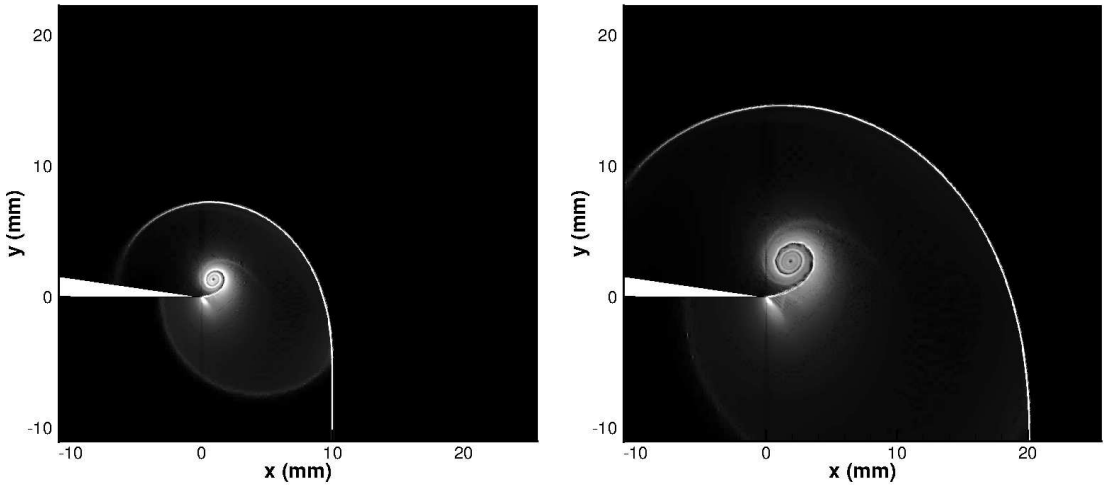

(a) 20 μs

(b) 40 μs

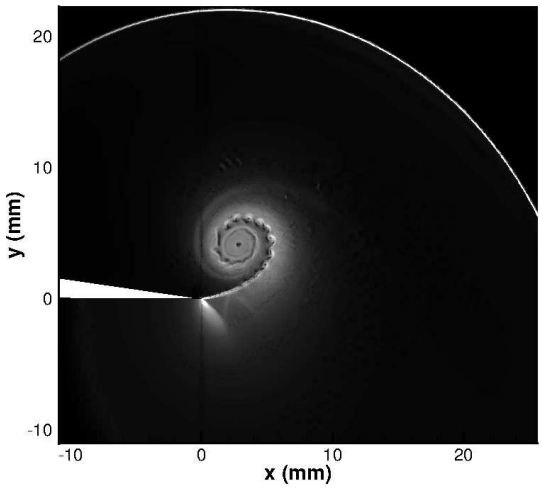

(c) 60 μs

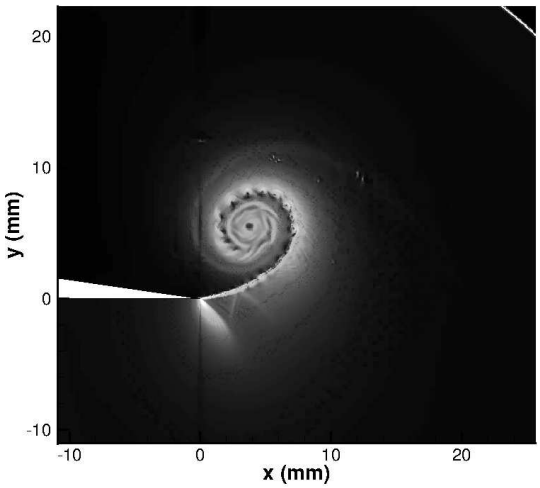

(d) 80 μs

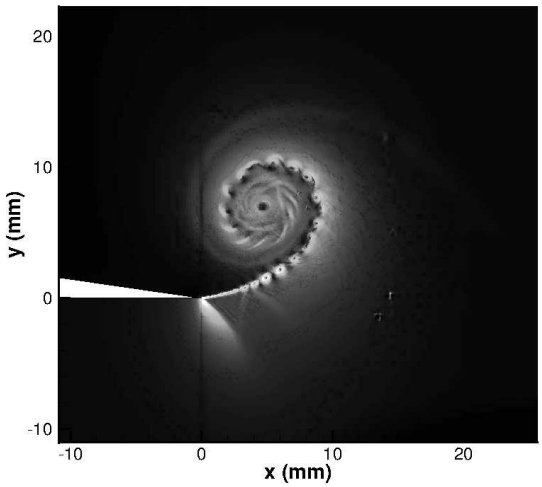

(e) 100 μs

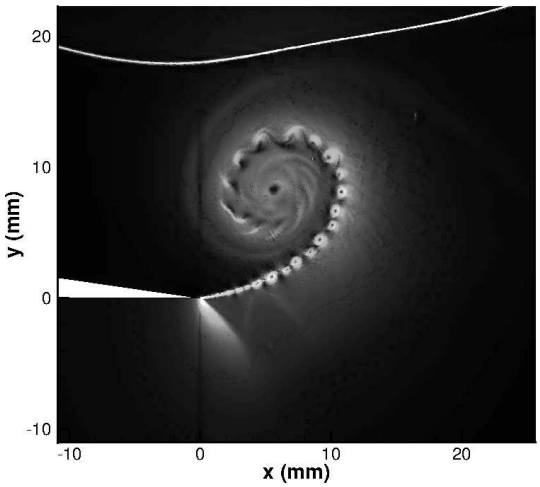

(f) 120 μs

Figure 5.11: Close-up numerical schlieren of $M_i = 1.46$ shock diffraction process around a sharp geometry

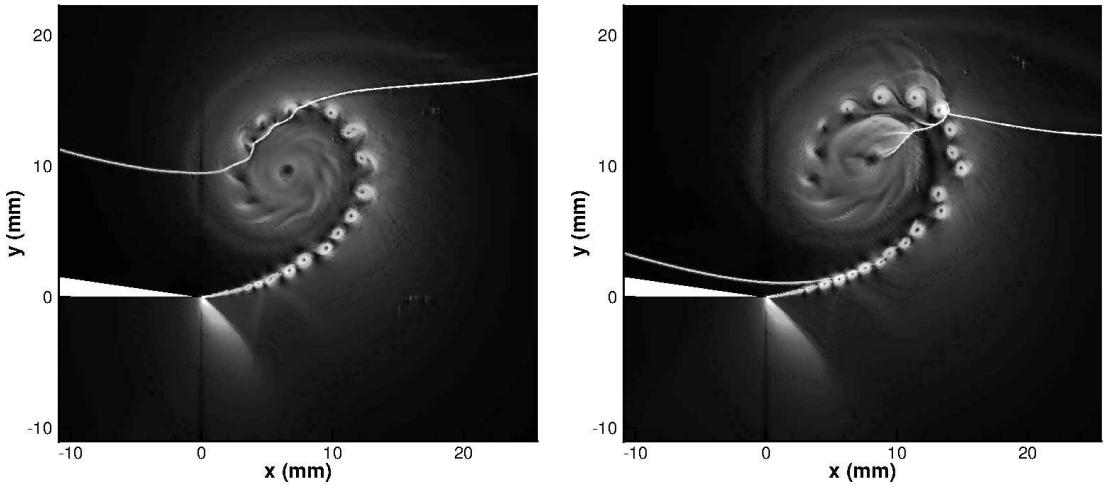

(g) 140 μs

(h) 160 μs

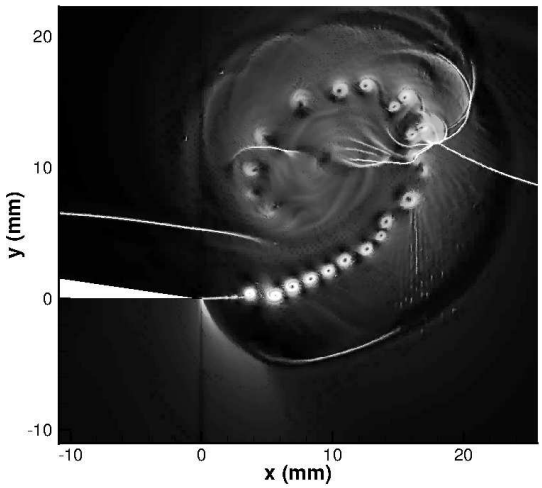

(i) 180 μs

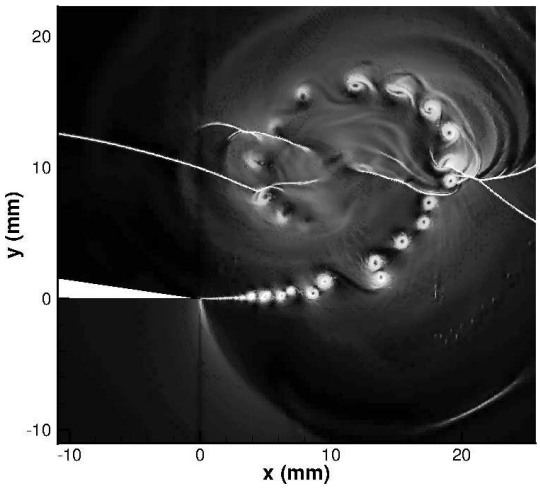

(j) 200 μs

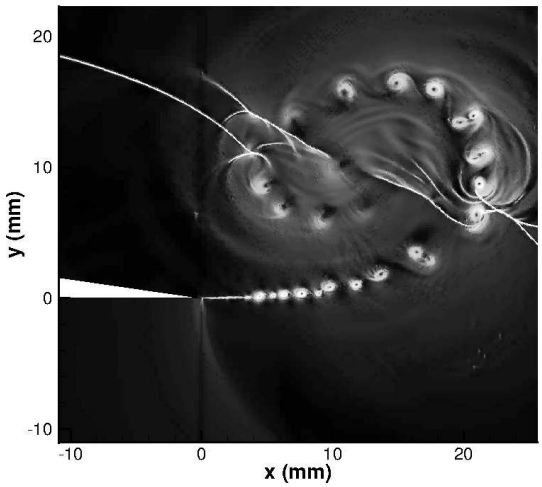

(k) 220 μs

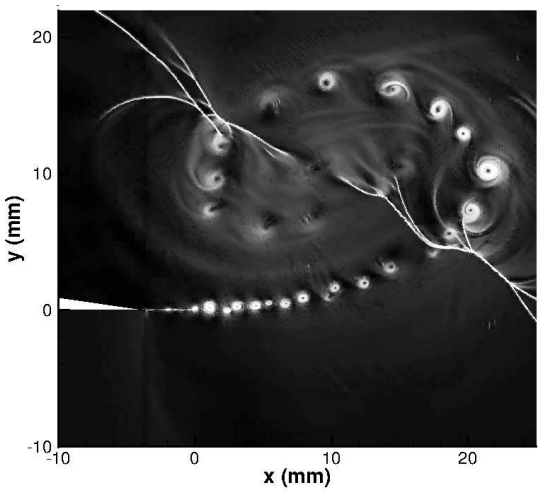

(l) 240 μs

Figure 5.11: Close-up numerical schlieren of $M_i = 1.46$ shock diffraction process around a sharp geometry

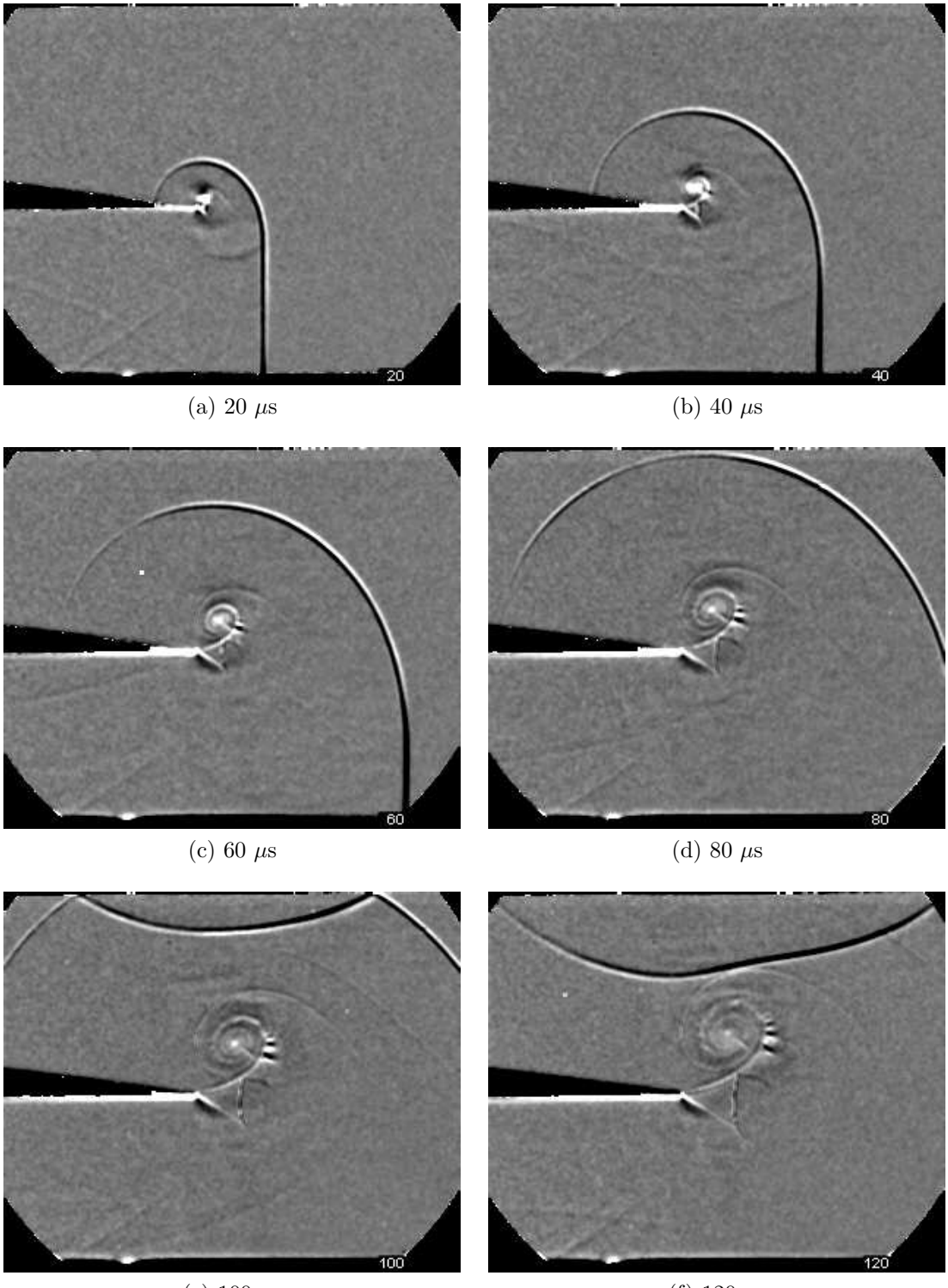

(a) 20 μs (b) 40 μs

(c) 60 μs (d) 80 μs

(e) 100 μs (f) 120 μs

Figure 5.12: Full-field shadowgraph of $M_i = 1.55$ shock diffraction process around a sharp geometry

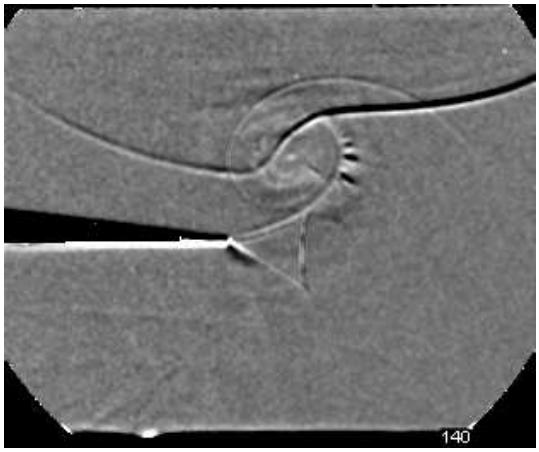

(g) 140 μs

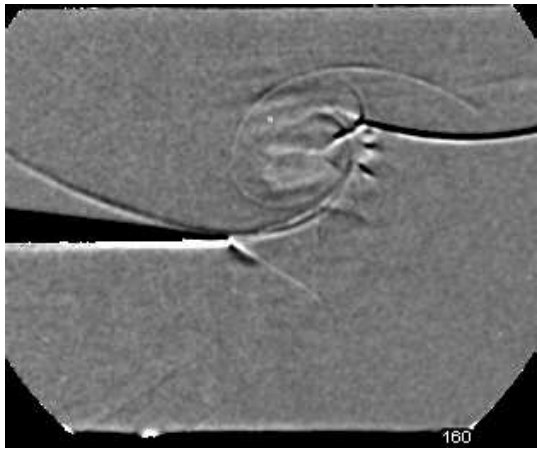

(h) 160 μs

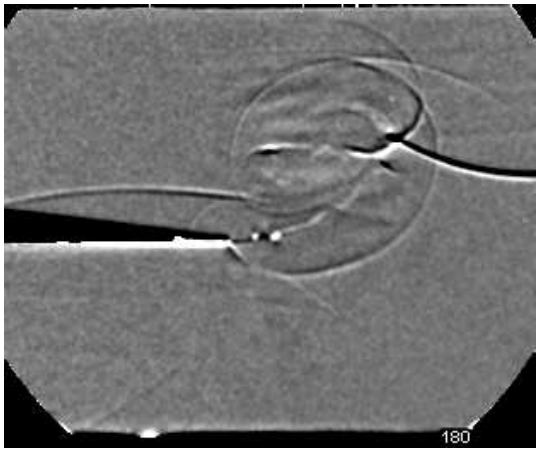

(i) 180 μs

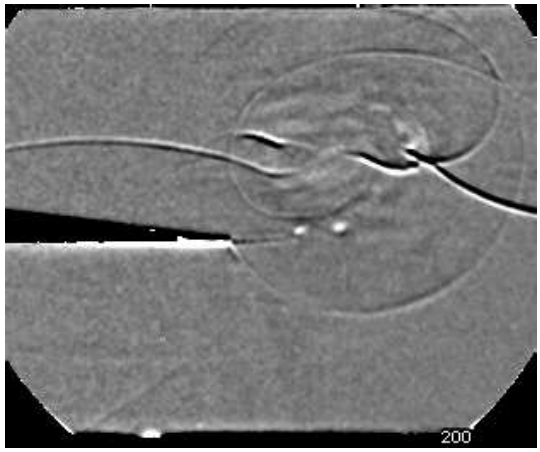

(j) 200 μs

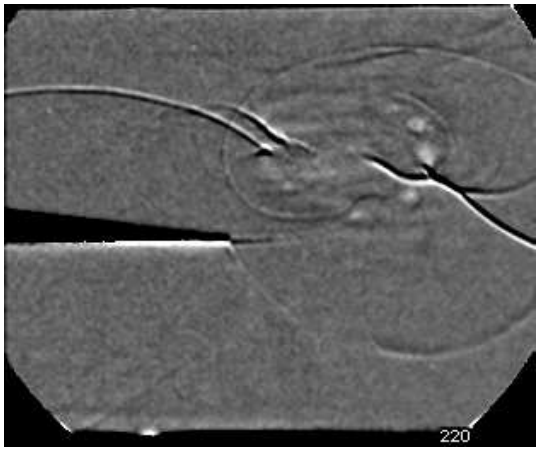

(k) 220 μs

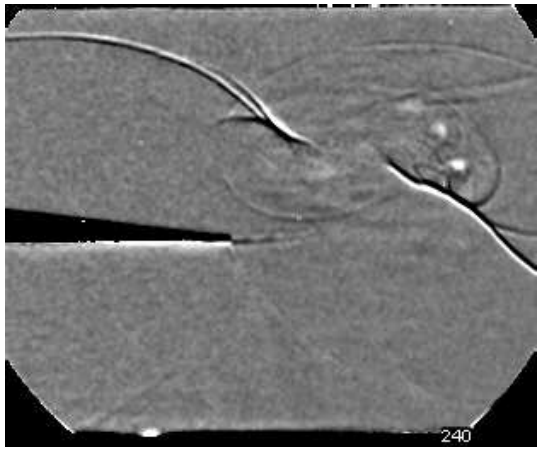

(l) 240 μs

Figure 5.12: Full-field shadowgraph of $M_i = 1.55$ shock diffraction process around a sharp geometry

Examining Fig.5.14f more closely, we can see that there are no apparent disturbances on the shear layer until the end of the structures seen on the outside of it (approximately 100° around the vortex). After this point, there are structures which can faintly be seen on the shear layer, suggesting that the K-H instability is more heavily damped in regions where one side of the shear layer has localised supersonic flow. Such a result is in accordance of the work of Papamoschou & Roshko [52] and Miles [1].

The embedded shock wave can partially be seen in Figs.5.13d to 5.13g, but is more clearly seen in Fig.5.14, specifically in Figs.5.14f & 5.14g. The shear layer in the vortex roll-up process can be thought of as a solid line which fluid cannot pass over. The main vortex induces velocity above the shear layer and the figures clearly show that the shear layer rolls up around the vortex. If the shear layer can be thought of as a boundary, then the fluid in this region is passing through a reduction in area and could be accelerated up to sonic speeds. This acceleration will come hand-in-hand with a reduction in pressure. Therefore, a shock wave is required to *balance* the pressure on either side of the shear layer.

Figs.5.13k & 5.13l show that, after the passage of the returning shock wave through the shear layer, there are some disturbances present on the shear layer, indicating the early stages of a further K-H instability. Instabilities which passed down the shear layer at this point are broken up into patches of turbulence by the shock vortex interaction, as can be seen on the far right of Figs.5.13k & 5.13l. The centre of the main vortex also displays the properties of a strong patch of turbulence.

Fig.5.13l shows that the main vortex has been severely distorted by the passage of the returning diffracted shock wave. The vortex has been stretched in the horizontal direction, giving it an elliptical shape.

5.1.1.6 Mi = 1.55 Numerical Results

The numerical schlieren results for Mi=1.55 are presented in Figs.5.16 & 5.17. The basic wave structure is well captured, so the main focus will be on the complex region.

Similar to the previous case, shown in Fig.5.11, the lambda structures below the shear layer are not well defined by the simulation. Figs.5.16b to 5.16d show the first and second lambda structure, but after this time the second one becomes more and more diffuse. The vortex shock seen in the experimental results is captured, although it does not seem to extend as far as the shear layer. It is interesting to note that the wave structures seen on the outside of the shear layer (90° around the vortex in Fig.5.16b onwards) appear to have been resolved, even though the lambda structures leading up to them have not. This suggests that the structures are not a continuation of the lambda shocks, but are, in fact, a function of something else.

The instability of the shear layer appears to be overpredicted in the numerical results, as there was little indication from Figs.5.12, 5.13 & 5.14 that so many vortices were produced so quickly.

The shock-vortex interaction shown in the latter images of Fig.5.16 and Fig.5.17 proceeds in a very similar manner to the experiments. The impact of the returning shock generates the two strong vortices, which immediately begin to pull another, weaker, vortex around them. As in the previous numerical cases, a secondary K-H instability is generated. This instability develops much more quickly than the

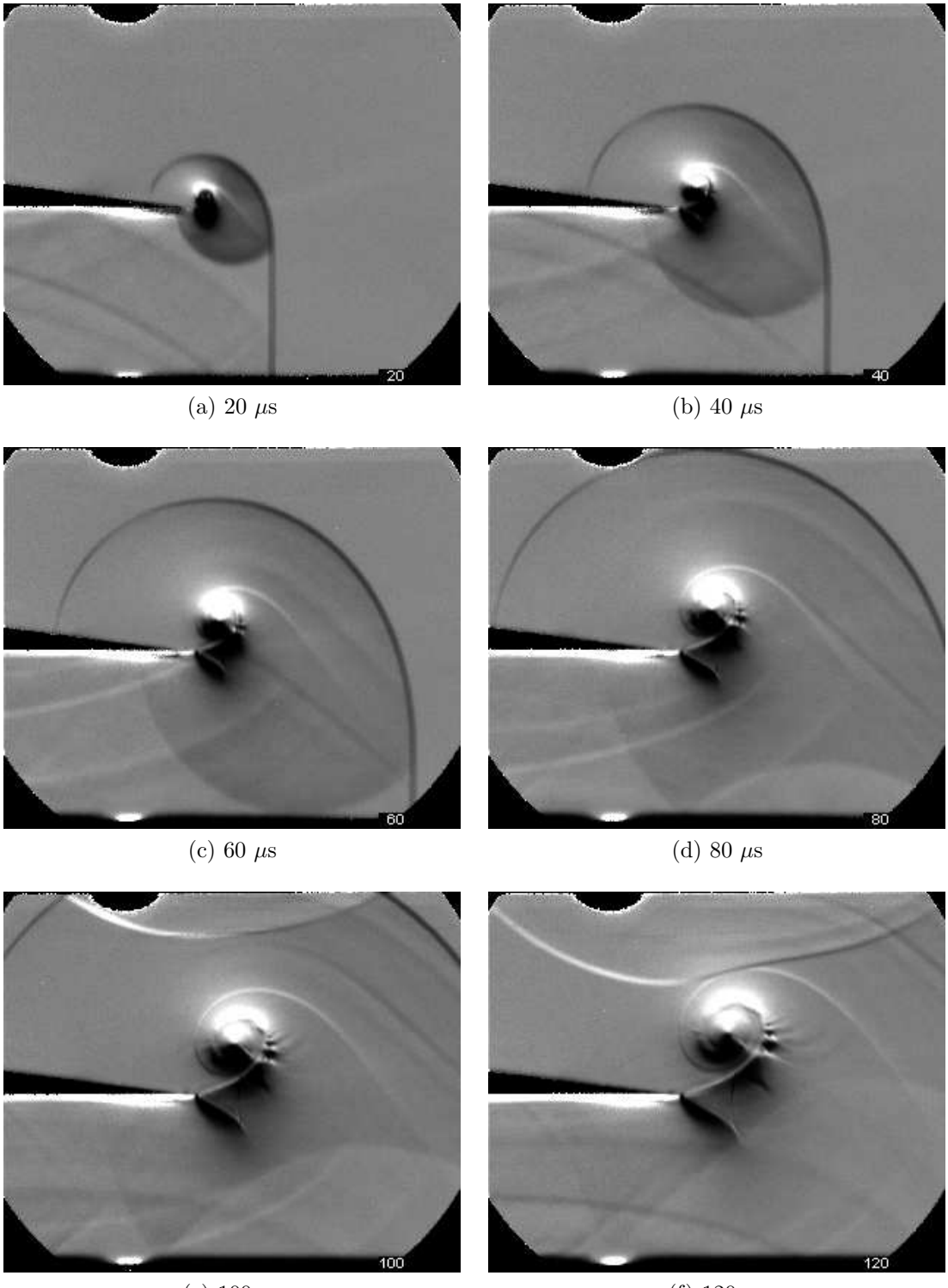

(a) 20 μs (b) 40 μs

(c) 60 μs (d) 80 μs

(e) 100 μs (f) 120 μs

Figure 5.13: Full-field schlieren of $M_i = 1.55$ shock diffraction process around a sharp geometry

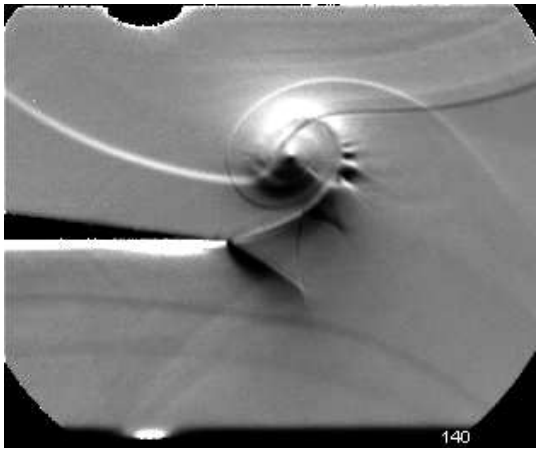

(g) 140 μs

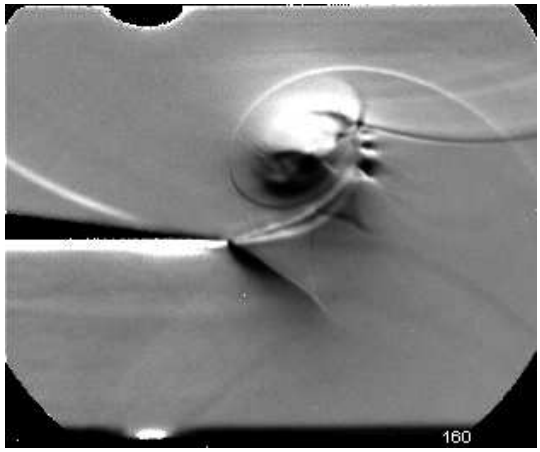

(h) 160 μs

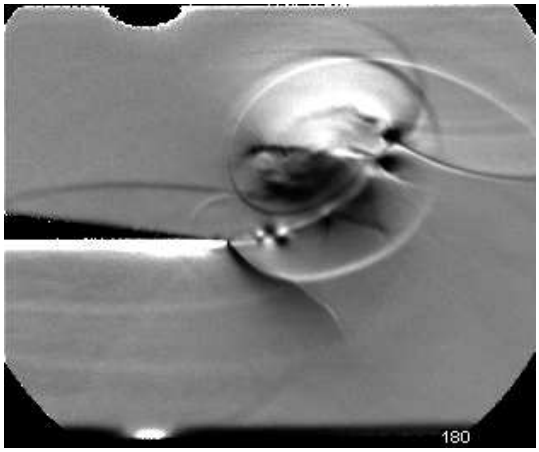

(i) 180 μs

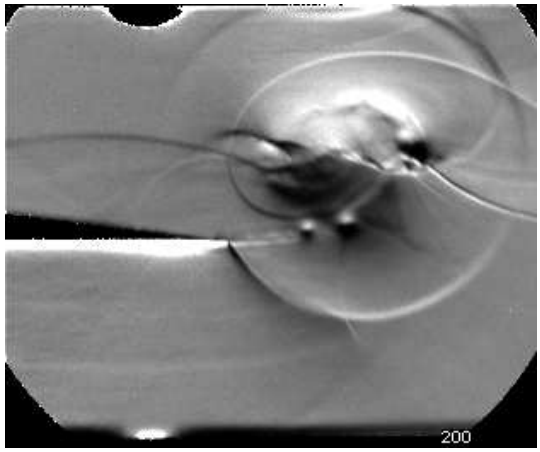

(j) 200 μs

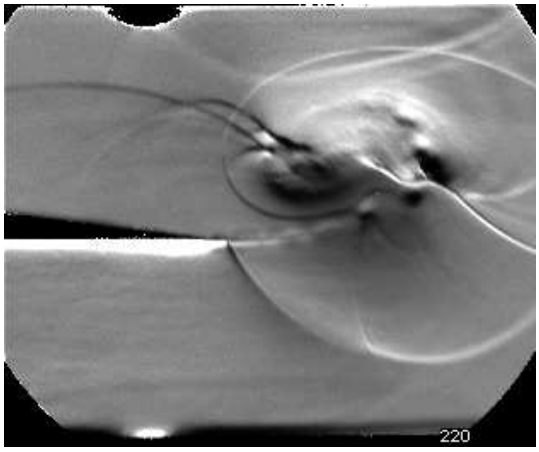

(k) 220 μs

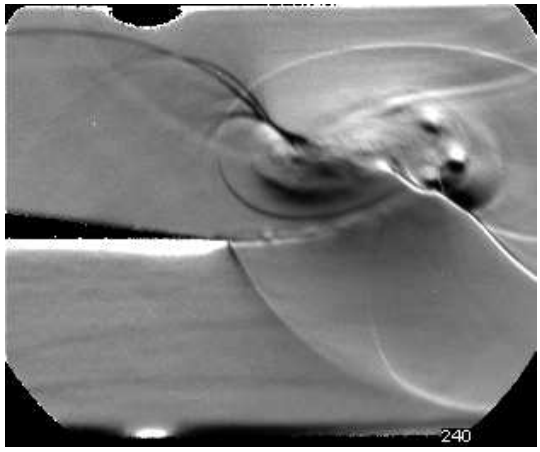

(l) 240 μs

Figure 5.13: Full-field schlieren of $M_i = 1.55$ shock diffraction process around a sharp geometry

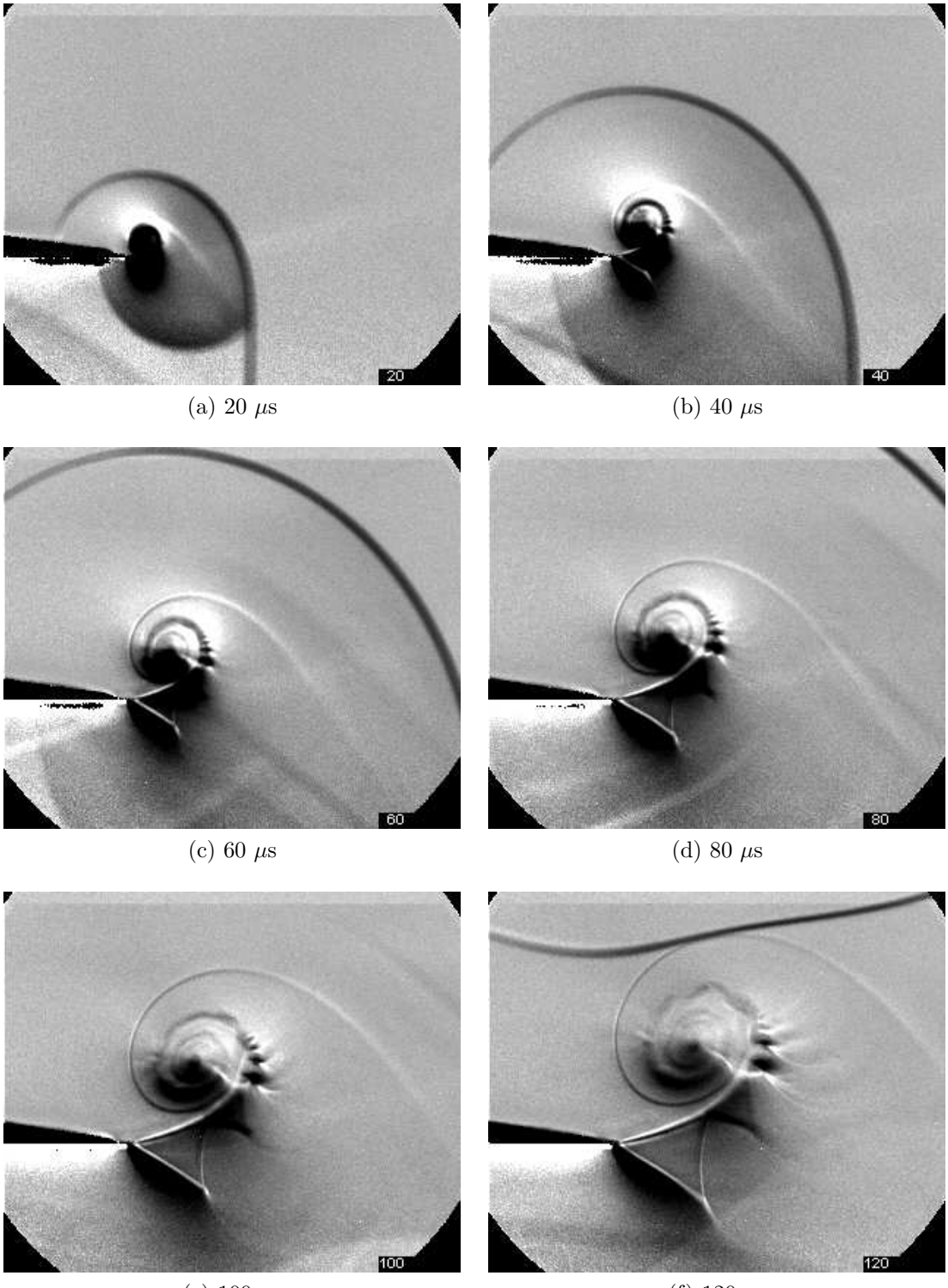

(a) 20 μs

(b) 40 μs

(c) 60 μs

(d) 80 μs

(e) 100 μs

(f) 120 μs

Figure 5.14: Close-up schlieren of $M_i = 1.55$ shock diffraction process around a sharp geometry

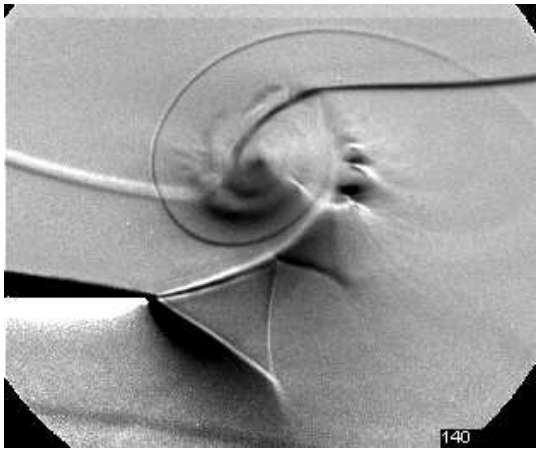

(g) 140 μs

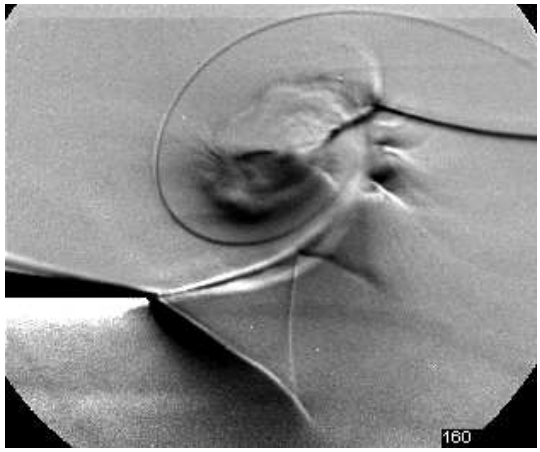

(h) 160 μs

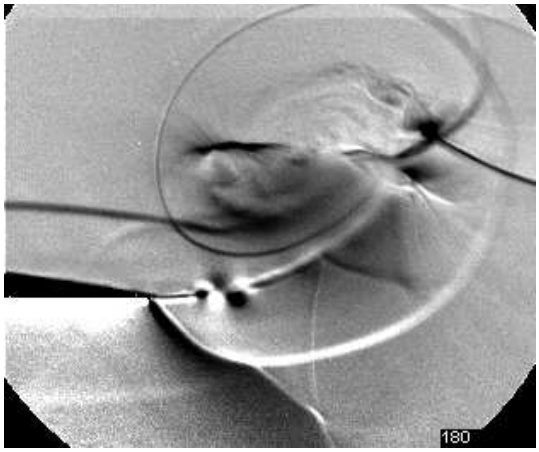

(i) 180 μs

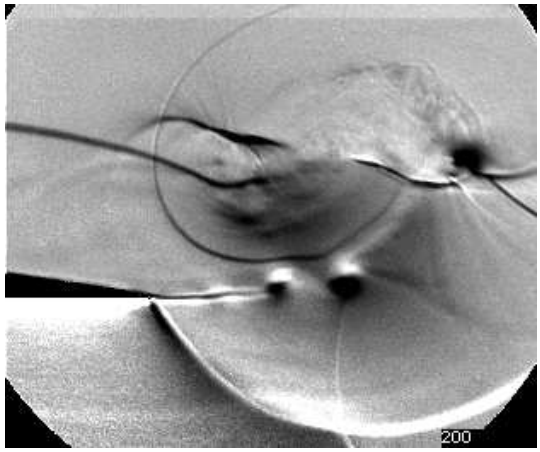

(j) 200 μs

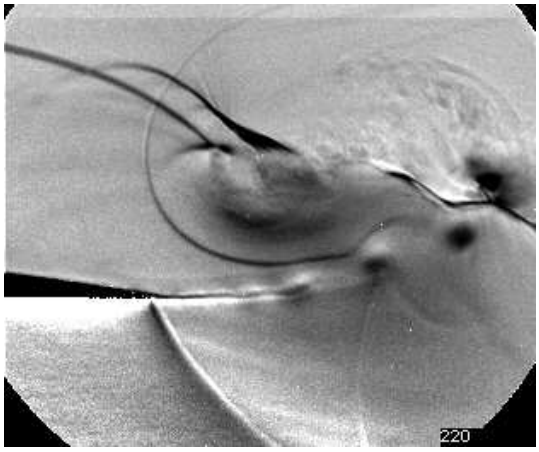

(k) 220 μs

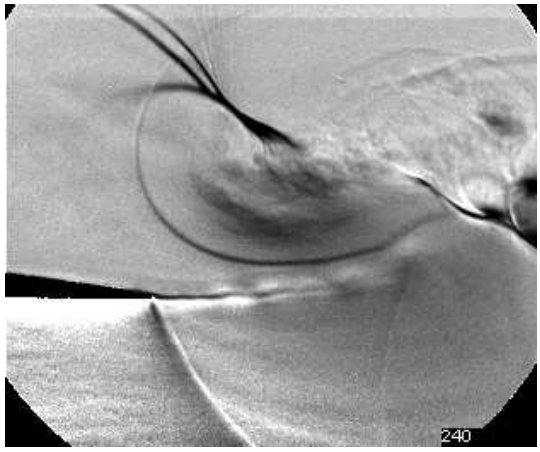

(l) 240 μs

Figure 5.14: Close up schlieren of $M_i = 1.55$ shock diffraction process around a sharp geometry

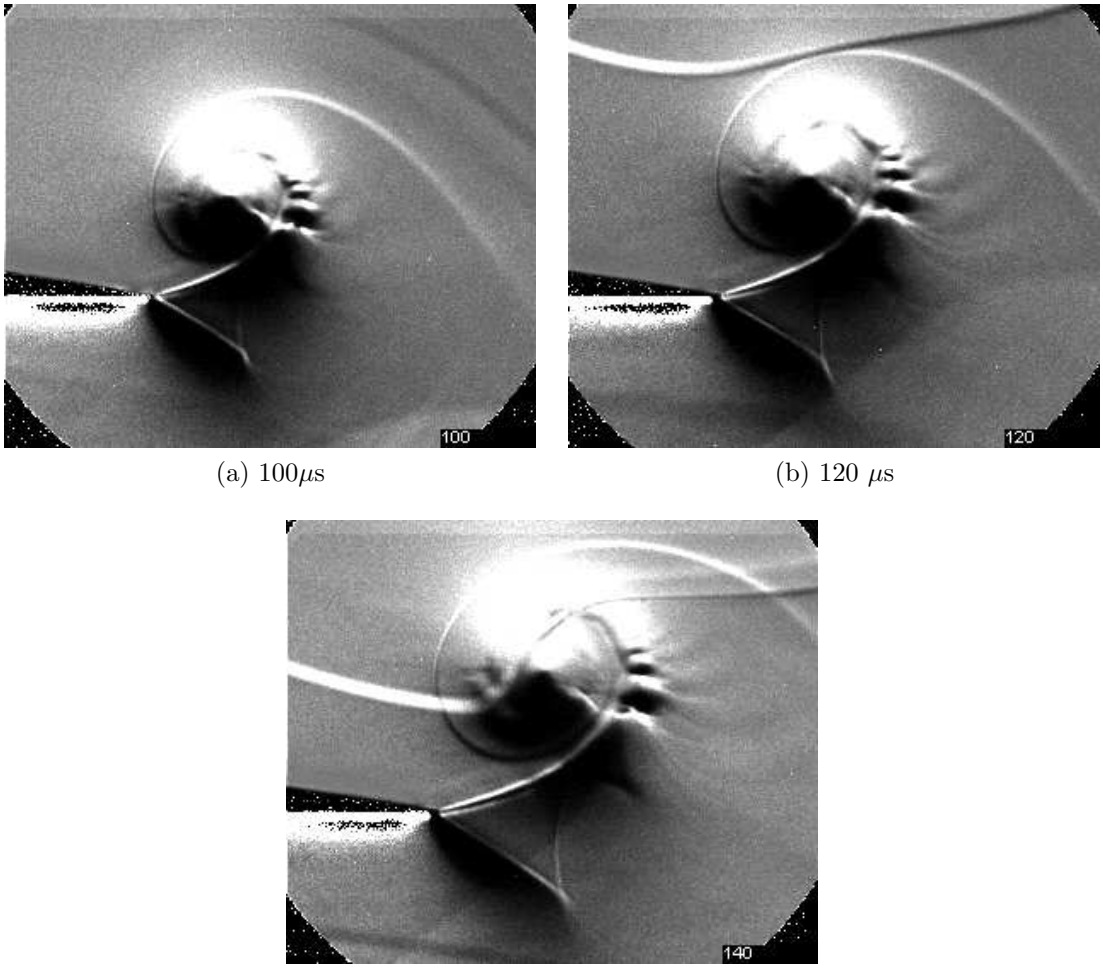

(a) 100μs

(b) 120 μs

(c) 140 μs

Figure 5.15: Close up schlieren of $M_i = 1.55$ shock diffraction process around a sharp geometry

experimental disturbances seen in Figs.5.14k & 5.14l.

5.1.1.7 Conclusions

The process of shock wave diffraction around a sharp corner has been studied using a variety of optical setups. The shock wave systems generated are different over a relatively narrow range of incident Mach numbers. A $M_i = 1.28$ does not generate any visible lambda structures underneath the shear layer, leading to the conclusion that the flow in this region is entirely subsonic. This is consistent with the critical Mach number theory presented by Sun & Takayama [36]. Both of the higher Mach number cases ($M_i = 1.46$ and $M_i = 1.55$) show a series of lambda structures underneath the shear layer in the expansion region. The $M_i = 1.46$ case shows many small lambda structures which eventually degenerate into structures too small to distinguish; however, the $M_i = 1.55$ shows a significantly larger initial lambda structure with fewer subsequent lambda structures. This leads to the conclusion that the flow is tending towards the strong shock solution presented in Fig.2.12c. The contact surface between the gas affected by the normal shock compared to the curved, diffracted portion, is swept up into the main vortex.

The results in this section show that the instabilities present on the shear layer created during shock wave diffraction can only be clearly seen by using a focused shadowgraph system with a shallow depth of field in conjunction with an ultra-high-speed camera. Previous experimental tests have only been conducted using schlieren or one shadowgraph setup. Schlieren systems are easily overranged, especially in the region of the main vortex, as the density changes in this region are especially strong, leading to some flow features being missed.

The shear layer created in this experiment is extremely thin, due to the nature of the corner geometry. The shear layer is so thin that it is almost impossible to accurately estimated its width given the limited spatial resolution. This thin shear layer is closer to the vortex sheet approximation made in Section 2.5 than in other work, such as that by Skews [32]. This thinner shear layer can act in a more inviscid manner than the thicker ones generated by shallower corner angles and can rapidly develop instabilities. Other tests, such as the 90° corner, will generate instabilities eventually, such as those seen by Skews [33]. An increase in incident shock Mach number seems to inhibit the growth of the instabilities, especially around the lambda structure region where the flow is locally supersonic on one side of the shear layer. It is a known phenomena that as the velocity ratio increases across a shear layer, particularly to a locally supersonic speed, instabilities can be damped out. Further to this, the majority of work performed on this problem involves using a 90° corner as the test geometry. In these tests the vortex is in such close proximity to the wall, that a *wall shock* formed. This will compress the flow in this region, thus increasing its density. If the density on the low-speed side of the shear layer is higher, the flow is less susceptible to small wavelengths, as the complex part of Equation 2.55 is smaller.

The diffraction process appears to be self-similar in time, with the exception of the shear layer instabilities. The instabilities on the shear layer will take a finite time to develop and as a result the flow cannot be considered completely self-similar in time.

The interaction of the cylindrical diffracted shock wave and the main vortex

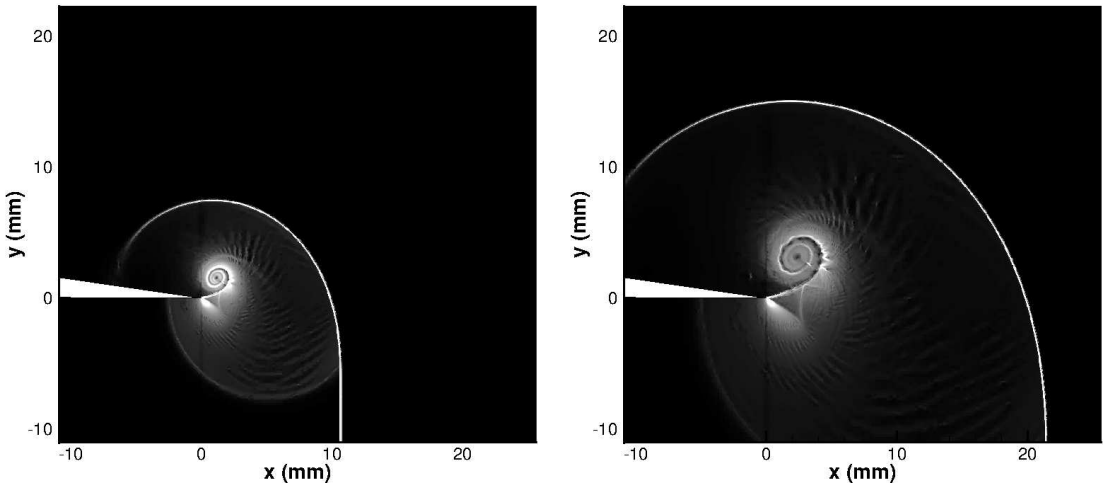

(a) 20 μs

(b) 40 μs

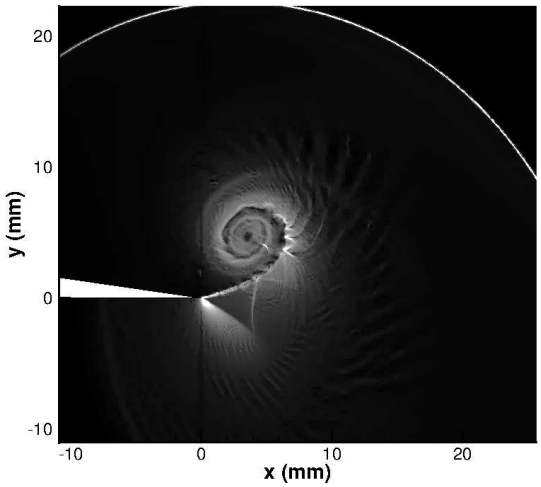

(c) 60 μs

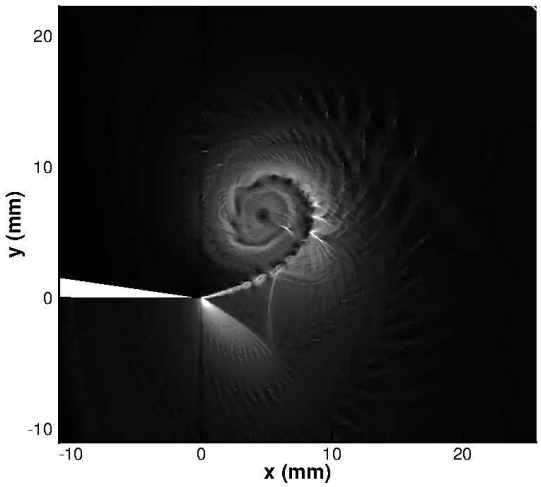

(d) 80 μs

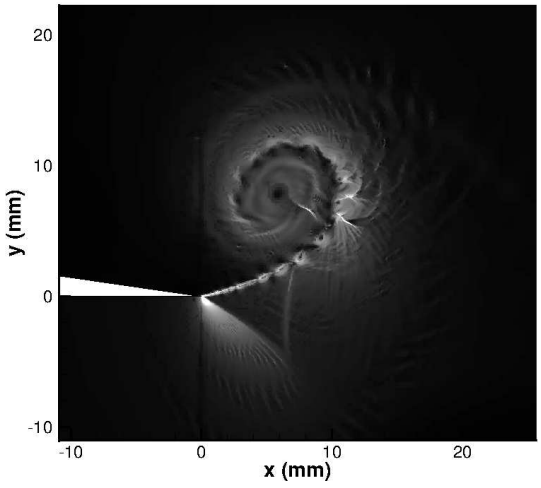

(e) 100 μs

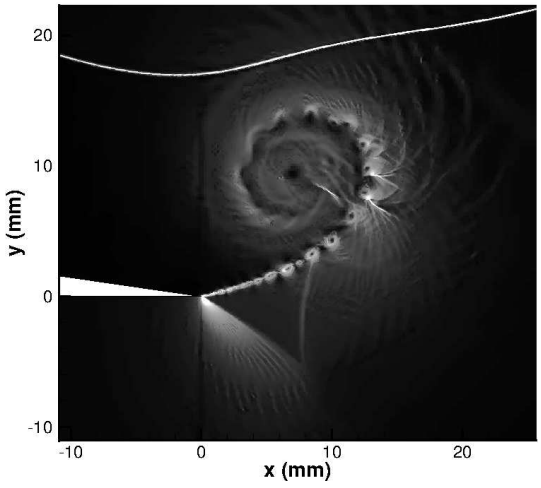

(f) 120 μs

Figure 5.16: Close-up numerical schlieren of $M_i = 1.55$ shock diffraction process around a sharp geometry

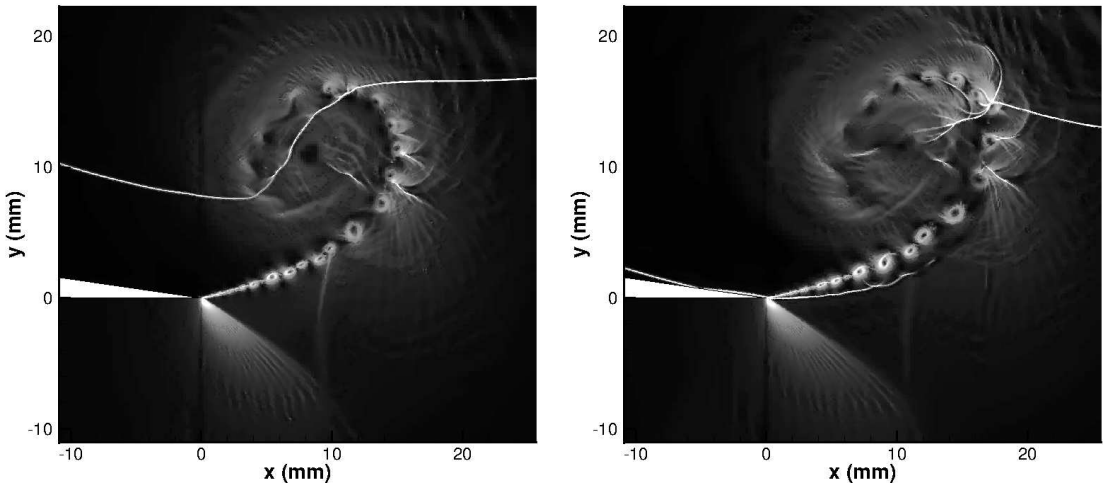

(g) 140 μs (h) 160 μs

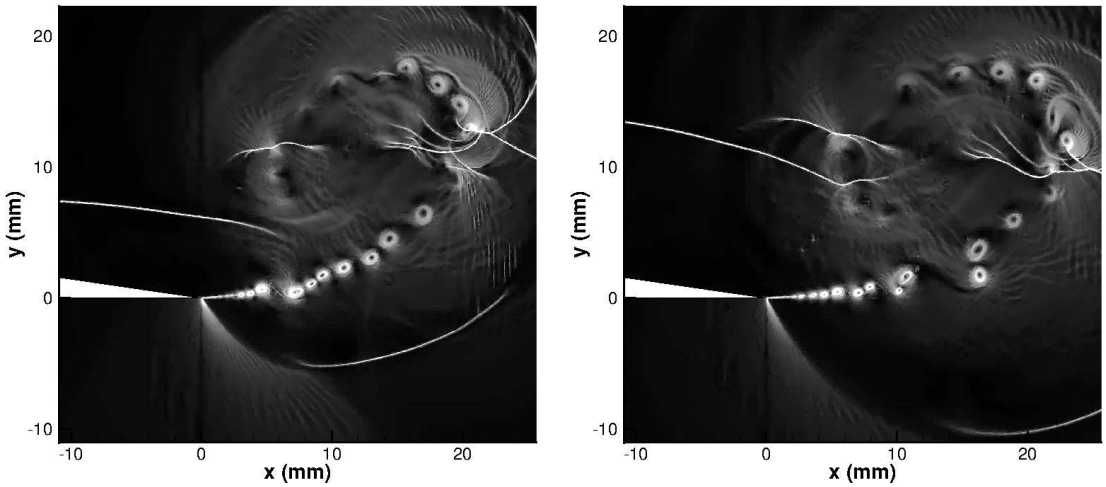

(i) 180 μs (j) 200 μs

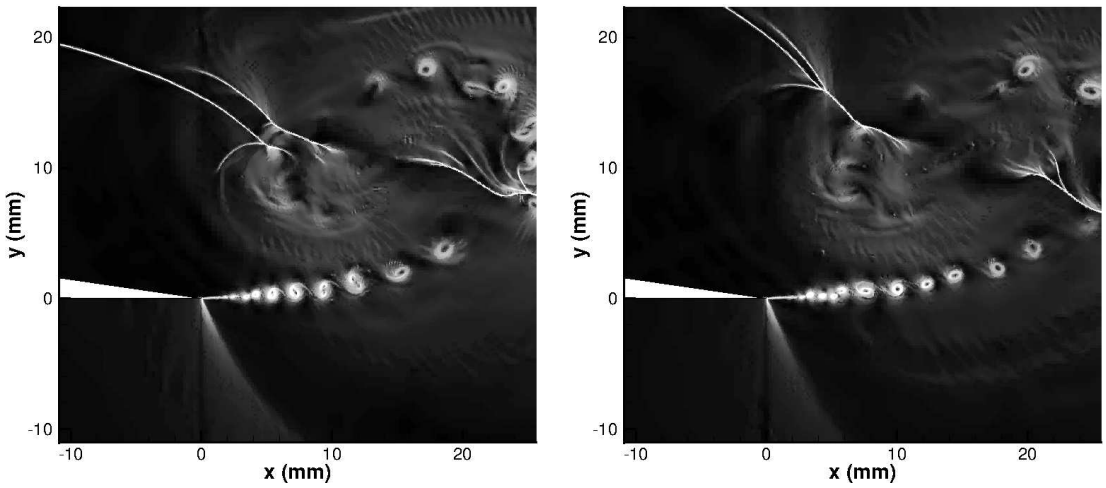

(k) 220 μs (l) 240 μs

Figure 5.16: Close-up numerical schlieren of $M_i = 1.55$ shock diffraction process around a sharp geometry

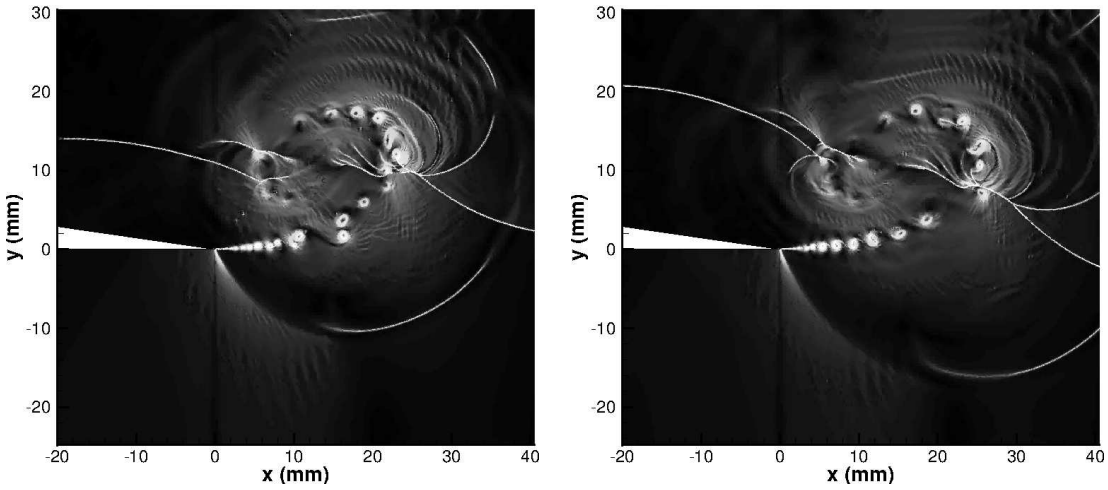

(a) 200 μs

(b) 220 μs

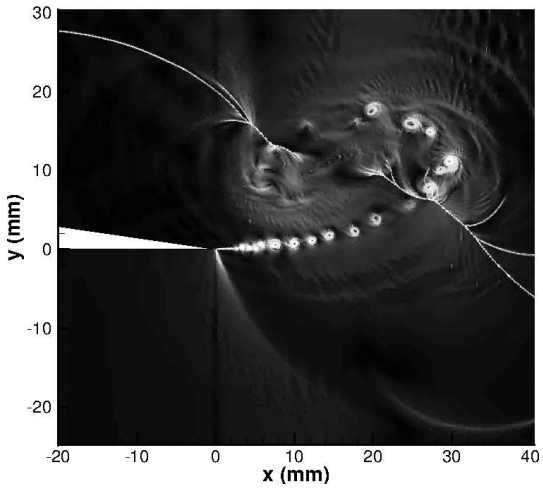

(c) 240 μs

Figure 5.17: Full-field numerical schlieren of $M_i = 1.55$ shock diffraction process around a sharp geometry

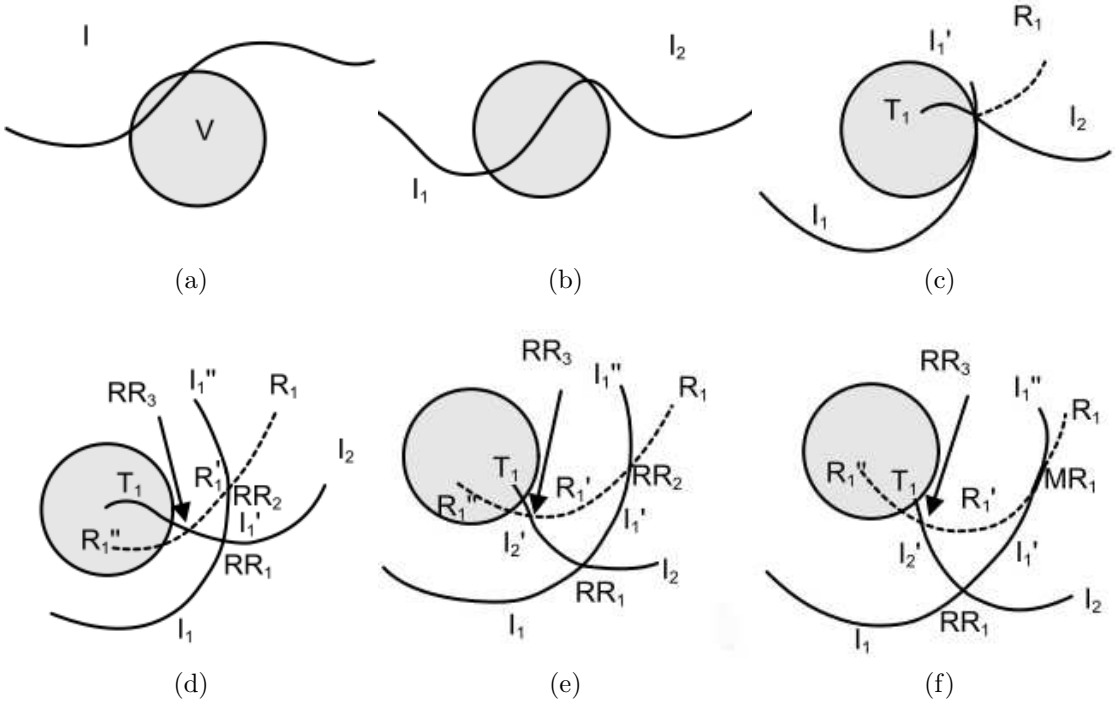

Figure 5.18: Schematic showing the different stages of shock-vortex interaction

has been captured in detail. The most interesting interactions are found on the right-hand side of the vortex, as the oncoming flow in this region opposes the shock. The interaction is difficult to see at $M_i = 1.28$, as the waves involved are very weak. However, as M_i is increased, the diffracted shock wave increases in strength and is much more visible. The wave pattern discussed below is very similar for all incident shock Mach numbers tested; however, the exact position of the reflection type transition may differ slightly due to different wave propagation speeds and vortex strengths. After the diffracted shock reflects off the upper wall, it interacts with the main vortex (Fig.5.18a). At this point the shock can be considered one wave, I, because it is relatively undistorted. The shock wave is then split up into two different shock waves, I_1 and I_2, because one half of the shock is accelerated by the vortex and one half is decelerated (Fig.5.18b). The wave I_2 is still connected to the vortex centre by a transmitted wave, T_1. A reflected wave, R_1, is also formed at this stage (Fig.5.18c). At this point there is a slight difference between the $M_i = 1.28$ case and the stronger waves. For the weaker incident shock strengths, there does not appear to be any shock waves transmitted inside the shear layer - only weak compression waves that can be seen in Fig.5.3k, despite the same wave structure propagating outside.

The incident wave I_1 now propagates outside the vortex and forms a regular reflection, RR_1, with the wave I_2. The waves I_1 and I_1' continue to propagate radially from the vortex core, creating several more reflections. A regular reflection, RR_2, is formed between waves R_1, R_1', I_1', and I_1''. Another regular reflection, RR_3, is formed between R_1', R_1'', I_2' and T_1 (Fig.5.18d). The transition between Fig.5.18d and Fig.5.18e is purely that the wave system has propagated further downstream and the distance between each reflection has increased.

In Fig.5.18f, RR_2 has matured into a Mach reflection, MR_1. This can be seen for all Mach numbers. The $M_i = 1.28$ case has the weakest waves and so is the most difficult to see, but the Mach reflection is faintly visible in Figs.5.2j to 5.2l. The $M_i = 1.46$ case shows a clear transition from regular to Mach reflection between Figs.5.9c & 5.9d. The final transition is from regular to Mach reflection for RR_3 between 180 and 200 μs in Figs.5.14i & 5.14j. The Mach reflection MR_3, formed from RR_3, appears to be the strongest shock wave formed during the shock vortex interaction, as it shows strong dark regions in the schlieren results for all three Mach numbers.

The regular reflection RR_1 transitions to a Mach reflection more quickly at higher Mach numbers, with the waves in the $M_i = 1.28$ case being so weak that the flow more closely resembles a von Neumann reflection. The other two cases show transition to a Mach reflection at approximately 200 μs. From the schlieren results, these Mach reflections appear to be very strong (Fig.5.9d & 5.14j).

5.1.2 Round Geometry

This section looks at the shock wave profiles and the interactions of a moving normal shock wave with a rounded geometry.

5.1.2.1 Mi = 1.28 Experimental Results

Fig.5.19 shows the full-field diffraction process of a $M_i = 1.28$ shock wave diffracting around a rounded corner. The shock wave profile is slightly different from previous cases, as the strength of the diffracted shock wave appears to diminish at a faster rate. Figs. 5.19a & 5.19b suggest that the shock travelling upstream above the splitter is extremely weak, as it is barely visible. It is difficult to see any interactions in the complex region at early times (less than 100 μs). The complex structures do not expand as quickly as was seen for the sharp geometry, and as such it is difficult to explain the flow from the full-field images. There is an interaction occurring below the apex of the splitter from as early as 20 μs, but it is not until 100 μs that we can begin to understand what is happening. A shear layer is formed due to the boundary layer separating on the round corner, which rolls up into a very tight vortex. A structure can be seen above the splitter, and there are some changes in light intensity (and therefore density) below the shear layer.

The wave structures below the shear layer grow into a visible lambda shock structure in Fig.5.19f, indicating that the reflected expansion wave is strong enough to induce a region of supersonic flow, even with such a low incident shock Mach number. Initially the lambda structure, consisting of the terminating shock and the last running expansion wave, is sharply defined with the appearance of distinct waves; however, later images Fig.5.20e and more evident in Fig.5.20g appear to show that the structure is made up of several smaller, finer waves. This indicates unsteadiness in the wave positions and that at this instant in time they are not planar; rather, they are disturbed along the span of the shock tube. This is likely to be due to the incoming boundary layer transitioning to turbulence, creating random fluctuations which will propagate down the shear layer and along any associated wave structures; however, as the boundary layer is not visible it is not possible to make firm conclusions based on these results alone.

Using the temperature rise given by Equation 2.13, the kinematic viscosity can be estimated. We can replace the length scale in the standard equation for Reynolds number with the induced velocity behind the shock wave and a time scale. This allows us to estimate the boundary layer characteristics at a certain time after the shock has passed. Based on a transition Reynolds number of $Re \approx 10^5$, the time for transition to a turbulent boundary layer is $t_{tr} = 100$ μs, agreeing well with the experimental evidence. This estimate is only used as a very rough guide, as there are no accounts taken for the roughness of the pipe, the heat transfer, or any effects due to the reflected expansion wave, and as a result should only be interpreted as an order of magnitude estimate.

By Fig.5.19h, a second lambda structure can be seen underneath the shear layer and the returning shock wave is impacting on the top surface of the splitter. The shock-vortex interaction shown in the subsequent images seems to pull the lambda structures upstream as they join with the left-hand returning shock wave.

In Figs.5.19j & 5.19k there is a faint shock wave embedded inside the vortex at approximately 325° around the vortex. The shock wave on the right hand side of the vortex has a large kink in it close to the vortex in Fig.5.19j. In subsequent images this kink splits off into a shock in its own right.

There is almost no information to be gained about the structure of the shear layer from Fig.5.19.

The close-up shadowgraph images afford us much more information about the structure of the complex region near the splitter apex. Fig.5.20b shows strong density gradients attached to the curved wall, indicating an unsteady boundary layer separation process. Later, in Fig.5.20c, we can see the early signs of a vortex forming (the bright circular region) along with the early formation of a lambda structure. There is also a structure propagating along the surface above the vortex. It is difficult to quantitatively predict the location of the boundary layer separation, as the radius of the corner is very small and the resolution of the optical system is limited; however, it can be seen that the separation point travels back upstream almost to the beginning of curvature. Fig.5.20d shows this much more clearly as the flow begins to develop. There are now two lambda structures developing (the second one is significantly smaller than the first) and the structure above the vortex has grown in size. By Fig, 5.20e the structure above the vortex has propagated out of sight, but we can begin to see the formation of some shock waves attached to the wall and reaching out to the vortex.

Moving forward in time to just before the returning shock wave impacts, in Fig.5.20g, the shock wave structure between the vortex and wall bears some resemblance to the lambda structure underneath the shear layer. A schematic of the flow is given in Fig.5.21, where the shaded regions represent supersonic flow. The main vortex induces flow, this is the same regardless of the geometry of the splitter, and the shear layer can be considered a solid boundary which the induced flow may not cross. Due to the proximity and curvature of the wall, and the shear layer curving closely to the wall, these two features act as a convergent-divergent nozzle, accelerating the flow to supersonic speeds in this region. This supersonic speed and the associated pressure drop must be balanced with the pressure on the other side of the main shear layer, leading to the creation of an internal normal shock wave which terminates the supersonic region (**IT**). This induced flow, like the flow induced by the incident shock wave, cannot navigate such a corner, and as such will also lead to the creation of a shear layer on the top surface of the splitter (**ISL**).

The returning shock wave impacts on the splitter in Fig.5.20h and the shock-vortex interaction proceeds as was shown in Fig.5.19. This kink in the shock on the right-hand side of the vortex is caused by the oncoming flow parameters being different on either side of the shear layer.

In the final image of Fig.5.20 we can see that the strongest remaining shock wave appears to be the internal terminating shock. The position and orientation of this shock wave have barely changed, implying that the shock vortex interaction is not very strong at this Mach number.

As before, it is difficult to ascertain any information about the structure of the shear layer formed. Figs.5.20g to 5.20i show turbulent structures in the shear layer and the vortex core; however, there are no signs of organised structures.

Due to the strength of the initial interaction, the schlieren images showing the early diffraction process are of limited use, as the system is completely overranged

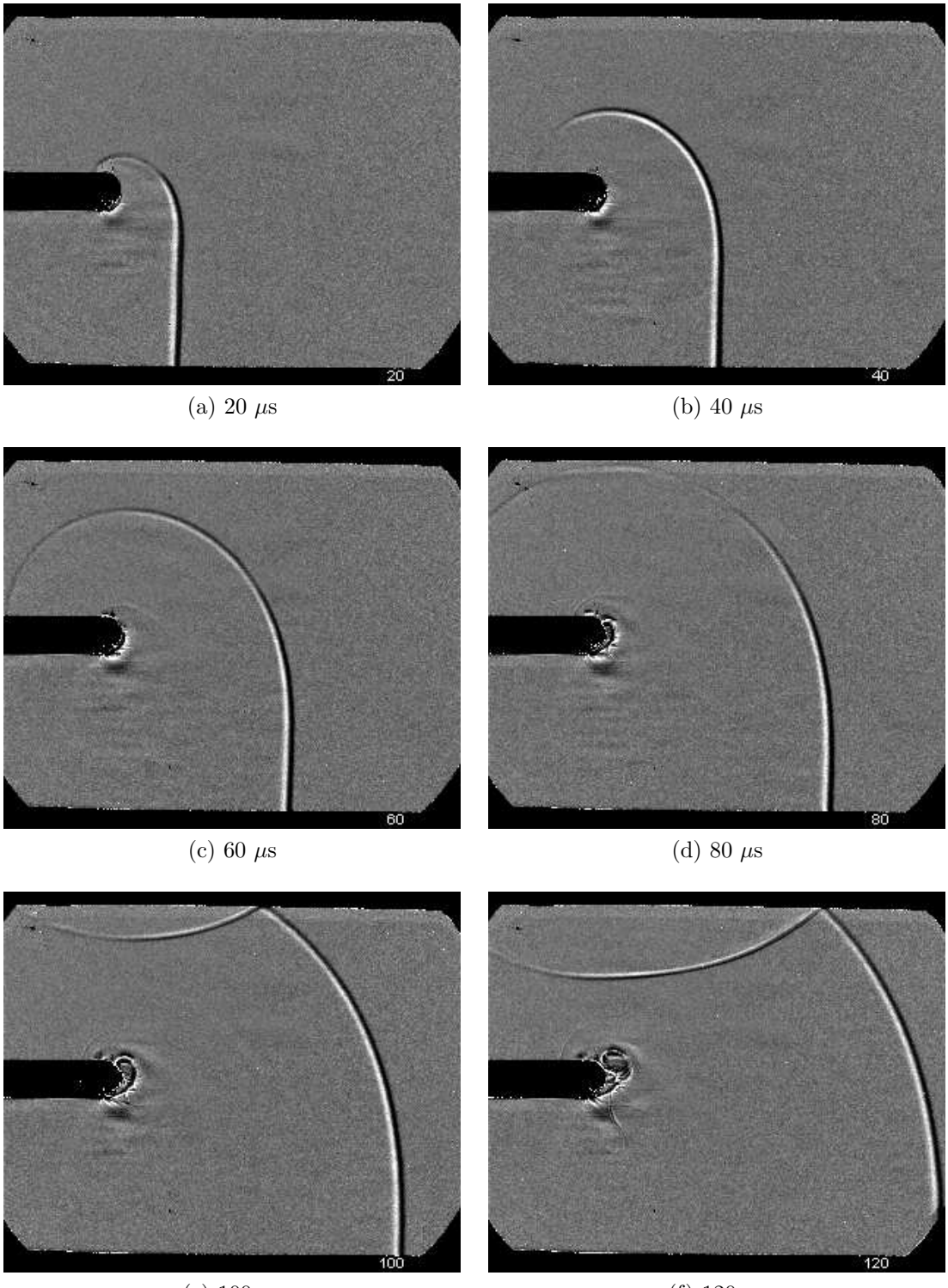

(a) 20 μs

(b) 40 μs

(c) 60 μs

(d) 80 μs

(e) 100 μs

(f) 120 μs

Figure 5.19: Full-field shadowgraph of $M_i = 1.28$ shock diffraction process around a round geometry

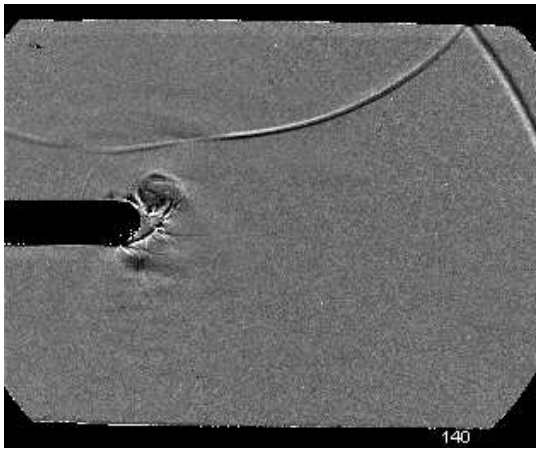

(g) 140 μs

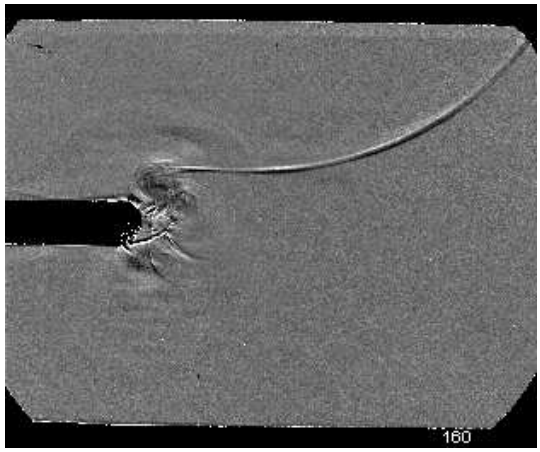

(h) 160 μs

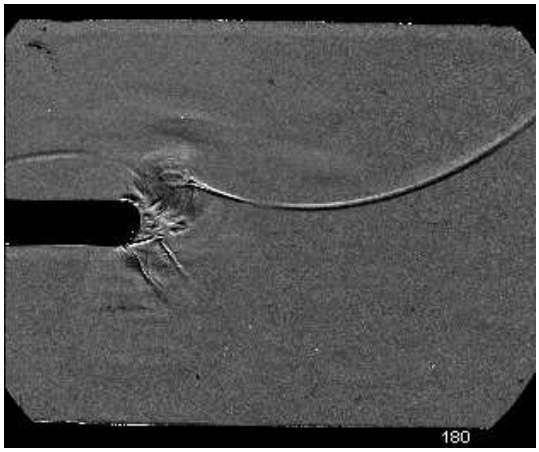

(i) 180 μs

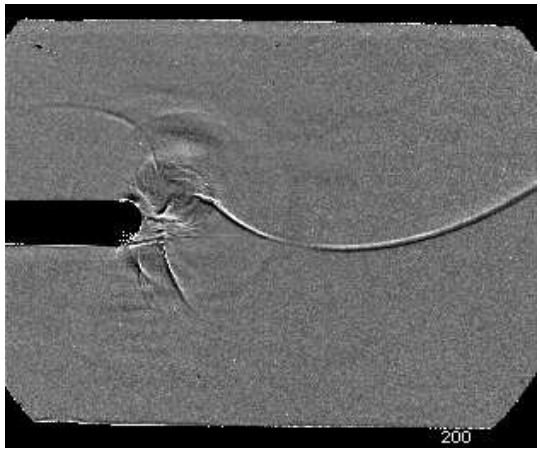

(j) 200 μs

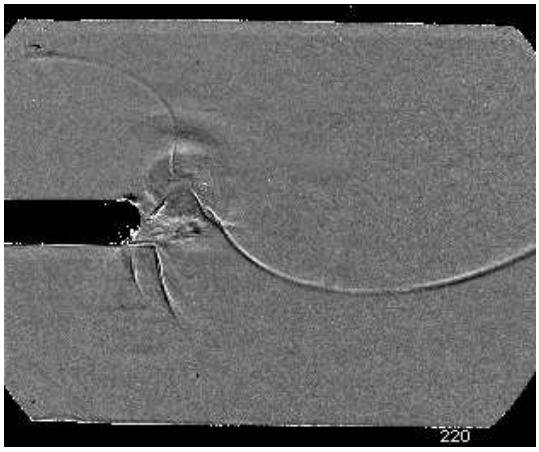

(k) 220 μs

(l) 240 μs

Figure 5.19: Full-field shadowgraph of $M_i = 1.28$ shock diffraction process around a round geometry

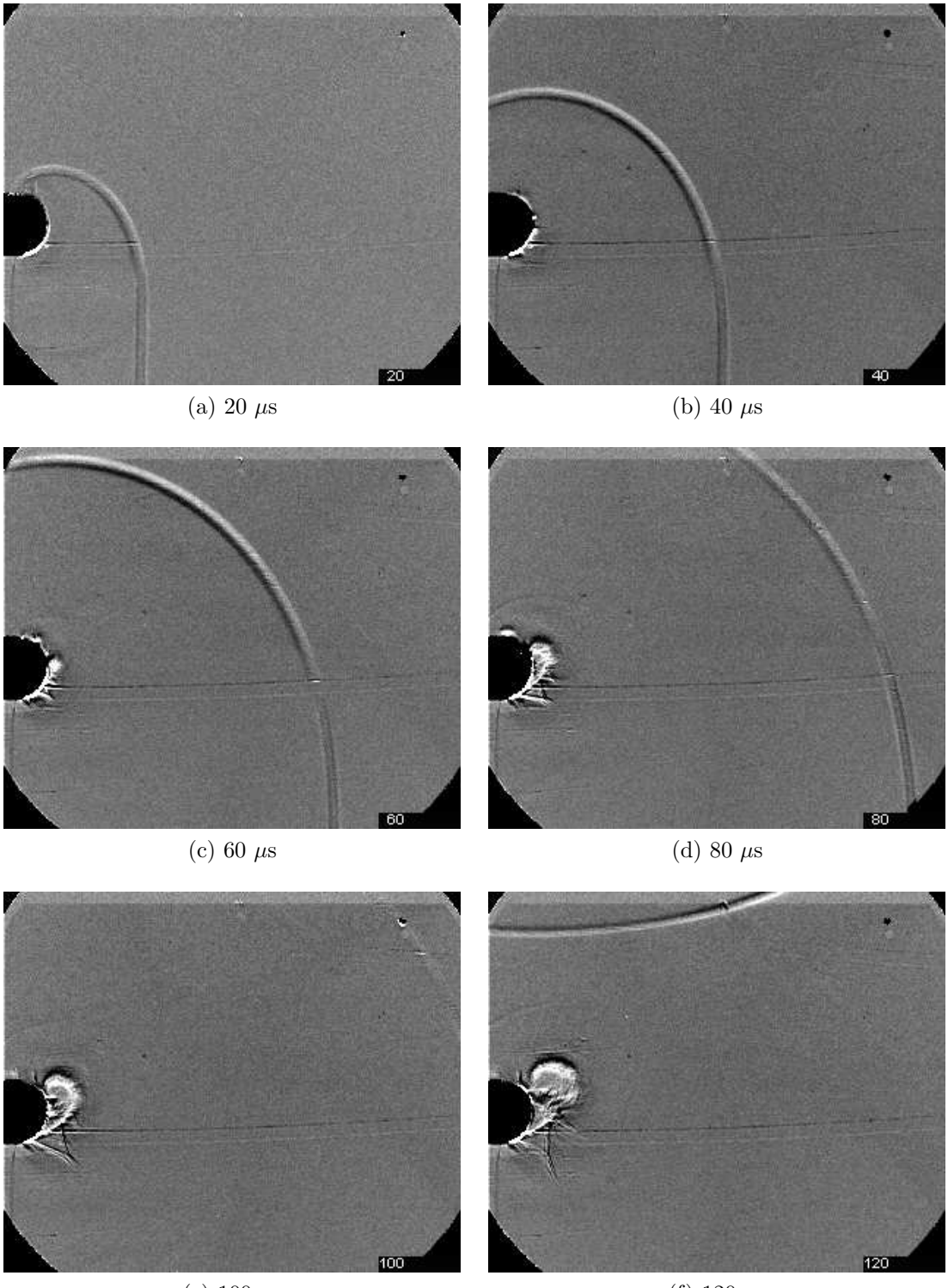

(a) 20 μs (b) 40 μs

(c) 60 μs (d) 80 μs

(e) 100 μs (f) 120 μs

Figure 5.20: Close-up shadowgraph of $M_i = 1.28$ shock diffraction process around a round geometry

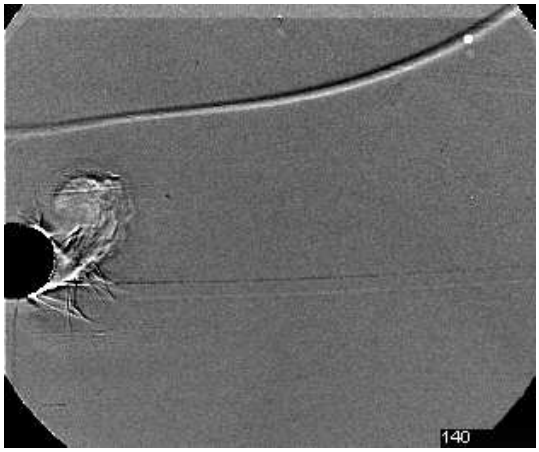

(g) 140 μs

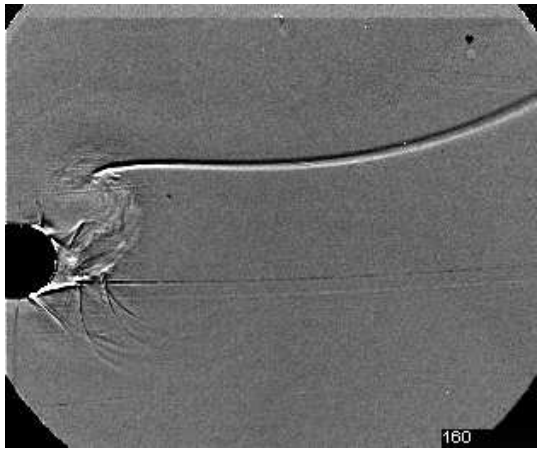

(h) 160 μs

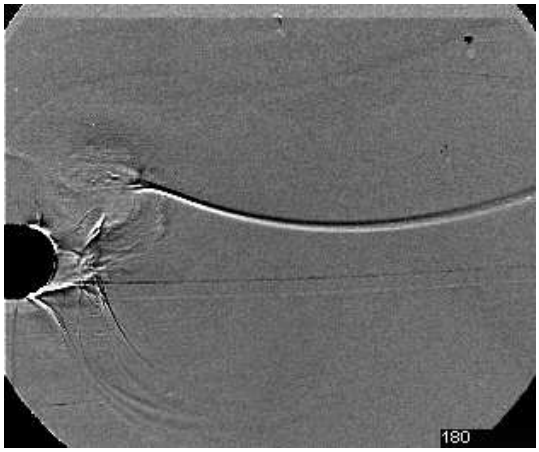

(i) 180 μs

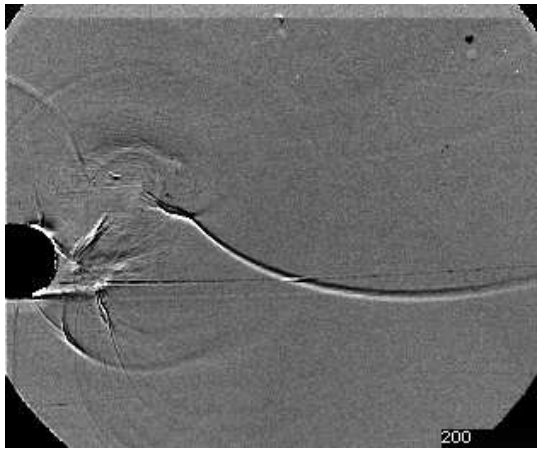

(j) 200 μs

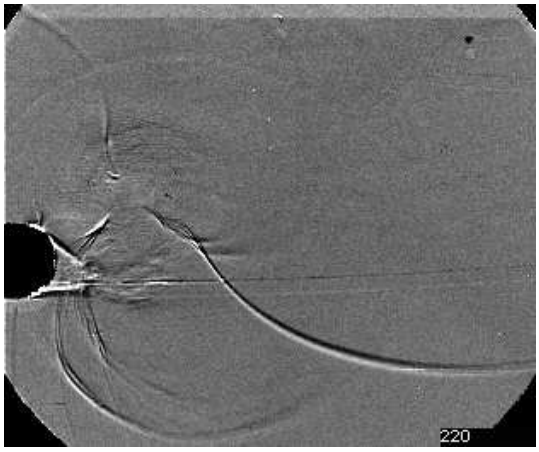

(k) 220 μs

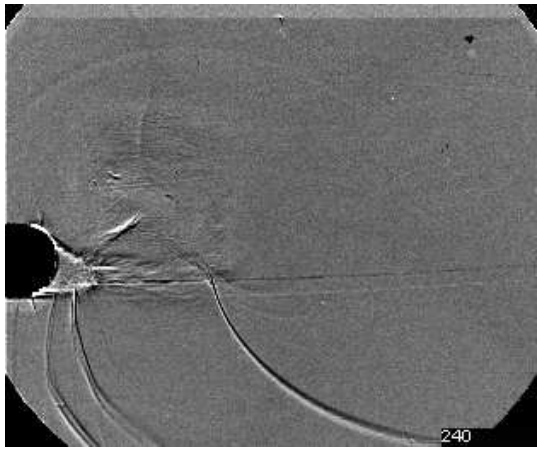

(l) 240 μs

Figure 5.20: Close-up shadowgraph of $M_i = 1.28$ shock diffraction process around a round geometry

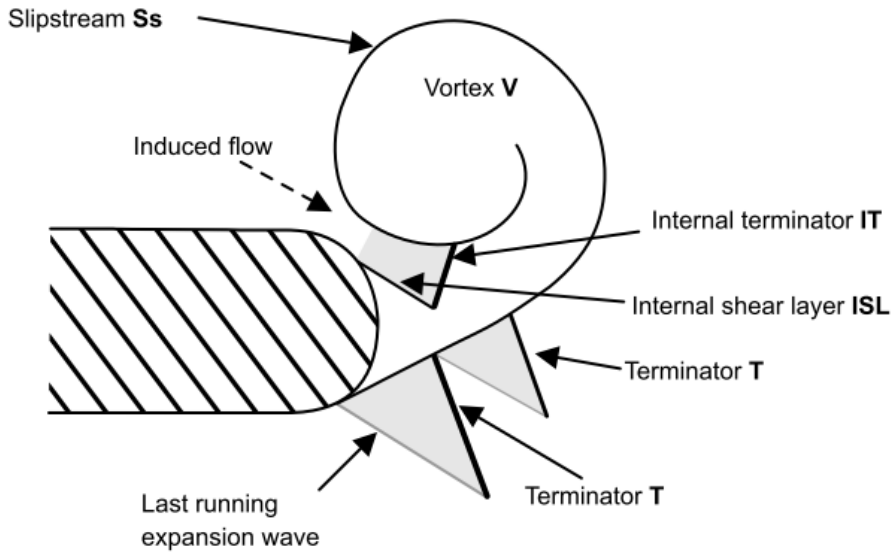

Figure 5.21: Schematic of complex region behind a $M_i = 1.28$ shock diffracting around a rounded corner

close to the wall (Fig.5.22a). Fig.5.22b shows the reflected expansion wave travelling away from the first point of area change. Later images, in particular Fig.5.22h, show a discontinuous change in intensity at approximately 300° around the vortex, corresponding to the internal terminating shock mentioned previously. Also in this figure, the internal shear layer shows a strong change in density across it.

The schlieren images do have the advantage that they show the outline of the vortex much more clearly than the shadowgraph images. From Fig.5.22l we can determine that the shock-vortex interaction is very weak for this case, as the main vortex is almost unchanged in shape and retains the circular profile developed by Fig.5.22g. As with the shadowgraph results, the schlieren setup has shown no signs of organised structures on the shear layer despite the extra sensitivity available.

5.1.2.2 Mi = 1.28 Numerical Results

The numerical results of the diffraction process capture some of the large features present but are not as reliable as the results were for the sharp geometry. Fig.5.23c agrees well with the experimental shadowgraph results at 60 μs, in that the boundary layer separation process is just taking place. The location of the separation point is well predicted, as is its movement back upstream in the subsequent figures; however, the lambda structures are not formed as early as the experimental results. The next image shows the formation of the lambda structures and a shed vortex above the main one, presumably a function of the stagnation point on the curved wall caused by the induced flow from the vortex. Between the shear layer and the wall there are no fewer than five discrete vortices, which are not seen in the experimental results. The shape of the main vortex is slightly different between the experimental and numerical results. Fig.5.23e shows the main vortex as elongated in the vertical direction, whereas in the corresponding experimental figure the vortex is more circular in profile. The lambda structures underneath the shear layer show curved tails, something which is not seen clearly in the shadowgraph results and

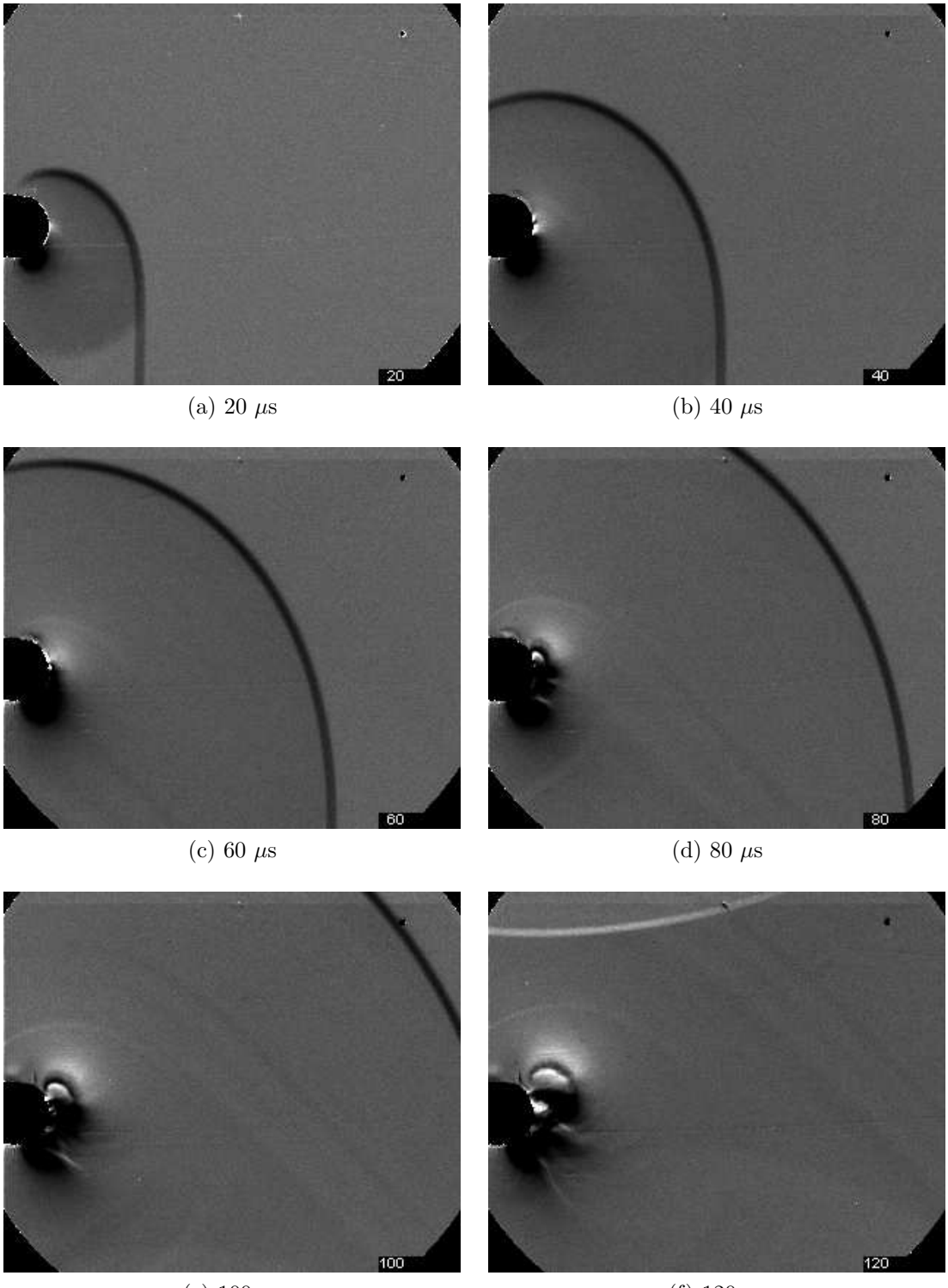

(a) 20 μs

(b) 40 μs

(c) 60 μs

(d) 80 μs

(e) 100 μs

(f) 120 μs

Figure 5.22: Close-up schlieren of $M_i = 1.28$ shock diffraction process around a round geometry

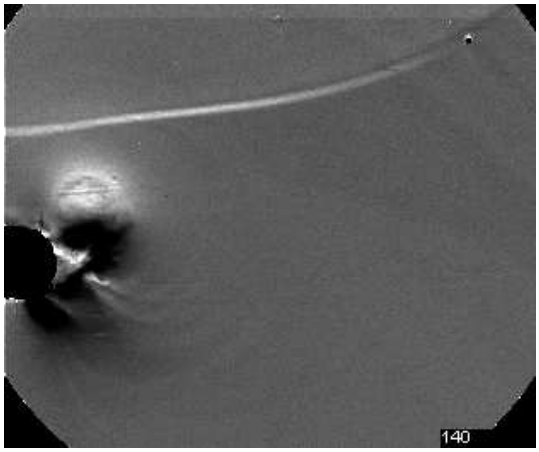

(g) 140 μs

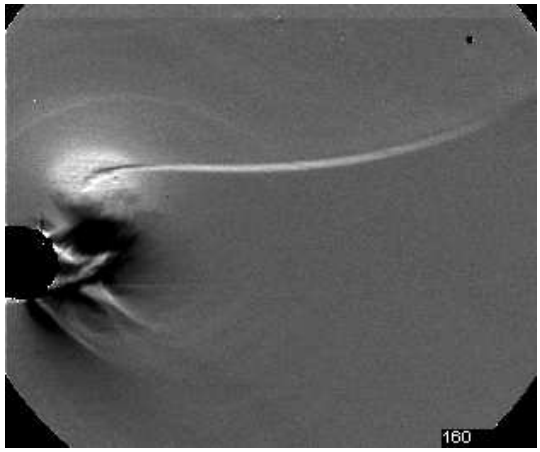

(h) 160 μs

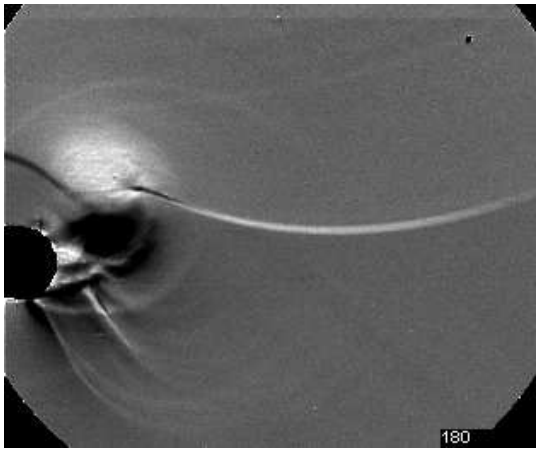

(i) 180 μs

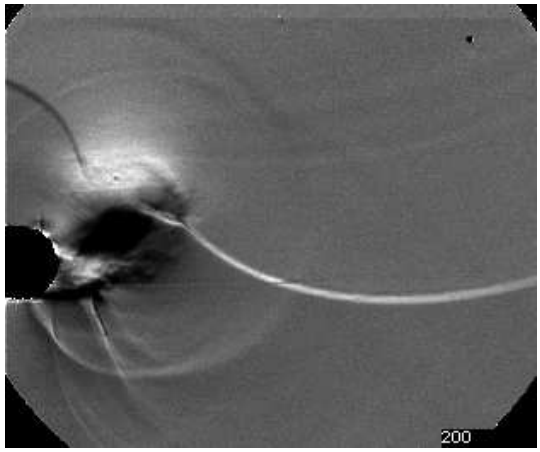

(j) 200 μs

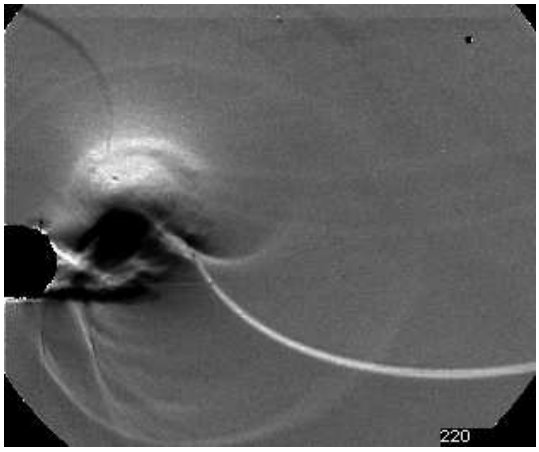

(k) 220 μs

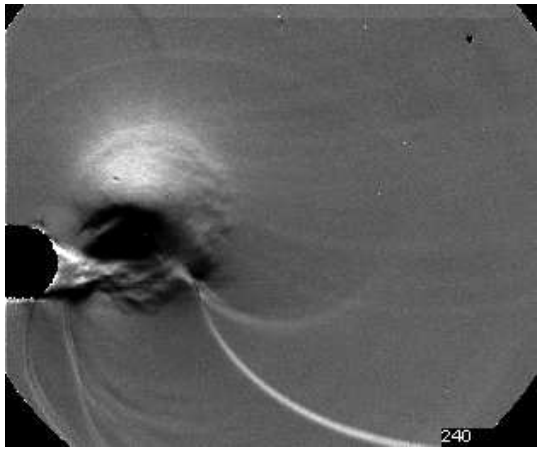

(l) 240 μs

Figure 5.22: Close-up schlieren of $M_i = 1.28$ shock diffraction process around a round geometry

only faintly seen at a later time in the schlieren results. There are two faint shock waves on top of the vortex which are not seen in any experimental results (Figs.5.23f & 5.23g).

The internal shock wave structure of the internal shear layer appears to be significantly more complex in Fig.5.23g than in the experimental results, with what appears to be a triple shock system.

The shock-vortex interaction (Fig.5.23h onwards) is more complex in the numerical results than in the experimental ones. It is not surprising from the experimental results that the shock above the vortex created in the shock vortex interaction (see Fig.5.20k) is so weak that it is not visible in the numerical results. Some of the basic wave structures are the same, such as the shock of the right-hand side of the vortex; however, the internal structure of the vortex and the shear layer vary quite drastically from the experimental results. From as early as Fig.5.23h there are discrete vortices being generated, initially outside the vortex but eventually inside from the exit of the last lambda structure.

The transition to a turbulent boundary layer, as indicated in the experimental results at approximately 100 μs, means that the assumptions of the laminar model are no longer valid, and it is not surprising to find that after this point the simulation begins to depart from reality. The numerical results from Fig.5.23h onwards display such little correlation with experimental results that any further discussion of them is not warranted.

5.1.2.3 Mi = 1.46 Experimental Results

The experimental close-up shadowgraph results for the $M_i = 1.46$ shock are shown in Fig.5.25. In these results it is easier to analyse the complex shock profile as the vortex propagation velocity is larger. Fig.5.25a shows the start of the boundary layer separation on the curved edge, with the next image showing the development of the lambda structure and the vortex. There is still a separate structure seen above the vortex but inside the contact surface. Noticeably, the contact surface is much more visible in this test. The contact surface joins the wall on the top surface of the splitter and is propagating upstream from the apex. Fig.5.26 shows a strong kink in the contact surface as it is swept up into the vortex. The lambda structure developing in Fig.5.25c is far more complex than in the previous case and is beginning to move upstream and face the oncoming flow over the subsequent images. The size of the lambda structure indicates that the strength of the expansion in this region is larger than in the previous case. The main vortex has developed a recompression shock at approximately 100° (Fig.5.25d), indicating that it is inducing large velocities. The secondary expansion region, consisting of the internal shear layer and the internal terminating shock wave, is seen in Fig.5.25e.

The initial portion of the main shear layer is curved, indicating that there is a difference in pressure from one side of it to the other. This is caused by the internal terminating shock wave. The curvature of the shear layer leads to the creation of the more complex lambda structure which resembles a distributed compression corner, creating a lambda shock after the last running expansion wave (Figs.5.25e & 5.25f). A schematic is given in Fig.5.24.

The schlieren results (Figs.5.27f & 5.27g specifically) show that after the lambda shock structure there is a large dark region which is not present in the shadowgraph

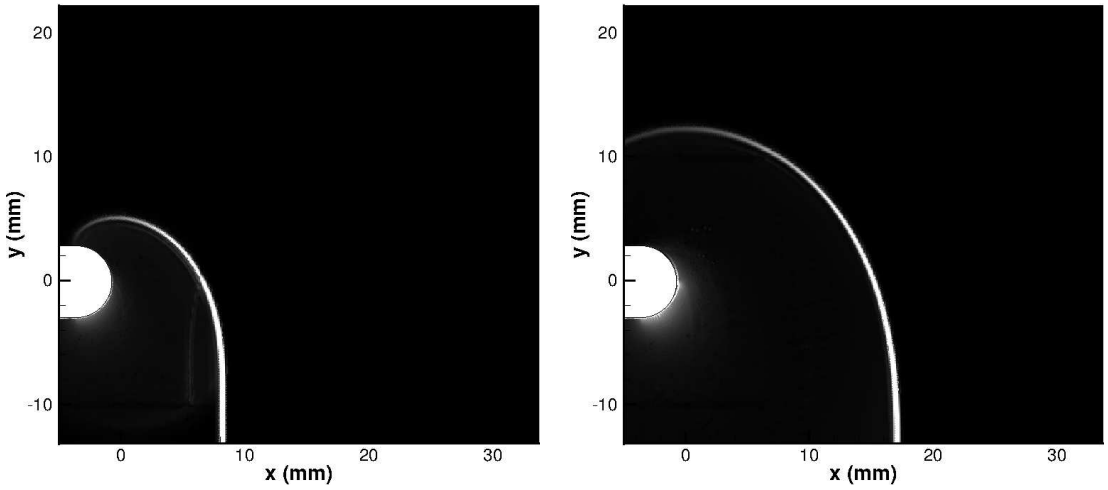

(a) 20 μs

(b) 40 μs

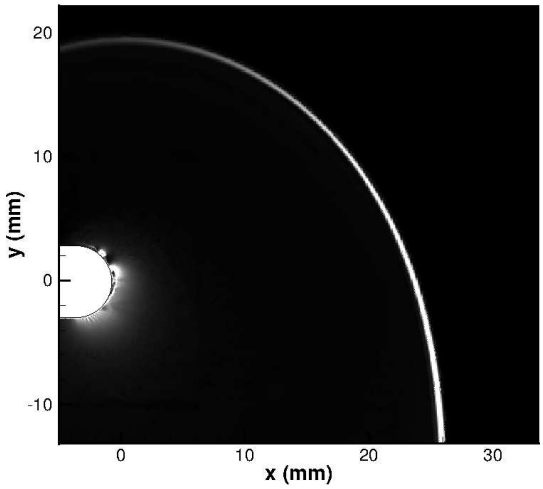

(c) 60 μs

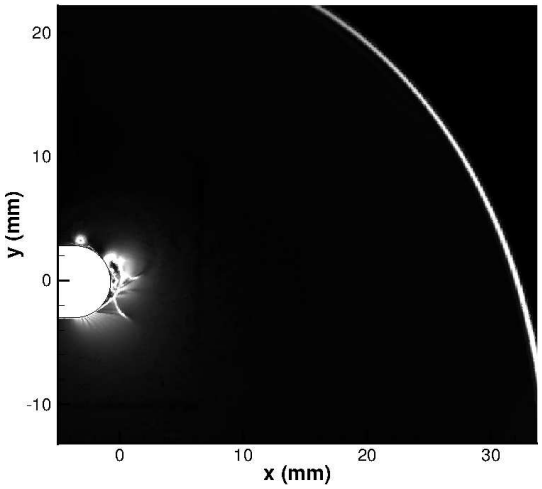

(d) 80 μs

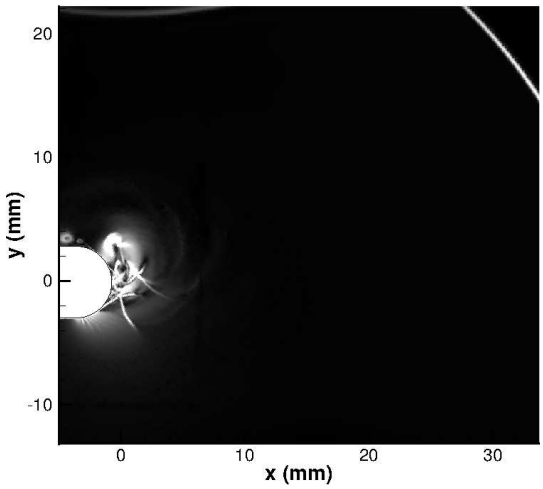

(e) 100 μs

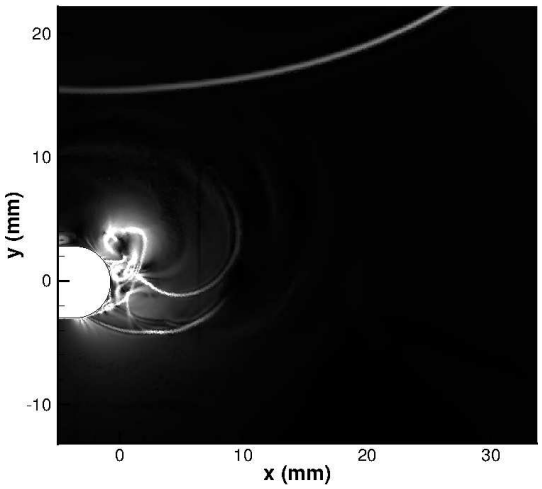

(f) 120 μs

Figure 5.23: Close-up numerical schlieren of $M_i = 1.28$ shock diffraction process around a round geometry

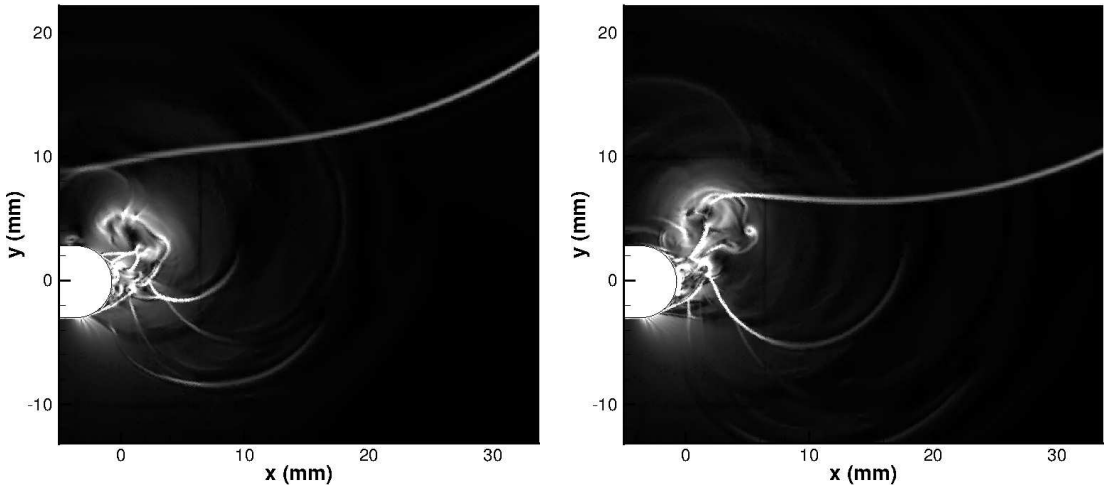

(g) 140 μs

(h) 160 μs

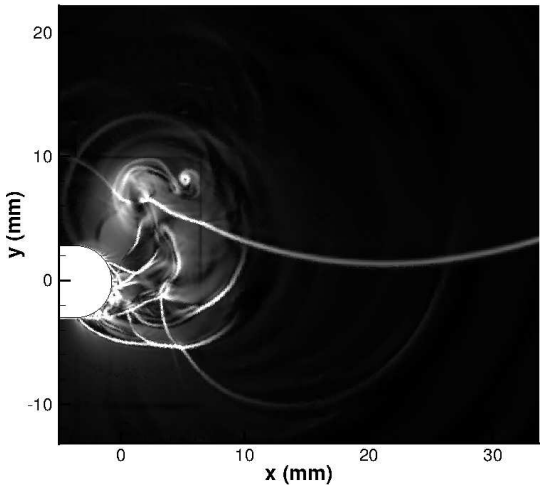

(i) 180 μs

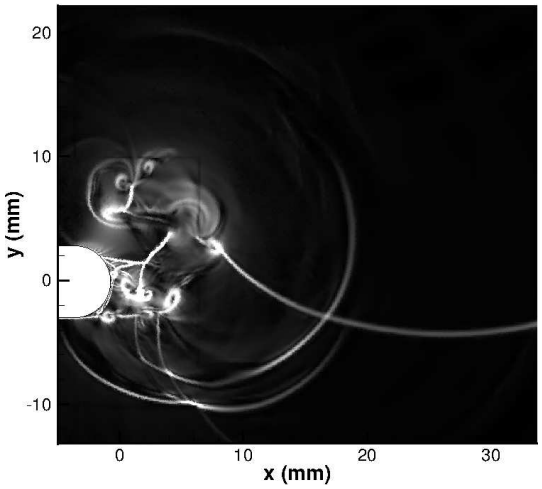

(j) 200 μs

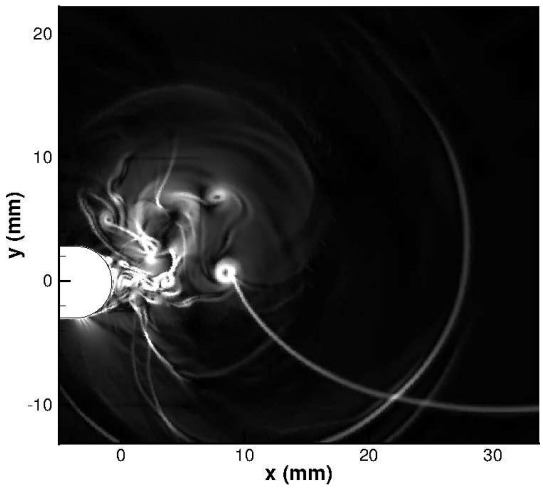

(k) 220 μs

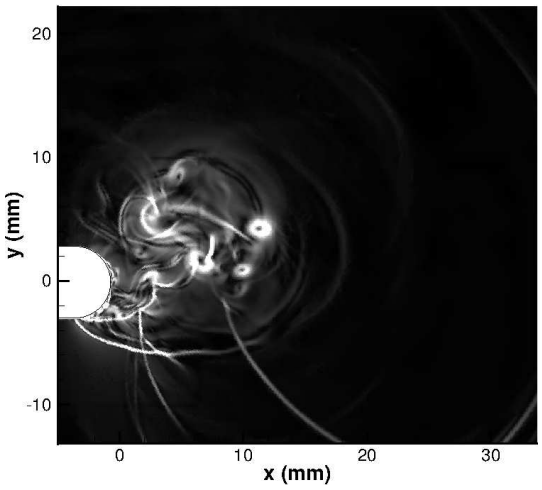

(l) 240 μs

Figure 5.23: Close-up numerical schlieren of $M_i = 1.28$ shock diffraction process around a round geometry

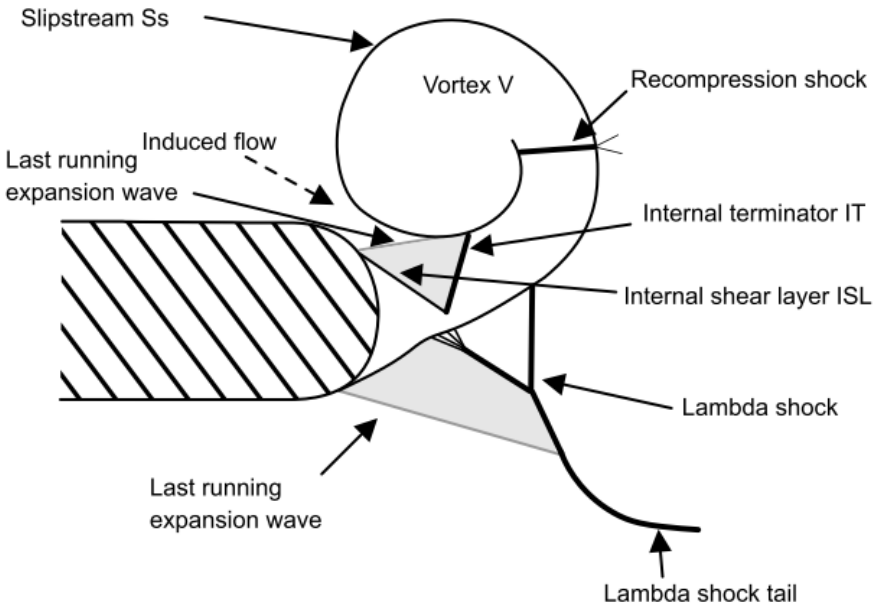

Figure 5.24: Schematic of complex region behind a $M_i = 1.46$ shock diffracting around a rounded corner

results. As there are no discontinuities visible in this region, it is assumed that this is another expansion wave and the flow is again accelerating up to a much weaker terminating shock wave at approximately 90° around the vortex.

The impact of the last running expansion wave on the tail of the lambda shock structure causes it to curve. The previous case did not show this clearly, as the tail of the lambda shock is weaker and as a result much shorter. The previous case showed that after 100 μs the lambda structure began to oscillate. In this case the long tail of the lambda shock gives a clearer indication of when this transition has begun to significantly effect the flow (Fig.5.25g); however, early signs can be seen inside the lambda structure in Fig.5.25e. The estimated time to transition, based on the simple Reynolds number criteria mentioned previously, is 50 μs.

The shear layer begins to straighten out in Fig.5.25f as the waves expand in time and the internal terminating shock is not as close to the shear layer. This means that the flow can expand again to match the pressure condition on the other side of the shear layer, as indicated in the schlieren results (Fig.5.27f shows a good example of this).

Fig.5.25g shows the beginning of the shock-vortex interaction and Fig.5.25h shows that the internal terminating shock is beginning to break down into much weaker waves. The returning shock wave has removed the pressure requirement for the internal terminating shock by compressing the flow in the secondary expansion region. The shock reflected from the splitter geometry travels around the outside of the vortex and is stronger than the one in the previous case (Fig.5.27j). Meanwhile, on the right-hand side of the vortex, the returning shock wave develops a kink, as it is slowed by the high velocity fluid close to the vortex core (Figs.5.27h & 5.25h). This kink develops into a Mach reflection with the triple point (Figs.5.27i & 5.25i) originating on the main shear layer and a curved region of the Mach stem (Figs.5.27j

& 5.25j). It is interesting to note that there appears to be a region of relatively uniform flow between the outer spiral of the shear layer and the outermost layer of the vortex in Fig.5.27l. This explains the curvature of the shock wave in both of these layers and the uniform shock region in between. This Mach stem shows a *split foot* connecting it to the vortex core, perhaps indicating the turbulent nature of the vortex core.

Although it is difficult to tell conclusively from the shadowgraph results, there does not appear to be any coherent structures on the shear layer. The schlieren results in Fig.5.27 give more information about the structure of the vortex and the shear layer. In all twelve of the images in Fig.5.27 there do not appear to be any coherent structures on the shear layer; rather, there appears to be turbulence.

5.1.2.4 Mi = 1.46 Numerical Results

Up to approximately 140 μs, the numerical simulations capture the shock wave structures well. After this point, instabilities begin to form on the shear layer as, unlike the real flow, there is no turbulent mixing acting to dissipate these structures. As the vortex propagation speed is higher in this case than in the previous one, the simulation captures the vortex shape and development well in Figs.5.28a to 5.28d. Between the main and the internal shear layers there are two trapped, counter-rotating vortices similar to those found behind a bluff body at very low Reynolds number. The secondary expansion process, including the last running wave and the internal terminating shock, are captured and are visible in Figs.5.28d & 5.28e.

The shock seen in the experimental results at approximately 100° around the vortex (Fig.5.25d) is not seen in the simulations at the same time step; however, it does eventually develop by Fig.5.28f.

From Fig.5.28g onwards, instabilities are developing on the shear layer. These instabilities do not seem to interact with the returning shock wave significantly and the wave profile is similar to the experimental results. In the numerical results (Fig.5.28i specifically), the internal terminating shock wave is not broken down into smaller compression waves as it is in the experimental results, and persists in this location. The curved Mach reflection created by the returning shock on the right-hand side of the vortex is captured. The left-hand wave does not show any particular reflection type; rather, it appears as a normal wave. There is another shock formed from the internal terminating shock which is not seen in the experiments. This indicates an overexpansion predicted by the simulation in this region.

5.1.2.5 Mi = 1.55 Experimental Results

The final case to be covered is the $M_i = 1.55$ shock. Fig.5.30 shows the development of this shock around the rounded corner. The development, although more complex than in the previous cases, is easier to visualise, due to the higher propagation velocity of the main vortex spreading the waves out. Figs.5.30a & 5.30b show very similar development to the previous case, albeit with stronger shock waves. Fig.5.30c shows a kink in the contact surface as it is drawn into the internal expansion region. The internal and external expansion regions are well formed by Fig.5.30d. The initial concave curvature of the main shear layer gives the already supersonic flow in this region space to expand more and reach a higher velocity before the direction

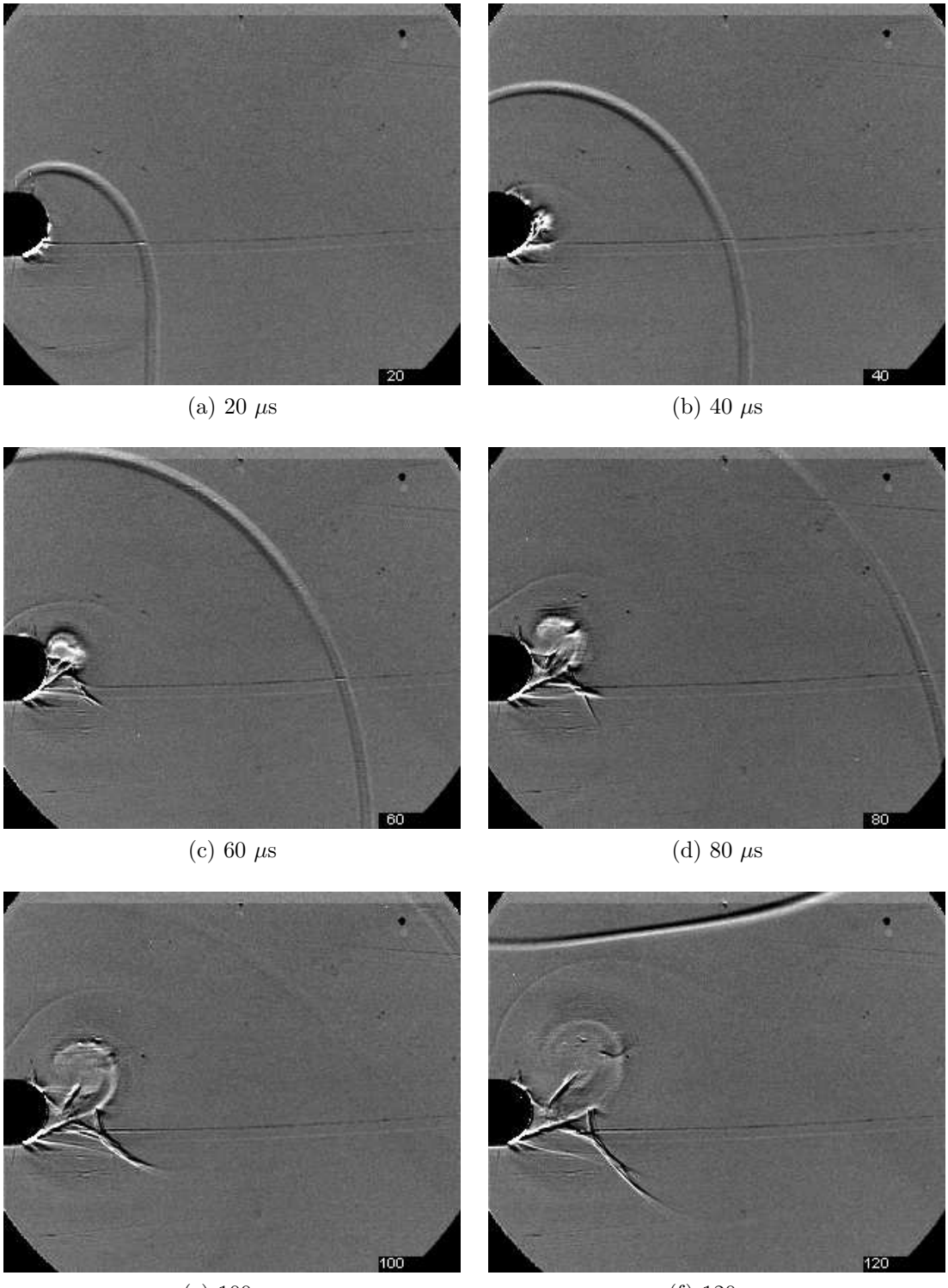

(a) 20 μs (b) 40 μs

(c) 60 μs (d) 80 μs

(e) 100 μs (f) 120 μs

Figure 5.25: Close-up shadowgraph of $M_i = 1.46$ shock diffraction process around a round geometry

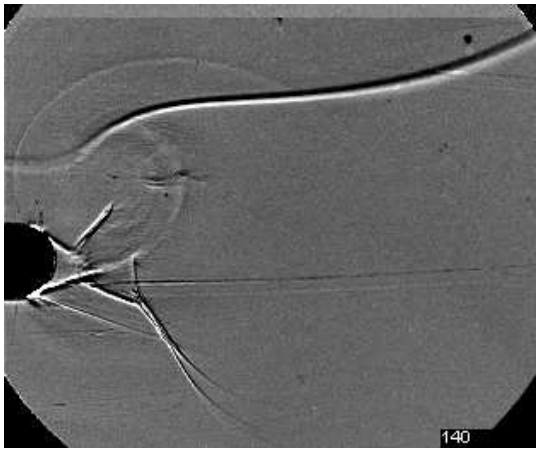

(g) 140 μs

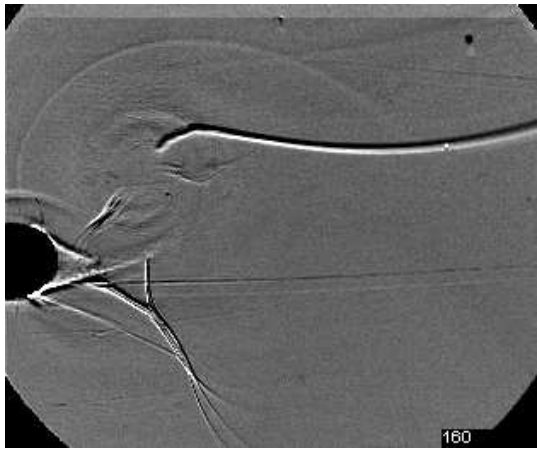

(h) 160 μs

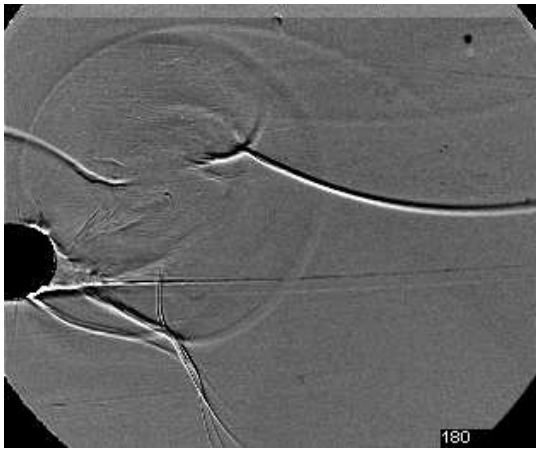

(i) 180 μs

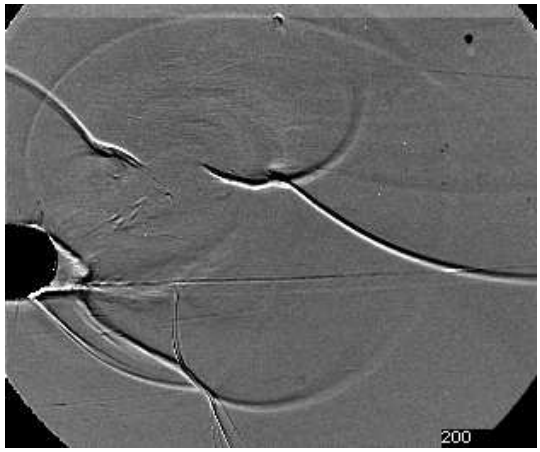

(j) 200 μs

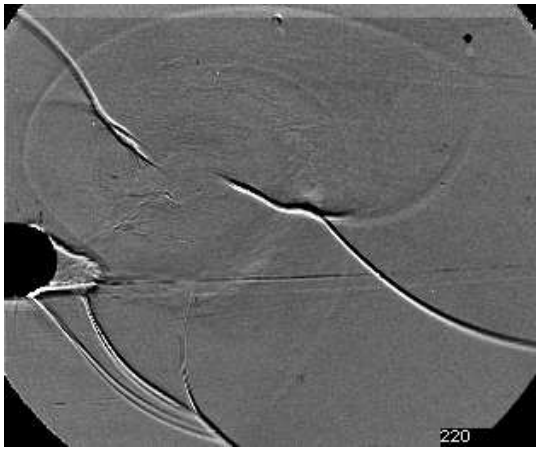

(k) 220 μs

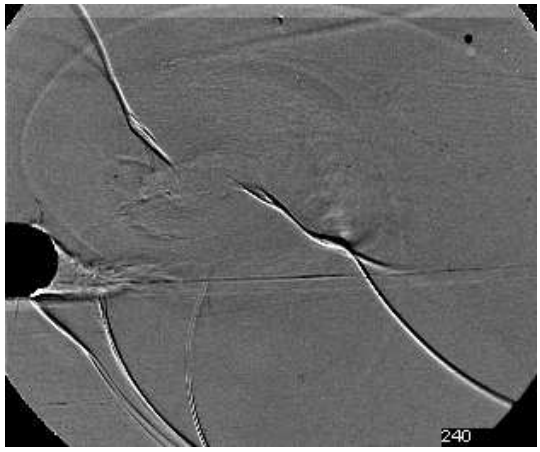

(l) 240 μs

Figure 5.25: Close-up shadowgraph of $M_i = 1.46$ shock diffraction process around a round geometry

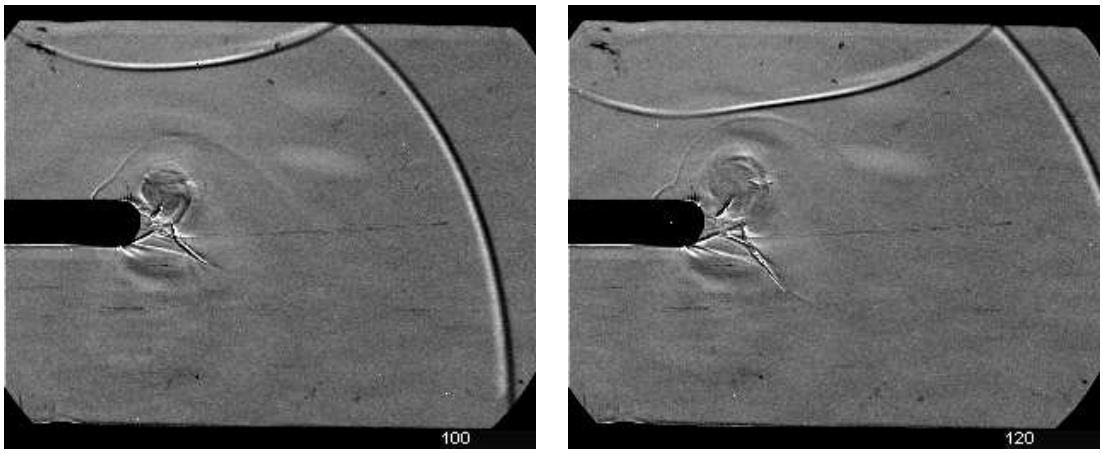

(a) 100 μs (b) 120 μs

Figure 5.26: Full-field shadowgraph of $M_i = 1.46$ shock diffraction process around a round geometry

of curvature changes. The higher speed means that stronger compression waves are required to slow the flow down. This is the reason for the formation of a much stronger lambda shock system than was seen in the previous case. The lambda shock structure underneath the shear layer appears to have generated a visible shear layer between the gas which has passed through the two oblique shocks and the normal shock (Figs.5.30d & 5.31b). This shear layer is swept up into the main vortex and acts as the outer boundary for the shock wave, recompressing the flow around 100° around the vortex (Figs.5.30d onwards). There is a second lambda system present which is only hinted at in Fig.5.30d, but, which is much clearer in a repeat experiment with a lower depth of field (Figs. 5.31b & 5.31c). A schematic of the complex region is given in Fig.5.29, showing the three strong shocks penetrating the vortex core.

After the internal terminating shock, the flow is forced through another area decrease between the initial part of the main shear layer and the curved part of it inside the vortex core. This nozzle effect leads to the flow expanding again and requiring a secondary internal shock wave to attempt to match the pressure condition on either side of the shear layer. This shock is connected to the lambda shock outside the shear layer, as at their point of contact as the pressure must be matched on both sides of the shear layer.

Boundary layer transition appears to take place around 60 μs, as the waves in the lambda shock are no longer distinct individual lines. The individual turbulent structures in the boundary layer cause oscillations in the position of the lambda shock which (due to the three-dimensional nature of turbulence) are not uniform in the spanwise direction. This manifests itself as several shock waves that appear to be overlapping on the shadowgraph images, due to the integrative nature of the technique. The estimated time for transition, based on the very simple theory mentioned previously, is 40 μs. As mentioned before, this is a rough estimate and can only be considered accurate to (at best) an order of magnitude.

The schlieren results give us more information about the structure of the shear layer and the vortex core and the shock-vortex interaction. Neither the schlieren or shadowgraph images show any coherent structures on the shear layer at any point

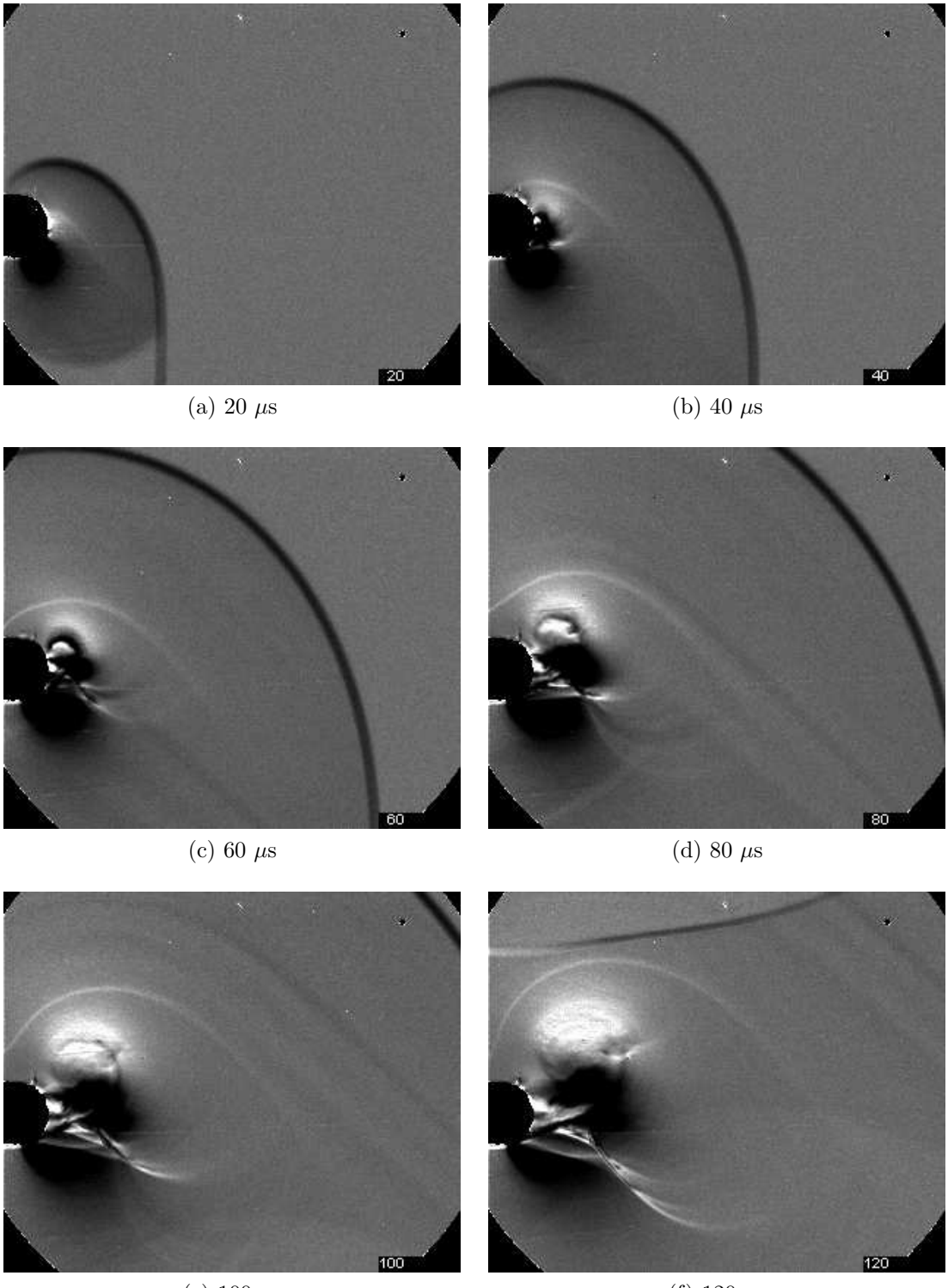

(a) 20 μs

(b) 40 μs

(c) 60 μs

(d) 80 μs

(e) 100 μs

(f) 120 μs

Figure 5.27: Close-up schlieren of $M_i = 1.46$ shock diffraction process around a round geometry

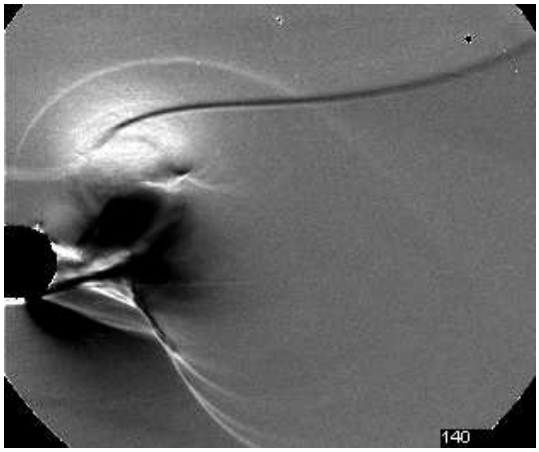

(g) 140 μs

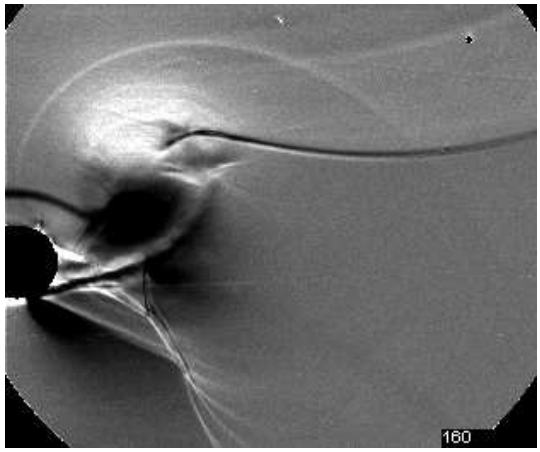

(h) 160 μs

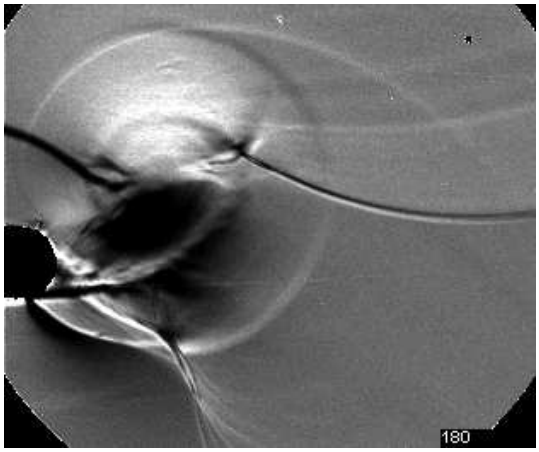

(i) 180 μs

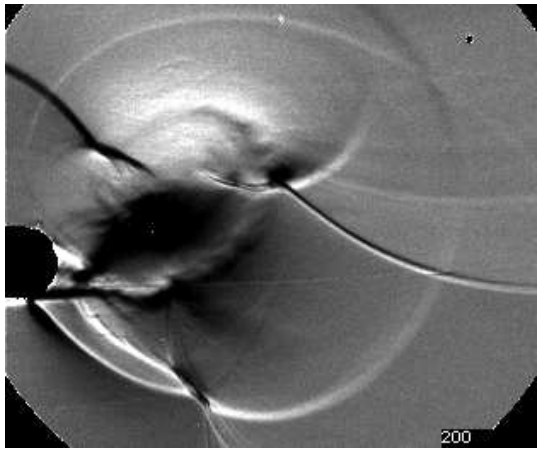

(j) 200 μs

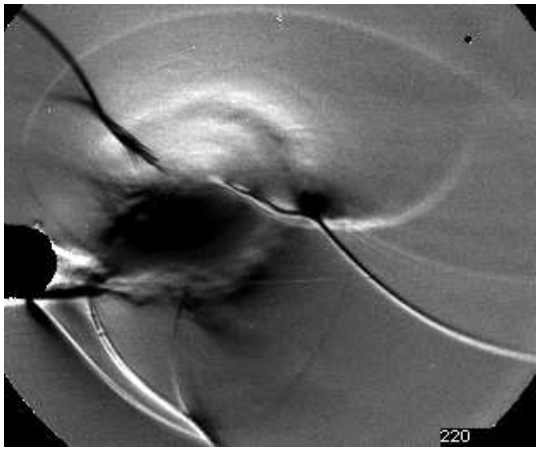

(k) 220 μs

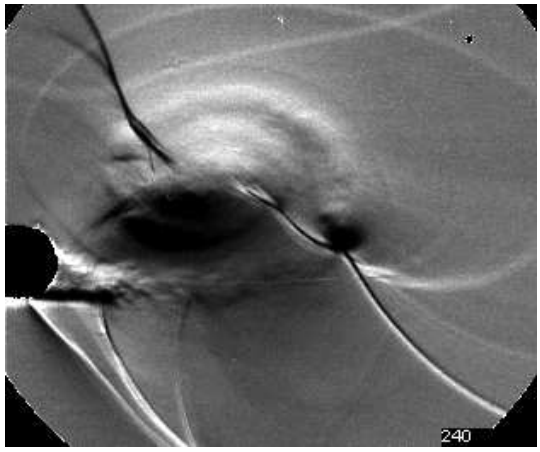

(l) 240 μs

Figure 5.27: Close-up schlieren of $M_i = 1.46$ shock diffraction process around a round geometry

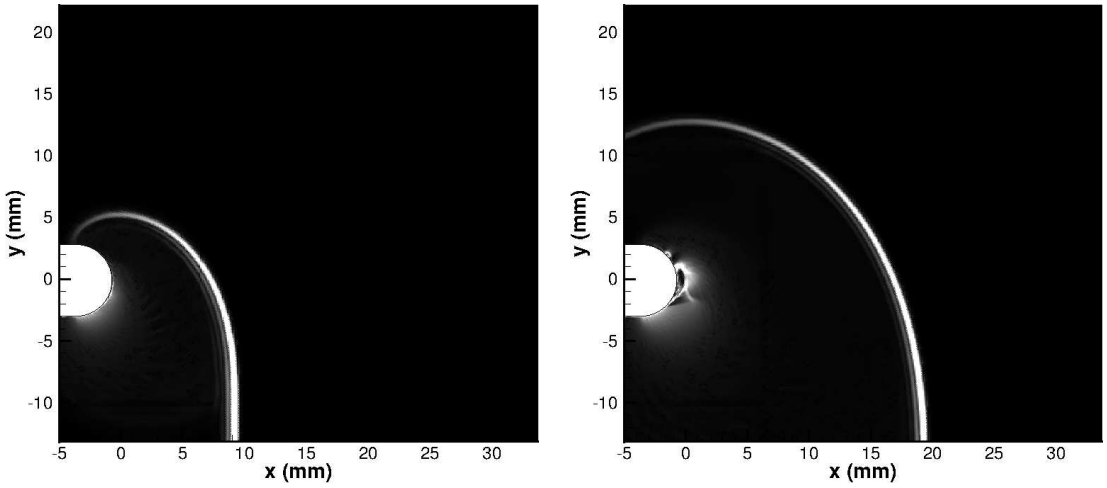

(a) 20 μs

(b) 40 μs

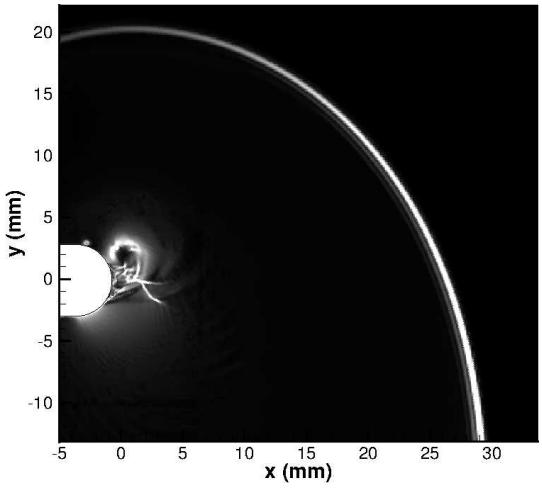

(c) 60 μs

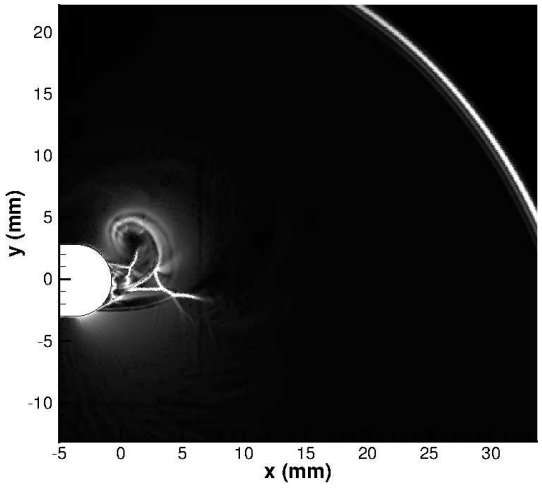

(d) 80 μs

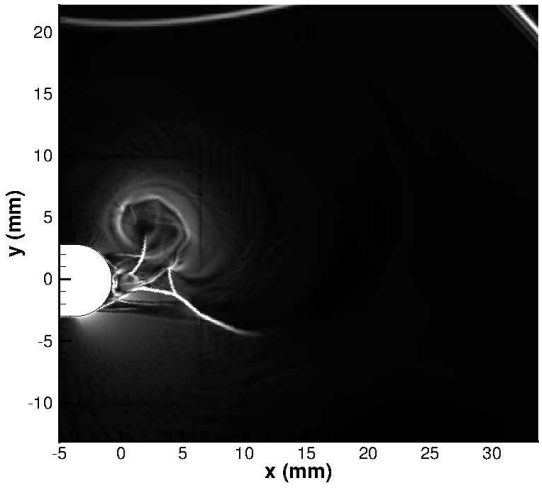

(e) 100 μs

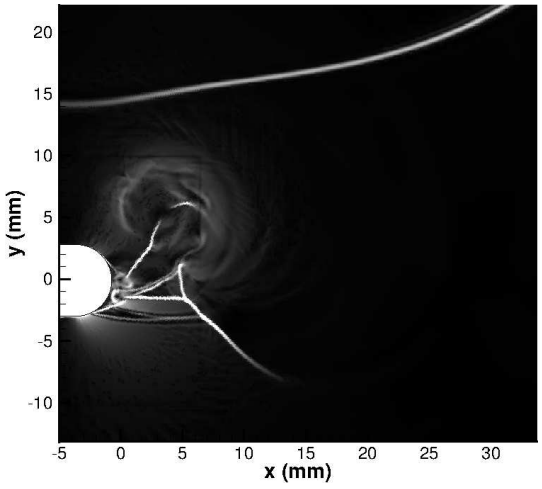

(f) 120 μs

Figure 5.28: Close-up numerical schlieren of $M_i = 1.46$ shock diffraction process around a round geometry

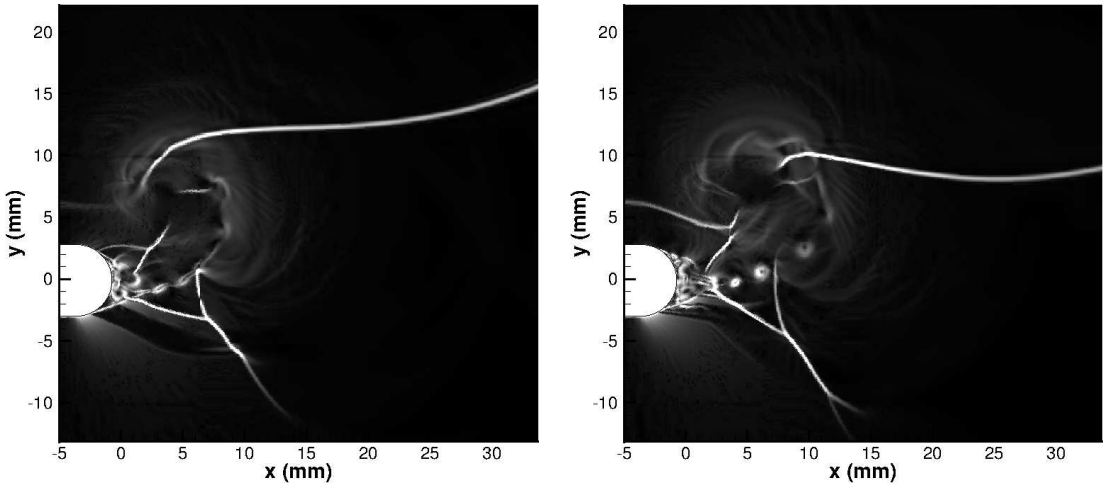

(g) 140 μs (h) 160 μs

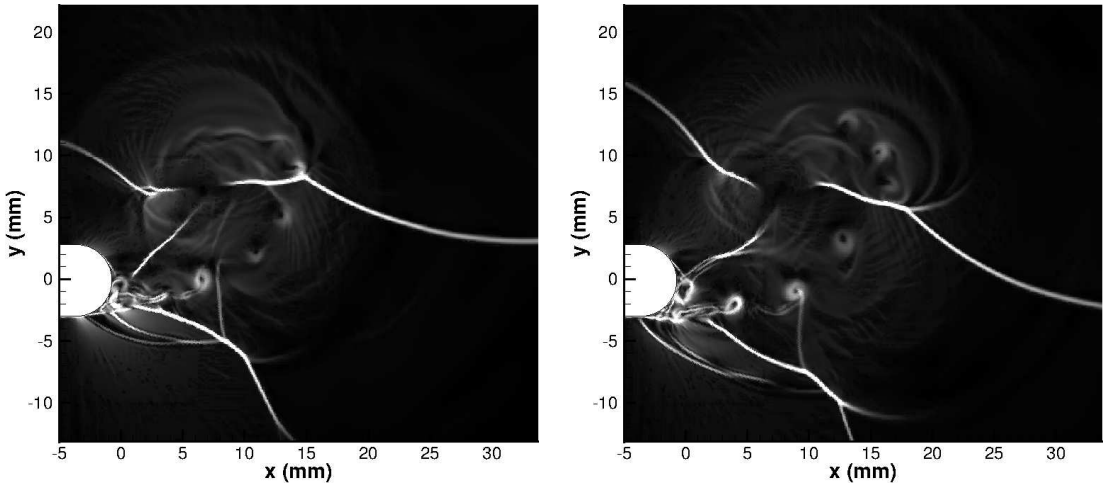

(i) 180 μs (j) 200 μs

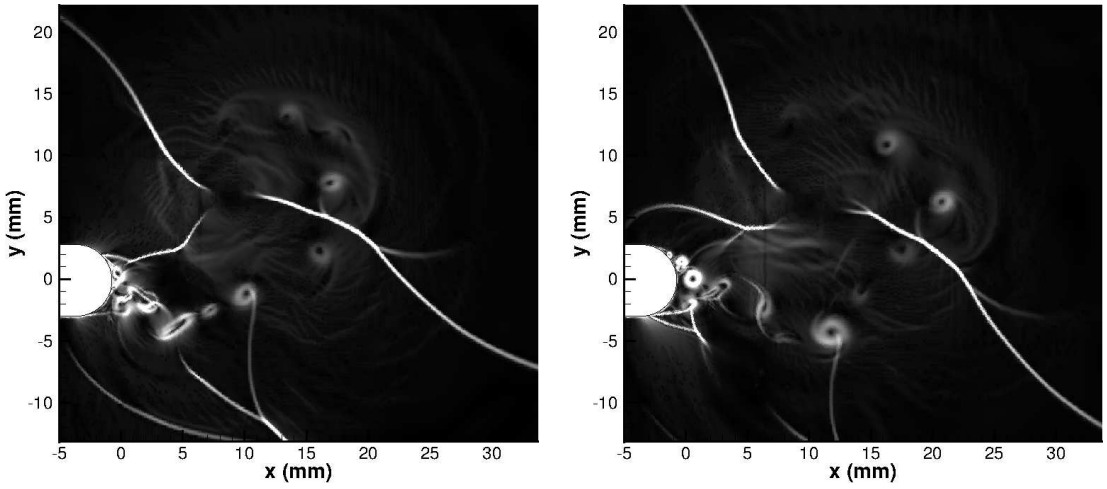

(k) 220 μs (l) 240 μs

Figure 5.28: Close-up numerical schlieren of $M_i = 1.46$ shock diffraction process around a round geometry

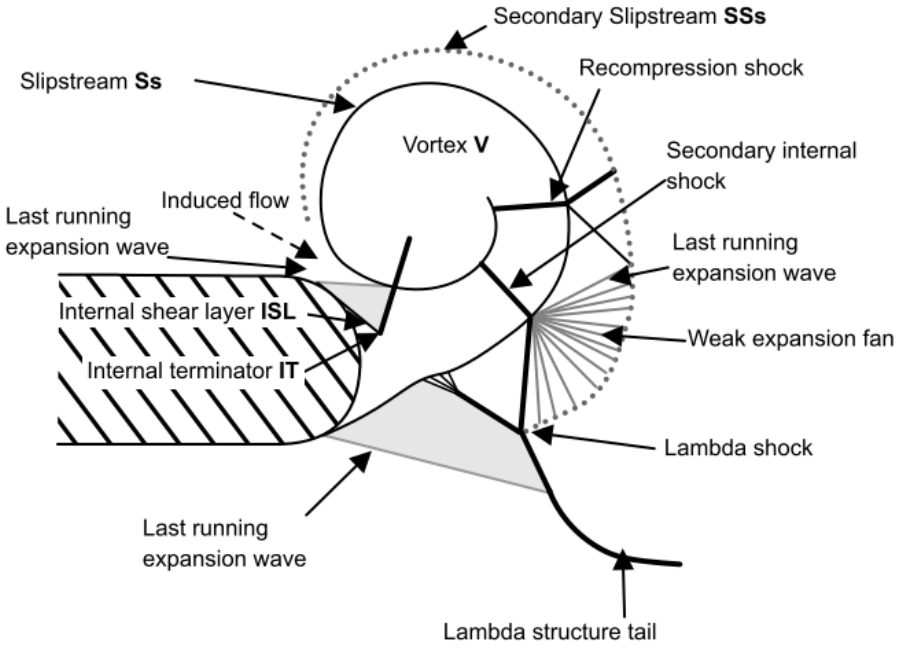

Figure 5.29: Schematic of complex region behind a $M_i = 1.55$ shock diffracting around a rounded corner

during the experiment. Fig.5.32 does show the turbulent nature of the vortex core, especially after the shock vortex interaction.

The returning shock-vortex interaction begins to take place from 140 μs onwards (Fig.5.32a) and appears to be stronger than in the previous cases. The first thing to note is that, as before, the internal terminating shock is broken down into smaller compression waves and eventually degenerates as the pressure balance requirements for its existence are removed by the shock-vortex interaction (Fig.5.30i). On the right-hand side of the vortex, the returning shock wave combines with the recompression shock as it propagates. The kink in the shock wave structure that connects it to the vortex core is visible. The schlieren results indicate the strength of the shock waves by the dark regions behind them. The Mach reflection connecting the returning shock to the vortex core on the right hand side of the vortex is very strong, as it has a large dark region behind the kink in the Mach stem (Fig.5.32f). The lambda shock, following the main expansion region (Fig.5.29), is swept upstream by the returning shock wave in Fig.5.32f. Both of the shock waves connected to the vortex core exhibit a *split foot*. This is likely to be due to the turbulence generated in the vortex core disturbing the otherwise planar shock wave. Both of the waves exhibit strong kinks in the region of the main shear layer and have diverging acoustic waves travelling along their length due to the vortex splitting the shock wave, as covered in Section 2.6.

5.1.2.6 Mi = 1.55 Numerical Results

The final set of numerical schlieren results are shown in Fig.5.33. Early in the diffraction process (i.e. before the effects of turbulence become significant), the simulations agree well with the experimental data. Fig.5.33d shows a very good representation

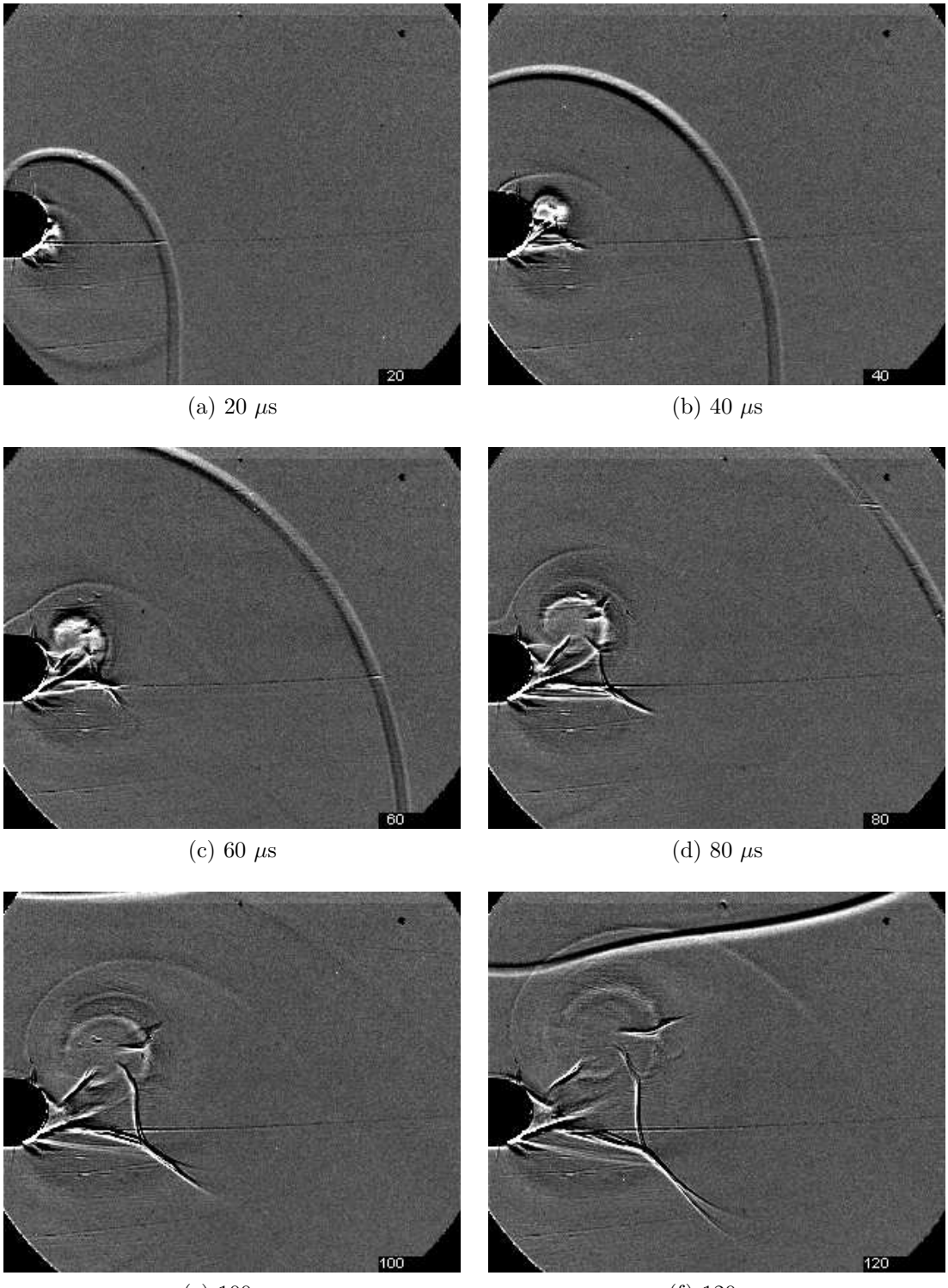

(a) 20 μs

(b) 40 μs

(c) 60 μs

(d) 80 μs

(e) 100 μs

(f) 120 μs

Figure 5.30: Close-up shadowgraph of $M_i = 1.55$ shock diffraction process around a round geometry

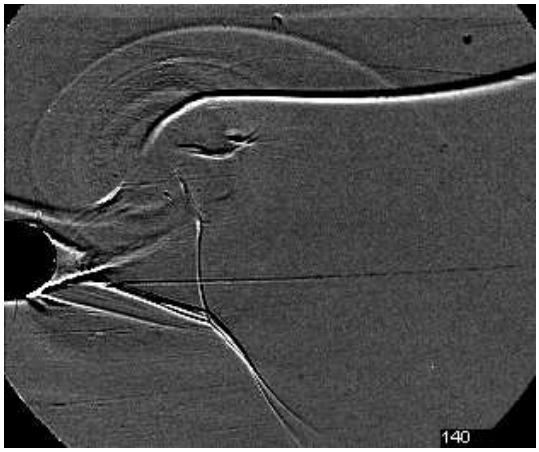

(g) 140 μs

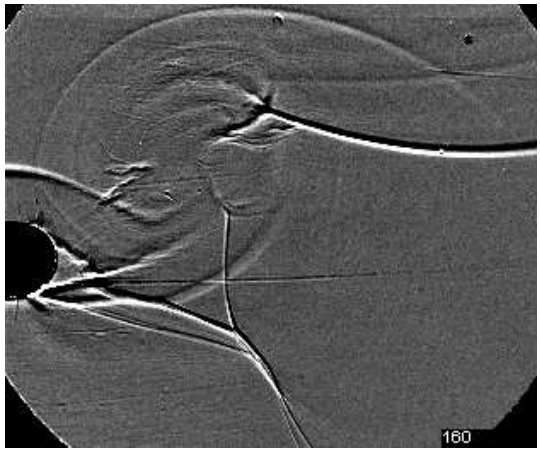

(h) 160 μs

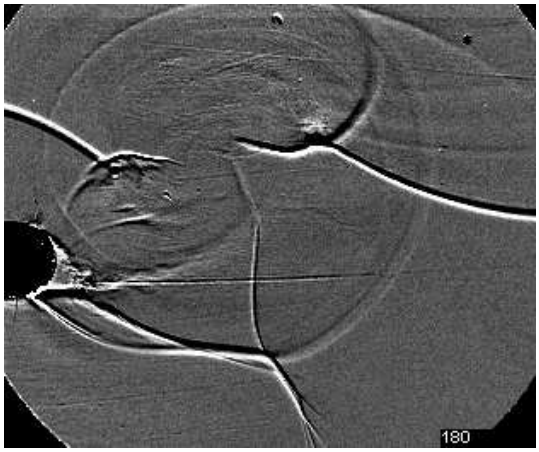

(i) 180 μs

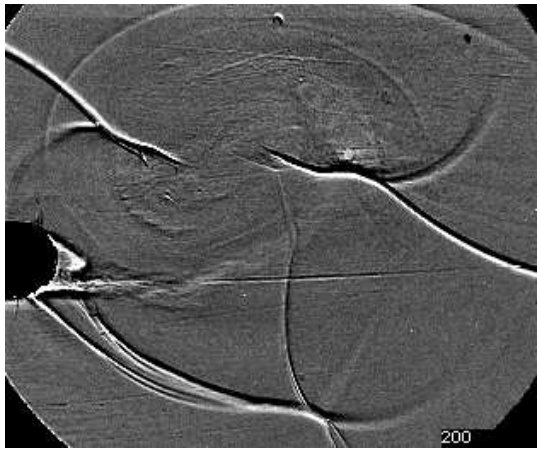

(j) 200 μs

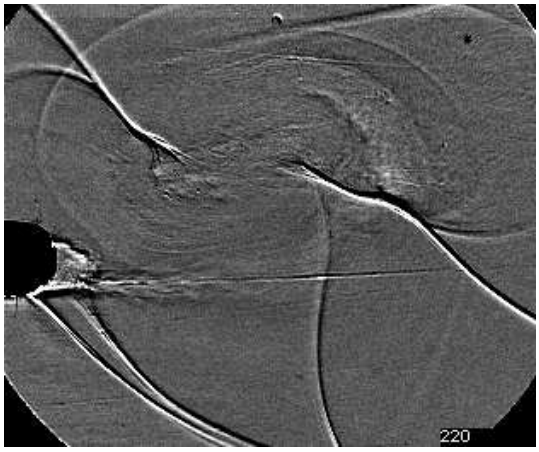

(k) 220 μs

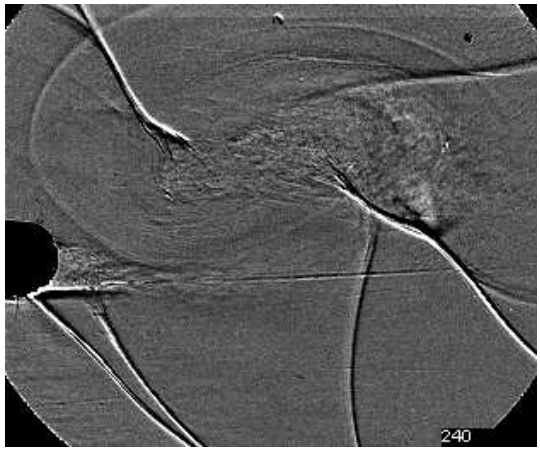

(l) 240 μs

Figure 5.30: Close-up shadowgraph of $M_i = 1.55$ shock diffraction process around a round geometry

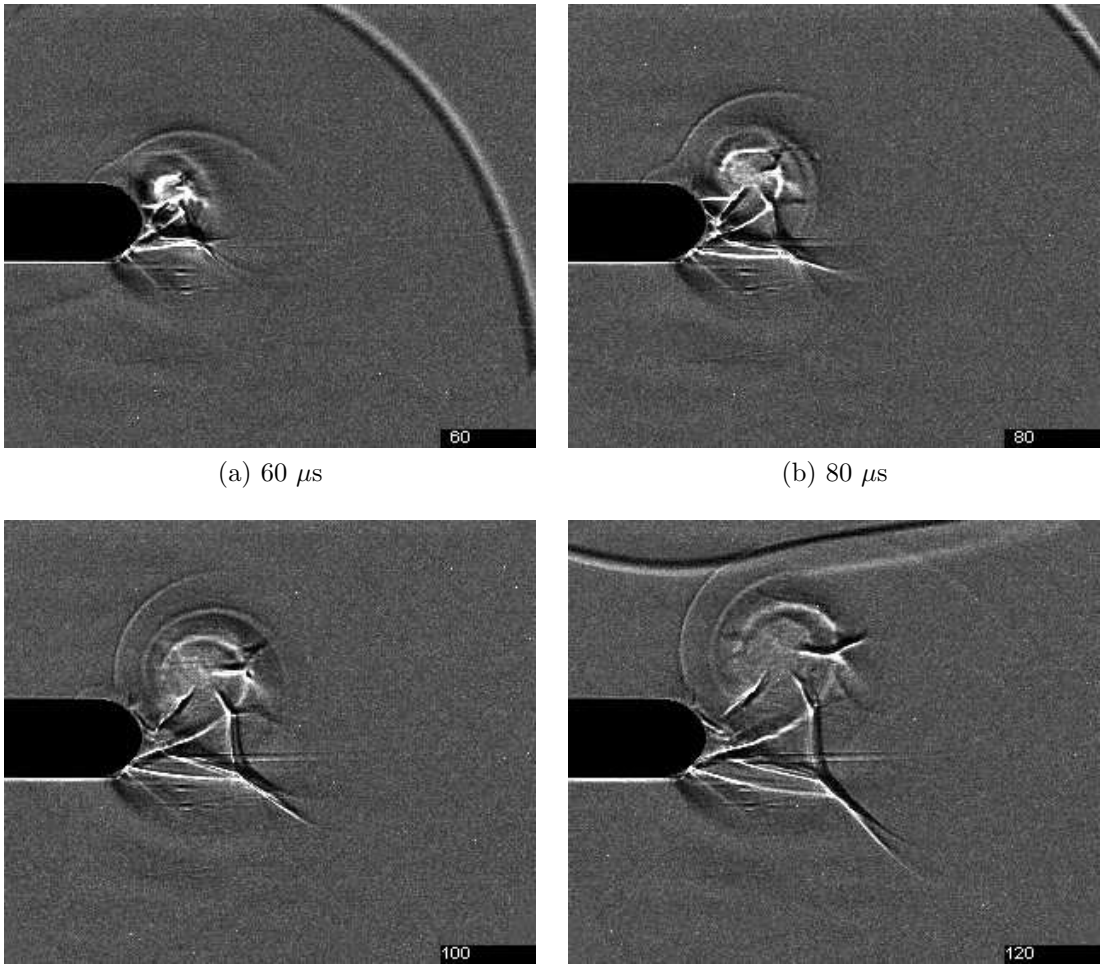

(a) 60 μs

(b) 80 μs

(c) 100 μs

(d) 120 μs

Figure 5.31: Close-up shadowgraph of $M_i = 1.55$ shock diffraction process around a round geometry with a lower depth-of-field

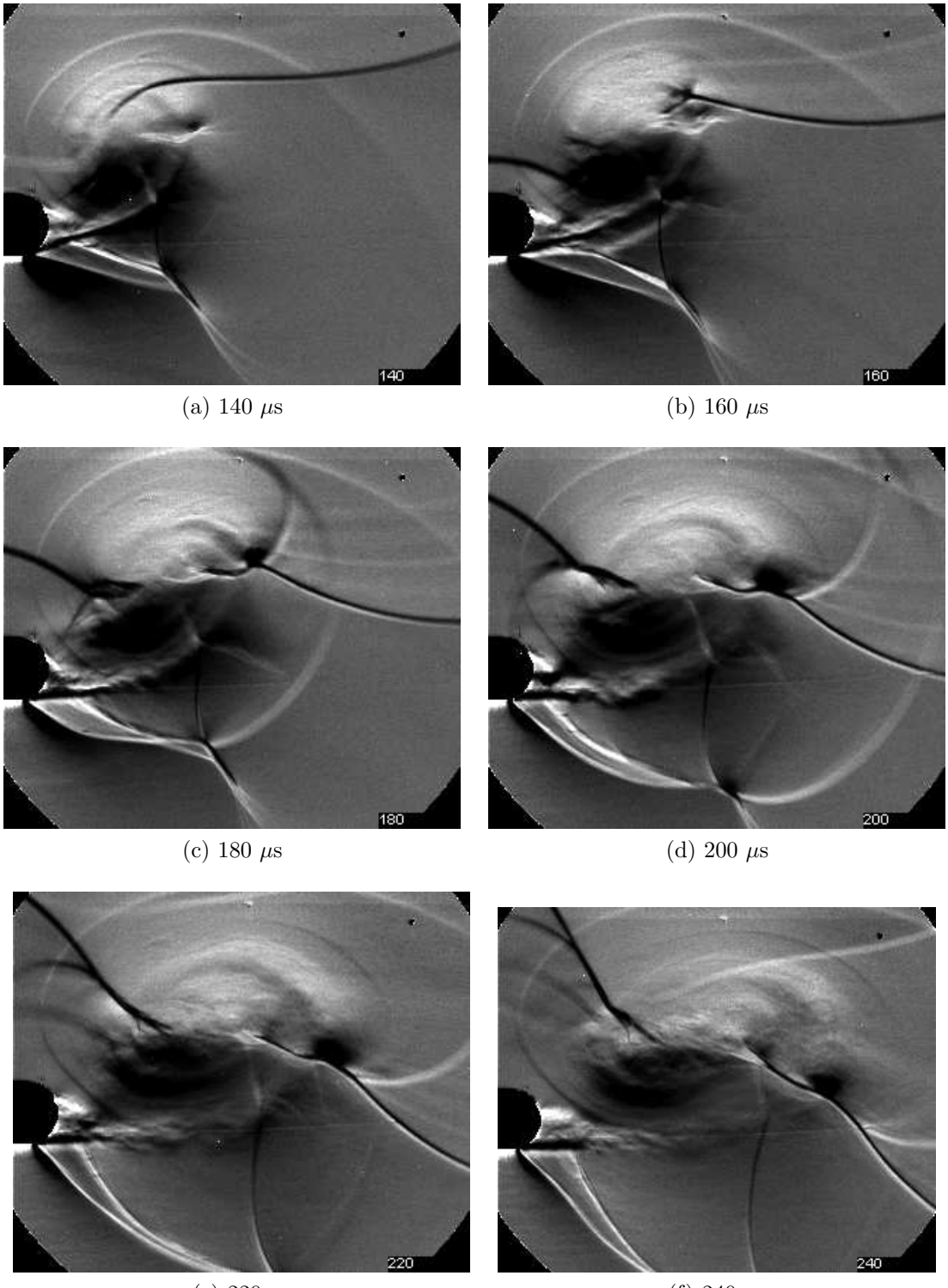

(a) 140 μs (b) 160 μs

(c) 180 μs (d) 200 μs

(e) 220 μs (f) 240 μs

Figure 5.32: Close-up schlieren of $M_i = 1.55$ shock diffraction process around a round geometry

of the actual expansion region underneath the shear layer. The lambda shock is well represented, as is its tail. The last running expansion wave begins to curve the lambda shock, although not as significantly as in previous cases. The secondary expansion region is captured, including the last running expansion wave and the internal terminating shock and shear layer. In the subsequent figure (slightly later than in the experiments), the secondary internal shock is visible, as is the recompression shock. From Fig.5.33e onwards, the shear layer begins to develop the instabilities seen in previous numerical results; however, the period of these instabilities is significantly shorter, as they are generated at a faster rate. Despite this, they are sufficiently weak so as not to significantly interfere with the shock wave structure during the shock-vortex interaction.

The terminating internal shock is broken down into weaker waves by the impact of the returning diffracted wave, although it never fully disappears as it does in the experimental results. The progress of the shock on the left-hand side of the vortex is well reproduced, complete with the kink caused by the shear layer. On the other side of the vortex the shock is split, as would be expected and a Mach reflection is formed, travelling upstream to face the oncoming flow. There is no *split foot* connecting any of the shocks to the vortex core, as seen in the experimental results.

5.1.2.7 Conclusions

Shock wave diffraction has been studied around a rounded corner using several different optical setups and numerical results have been provided for comparison with the experiments. At different Mach numbers the shock wave structures show common features; however, the spacing and layout of these varies accordingly. Unlike the sharp geometry, the main shock wave structures do not grow in a self-similar fashion, due the associated length scale (the radius of the corner). For example, the main expansion region causes a lambda structure which, over time, changes in orientation to face upstream. The diffracted shape of the initial shock wave is largely similar to the previous case; however, the complex region it generates is significantly more complicated.

The rounded geometry leads to the generation of a strong vortex; however, this formation of this vortex is more difficult to see, due to its proximity to the wall. The main vortex has a lower propagation velocity; this is especially evident for the $M_i = 1.28$ case. The close proximity of the vortex to the wall leads to the creation of a secondary expansion region, consisting of the flow induced by the main vortex. This internal expansion region is created by the convergent divergent nature of the geometry of the rounded corner and the main shear layer, which can be thought of as a solid boundary. The induced flow reaches supersonic velocity and is decelerated by an internal terminating shock wave. This internal expansion region is almost impossible to visualise using the schlieren technique, as the shock wave interactions in this region overrange the system (even with a small amount of cut-off). Only the shadowgraph technique is capable of resolving the flow features in this region. However, the shock vortex interaction is not well captured by the shadowgraph results as it appears that the vortex is not as strong for this geometry. The schlieren results show the contact surface and other weak flow features well.

The lowest Mach number case, $M_i = 1.28$, has a lambda-shaped structure underneath its main shear layer, indicating that it has a region of supersonic flow. This is

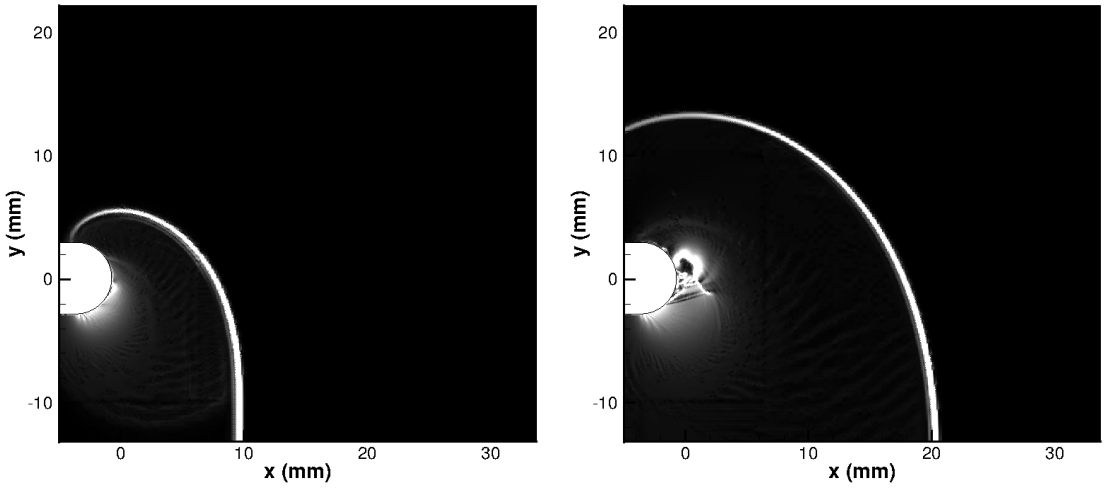

(a) 20 μs

(b) 40 μs

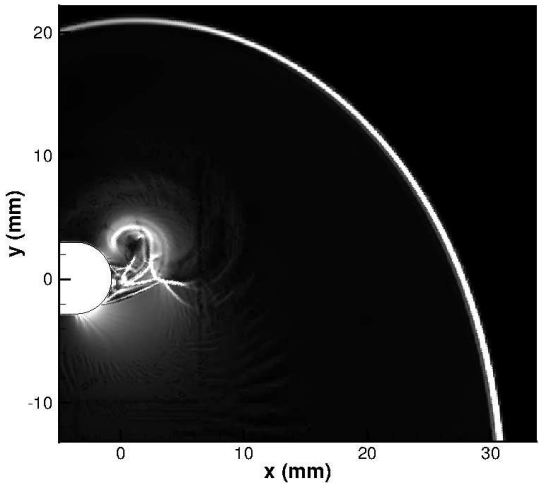

(c) 60 μs

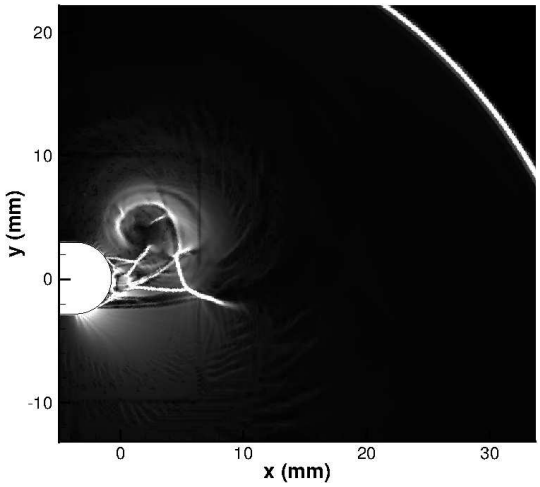

(d) 80 μs

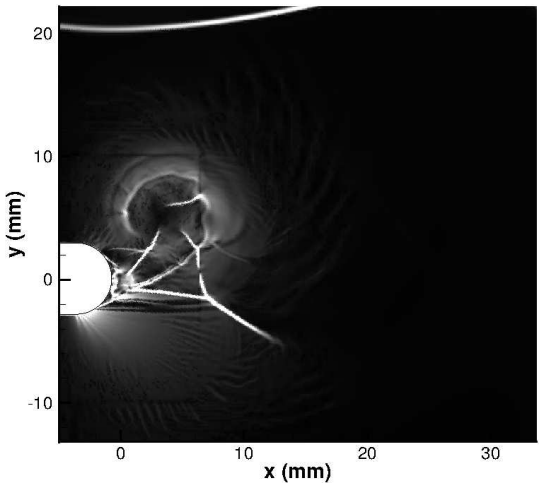

(e) 100 μs

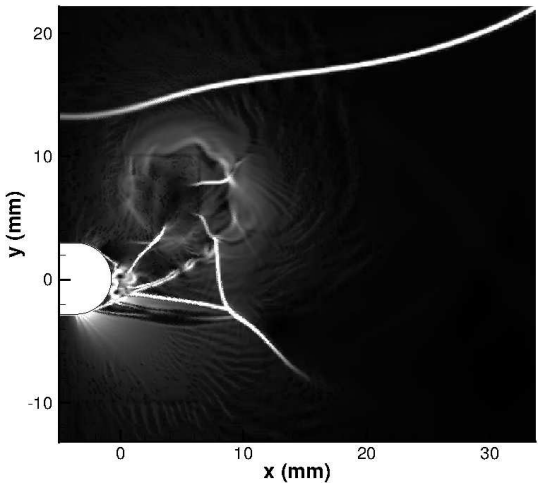

(f) 120 μs

Figure 5.33: Close-up numerical schlieren of $M_i = 1.55$ shock diffraction process around a round geometry

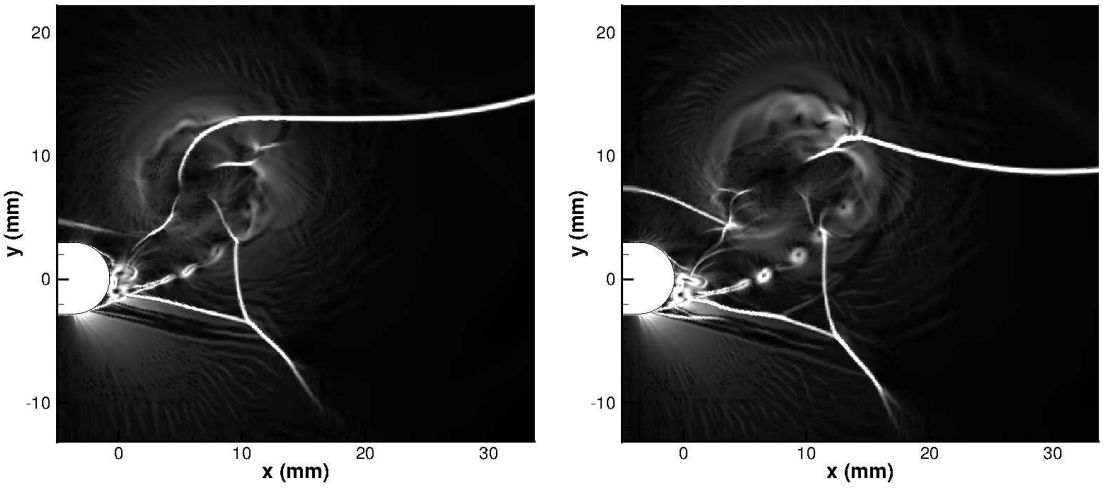

(g) 140 μs (h) 160 μs

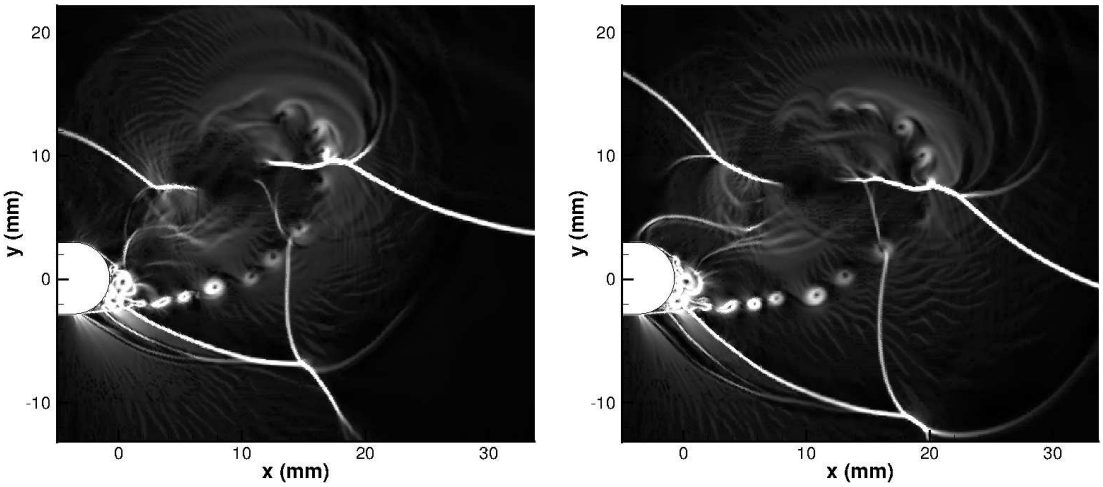

(i) 180 μs (j) 200 μs

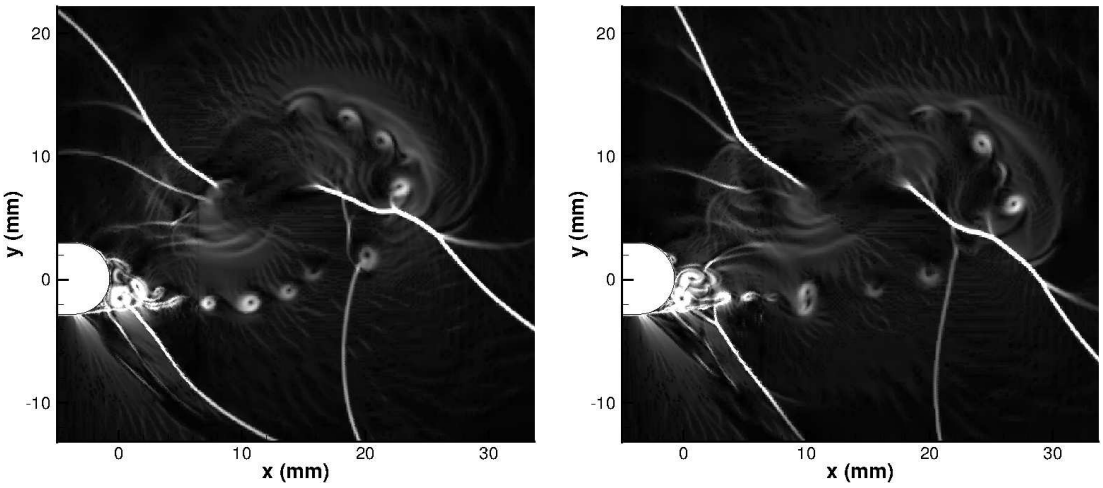

(k) 220 μs (l) 240 μs

Figure 5.33: Close-up numerical schlieren of $M_i = 1.55$ shock diffraction process around a round geometry

in contrast with the theory of Sun & Takayama [36], which predicts that the critical incident shock Mach number for a region of supersonic expansion is $M_i = 1.35$. The expansion wave in this flow has a larger area to act over, given the distributed nature of the geometry involved. This will be expanded upon further in Section 5.4.2.

The lambda structures indicate an incorrectly expanded region, followed by a shock required to match the pressure condition imposed elsewhere in the flow field. The $M_i = 1.28$ case showed a pair of these lambda structures; however, subsequent Mach number cases showed a more complex, albeit single, wave pattern. Higher Mach number cases exhibited a concave shear layer (unlike the $M_i = 1.28$ case), allowing the already supersonic flow to expand more. This is especially evident at $M_i = 1.55$. The internal terminating shock wave creates a jump in pressure which causes a change of curvature of the main shear layer, leading to the creation of a compression corner and the subsequent lambda shock.

The numerical simulations accurately predicted the boundary separation and the movement of the separation point. The basic wave structures are captured, including the internal expansion region. For this geometry, the shear layer is created by a separated boundary layer which will be thicker than the one created by a sharp corner, which can be thought of as inviscid separation. The presence of viscosity plays an important role in the development of the flow around a rounded geometry and, as such, it should be expected that a laminar model can only represent a finite amount of flow development. Due to the high flow speeds involved, it will not take long for the boundary layer to become turbulent and begin to invalidate the assumptions of the laminar model used. This is especially a problem in the $M_i = 1.28$ case, where the simulation begins to depart from the experiments after 160 μs, as the structures created are strong enough to interfere with the main wave pattern development. Another manifestation of this problem can be found on the main shear layer at higher Mach numbers. The numerical results develop instabilities similar to those seen for the sharp geometry, which were not seen in the experimental results. After a finite time, the real boundary layer will transition to turbulence, providing a mechanism for energy transfer in the flow which is not reproduced in the laminar simulations. This leads the laminar simulations to create sinks for energy which cannot be transported elsewhere in the flow and is not lost through viscous dissipation, i.e. vortices on the shear layer.

Thus far, it has been assumed that the flow in the shock tube is completely two-dimensional. However, the shadowgraph results indicate that some of the waves are no longer planar. This is caused by the turbulence in the boundary layer, as turbulence is an inherently three-dimensional phenomenon. Although the flow is no longer completely two-dimensional, the disturbances introduced do not appear large enough to significantly affect the flow development. This means that the two-dimensional simulations are still of use for comparison with the experimental results in subsequent sections.

The shock vortex interaction is largely similar to the one presented for the sharp geometry, with some minor differences. The waves T_1 and RR_1'' in Fig.5.18 propagate more slowly around the vortex. This indicates that the oncoming flow is much faster than for the sharp geometry. The lack of coherent structures propagating along the shear layer means that the shock vortex interaction does not have the same diverging acoustics created by the serially arranged K-H vortices found for the sharp case. The strongest wave seen is the wave **MR3** which is followed by a large change in image

intensity, indicating its strength.

5.2 Particle-Based Results

In this section, numerical velocity flood plots will be compared to the experimental PIV data and a selection of raw PIV images in order to highlight certain flow features which are ambiguous based on the results seen so far. The time advancement of the experimental results is more staggered than for the density-based results. Velocity flood plots are presented in lieu of velocity vectors, as the adaptive grid scheme means that there are many more velocity vectors in certain regions, which can be misleading. As before, sharp and round geometries will be discussed separately.

A comparison of the induced velocities expected from theory and measured using PIV can be seen in Tab.3.6.

5.2.1 Sharp Geometry

5.2.1.1 Mi = 1.28 Experimental Results

Fig.5.34 shows the velocity vector evolution of the shock diffraction process. Figs. 5.34a to 5.34c show that in the inlet of the test section the flow is of uniform velocity with no vertical component. The measured velocity of 148 ms^{-1} is very close to the predicted velocity (143 ms^{-1}) based on the experimental Mach number measured from the density-based results. The reflected expansion wave emanating from the splitter apex travels back upstream in these figures, inducing a vertical component of velocity, and spreads downwards from the start of curvature of the incident shock wave. In the vortex core there are no velocity vectors; this is due to the inertial effects of the tracer particles. This problem is expected to get worse as the vortices become stronger and the centrifugal forces increase. Fig.5.34c shows significant holes in the vector plot in the region of the reflected expansion wave. As the flow begins to turn around the corner, it is ejected away from the centre of rotation, making measurements in this region difficult. Fig. 5.34e shows the expansion region under the shear layer as a clear region of high velocity fluid. The velocity measured in this region is 342 ms^{-1}. Based on the theory presented in Sections 2.2.1 & 2.4.1, the sonic velocity in this region is 348 ms^{-1}, meaning that the flow is almost sonic. The velocity induced by the diffracted wave, above the splitter, is extremely small, implying that the wave has degenerated into an acoustic level wave by this point.

In Figs.5.34e & 5.34f, the returning shock wave can be seen clearly on the right-hand side of the vortex, as the fluid is forced to change direction by this shock. The vertical component of the velocity in this region is reduced, with the flow having a larger horizontal component. This is most evident around the stagnation point on the top wall, caused by the returning diffracted shock wave.

At approximately 30° & 210° around the vortex, inside the shear layer, there is a region of fluid which is significantly faster than the rest of the fluid in the vortex region; this is most evident in Fig.5.34j. From the density-based results, by 232 μs, we know that the returning shock wave on the right-hand side of the vortex is now traversing the region containing the highest flow velocity. This is evident in Figs. 5.34j to 5.34l, as the region of high velocity fluid contains a sharp deceleration, both inside and outside the shear layer.

None of the experimental velocity vector plots show any sign of shear layer instabilities.

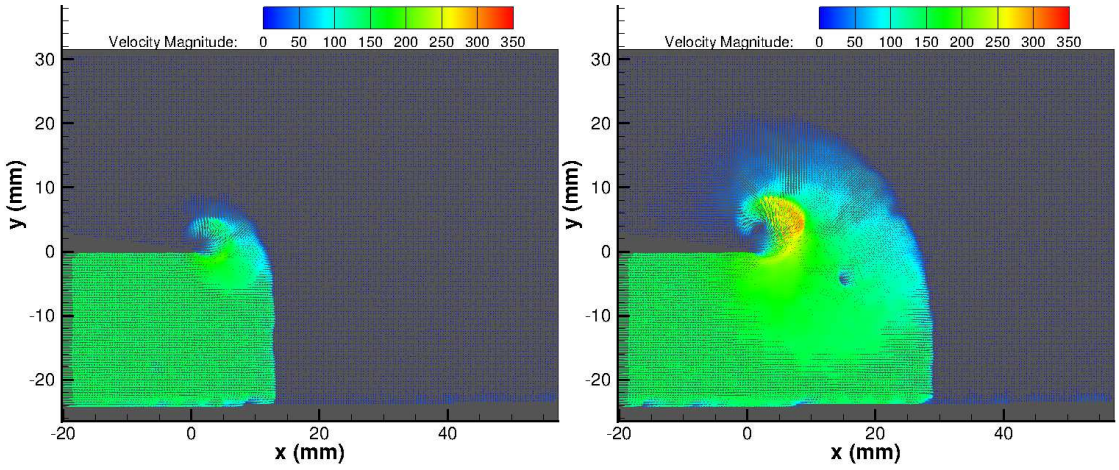

(a) 30 μs

(b) 64 μs

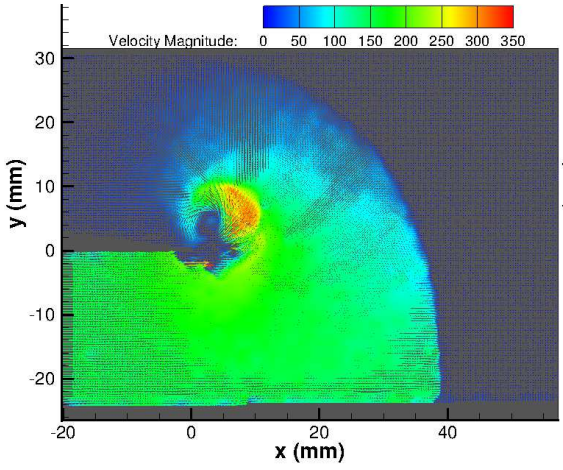

(c) 88 μs

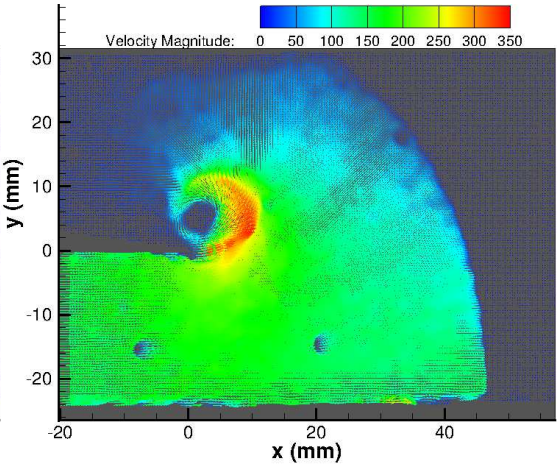

(d) 104 μs

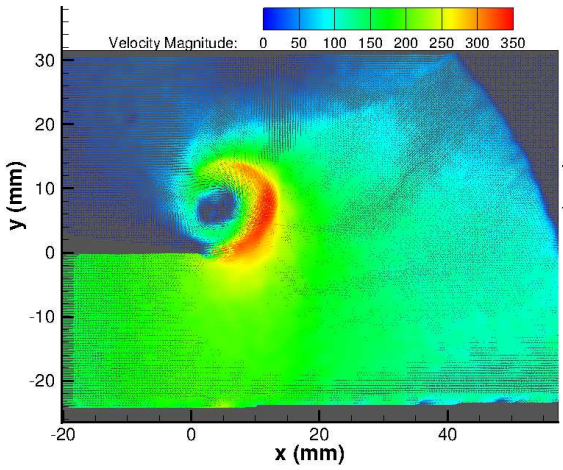

(e) 140 μs

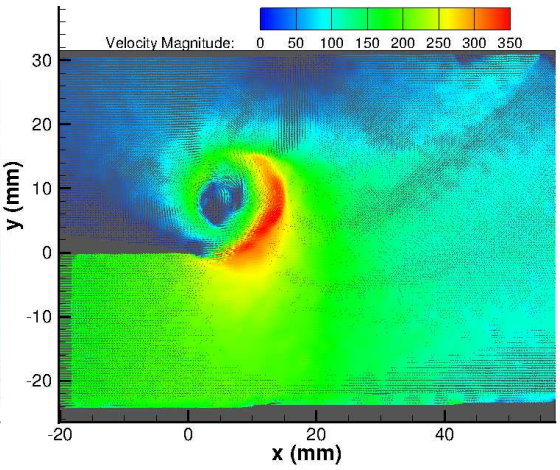

(f) 164 μs

Figure 5.34: PIV vector plot of $M_i = 1.28$ shock diffraction process around a sharp geometry

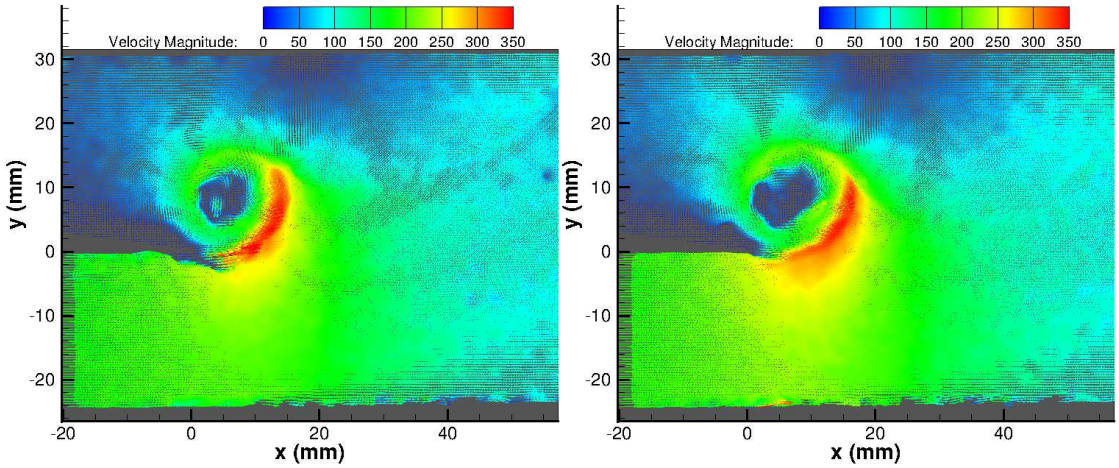

(g) 180 μs (h) 200 μs

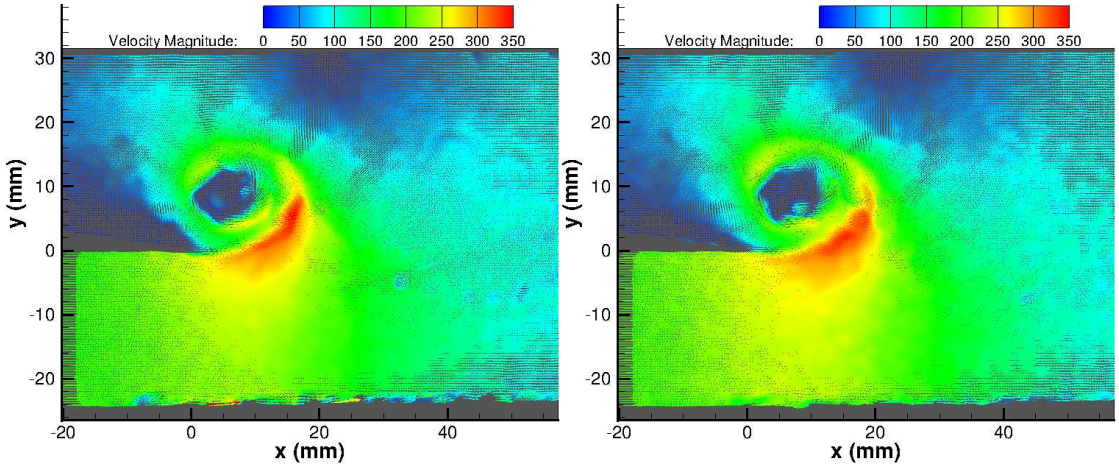

(i) 212 μs (j) 232 μs

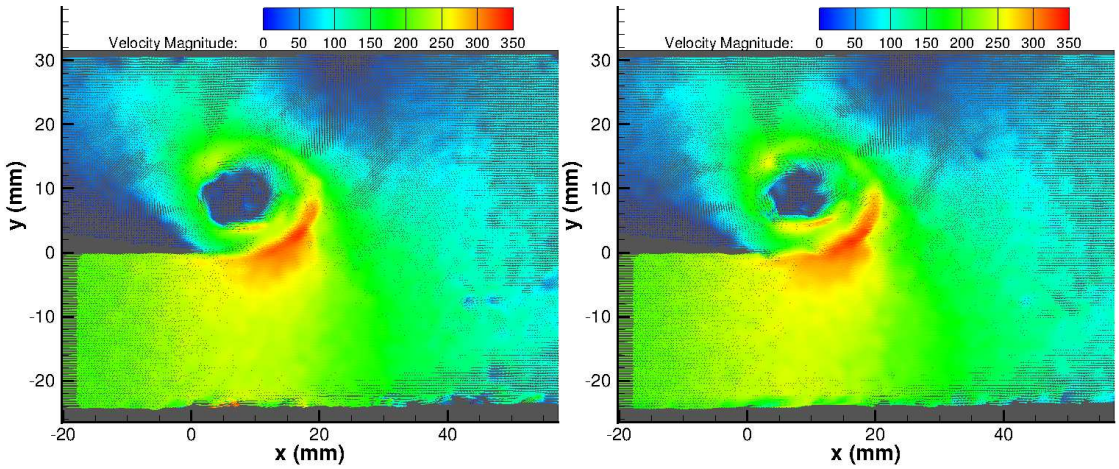

(k) 240 μs (l) 244 μs

Figure 5.34: PIV vector plot of $M_i = 1.28$ shock diffraction process around a sharp geometry

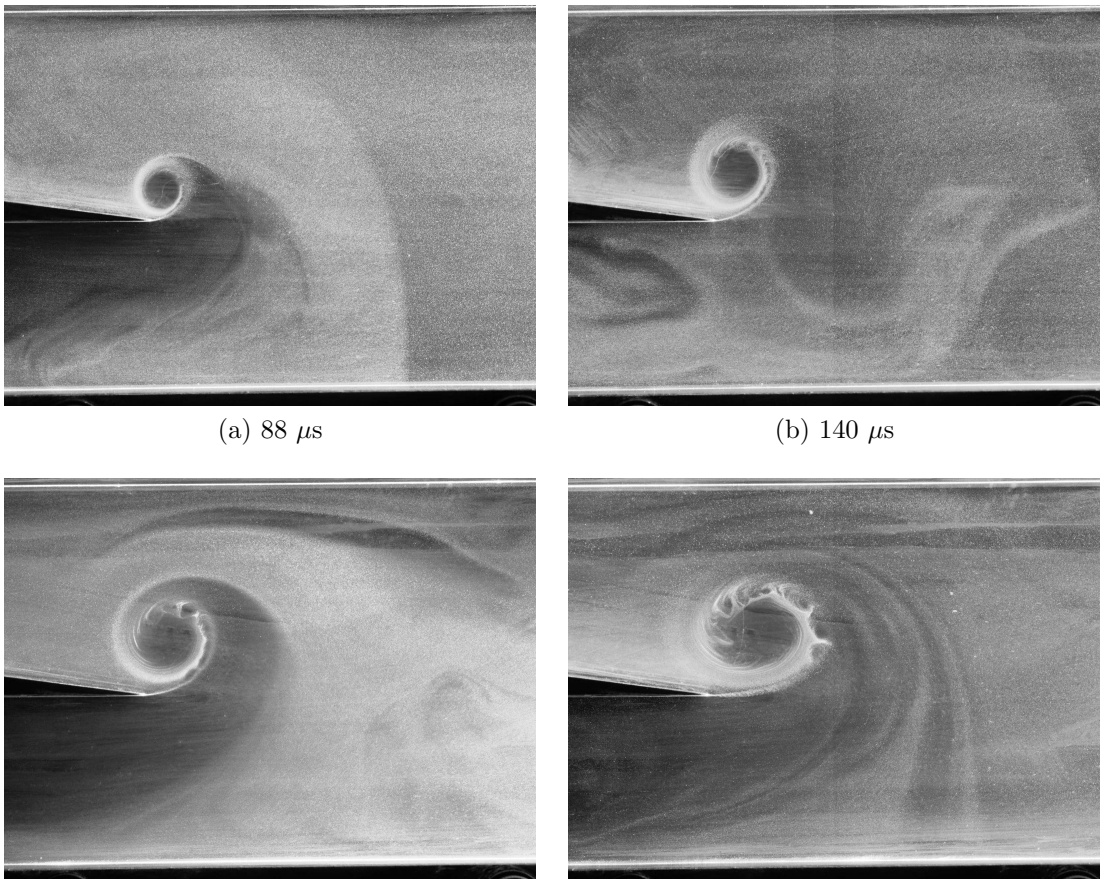

(a) 88 μs (b) 140 μs

(c) 200 μs (d) 244 μs

Figure 5.35: PIV raw images of $M_i = 1.28$ shock diffraction process

Raw PIV images can be used as particle flow-visualisation to give us qualitative information about certain types of flow phenomena, such as vortices. Fig.5.35 shows the development of the flow using raw PIV images. In Fig.5.35a there are very faint signs of flow instabilities on the shear layer. However, as the flow expands in time, Figs. 5.35b, 5.35c & 5.35d show the instabilities on the shear layer very clearly. Furthermore, from the density-based results we could not determine what the flow structure of the shear layer was after the returning shock wave had impacted on it. Fig.5.36 shows the flow structure very clearly. The previous instability has been slowed and is beginning to break up; however, there is a new high-frequency K-H instability on the shear layer, as predicted by the numerical simulations.

The boundary layer thickness in this flow is difficult to estimate as it is developing in time and is not spatially uniform. Also, as it is not possible to extract time-averaged data, there is no way to conclusively estimate its thickness. However, based on the raw PIV image shown in Fig. 5.37 the average structure height appears to be approximately 0.7 mm.

5.2.1.2 Mi = 1.28 Numerical Results

Numerical flood plots of velocity are presented in Fig.5.38. The velocity magnitude plots agree very well with the experimental results, with a few minor exceptions. The uniform region behind the incident shock wave has an induced velocity of 145 ms^{-1},

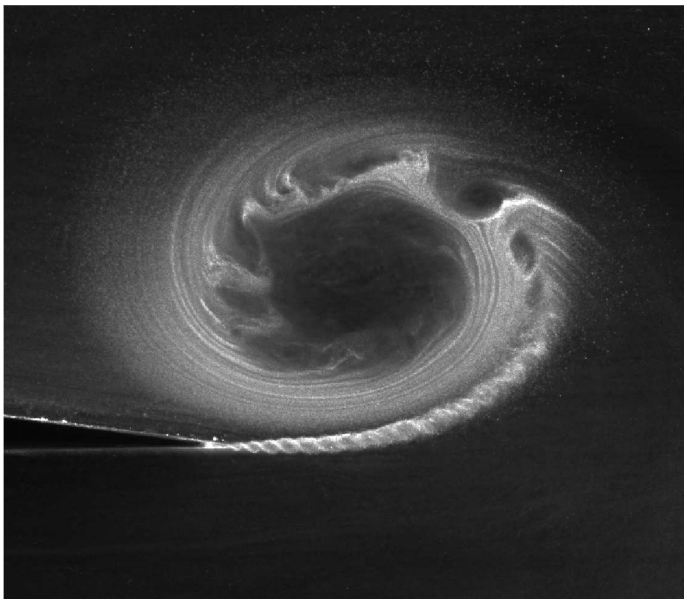

Figure 5.36: Close-up PIV raw image of the complex region at 240 μs

Figure 5.37: Close-up PIV raw image of the boundary layer $M_i = 1.28$ shock at 240 μs

which compares very well with the experimental and analytical values. The region of high-velocity fluid has a slightly higher velocity in the simulations compared to the experiments, with a maximum of 369 ms^{-1}, meaning that there are localised pockets of supersonic flow. The maximum values are around the shear layer instabilities, although they do not have as large an influence here as in subsequent tests. The velocity just outside the shear layer reached 352 ms^{-1}. In the simulations it is predicted to be slightly supersonic, which disagrees with the theory presented by Sun & Takayama [36] which states that the critical Mach number is $M_i = 1.346$. The stagnation point on the top surface of the test section can clearly be seen from Fig.5.38e onwards. The region of high-velocity fluid on either side of the vortex inside the shear layer can be seen in Fig.5.38j onwards. Figs.5.34l & 5.38l show the decrease in velocity due to the returning diffracted shock wave as it passes through the expansion region very clearly.

The numerical velocity flood plots show evidence of the shear layer instabilities seen in the previous section.

5.2.1.3 Mi = 1.46 Experimental Results

Fig.5.39 shows the PIV vector plot of the $M_i = 1.46$ shock diffraction process. The first thing to note in these images is the higher inlet velocity, 216 ms^{-1}, induced by the stronger incident shock wave; this compares well with the experimental Mach number prediction of 221 ms^{-1}. Velocity measurements in the vortex core remain a problem, with little to no information available in those regions. Fig.5.39c shows that the high velocity region is significantly larger in this case than in the previous one, with a maximum velocity of 469 ms^{-1}. However, there is no sign of the lambda shock structures seen in the density-based results. Although the expansion in this region is stronger and therefore the velocity is higher, the lambda waves are not strong enough to significantly change the velocity. The lambda structures are also small enough that they are on the limit of what the PIV particles can be expected to resolve given their relaxation time (Section 3.2.3) and could be smoothed out by particle intertia. As in the previous case, the velocity induced by the diffracted wave, above the splitter, is extremely small.

The stagnation region, seen as early as 104 μs, on the top surface of the test section is larger in this test, indicating that the strength of the returning shock wave is greater than before. The returning wave is again more visible to the right of the vortex, due to the larger changes in flow direction in this region (Figs. 5.39f to 5.39h).

Fig.5.39g onwards show regions of high-velocity fluid on the top side and bottom side of the vortex. These are especially noticeable from Fig.5.39i onwards, where the double shock structure to the left of the vortex (see Fig.5.8j to 5.8l) seems to end the region of high-speed flow. Below the vortex but above the shear layer, the flow is accelerated to speeds approaching those seen below the shear layer (Figs.5.39j to 5.39l). The regions both inside and outside the shear layer are decelerated by the returning shock wave, as seen in Fig.5.8k; however, the region inside is decelerated further upstream, as the shock has been able to propagate faster in this region due to the slower oncoming flow.

After the returning shock has impacted on the shear layer, the expansion region is drawn further and further towards the bottom of the test section, inducing a high

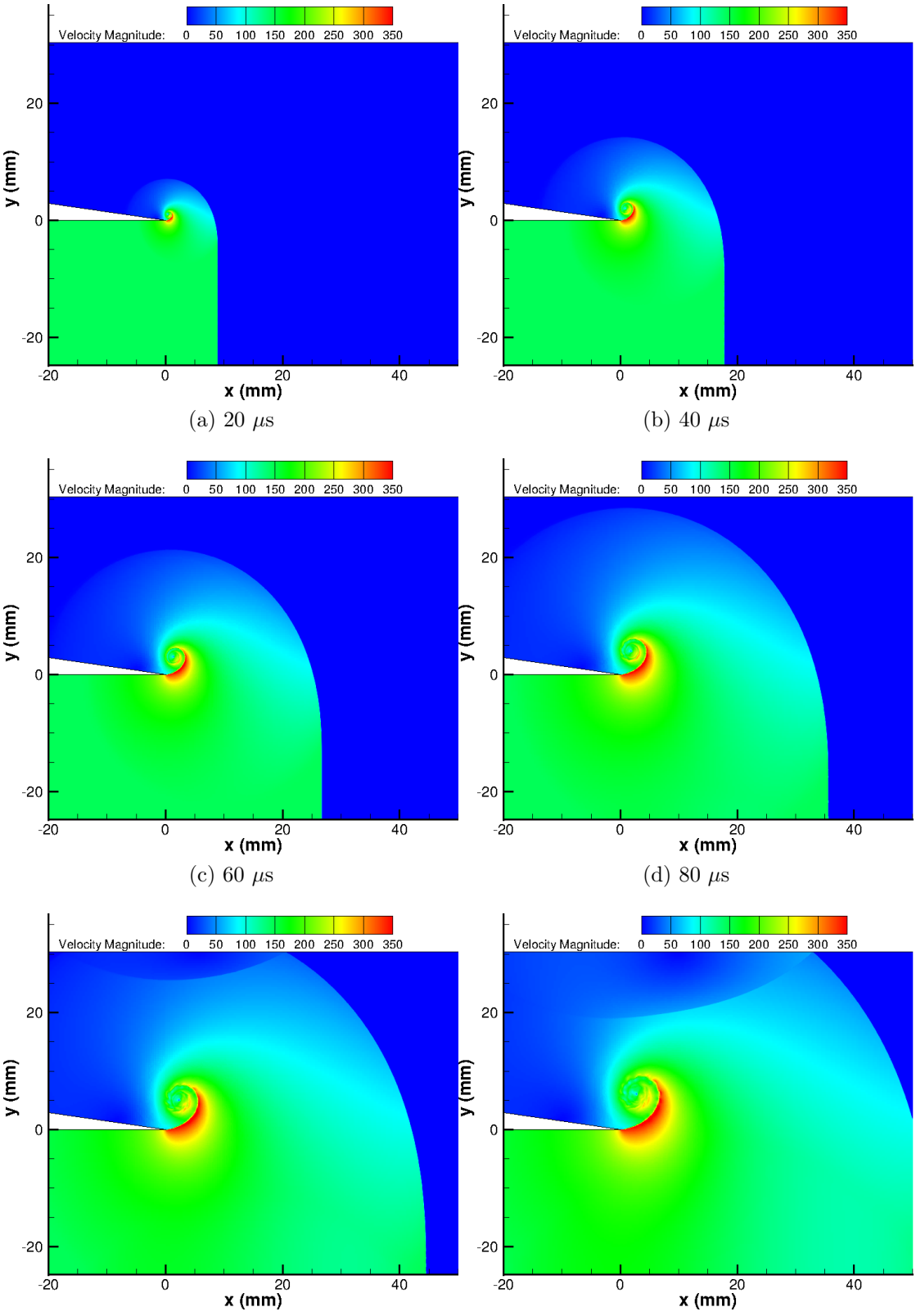

(a) 20 μs (b) 40 μs

(c) 60 μs (d) 80 μs

(e) 100 μs (f) 120 μs

Figure 5.38: Numerical velocity flood plot of $M_i = 1.28$ shock diffraction process around a sharp geometry

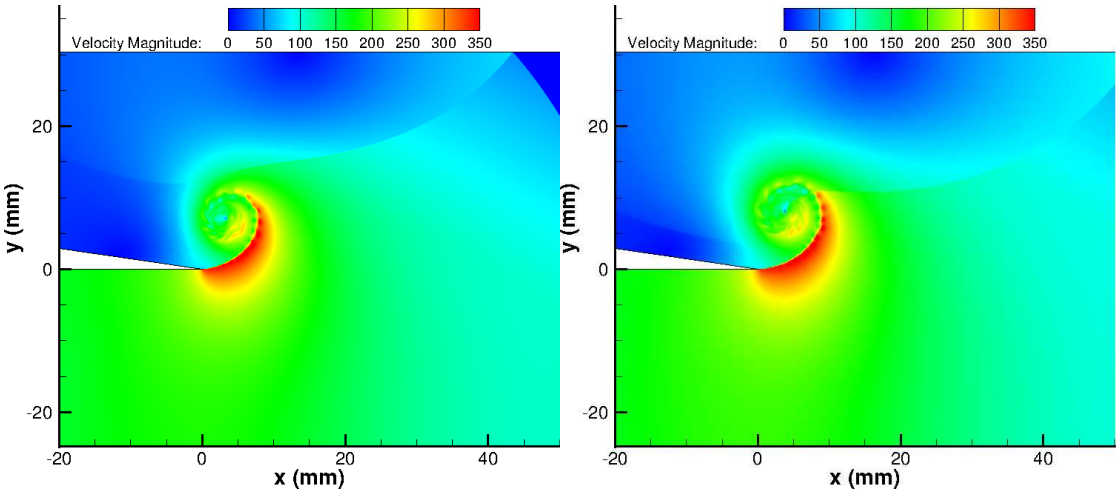

(g) 140 μs (h) 160 μs

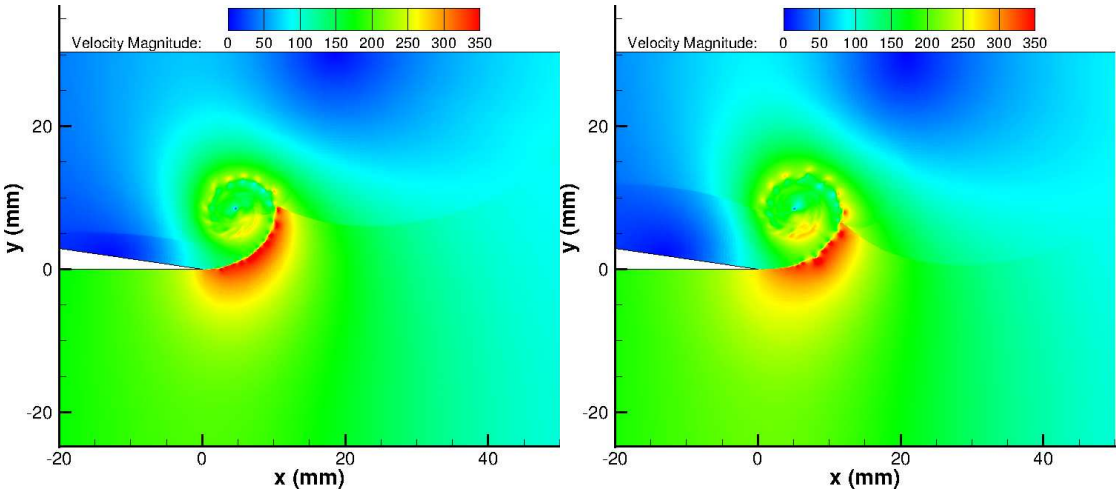

(i) 180 μs (j) 200 μs

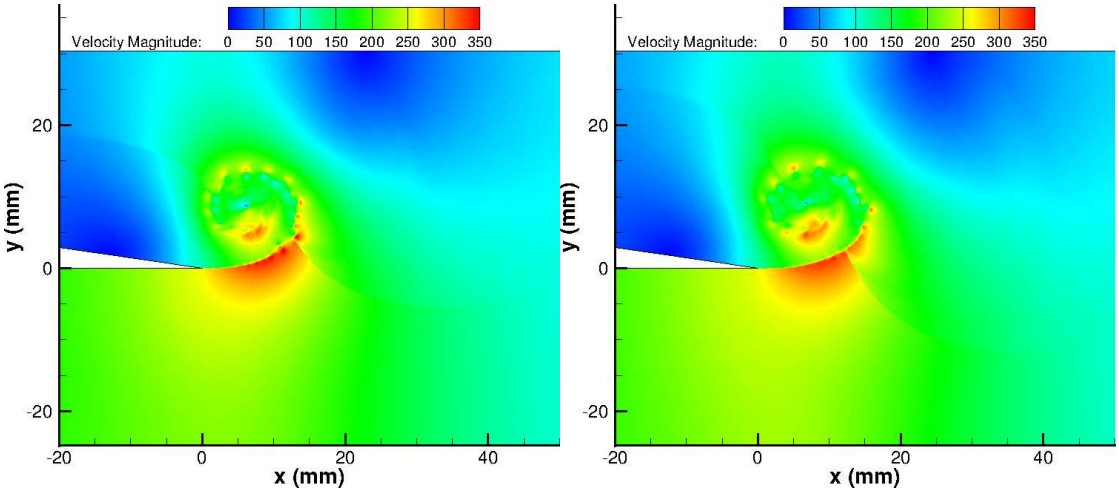

(k) 220 μs (l) 240 μs

Figure 5.38: Numerical velocity flood plot of $M_i = 1.28$ shock diffraction process around a sharp geometry

velocity over a larger region than was seen in the previous case.

Again, due to the limited resolution of the velocity vectors, it is not possible to see any instabilities on the shear layer. This is not surprising, as the instabilities appeared to be more inhibited as the incident Mach number is increased from its lowest value. The raw PIV images shown in Fig.5.40 show that these instabilities are present on the shear layer. Figs.5.40a & 5.40b are before the returning shock wave has reached the shear layer around the vortex. The individual vortices are only seen from approximately 90° around the vortex, and they appear to have completely dispersed by 270°. This indicates that the supersonic flow in the expansion region below the shear layer inhibits the growth of the instabilities. After the impact of the returning shock (Figs. 5.40c & 5.40d), once again the movement of the instabilities is slowed and they begin to expand and disperse. The two strong vortices generated by the impact of this shock wave can be seen in Fig.5.41 as the last two coherent structures moving away from the splitter tip. Unlike in the previous case, there does not appears to be any coherent structure generated in the shear layer after the passage of the returning shock wave.

The boundary layer behind a $M_i = 1.46$ shock should be slightly thicker at the same time step given the higher induced velocity behind the shock. Fig. 5.42 shows that the boundary layer is slightly thicker for this case compared to the previous one. The average structure height seen in Fig. 5.42 is approximatly 0.95 mm.

5.2.1.4 Mi = 1.46 Numerical Results

The numerical results for $M_i = 1.46$ show good agreement with the experimental results. The incident shock-induced velocity is 224 ms^{-1}, which compares well with the experimental results presented above. Similarly to the first test case, the maximum velocity predicted in the expansion region is found around the instabilities on the shear layer, where locally the velocity is as high as 550 ms^{-1}. Outside of the influence of the instabilities, the maximum velocity is 490 ms^{-1}, still 4.5 % higher than the experimental values.

The qualitative velocity profile in this region is almost exactly the same as the experimental results. This is likely to be because the lambda structures are not predicted correctly, as seen in the numerical schlieren results. The region of high-speed flow inside the shear layer is well predicted and can be seen as early as Fig.5.43b. The effect of the returning shock wave on this region is also well predicted (Fig.5.43i), as is the ingress of the shock wave both inside and outside of the shear layer (Fig.5.43l). The shear layer instabilities are seen in the velocity flood plots both before and after the impact of the returning shock wave.

The size of the expansion region after the returning shock wave impacts on the shear layer and diffracts around the splitter is very well predicted by the numerical simulations.

5.2.1.5 Mi = 1.55 Experimental Results

Measurements at $M_i = 1.55$ proved more challenging than at lower Mach numbers. The stronger expansion fan under the shear layer and higher velocities found around the vortex ejected particles more readily from the vortex core. This led to fewer full vector plots being gathered, making the time stepping in the results more sporadic.

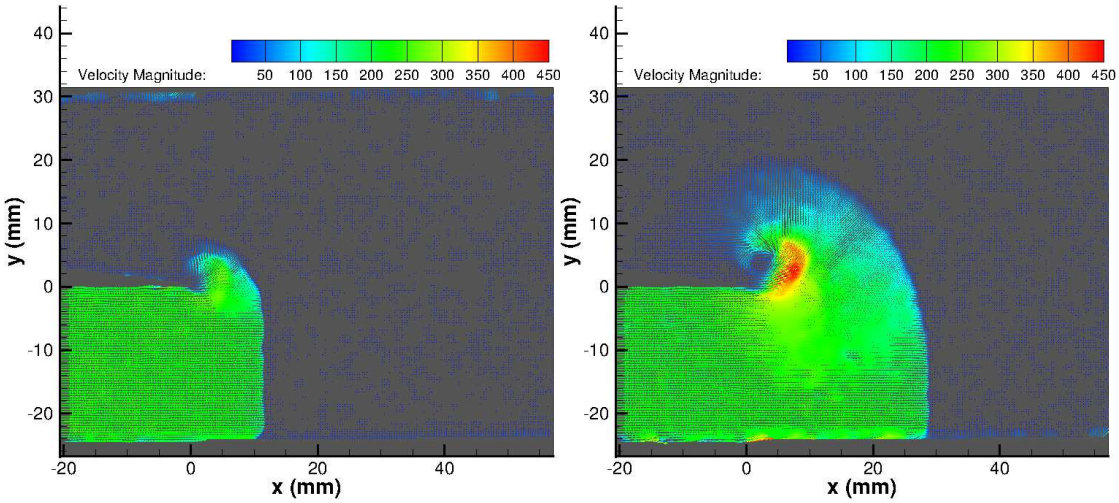

(a) 20 μs (b) 56 μs

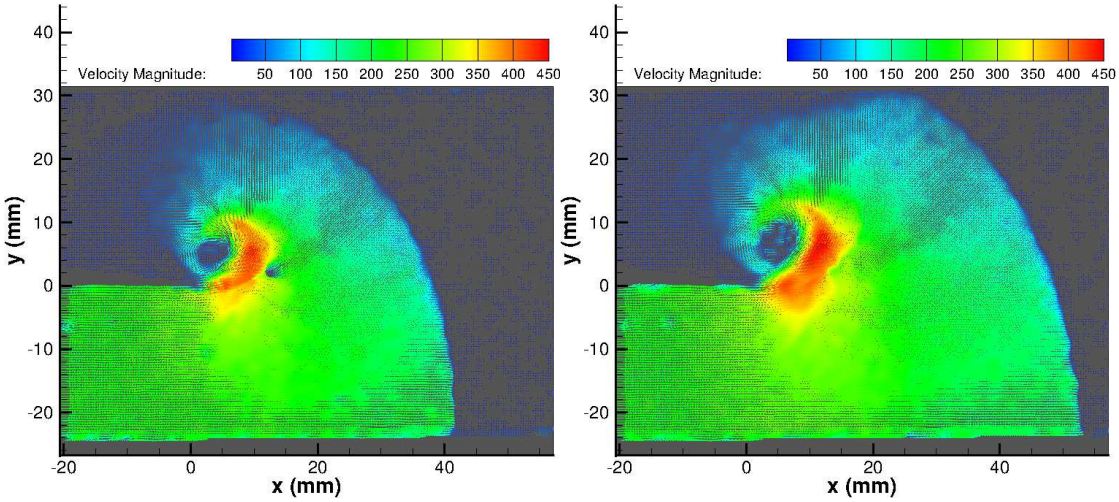

(c) 80 μs (d) 104 μs

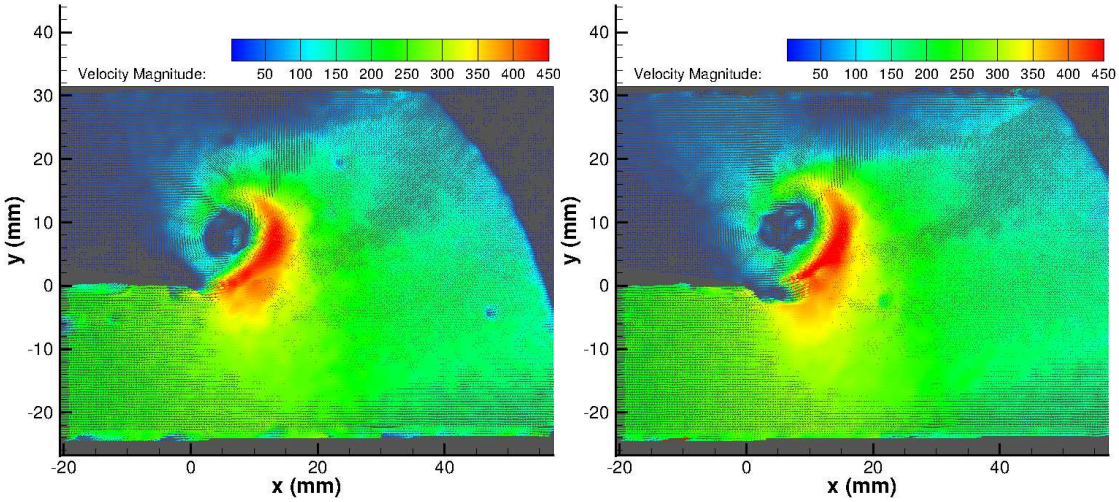

(e) 116 μs (f) 136 μs

Figure 5.39: PIV vector plot of $M_i = 1.46$ shock diffraction process around a sharp geometry

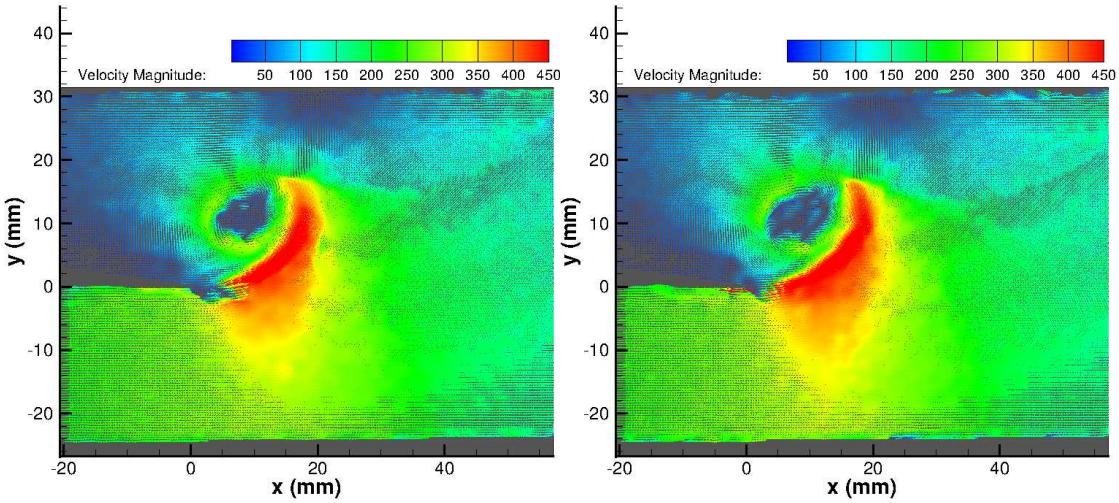

(g) 160 μs (h) 168 μs

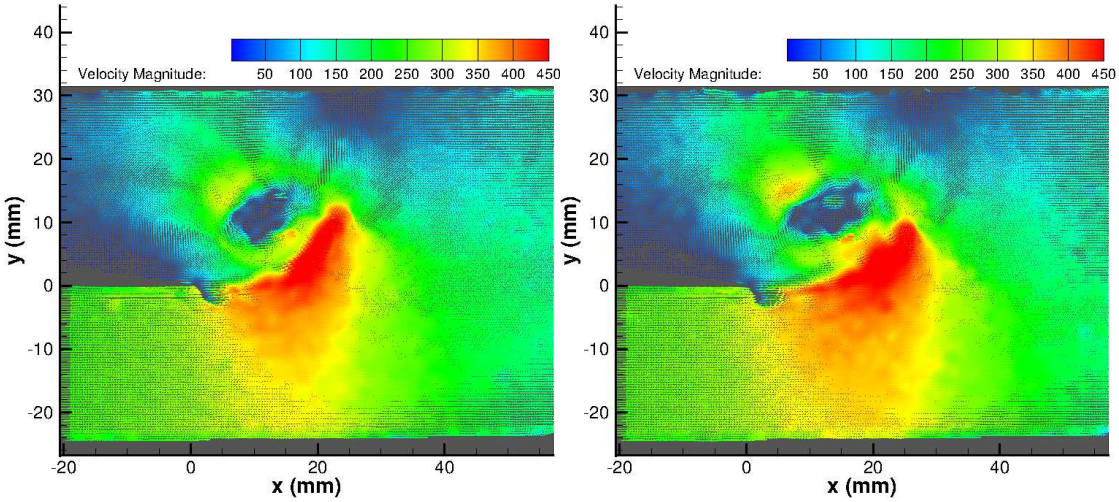

(i) 200 μs (j) 216 μs

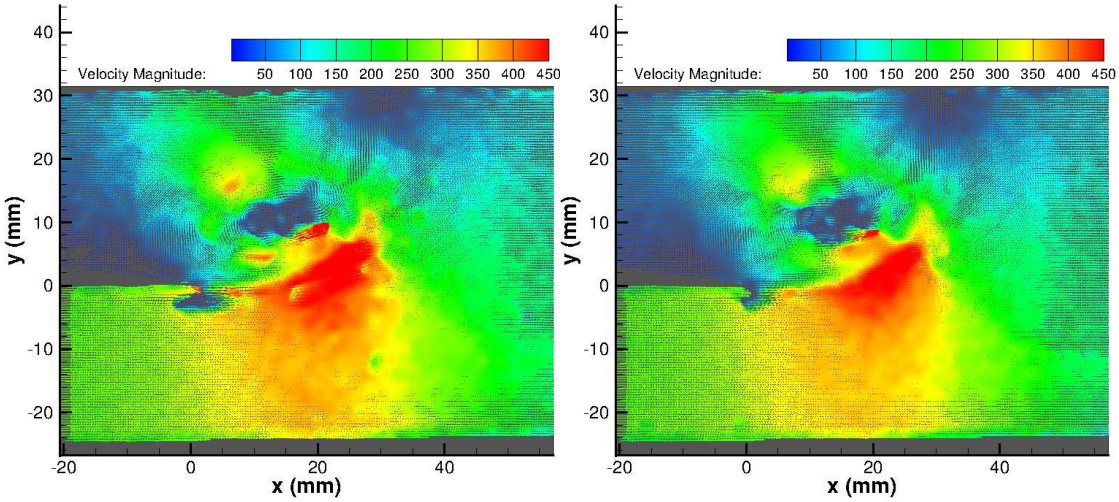

(k) 236 μs (l) 244 μs

Figure 5.39: PIV vector plot of $M_i = 1.46$ shock diffraction process around a sharp geometry

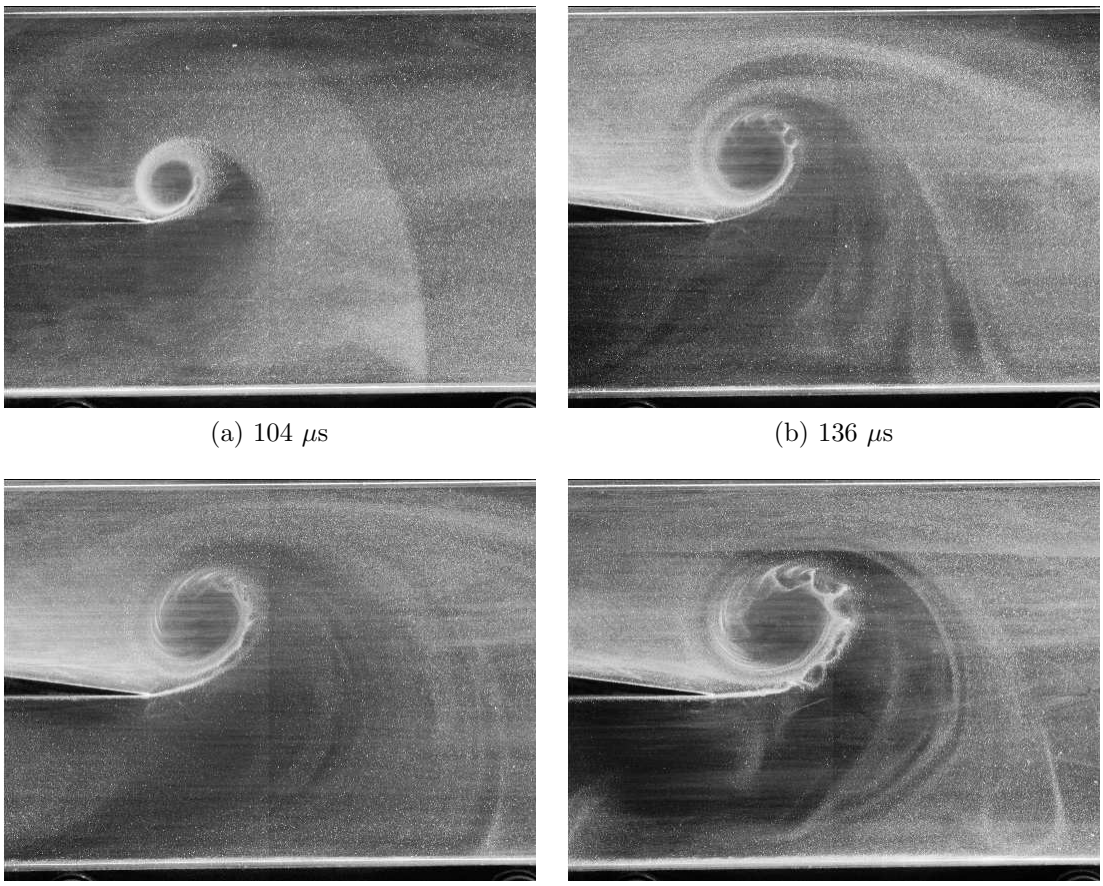

(a) 104 μs (b) 136 μs

(c) 168 μs (d) 216 μs

Figure 5.40: PIV raw images of $M_i = 1.46$ shock diffraction process

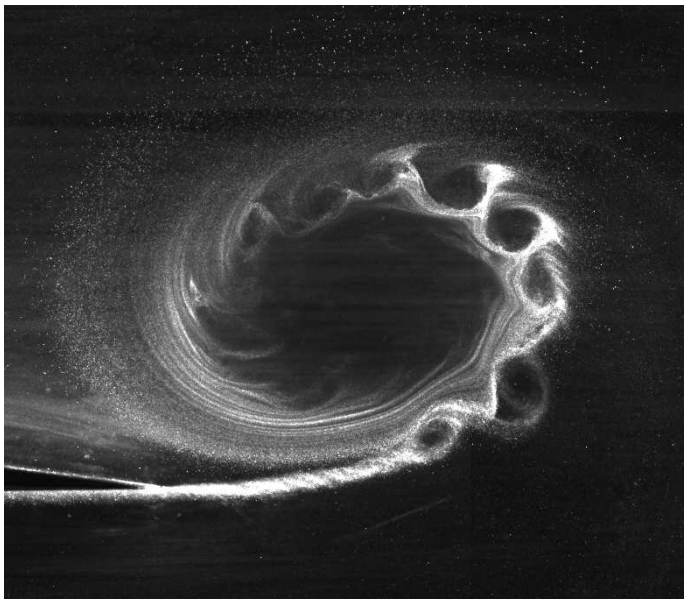

Figure 5.41: Close-up PIV raw image of the $M_i = 1.46$ complex region at 236 μs

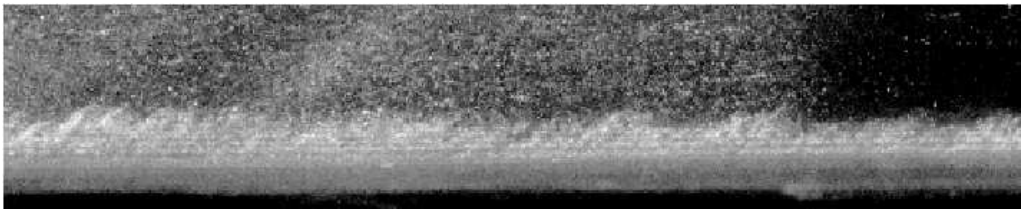

Figure 5.42: Close-up PIV raw image of the boundary layer $M_i = 1.46$ shock at 236 μs

Fig.5.44 shows the PIV vector plot of the shock diffraction and shock-vortex interaction process. Fig.5.44a shows the point at which the shock wave arrives at the apex of the corner. The induced velocity profile is uniform and horizontal, with an average induced velocity of 264 ms^{-1}.

The subsequent figures (5.44b to 5.44d) show the development of the velocity profile before the diffracted shock wave impacts on the top wall of the test section. In these figures, the velocity change induced by the reflected expansion wave does not propagate as far upstream, due to the increased induced velocity.

The lambda structures seen in the density-based results are not repeated here; this is most likely as a result of the relaxation length of the seeder particles. Again, the diffracted wave appears to have degenerated into an acoustic level wave above the splitter. Figs. 5.44e & 5.44f show the difficulties in measuring the velocity of the fluid in the expansion region under the shear layer. There are several holes in the vector plot where there were insufficient particles. Increasing the number of particles had the effect of saturating the camera in the regions around the shear layer (see Fig.5.45) and still did not yield improved results in this region.

Fig.5.44h begins to show signs of the accelerated flow inside the shear layer. Approximately 45° around the vortex, a region of high-speed fluid can be seen inside the shear layer. This position agrees well with the embedded shock seen in the density-based results, as shown in Fig.5.14.

The effect of the returning diffracted shock wave can most clearly be seen to the top left and bottom right of the main vortex. In these regions the vector plot shows sharp changes in velocity, corresponding to the shock waves seen in Fig.5.14. The maximum velocity shown in the vector plots increases from Fig.5.44j onwards. This corresponds to a broadening of the expansion region due to the effect of the returning diffracted shock. As the region broadens, the acceleration of the seeder particles can take place over a larger area, meaning that the particles have a longer time to reach the flow velocity. As before, the returning diffracted shock wave makes more progress upstream inside of the shear layer than outside, due to the smaller induced velocity in this region.

The distortion of the main vortex due to the shock-vortex interaction is clearly seen in the latter images of Fig.5.44. The vortex appears to become more elongated and narrow as time progresses.

Unsurprisingly, Fig.5.44 showed no sign of instabilities on the shear layer. However, the raw PIV images do show some disturbances propagating around the main vortex, both before and after the impact of the returning shock wave. Fig.5.45a shows some disturbances around the shear layer from approximately 50° around the

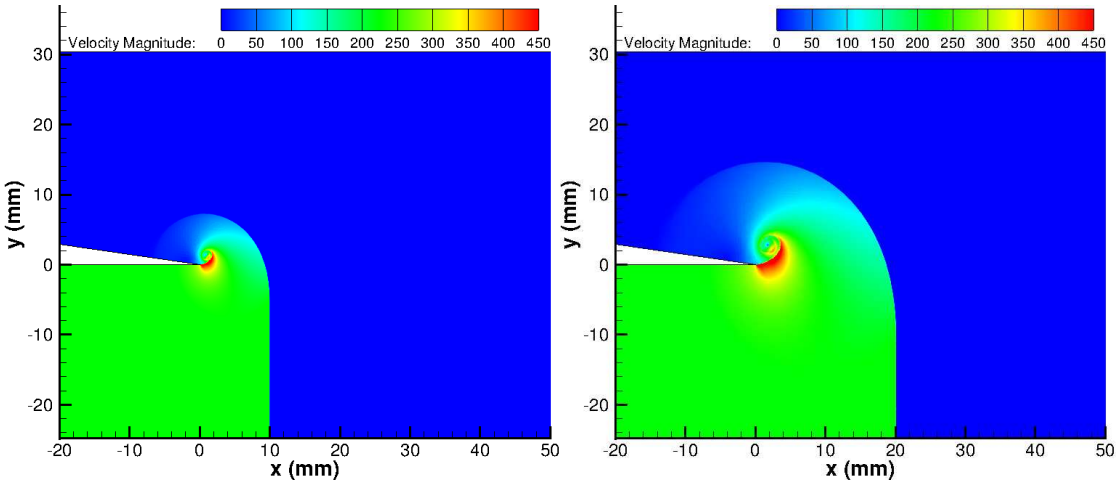

(a) 20 μs (b) 40 μs

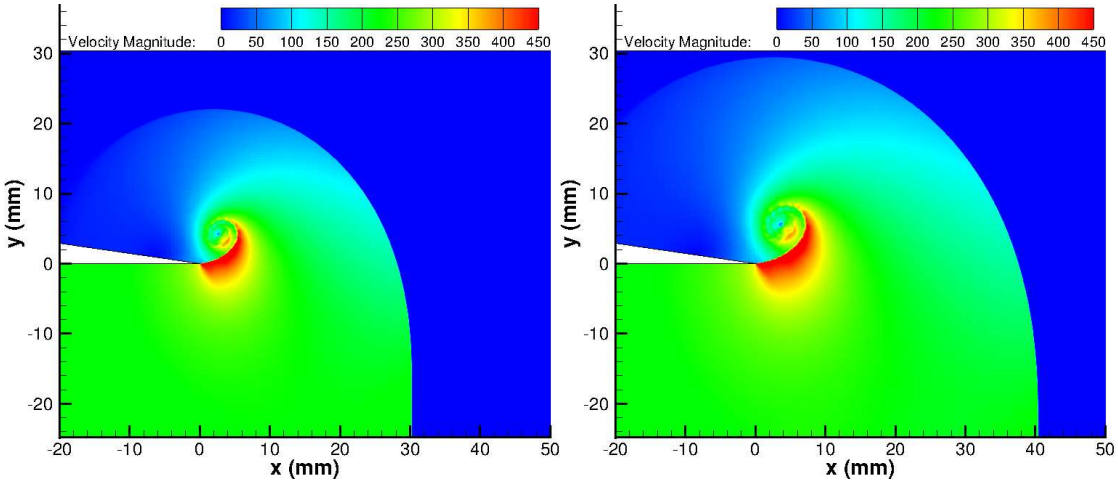

(c) 60 μs (d) 80 μs

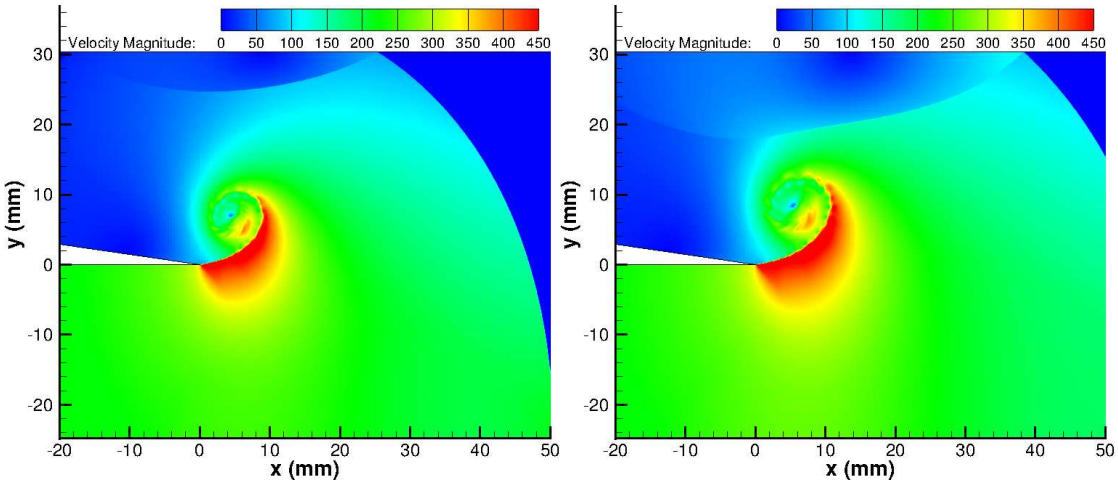

(e) 100 μs (f) 120 μs

Figure 5.43: Numerical velocity flood plot of $M_i = 1.46$ shock diffraction process around a sharp geometry

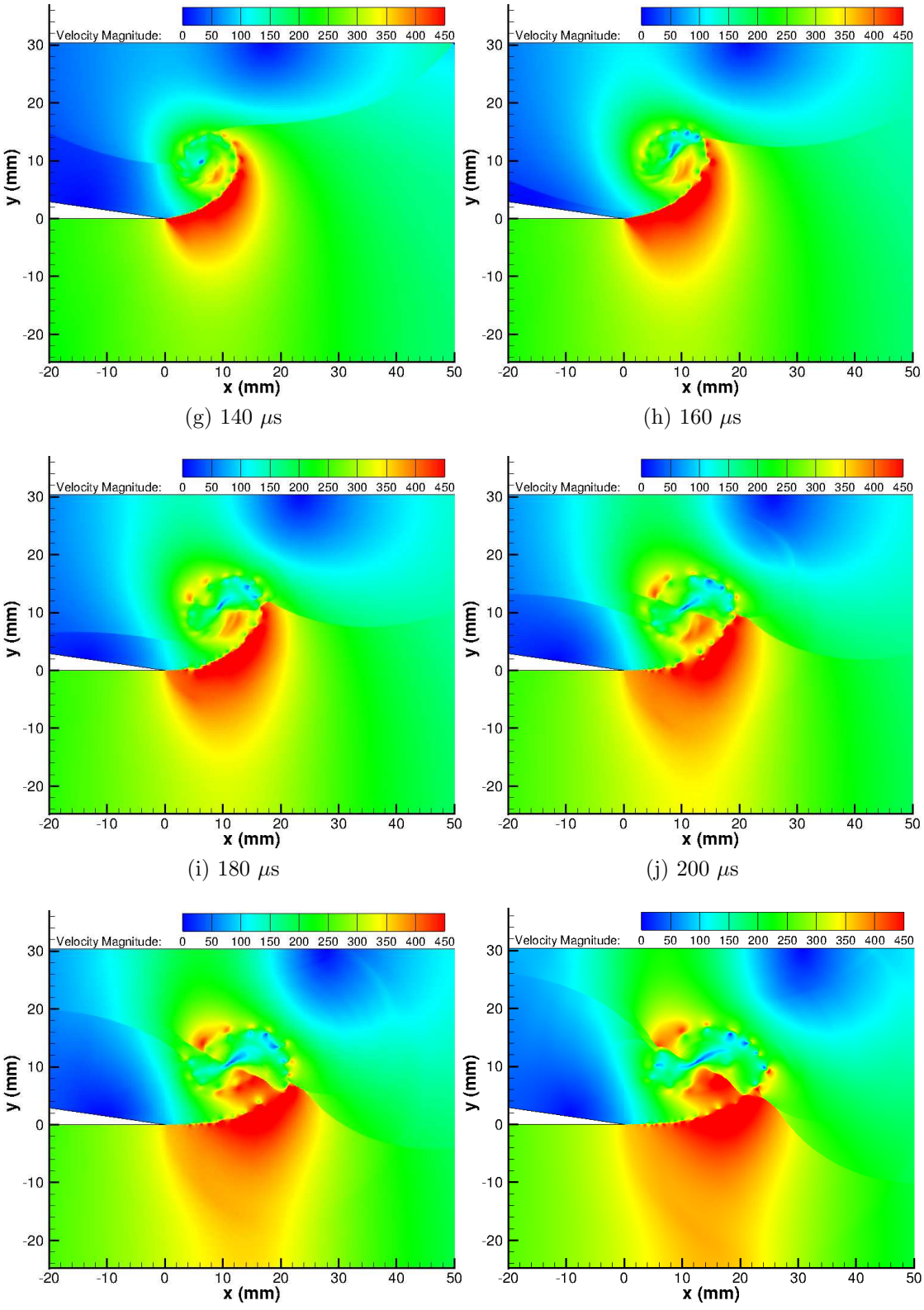

(g) 140 μs (h) 160 μs

(i) 180 μs (j) 200 μs

(k) 220 μs (l) 240 μs

Figure 5.43: Numerical velocity flood plot of $M_i = 1.46$ shock diffraction process around a sharp geometry

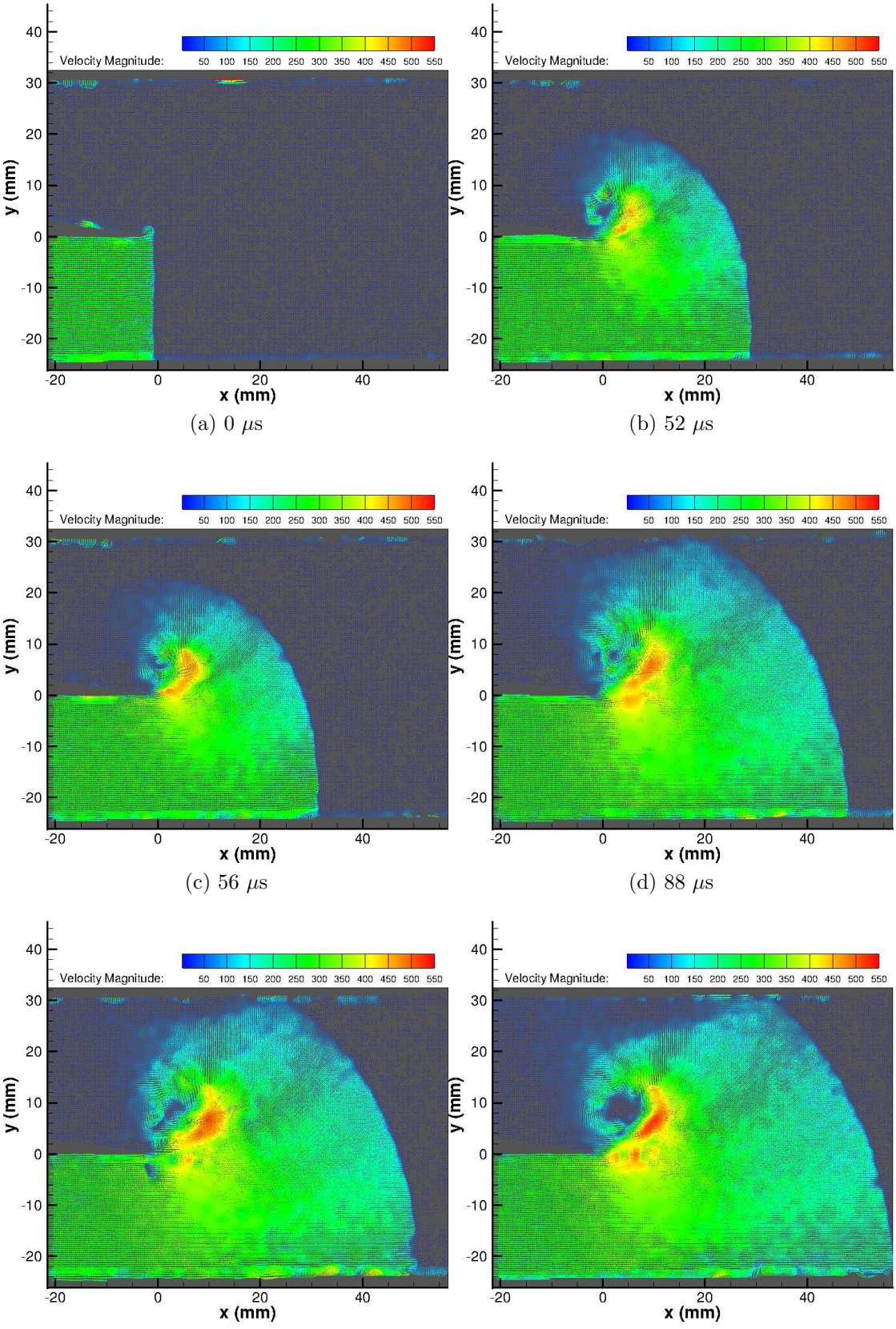

(a) 0 μs (b) 52 μs

(c) 56 μs (d) 88 μs

(e) 96 μs (f) 104 μs

Figure 5.44: PIV vector plot of $M_i = 1.55$ shock diffraction process around a sharp geometry

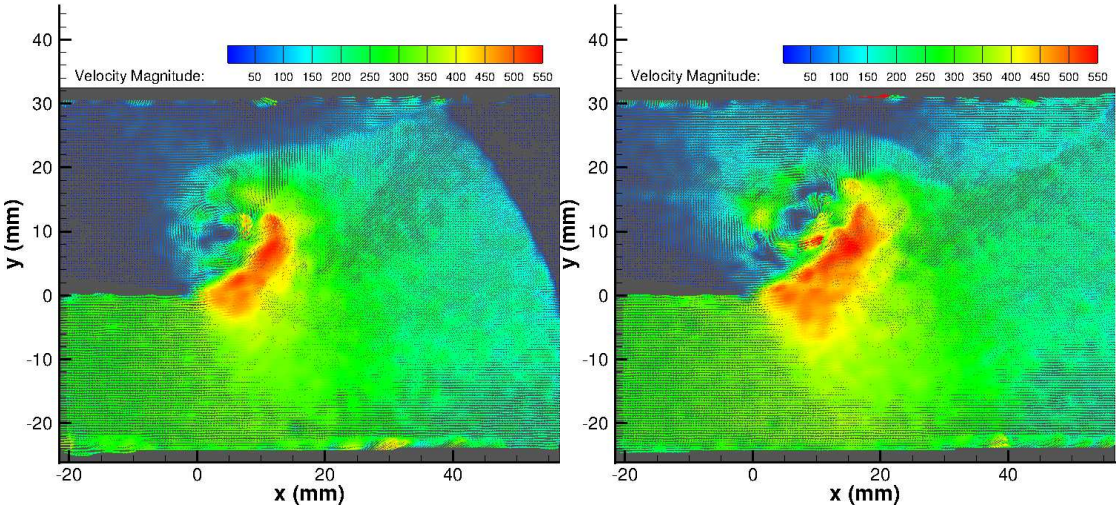

(g) 116 μs (h) 148 μs

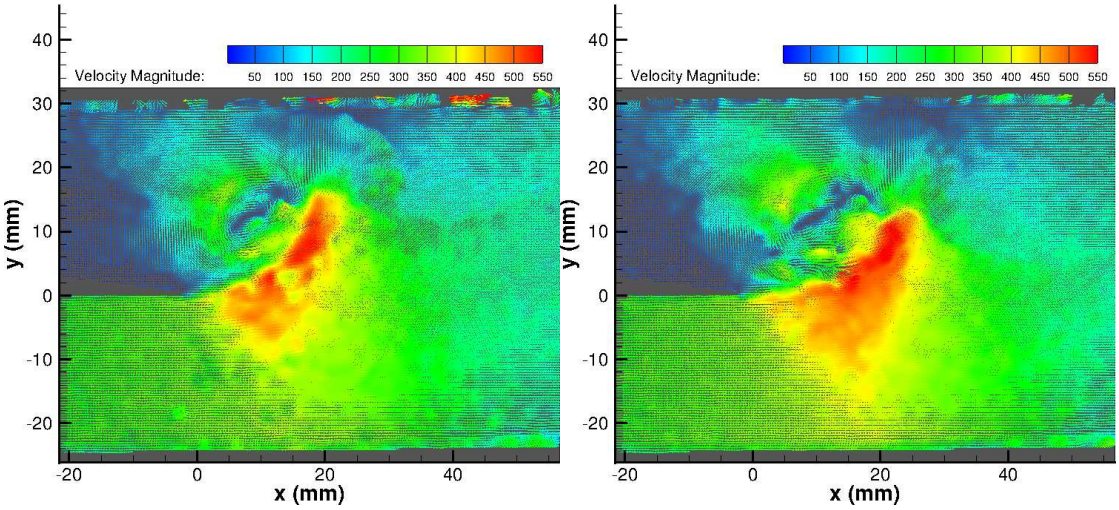

(i) 176 μs (j) 196 μs

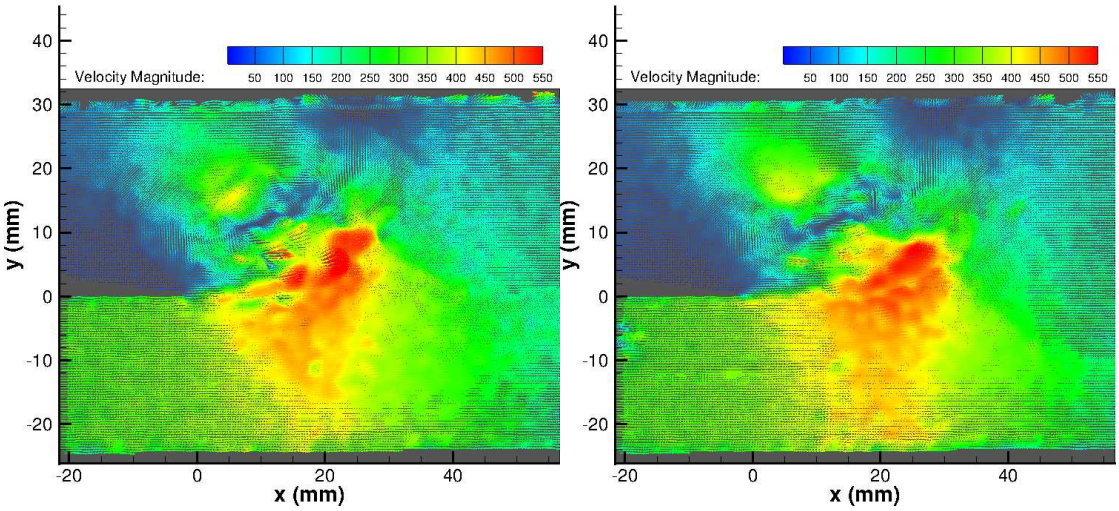

(k) 220 μs (l) 260 μs

Figure 5.44: PIV vector plot of $M_i = 1.55$ shock diffraction process around a sharp geometry

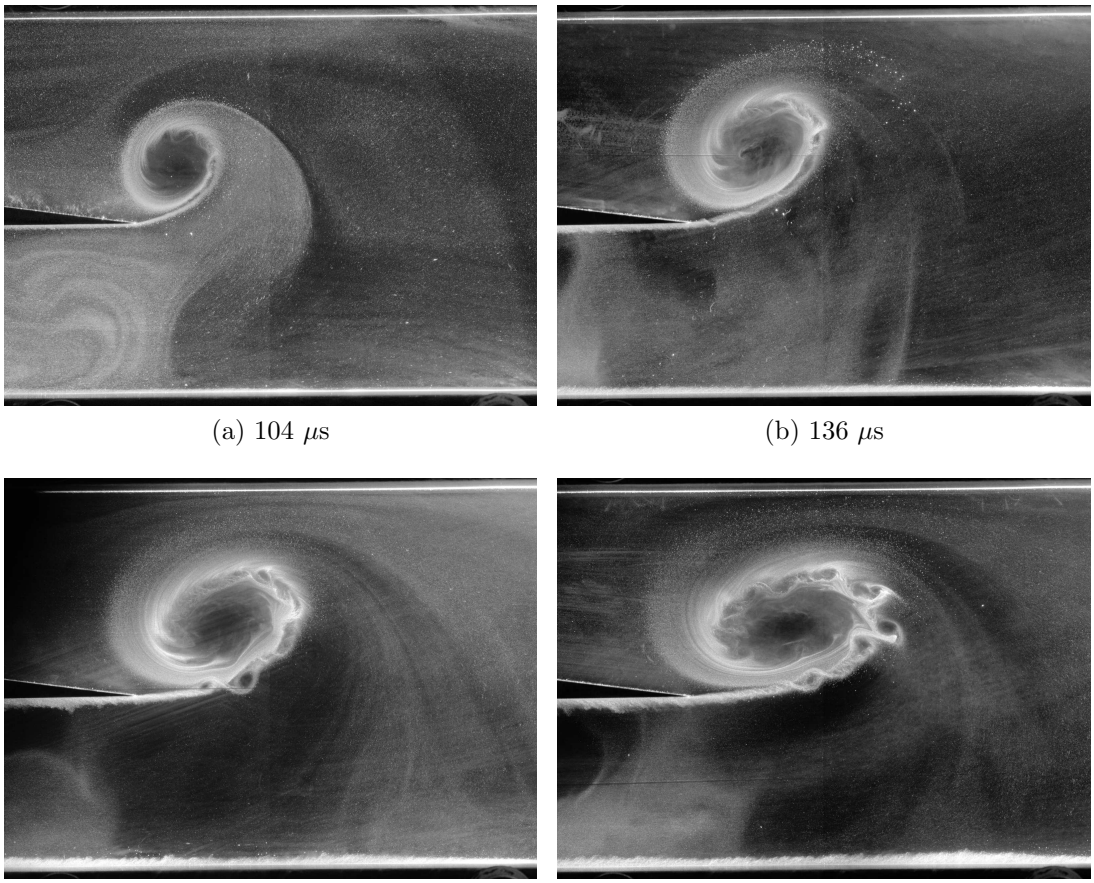

(a) 104 μs (b) 136 μs

(c) 168 μs (d) 216 μs

Figure 5.45: PIV raw images of $M_i = 1.46$ shock diffraction process

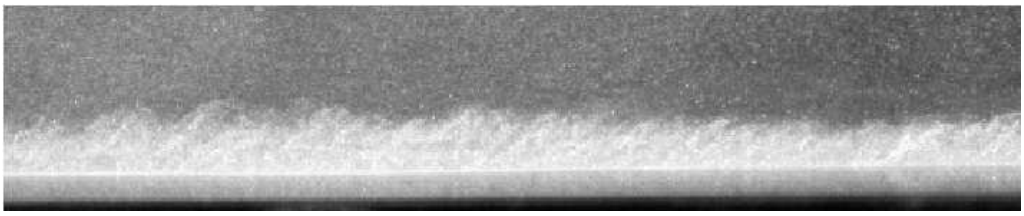

Figure 5.46: Close-up PIV raw image of the boundary layer behind a $M_i = 1.55$ shock at 244 μs

vortex until they dissipate completely by around 300°. After the impact of the returning shock wave in Fig.5.45b, each individual instability is slowed and becomes more visible. Fig.5.45c shows the two strong vortices generated by the impact of the returning shock wave on the splitter. Similarly to the $M_i = 1.46$ case, there do not appear to be any coherent structures on the shear layer after the generation of the two strong vortices.

The boundary layer for the $M_i = 1.55$ case is, as expected, slightly thicker than the previous cases with an average structure height of approximately 1.19 mm (Fig. 5.46). This figure shows a greater variation in boundary layer thickness across the image compared to Figs. 5.37 & 5.42, indicating a higher turbulent intensity.

5.2.1.6 Mi = 1.55 Numerical Results

As before, the numerical simulations appear to agree very well with the experimental results. The velocity profiles are qualitatively similar; however, there are some small differences. The incident shock-induced velocity is 262 ms^{-1}, which is slightly higher than the experimental and analytical values. The velocity predicted below the shear layer in Figs. 5.47a to 5.47e is higher than the experimental values. In the region of the instabilities on the shear layer, the velocity is as high as 620 ms^{-1}. However, just outside the region of influence of the instabilities the velocity is approximately 540 ms^{-1}, only 3% higher than the experimental value of 524 ms^{-1}. As the simulation is completely inviscid, the velocities predicted may be slightly too high due to the lack of viscous losses; however, the difficulty in adequately seeding the flow in this region makes this conclusion less certain. Individual lambda structures at 90° around the vortex are reasonably well resolved by the numerical velocity flood plots; however, as in the numerical density-based results, the second large lambda structure is not clearly seen.

The region of high velocity fluid inside the shear layer is seen from 5.47b onwards and is curtailed by a shock wave corresponding to the same location around the vortex, as was seen in the vector plots.

The shock-vortex interaction seen from Fig.5.47g onwards corresponds very well with the experimental results, showing the region of high velocity to the top left of the vortex and the shock wave that ends it. The progress of the returning shock on the right-hand side of the vortex is again well reproduced. The velocity profile at 220 μs is almost exactly the same, both qualitatively and quantitatively, showing that the simulations have reproduced this behaviour very accurately.

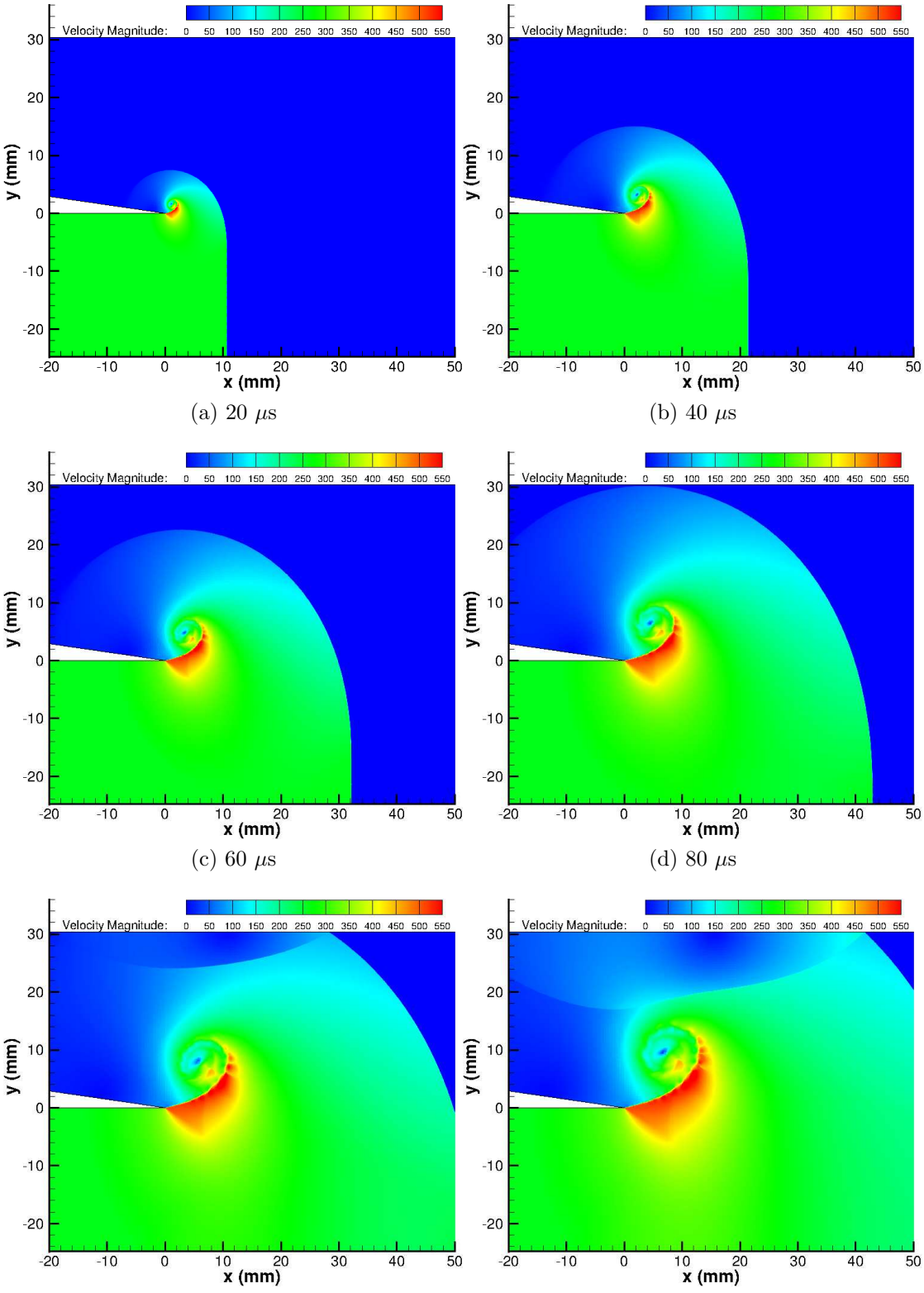

(a) 20 μs (b) 40 μs

(c) 60 μs (d) 80 μs

(e) 100 μs (f) 120 μs

Figure 5.47: Numerical velocity flood plot of $M_i = 1.55$ shock diffraction process around a sharp geometry

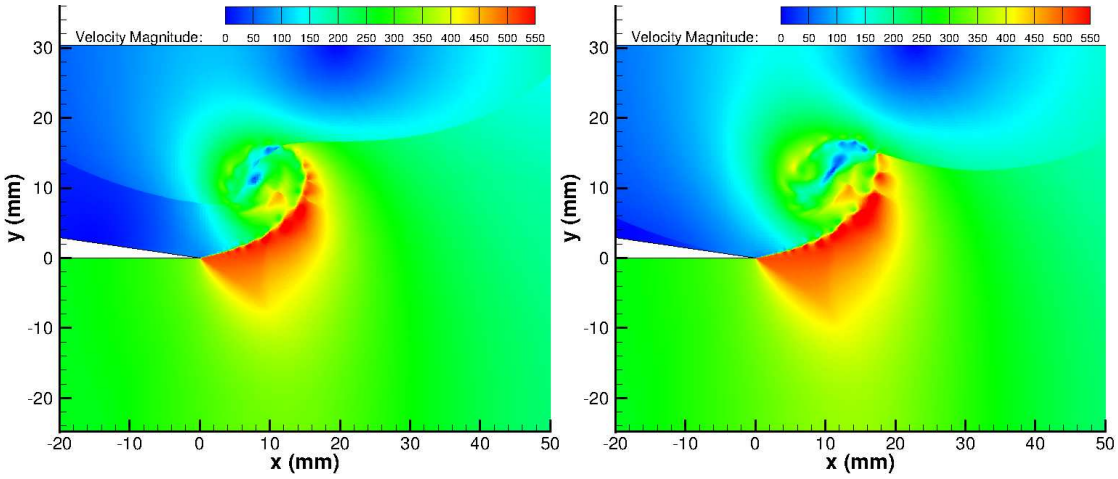

(g) 140 μs (h) 160 μs

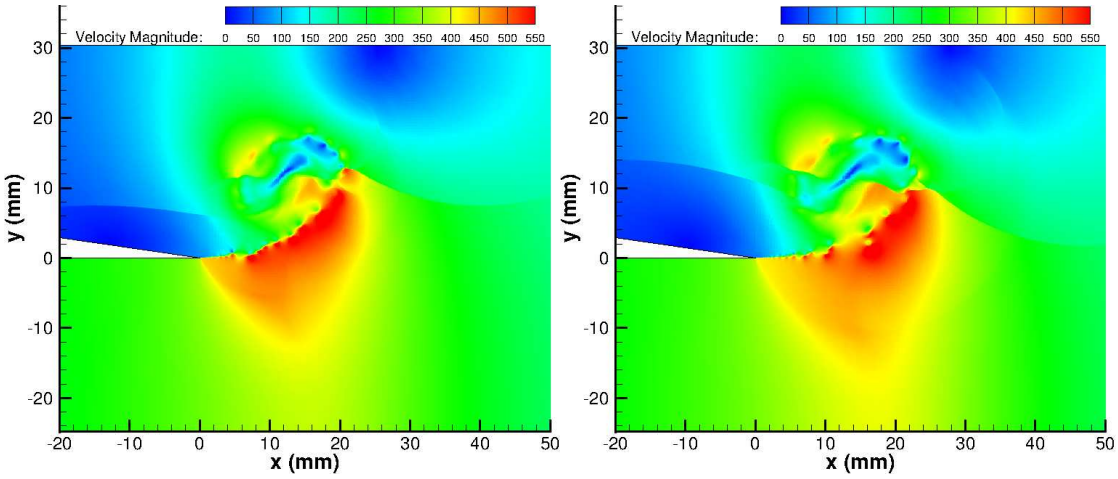

(i) 180 μs (j) 200 μs

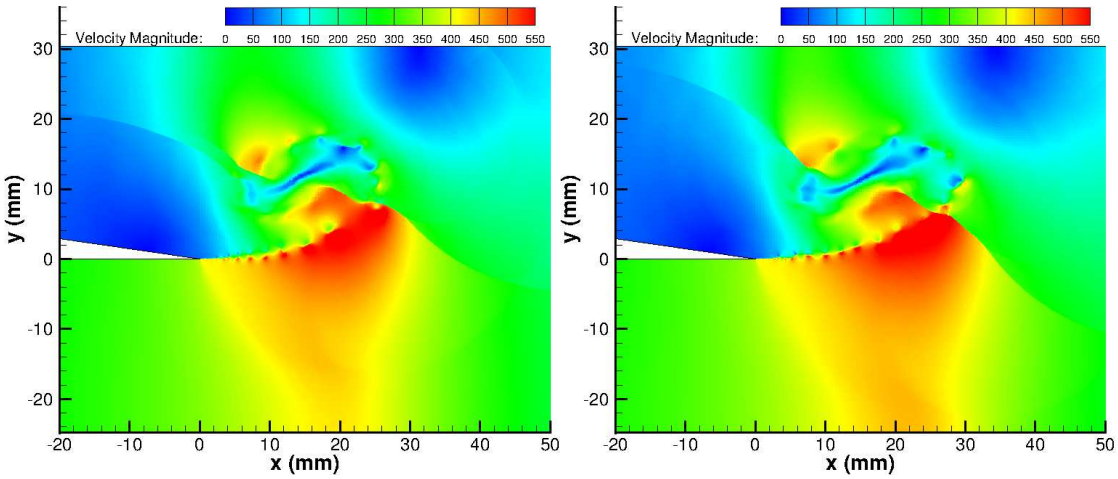

(k) 220 μs (l) 240 μs

Figure 5.47: Numerical velocity flood plot of $M_i = 1.55$ shock diffraction process around a sharp geometry

5.2.1.7 Conclusions

Particle image velocimetry has been successfully applied to the problem of shock wave diffraction and shock-vortex interaction for the first time. The velocity induced behind the incident shock wave is measured and the front of the shock wave is well resolved. The unsteady nature of the flow led to significant timing problems, with only a limited degree of control over each individual time step being possible. The expansion region underneath the shear layer shows a clear increase in velocity compared to the rest of the flow behind the incident shock wave. The biggest variation between experimental and simulation results can be found in this region, as the simulations predict a significantly higher velocity than was measured in the experiments. It is very difficult to separate the effects of the seeder particle inertia over such a small expansion region and the possible overprediction from simulations. As opposed to the experiments, simulations predict that the maximum velocity in this region is affected by the instabilities present on the shear layer. The velocity in the rest of the expansion region, for all three incident Mach numbers, agrees very well between the experiments and simulations. It is curious to note that in the $M_i = 1.28$ simulations, the expansion region shows pockets of slightly supersonic flow ($1.00 < M < 1.01$) with no associated shock waves slowing the flow down again.

Measurements in vortex cores is always challenging in PIV experiments; however, none more so than this flow. Taking one example of the $M_i = 1.28$ case at 140 μs (Fig.5.34e) we can see that the velocity around the top of the vortex is approximately 250 ms^{-1}. Given that the radius from the vortex core to that point is approximately 6 mm, the centripetal acceleration is approximately $10^6 g$. As a result of such large centripetal forces, it is not surprising that even nano-particles are ejected from the vortex, making PIV measurements in the core practically impossible. Despite the difficulties in attaining quantitative data inside the vortex core, the particle inertia does allow us to use the raw PIV images as flow visualisation. The inertial characteristics of the seeder particles highlight the vortex core and show an outline of the flow instabilities on the shear layer. The evidence of these instabilities is clearer in these results than in any others presented. Figs.5.35, 5.40 & 5.45 show how the growth of the shear layer instabilities slows as the incident Mach number increases. This agrees well with the results presented in Section 5.1.1. The secondary instabilities created after the returning shock wave has impacted on the shear layer, highlighted in Fig.5.36, are only present in the $M_i = 1.28$ and are not conclusively visible in subsequent cases. The two large vortices created are present for all of the Mach numbers tested. Despite this, the numerical simulations predicted that all of the cases showed the secondary stream of instabilities. Given that in the simulations the grid spacing is extremely small and the flow is inviscid, the shear layer acts as a vortex sheet, as discussed in Section 2.5. The $M_i = 1.28$ case shows that the boundary layer is hardly thickened as the flow proceeds in time (Fig.5.36); however, the higher Mach number cases show a thickening of the boundary layer (Figs. 5.41 & 5.45). This thickening means that the shear layer will be significantly thicker and, as discussed in Section 2.5, thicker shear layers act in a more viscous manner and can be stable for short wavelengths.

The shock-vortex interaction was captured with some success using PIV. The strength of the shock wave returning from the top surface and the subsequent shocks it generates vary wildly in strength; as such, it is unreasonable to expect PIV to

resolve all of the flow features present. The strongest returning shock wave is found on the right-hand side of the main vortex. This is particularly evident in the latter images of Figs.5.39 & 5.44, where the large expansion region clearly has a discontinuous velocity decrease. The returning shock wave has the effect of slowing the flow down in the upper right region of Fig.5.47k, for example. This stagnation region was well captured in both the experiments and the simulations.

5.2.2 Round Geometry

5.2.2.1 Mi = 1.28 Experimental Results

Fig.5.48 shows the time evolution of the flow around a rounded corner. As with the sharp geometry, there is no vertical component of velocity until the influence of the reflected expansion wave is felt by the flow. The inlet velocity is 141 ms^{-1}, which compares very well with the predicted velocity of 143 ms^{-1}. The shock front is well resolved and shows the expected curvature as it diffracts around the corner. Figs. 5.48a & 5.48b show no signs of flow separation around the corner, as there are no holes in the vector plot and no recirculation in the flow. However, by 64 μs (Fig.5.48c), there are signs of recirculation and some noticeable gaps in the data due to non-uniform seeding. The velocity in the complex region is higher than in the uniform inlet region, indicating the strength of the main vortex. The lack of uniform seeding, especially inside the vortex, makes quantitative interpretation of the PIV results in this area very difficult, as we know from the schlieren images that the main vortex remains in close proximity to the wall for a significant amount of time. There are regions of very high velocity fluid below the shear layer corresponding to the expansion wave in this region; however, we know from the density-based results that this structure is not very large, a finding repeated from the PIV results, as this region is relatively small.

As the wave pattern expands in time, a stagnation point moves along the top surface of the splitter in the corresponding location to the contact surface seen in the density-based results. This observation indicates that the conclusion by Skews [32] that the contact surface is a good indication of fluid motion is justified. Figs.5.48e & 5.48f show the diffracted shock wave reflecting off the top surface of the test section and propagating downwards towards the complex region. By Fig.5.48h the vortex has grown in size and strength to begin to eject particles from its core, leaving holes in the vector plot indicating its centre. In this figure we can see that there is a region of high-speed fluid between the vortex core and the rounded corner of the splitter. This region of high-speed fluid corresponds to the location of the internal expansion region discussed in Section 5.1.2. The slug of high-speed fluid persists in all of the subsequent PIV vector plots and is terminated at the same location as the internal terminating shock seen in Figs.5.19 & 5.20. Fig.5.48l shows a region of very high-velocity fluid just below the vortex core. This high-velocity fluid corresponds to the location of the strongest shock seen in the density-based results, MR_3, as discussed in Sections 5.1.1.7 & 5.1.2.7.

With the exception of the wave MR_3, the shock-vortex interaction does not appear to have significantly affected the flow, apart from transforming the vortex into a more circular shape as there are no more strong discontinuities.

Throughout the development seen in Fig.5.48, there is no information available about the structure of the shear layer(s) and the region immediately adjacent to the splitter edge. The early raw PIV images show no distinct shear layer (Fig.5.49a). At later times, after the shock-vortex interaction, the shear layer is more visible (Fig.5.49b), although there does not appears to be any coherent structures present, just random structures with no discernible pattern. Fig.5.49a shows the contact surface and its impact point on the splitter clearly, along with the kink seen in the schlieren images, indicating that the flow is being drawn into the vortex in

the internal expansion region. The raw PIV images also give us some qualitative information on the development of the incoming boundary layer that separates from the curved edge. Fig.5.50 shows the boundary layer at two time steps. At 100 μs the boundary layer is still relatively thin; however, at 180 μs it has thickened considerably and is showing signs of turbulence, as it is no longer uniform in height[2].

5.2.2.2 Mi = 1.28 Numerical Results

Numerical velocity flood plots are presented in Fig.5.51. Based on the evidence from the density-based results, no data will be shown from 160 μs onwards as the wave patterns are not similar to those seen in the experiments. Initially (20 to 60 μs) the simulations qualitatively and quantitatively agree with the experimental results. The strong influence of the contact surface can be seen in both the numerical and experimental results. After the flow begins to separate, the magnitude of the velocity in the numerical simulations is significantly higher than that found in the experimental results. Unfortunately, due to the lack of repeatable seeding available in the region close to the main vortex, it is not possible to say whether the simulations overpredict the velocity or whether the experiments are seriously affected by particle lag (and lack of seeding). However, it is likely to be a combination of both of these factors. Given our experience with simulations predicting higher than measured velocities for the sharp geometry, even where adequate seeding was available, it is not unreasonable to expect this again. It is known that the seeder particles underpredict changes in velocity, so the real flow value in the complex region is likely to be between the simulated and measured values. The returning shock wave causes a stagnation point on the top wall of the test section, which agrees well with the experimental results.

It is interesting to note that, along with the expansion region and its associated shocks on the outside of the vortex, there is a region of high-velocity fluid (barely visible in Fig.5.51e but clearer in Fig.5.51f) corresponding to the internal expansion region. The magnitude of the velocity in this region is again higher in the simulations than in the measurements.

5.2.2.3 Mi = 1.46 Experimental Results

The PIV results for the $M_i = 1.46$ case show more of the complex region behind the diffracting shock wave, most likely due to the structures being more spread out and the interactions themselves being stronger. However, as the interactions in this case are stronger than in the previous case, attaining uniform seeding is a more significant problem. As a result of this, the velocity vector plots contain a significant degree of spatial noise in the complex region as it is developing, and elsewhere in the flow field at later times.

The initial diffraction profile (Figs.5.52a & 5.52b) is similar to the previous case, as the complex region has not begun to develop yet. The velocity induced behind the incident shock is measured as 214 ms^{-1}, agreeing very well with inviscid theory. In the subsequent images the influence of the reflected expansion wave can be seen

[2]A time-averaged measurement of the boundary layer would reveal a uniform thickness with the expected steep wall gradients; however, this is an instantaneous snapshot of the boundary layer, and as such it will not be uniformly thick

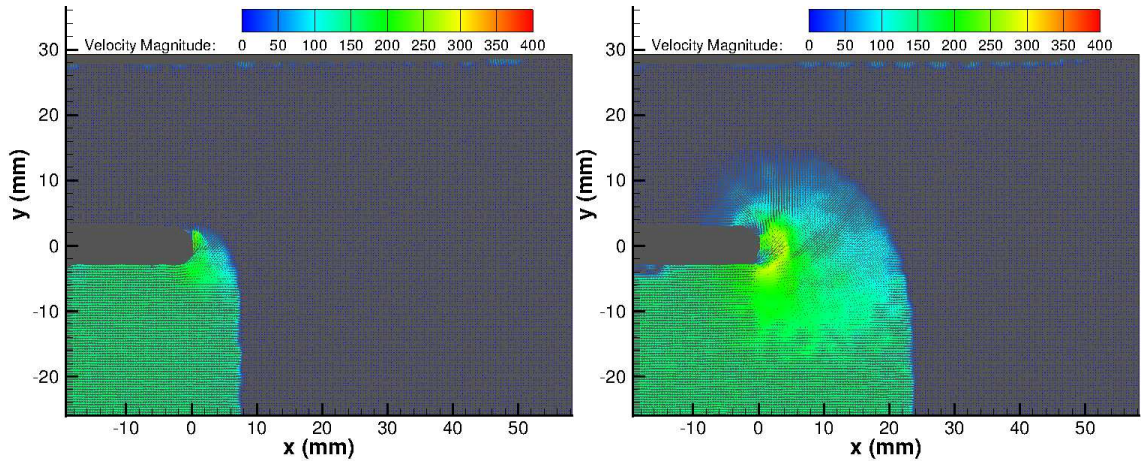

(a) 16 μs

(b) 52 μs

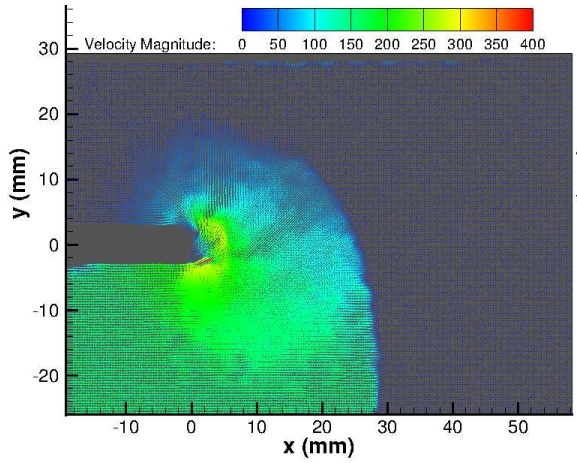

(c) 64 μs

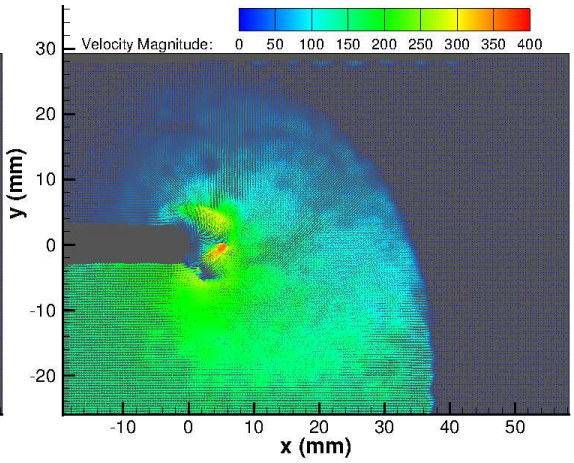

(d) 84 μs

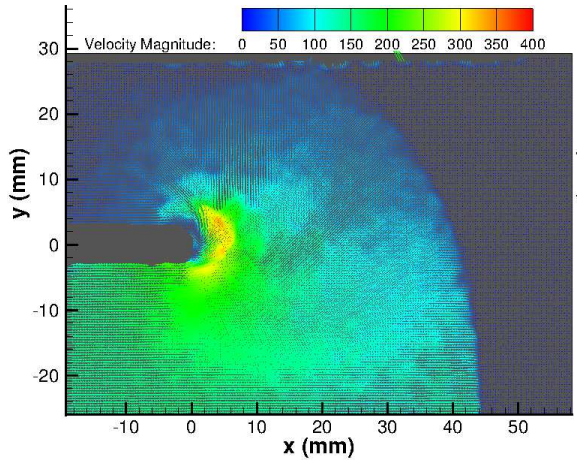

(e) 100 μs

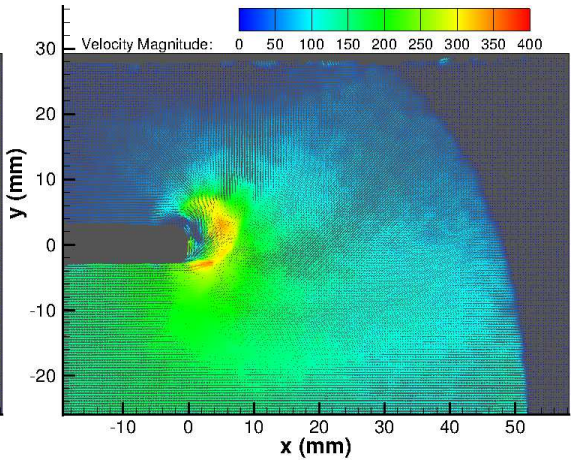

(f) 116 μs

Figure 5.48: PIV vector plot of $M_i = 1.28$ shock diffraction process around a round geometry

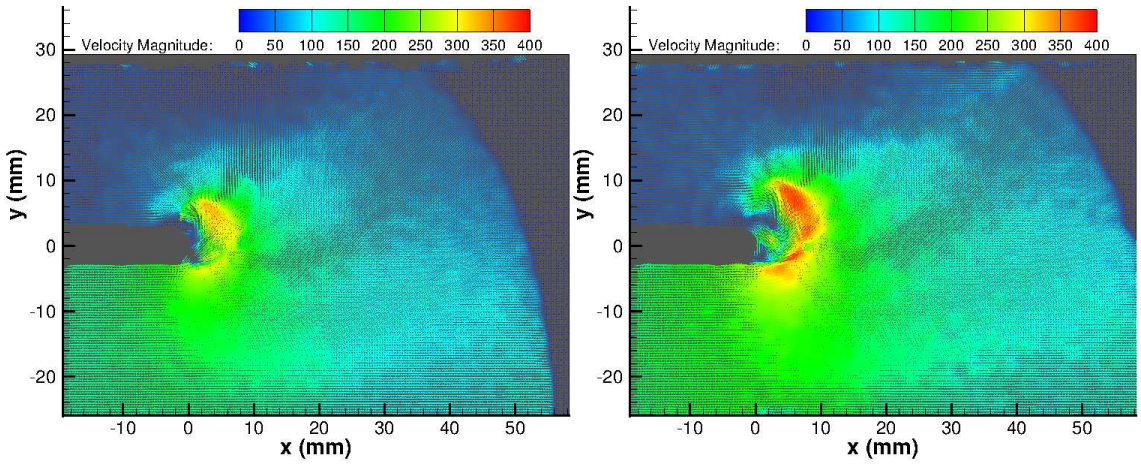

(g) 128 μs (h) 136 μs

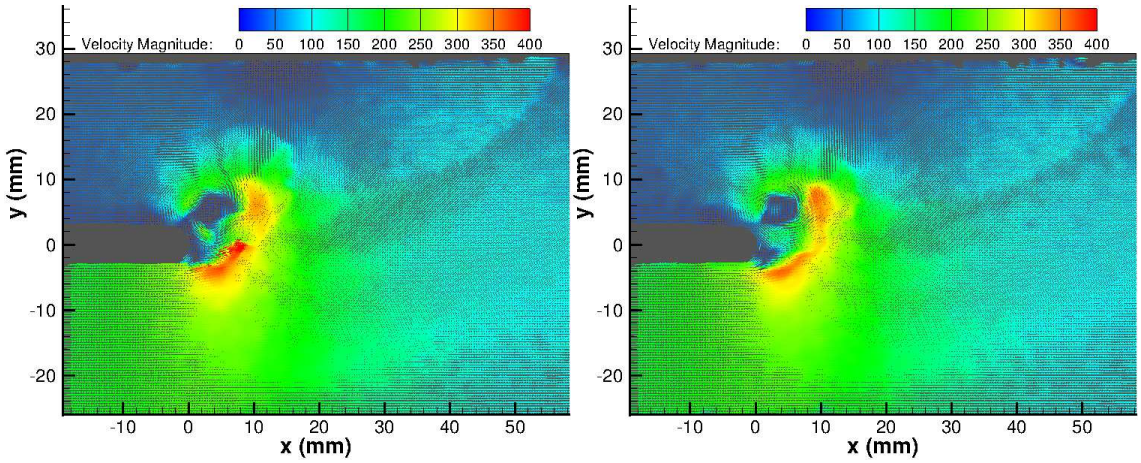

(i) 168 μs (j) 180 μs

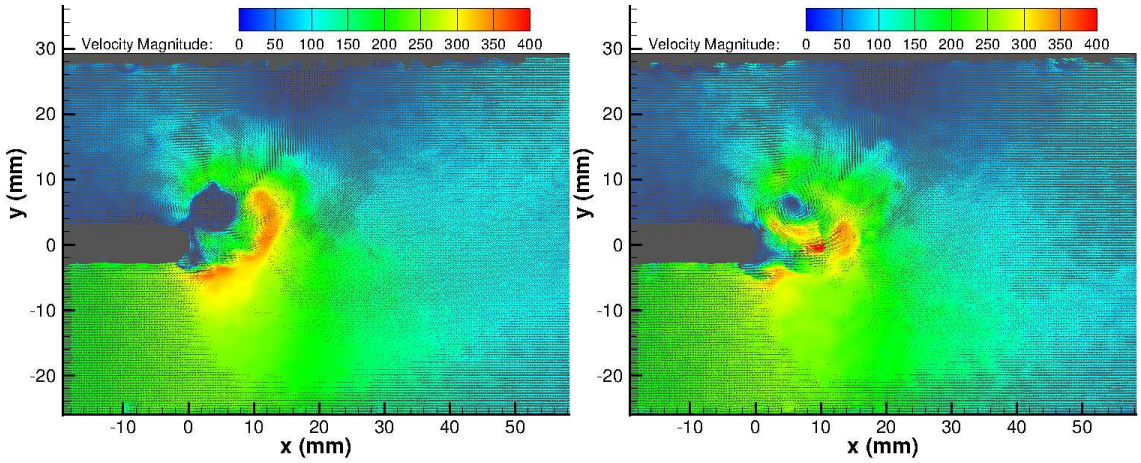

(k) 196 μs (l) 232 μs

Figure 5.48: PIV vector plot of $M_i = 1.28$ shock diffraction process around a round geometry

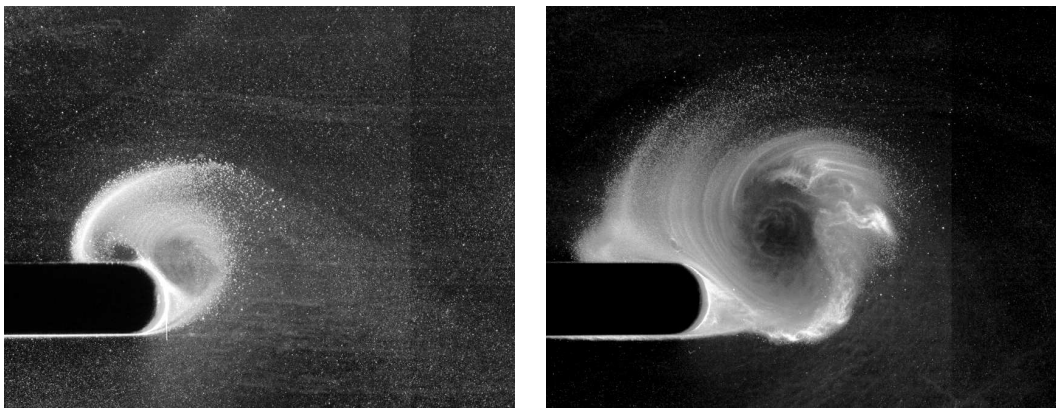

(a) 128 μs (b) 232 μs

Figure 5.49: Close-up PIV raw image of the complex region generated by a $M_i = 1.28$ shock

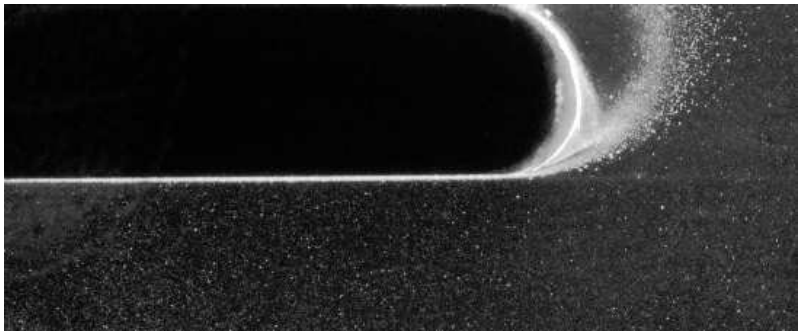

(a) 100 μs

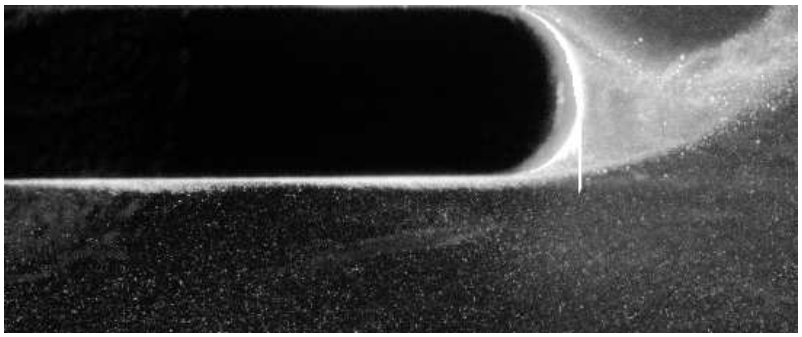

(b) 180 μs

Figure 5.50: PIV raw images of $M_i = 1.28$ boundary layer development

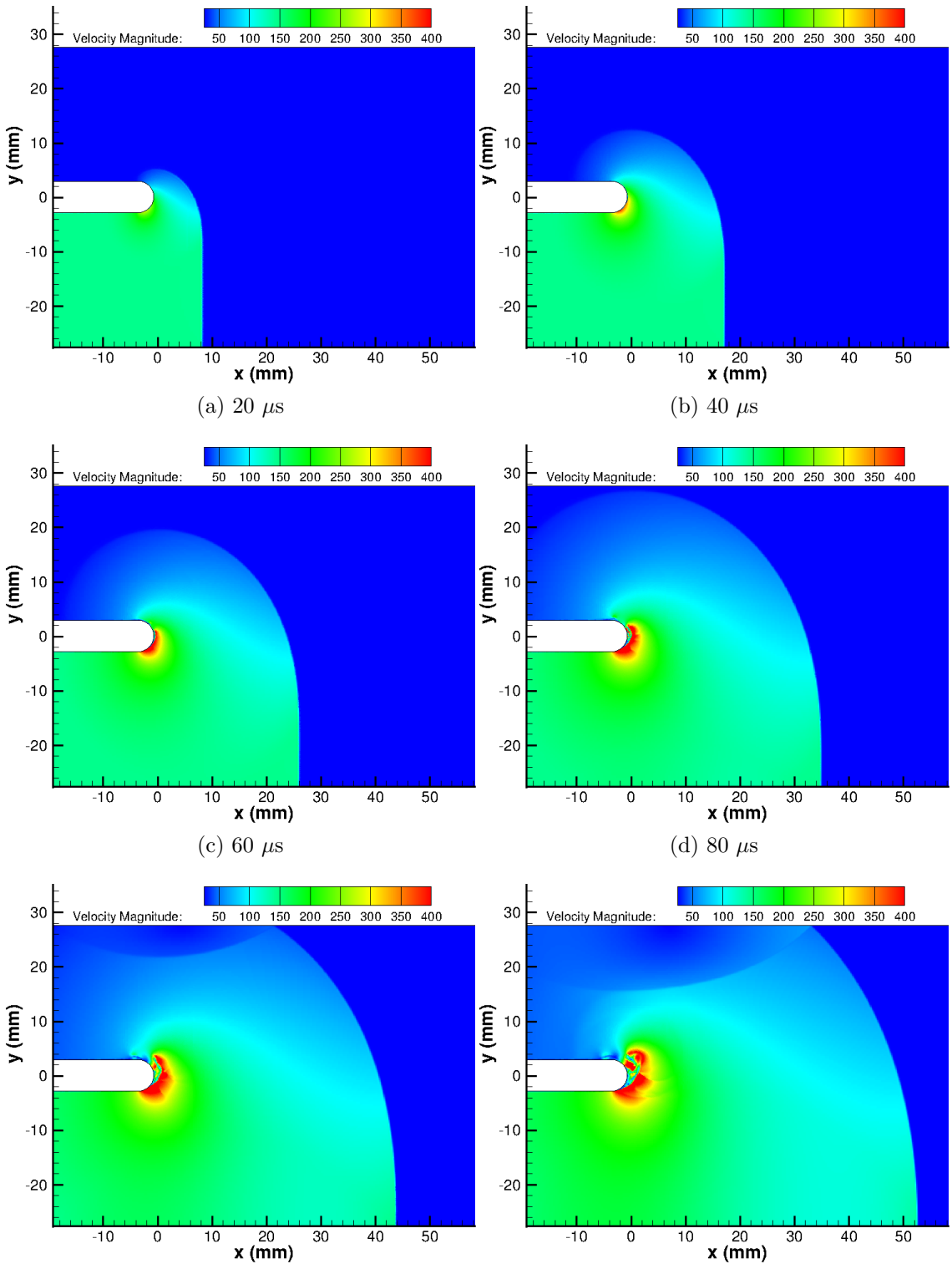

(a) 20 μs (b) 40 μs

(c) 60 μs (d) 80 μs

(e) 100 μs (f) 120 μs

Figure 5.51: Numerical velocity flood plot of $M_i = 1.28$ shock diffraction process around a round geometry

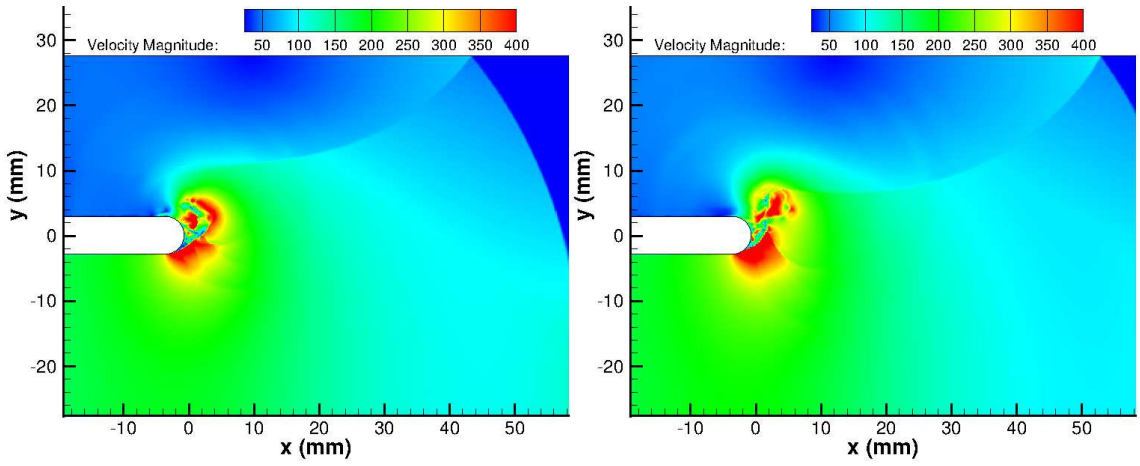

(g) 140 μs (h) 160 μs

Figure 5.51: Numerical velocity flood plot of $M_i = 1.28$ shock diffraction process around a round geometry

as the flow accelerates underneath the main vortex (Figs.5.52c & 5.52d). At 96 μs the expansion region and its associated lambda shock structure can be seen underneath the main shear layer. Fig.5.52f shows two regions of high velocity outside the shear layer, the top of which extends inside the shear layer. This correlates well with the results found in Figs.5.27f & 5.27g and the suspected expansion wave. The dark region in the schlieren images corresponds to the same location as the second increase in velocity which appears to have terminated by approximately 90° around the vortex; this is the location of the weak terminating shock. The schlieren results show that the terminating shock arises inside the shear layer and propagates across it, implying that there should be a region of high-speed, expanded fluid inside the shear layer too, as is seen in Fig.5.52f. The highest velocity measured in the expansion region at 132 μs is 471 ms^{-1}.

The internal expansion region and its terminating shock are faintly visible in Figs.5.52f & 5.52g, although the usual issues with non-uniform seeding hamper the results. The internal terminating shock seen in the density-based results is not well captured by the PIV measurements. This is not too surprising given the rotational velocity of the flow in this region. The expansion region below the main shear layer is growing in size but weakening in strength over the remainder of the PIV images. The schlieren results showed that the shock vortex interaction caused the waves in the first lambda structure to be swept upstream and therefore increasing their region of influence. This is noticeable from Fig.5.52i onwards as the expansion region below the shear layer grows rapidly in size, albeit at the cost of its strength. Around the top of the vortex there is a small region of accelerated flow which corresponds to the location of the left-hand shock-vortex interaction. However, the right-hand side of the shock-vortex interaction is considerably stronger. The expansion region containing the highest velocity fluid in Fig.5.52l is terminated by a strong discontinuity correlating to the strongest wave seen in Figs. 5.25k & 5.27k.

As before, there is no information about the shear layer structure in the vector plots, so we must resort to the raw PIV images to analyse this part of the flow. Fig.5.53 shows the complex region both before (Fig.5.53a) and after (Figs.5.53b &

5.53c) the shock vortex interaction. Fig.5.53a shows the kink in the contact surface as it is swept up into the main vortex core. The region bounded by the external and internal shear layers appears to show a trapped vortex, something not visible in the density-based results. The main shear layer does not show any coherent structures along its length; rather, just turbulent fluctuations are visible. Later images, after the shock-vortex interaction, shows that the shear layer contains several structures, but none of them are repetitive or ordered. Other raw PIV images at similar times show that the basic shape of the shear layer is the same but that the structures are not ordered, indicating turbulence rather than coherent instabilities. The proximity of the vortex to the wall at early times means that the particles which are ejected from the vortex actually impact on the rounded corner, making measurements in the internal expansion region extremely difficult until later times when the vortex has propagated away from the corner.

Fig.5.54 shows the boundary layer at two different time steps. At 100 μs the boundary layer contains some fluctuations but is still relatively thin, indicating that it is transitioning to turbulence. However, by 180 μs the boundary layer is much thicker and has completely transitioned to turbulence.

5.2.2.4 Mi = 1.46 Numerical Results

The numerical results for $M_i = 1.46$ are presented in Fig.5.55. The initial diffraction profile shown in Fig.5.55a agrees well with the measured velocity profile from the PIV experiments, with an induced velocity of 224 ms^{-1}. However, subsequent results show that the numerical velocity is significantly higher in the complex region. The expansion region below the main shear layer is much stronger and larger than the experimental results. The maximum velocity in the numerical results is 634 ms^{-1}, whereas the experimental value is 471 ms^{-1} . This value, although localised to one cell, is still significantly above the velocity measured using PIV.

Despite the quantitative disagreement between the numerical and experimental results, the qualitative agreement is very good. The shape of the expansion region is well captured, as is the second region of high-speed fluid outside the shear layer. After the lambda shock, there is a second expansion region in the same place as the experimental results (comparing Figs.5.52e & 5.55e shows this well).

The internal expansion region is resolved as a region of high-speed fluid which is ended by the internal terminating shock. The fluid passing through this shock is then accelerated again until it is stopped by the recompression shock (see Fig.5.24).

As in the experimental results, the shock-vortex interaction has the effect of spreading the main expansion region upstream at the expense of its strength. Comparing Figs. 5.52l & 5.55k shows the influence of the shock-vortex interaction on both sides of the vortex. On the left-hand side the simulations show two regions of high-velocity fluid which are seen in the experimental results (although the experimental magnitudes are significantly lower). Meanwhile, on the right-hand side, the strong shock wave **MR3** is terminating the supersonic region. The numerical results show this as a smooth shock wave, whereas the experimental results show this shock to have a strong kink in it. Based on the schlieren and shadowgraph results, the experimental results show the true profile more accurately, as there is a kink in the shock wave at that location (see Fig.5.25k). The numerical results also show a significant influence of the instabilities seen in the density-based numerical

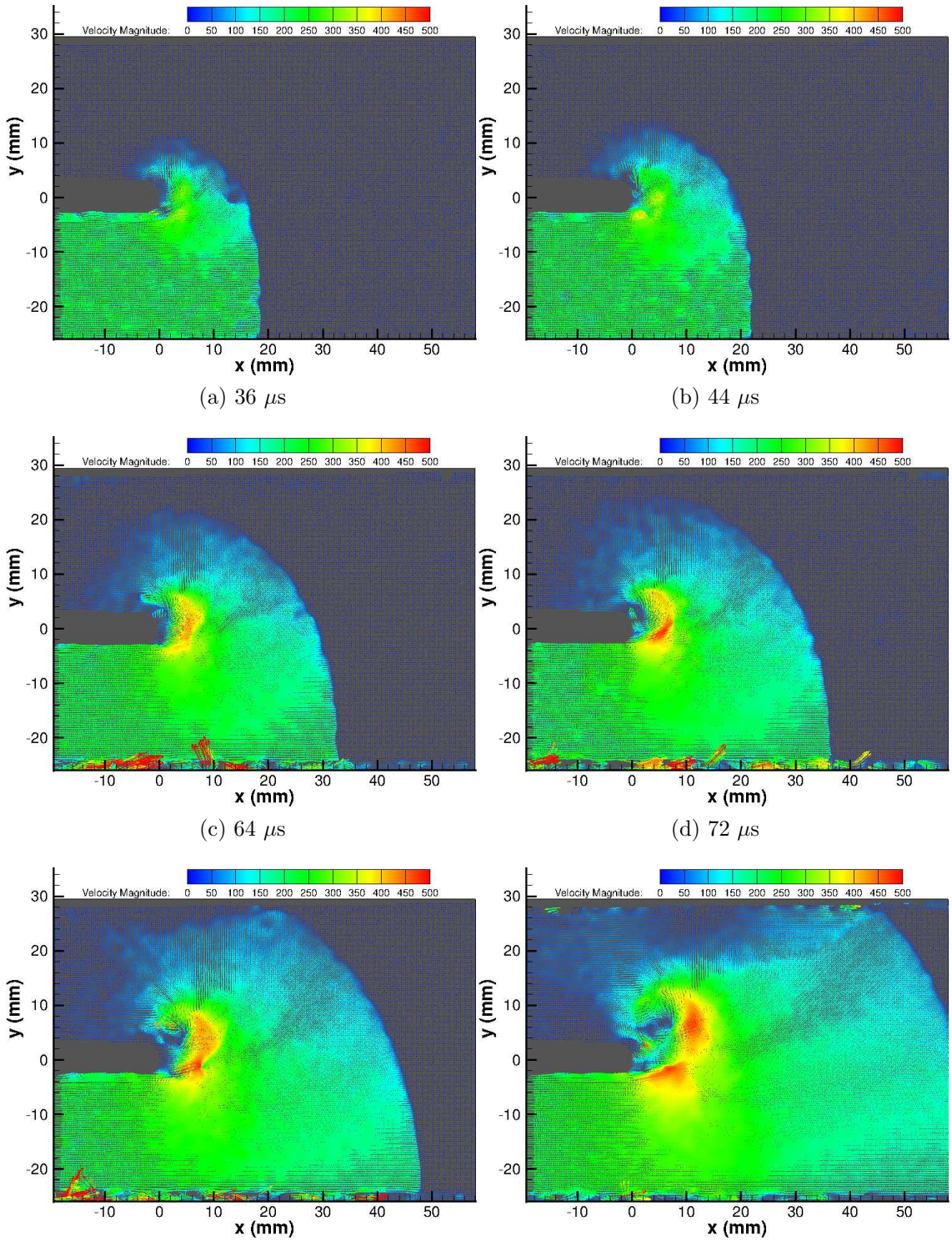

(a) 36 μs (b) 44 μs

(c) 64 μs (d) 72 μs

(e) 96 μs (f) 132 μs

Figure 5.52: PIV vector plot of $M_i = 1.46$ shock diffraction process around a round geometry

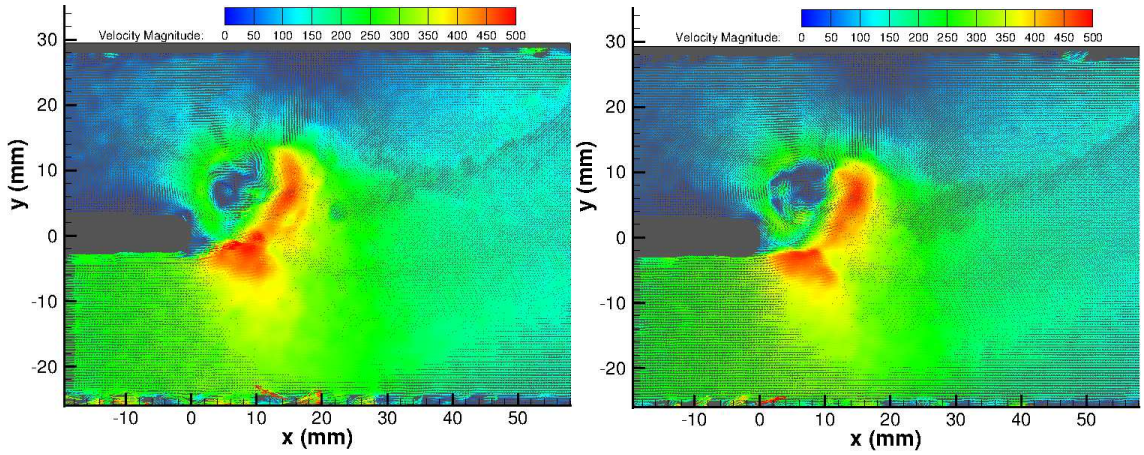

(g) 164 μs (h) 168 μs

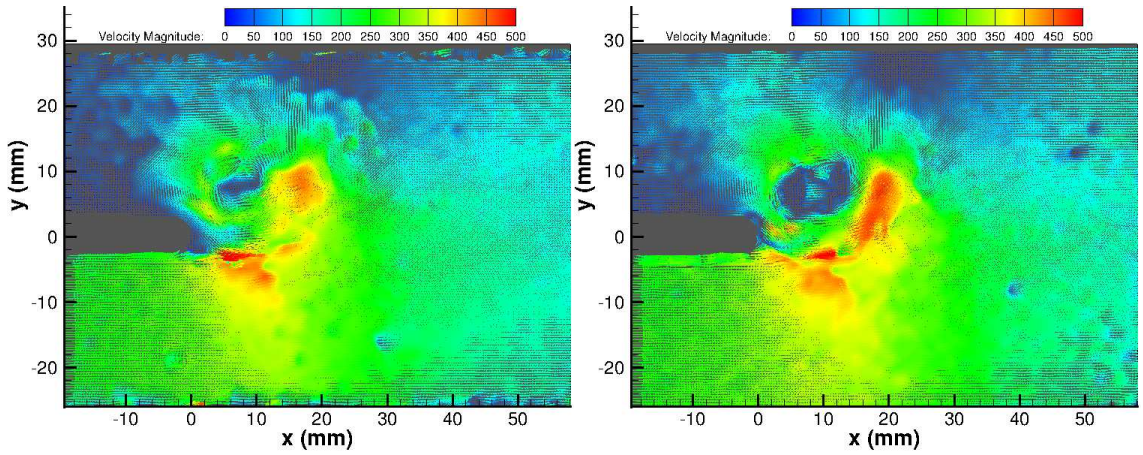

(i) 184 μs (j) 196 μs

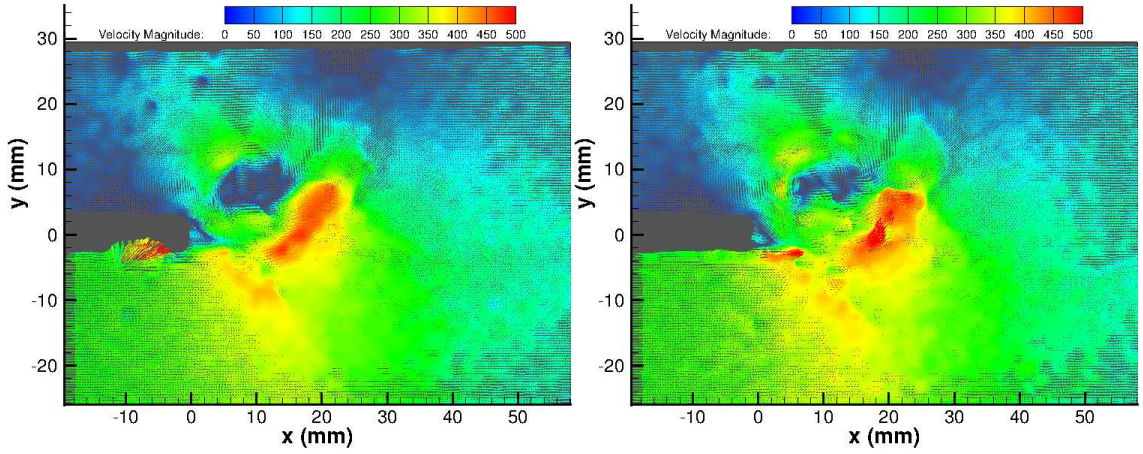

(k) 212 μs (l) 220 μs

Figure 5.52: PIV vector plot of $M_i = 1.46$ shock diffraction process around a round geometry

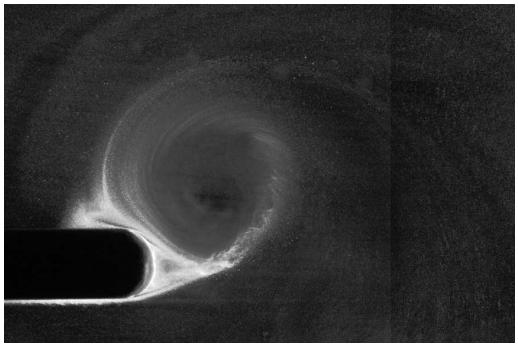

(a) 132 μs

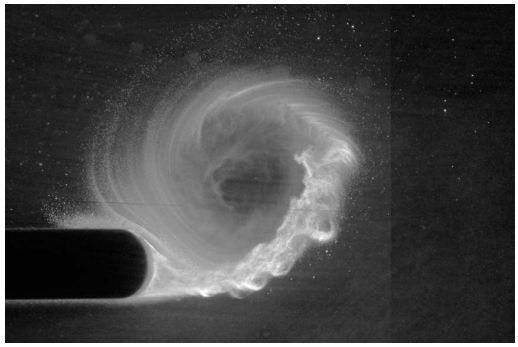

(b) 184 μs

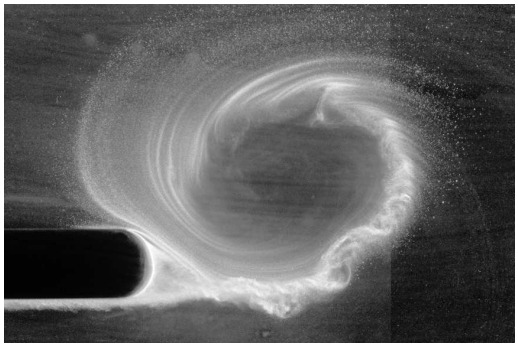

(c) 220 μs

Figure 5.53: PIV raw images of $M_i = 1.46$ complex region

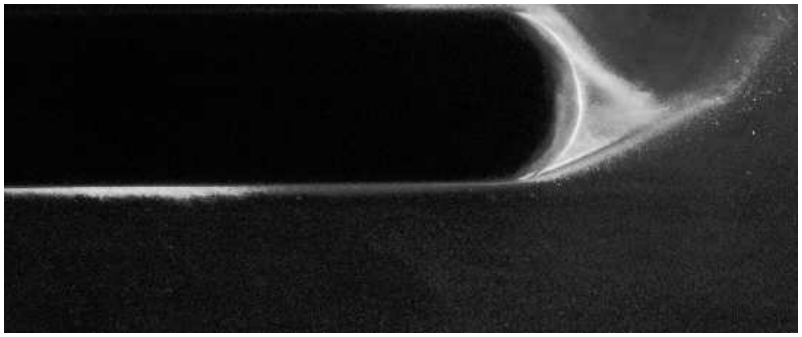

(a) 100 μs

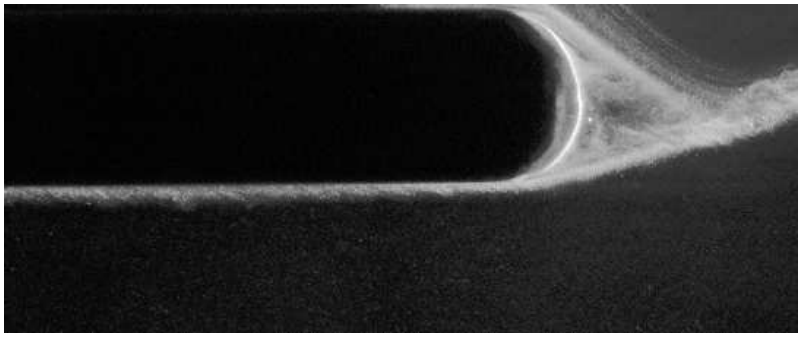

(b) 180 μs

Figure 5.54: PIV raw images of $M_i = 1.46$ boundary layer development

results, especially at later times.

5.2.2.5 Mi = 1.55 Experimental Results

In a similar fashion to the results for the sharp geometry, measurements in and around the vortex core proved impossible for this Mach number, due to the high velocities found in the region ejecting particles. Despite these difficulties, the vector plots are shown in Fig.5.56. The uniform region behind the incident shock wave has an average velocity of 236 ms^{-1} in Fig.5.56a. For the reasons mentioned previously, it was always unlikely that any measurements in the internal expansion region would be possible at this Mach number, and so it proved.

Fig.5.56a shows an increase in velocity in the complex region close to the rounded corner, but it is difficult to see the exact flow features until Fig.5.56c. In Fig.5.56c the expansion wave induces a large velocity underneath the shear layer which only appears to be significant at a reasonably large distance around the corner. This corresponds well with the density-based results, which showed the lambda shock structure to be almost horizontal in Fig.5.30d. In Figs.5.56d & 5.56e the flow is beginning to develop in the expected pattern, with the influence of the expansion wave being felt across a wider region. The velocity measured in the main expansion region at 100 μs is 625 ms^{-1}. The first expansion region is ended by a lambda shock (Fig.5.56e) with a subsequent expansion region after it. The region of high-velocity fluid in the secondary expansion region appears to be bounded by the secondary slipstream generated by the strong lambda shock (Fig.5.29). The recompression shock then terminates the region of high-velocity fluid abruptly at approximately 110° around the vortex (Fig.5.56f).

The influence of the shock-vortex interaction is similar to that discussed for the previous cases, with a small region of high-speed fluid induced by the vortex. This region is terminated by the left-hand returning shock wave after it has reflected off the splitter and is travelling clockwise around the vortex (Figs.5.56k & 5.56l). The portion of the left-hand shock which passes the splitter draws the lambda shock further into the flow field, opposing the increase in velocity caused by the main expansion wave. On the right-hand side of the vortex, the secondary expansion region is terminated by the returning shock wave, which again shows a strong kink in Fig.5.56k. This discontinuity is very sharply resolved, which is unsurprising given that it is a very strong shock wave with a low propagation velocity (at least when compared to the others present in the flow).

The raw PIV results, shown in Fig.5.57, show that the strength of the vortex is such that almost all of the particles are ejected from it and are either forced into the main shear layer or the internal shear layer. Fig.5.57a shows the region bounded by the two shear layers and appears to contain a pair of counter-rotating vortices, although it is difficult to confirm this from the limited data available. The internal shear layer is shown in this figure and it exhibits a discontinuous kink in its shape. From looking at the corresponding density-based results, we can say that the kink is caused by the internal terminating shock. Fig.5.57b shows the structure of the shear layer after the shock-vortex interaction. The shear layer contains several discrete structures, although they do not appear to be organised, at least not to the same extent as in Fig.5.45. It would be expected that the boundary layer for the highest Mach number case transitions fastest. Fig.5.58 shows that even as early as 100 μs,

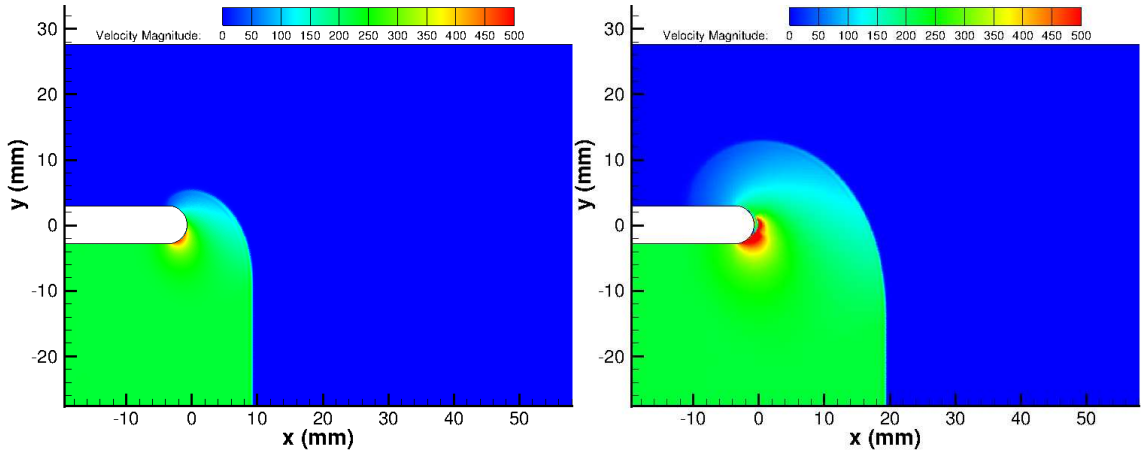

(a) 20 μs

(b) 40 μs

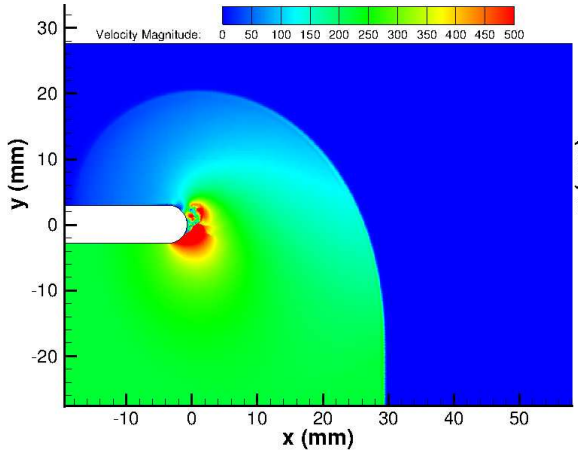

(c) 60 μs

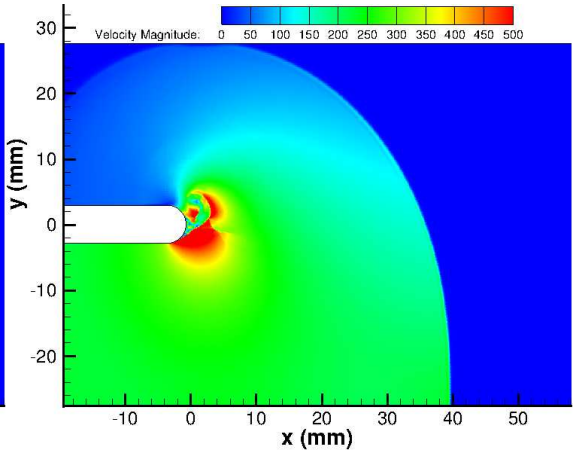

(d) 80 μs

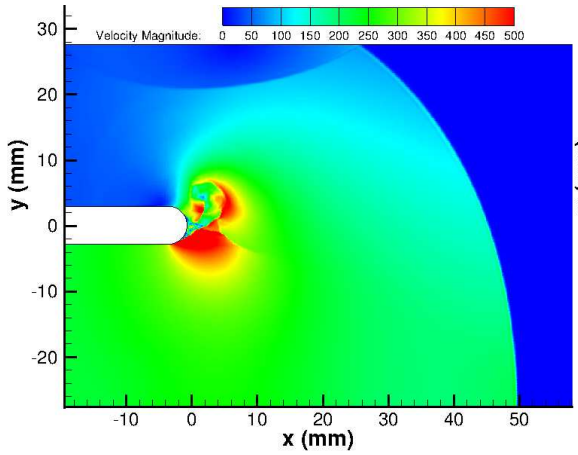

(e) 100 μs

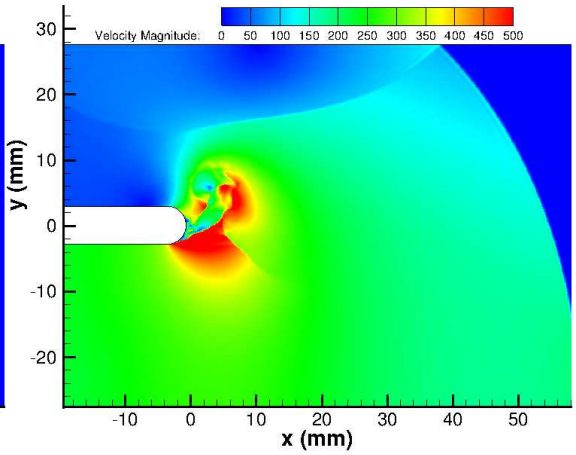

(f) 120 μs

Figure 5.55: Numerical velocity flood plot of $M_i = 1.46$ shock diffraction process around a round geometry

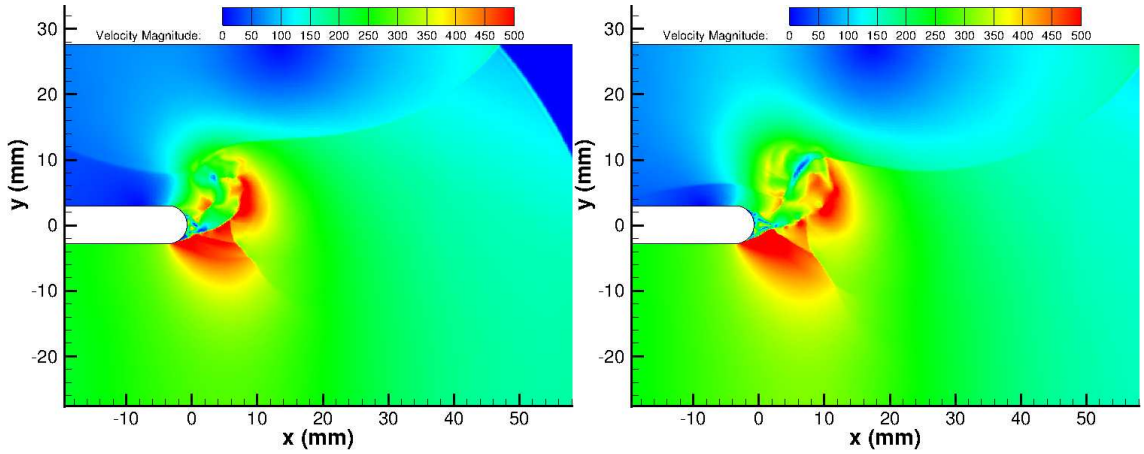

(g) 140 μs (h) 160 μs

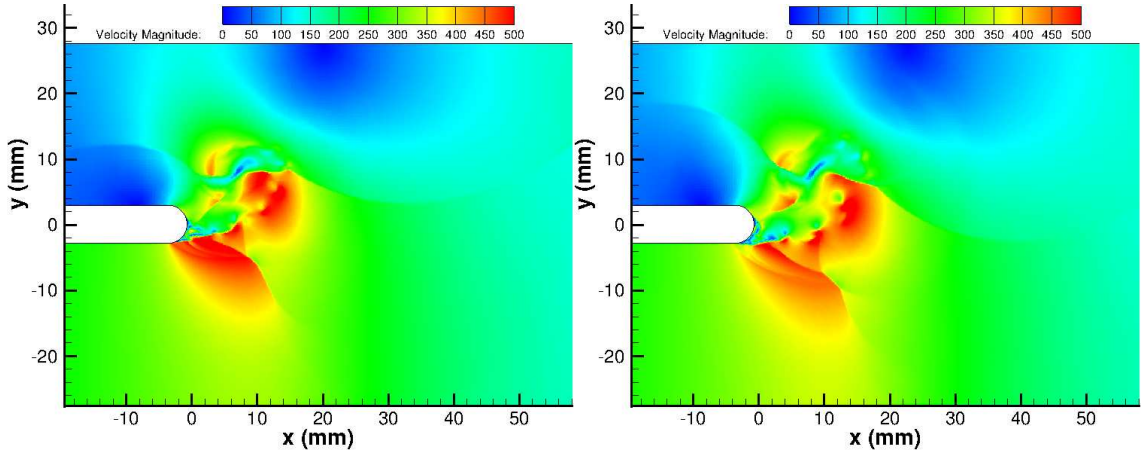

(i) 180 μs (j) 200 μs

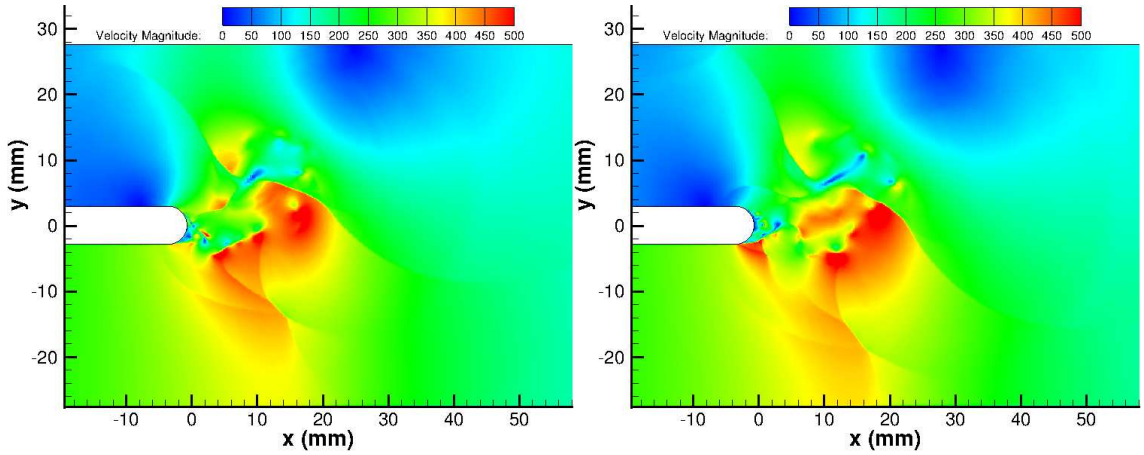

(k) 220 μs (l) 240 μs

Figure 5.55: Numerical velocity flood plot of $M_i = 1.46$ shock diffraction process around a round geometry

the boundary layer has grown to be significantly thicker than in the previous two cases, indicating that it transitioned faster.

5.2.2.6 Mi = 1.55 Numerical Results

The agreement between numerical and experimental velocity profiles is better for this Mach number than for any other presented on the round geometry. Initial agreement between the two is poor, possibly due to the strength of the interactions in the complex region and their close proximity to each other. However, from 80 μs onwards, the agreement is good, both qualitatively and quantitatively. The maximum velocity is 651 ms^{-1} at 100 μs; however, this is localised to one cell. The velocity in this region (distributed over a small area) at 100 μs is 630 ms^{-1}, which agrees well with the experimental results.

The lambda shock system is well resolved in Fig.5.59. The internal expansion region can be seen in Fig.5.59c and reaches a maximum size in Fig.5.59d. After 80 μs, the strength of the internal expansion region begins to decay due to the propagation of the vortex away from the wall, effectively removing the nozzle effect created by the shear layer and the corner geometry. After the internal terminating shock, there is a very small and complex interaction. The waves in this region correspond to the secondary internal shock and the recompression shock shown in Fig.5.29.

The shock-vortex interaction is well represented in the numerical results. The basic wave structures are the same as the experimental results; however, their individual contributions is easier to distinguish. The slug of high-speed fluid above the vortex is well captured, as is the shock wave terminating it. The right-hand side of the vortex shows the returning shock decelerating the fluid both inside and outside of the shear layer (Fig.5.59i onwards). The position and strength of the lambda shock after the shock vortex interaction agrees well with the experimental results (Figs.5.59k & 5.59l).

5.2.2.7 Conclusions

Particle image velocimetry has been applied to the problem of shock wave diffraction around a rounded corner. As with the sharp case, the velocity measured behind the incident shock shows excellent agreement with inviscid theory, with numerical simulations producing almost identical values. However, the complex region generated by a rounded corner is significantly more complex than for a sharp case and, as such, is considerably more challenging to measure. As the vortices generated here appear to be smaller than the ones produced by the sharp geometry, with equally high associated velocities, the centripetal acceleration will be even higher.

For the $M_i = 1.28$ case, the complex region, including the vortex and its associated shear layers and expansions, are in so small in size and in such close proximity to the wall that they are almost impossible to measure quantitatively, even using nano-particles. This test produced the worst agreement between experimental and numerical results seen in all of this project, and it is believed that this is solely due to the size of the interactions. The raw PIV measurements showed that the vortex core is only 6 mm in diameter after 128 μs, much smaller for this case than in any other investigated. Therefore, this discussion will focus on the two higher Mach number cases.

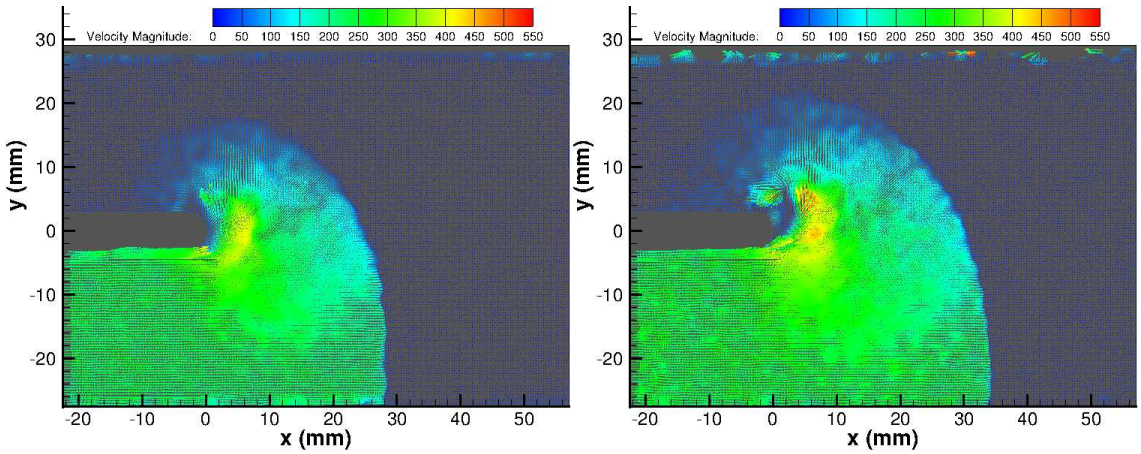

(a) 56 μs

(b) 64 μs

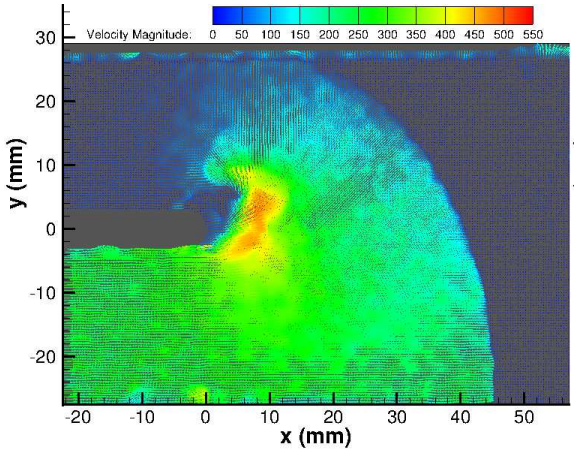

(c) 76 μs

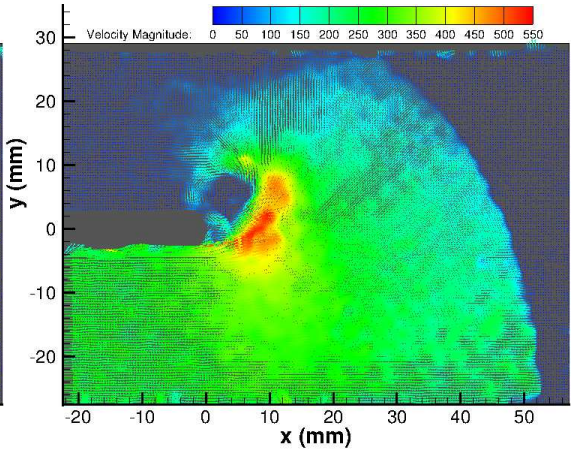

(d) 88 μs

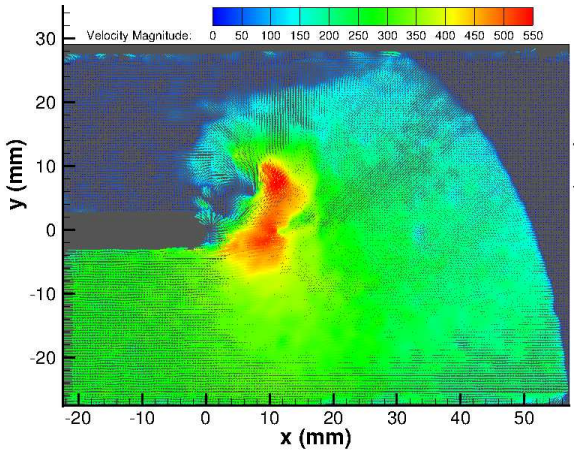

(e) 100 μs

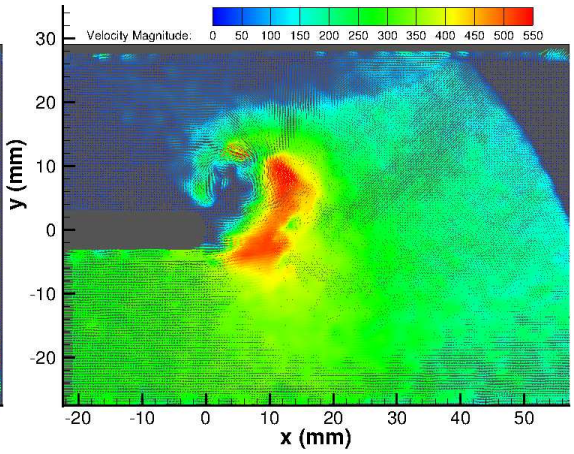

(f) 116 μs

Figure 5.56: PIV vector plot of $M_i = 1.55$ shock diffraction process around a round geometry

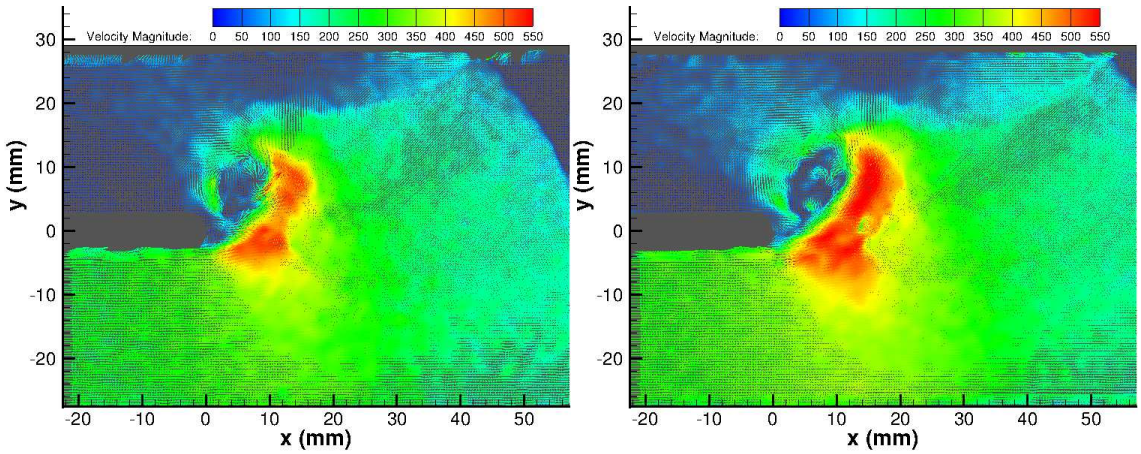

(g) 124 μs (h) 140 μs

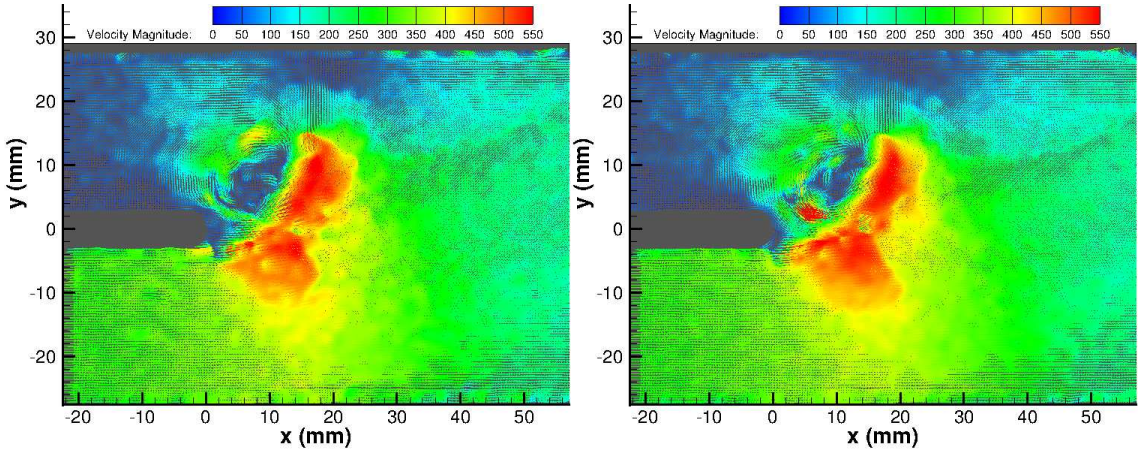

(i) 156 μs (j) 164 μs

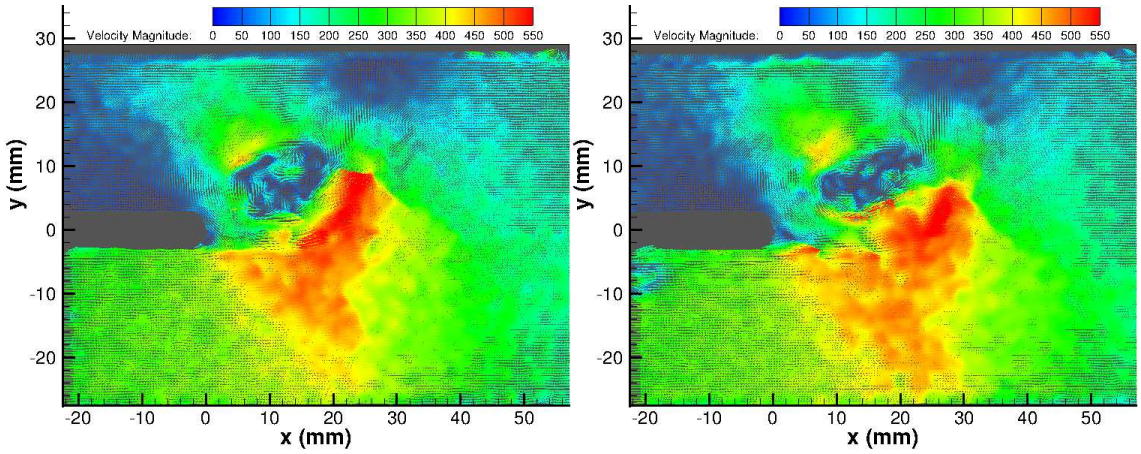

(k) 208 μs (l) 224 μs

Figure 5.56: PIV vector plot of $M_i = 1.55$ shock diffraction process around a round geometry

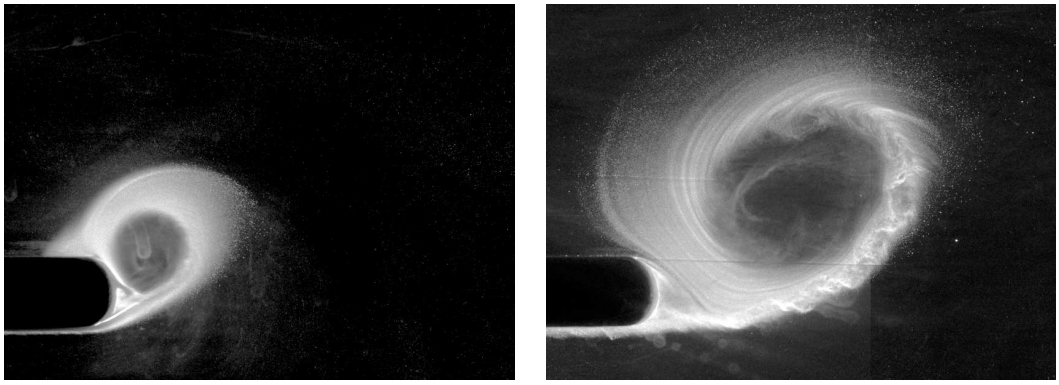

(a) 76 μs (b) 208 μs

Figure 5.57: PIV raw images of $M_i = 1.55$ complex region

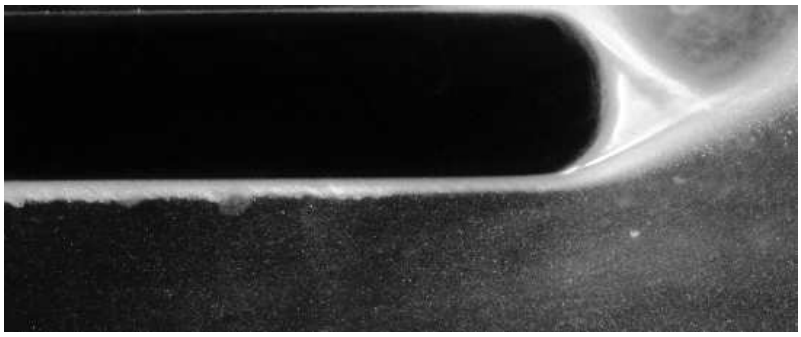

(a) 100 μs

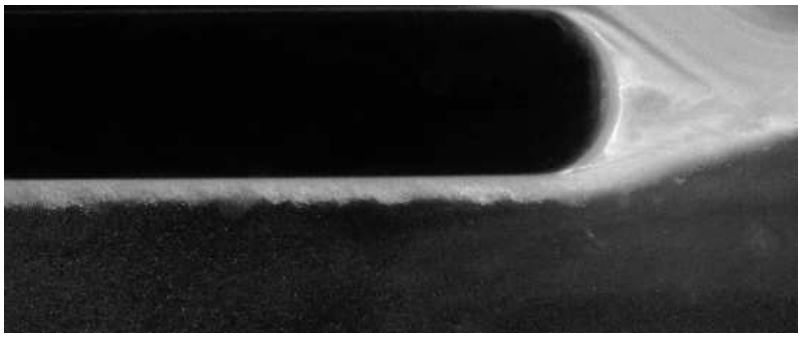

(b) 180 μs

Figure 5.58: PIV raw images of $M_i = 1.55$ boundary layer development

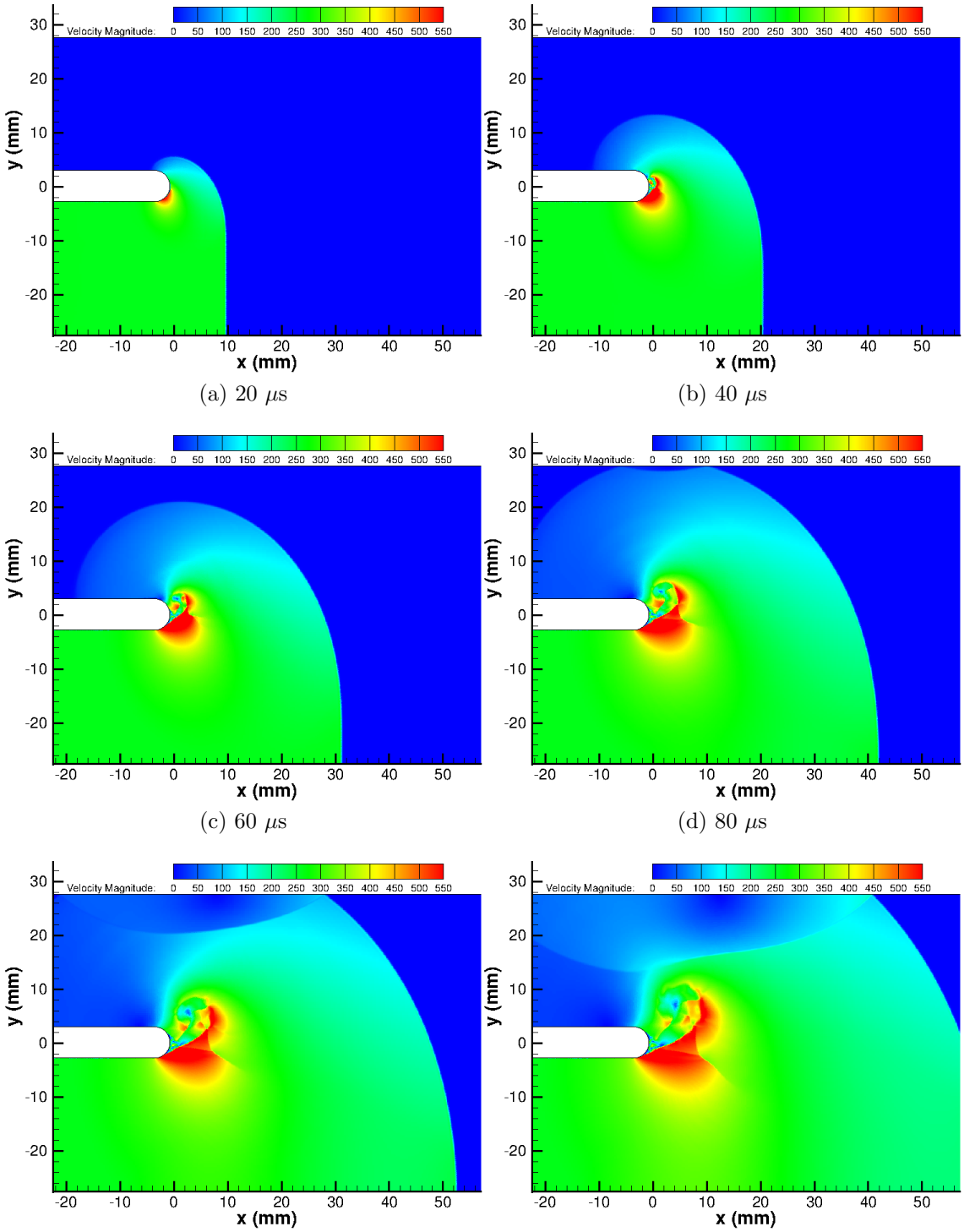

(a) 20 μs (b) 40 μs

(c) 60 μs (d) 80 μs

(e) 100 μs (f) 120 μs

Figure 5.59: Numerical velocity flood plot of $M_i = 1.55$ shock diffraction process around a round geometry

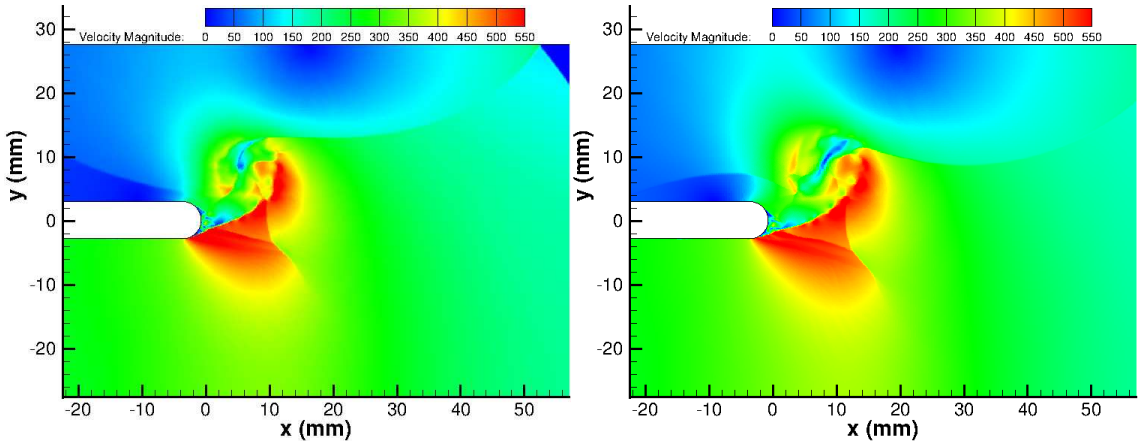

(g) 140 μs (h) 160 μs

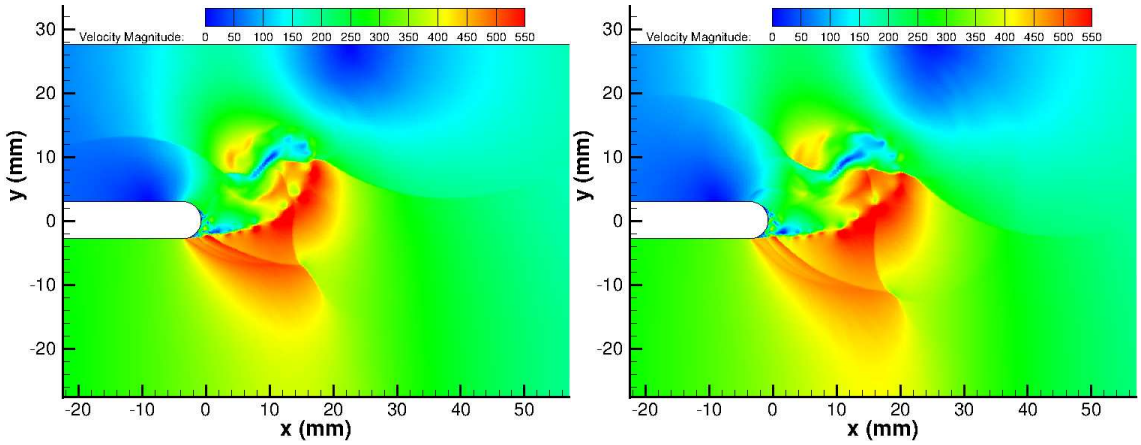

(i) 180 μs (j) 200 μs

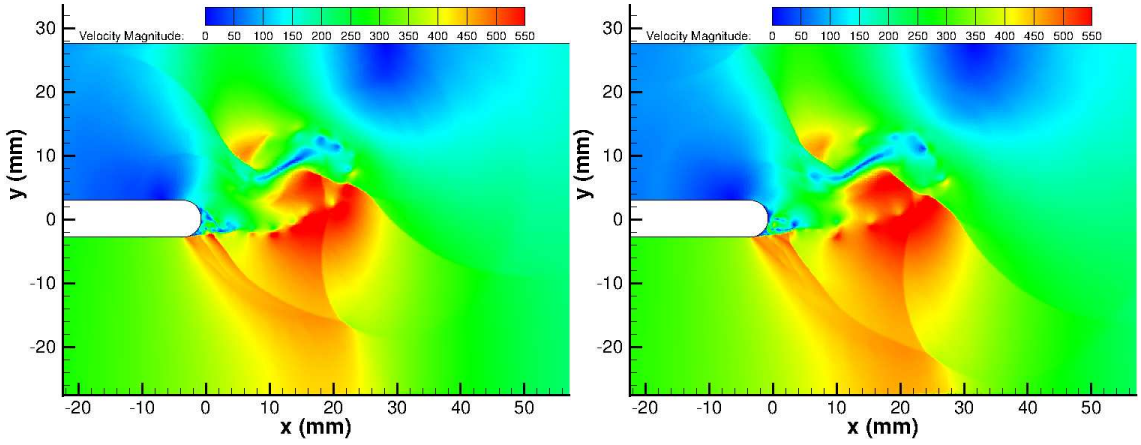

(k) 220 μs (l) 240 μs

Figure 5.59: Numerical velocity flood plot of $M_i = 1.55$ shock diffraction process around a round geometry

The $M_i = 1.46$ case showed a very strong expansion region terminated by a lambda shock, with a further expansion region after it. This was captured both experimentally and numerically. As the flow grows faster in time for higher Mach numbers, the $M_i = 1.55$ case showed the lambda structures even more clearly. The secondary expansion region was well captured, as was the shock vortex interaction. The problem of acquiring measurements in vortex cores is still an unresolved issue. The proximity of the internal expansion region to the vortex core means that we are extremely unlikely to obtain reliable quantitative data in this region. However, as the numerical simulations do not suffer from this problem, they resolved the internal expansion region well for all three Mach numbers, indicating that the interpretation of the density-based results is correct.

From the density-based results, it was not possible to conclude much about the structure of the main shear layer, as there was little visible in the shadowgraph or schlieren results[3]; however, the raw PIV images showed that there are no instabilities present for this geometry like there were for the sharp corner. The numerical simulations predicted that a series of K-H style vortices would be present on the shear layer; however, the raw PIV images showed that the shear layer is made up of turbulent fluctuations. This level of turbulence, not present in the assumptions of the simulation, gives an extra method of dissipation and damps out the instabilities from the experimental results.

The incoming boundary layer is not visible in the density-based results section; however, the raw PIV images highlight it well and allow us to see an instantaneous snapshot of the structure of the boundary layer. The size of the boundary layers is such that it was not possible to gain quantitative data from the results presented here; a different experimental setup would be required and, as the flow is transient, it would be unnecessary, and probably impossible, to gain statistical data about the fluctuations in the boundary layer. The raw PIV images show the growth of the boundary layer and some results indicate that there are structures aligned at approximately 45° to horizontal. These structures are likely to be packets of vorticity, possibly in the form of hairpin vortices, similar to those seen by Adrian et al. [200].

[3]This has been the case for many researchers in the past looking at similar problems to this; therefore more conclusive evidence is needed.

5.3 Pressure Transducer Measurements

In this section, pressure transducer measurements at discrete points will be presented, along with virtual transducers from the simulations at the same locations. Each one of the experimental results presented is an ensemble average of five individual test runs. The implication of these results will not be discussed in great detail, as the pressure-sensitive paints results section follows this one. The size of the virtual transducer is one cell in the simulation, whereas the actual transducer has a finite size (3.8 mm diameter sensor head) and as such will suffer from some spatial averaging.

5.3.1 Sharp Geometry

5.3.1.1 Mi = 1.28 Results

Fig.5.60 shows the pressure history along the side wall of the shock tube test section as measured by the three Kulite transducers mentioned in Section 3.3. **K4** is the first transducer to be influenced by the flow and gives a pressure rise to a maximum of 1.84 bar. This decays as the reflected expansion wave propagates upstream. **K2** shows a very sharp pressure rise 50 μs later but only to 1.53 bar. This lower pressure peak is due to the diffracted shock wave being weaker than the incident one from which it spawns. **K2** also shows a rise in pressure, a slow decay and then another rise. This pattern is due to the initial shock and then the expansion region underneath the shear layer. The second pressure rise is almost certainly the passage of the returning diffracted shock. **K1** is the last transducer to be effected and shows a two-stage pressure rise to a maximum of 1.63 bar. This is due to the diffracted shock wave reflecting off the top surface of the test section and therefore compressing the flow over this transducer twice.

The numerical transducers agree very well with the Kulites. The rises and falls are well predicted in terms of both time and magnitude. The numerical incident shock is very sharply resolved with no discernible overshoot in pressure. Obviously the numerical transducers will have a smoother profile as they were taken at each time step in the simulation, whereas the Kulites cannot be used reliably past 100kHz.

The schlieren images, and to some extent the PIV vectors, showed the main vortex being distorted by the returning diffracted shock wave. The higher the incident Mach number, the larger the distortion. In this case, the distortion of the vortex is so slight that it appears to have convected away in between **K1** and **K2**, as these transducers show no significant pressure drop.

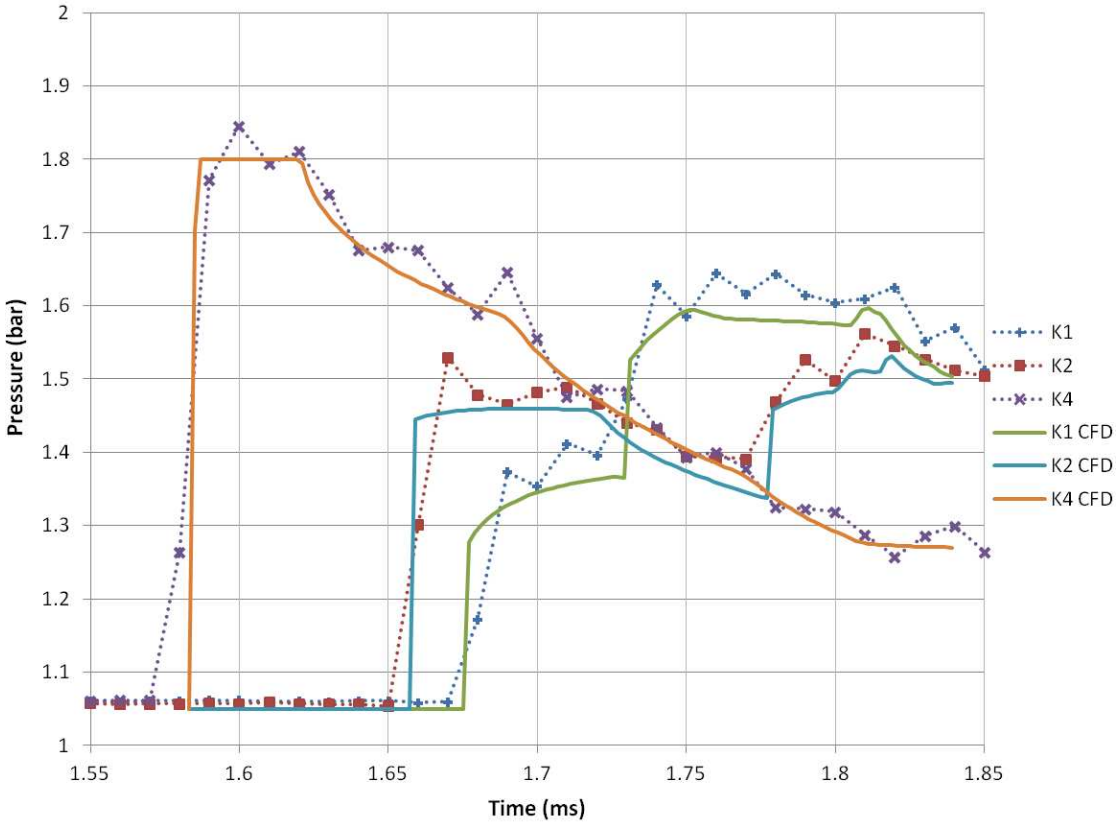

Figure 5.60: Pressure transducer measurements of Mi=1.28 shock diffraction process around a sharp geometry

5.3.1.2 Mi = 1.46 Results

Fig.5.61 shows a qualitatively similar initial pressure profile (over the first 200 μs). **K4** shows the characteristic ringing mentioned in Section 3.3, as the pressure over this transducer only slowly changes after an initial step change from ambient to 2.38 bar. The other two transducers both show an initial increase in pressure due to the diffracted shock wave. **K2** shows a decrease as the vortex begins to propagate towards it. A second pressure increase in both **K1** & **K2** is due to the returning diffracted shock wave. The second pressure jump shown by **K1** is significantly larger than the previous test case, implying that the shock wave returning from the top wall of the test section is much stronger for this Mach number. **K2** reaches a maximum of 1.79 bar, while **K1** reaches a peak of 2.14 bar.

Similarly to the $M_i = 1.28$ results, the real and virtual transducers agree very well in both magnitude and time. There is some degree of spatial noise on the Kulite measurements; however, this is to be expected. The initial (and for **K1** & **K2**, the secondary) pressure increase is very well represented.

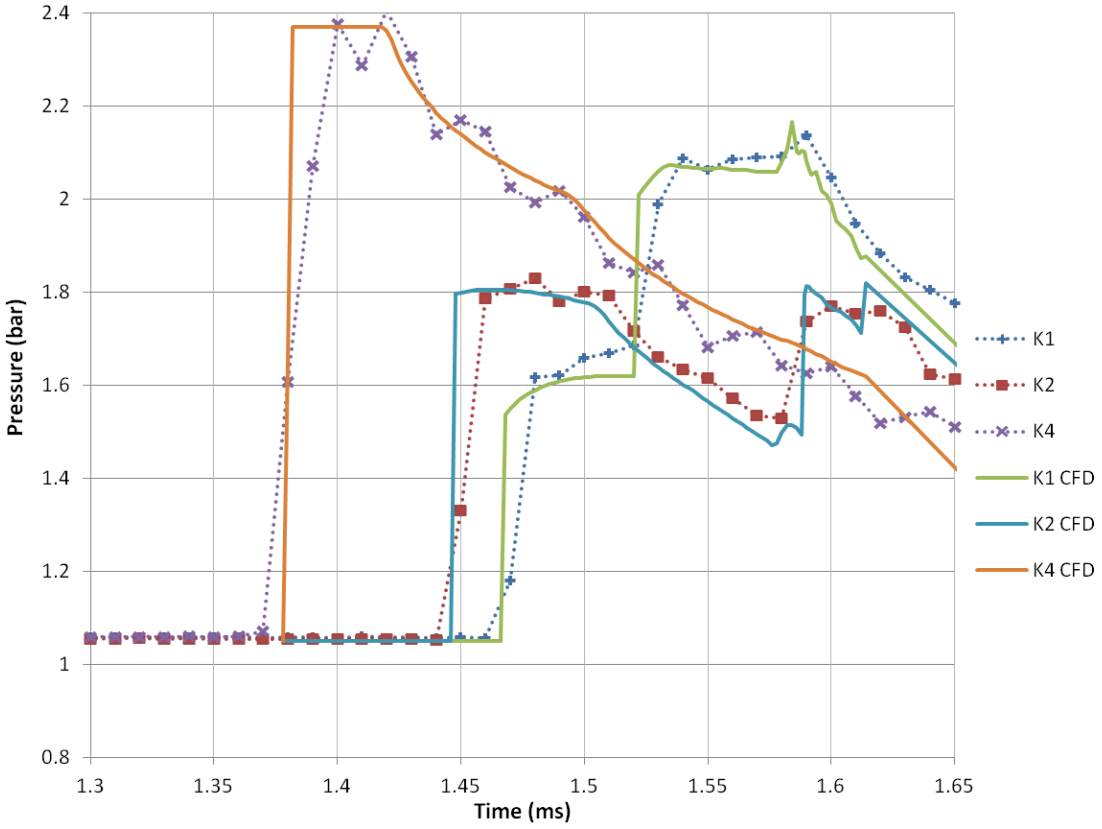

Figure 5.61: Pressure transducer measurements of Mi=1.46 shock diffraction process around a sharp geometry

5.3.1.3 Mi = 1.55 Results

The final pressure history for sharp geometries is shown in Fig.5.62. **K4** shows the highest initial pressure rise at 2.62 bar with a similar attenuation to those seen in the previous cases. **K1** shows a two-stage pressure rise similar to the previous cases, leading to a maximum of 2.38 bar. Although **K2** shows a secondary pressure rise, it is not as significant as in the previous cases, with a maximum pressure reading of 1.96 bar. This value indicates a fundamental change in the pressure history. This is likely to be due to the higher induced velocity in the expansion region and behind the incident shock wave in general. This increase in velocity has slowed the progress of the returning diffracted shock wave before the vortex is conducted away, therefore eliminating the second pressure rise within the time frame of Fig.5.62.

There are some large discrepancies between real and virtual transducers at this Mach number. After the initial shock wave, the numerical values of **K4** are slightly higher than the measured values from the Kulites. The second pressure jump seen in the **K1** measurements arrives slightly earlier in the numerical simulation than in the real measurements. This is not a significant error as the actual transducers are finite in size, whereas the virtual transducers are point measurements at the centre of the real transducer location. The most significant discrepancy is seen between the real and numerical **K2** transducers. The numerical results seem to have significantly over-predicted the influence of the vortex after the shock-vortex interaction, causing a large decrease in pressure at the **K2** location.

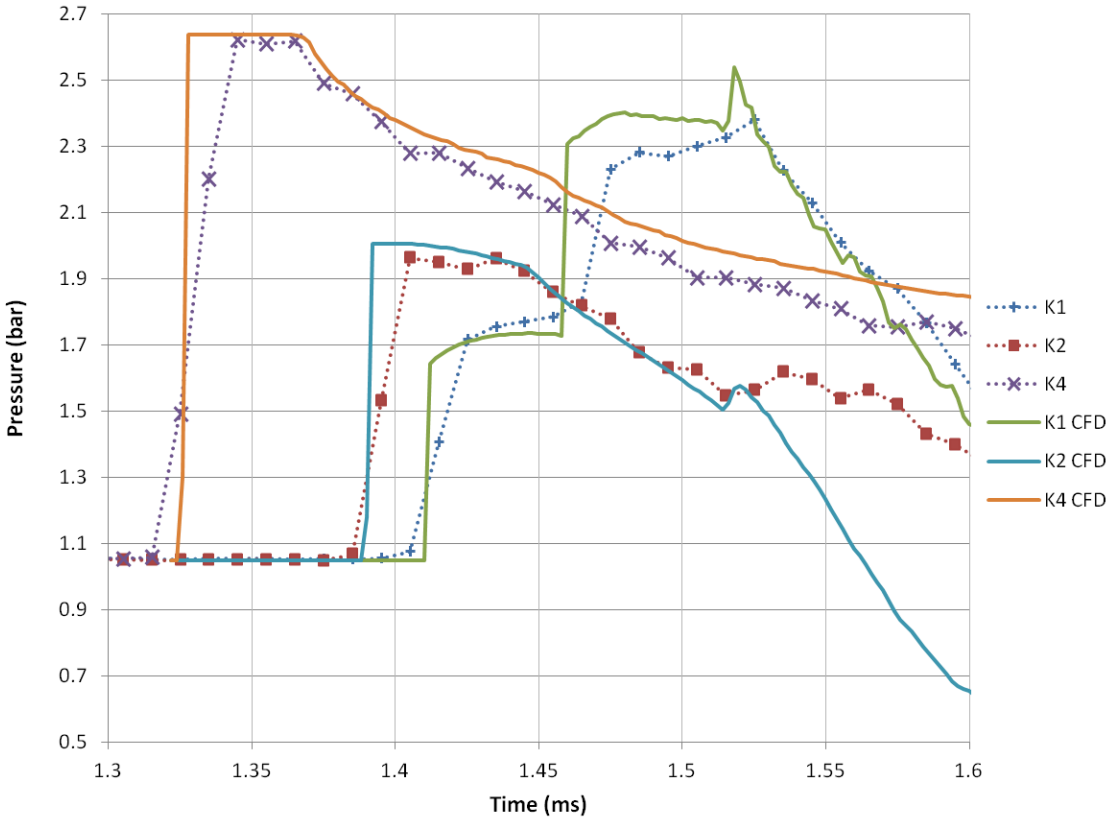

Figure 5.62: Pressure transducer measurements of Mi=1.55 shock diffraction process around a sharp geometry

5.3.1.4 Conclusions

The results in this section have shown that the Kulite XT-190M pressure transducers are capable of capturing the initial pressure rise and then the time history of the pressure during the shock diffraction process. Numerical simulations,for the most part, agreed well with the actual pressure measurements on the wall, with the exception of the $M_i = 1.55$ case. The numerical simulation overpredicts the expansion region after the shock-vortex interaction and gives a significantly lower pressure in this region than that measured by the transducer.

The good agreement between the expereimental pressure measurements and the simulations highlights the two-dimensionality of the flow as the kulites were flush mounted to the side wall.

5.3.2 Round Geometry

5.3.2.1 Mi = 1.28 Results

Fig.5.63 shows the experimental and numerical pressure history for the $M_i = 1.28$ diffraction process. **K4** is the first transducer affected by the flow and shows the largest pressure rise, as the shock is still planar at this point. It reaches a maximum of 1.78 bar, which agrees very well with the theoretical value of 1.75 bar. The reflected expansion wave then causes this maximum to decay in the same way as the the sharp cases. **K1** & **K2** both show a double pressure rise, the first which

corresponds to the initial curved shock (hence its lower strength) and the second is produced by the shock reflecting off the top surface of the test section and compressing the flow again. Initially, **K1** reaches a pressure of 1.37 bar and **K2** reaches 1.45 bar. The delay for the second pressure rise at **K2** is due to the high-speed fluid underneath the shear layer opposing the motion of the returning diffracted shock wave, slowing it down. With the second pressure rise, **K1** reaches a maximum pressure of 1.57 bar while **K2** peaks at 1.49 bar.

The numerical transducers agree well with the Kulites in terms of both pressure rise magnitude and shock arrival time. All of the numerical transducers show a sharp increase in pressure towards the end of Fig.5.63 which is not seen in the experimental results. This will be discussed in Section 5.4.2.2.

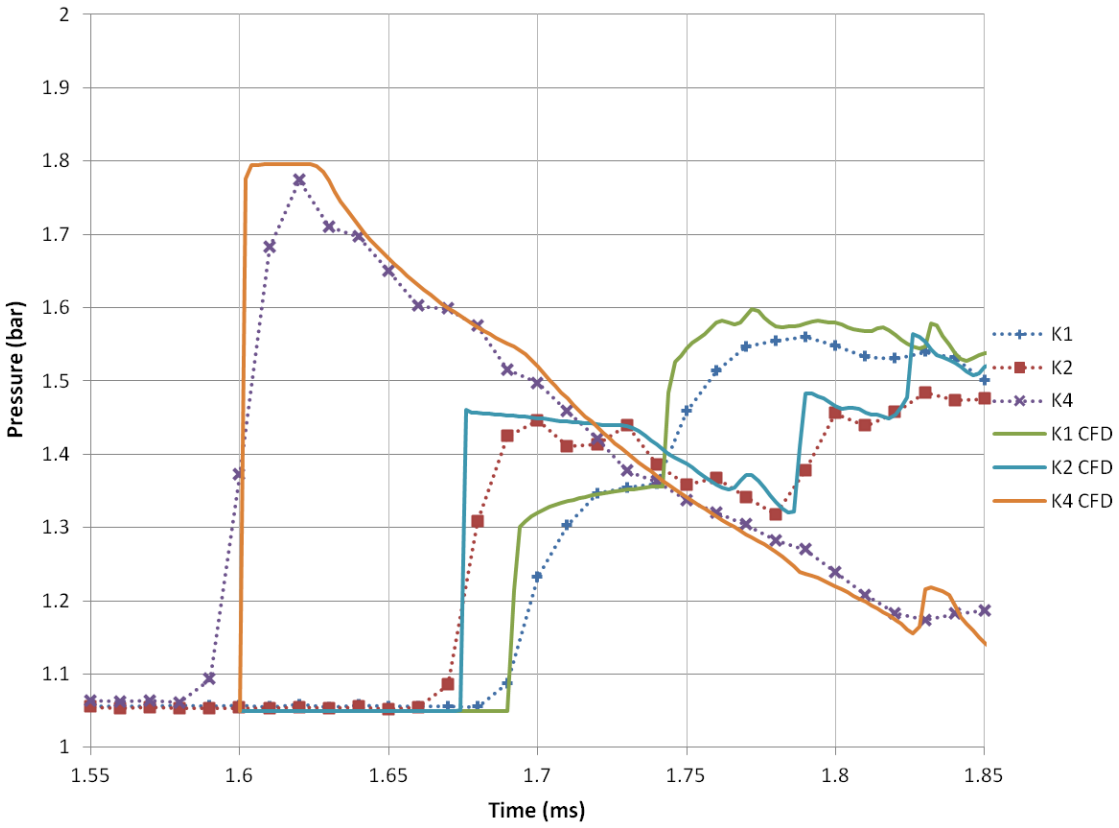

Figure 5.63: Pressure transducer measurements of Mi=1.28 shock diffraction process around a round geometry

5.3.2.2 Mi = 1.46 Results

As with the sharp geometry, the pressure profile for the $M_i = 1.46$ case is largely similar to that of the $M_i = 1.28$ case. In Fig.5.64, **K4** measures the pressure rise, given by the incident shock as 2.38 bar, agreeing well with the theoretical value of 2.32 bar. The other two Kulites experience a two-stage pressure rise as before; however, the pressure rise seen by **K1** is much stronger, and again occurs earlier than the rise seen by **K2**. **K1** reaches an initial pressure of 1.66 bar and peaks at 2.09 bar with the help of the returning diffracted shock. **K2** sees an initial pressure rise to 1.80 bar, followed by a decrease due to the expansion region under the shear

layer, followed by a second compression to 1.81 bar.

The numerical transducers show good correlation with the experimental results. The pressure rises seen in the numerical results appear sharper than that of their experimental counterparts, highlighting the limitations of the XT190-M transducers and the DAQ system. However, the magnitude of the pressure changes show excellent agreement for all transducers.

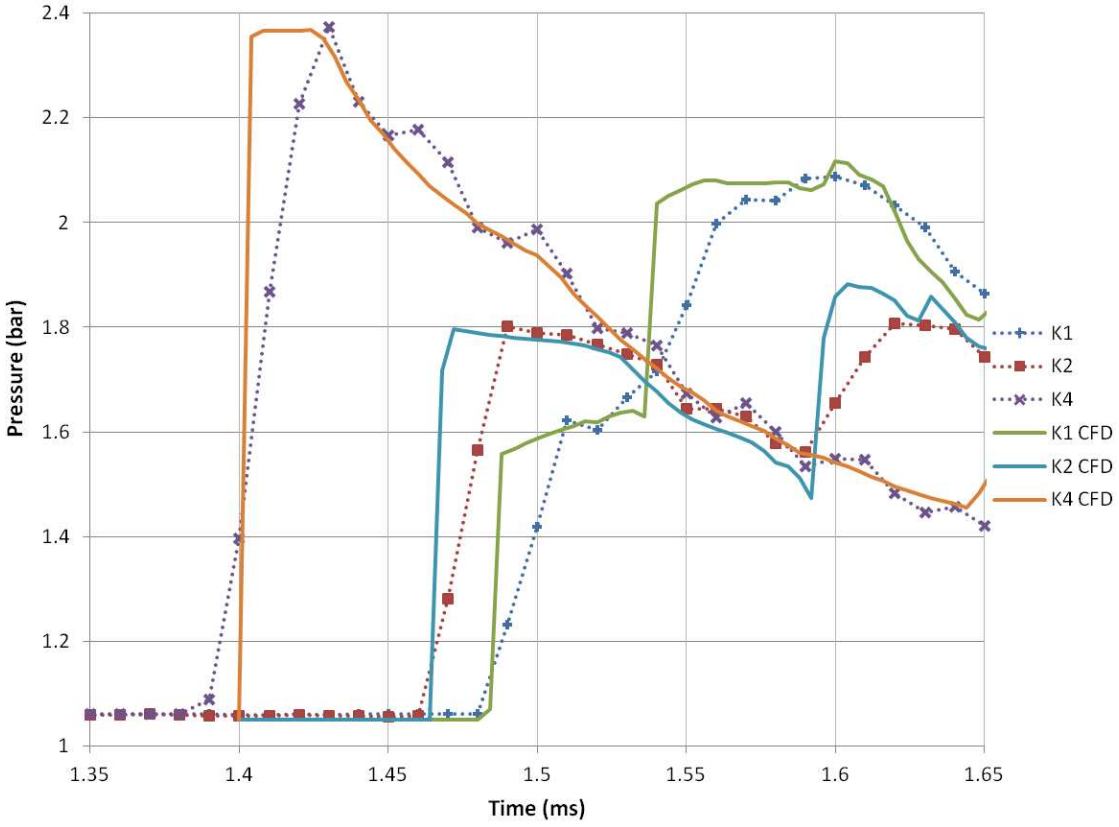

Figure 5.64: Pressure transducer measurements of Mi=1.46 shock diffraction process around a round geometry

5.3.2.3 Mi = 1.55 Results

Fig.5.65 shows the final set of transducer measurements for the round geometry (notice the different scale from that of the sharp case). The transducer **K4** reaches a maximum value of 2.67 bar, agreeing well with the theoretical value of 2.64 bar. **K1** shows two sharp pressure rises, initially to 1.84 bar and eventually to 2.43 bar. As with the sharp case, the transducer **K2** shows no significant secondary pressure rise after reaching its initial maximum of 2.06 bar.

The numerical transducers corresponding to **K1** & **K4** agree very well with the experimental results over the whole time range shown. However, as with the sharp geometry, **K2** initially agrees well but begins to diverge from the experimental results after approximately 150 μs. There is a small secondary pressure increase, followed by a decrease. On closer inspection of the schlieren results, it is found that the returning shock on the right-hand side of the vortex only skims across the location of **K2**. The transducer is half affected by the shock and half not, whereas

the numerical transducer is based on one cell at the centre of the transducer location.

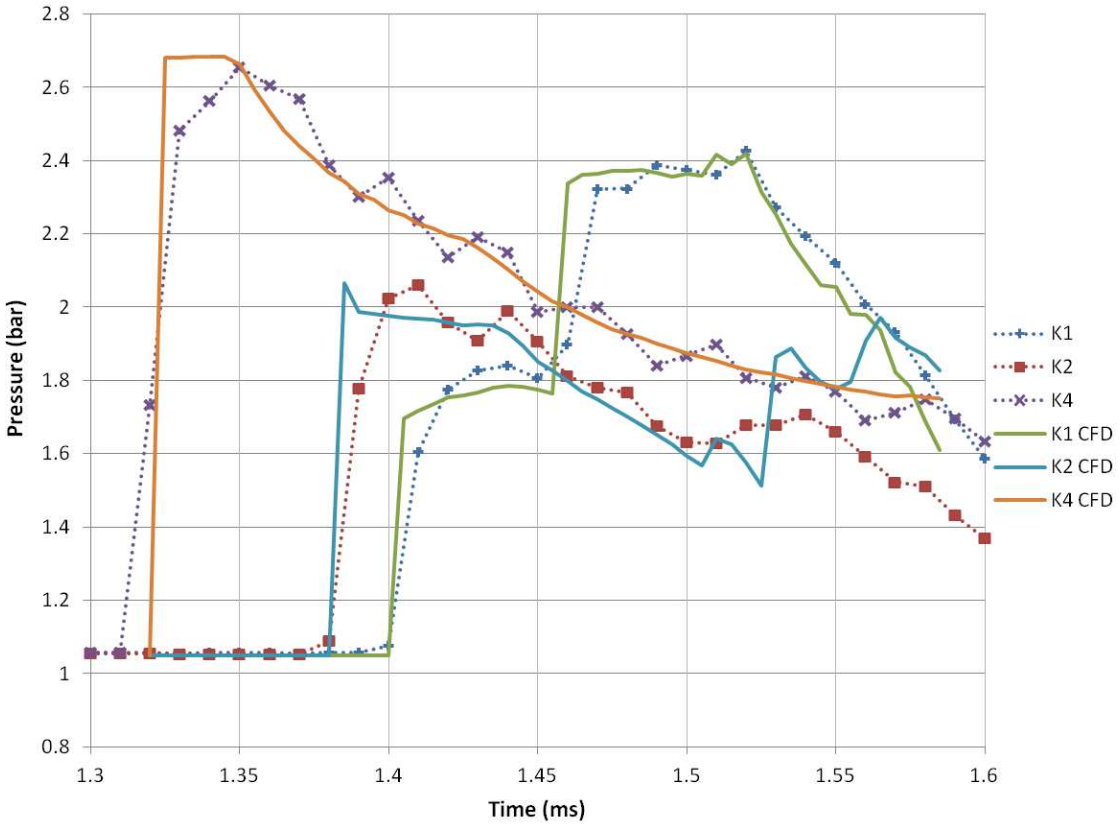

Figure 5.65: Pressure transducer measurements of Mi=1.55 shock diffraction process around a round geometry

5.3.2.4 Conclusions

The pressure transducer results presented in this section show good agreement with inviscid theory for the initial pressure rise, and make sense given the results we have seen so far. Numerical simulations agree well with the experimental data, given the limiting assumption that transducers measure *point* values. The diameter of a Kulite XT190-M transducer sensor head is 3.8 mm, meaning that we are spatially averaging the pressure rise over that area, whereas the virtual transducers are based on one cell and do not suffer from this problem.

5.4 Pressure-Sensitive Paint Measurements

This section shows the test section side wall static pressure development as measured by thin layer chromatography-based pressure-sensitive paint.

5.4.1 Sharp Geometry

5.4.1.1 Mi = 1.28 Experimental Results

Fig.5.66a shows the incident shock wave and the pressure rise behind it. There is a significant degree of spatial noise, despite taking an ensemble average of three individual tests and using a 3×3 linear filter to process the results. The pressure rise of 1.68 bar correlates well with the expected value of 1.75 bar given by inviscid theory based on M_{ie}. Fig.5.66b begins to show the vortex shed from the apex. Subsequent figures (5.66c onwards) show the pressure drop in the centre of the vortex to its lowest value of 0.46 bar. The vortex remains approximately the same size from Fig.5.66f onwards. In the same images, the reflected expansion wave can be seen to be propagating upstream and downwards from the apex, as the pressure in this region is reduced compared to the region of uniform high pressure at the inlet to the test section. The pressure above the splitter does not change significantly over the first few images, indicating that the diffracted shock wave in this region is extremely weak.

Fig.5.66e shows the diffracted shock just as it is returning from the top wall. There is a small pressure rise behind it, which is more clearly seen in Fig.5.66f. The pressure rise is not uniform along the length of the returning shock wave, as it is barely noticeable on the left-hand side of the vortex and significantly stronger on the right hand side. This region of high pressure grows as the returning wave propagates towards the vortex. The pressure in this region attains values close to that behind the incident shock wave; reaching a value of 1.60 bar. There are no significant pressure changes on the left-hand side of the vortex due to the shock-vortex interaction. By 240 μs the high-pressure region behind the returning diffracted shock wave is attenuating. As was expected from the density- and particle-based results, there is very little change in the shape of the vortex, indicating a very weak shock-vortex interaction.

Due to the high degree of spatial noise, it is impossible to make any comments about the shear layer and its structure.

5.4.1.2 Mi = 1.28 Numerical Results

The numerical pressure profile is presented in Fig.5.67. The numerical results qualitatively agree with the PSP measurements; however, there are some discrepancies. The simulated pressure behind the incident shock is slightly higher than the PSP measurements, albeit within experimental error. This is likely to be a function of the diffusion time through the PSP layer rather than an overprediction by the simulation.

The reflected expansion wave can be see propagating upstream and is reflected from the bottom wall of the test section in Fig.5.67d. The vortex is a clear region of low pressure, with pressures as low as 0.23 bar. This value is significantly lower

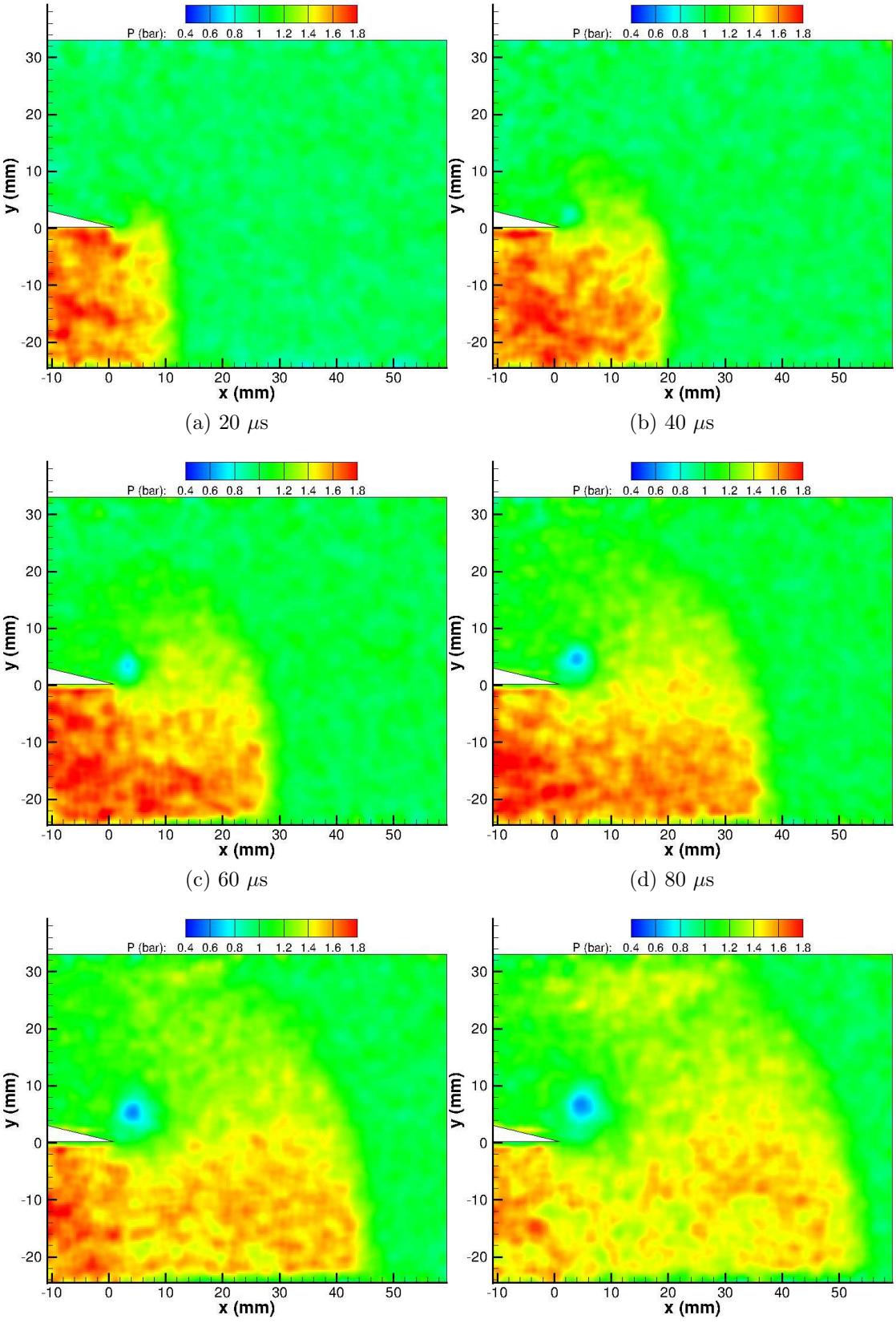

(a) 20 μs (b) 40 μs

(c) 60 μs (d) 80 μs

(e) 100 μs (f) 120 μs

Figure 5.66: PSP map of $M_i = 1.28$ shock diffraction process around a sharp geometry

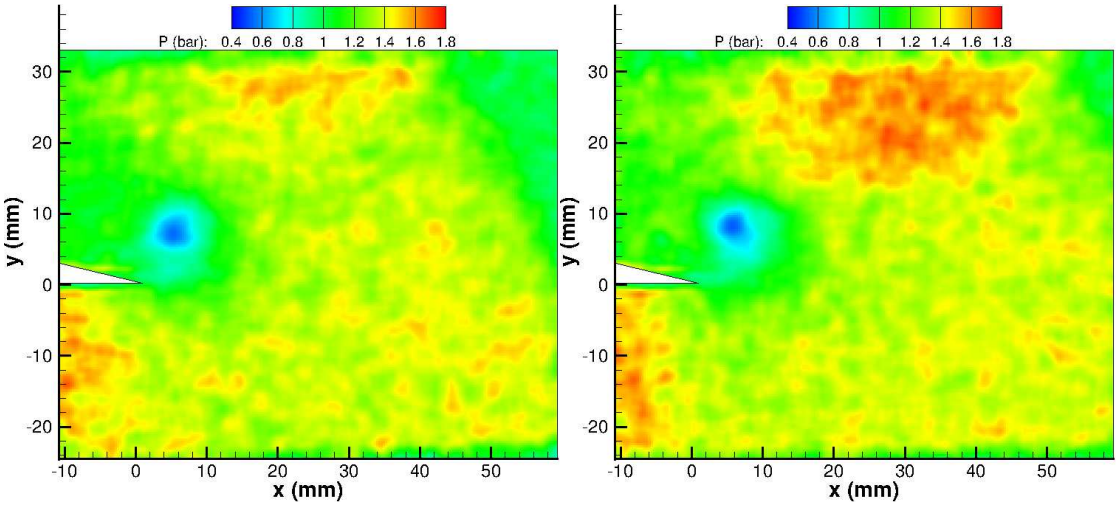

(g) 140 μs (h) 160 μs

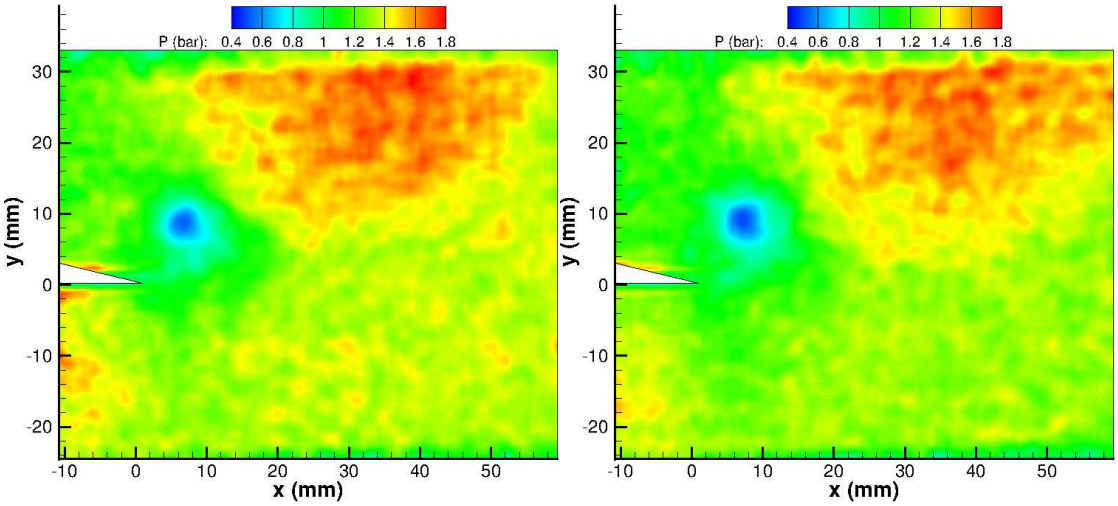

(i) 180 μs (j) 200 μs

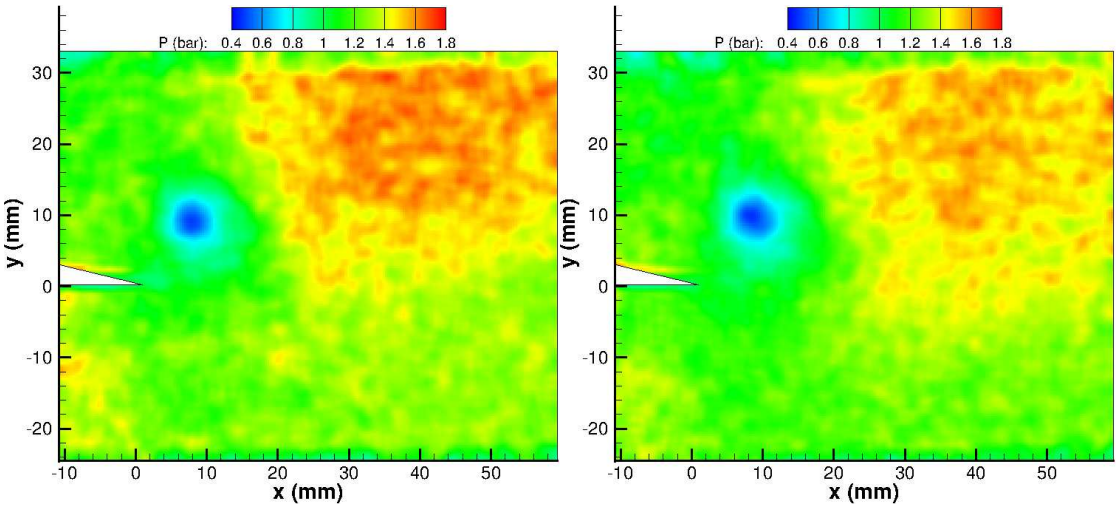

(k) 220 μs (l) 240 μs

Figure 5.66: PSP map of $M_i = 1.28$ shock diffraction process around a sharp geometry

than that measured in the experimental results. This will be discussed further in Section 5.4.1.7.

The diffracted shock wave is clearly losing strength along its length from the triple point, where it causes hardly any pressure change above the splitter. The diffracted shock wave is reflected from the top wall of the test section and it is clear that it differs in strength along its length. The main vortex grows in size until 120 μs (Fig.5.67f) and remains at approximately a constant size from then on, including after the shock-vortex interaction.

The shock-vortex interaction shown in Fig.5.67i onwards appears to be very weak and to have little impact on the pressure profile. As is to be expected, the pressure varies slowly across the shear layer (owing to its steady curvature) and as such there is very little information available about it.

The reflected diffracted shock wave, returning back from the top wall of the test section in Figs.5.67g to 5.67g, gives a pressure of up to 1.60 bar, agreeing almost perfectly with the experimental values.

5.4.1.3 Mi = 1.46 Experimental Results

Fig.5.68 shows the time development of the shock diffraction process as measured by the TLC PSP. Initially, the shock appears to be spread over a slightly larger distance than in the previous case. This is to be expected due to its higher velocity. The measured pressure rise is 2.21 bar behind the incident shock. The vortex core is easily identified in Fig.5.68b as a clear region of sub-atmospheric pressure. The curved portion of the shock shows variable strength along its length. The influence of the reflected expansion wave can be seen from Fig.5.68b onwards as the initial pressure rise is reduced. The vortex core has a lower pressure than the previous case, with a minimum of 0.34 bar. There appears to be no influence on pressure due to the region of lambda shocks seen in the density results.

The returning diffracted shock wave shows a large pressure rise from Fig.5.68f onwards, due to the double compression of the flow. The maximum pressure is measured to be almost exactly the same as the value behind the incident shock of 2.20 bar. On the left-hand side of the vortex there appears to be very little pressure change due to the shock-vortex interaction (Fig.5.68i onwards). However, there does seem to be a decrease in pressure in later images (Fig.5.68j onwards), which is associated with the increase in velocity seen in this region seen in the PIV measurements (Fig.5.39i).

Fig.5.68l shows a discontinuous change in pressure around the right-hand side of the vortex core. This is associated with the shock-vortex interaction and can be seen clearly in Fig.5.8l. The shape of the low pressure region corresponding to the vortex is much more distorted by the shock-vortex interaction in this case. The low-pressure region is distorted from a circular region to an elliptical shape. This corresponds well with the density-based results and the regions of low pressure correspond to the regions of high velocity in the PIV measurements.

5.4.1.4 Mi = 1.46 Numerical Results

The numerical results of the $M_i = 1.46$ shock diffraction and shock-vortex interaction process are given in Fig.5.69. As in the previous comparison, the initial pressure rise

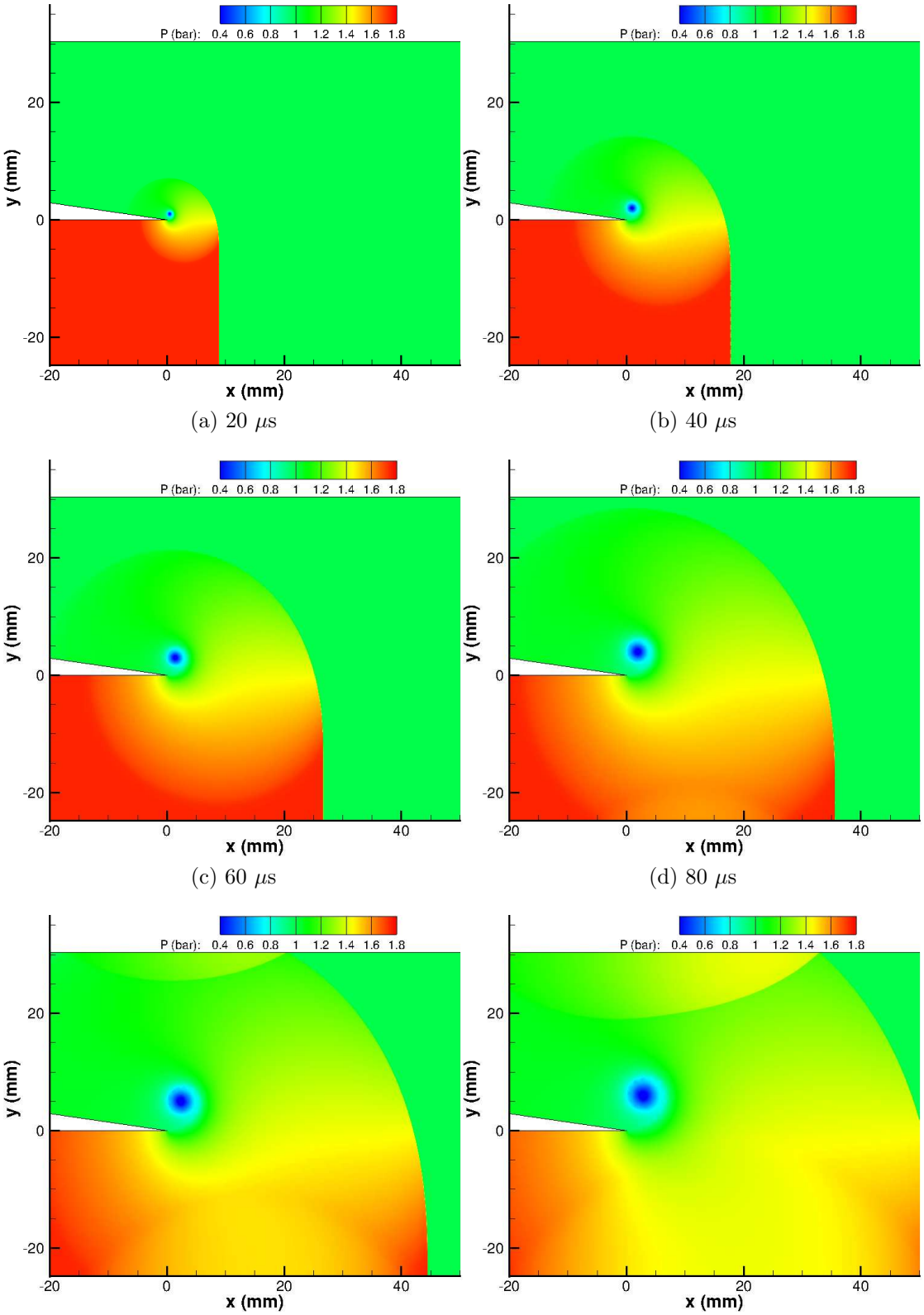

(a) 20 μs (b) 40 μs

(c) 60 μs (d) 80 μs

(e) 100 μs (f) 120 μs

Figure 5.67: CFD pressure map of $M_i = 1.28$ shock diffraction process around a sharp geometry

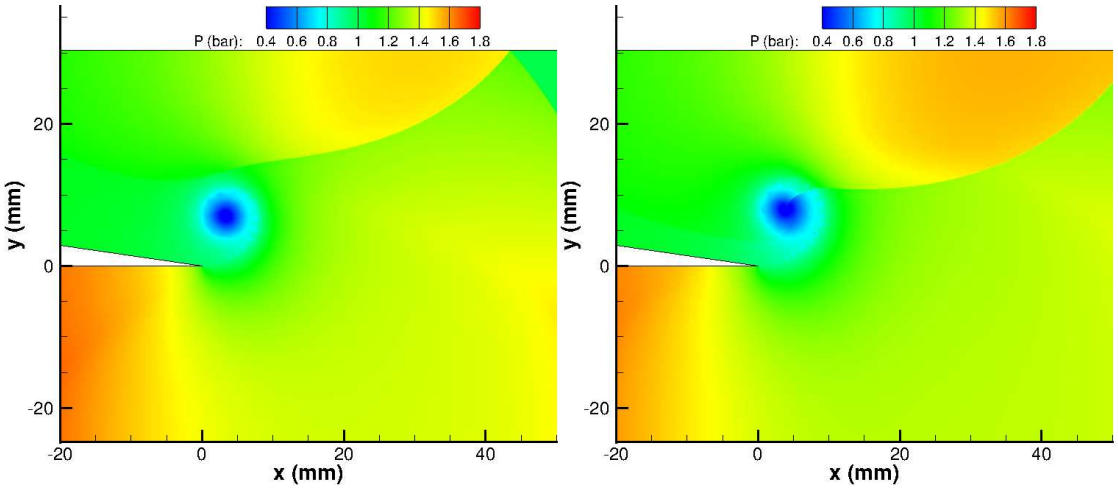

(g) 140 μs (h) 160 μs

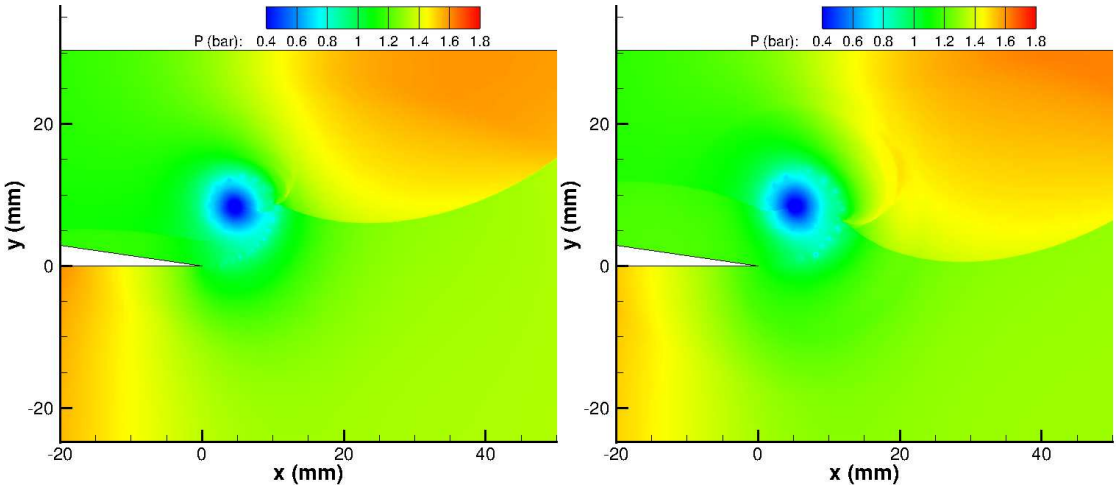

(i) 180 μs (j) 200 μs

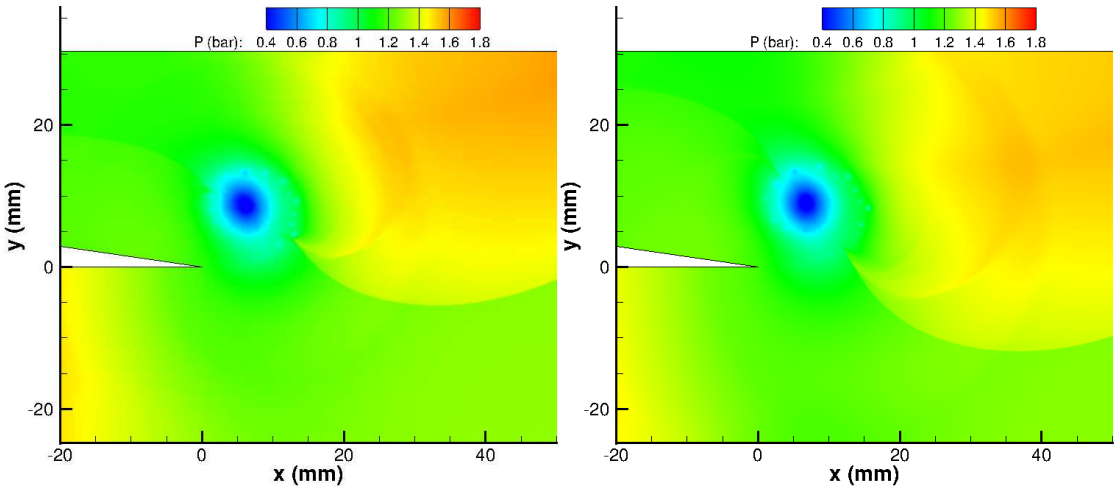

(k) 220 μs (l) 240 μs

Figure 5.67: CFD pressure map of $M_i = 1.28$ shock diffraction process around a sharp geometry

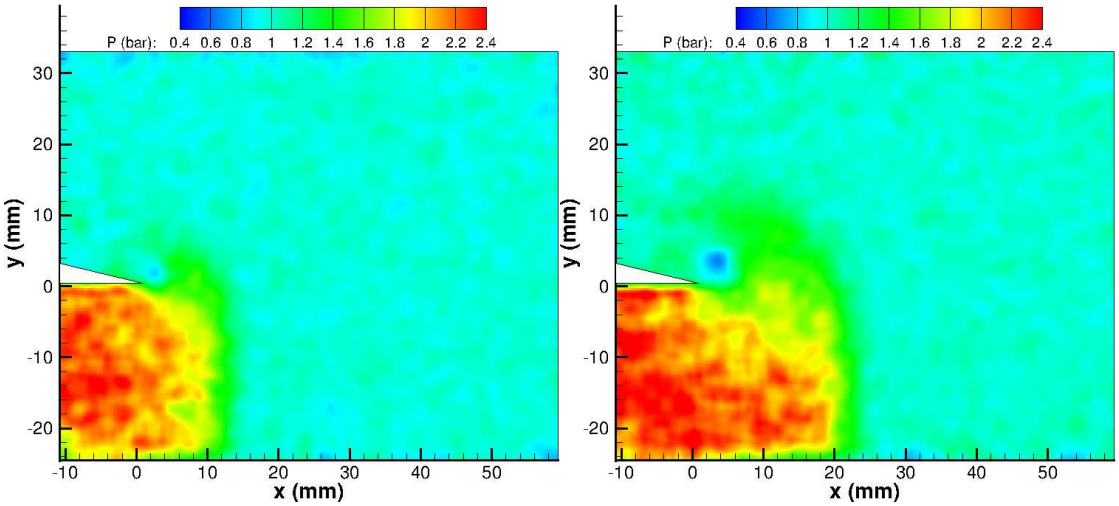

(a) 20 μs

(b) 40 μs

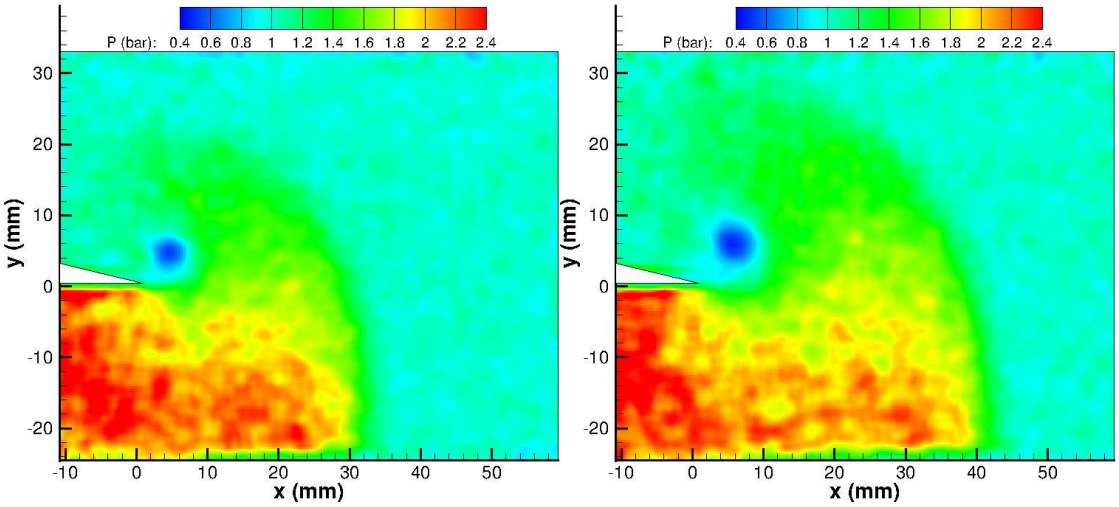

(c) 60 μs

(d) 80 μs

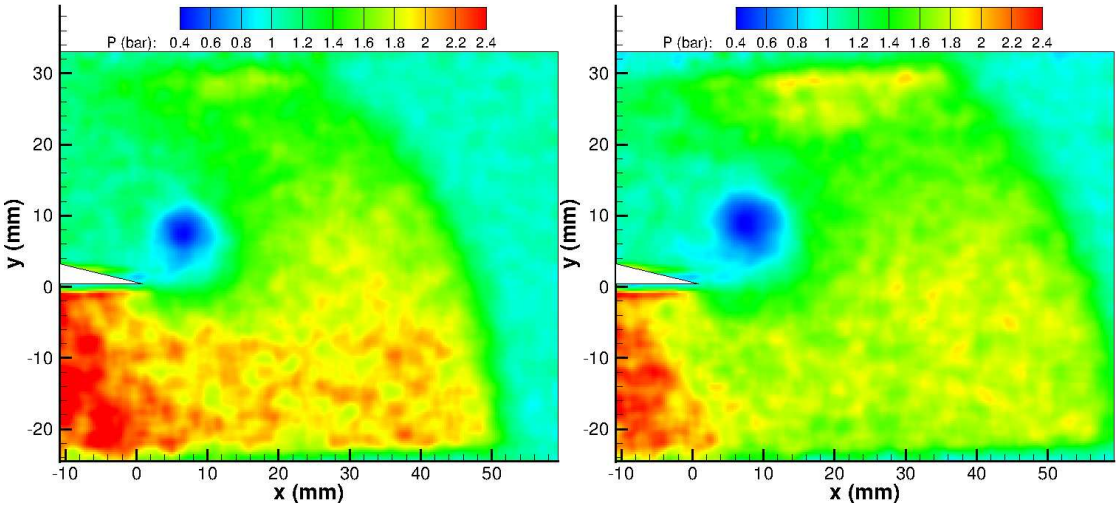

(e) 100 μs

(f) 120 μs

Figure 5.68: PSP map of $M_i = 1.46$ shock diffraction process around a sharp geometry

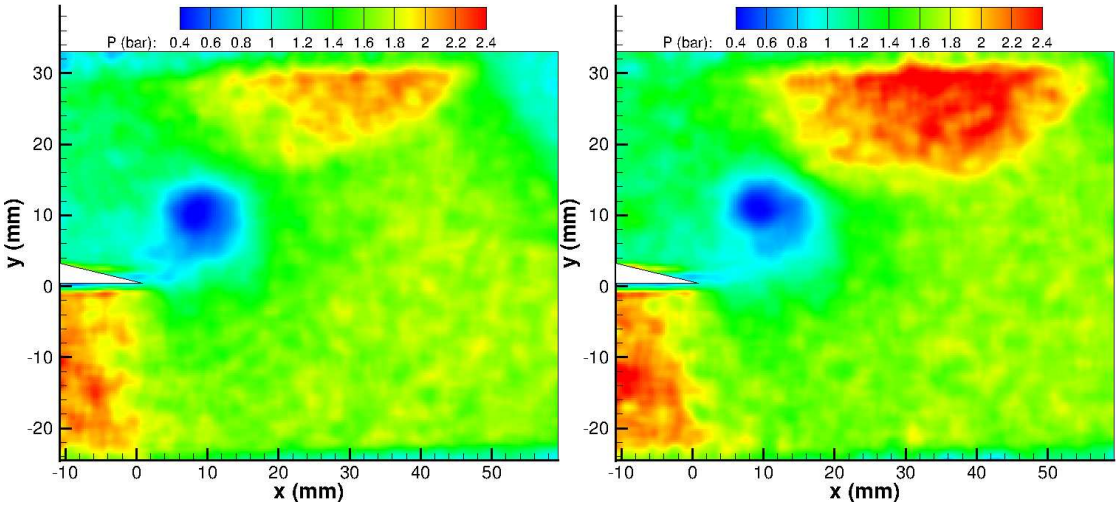

(g) 140 μs (h) 160 μs

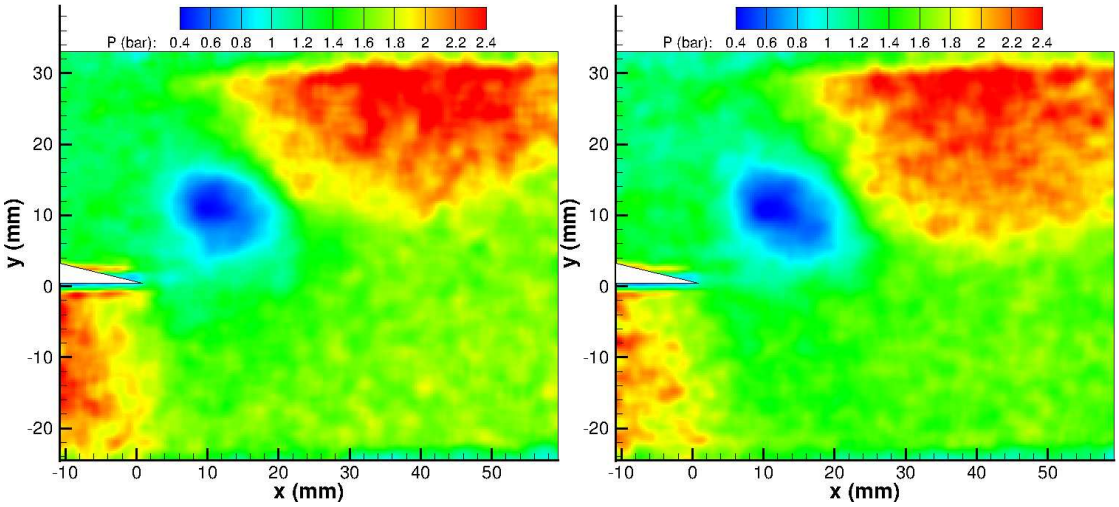

(i) 180 μs (j) 200 μs

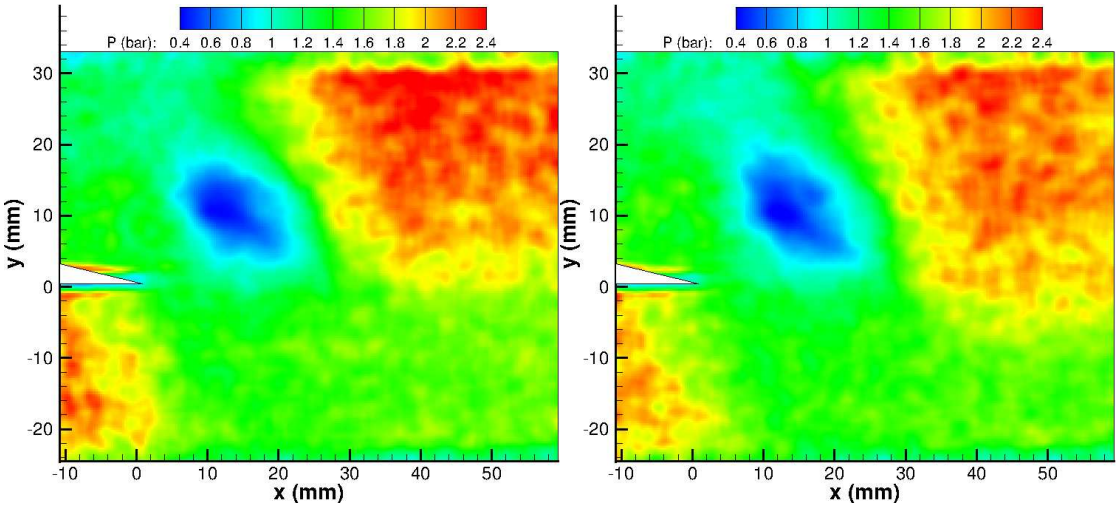

(k) 220 μs (l) 240 μs

Figure 5.68: PSP map of $M_i = 1.46$ shock diffraction process around a sharp geometry

in the CFD data is almost discontinuous as there is no associated exposure time, reaching a maximum of 2.62 bar. The vortex core can clearly be seen as a region of low pressure from 20μs onwards. The reflected expansion wave propagates upstream, causing a decrease in pressure below the splitter, as seen in the experimental results. The last running expansion wave can be seen in Fig.5.69d; however, subsequent waves in this region cannot be seen. The vortex core has an extremely low pressure, 0.12 bar, which is lower than the PSP results, although still within experimental error.

The returning diffracted shock wave shows a pressure increase, as the flow is compressed twice (Fig.5.69f onwards); however, the magnitude of the compression is significantly lower than the experimental PSP results show at the same time step. Of note is the presence of the instabilities on the shear layer. The numerical simulation predicts that these are strong enough to cause significant change in the pressure plot, possibly implying that their strength is overpredicted numerically.

From Fig.5.69g onwards, the shock-vortex interaction proceeds as expected, with the returning wave being split by the vortex. Similarly to the experimental results, the left-hand side of the vortex is associated with a region of low pressure while the right-hand side is compressed to up to 2.1 bar. The impact of the returning shock on the shear layer creates the two strong vortices seen previously which begin to rotate around each other (Fig.5.69j). In the latter images (Figs.5.69k & 5.69l) the shock vortex interaction has created a noticeable step change in pressure at approximately 50° around the vortex as the returning shock wave is slowed by the high-velocity fluid under the shear layer. The location of this pressure change agrees well with the experimental PSP results at the same time step. The distortion to the vortex, evident in the latter images of Fig.5.69, shows the pattern as the PSP results; however, the low-pressure regions extending from the vortex core extend further in the CFD results.

5.4.1.5 Mi = 1.55 Experimental Results

The final PSP results of the sharp geometry are presented in Fig.5.70. The initial pressure rise due to the incident shock wave appears to be spread out over a significantly larger distance than in the previous cases. This could be due to the higher shock speed or due to the larger step change in pressure. The pressure rise behind the shock is measured as 2.54 bar. This values compares reasonably well with the inviscid theory based on M_{ie}, which gives a pressure rise of 2.64 bar. The vortex core is easily identifiable, as is the reflected expansion wave and its associated pressure drop. The lowest pressure measured in the vortex core is 0.40 bar. The pressure gradually increases from the vortex core, with no discontinuities nearby such as the embedded shock seen in the schlieren results. Surprisingly, the pressure at the centre of the vortex in this case is higher than in the previous case.

Figs.5.70e & 5.70f begin to show the initial two lambda shock structures underneath the shear layer. These structures can be seen more clearly by changing the colour map and zooming in (see Fig.5.71). The returning shock wave propagates as before, with an increase in pressure on the right-hand side of the vortex. The slowed returning shock wave can be seen on the PSP figures from Fig.5.70j onwards as an increase in pressure close to the vortex core. There is a pressure increase on the other side of the vortex core (approximately 210° around the vortex) which is

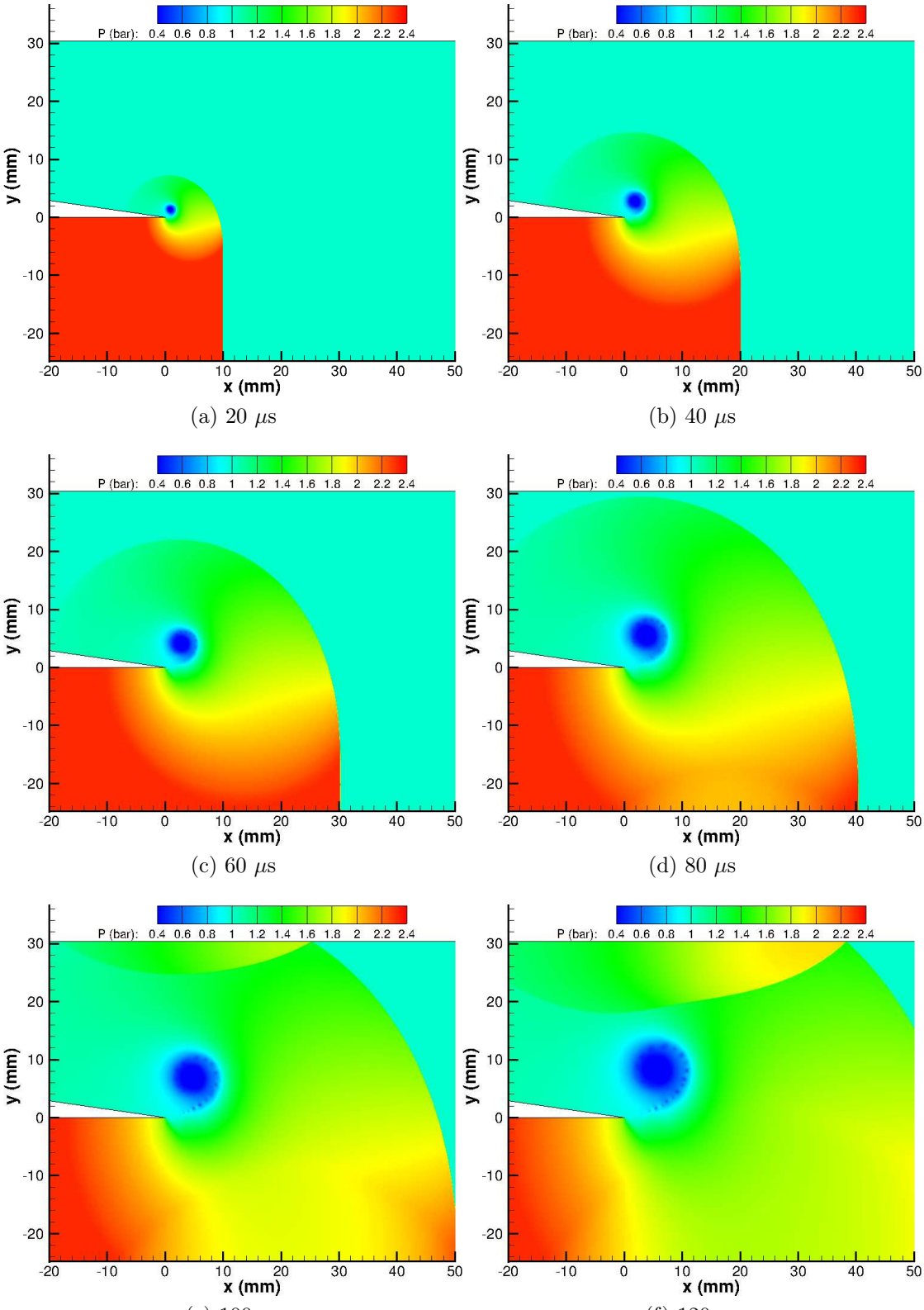

(a) 20 μs (b) 40 μs

(c) 60 μs (d) 80 μs

(e) 100 μs (f) 120 μs

Figure 5.69: CFD pressure map of $M_i = 1.46$ shock diffraction process around a sharp geometry

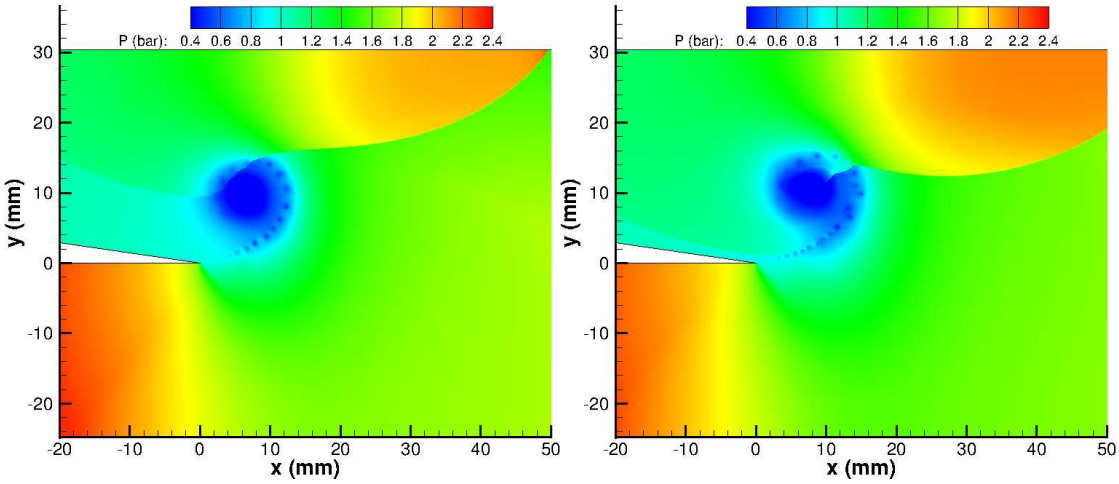

(g) 140 μs (h) 160 μs

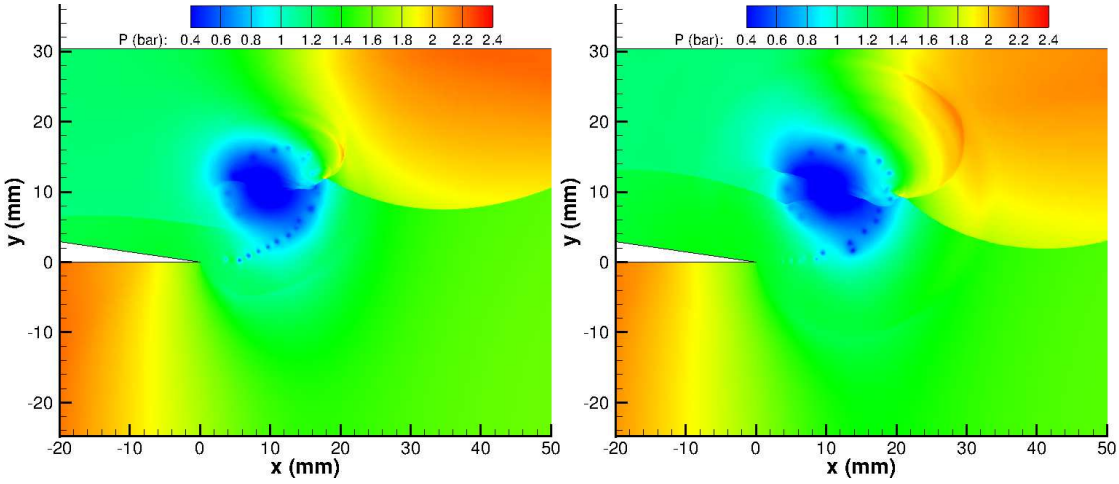

(i) 180 μs (j) 200 μs

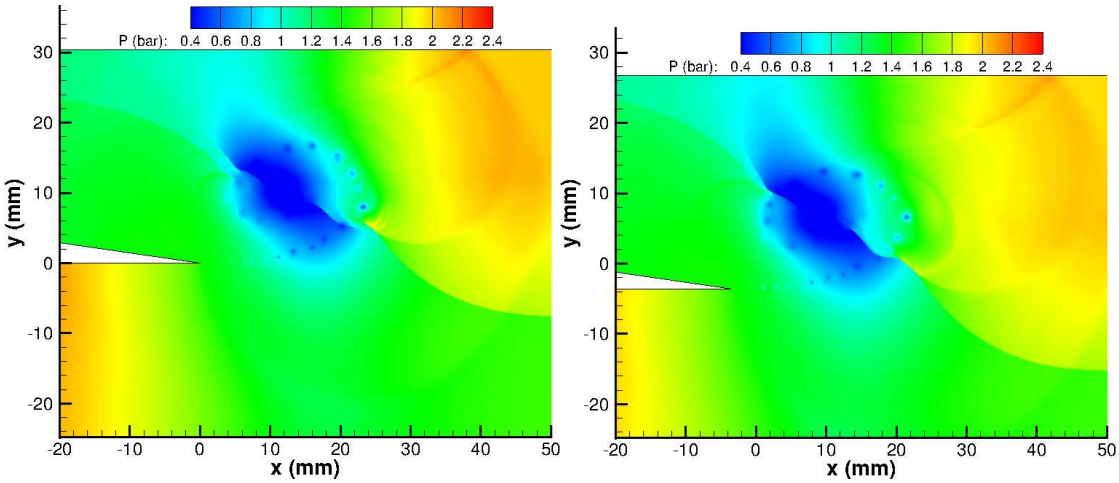

(k) 220 μs (l) 240 μs

Figure 5.69: CFD pressure map of $M_i = 1.46$ shock diffraction process around a sharp geometry

not as well defined as a discontinuity, possibly due to its lower strength.

The main vortex is heavily distorted during the shock-vortex interaction. The once circular vortex has now been stretched to form an elliptical shape aligned at approximately 45° to the horizontal.

5.4.1.6 Mi = 1.55 Numerical Results

The numerical simulations of a $M_i = 1.55$ shock diffracting around a sharp corner are presented in Fig.5.72. The same flow features seen in the previous case are well represented, with the noticeable inclusion of the embedded shock wave between the shear layer and the vortex core, which can be faintly distinguished from Fig.5.72c onwards. The predicted pressure in the vortex core is significantly lower than the experimental value, at 0.12 bar. This value is almost identical (to five decimal places) to the pressure at the centre of the $M_i = 1.46$ numerical simulations, perhaps indicating that the pressure plateaus at a minimum value at this Mach number.

The predicted maximum pressure due to the returning shock wave is 2.41 bar, which agrees well with the experimental results (Figs.5.70h & 5.72h). The diverging acoustic waves, generated by the interaction of the returning shock with the shear layer instabilities (Fig.5.72j), appear significantly stronger in this case than compared to all of the others covered so far. This implies that both the returning shock and the instabilities are significantly stronger in this case.

The shock structure created by the shock-vortex interaction is very sharply defined in Figs. 5.72k & 5.72l. The position of the interaction agrees well with the PSP results at the same time step; however, the PSP results are obviously not as sharply defined.

In the latter images for Fig.5.72, the low-pressure region associated with the vortex appears to be spreading quickly along the upstream side of the shock wave system created by the shock vortex interaction. The scale of this expansion region is much larger than that seen in the PSP results (Figs.5.70l & 5.72l). This larger expansion region explains the large discrepancy between the real and numerical transducers seen in Section 5.3.1.3.

5.4.1.7 Conclusions

Thin layer chromatography-based pressure-sensitive paint has been successfully applied to give quantitative measurements of the static pressure during the shock diffraction process. These results represent one of the first successful attempts to measure a truly transient process using a camera rather than a PMT. The rise in pressure due to the shock wave and the decrease in pressure due to the vortex are well captured. There is some disagreement between the pressure measured in the vortex core and the numerical results. The spatial resolution of the numerical results is significantly higher than the experimental results, meaning that the exact centre of the vortex (i.e. the cell of lowest pressure) can be captured more accurately.

The initial shock wave is captured, although it is not represented as a discontinuity. The shock wave is smeared due to the finite exposure time of 9.6 μs. However, this alone does not explain the total shock spread distance. The finite luminescent lifetime of the ruthenium complex used accounts for more of the shock-spreading distance, as was shown in Fig.3.37.

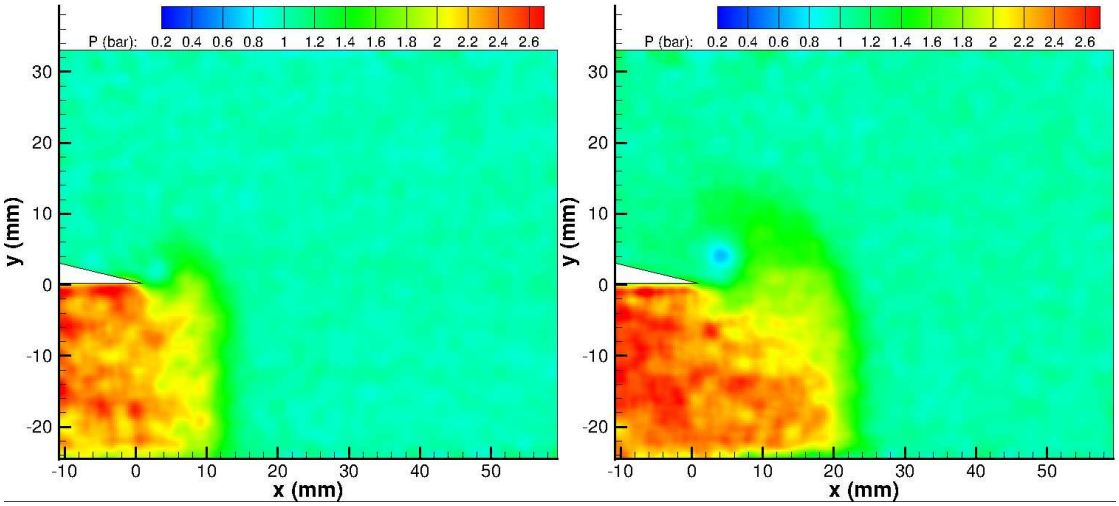

(a) 20 μs (b) 40 μs

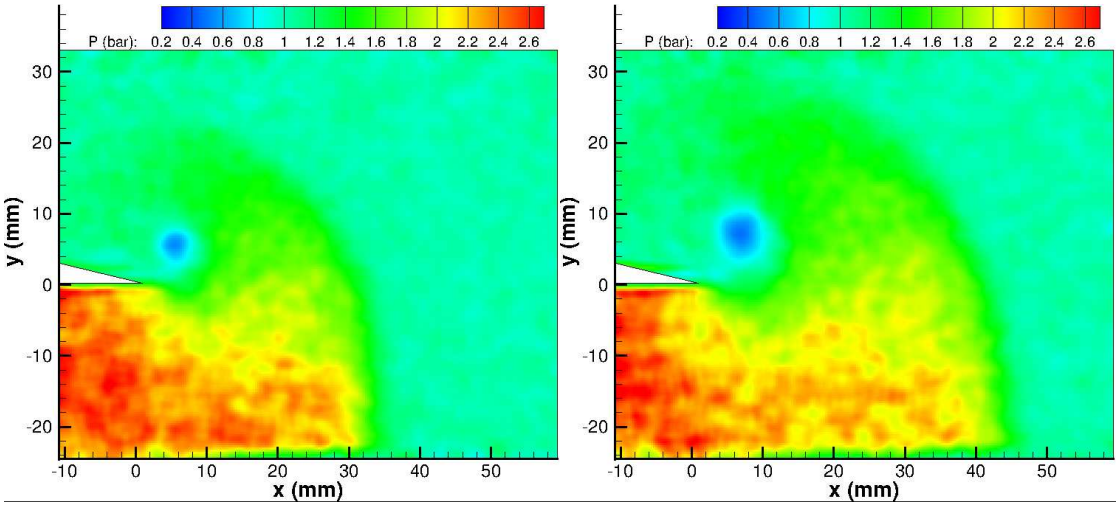

(c) 60 μs (d) 80 μs

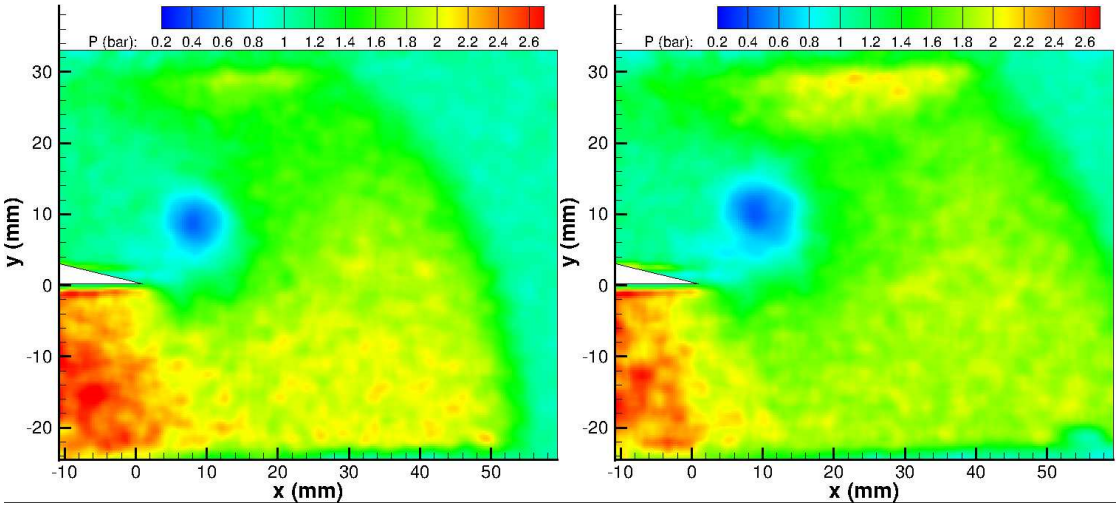

(e) 100 μs (f) 120 μs

Figure 5.70: PSP map of $M_i = 1.55$ shock diffraction process around a sharp geometry

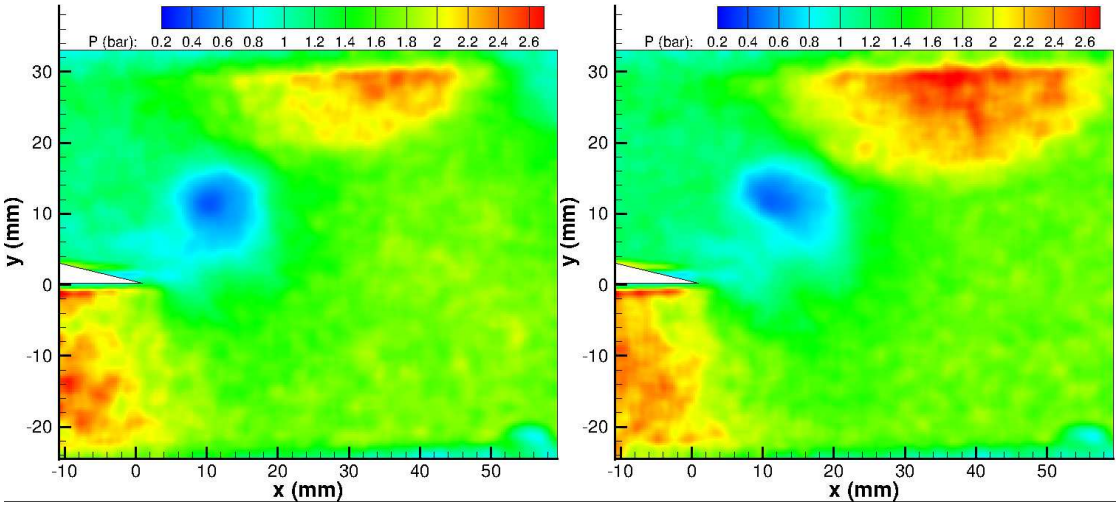

(g) 140 μs (h) 160 μs

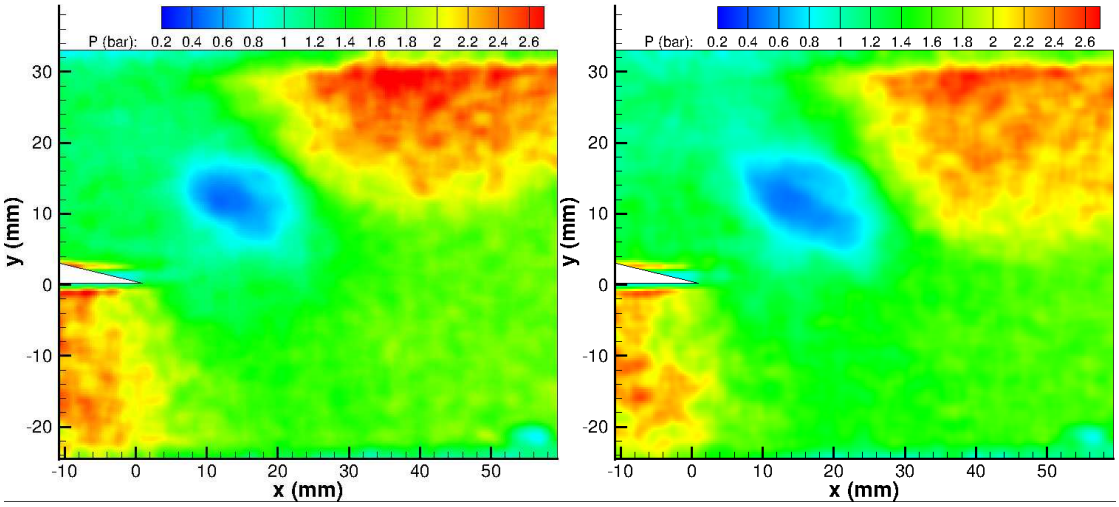

(i) 180 μs (j) 200 μs

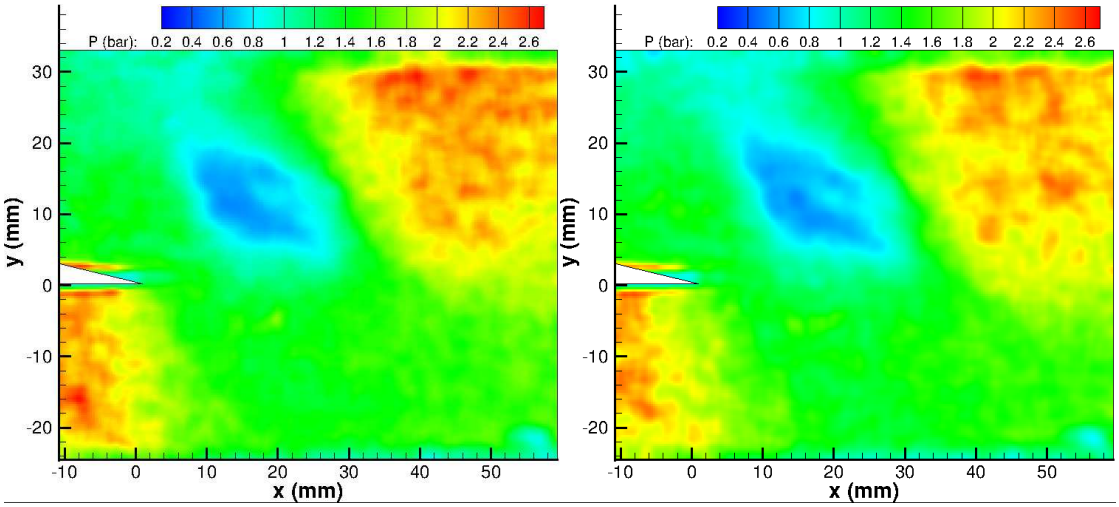

(k) 220 μs (l) 240 μs

Figure 5.70: PSP map of $M_i = 1.55$ shock diffraction process around a sharp geometry

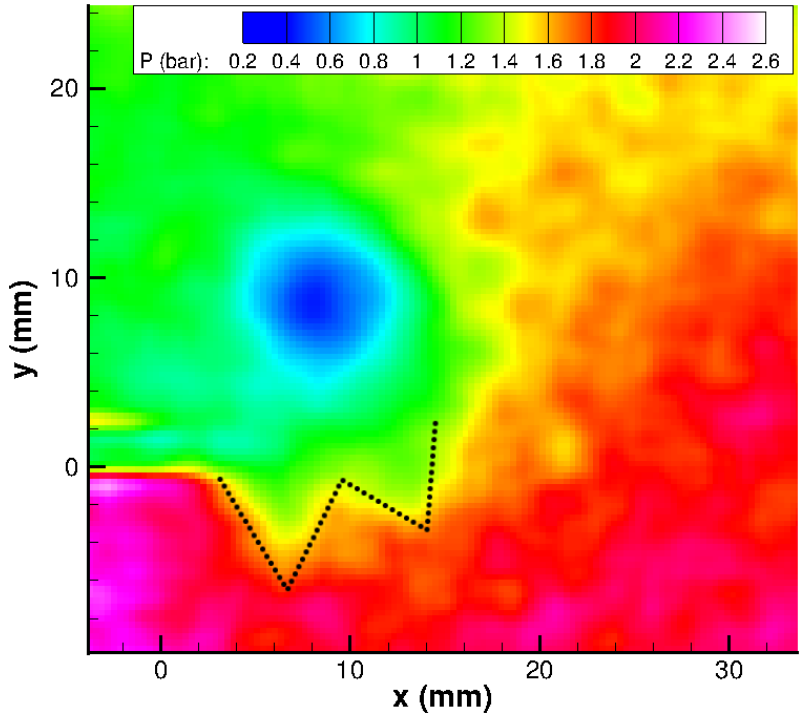

Figure 5.71: Pressure map showing the lambda structures underneath the shear layer at 100 μs

The reflected expansion wave can be seen propagating away from the splitter tip at all three test conditions. In the $M_i = 1.55$ case, faint traces of the lambda wave structure can be seen underneath the shear layer in the density-based results. These lambda structures are clearly not very strong, as they are poorly resolved in both the pressure measurements and the particle-based measurements. The pressure measured in the expansion region is approximately 1 bar regardless of the incident shock Mach number, validating one of the assumptions made in the secondary shock analysis in Section 2.4.1.

The reflection of the diffracting shock wave from the top wall of the test section can be seen in all three cases as a secondary increase in pressure. The pressure reached in this region is almost the same magnitude as the pressure behind the incident shock wave for all three cases. This is the region of stagnant fluid mentioned in Section 5.2.1.7.

The shock-vortex interaction, specifically the progress of the shock on the right-hand side of the vortex, is captured well and represents the sharpest discontinuity measured by the PSP. This is not surprising, as this shock wave moves significantly more slowly than the incident shock and produces a similar magnitude of pressure jump. The shock on the left-hand side of the vortex is not well captured by the PSP, indicating that it is significantly weaker, a finding expected from the particle-based results. The distortion of the main vortex, caused by the returning diffracted shock wave, is reflected in the PSP results. For the $M_i = 1.28$ case, the distortion is barely noticeable and the vortex remains a circular region of low pressure. However, the subsequent cases show that the vortex is heavily distorted, with the regions of high velocity from the PIV results manifesting as regions of low pressure. This is particularly noticeable in the $M_i = 1.55$ case, as a discontinuity near the vortex core

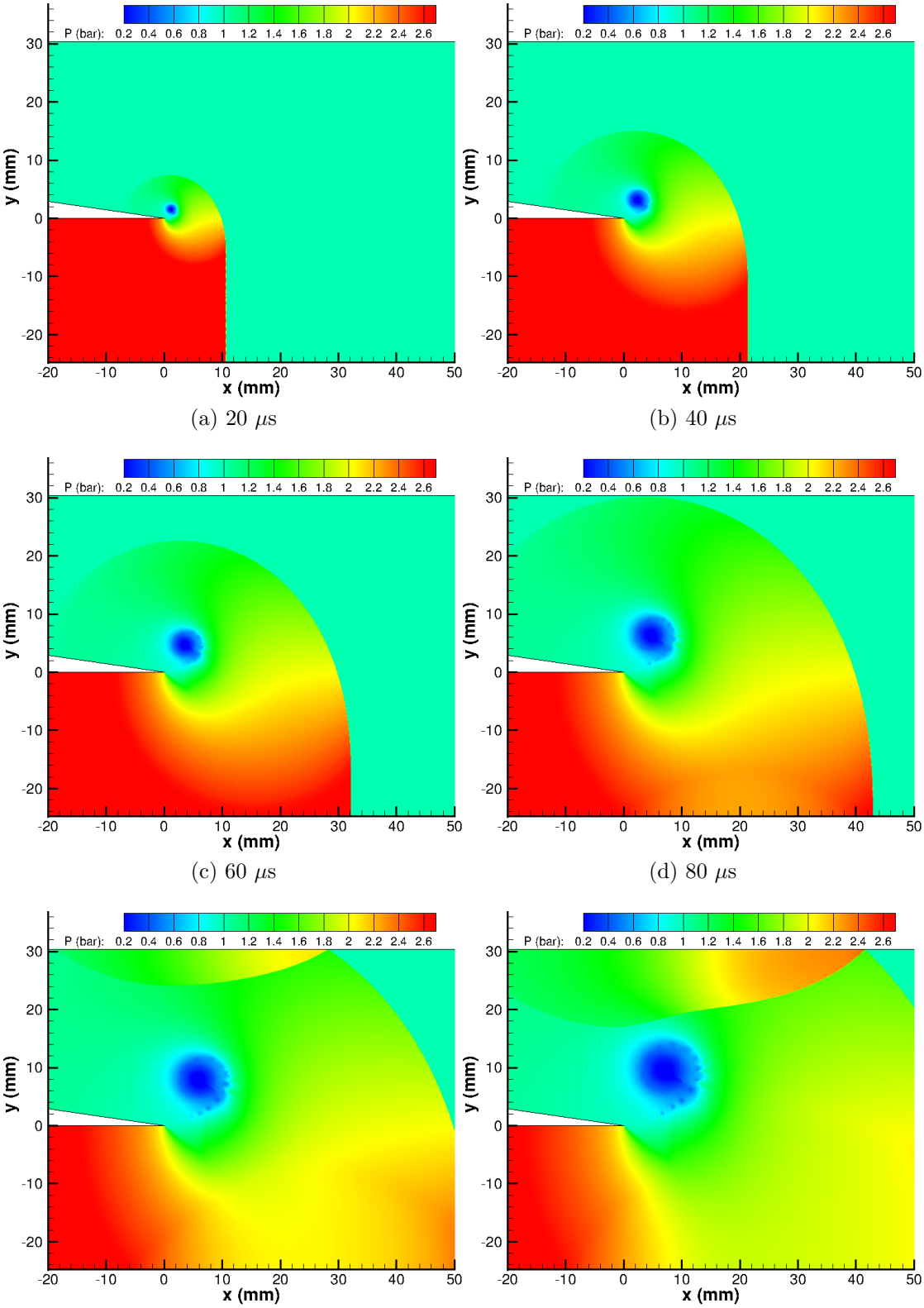

(a) 20 μs (b) 40 μs

(c) 60 μs (d) 80 μs

(e) 100 μs (f) 120 μs

Figure 5.72: CFD pressure map of $M_i = 1.55$ shock diffraction process around a sharp geometry

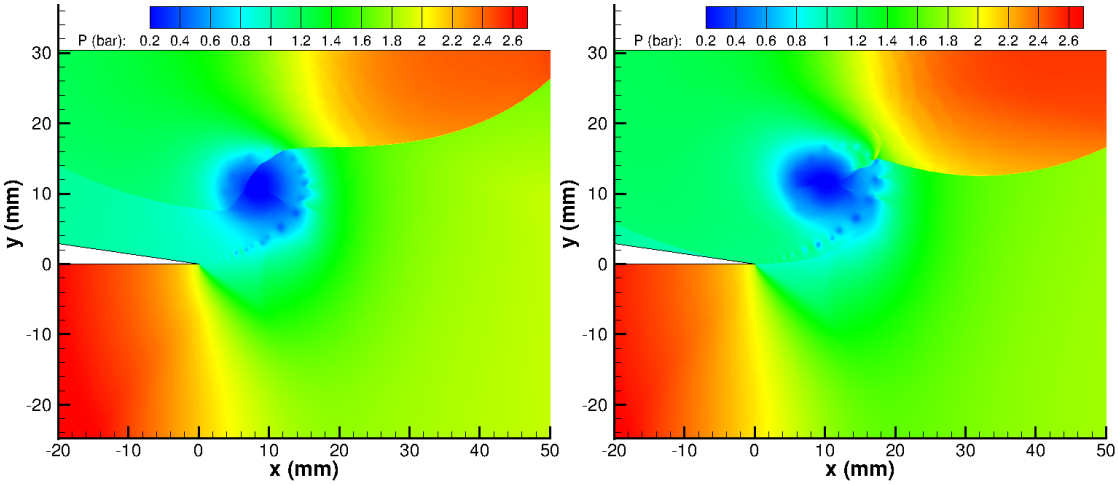

(g) 140 μs (h) 160 μs

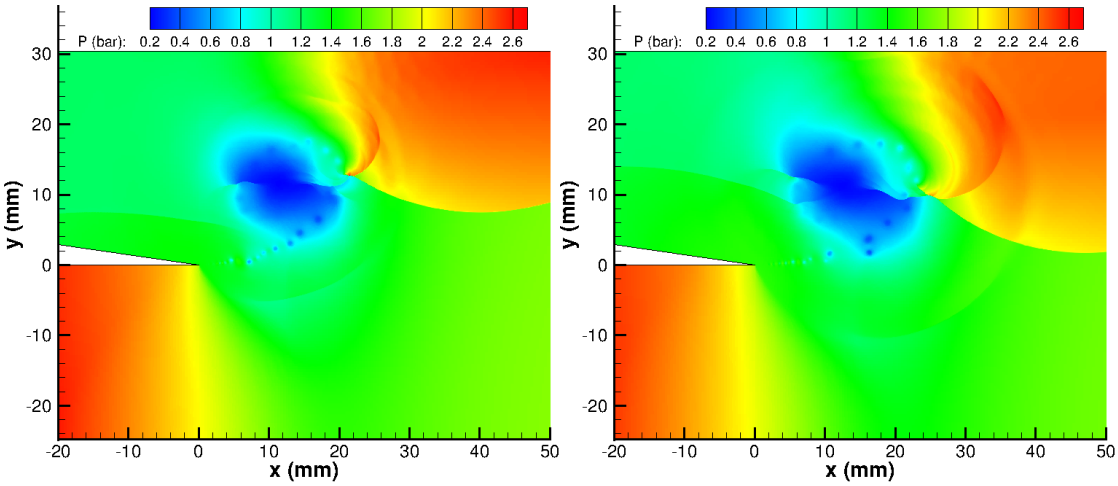

(i) 180 μs (j) 200 μs

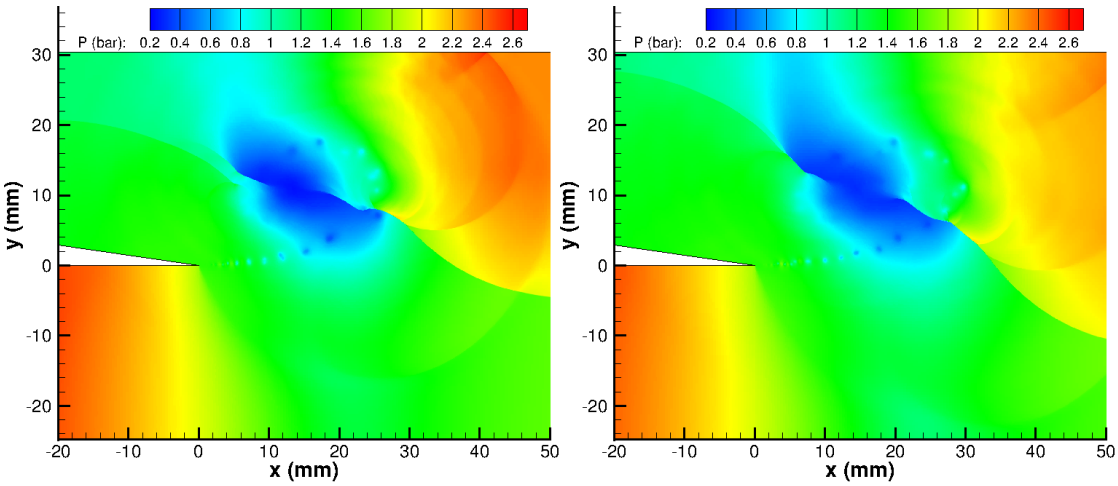

(k) 220 μs (l) 240 μs

Figure 5.72: CFD pressure map of $M_i = 1.55$ shock diffraction process around a sharp geometry

can be seen. The pressure spike seen by Skews et al. [71] is not seen in either the numerical or experimental results.

The *low* spatial resolution of the PSP results and relatively high degree of spatial noise means that no information can be gathered about the shear layer. It would be expected that, initially, where the shear layer is straight, the pressure on either side would be equal, meaning that PSP would not give significant information. To begin with, the same is true in the numerical results; however, eventually the instabilities on the shear layer become strong enough to manifest themselves in the static pressure field.

There is a significant degree of spatial noise present in the experimental results. This is primarily due to the shot noise, as was shown in Section 3.4.10. The spatial noise can only be reduced by ensemble-averaging multiple runs, as it consists of random fluctuations. Future improvements in CCD technology should also reduce this problem. Despite the high level of spatial noise, the experimental and numerical results agree within experimental error, with the exception of the exact vortex core pressure. The PSP measurements also show that the influence of the low-pressure region after the $M_i = 1.55$ shock-vortex interaction is not as strong as the numerical predictions, agreeing with the conclusion of Section 5.3.1.4. This is likely to be a numerical error rather than the PSP not responding quickly enough, as the results of Gregory & Sullivan show that PSP responds to a decrease in pressure more quickly than to an increase in pressure [184].

5.4.2 Round Geometry

5.4.2.1 Mi = 1.28 Experimental Results

Fig.5.73 shows the static pressure map of a $M_i = 1.28$ shock wave diffracting around a rounded corner. The spatial noise present on the sharp corner is ever present here, despite attempts to improve the processing algorithm to minimise its impact. The initial pressure rise shock in Fig.5.73a is 1.68 bar, identical to the result for a sharp corner. The low-pressure region corresponding to the vortex core does not become clearly visible until Fig.5.73d. This corresponds well with the density- and particle-based results, which showed that the boundary layer separation process for a rounded corner takes a finite length of time, unlike that for a sharp corner. The pressure in the vortex core goes on to reach a minimum of 0.42 bar, a value slightly lower than the corresponding result for a sharp geometry. The diffracted part of the shock appears very faintly in Fig.5.73, suggesting that it loses its strength quickly. This correlates with the slightly lower initial pressure rises given by the pressure transducers. The reflected expansion wave is noticeable in Fig.5.73b onwards as it propagates away from the change in curvature, reducing the pressure in the test section.

It is interesting to note that the location at which the contact surface impacts on the top surface of the splitter (see Fig.5.19) shows almost no change in pressure, indicating that the stagnation region seen in Fig.5.48 is not strong in comparison with the rest of the flow features.

By 100 μs (Fig.5.73e) the low-pressure region caused by the vortex appears as a stretched vertical structure, rather than the rounded low-pressure region seen for the sharp geometry. In Fig.5.73f, the vortex core is rounded in shape; however, there is a region of low pressure connecting it to the splitter edge. This low-pressure region corresponds to the internal expansion region and the region bounded by the main and internal shear layers seen in the density-based results.

At 120 μs the diffracted shock wave has reached the top wall of the test section and is beginning to reflect back through the test section. The flow is then compressed again to a maximum value of 1.53 bar. This value is slightly lower than the one for a sharp geometry, indicating that the rounded corner has reduced the strength of the shock wave. The region of highest pressure is in the same location as the stagnation region seen in the PIV results. The strength of the double compression is almost constant from Fig.5.73i to Fig.5.73k; however, by 240 μs, the pressure in this region is beginning to slowly decrease. The reflected shock is much weaker on the left-hand side than on the right; this is to be expected, as the diffracted shock loses strength along its length. There is no sign that the shock-vortex interaction creates strong enough diverging waves to influence the PSP measurements.

5.4.2.2 Mi = 1.28 Numerical Results

The numerical pressure profile is presented in Fig.5.74. The discontinuous pressure jump created by the incident shock wave is, as expected, more sharply resolved in the numerical results than in the PSP results and reaches a steady maximum of 1.75 bar, identical to the result predicted by inviscid theory. The curved portion of the diffracted shock wave rapidly loses its strength along its length, as shown in the experimental results. The numerical incident shock pressure ratio is not limited

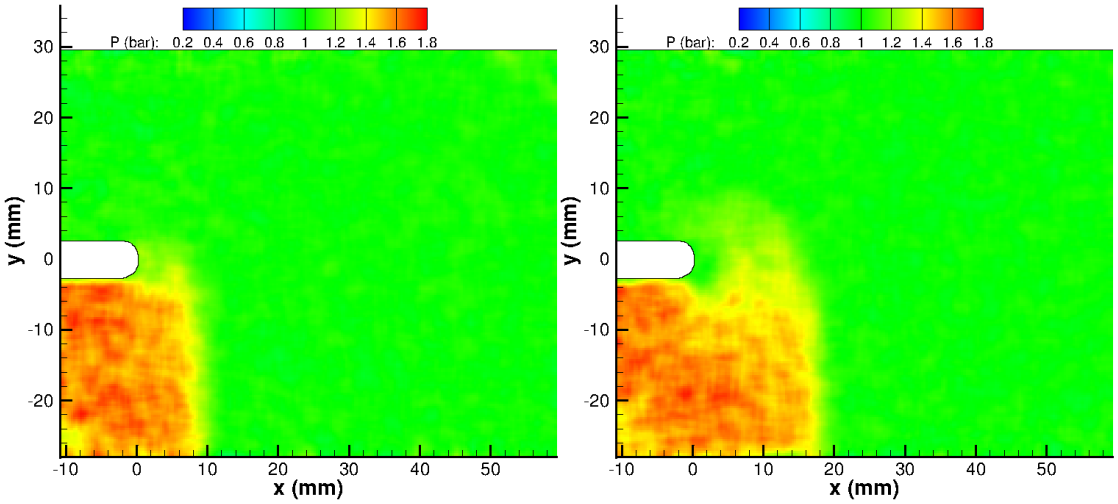

(a) 20 μs

(b) 40 μs

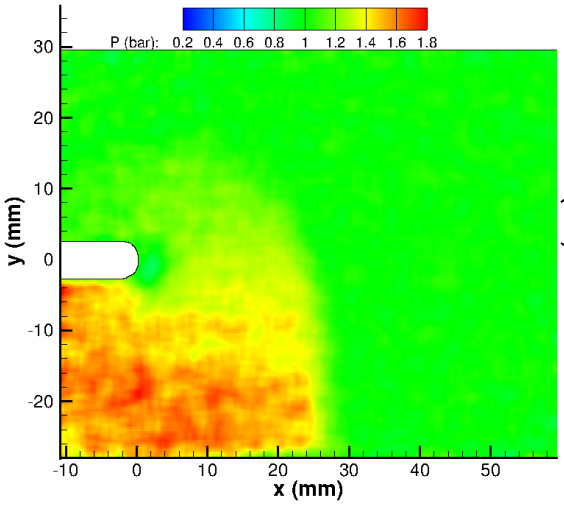

(c) 60 μs

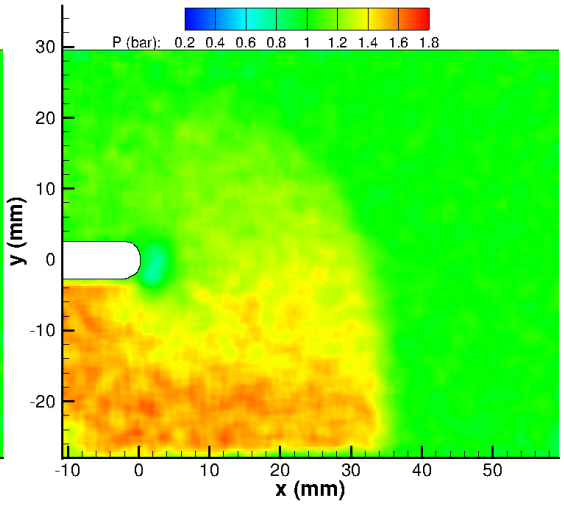

(d) 80 μs

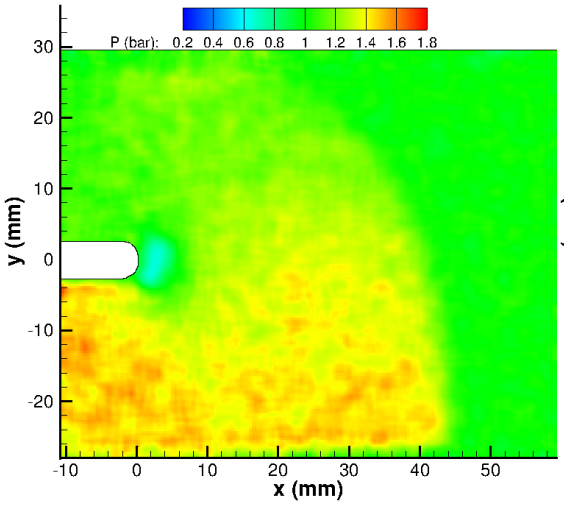

(e) 100 μs

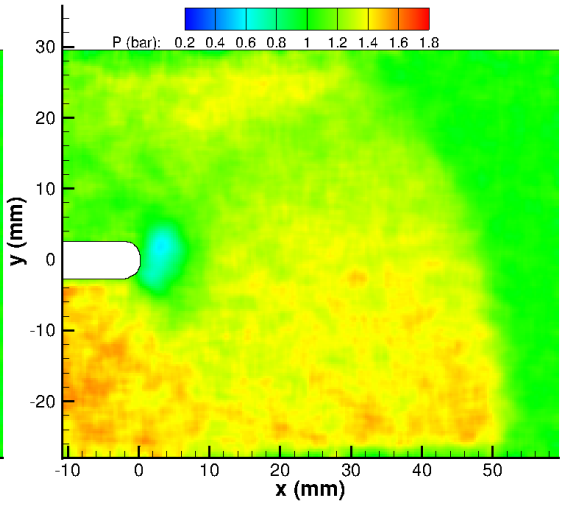

(f) 120 μs

Figure 5.73: PSP map of $M_i = 1.28$ shock diffraction process around a round geometry

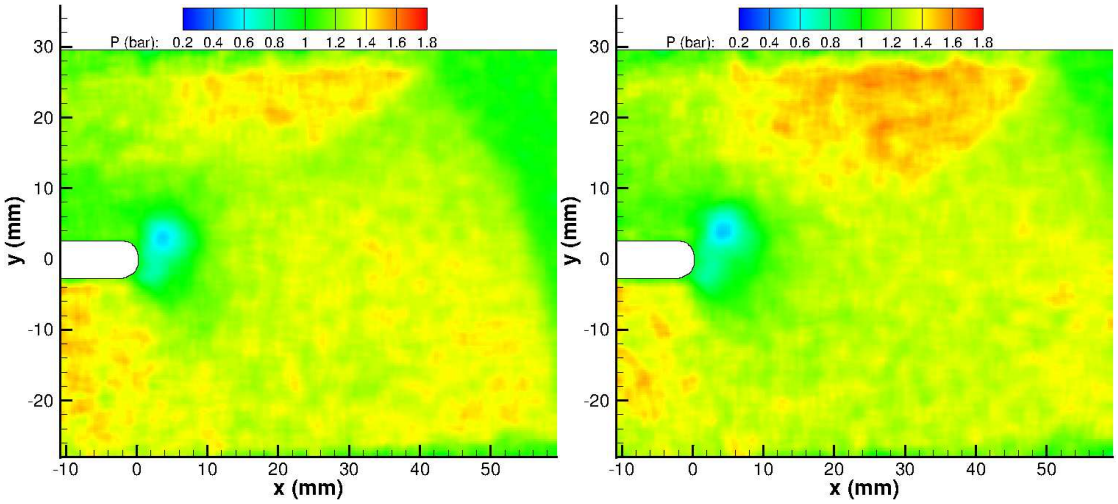

(g) 140 μs

(h) 160 μs

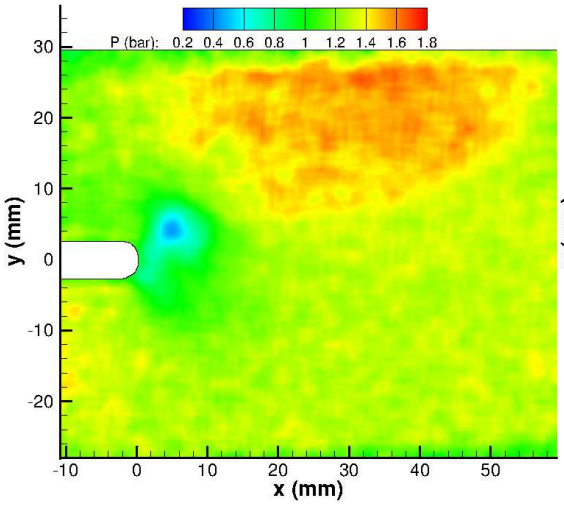

(i) 180 μs

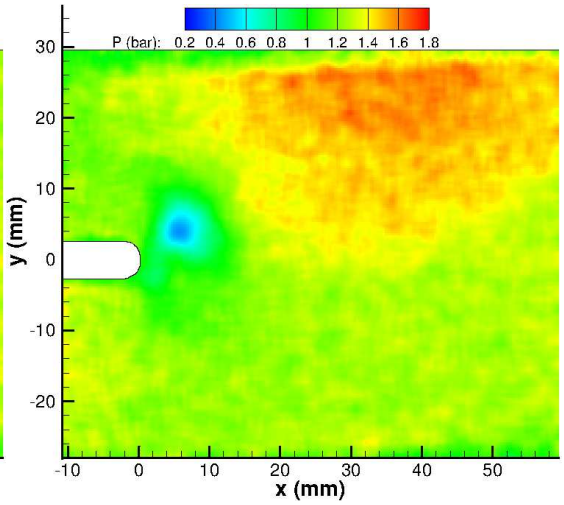

(j) 200 μs

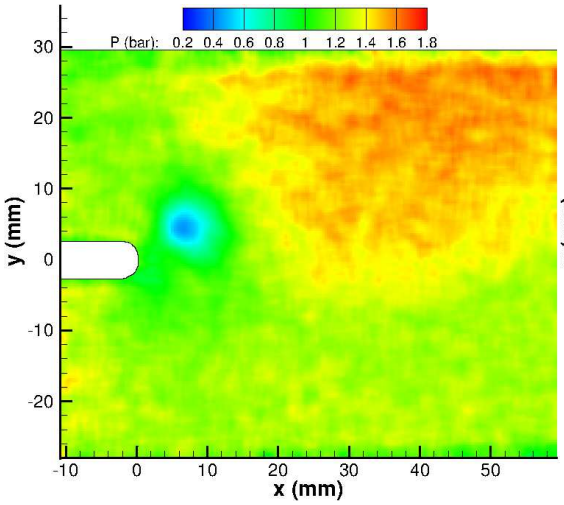

(k) 220 μs

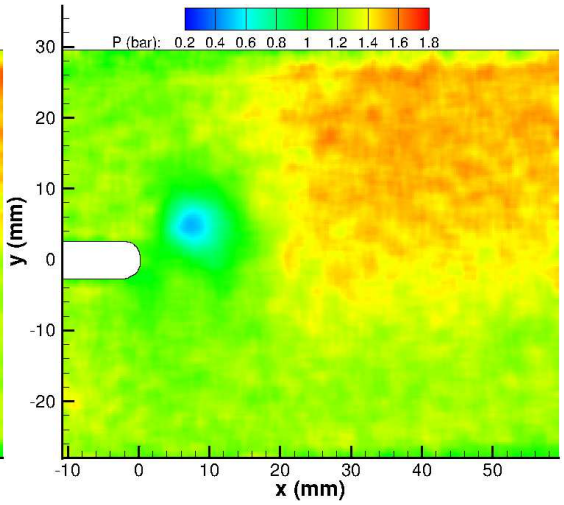

(l) 240 μs

Figure 5.73: PSP map of $M_i = 1.28$ shock diffraction process around a round geometry

by physical processes, such as diffusion or deactivation time, as is the case of the experimental results, and as such it reaches the maximum much more quickly.

As the process evolves in time, the reflected expansion wave, although not easily distinguishable as an individual wave, lowers the pressure behind the incident shock wave to similar levels, as was seen in the experimental results. The numerical results agree with the experimental results in that the stagnation region on the top surface of the splitter in the vicinity of the contact surface does not create any significant changes in pressure.

The low-pressure region associated with boundary layer separation and vortex formation can be seen as early as 60 μs in Fig.5.74c. The low-pressure region is the same size and shape as the experimental results; however, the lowest pressure in the vortex core is measured at 0.08 bar, significantly lower than in the experimental results. The discrepancy between numerical and experimental results will be discussed in the conclusions of this section. The vortex core goes on to develop a rounded shape similar to the experimental results with an associated low-pressure region attached to the rounded corner. Fig.5.74g shows the internal expansion region and the last running expansion wave coming from it. The internal terminating shock is also well-resolved in this figure.

The pressure profile created by the reflected diffracted shock wave is almost identical to the experimental results in terms of both shape and magnitude (Figs.5.74f to 5.74h). The pressure rise seen by the double compression is 1.55 bar and the pressure in this region begins to attenuate by 240 μs. However, the shock-vortex interaction causes waves which are significant enough to increase the pressure by approximately 0.2 bar. The compression waves created in the interaction account for the two pressure rises seen at transducers **K1 CFD** & **K2 CFD** in Fig.5.63, which are barely detected by the actual transducers. These waves are not seen in the PSP map, although they are within the experimental error of the current setup given in Section 3.4.10.

5.4.2.3 Mi = 1.46 Experimental Results

Fig.5.75 shows the static pressure history of a $M_i = 1.46$ shock diffracting around a sharp corner as measured by the TLC PSP. The pressure rise behind the incident shock in Fig. 5.75a is 2.28 bar; this is slightly lower than the expected value based on inviscid theory (2.32 bar) but still well within experimental error. In Fig.5.75b the shock front shape seems more easily defined than in the previous case. This is partly due to the stronger shock, but it is also a function of the visibility of the colour map range. Even at this early time (40 μs) the low-pressure region associated with the separation process and the vortex is faintly visible. The reflected expansion wave makes slower progress into the uniform flow behind the incident shock in this case, due to the higher induced velocity. Despite this, the pressure is still dropping in this region (Fig.5.75b onwards). By 100 μs the vortex has appeared as a distinct rounded region of low pressure with a further region of low pressure connecting it to the expansion region. The minimum pressure measured in the vortex core is 0.28 bar. In Figs.5.75e & 5.75f the region of low pressure below the vortex is beginning to resemble the lambda structure seen in the density-based results. The region between the main and internal shear layers appears as a clear region of low pressure.

The shock wave reflecting off the top surface and propagating towards the vortex

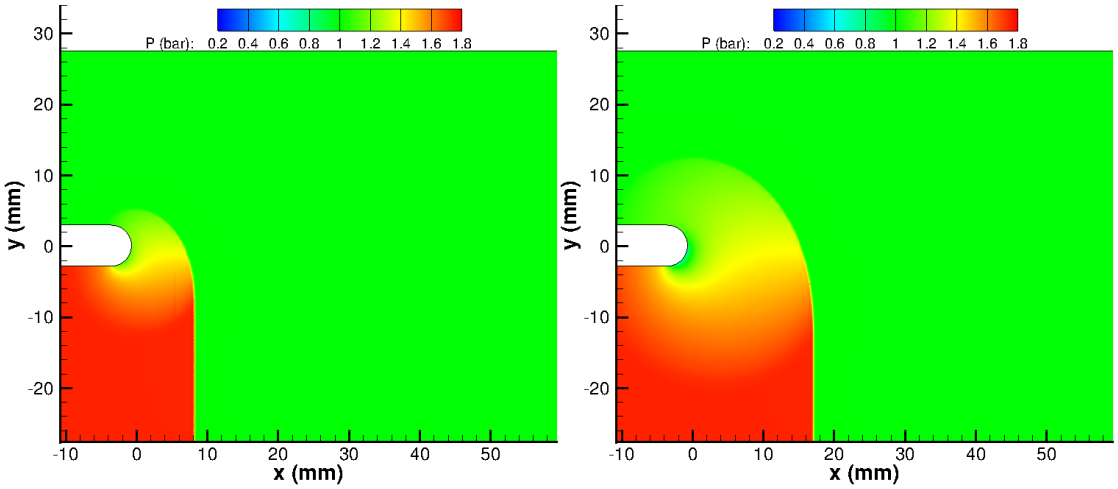

(a) 20 μs

(b) 40 μs

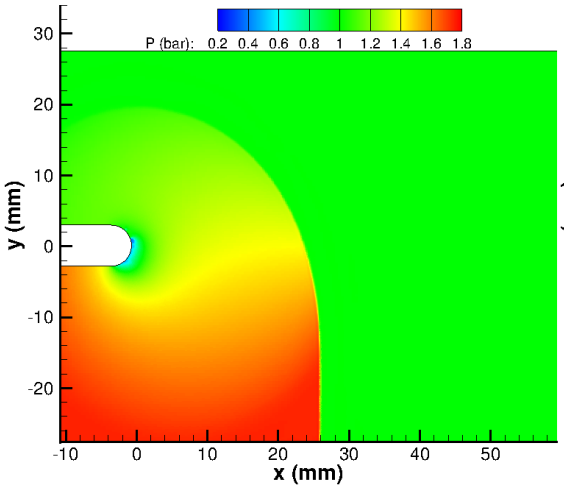

(c) 60 μs

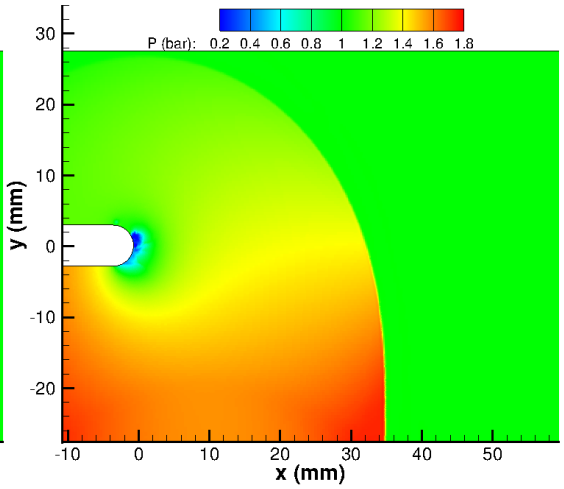

(d) 80 μs

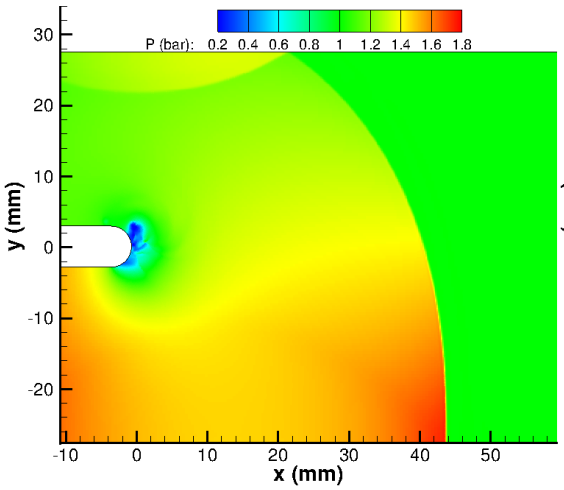

(e) 100 μs

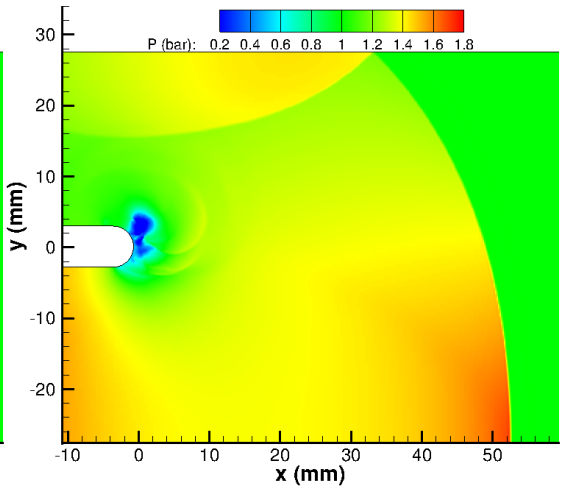

(f) 120 μs

Figure 5.74: CFD pressure map of $M_i = 1.28$ shock diffraction process around a round geometry

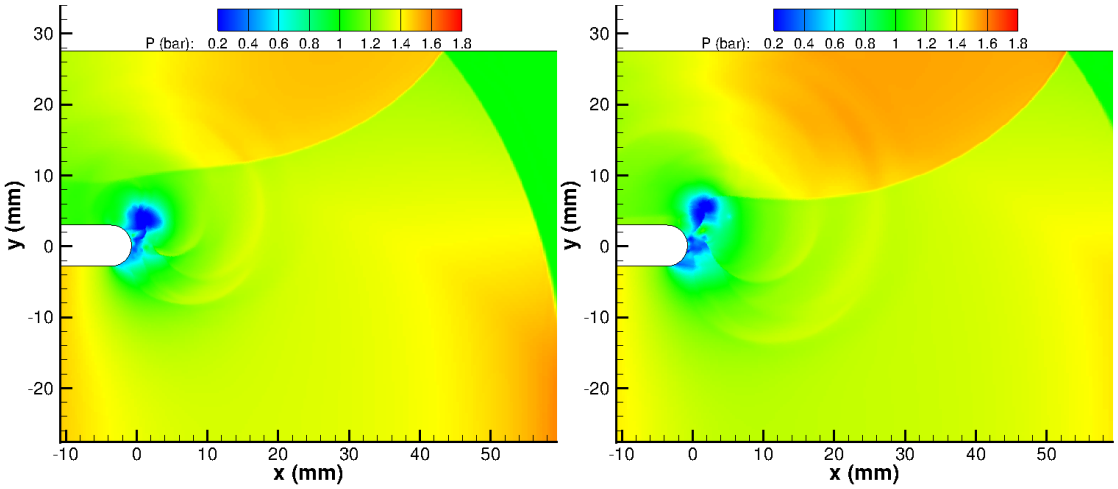

(g) 140 μs (h) 160 μs

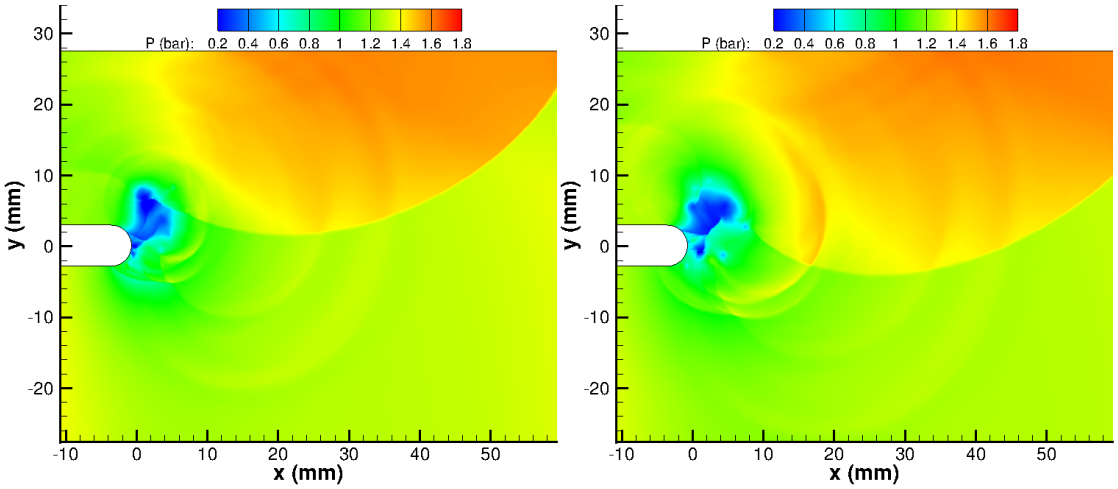

(i) 180 μs (j) 200 μs

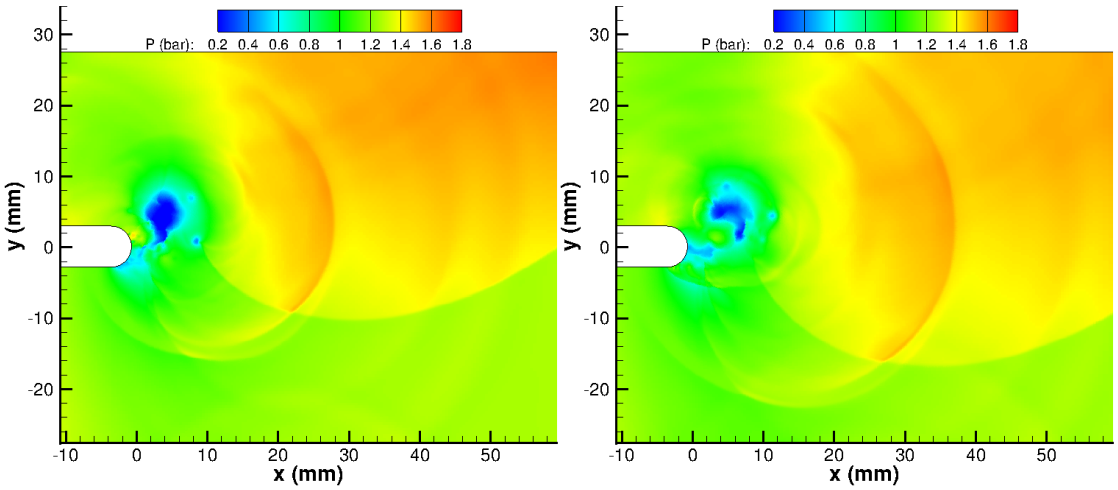

(k) 220 μs (l) 240 μs

Figure 5.74: CFD pressure map of $M_i = 1.28$ shock diffraction process around a round geometry

is visible from 100 μs onwards. The double compression raises the pressure in this region to 2.21 bar, significantly higher than in the $M_i = 1.28$ case, showing the increased strength of the shock. Just prior to the shock-vortex interaction, the lambda wave structures underneath the shear layer can be seen most clearly. Fig.5.76 shows a close-up of this region with a different colour map to aid visibility of the wave structures. The las running expansion wave and its associated lambda shock have been highlighted.

The shock-vortex interaction has a significantly greater impact on the flow than in the previous case. The vortex contains a weak discontinuity at approximately 45°. This shock corresponds to the right-hand shock during the shock vortex interaction, as seen in the density-based results. However, the PIV results suggested that this shock would be significantly stronger than it appears to be in the PSP map. The static pressure directly below the vortex in Figs.5.75k & 5.75l is significantly reduced as the last running expansion wave is drawn downwards by the returning diffracted shock. This correlates well with the large increase in velocity seen in the PIV measurements in this region.

5.4.2.4 Mi = 1.46 Numerical Results

The numerical results of a $M_i = 1.46$ shock are presented in Fig.5.77. The initial pressure rise behind the incident shock is 2.31 bar, agreeing almost perfectly with inviscid theory. The diffraction profile agrees well with the experimental results, as well as the size of the vortex in the complex region. The absolute pressure in the vortex core is 0.07 bar, which is much lower than the experimental value. The reflected expansion wave makes slower progress through the test section in this case but the influence of the corner is stronger. The expansion wave generated at the corner lowers the pressure dramatically before it is recompressed by the lambda shock attached to the main shear layer. From Fig.5.77e onwards, the internal terminating shock wave can be seen connecting the vortex core and the internal shear layer. After this shock wave the pressure is increased to a value slightly higher than that on the other side of the shear layer. This accounts for the curvature seen in the density-based results, leading to the generation of a compression corner and, as a result, a stronger lambda shock. The internal terminating shock wave persists during the shock-vortex interaction (Fig.5.77h onwards), connecting the rounded corner and the vortex core. This was not seen in the PSP results. Density-based results show that this shock is broken down into compression waves, perhaps indicating that the numerical simulations overpredict the velocity induced by the vortex and the internal expansion region.

The returning diffracted shock wave strongly compresses the flow above and to the right of the vortex. The pressure in this region reaches 2.17 bar, close to the experimental value of 2.21 bar. The shock-vortex interaction creates several compression waves which are most easily visible in Fig.5.77j. These waves are approximately the same strength as those seen in the previous case, although they are relatively weaker given the stronger waves found elsewhere in the flow at this higher Mach number. By 240 μs, the shock-vortex interaction has created two alternating regions of high and low pressure around the vortex core which agree with the PIV results. The shock at approximately 60° around the vortex is clearly visible in both the density-based results (Fig.5.25l) and the PIV results (Fig.5.52l). The shock wave

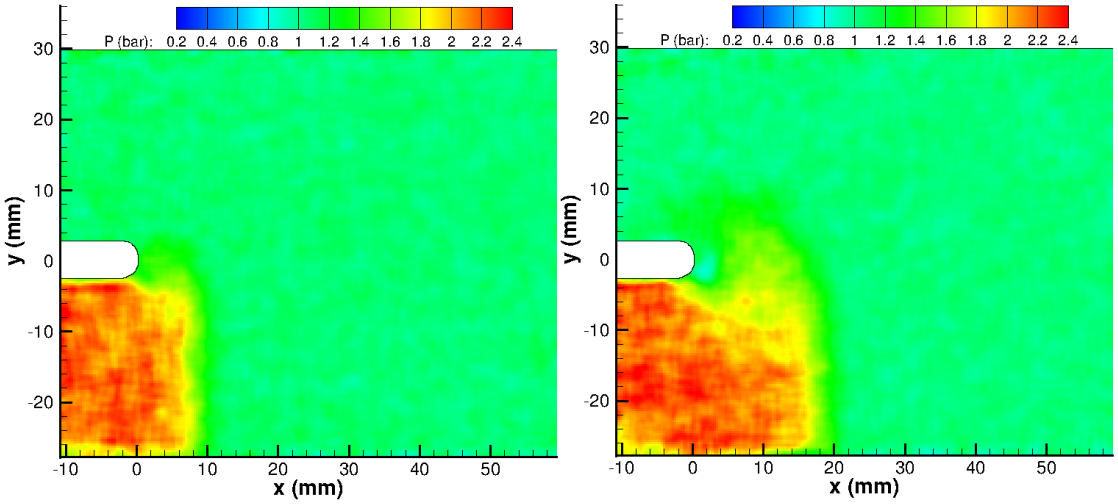

(a) 20 μs

(b) 40 μs

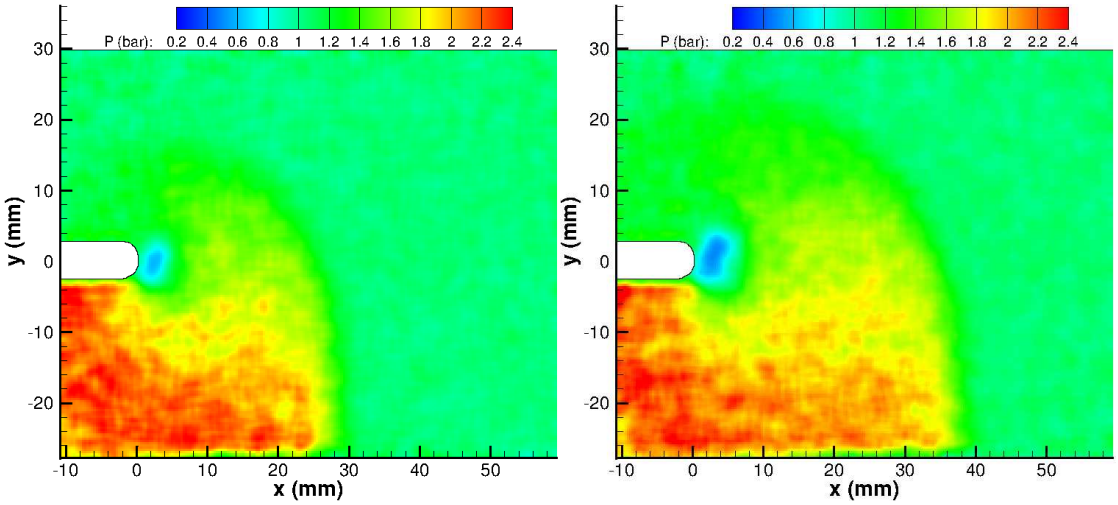

(c) 60 μs

(d) 80 μs

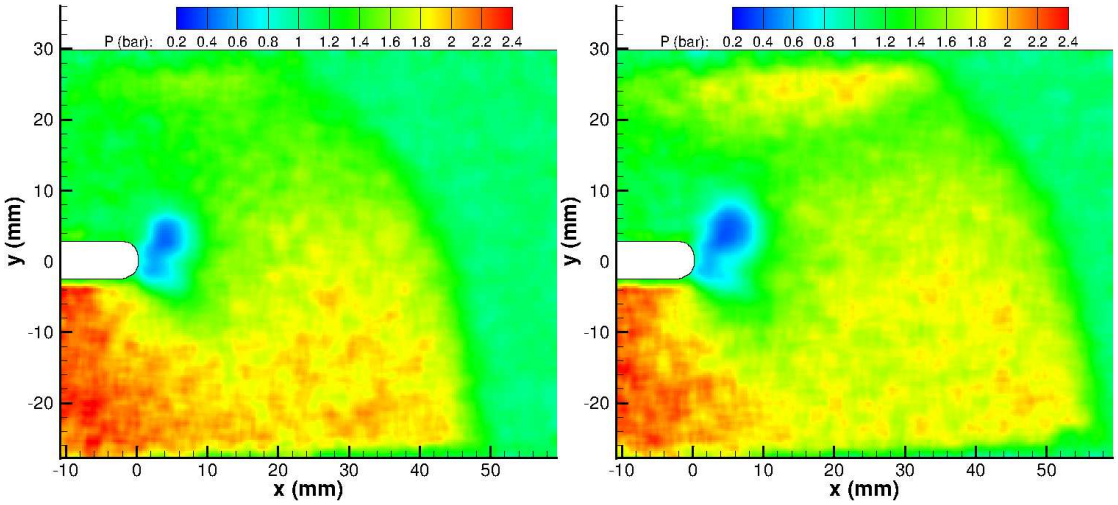

(e) 100 μs

(f) 120 μs

Figure 5.75: PSP map of $M_i = 1.46$ shock diffraction process around a round geometry

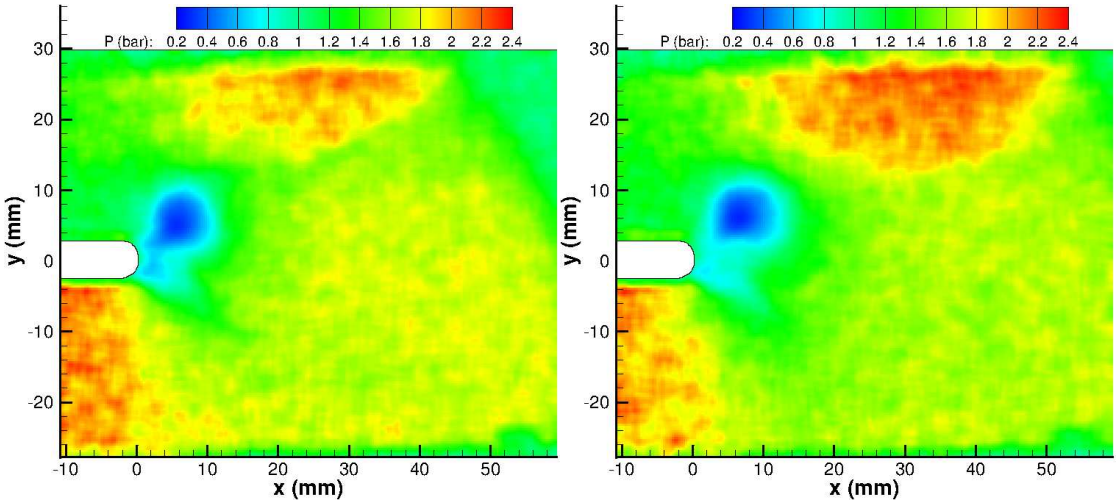

(g) 140 μs (h) 160 μs

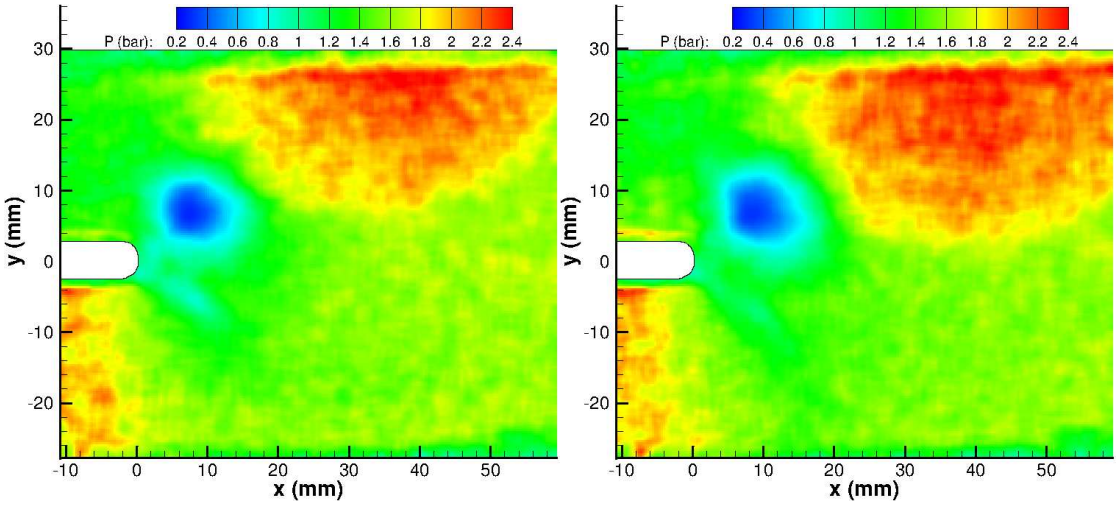

(i) 180 μs (j) 200 μs

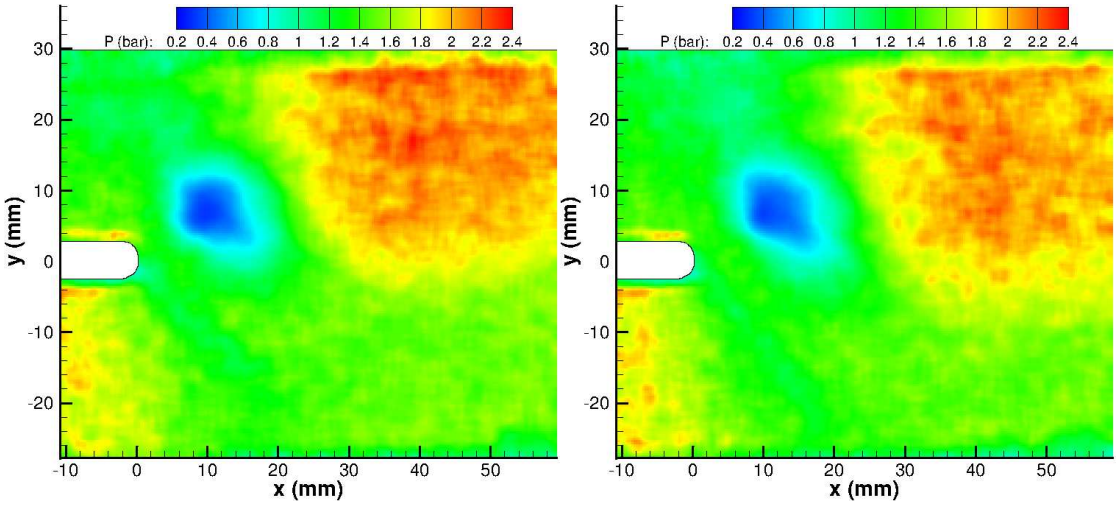

(k) 220 μs (l) 240 μs

Figure 5.75: PSP map of $M_i = 1.46$ shock diffraction process around a round geometry

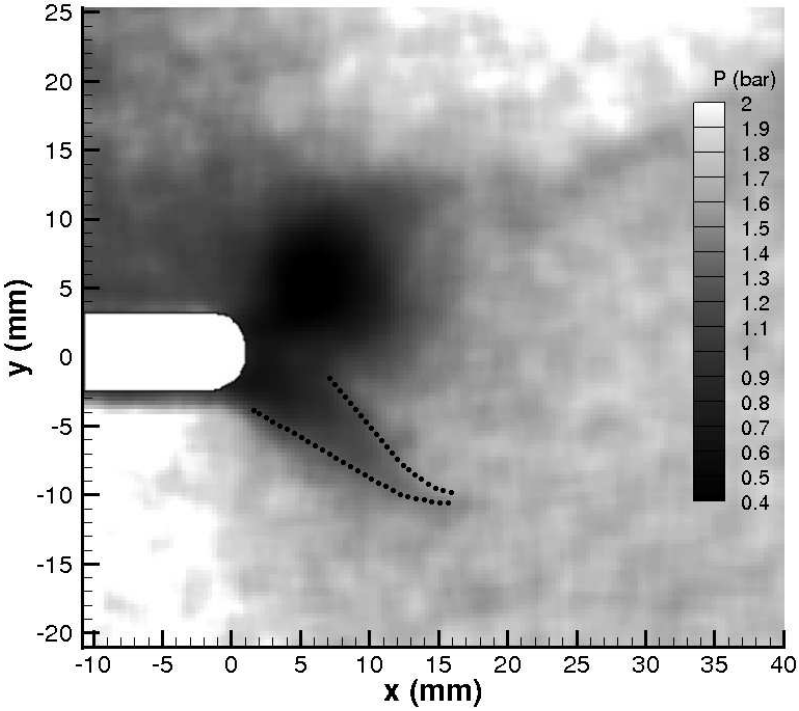

Figure 5.76: Close-up PSP map of the $M_i = 1.46$ complex region at 140 μs

opposite (approximately 220°) around the vortex is not well represented in the PIV results but is visible in the density-based results, implying that the expansion region growing from the main vortex has been overpredicted, as was seen in Sections 5.3.1.3 & 5.4.1.6.

The numerical density-based results showed some instabilities generated along the shear layer (Fig.5.28). These instabilities are strong enough to manifest themselves significantly in the pressure map results. Even if these vortices were seen in the experimental results (most likely in the density-based and raw PIV results), the numerical size of these vortices is of the same scale as the spatial noise in the PSP images and would therefore not be reliably detected.

5.4.2.5 Mi = 1.55 Experimental Results

The final set of PSP results show a $M_i = 1.55$ shock diffracting around the rounded corner. Fig.5.78a shows that the initial pressure rise behind the shock is more spread out than for the previous cases, reaching a steady level of 2.52 bar, slightly lower than the theoretical inviscid value of 2.64 bar, although still within experimental error. The diffracted shock wave propagating along the top surface of the splitter is slightly more visible in this test, indicating that it is stronger than for the lower Mach numbers. The reflected expansion wave and the expansion at the beginning of curvature are stronger in this case than any other and significantly affect the flow field. From the density-based results we know that the growth of the complex region, both spatially and temporally, is faster for this Mach number, potentially meaning that more of the structures are visible.

The separation region and the vortex are visible in Fig.5.78b onwards, with the vortex core reaching a minimum pressure of 0.27 bar. Fig.5.78e shows the expansion

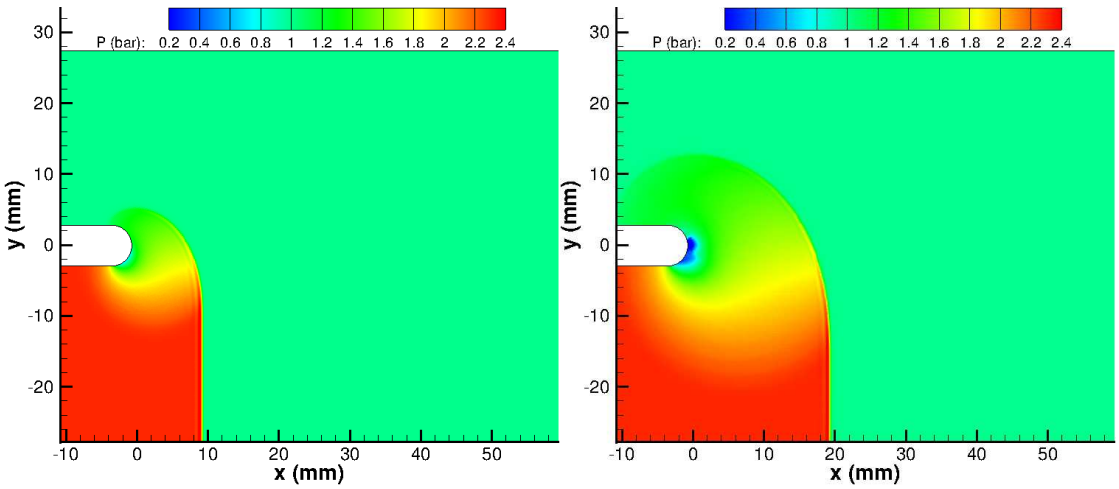

(a) 20 μs

(b) 40 μs

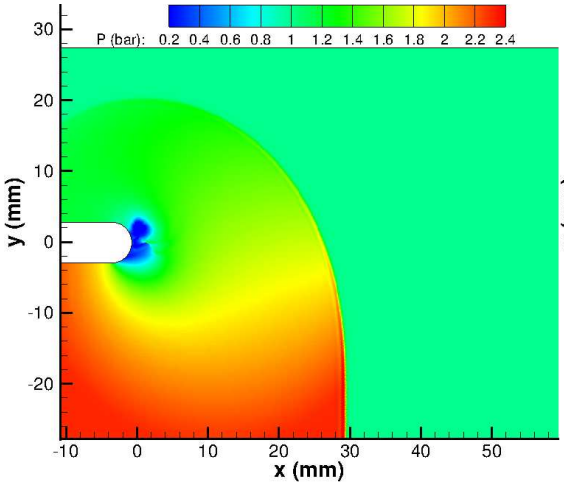

(c) 60 μs

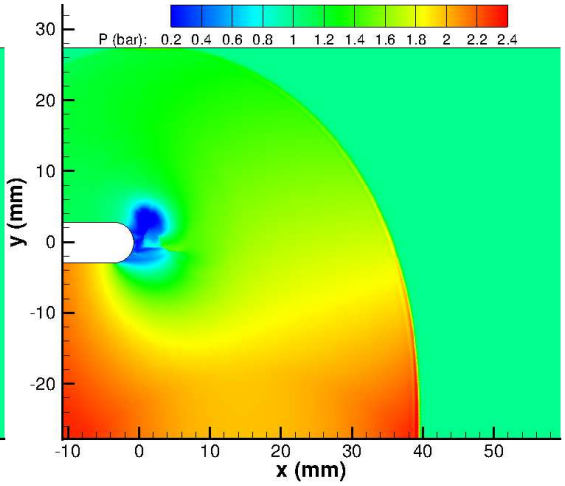

(d) 80 μs

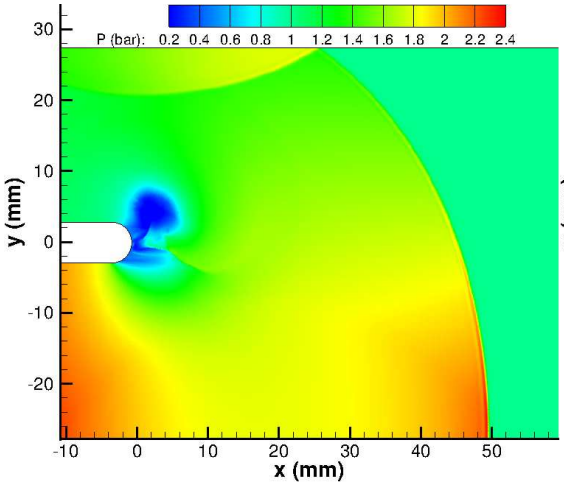

(e) 100 μs

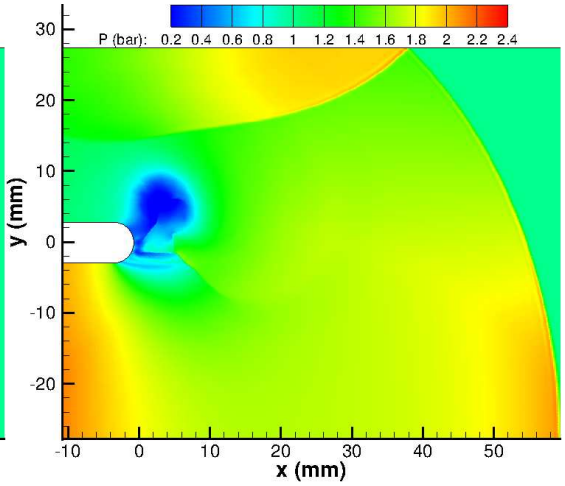

(f) 120 μs

Figure 5.77: CFD pressure map of $M_i = 1.46$ shock diffraction process around a round geometry

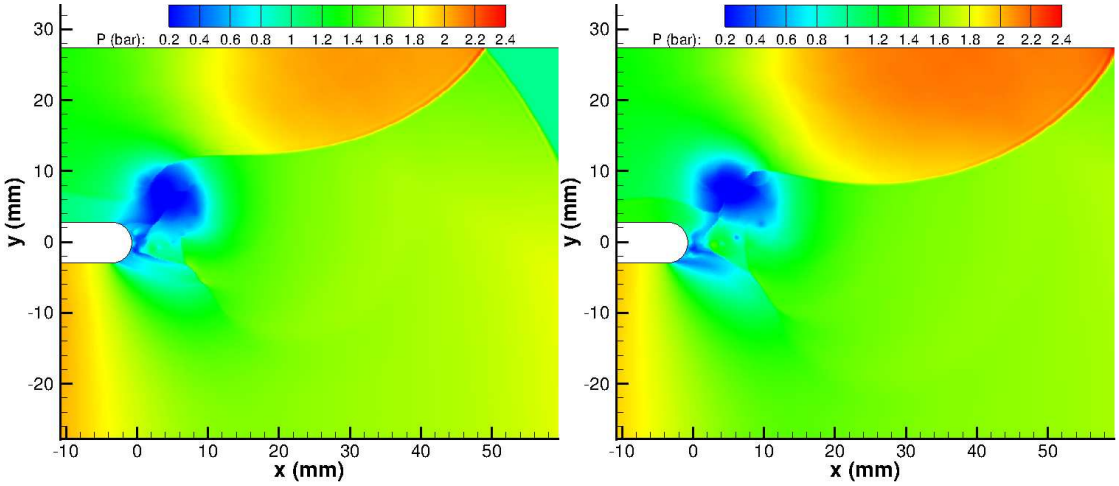

(g) 140 μs (h) 160 μs

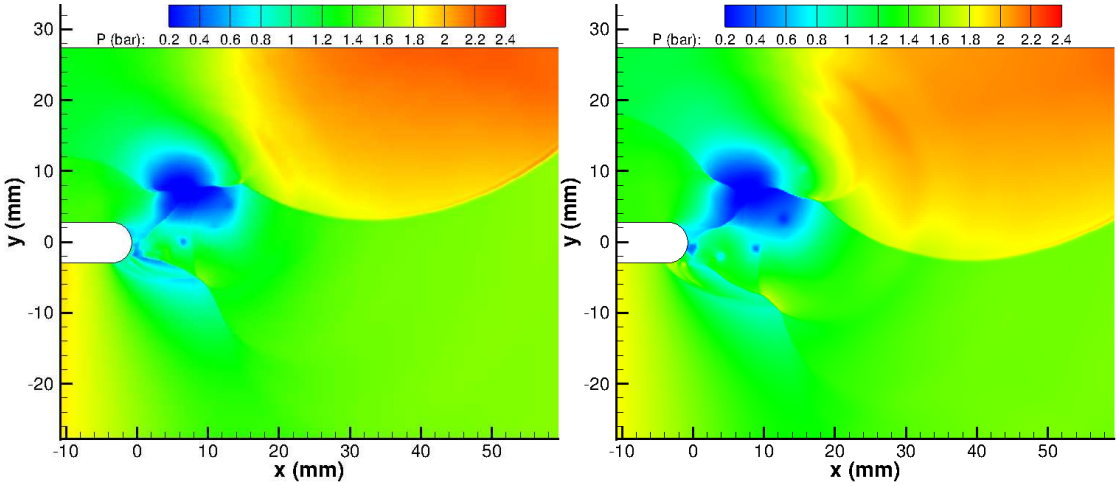

(i) 180 μs (j) 200 μs

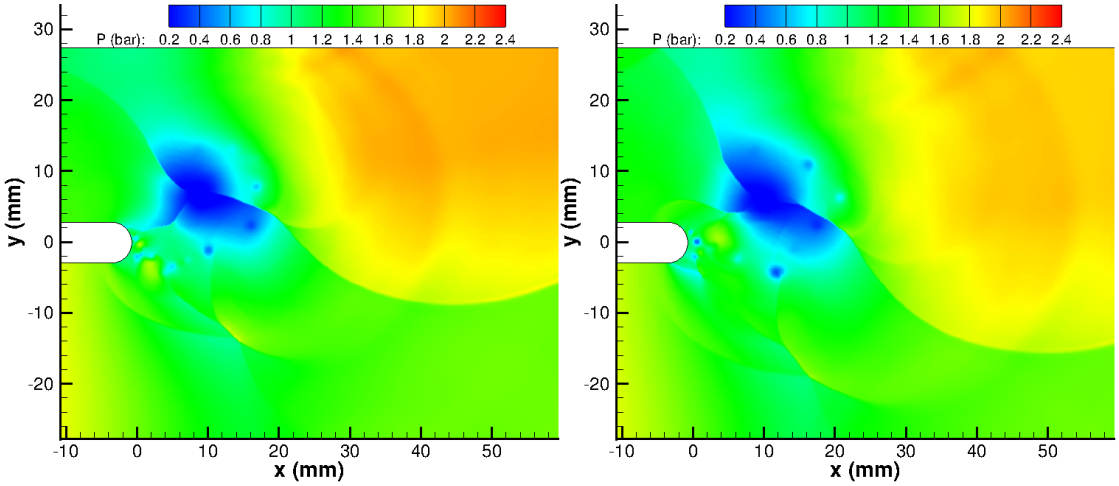

(k) 220 μs (l) 240 μs

Figure 5.77: CFD pressure map of $M_i = 1.46$ shock diffraction process around a round geometry

region below the main shear layer and the lambda shock structure following it. The subsequent two images allow us to begin to see into the internal expansion region before the interference of the returning diffracted shock wave. A close-up of the PSP results at 140 μs is presented in Fig.5.79, again with an altered colour map to aid the reader. In this figure the black dotted lines show the last running expansion wave and the first shock of the lambda shocks (see Fig.5.30g), while the white dotted line indicates the position of the internal terminating shock. The pressure rise from this shock can faintly be seen, although it is almost the same magnitude as the experimental uncertainty.

The returning diffracted shock wave recompresses the flow to 2.45 bar. The shock-vortex interaction is significantly stronger for this Mach number, due to the increased strength of both the main vortex and the returning shock. Fig.5.78j shows that the region of low pressure is being stretched due to the shock-vortex interaction. The final figure (Fig.5.78l) shows that there is a large region of low pressure above the main vortex terminated by the left-hand shock in the shock-vortex interaction. The position of this shock agrees very well with the density-based results and the PIV results where a small region of accelerated flow can be seen above the vortex. The discontinuity on the right-hand side of the vortex is much more difficult to see, as the progress of the shock wave on this side is slowed by the high velocity of the induced flow in this region. The foot of this shock (which connects it to the vortex core) appears as a sharp shock wave, indicating that it is much stronger in this region than elsewhere along its length.

5.4.2.6 Mi = 1.55 Numerical Results

The numerical results in Fig.5.80 show that the incident shock follows the expected diffraction pattern and loses strength along its length from its initial pressure rise of 2.63 bar. The structures in the complex region are much more spread out at this Mach number, making interpretation of the results significantly easier. The strength of the expansion wave under the main shear layer is evident early on in the flow development. The highly inclined lambda shock is visible in Fig.5.80d. Also in this figure, the internal expansion region and the internal terminating shock are visible. The secondary terminating shock and recompression shock are visible in Fig.5.80f (see Fig.5.29).

The vortex is clearly much stronger at this Mach number and reaches a minimum pressure of 0.06 bar, much lower than the experimental value. This value shows a similar trend to that of the sharp geometry, namely that the minimum pressure in the vortex core appears to plateau. The returning shock wave from the top surface of the test section compresses the flow to 2.52 bar, a value similar to that seen in the experiments. The stronger vortex leads to a stronger shock-vortex interaction. By Fig.5.80j the vortex has been compressed vertically and stretched horizontally. As the two shock waves propagate around the vortex in a clockwise direction they strongly compress the expanded flow. The location and magnitude of both of the compression waves agree well with the experimental results. The right-hand shock appears much more sharply in the numerical results and has propagated further than then experimental results show. This explains the secondary increase in pressure seen by the transducer **K2** in Fig.5.62.

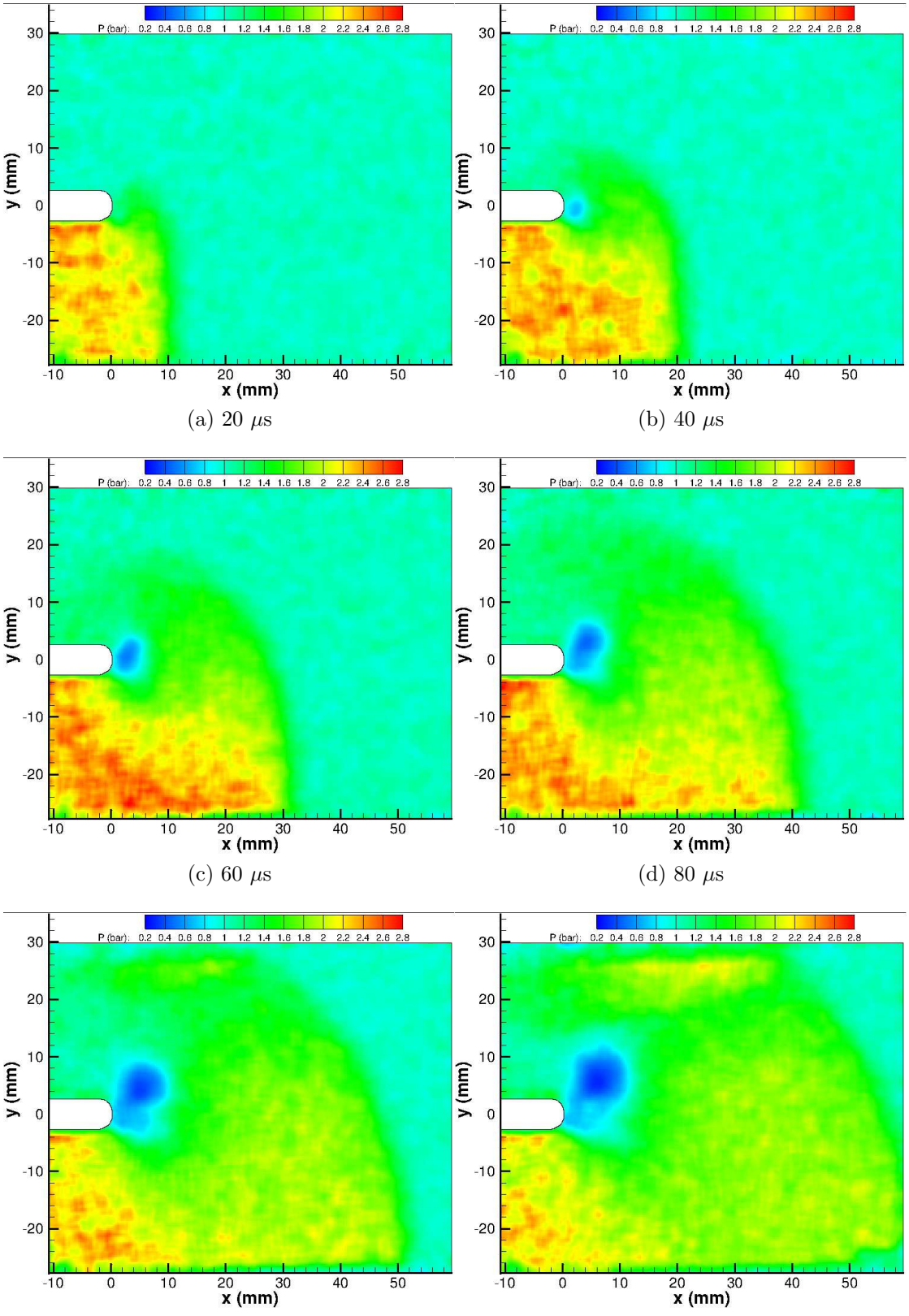

(a) 20 μs (b) 40 μs

(c) 60 μs (d) 80 μs

(e) 100 μs (f) 120 μs

Figure 5.78: PSP pressure map of $M_i = 1.55$ shock diffraction process around a round geometry

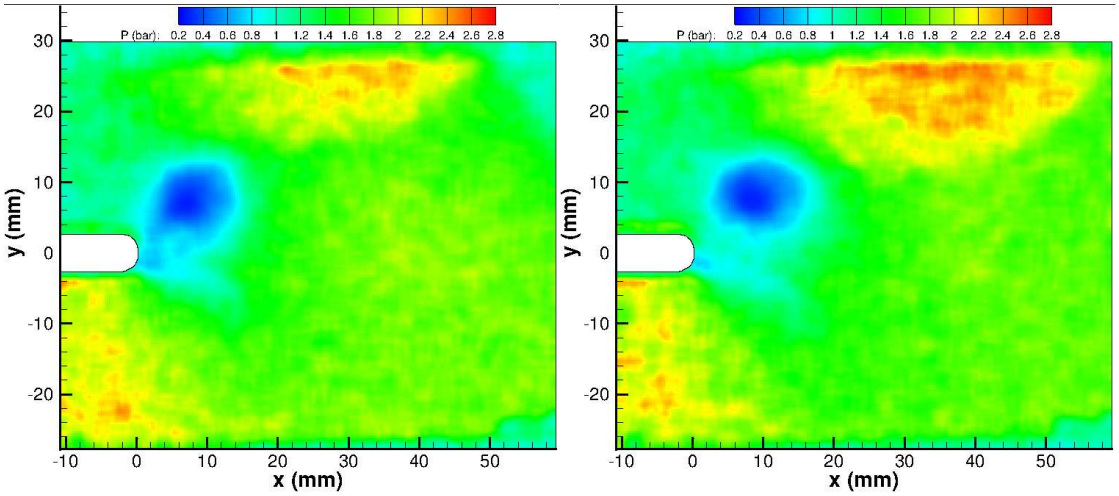

(g) 140 μs (h) 160 μs

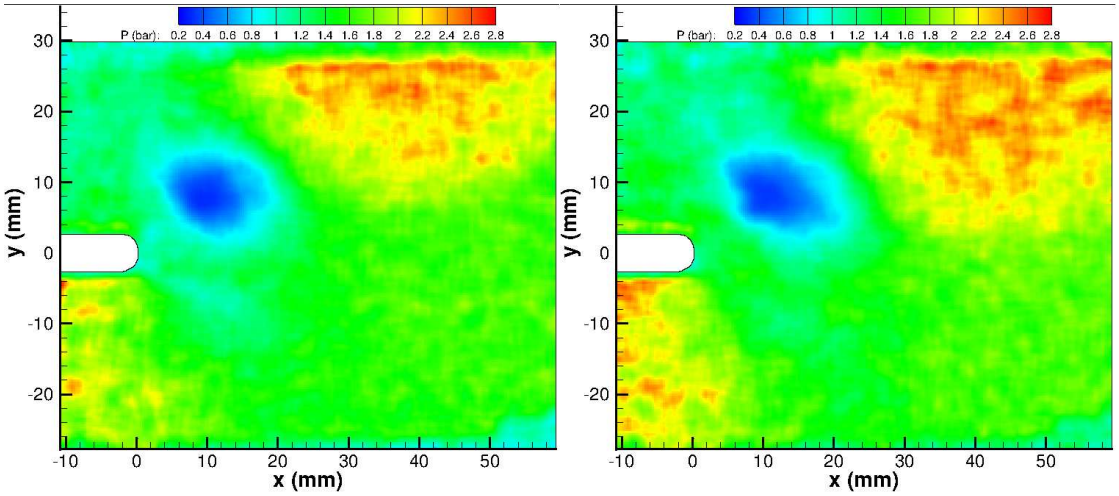

(i) 180 μs (j) 200 μs

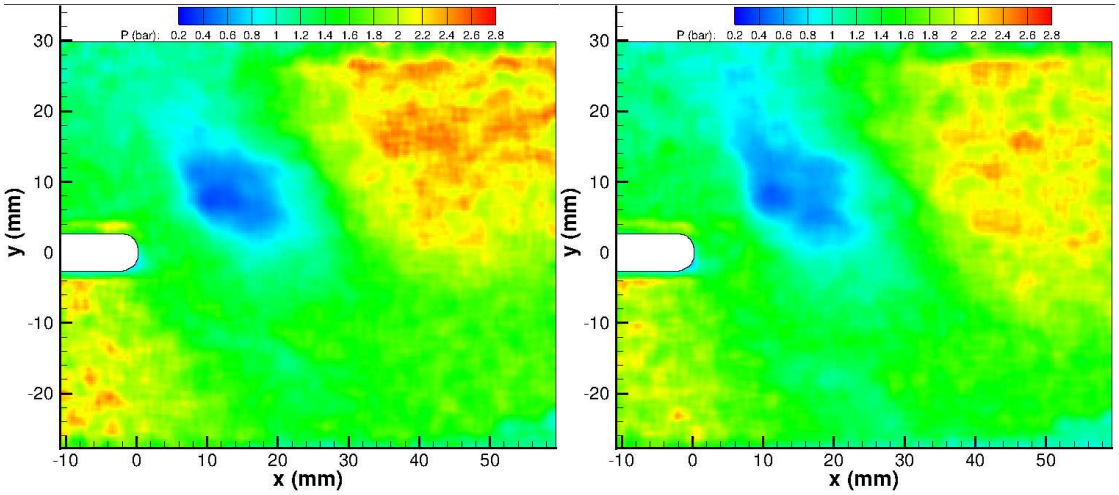

(k) 220 μs (l) 240 μs

Figure 5.78: PSP pressure map of $M_i = 1.55$ shock diffraction process around a round geometry

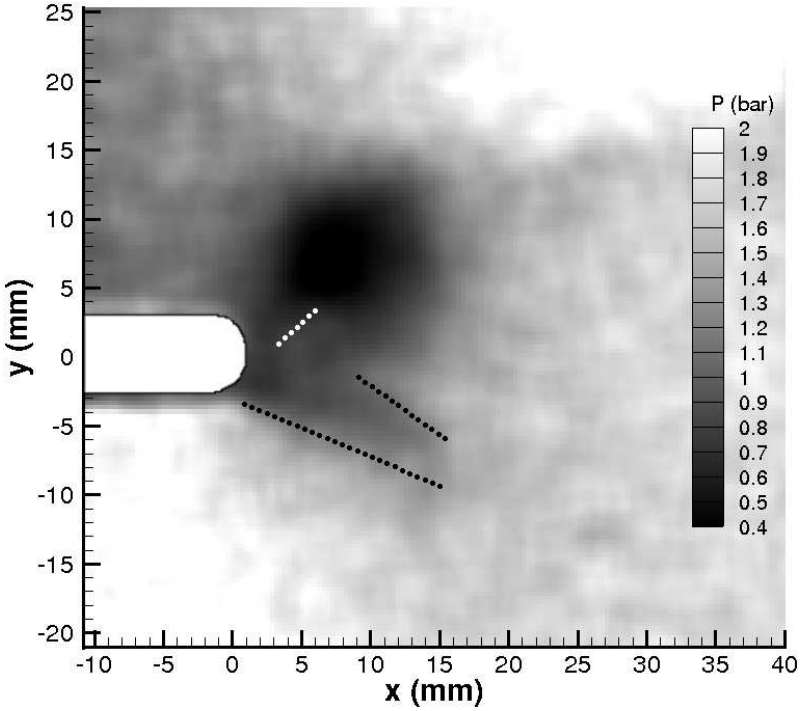

Figure 5.79: Close-up PSP map of the $M_i = 1.55$ complex region at 140 μs

5.4.2.7 Conclusions

The conclusions presented in this section will not repeat conclusions already made in Section 5.4.1.7 about the PSP technique and its limitations.

Pressure-sensitive paint has been applied to quantitatively measure the pressure profile behind a shock wave diffracting around a rounded geometry. The complex region behind a shock diffracting around a rounded corner is very difficult to measure, due to its slow spatial growth and given the already discussed spatial noise of the high-speed TLC PSP technique used here.

Similarly to the sharp geometry, there is some disagreement between the experimental and numerical results regarding the pressure in the vortex core. The pressure in the vortex core is lower for the rounded geometry and the vortex is smaller in size, especially for lower Mach numbers. However, initial shock wave profiles and strengths agree well with the values from inviscid theory based on the experimental Mach number measured from the density-based results, as do the values for the secondary compression region caused by the diffracted shock reflecting off the top wall.

The $M_i = 1.55$ case allows us to see some of the internal waves in the complex region. The internal terminating shock wave can faintly be seen in the experimental results and is easily visible in the numerical results.

It is interesting to note that the pressure in the expansion region under the main shear layer is significantly lower than atmospheric (as was the case for the sharp geometry). As the last running expansion wave has a larger turning angle (i.e. the angle between horizontal and the main shear layer), the expansion is much stronger than that of the sharp geometry; on a local level, this leads to much higher velocities and stronger interactions. The theory of Sun & Takayama [36] predicts that, for the $M_i = 1.28$ case, the pressure after the expansion wave must be 0.83 bar or lower for

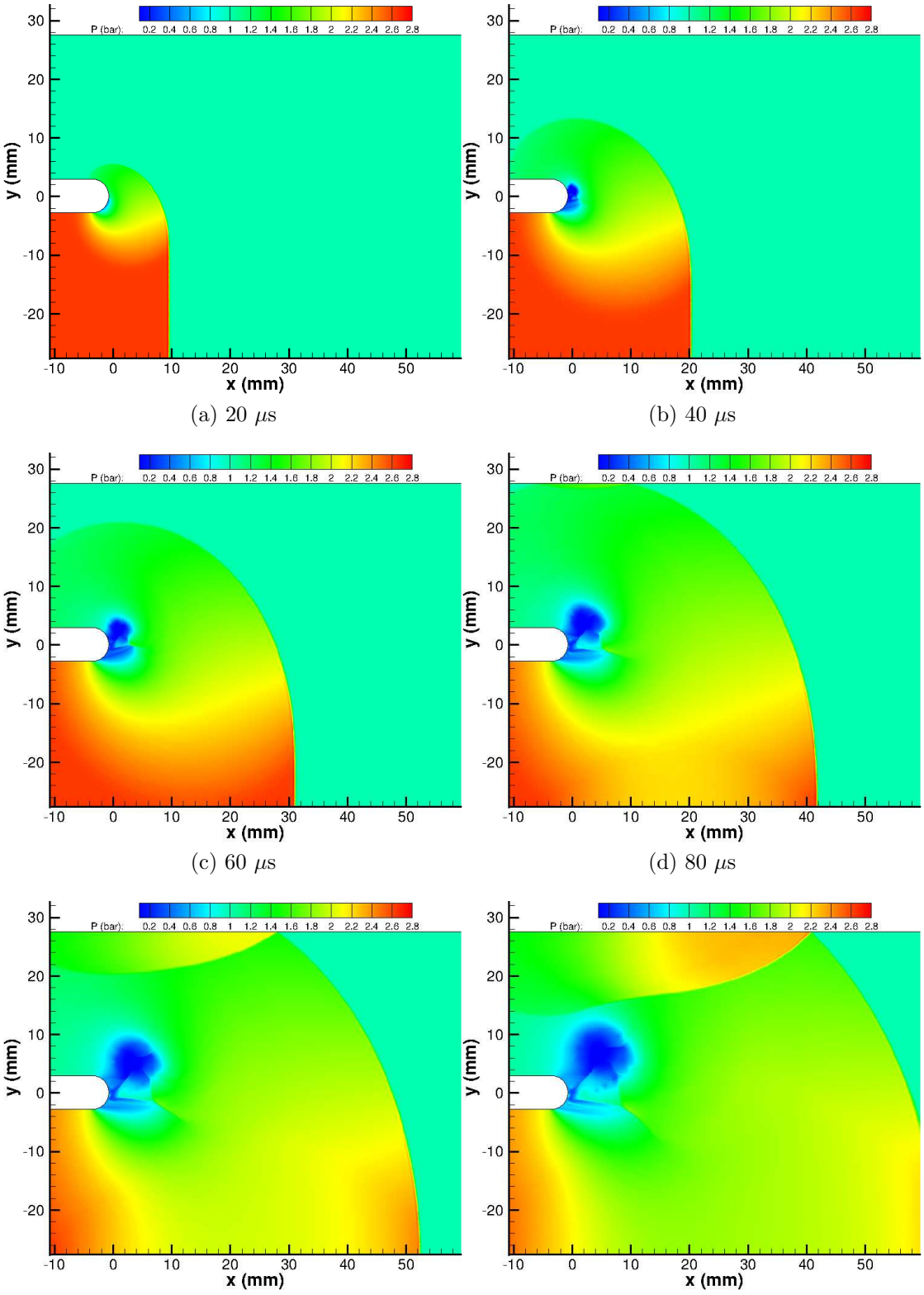

(a) 20 μs (b) 40 μs

(c) 60 μs (d) 80 μs

(e) 100 μs (f) 120 μs

Figure 5.80: CFD pressure map of $M_i = 1.55$ shock diffraction process around a round geometry

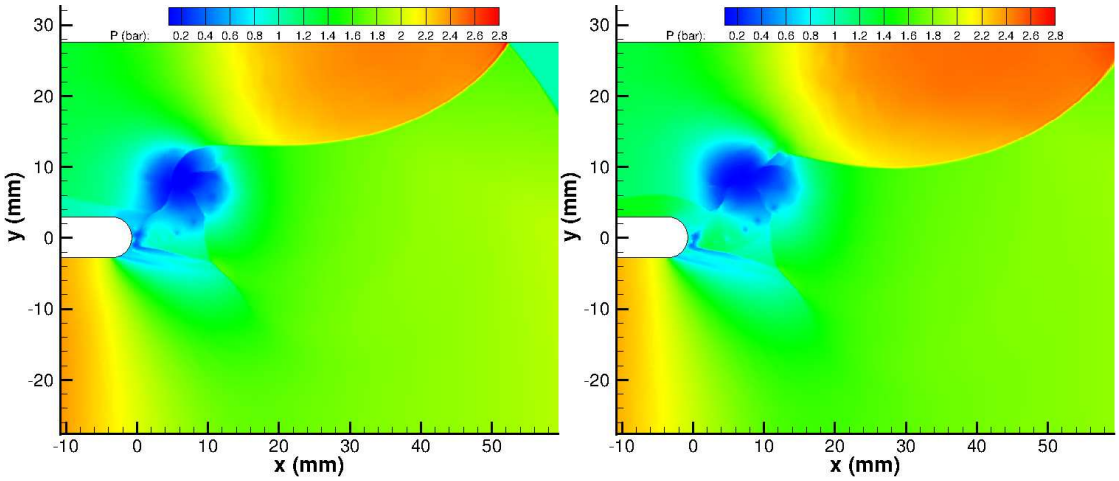

(g) 140 μs (h) 160 μs

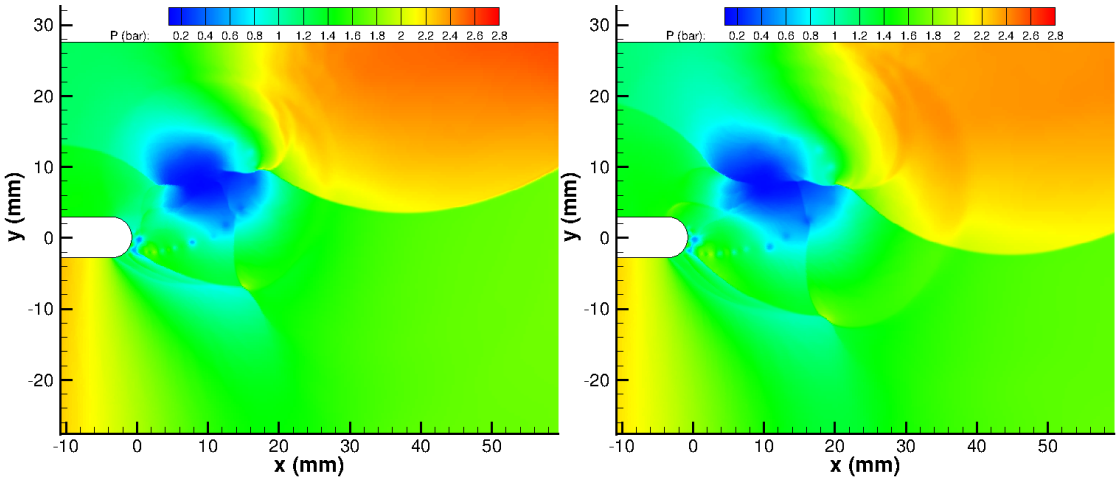

(i) 180 μs (j) 200 μs

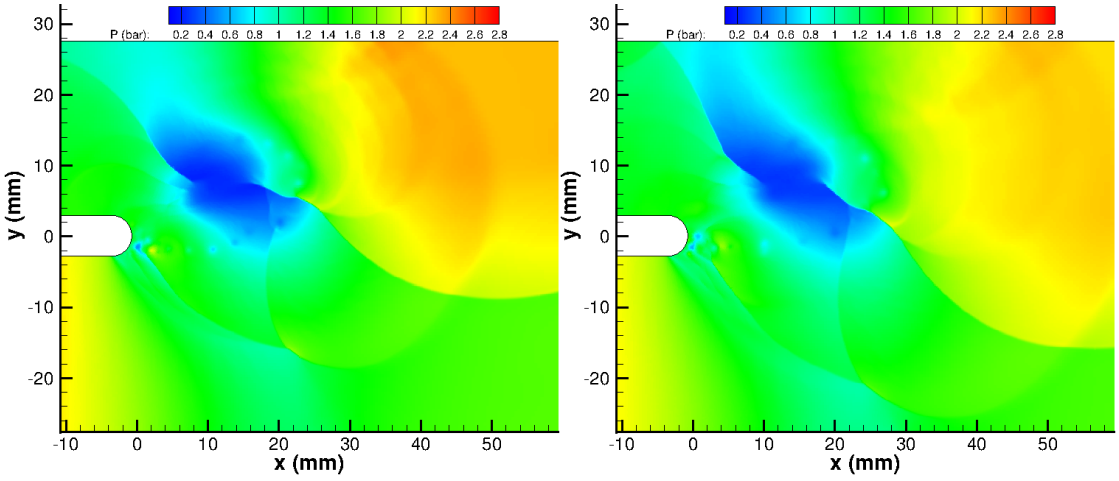

(k) 220 μs (l) 240 μs

Figure 5.80: CFD pressure map of $M_i = 1.55$ shock diffraction process around a round geometry

the flow to be sonic. The value in both the numerical and experimental results is significantly lower than this, meaning that, based on that pressure ratio, we should expect regions of locally supersonic flow.

The numerical simulations predicted the progress of the right-hand shock during the shock-vortex interaction to be faster than was measured in the experiments. This result is difficult to explain, given that the PIV measurements and numerical velocity plots agreed very well in the region into which this shock propagates.

Chapter 6

Conclusions

> *To be suspicious is not a fault. To be suspicious all the time without coming to a conclusion is the defect.* - Lu Xun

The conclusions of this study are divided into three main sections:

1. investigation of the sharp geometry
2. investigation of the round geometry
3. applicability of flow diagnostics and their results

6.1 Sharp Geometry

The flow field generated by a shock wave diffracting around a sharp corner has been investigated using different flow diagnostic techniques. The lowest Mach number case showed no secondary shock wave underneath the shear layer formed at the splitter tip. Subsequent higher Mach number cases showed small lambda structures, indicating a cycle of expansion and compression. As the Mach number was increased, the lambda structures grew stronger and fewer in number, indicating the trend towards the recognised *strong shock* solution. The flow appears to grow in a self-similar fashion, as the relative location of all of the wave structures remains the same, with the exception being disturbances on the shear layer.

Kelvin-Helmholtz instabilities in the shear layer, a source of much discussion in the field, have been experimentally resolved using density-based optics for the first time at such small scales. The shear layer in this experiment is extremely thin and as a result is a good approximation of a vortex sheet, a fundamentally unstable configuration. Increasing incident shock Mach number had the effect of reducing the growth rate of these instabilities; although the instabilities were still present, albeit more difficult to visualize. At the highest Mach number, the instabilities could only be imaged by using a very short depth-of-field shadowgraph system. It is unsurprising to find that other researchers have struggled to find these instabilities using density-based techniques.

The shock-vortex interaction was investigated using all of the available experimental techniques. It was shown that the most significant wave is the one propagating on the right-hand side of the main vortex, opposing the flow direction. This

wave is significantly stronger than any of the others generated. The instabilities present on the shear layer affected the impinging shock wave and created a series of diverging acoustic level waves.

The impingement of the returning shock wave on the shear layer caused two very strong vortices to be generated, which began to propagate around the main vortex. The $M_i = 1.28$ case showed a further series of secondary instabilities at a much higher spatial frequency than the initial ones. This secondary stream of coherent structures was not seen in the higher Mach number cases using any of the experimental techniques.

Numerical simulations performed well with this flow, as it can be modelled inviscidly. With inviscid simulations containing instabilities, the only parameter affecting the growth rate of unstable modes is the numerical viscosity. As the numerical viscosity is reduced by increasing the number of cells, the instabilities grow at a faster rate, meaning the simulation will never be truly grid-independent. Despite this, the numerical simulation gave excellent agreement with the experimental results, with one small exception. The stream of secondary instabilities (after the impact of the returning shock on the shear layer) was predicted for every Mach number. Raw PIV results show that the incoming boundary layer grows significantly thicker over the test and transitions to turbulence. This means that small instabilities are easily damped out, as the boundary layer is not resolved in the simulations, it is not surprising that the numerical results depart from the experimental results in this region. Furthermore, the growth rate of the instabilities is overpredicted for every Mach number; however, this is likely due to be due to a mismatch between the actual viscosity of the flow and the numerical viscosity in the simulation.

6.2 Round Geometry

The complex region generated by the round geometry has been investigated using numerous experimental techniques for the first time. Unlike for the sharp geometry, the shear layer is not generated by a sharp corner, meaning that there is a boundary layer separation process which takes place after a certain distance around the model. This means that the flow cannot be considered self-similar in time, as it has an associated length and time scale. Once the shear layer and vortex have begun to develop, the complex region attains a quasi-steady structure, lasting for approximately 80 μs before the shock-vortex interaction begins. Despite the flow structure being qualitatively similar for some time, the actual waves are changing in location and strength. The main shear layer forms a much larger angle to the horizontal for the rounded case, meaning that the expansion wave at the corner can accelerate the flow more, leading to a lambda shock structure under the shear layer for all Mach numbers.

The shear layer formed by the boundary layer separation rolls up into a tight vortex. The strength and proximity of the main vortex to the round corner means that the induced flow is forced through a convergent-divergent geometry consisting of the model geometry and the shear layer swept up into the vortex. This accelerates the flow to supersonic speeds ,which is then decelerated by an internal terminating shock wave. As the vortex propagates away from the corner during the test, the effective area of the convergent-divergent nozzle is increased to the point where the

flow no longer becomes sonic at the throat. As such, the internal terminating shock wave becomes weaker in strength and begins to degenerate into a series of weak compression waves. The higher Mach number test cases showed that this internal terminating shock wave is strong enough to compress the flow to a higher pressure than is found on the other side of the main shear layer, causing it to curve in the opposite direction. This change in curvature leads to a distributed compression corner, further complicating the flow after the main expansion region.

The flow in the internal expansion region is not capable of following the geometry of the rounded corner and separates from the wall, creating an internal shear layer. The internal and external expansion and compression cycle becomes more complex as the incident Mach number is increased. Unlike the sharp geometry, this does not show any trend towards a *strong shock* solution.

From the density-based results it is not possible to make any firm conclusions about the structure of the main shear layer. Although there are no coherent structures seen in the density-based results, that does not mean that they are not there. The raw PIV images confirm that the shear layer does not contain any coherent structures; rather, only turbulence is present. The raw PIV images also show the size and structure of the incoming boundary layer. The incoming boundary layer transitions to turbulence, providing a mechanism of energy transfer and suppressing any would-be instabilities in the shear layer.

The numerical simulations proved significantly more challenging for the round geometry due to the presence of viscous phenomena in the flow. Laminar simulations were capable of resolving the boundary layer separation and growth of the flow field for the early portion of the diffraction process. The wave structure, including the complex internal expansion region, were captured at all Mach numbers. However, after the incoming boundary layer transitioned to turbulence, the simulations began to depart from the experimental results, especially at lower Mach numbers. The lack of turbulence to act as an energy transfer mechanism led to the creation of spurious vortices in the flow. Despite the different wave structure, the simulations agreed well with the PIV and PSP results both qualitatively and quantitatively.

6.3 Diagnostics

Density-based diagnostics yielded the most information about the wave structures and the flow field in general. The strength of the interactions meant that schlieren results were often overranged during the early stages of the diffraction process (especially for the round geometry) but gave valuable information at later times. The shadowgraph results with a low depth-of-field gave information about the structure of the shear layer and the local lambda shock configurations; however, several waves were often missed during the shock vortex interaction due to the limited sensitivity. Only an effective combination of both of the density-based techniques (including two variants of the shadowgraph setup) allowed for all of the waves and structures to be visualised and understood.

Particle image velocimetry was successfully used to give both quantitative and qualitative information about the strength of the waves present in the flow. Particle inertia was both a blessing and a curse in that it highlighted any vortices present, conclusively proving their existence, yet also prevented any velocity information

inside the shear layer from being gathered. The initial velocity rise and the moving shock front was well-captured, as were regions of expanded flow. Lambda shocks seen in the density-based results were not well-resolved, indicating that they are very weak in comparison with the rest of the waves present in the flow. Improvements in the PIV measurements are only possible if a seeder material with even lower inertia is available to use (acetone fog, for example); however, these represent even greater health risks than inert nano-particles, and the improvement in measurement must be balanced against the potential safety risks.

Pressure-sensitive paint has been successfully applied to the problem of shock wave diffraction for the first time. A new transient *in-situ* calibration technique has been applied, yielding a thorough calibration map using only three electro-mechanical transducers. The shock front was well-resolved by the PSP, as was the lower pressure region corresponding to the vortex core. The reflected shock-vortex interaction was also captured, giving the relative strength of each wave. To the author's knowledge, this is the first quantitative measurement of pressure in a shock tube using a CCD camera rather than a PMT. Previous attempts have only contained vague details of the experiment and have not quantified the errors involved. Improvements to the PSP technique are mentioned in Section 7.

The results have shown that only by using a combination of techniques can a problem such as shock diffraction be fully understood. The difference in strength of phenomena means that one application of a density-based technique alone is not enough to conclusively resolve all of the flow features. The optical sensitivity of the shadowgraph technique is crucial to resolving some flow features, and very close attention should be paid to it when setting up any optical experiment. The circle of confusion of the system should be tuned to match the resolution of the camera in order to yield the best results. Some techniques, such as raw PIV, are more suited to capturing shear layer instabilities.

Chapter 7

Future Work

Prediction is very difficult, especially if it's about the future. - Niels Bohr

Although a large number of experiments have been performed in this project and several conclusions drawn, there is more work that the author would have liked to have undertaken. The main of which would involve a redisign of the experimental rig to allow for depressurisation of the test section, allowing for improved signal to noise ratio in the PSP measurements. Ideally illumination would come from a series of high-power UV LEDS rather than a broadband light source to avoid excessive thermal stress on expensive components. The PSP measurements shown in this project show that the flow can be imaged reliably using; however, the measurement error of approximately 10% highlights that more work needs to be done on this area before it can be reliably used or industrialised.

A brief summary of future work will be discussed in the following sections.

7.1 Increased Mach Number Range

The Mach number range tested in this project is rather limited. During the calibration of the shock tube (measuring formation decrement and arrival times) for future time-sensitive work, six Mach numbers were tested. Only three of these were heavily investigated in this project, ranging from M= 1.28 to 1.55. As the test section was open to the atmosphere, the only way to increase the driver pressure ratio (and therefore the incident shock Mach number) was to increase the driver pressure; however, the experimental rig is only pressure-rated to 14 bar. This would require a redesign of the test section to be closed to the atmosphere and evacuated before the test, thereby increasing the pressure ratio. If this were achieved and the pressure in the test section were sub-atmospheric, then density-based diagnostics would be less sensitive, as the refraction angle (ϵ) is dependent on density. This effect could also be achieved by varying the driver gas; however, given the potential advantages to PSP experiments, evacuating the test section would be the preferable option.

The stability of higher Mach number shear layers has not been investigated for the sharp geometry and could be a project for future students. As mentioned in Section 6.2, the round geometry did not show convergence towards a known *strong shock* solution. This should be investigated using the techniques presented in this project.

7.2 Variation of Splitter Geometry

In order to ascertain the variation of flow parameters with apex angle, more investigations are needed with different corner geometries. Skews [32][34] has performed numerous investigations on angles smaller than 90°; however, there is limited existing work on angles greater than 90°. As we have shown, the flow can only be completely understood by combining diagnostic techniques; therefore, the flow around different sharp corner angles should be investigated using the combined approach presented here.

The radius of the rounded corner appears to change the flow features by changing the associated length scale [42][46]. The combined diagnostic approach should be applied to different corner radii to investigate this effect. In order to do this, a significantly larger shock tube test section would be needed to allow for the longer development time.

Three-dimensional geometries have been briefly investigated during this project (geometric details are given in Appendix A). Appendix B shows some of the density-based results. Due to the three-dimensionality of the flow, two-dimensional PIV measurements would not be suitable. Either a stereoscopic or volumetric approach should be used. Further to this, numerical simulations of this flow would not be possible using the version of Fluent available during this project, which was running on a desktop PC and was limited to 450,000 cells.

7.3 Investigations of Shock Motion with Co-Flow

Density-based results were gathered on the diffraction process of shocks around the two geometries presented so far (and the four mentioned above) with a subsonic and supersonic co-flow. As these investigations were only possible using density-based techniques (PSP is possible but was not performed due to time constraints of the loaned equipment), they do not give a complete understanding of the flow. Despite this, a portion of the preliminary results is presented in Appendix C.

7.4 Further Numerical Simulations

Numerical simulations performed in this project were limited by the computational power and software available. This restricted the use of more modern turbulence models and also limited the use of Reynolds stress models. Inviscid and laminar simulations performed well; however, these had a very strong grid dependency, which required a very good understanding of the flow already to be able to tailor the numerical viscosity to act as a damping function. Future work on the topic should consider using a GPU enabled code, as the benefits of such high-performance computing can be an increase in processing speed of up to 100 times.

7.5 PSP Chemical Composition Optimisation

Due to the scope of the experimental work performed during this project, it was not possible to completely optimise the chemical composition of the PSP samples.

Ideally, a study similar to those performed by Sakaue et al. [185][196][170], where each independent parameter such as solvent polarity or solution concentration is varied across a wide range, would be conducted. This parametric variation could allow for great increases in the PSP signal output and pressure sensitivity, and is the logical extension of the paper published by the author in the Sensors Journal [156].

Other luminophores were investigated during this project, namely PtTFPP (Platinum tetrakis-pentafluorophenyl Porphyrin) and PBA (Pyrene Butyric Acid). The luminescent lifetime of PtTFPP is too long to be of use in this research; however, PBA has a lifetime of the order of nanoseconds. As this value represents the absolute minimum response time, theoretically at least, PBA is capable of much faster PSP measurements than the Ruthenium complex used. The disadvantage of PBA is that its excitation wavelength is mid to high UV. Not only is this range of light dangerous to work with, but it is also very difficult to find a light source with enough power to give a meaningful signal. Filtering broadband light sources is not an option, as regular filters cannot withstand the light throughput; therefore, a UV solar simulator, primarily used for biological applications, seems to be the only possible option. However, these are prohibitively expensive and can be dangerous to operate. Other possible alternatives include UV LED flash lamps, although these suffer from cooling issues and are not always repeatable from flash to flash.

7.6 Pressure-/Temperature-Sensitive Velocimetry

The lifetime-based method uses the luminescent lifetime of the photo-active molecules to calculate the surface pressure. The reduction of luminescent intensity after an initial excitation follows an exponential decay, which is a function of the partial pressure of oxygen (Fig.7.1). A simple derivation of the theory behind this is given by Gregory et al. [143] and also by Lui & Sullivan [153]. A sample is exposed to a known pressure and then excited by a short pulse of light, typically from a laser. The emission from the excited sample decays at a certain rate, depending on the pressure (and temperature) on the surface. The rate of this decay is directly related to the pressure by the Stern-Volmer equation shown in Section 3.4.2.

Fig.7.1 shows a typical intensity decay rate for an excited luminophore. The intensity is measured at various points during the decay in order to calculate the decay rate. This is typically modelled by a single exponential, but can be modelled by multiple exponentials [153].

The lifetime-based method has the advantages that it is insensitive to luminophore and light non-uniformity and does not require a wind-off image. A possible application of lifetime-based decay is a hybrid method of PSP and PIV, which will be referred to as pressure-sensing velocimetry (PSV).

This method involves seeding atomised luminophores into the flow and using them as the tracer particles for PIV measurements. The flow would be illuminated as shown in Fig.3.18; however, the laser used would emit light in the absorption range of the PSP spectra. The luminophore would then emit a certain amount of light (dependent on the pressure at that point) and lifetime calculations can be made. As the luminescent lifetime of most luminophores is extremely short (O 100ns s), the flow would appear frozen in lifetime measurements. A second laser pulse would

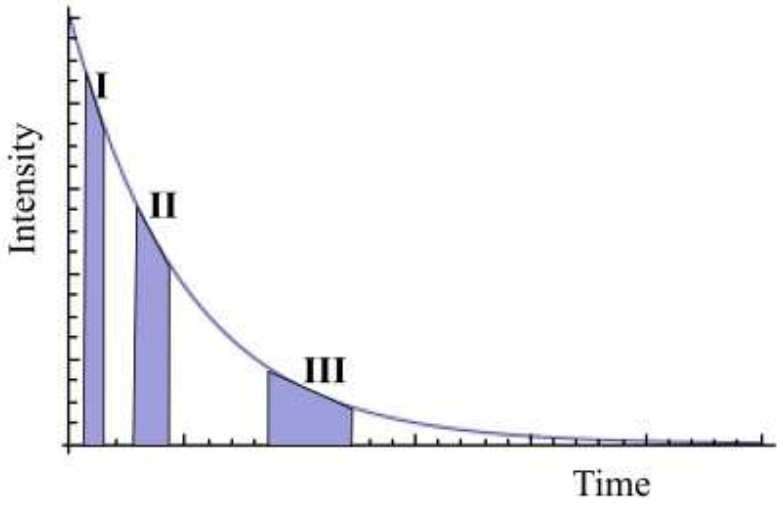

Figure 7.1: Decay of intensity and camera gates

excite the flow again at time ΔT later so that PIV calculations can be made. This concept has been tested with some success by Kimura et al. [201]. It was suggested in this study that one of the largest sources of error in the PSP measurements was, as usual, the temperature-induced effects. However, if a second luminophore could be introduced into the tracer particle, as shown by Hradil et al. [180], the dual lifetime method could allow for the measurement of pressure, temperature and velocity in one single run. The combination of velocity and two independent thermodynamic variables means that all of the flow parameters can be calculated.

The potential advantages of this technique are clear to see; however, the technical difficulties associated with it are far from trivial. The selection of a carrier particle for the luminophore(s) has conflicting requirements. The particle must be large enough to carry a sufficient amount of luminophore to give a detectable signal while still being small enough to follow the flow closely. The luminescent decay must be fast enough to be considered stationary by the PIV measurements. Initial research has been done in this area by Kimura et al. [202].

This hybrid method has been suggested by researchers Abe et al. [203], Song et al. [204] and Kimura et al. [201], but has never been perfected or applied to an actual flow. This is an interesting area of research and should be explored, as the potential benefits could be revolutionary.

Bibliography

[1] J. W. Miles. On the disturbed motion of a plane vortex sheet. *Journal of Fluid Mechanics*, 4(5):538–552, 1958.

[2] D. I. Pullin and A. E. Perry. Some flow visualization experiments on the starting vortex. *Journal of Fluid Mechanics*, 97(02):239–255, 1980.

[3] J-P. Marat. *Recherches physiques sur le feu*. Jombert, Paris, 1780.

[4] Fluorophores.org Database of Fluorescent Dyes Properties and Applications.

[5] A. Price. *The Spitfire Story*. Jane's Information Group Incorporated, 1982.

[6] F. Ma, J-Y. Choi, and V. Yang. Propulsive Performance of Airbreathing Pulse Detonation Engines. *Journal of Propulsion and Power*, 22(6):1188–1203, 2006.

[7] I. I. Glass. *Shock Waves & Man*. University of Toronto Institute for Aerospace Studies, Toronto, 1974.

[8] C. Chaussy and E. Schmiedt. Shock wave treatment for stones in the upper urinary tract. *The Urologic Clinics of North America*, 10(4):743, 1983.

[9] N. Sultan-Bichat, J. Menard, G. Perceau, F. Staerman, P. Bernard, and Z. Reguia. Treatment of calcinosis cutis by extracorporeal shock-wave lithotripsy. *Journal of the American Academy of Dermatology*, 66(3):424–429, 2012.

[10] M. H. Anderson, B. P. Puranik, J. G. Oakley, P. W. Brooks, and R. Bonazza. Shock tube investigation of hydrodynamic issues related to inertial confinement fusion. *Shock Waves*, 10(5):377–387, 2000.

[11] Formula1.com. Virgin Racing reveal details of the VR-01.

[12] TotalF1.com. Virgin to rely on CFD again, 2010.

[13] J. Allen. Virgin moves shows Marussia's statement of intent to move up the grid, 2011.

[14] TotalF1.com. Virgin gives up on all-CFD approach to F1, 2011.

[15] J. K. Wright. *Shock Tubes*. Methuen's Monographs On Physical Subjects. Spottiswoode, London, 1961.

[16] J. D. Anderson. *Modern Compressible Flow With Historical Perspective*. McGraw-Hill, 3 edition, 2004.

[17] S. C. Lin. Rate of Ionization Behind Shock Waves in Air. *Planetary and Space Science*, 6:94–99, 1961.

[18] R. Mariani. *Experimental Studies on Compressible Vortex Loops*. PhD thesis, Manchester, 2012.

[19] H. Zare-Behtash, N. Gongora-Orozco, and K. Kontis. Global Visualization and Quantification of Compressible Vortex Loops. *Journal of Visualization*, 12(3):233–240, 2009.

[20] I. I. Glass, W. Martin, and G. N. Patterson. A Theoretical and Experimental Study of The Shock Tube, 1953.

[21] G. Ben-Dor. *Shock Wave Reflection Phenomena*. Springer, New-York, 1991.

[22] G. Ben-Dor. A State-of-the-Knowledge Review on Pseudo-Steady Shock-Wave Reflections and their Transition Criteria. *Shock Waves*, 15(3):277–294, 2006.

[23] B. W. Skews and J. T. Ashworth. The Physical Nature of Weak Shock Wave Reflection. *Journal of Fluid Mechanics*, 542:105–114, 2005.

[24] T. V. Bazhenova, L. G. Gvozdeva, and M. A. Nettleton. Unsteady interactions of shock waves. *Progress in Aerospace Sciences*, 21(0):249–331, 1984. doi: 10.1016/0376-0421(84)90007-1.

[25] G. B. Whitham. A New Approach to Problems of Shock Dynamics Part 1: Two-Dimensional Problems. *Journal of Fluid Mechanics*, 2:145–171, 1957.

[26] G. B. Whitham. A new approach to problems of shock dynamics Part 2: Three-dimensional problems. *Journal of Fluid Mechanics*, 5(03):369–386, 1959.

[27] Z. Han and X. Yin. *Shock Dynamics*. Kluwer Academic, Dordrecht, 1993.

[28] B. W. Skews. The Shape of a Diffracting Shock Wave. *Journal of Fluid Mechanics*, 29(2):297–304, 1967.

[29] K. Oshima, K. Sugaya, M. Yamamoto, and T. Totoki. Diffraction of a Plane Shock Wave Around a Corner. *ISAS report*, 30(2):51–82, 1965.

[30] J. Rosciszewski. Propagation of waves of finite amplitude along a duct of non-uniform cross-section. *Journal of Fluid Mechanics*, 8(04):625–633, 1960.

[31] R. F. Chisnell. The motion of a shock wave in a channel, with applications to cylindrical and spherical shock waves. *Journal of Fluid Mechanics*, 2(03):286–298, 1957.

[32] B. W. Skews. The Perturbed Region Behind a Diffracting Shock Wave. *Journal of Fluid Mechanics*, 29(4):705–719, 1967.

[33] B. W. Skews, C. Law, A. Muritala, and S. Bode. Shear layer behavior resulting from shock wave diffraction. *Experiments in Fluids*, 52(2):417–424, 2012.

[34] B. W. Skews, C. Law, A. Muritala, and S. Bode. Shear Layer Evolution in Shock Wave Diffraction. In K Kontis, editor, *28th International Symposium on Shock Waves*, Manchester, UK, 2011. Springer.

[35] T. V. Bazhenova, L. G. Gvozdeva, V. S. Komarov, and B. G. Sukhov. Diffraction of strong shock waves by convex corners. *Fluid Dynamics*, 8(4):611–619, 1973.

[36] M. Sun and K. Takayama. The Formation of a Secondary Wave Behind a Shock Wave Diffracting at a Convex Corner. *Shock Waves*, 7:287–295, 1997.

[37] H. Kleine, E. Ritzerfeld, and H. Groenig. Shock wave diffraction: new aspects on an old problem. In R Brun and L Z Dumitrescu, editors, *19th International Symposium on Shock Waves*, Marseille, France, 1995. Springer.

[38] R. Hillier. Computation of Shock Wave Diffraction at a Ninety Degrees Corner. *Shock Waves*, 1:89–98, 1991.

[39] T. V. Bazhenova, S. B. Bazarov, O. V. Bulat, V. V. Golub, and A. M. Schul'meister. Experimental and numerical study of shock wave attenuation at the outlet of two-dimensional and axisymmetric ducts. *Fluid Dynamics*, 28(4):590–593, 1993.

[40] S-M. Chang, K-S. Chang, and S. Lee. Reflection and Penetration of a Shock Wave Interacting with a Starting Vortex. 42(4):796–805, 2004. Korea Advanced Institute of Science and Technology (KAIST) [http://koasas.kaist.ac.kr/dspace-oai/request] (Korea, Republic of) ER.

[41] N. Gongora-Orozco, H. Zare-Behtash, K. Kontis, and C. Hale. Particle Image Velocimetry Studies on Shock Wave Diffraction with Co-Flow Jet. In K C Kim and S J Lee, editors, *14th International Symposium on Flow Visualization*, Daegu, Korea, 2010.

[42] B. W. Skews. Shock Diffraction on Rounded Corners. In *Thrid Australasian conference on Hydraulics and Fluid Mechanics*, Sydney, Australia, 1968.

[43] Y. P. Lagutov. Shape of a shock wave diffracted by a rounded corner. *Fluid Dynamics*, 18(3):484–487, 1983.

[44] C. Law, S. Menon, and B. W. Skews. Near-wall features in transient compressible flow on convex walls. In G Jagadeesh, editor, *25th International Symposium on Shock Waves*, Bangalore, India, 2005.

[45] M. Sun and K. Takayama. Vorticity Production in Shock Diffraction. *Journal of Fluid Mechanics*, 478:237–256, 2003.

[46] A. Muritala, C. Law, and B. W. Skews. Shock wave diffraction on convex curved walls. In K Kontis, editor, *28th International Symposium on Shock Waves*, Manchester, UK, 2011. Springer.

[47] H. Hasegawa, M. Fujimoto, T-D. Phan, H. Reme, A. Balogh, M. W. Dunlop, C. Hashimoto, and R. TanDokoro. Transport of solar wind into Earth's magnetosphere through rolled-up Kelvin-Helmholtz vortices. *Nature*, 430:755–758, 2004.

[48] P. G. Drazin and W. H. Reid. *Hydrodynamic Stability*. Cambridge Monographs on Mechanics. Cambridge University Press, Cambridge, 1982.

[49] R. Betchov and Criminale W. O. *Stability of Parallel Flows*. Academic Press, New York, 1967.

[50] E. M. Greitzer, C. S. Tan, and M. B. Graf. *Internal Flow: Concepts and Applications*. Cambridge University Press, New York, 2004.

[51] R. F. Davey and A. Roshko. The effect of density difference on shear-layer instability. *Journal of Fluid Mechanics*, 53(3):523–543, 1972.

[52] D. Papamoschou and A. Roshko. The Compressible Turbulent Shear Layer: An Experimental Study. *Journal of Fluid Mechanics*, 197:453–477, 1988.

[53] P. A. Monkewitz and P. Huerre. Influence of the velocity ratio on the spatial instability of mixing layers. *Physics of Fluids*, 25(7):1137–1143, 1982.

[54] J. Abraham and V. Magi. Exploring Velocity and Density Ratio Effects in a Mixing Layer Using DNS. *International Journal of Computational Fluid Dynamics*, 8(2):147–151, 1997. doi: 10.1080/10618569708940801.

[55] Lord Rayleigh. On the Dynamics of Revolving Fluids. *Proceedings of the Royal Society of London. Series A, Containing Papers of a Mathematical and Physical Character*, 93(648):148–154, 1880.

[56] G. L. Brown and A. Roshko. On Density Effects and Large Structure in Turbulent Mixing Layers. *Journal of Fluid Mechanics Digital Archive*, 64(04):775–816, 1974.

[57] A. Roshko. Structure of Turbulent Shear Flows: A New Look. *AIAA Journal*, 14(10):1349–1357, 1976.

[58] D. W. Bogdanoff. Compressibility Effects in Turbulent Shear layers. *AIAA Journal*, 21(6):926–927, 1983.

[59] G. S. Elliott and M. Samimy. Compressibility Effects in Free Shear Layers. *Physics of Fluids*, 2(7):1231–1240, 1990.

[60] W. W. Liou. Linear instability of curved free shear layers. *Physics of Fluids*, 6(2):541–549, 1993.

[61] L. Prandtl and O. G. Tietjens. *Applied hydro-and aeromechanics*, volume 2. Dover publications, 1957.

[62] Q. Lian and Z. Huang. Starting flow and structures of the starting vortex behind bluff bodies with sharp edges. *Experiments in Fluids*, 8(1):95–103, 1989.

[63] D. W. Moore. A numerical study of the roll-up of a finite vortex sheet. *Journal of Fluid Mechanics*, 63(02):225–235, 1974.

[64] H. Kaden. *Aufwicklung einer unstabilen Unstetigkeitsflache*. PhD thesis, 1931.

[65] D. S. Dosanjh and T. M. Weeks. Interaction of a Starting Vortex as Well as a Vortex Street with a Travelling Shock Wave. *AIAA Journal*, 3(2):216–223, 1965.

[66] J. L. Ellzey, M. R. Henneke, J. M. Picone, and E. S. Oran. The Interaction of a Shock with a Vortex: Shock Distortion and the Production of Acoustic Waves. *Physics of Fluids*, 7(1):172–184, 1995.

[67] F. Grasso and S. Pirozzoli. Shock-Wave-Vortex Interactions: Shock and Vortex Deformations, and Sound Production. *Theoretical and Computational Fluid Dynamics*, 13:421–456, 2000.

[68] K-S. Chang and S-M. Chang. Scattering of Shock into Acoustic Waves in Shock-Vortex Interaction. *Materials Science Forum*, pages 131–138, 2004.

[69] K-S. Chang, H. Barik, and S-M. Chang. The Shock-Vortex Interaction Patterns Affected by Vortex Flow Regime and Vortex Models. *Shock Waves*, 19:349–360, 2009.

[70] A. Chatterjee and S. Vijayaraj. Multiple Sound Generation in Interaction of Shock Wave with Strong Vortex. *AIAA Journal*, 46(10):2558–2567, 2008.

[71] B. W. Skews. Curved shock wave interaction with a spiral vortex. In Z Jiang, editor, *24th International Symposium on Shock Waves*, volume 2, pages 1317–1322, Beijing, China, 2004. Springer.

[72] S-M. Chang and K-S. Chang. Successive Interactions of a Shock Wave with Serially Arranged Vortices. *KSME International Journal*, 18(4):664–670, 2004.

[73] F. J. Barbosa and B. W. Skews. Shock wave interaction with a spiral vortex. *Physics of Fluids*, 13(10):3049–3060, 2001.

[74] B. Strurtevant and V. A. Kulkarny. The focusing of weak shock waves. *Journal of Fluid Mechanics*, 73(4):651–671, 1976.

[75] G. A. Sod. A survey of several finite difference methods for systems of nonlinear hyperbolic conservation laws. *Journal of Computational Physics*, 27(1):1–31, 1978. doi: 10.1016/0021-9991(78)90023-2.

[76] K. Takayama and Y. Inoue. Shock Wave Diffraction over a 90 degree Sharp Corner. *Shock Waves*, 1:301–312, 1991.

[77] J. H. Ferziger and M. Peric. *Computation Methods for Fluid Dynamics*. Springer, Berlin, 3rd edition, 2002.

[78] M. Sun and K. Takayama. A Note on Numerical Simulation of Vortical Structures in Shock Diffraction. *Shock Waves*, 13:25–32, 2003.

[79] G. Abate and W. Shyy. Dynamic Structure of Confined Shocks Undergoing Sudden Expansion. *Progress in Aerospaces Sciences*, 38, 2002.

[80] S. M. Liang, W. T. Chung, H. Chen, and S-H. Shyu. Numerical Investigation of Reflected Shock Vortex Interaction Near an Open Ended Duct. *AIAA Journal*, 43(2):349–356, 2005.

[81] T. I. Tseng and R. J. Yang. Numerical Simulation of Vorticity Production in Shock Diffraction. *AIAA Journal*, 44(5):1040–1047, 2006.

[82] S. De and M. Thangadurai. Numerical Simulation of Shock Tube Generated Vortex Effect of Numerics. *International Journal of Computational Fluid Dynamics*, 25(6):345–354, 2011.

[83] N. Uchiyama and O. Inoue. Shock Wave/ Vortex Interaction in a Flow over a 90-deg Sharp Corner. *AIAA Journal*, 33(9):1740–1743, 1995.

[84] Z. Jiang, K. Takayama, H. Babinsky, and T. Meguro. Transient Shock Wave Flows in Tube with Sudden Change in Cross Section. *Shock Waves*, 7, 1997.

[85] K. D. Jensen. Flow Measurements. *Journal of the Brazilian Society of Mechanical Sciences and Engineering*, 26:400–419, 2004.

[86] H. Kleine, H. Groenig, and K. Takayama. Simultaneous Shadow, Schlieren and Interferometric Visualization of Compressible Flows. *Optics and Lasers in Engineering*, 44:170–189, 2006.

[87] J. Rienitz. Optical inhomogeneities: schlieren and shadowgraph methods in the seventeenth and eighteenth centuries. *Endeavour*, 21(2):77–81, 1997.

[88] R. Hooke. *Micrographia: or some Physiological Descriptions of Minute Bodies made by Magnifying Glasses with Observations and Inquiries thereupon*. 1667.

[89] T. Birch. *The history of the Royal Society of London for improving of natural knowledge from its first rise, in which the most considerable of those papers communicated to the Society, which have hitherto not been published, are inserted as a supplement to the Philosophical Transactions*, volume 3. Printed for A. Millar in the Strand, London, 1757. v. 3.

[90] M. Burgan. *Robert Hooke: Natural Philosopher and Scientific Explorer*. Compass Point Books, 2008.

[91] J. Rienitz. Schlieren experiment 300 years ago. *Nature*, 254:293–295, 1975.

[92] P. Heering. Public Experiments and their Analysis with the Replication Method. *Science & Education*, 2006.

[93] O. Reynolds. An Experimental Investigation of the Circumstances which determine whether the Motion of Water shall be Direct or Sinuous, and the Law of Resistance in Parallel Channels. *Philosophical Transactions of the Royal Society*, 174:935–982, 1883.

[94] J. Darius. Visions of sound. *New Scientist*, 16 May 1974 1974.

[95] L. Foucault. Memoire sur la construction des telescopes en verre argente. *Annales de l'Observatoire de Paris*, 5:197–237, 1859.

[96] P. Krehl and S. Engemann. August Toepler - the first who visualized shock waves. *Shock Waves*, 5:1–18, 1995.

[97] A. J. I. Toepler and A. Witting. *Beobachtungen nach einer neuen optischen methode: Ein beitrag experimentalphysik*. W. Engelmann, 1906.

[98] H. G. Taylor and J. M. Waldram. Improvements in the Schlieren method. *Journal of Scientific Instruments*, 10(12):378–389, 1933.

[99] T. Smith. Foucault or Toepler? *Journal of Scientific Instruments*, 11(32):32–33, 1934.

[100] H. Kleine and G. S. Settles. The art of shock waves and their flowfields. *Shock Waves*, 17:291–307, 2008.

[101] H. Kleine. Filming the invisible - time-resolved visualization of compressible flows. *The European Physical Journal Special Topics*, 180:3–34, 2010.

[102] G. E. A. Meier. Hintergrund Schlierenverfahren, 1999.

[103] M. Raffel, H. Richard, and G. E. A. Meier. On the applicability of background oriented optical tomography for large scale aerodynamic investigations. *Experiments in Fluids*, 28:477–481, 2000.

[104] G. E. A. Meier. Computerized background-oriented schlieren. *Experiments in Fluids*, 33:181–187, 2002.

[105] F. Leopold, D. Klatt, F. Jagusinski, and C. Demeautis. Error estimation for the colored background oriented schlieren techniques (CBOS). In *8th Pacific Symposium on flow Visualization and Image Processing*, Moscow, Russia, 2011.

[106] D. Papamoschou. A Two-Spark Schlieren System for Very-High Velocity Measurements. *Experiments in Fluids*, 7:354–356, 1989.

[107] G. S. Settles. *Schlieren and Shadowgraph Techniques*. Experimental fluid Mechanics. Springer, Berlin, 2001.

[108] W. Merzkirch. *Flow Visualization*. Academic Press Inc., Florida, second edition, 1987.

[109] M. M. Biss, G. S. Settles, M. J. Hargather, L. J. Dodson, and J. D. Miller. High-speed digital shadowgraphy of shock waves from explosions and gunshots. In Klaus Hannemann and Friedrich Seiler, editors, *26th International Symposium on Shock Waves*, Gottingen, Germany, 2007.

[110] R. J. Goldstein. *Fluid Mechanics Measurements*. Taylor & Francis, Washington DC, 2nd edition, 1996.

[111] G. S. Speak and D. J. Walters. Optical Considerations and Limitations of the Schlieren Method. Technical report, Aeronautical Research Council, 1954.

[112] C. M. Vest. *Holographic Interferometry*. John Wiley & Sons, New York, 1979.

[113] T. Kreis. *Handbook of Holographic Interferometry - Optical and Digital Methods*. Wiley-VCH, Weinheim, 2005.

[114] M. J. Hargather, G. S. Settles, and M. J. Madalis. Schlieren imaging of loud sounds and weak shock waves in air near the limit of visibility. *Shock Waves*, 20:9–17, 2010.

[115] H. Kleine and H. Groenig. Color schlieren methods in shock wave research. *Shock Waves*, 1:51–63, 1991.

[116] W. L. Howes. Rainbow schlieren and its applications. *Applied Optics*, 23(14):2449–2460, 1984.

[117] D. Pierce. Photographic evidence of the formation and growth of vorticity behind plates accelerated from rest in still air. *Journal of Fluid Mechanics*, 11(03):460–464, 1961.

[118] A. R. Greenleaf. *Photographic Optics*. The MacMillan Company, New York, 1950.

[119] L. Prandtl. Uber Flussigkeitsbewegung Bei Sehr Kleiner Reibung. In *verh iii Int. math. Kongr., Heidelberg*, pages 484–491, 1905.

[120] R. J. Adrian. Twenty years of particle image velocimetry. *Experiments in Fluids*, 39:159–169, 2005.

[121] G. E. Elsinga, B. Wieneke, F. Scarano, and A. Schroeder. Tomographic 3D-PIV and Applications. In A Schroeder and C E Willert, editors, *Particle Image Velocimetry: New Developments and Recent Applications*. Springer, Berlin, 2008.

[122] F. F. J. Schrijer, F. Scarano, and B. W. van Oudheusden. Application of PIV in a Mach 7 Double-Ramp Flow. *Experiments in Fluids*, 41:353–363, 2006.

[123] R. Theunissen, F. Scarano, and M. L. Tiethmuller. An Adaptive Sampling and Windowing Interrogation Method in PIV. *Measurement Science and Technology*, 18:275–287, 2007.

[124] M. Havermann, J. Haertig, C. Rey, and A. George. PIV Measurements in Shock Tunnels and Shock Tubes. In A Schroeder and C E Willert, editors, *Particle Image Velocimetry: New Developments and Recent Applications*. Springer, 2008.

[125] M. J. Molezzi and J. C. Dutton. Application of Particle Image Velocimetry in high-Speed Separated Flows. *AIAA Journal*, 31(3):439–446, 1993.

[126] M. Raffel, C. E. Willert, S. T. Wereley, and J. Kompenhans. *Particle Image Velocimetry: A Practical Guide*. Springer, Berlin, 2007.

[127] H. Ounis, G. Ahmadi, and J. B. McLaughlin. Brownian diffusion of submicrometer particles in the viscous sublayer. *Journal of Colloid and Interface Science*, 143(1):266–277, 1991. doi: 10.1016/0021-9797(91)90458-K.

[128] S. G. Jennings. The mean free path in air. *Journal of Aerosol Science*, 19(2):159–166, 1988. doi: 10.1016/0021-8502(88)90219-4.

[129] A. Melling. Tracer Particles and Seeding for Particle Image Velocimetry. *Measurement Science and Technology*, 8:1406–1416, 1997.

[130] M. Samimy and S. K. Lele. Motion of Particles with Inertia in a Compressible Free Shear Layer. *Physics of Fluids*, 3(8), 1991.

[131] D. Ragni, F. Schrijer, B. van Oudheusden, and F. Scarano. Particle tracer response across shocks measured by PIV. *Experiments in Fluids*, 50(1):53–64, 2011.

[132] S. Ghaemi, A. Schmidt-Ott, and F. Scarano. Nanostructured tracers for laser-based diagnostics in high-speed flows. *Measurement Science and Technology*, 21(10):105403, 2010.

[133] F. Scarano. Overview of PIV in Supersonic Flows. In A Schroeder and C E Willert, editors, *Particle Image Velocimetry: New Developments and Recent Applications*. Springer, 2008.

[134] C. Hale, R. Efrani, and K. Kontis. Plasma Actuators with Multiple Encapsulated Electrodes to Influence the Induced Velocity. In *48th AIAA Aerospace Sciences Meeting*, Orlando, Florida, 2010. AIAA.

[135] C. Hale, R. Efrani, and K. Kontis. Plasma Actuators with Multiple Encapsulated Electrodes to Influence the Induced Velocity: Further Configurations. In *40th AIAA Fluid Dynamics Conference and Exhibit*, Chicago, Illinois, 2010. AIAA.

[136] D. Ragni, A. Ashok, B. W. van Oudheusden, and F. Scarano. Surface Pressure and Aerodynamic Loads Determination of a Transonic Airfoil Based on Particle Image Velocimetry. *Measurement Science and Technology*, 20, 2009.

[137] J. Haertig, M. Havermann, C. Rey, and A. George. Particle Image Velocimetry in Mach 3.5 and 4.5 Shock-Tunnel Flows. *AIAA Journal*, 40(6):1056–1060, 2002.

[138] F. F. J. Schrijer, R. Caljouw, F. Scarano, and B. W. van Oudheusden. Three Dimensional Experimental Investigation of a Hypersonic Double-Ramp Flow. In A. Schroeder and C. E. Willert, editors, *Particle Image Velocimetry: New Developments and Recent Applications*, pages 719–724. Springer, 2008.

[139] R. A. Humble, F. Scarano, and B. W. van Oudheusden. Particle Image Velocimetry Measurements of a Shock Wave/Turbulent Coundary Layer Interaction. *Experiments in Fluids*, 43:173–183, 2007.

[140] R. A. Humble, G. E. Elsinga, F. Scarano, and B. W. van Oudheusden. Investigation of the Instantaneous 3D Flow Organization of a Shock Wave/Turbulent Bouldanr Layer Interaction using Tomographic PIV. In *37th AIAA Fluid Dynamics Conference and Exhibit*, Miami, Florida, 2007. AIAA.

[141] various. Particle Image Velocimetry. In C. Tropea, A. Yarin, and J. F. Foss, editors, *Springer Handbook of Experimental Fluid Dynamics*, pages 309–342. Springer, Berlin, 2007.

[142] G. E. Elsinga, B. W. van Oudheusden, and F. Scarano. Evaluation of Aero-Optical Distortion Effects in PIV. *Experiments in Fluids*, 39, 2005.

[143] J. W. Gregory, K. Asai, M. Kameda, T. Lui, and J. P. Sullivan. A Review of Pressure-Sensitive Paint for High Speed and Unsteady Aerodynamics. *Proceedings of the Institution of Mechanical Engineers, Part G: Journal of Aerospace Engineering*, 222(2):249–290, 2008.

[144] O. Stern and M. Volmer. On the quenching-time of fluorescence. *Physik Zeitschr*, 20:183–188, 1919.

[145] H. Kautsky and H. Hirsch. Detection of minutest amounts of oxygen by extinction of phosphorescence. *Z. Anorg. Allg. Chem*, 222:126, 1935.

[146] J. P. Crowder. Fluorescent Minitufts. In W-J. Yang, editor, *Handbook of Flow Visualization*. Taylor-Francis, 1989.

[147] B. G. McLachlan, J. L. Kavandi, J. B. Callis, M. Gouterman, E. Green, G. Khalil, and D. Burns. Surface Pressure Mapping Using Luminescent Coatings. *Experiments in Fluids*, 14:33–41, 1993.

[148] J. L. Kavandi, J. B. Callis, M. Gouterman, G. Khalil, D. Wright, E. Green, D. Burns, and B. G. McLachlan. Luminescent barometry in wind tunnels. *Review of Scientific Instruments*, 61(11):3340–3347, 1990.

[149] I. A. Zakharov, V. B. Aleskovsky, and T. I. Grishaeva. Phosphorescence of trypaflavin on silica and its quenching by oxygen. *Journal of Applied Spectroscopy*, 1964.

[150] M. M. Ardasheva, L. B. Nevskii, and G. E. Pervushin. Measurement of pressure distribution by means of indicator coatings. *Journal of Applied Mechanics and Technical Physics*, 26(4):469–474, 1985.

[151] C. M. McGraw, J. H. Bell, G. Khalil, and J. B. Callis. Dynamic Surface Pressure Measurements on a Square Cylinder with Pressure Sensitive Paint. *Experiments in Fluids*, 40:203–211, 2005.

[152] J. W. Gregory, H. Sakaue, J. P. Sullivan, and S. Raghu. Characterization of miniature fluidic oscillator flowfields using porous pressure sensitive paint. In *ASME Fluids Engineering Division Summer Meeting*, New Orleans, USA, 2001.

[153] T. Liu and J. P. Sullivan. *Pressure and Temperature Sensitive Paints*. Springer-Verlag, Berlin, 2005.

[154] J. H. Bell, E. T. Schairer, L. A. Hand, and R. D. Mehta. Surface Pressure Measurements Using Luminescent Coatings. *Annual Review of Fluid Mechanics*, 33:155–206, 2001.

[155] H. Sakaue. *Anodized Aluminum Pressure Sensitive Paint for Unsteady Aerodynamic Applications*. PhD thesis, Purdue University, 2003.

[156] M. K. Quinn, L. Yang, and K. Kontis. Pressure-Sensitive Paint: Effect of Substrate. *Sensors*, 11(12):11649–11663, 2011.

[157] H. Zare-Behtash. *Experimental Studies on Compressible Vortical Flows, Phenomena and Interactions*. PhD thesis, University of Manchester, 2009.

[158] B. J. Basu. Optical Oxygen Sensing Based on Luminescence Quenching of Platinum Porphyrin Dyes Doped in Ormosil Coatings. *Sensors and Actuators B*, 123:568/577, 2007.

[159] B. D. MacCraith and C. McDonagh. Enhanced Fluorescence Sensing Using Sol-Gel Materials. *Journal of Fluorescence*, 12(3/4):333–342, 2002.

[160] A. E. Baron, J. D. Danielson, M. Gouterman, J. R. Wan, J. B. Callis, and M. Blair. Submillisecond Response Times of Oxygen-Quenched Luminescent Coatings. *Review of Scientific Instruments*, 64(12):3394–3402, 1993.

[161] Y. Sakamura, M. Mamtsumoto, and T. Suzuki. High Frame-Rate Imaging of Surface Pressure Distribution Using a Porous Pressure-Sensitive Paint. *Measurement Science and Technology*, 16:759–765, 2005.

[162] N. Gongora-Orozco. *Experimental Studies on Internal Shock Wave Phenomenon and Interactions*. PhD thesis, University of Manchester, 2010.

[163] V. E. Mosharov, V. Radchenko, and S. Fonov. *Luminescent Pressure Sensors in Aerodynamic Experiments*. Central Aerodynamic Institute (TsAGI), Moscow, Russia, 1997.

[164] H. Sakaue and J. P. Sullivan. Time Response of Anodized Aluminium Pressure-Sensitive Paint. *AIAA Journal*, 39(10):1944–1949, 2001.

[165] M. Kameda, N. Tezuka, T. Hangai, K. Asai, K. Nakakita, and Y. Amao. Adsorptive Pressure-Sensitive Coatings on Porous Anodized Aluminium. *Measurement Science and Technology*, 15(3):489–500, 2004.

[166] T. Hangai, M. Kameda, K. Nakakita, and K. Asai. Time Response characteristics of Pyrene-Based Pressure-Sensitive Coatings on Anodic Porous Alumina. In *Proceedings of the 10th International Symposium on Flow Visualization*, volume 5, pages 1727–1738, Kyoto, Japan, 2002.

[167] S. Fang. *Application of Fast-Responding Pressure-Sensitive Paint to a Hemispherical Dome in Unsteady Transonic Flow*. PhD thesis, Ohio State University, 2010.

[168] M. Pastuhoff, N. Tillmark, and P. H. Alfredsson. Dynamic Calibration of Polymer/Ceramic Pressure Sensitive Paint Using a Shock Tube. In *Seventh International Conference on Flow Dynamics : Proceedings*, KTH Sweden, 2010.

[169] T. Hayashi, H. Ishikawa, and H. Sakaue. Development of Polymer-Ceramic Pressure-Sensitive Paint and Its Application to Supersonic Flow Field. In K Kontis, editor, *28th International Symposium on Shock Waves*, pages 607–613, Manchester, UK, 2011. Springer Berlin Heidelberg.

[170] H. Sakaue, T. Kakisako, and H. Ishikawa. Characterization and Optimization of Polymer-Ceramic Pressure-Sensitive Paint by Controlling Polymer Content. *Sensors*, 11(7):6967–6977, 2011.

[171] H. Sakaue. Luminophore Application Method of Anodized Aluminum Pressure Sensitive Paint as a Fast Responding Global Pressure Sensor. *Review of Scientific Instruments*, 76, 2005.

[172] H. Sakaue, T. Tabei, and M. Kameda. Hydrophobic monolayer coating on anodized aluminum pressure-sensitive paint. *Sensors and Actuators B: Chemical*, 119(2):504–511, 2006. doi: 10.1016/j.snb.2006.01.010.

[173] B. F. Carroll, J. D. Abbitt, and E. W. Lukas. Step Response of Pressure-Sensitive Paints. *AIAA Journal*, 34(3):521–526, 1996.

[174] J. P. Hubner, B. F. Carroll, K. S. Schanze, and H. F. Ji. Pressure-sensitive paint measurements in a shock tube. *Experiments in Fluids*, 28(1):21–28, 2000. Experiments in Fluids.

[175] C. McDonagh, P. Bowe, K. Mongey, and B. D. MacCraith. Characterisation of porosity and sensor response times of sol-gel-derived thin films for oxygen sensor applications. *Journal of Non-Crystalline Solids*, 306(2):138–148, 2002. doi:10.1016/S0022-3093(02)01154-7.

[176] M. Kameda, T. Tabei, K. Nakakita, H. Sakaue, and K. Asai. Image measurements of unsteady pressure fluctuation by a pressure-sensitive coating on porous anodized aluminium. *Measurement Science and Technology*, 16(12):2517, 2005.

[177] Y. Takeuchi, Y. Amao, G. Orellana, and M. Moreno-Bondi. Materials for Luminescent Pressure-Sensitive Paint. In *Frontiers in Chemical Sensors*, volume 3 of *Springer Series on Chemical Sensors and Biosensors*, pages 303–322. Springer Berlin Heidelberg, 2005.

[178] Y. Egami and K. Asai. Effect of antioxidants on photodegradation of porous pressure-sensitive paint. In *22nd AIAA Aerodynamic Measurement Technology and Ground Testing Conference*, St Louis, USA, 2002. AIAA.

[179] J. R. Lakowicz. *Principles of fluorescence spectroscopy*. Springer Science and Business Media, New York, 2010.

[180] J. Hradil, C. Davis, K. Mongey, C. McDonagh, and B. D. MacCraith. Temperature-Corrected Pressure-Sensitive Paint Measurements Using a Single Camera and A Dual-Lifetime Approach. *Measurement Science and Technology*, 13:1552–1557, 2002.

[181] M. K. Quinn, N. Gongora-Orozco, K. Kontis, and P. Ireland. Application of pressure-sensitive paint to low-speed flow around a u-bend of strong curvature. In *8th Pacific Symposium on Flow Visualization and Image Processing*, Moscow, Russia, 2011.

[182] M. K. Quinn, N. Gongora-Orozco, K. Kontis, and P. Ireland. Application of Pressure-Sensitive Paint to Low-Speed Flow around a U-Bend of Strong Curvature. *Experimental Thermal and Fluid Science*, 2013.

[183] B. G. McLachlan, J. H. Bell, H. Park, R. A. Kennelly, J .A. Schreiner, S. C. Smith, J. M. Strong, J. Gallery, and M. Gouterman. Pressure-Sensitive Paint Measurements on a Supersonic High-Sweep Oblique Wing Model. *Journal of Aircraft*, 32(2):217–227, 1995.

[184] J. W. Gregory, J. P. Sullivan, K. Asai, B. Carroll, W. Ruyten, H. Sakaue, and J. Bell. Effect of Quenching Kinetics on Unsteady Response of Pressure-Sensitive Paint. *AIAA Journal*, 44(3):634–645, 2006.

[185] H. Sakaue and K. Ishii. Optimization of Anodized-Aluminum Pressure-Sensitive Paint by Controlling Luminophore Concentration. *Sensors*, 10(7):6836–6847, 2010.

[186] R. H. Engler, C. Klein, and O. Trinks. Pressure Sensitive Paint Systems for Pressure Distribution Measurements in Wind Tunnels and Turbomachines. *Measurement Science and Technology*, 11:1077–1085, 2000.

[187] C. M. McGraw, H. Shroff, G. Khalil, and J. B. Callis. The Phosphorescence Microphone: A Device for Testing Oxygen Sensors and Films. *Review of Scientific Instruments*, 74(12):5260–5266, 2003.

[188] K. Nakakita. Unsteady Pressure Distribution Measurement around 2D-Cylinders Using Pressure-Sensitive Paint. In *25th AIAA Applied Aerodynamics Conference*, Miami, FL, 2007. AIAA.

[189] U. Henne. Application of the PSP Technique in Low Speed Wind Tunnels. In H-J. Rath, C. Holze, H-J. Heinemann, R. Henke, and H. Honlinger, editors, *New Results in Numerical and Experimental Fluid Mechanics V*, pages 41–49. Springer Berlin / Heidelberg, Berlin, 2006.

[190] H. Sakaue, J. P. Sullivan, Y. Egami, Y. Iijima, K. Asai, R. H. Engler, U. Beifuss, and F. Doring. Open-System Pressure Sensitive Paint for Surface Pressure Measurements in a Crogenic Wind Tunnel. In *19th International congress on instrumentation in aerospace simulation facilities*, Cleveland, USA, 2001. DLR Electronic Library [http://elib.dlr.de/perl/oai2] (Germany) ER.

[191] C. Klein, R. H. Engler, and U. Henne. Application of Pressure Sensitive Paint for Determination of the Pressure Field and Calculation of the Forces and Moments of Models in a Wind Tunnel. *Experiments in Fluids*, 39:475–483, 2005.

[192] H. Zare-Behtash, N. Gongora-Orozco, and K. Kontis. PSP Visualization Studies on a Convergent Nozzle with an Ejector System. *Journal of Visualization*, 12(2):157–163, 2009.

[193] R. H. Engler, M-C. Mrienne, C. Klein, and Y. Le Sant. Applications of PSP in Low Speed Flows. *Aerospace Science and Technology*, 6:313–322, 2002.

[194] Y. Sakamura and T. Suzuki. Surface Pressure Distribution Imaging at Frame Rates Over 1kHz Using Porous Pressure-Sensitive Paint. In *20th International Congress on Instrumentation in Aerospace Simulation Facilities*, pages 363–371, Gottingen, Germany, 2003.

[195] A. Mills. Optical Oxygen Sensors: Utilising the Luminescence of Platinum Metals Complexes. *Platinum Metals Review*, 41(3):115–127, 1997.

[196] H. Sakaue and K. Ishii. A Dipping Duration Study for Optimization of Anodized-Aluminum Pressure-Sensitive Paint. *Sensors*, 10(11):9799–9807, 2010.

[197] N. Gongora-Orozco, H. Zare-Behtash, and K. Kontis. Global Unsteady Pressure-Sensitive Paint Measurements of a Moving Shock Wave Using Thin-Layer Chromatography. *Measurement*, 43(1):152–155, 2009.

[198] H. Mori, T. Yoshimoto, J-K. Moon, and Y. Inoue. A Priori Calibration Of Pressure Sensitive Paint for Low-Speed Flows. In *14th International Symposium on Flow Visualization*, EXCO Daegu, Korea, 2010.

[199] T. Craft. Personal Communication, 2012.

[200] R. J. Adrian, C. D. Meinhart, and C. D. Tomkins. Vortex organization in the outer region of the turbulent boundary layer. *Journal of Fluid Mechanics*, 422:1–54, 2000.

[201] F. Kimura, J. McCann, G. Khalil, D. Dabiri, Y. Xia, and J. B. Callis. Simultaneous Velocity and Pressure Measurements using Luminescent Microspheres. *Review of Scientific Instruments*, 81, 2010.

[202] F. Kimura, M. Rodriguez, J. McCann, B. Carlson, D. Dabiri, G. Khalil, J. B. Callis, Y. Xia, and M. Gouterman. Development and Characterization of Fast Responding Pressure Sensitive Microspheres. *Review of Scientific Instruments*, 79, 2008.

[203] S. Abe, K. Okamoto, and H. Madarame. The Development of PIV-PSP Hybrid System Using Pressure Sensitive Particles. *Measurement Science and Technology*, 15:1153–1157, 2004.

[204] D. H. Song, H. D. Kim, S. Someya, and K. C. Kim. Development of Micro PSP-PIV System For Simultaneous Measurement of Oxygen Concentration and Velocity Fields. In *14th International Symposium on Flow Visualization*, Daegu, Korea, 2010.

Appendix A

Designs

A.1 Co-flow Nozzle

The nozzle was used for supersonic co-flow measurements (results shown in Appendix C) and was designed using a code written by the author based on the method of characteristics as presented by Anderson [16]. Only a half nozzle was used in order to reduce manufacturing time and also to avoid heavy modifications to the existing experimental setup. Viscous effects were considered in the design of the nozzle; however, it was discovered that the boundary layer would be smaller than the machining tolerances possible using in-house equipment and so they were neglected. In order to help maintain the validity of this assumption, the nozzle length was kept to be as short as possible as, the boundary layer mainly grows in the divergent part of the nozzle. The nozzle contour was numerically tested using the CFD program Fluent and produced uniformly expanded isentriopic Mach 1.5 flow.

The nozzle fits over a removed section of the existing pipework and is cut at angles in order to remove any freestanding faces which would be extremely difficult to seal.

A.2 Splitter Designs

This section contains the geometry of the splitters relevant to the results in Appendix B.

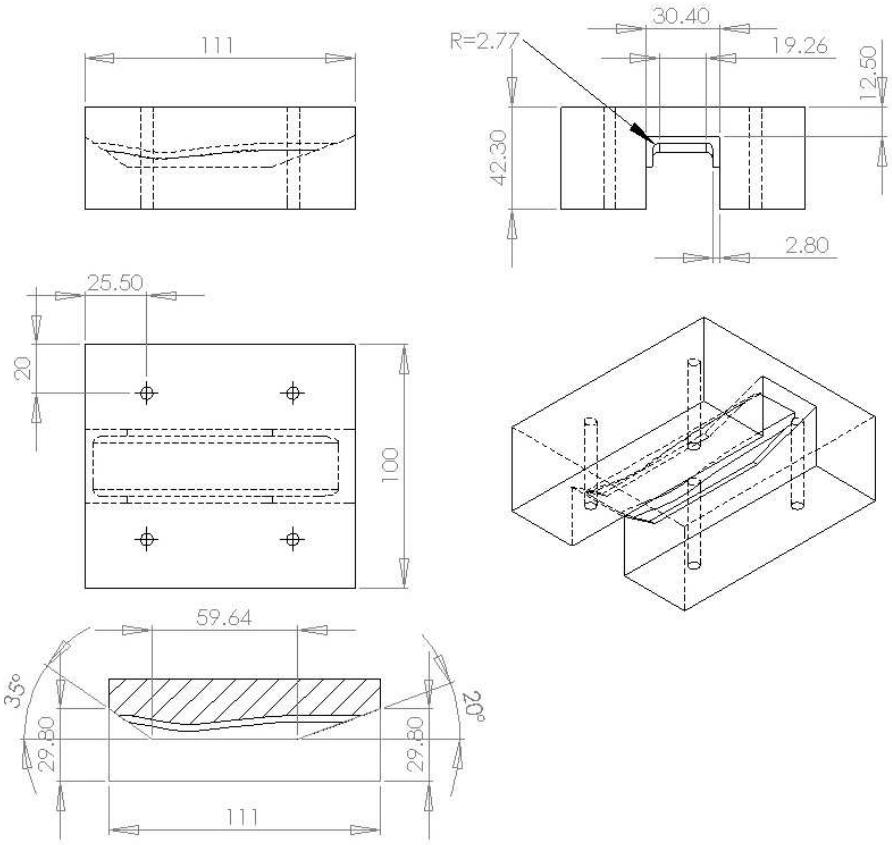

Figure A.1: Mach 1.5 nozzle design (all dimensions in (mm))

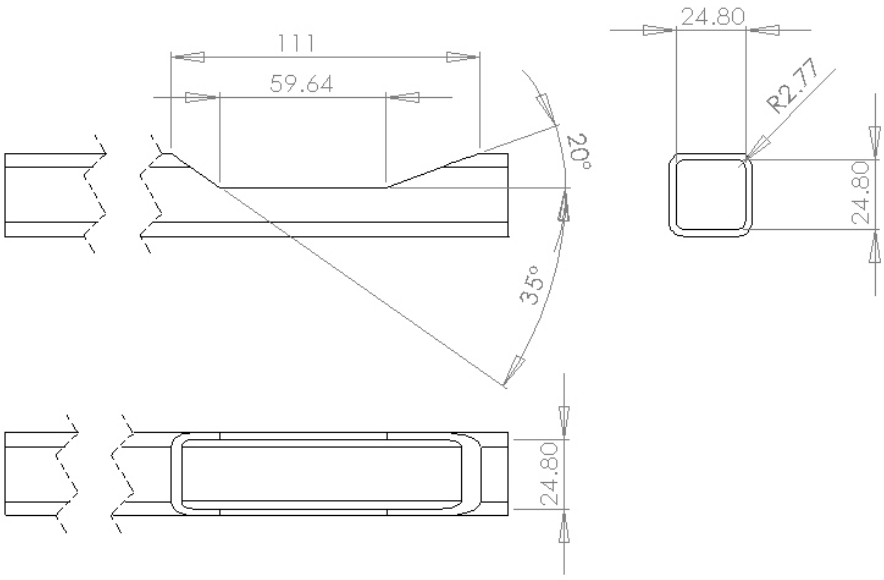

Figure A.2: Cut out section from existing pipework (all dimensions in (mm))

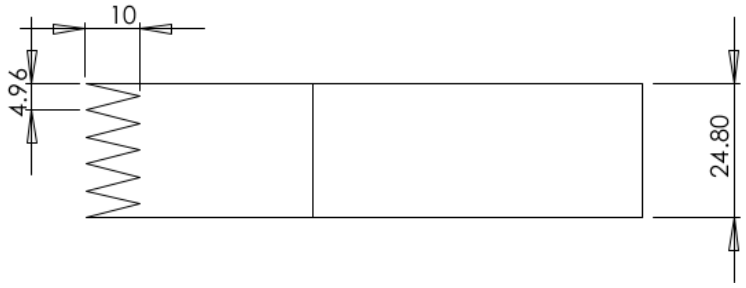

(a) Small Sawtooth

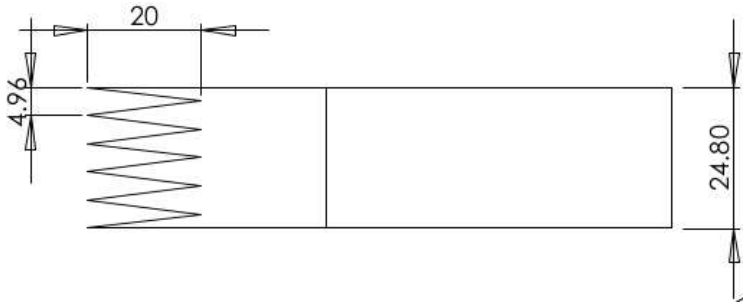

(b) Large Sawtooth

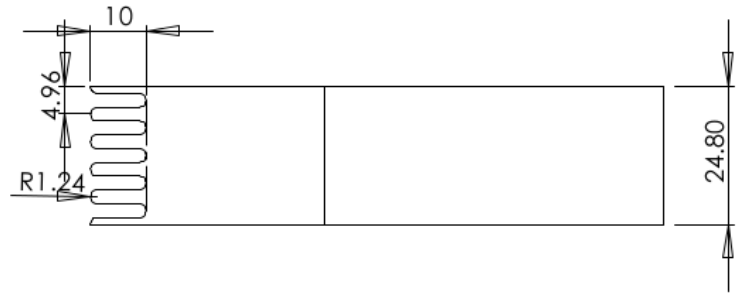

(c) Small Fingers

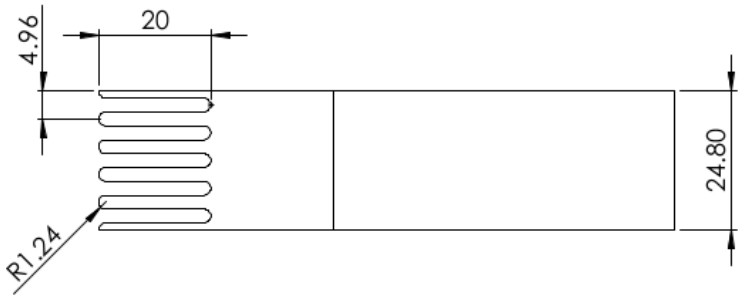

(d) Large Fingers

Figure A.3: Geometry of the extra splitters (all dimensions in (mm))

Appendix B

Preliminary Results with Three-Dimensional Splitters

The splitter designs shown in Appendix A.2 were tested using schlieren and shadowgraph imaging at all three of the pressure ratios discussed in the main body of the thesis. Only pressure ratios of 4 and 12 will be shown in the appendix.

B.1 Small Saw Geometry

B.1.1 P4/P1=4

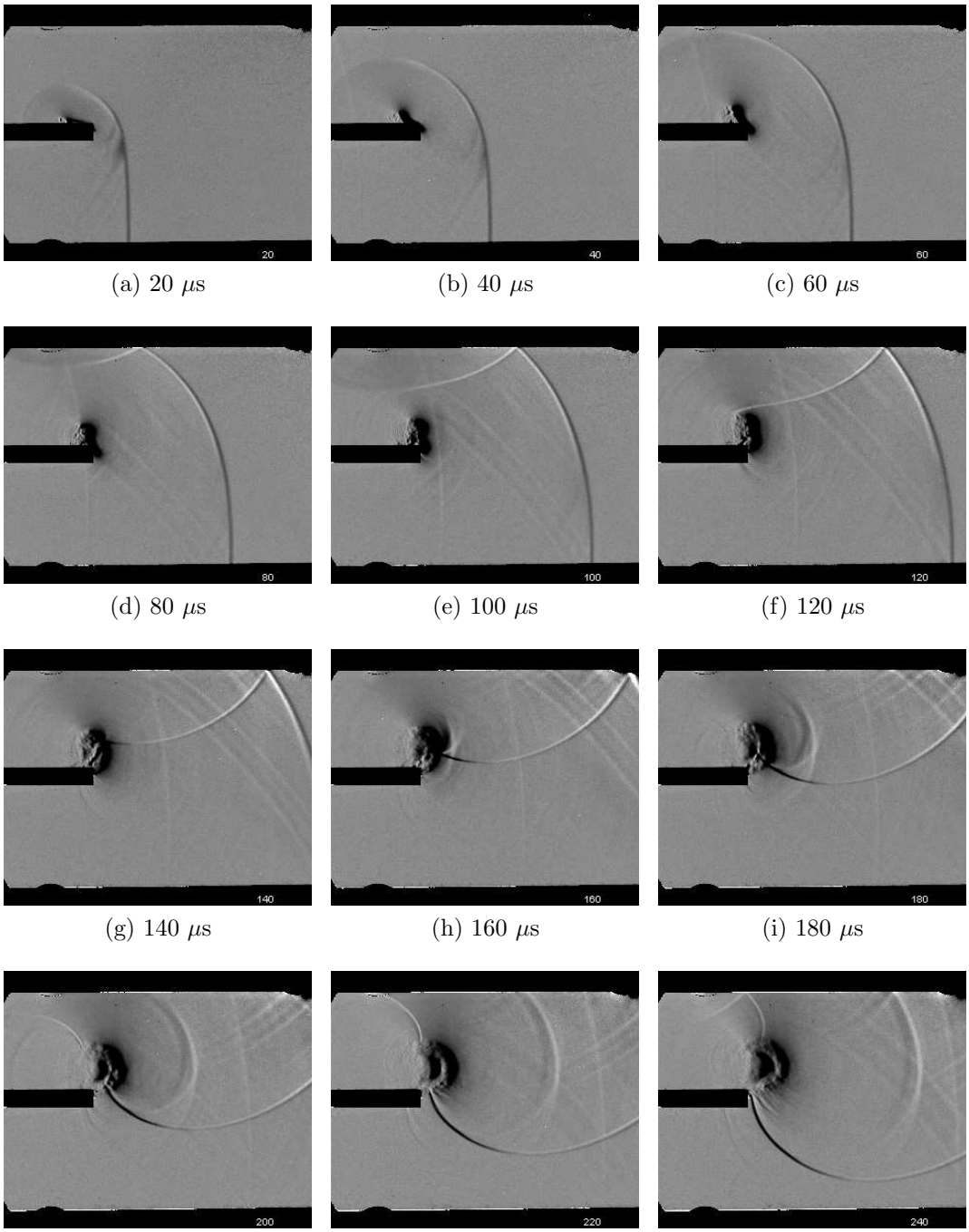

(a) 20 μs (b) 40 μs (c) 60 μs

(d) 80 μs (e) 100 μs (f) 120 μs

(g) 140 μs (h) 160 μs (i) 180 μs

(j) 200 μs (k) 220 μs (l) 240 μs

Figure B.1: Schlieren results of diffraction process around small saw geometry, $\frac{P_4}{P_1} = 4$

B.1.2 P4/P1=12

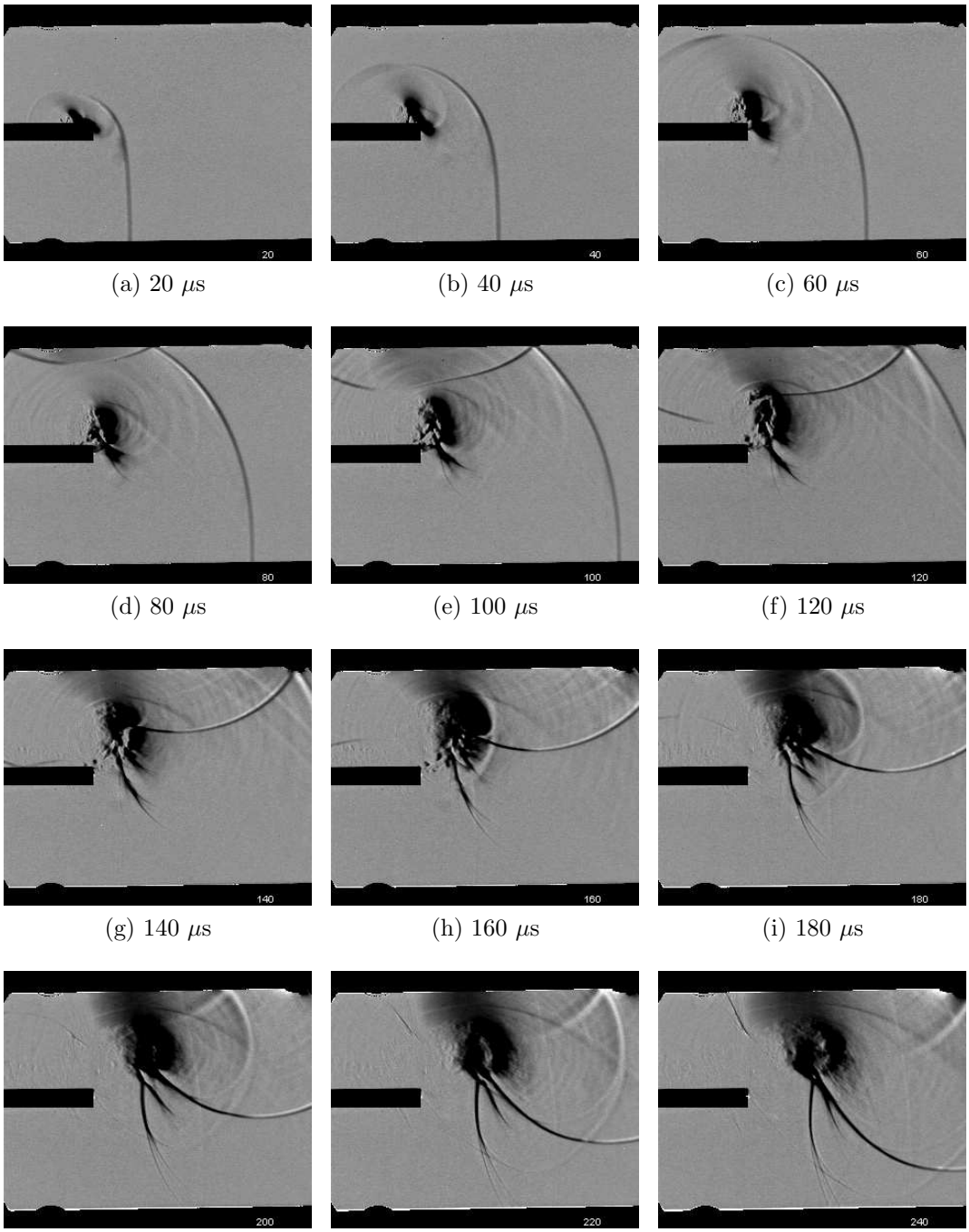

(a) 20 μs (b) 40 μs (c) 60 μs

(d) 80 μs (e) 100 μs (f) 120 μs

(g) 140 μs (h) 160 μs (i) 180 μs

(j) 200 μs (k) 220 μs (l) 240 μs

Figure B.2: Schlieren results of diffraction process around small saw geometry, $\frac{P_4}{P_1} = 12$

B.2 Large Saw Geometry

B.2.1 P4/P1=4

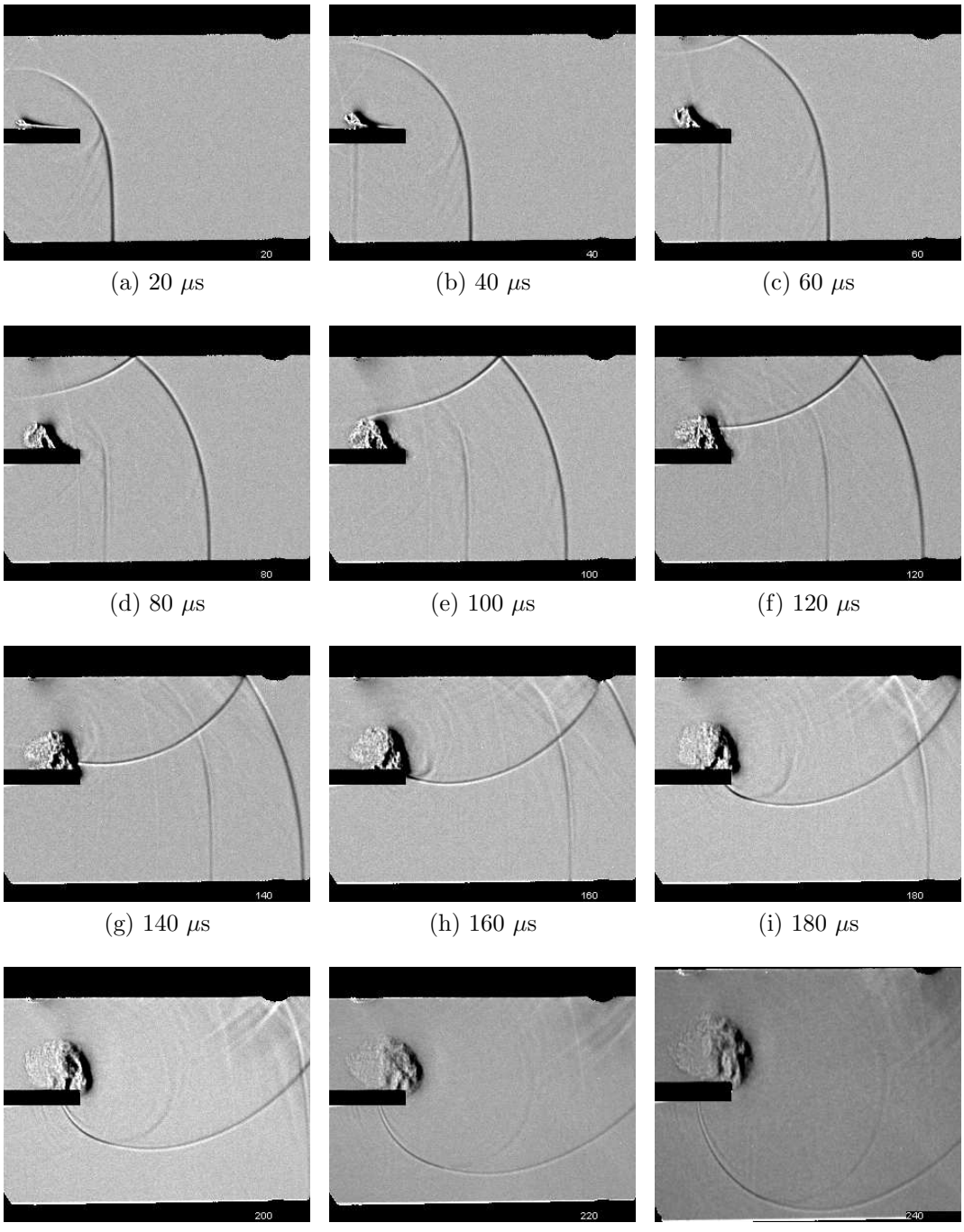

(a) 20 μs (b) 40 μs (c) 60 μs

(d) 80 μs (e) 100 μs (f) 120 μs

(g) 140 μs (h) 160 μs (i) 180 μs

(j) 200 μs (k) 220 μs (l) 240 μs

Figure B.3: Schlieren results of diffraction process around large saw geometry, $\frac{P_4}{P_1} = 4$

B.2.2 P4/P1=12

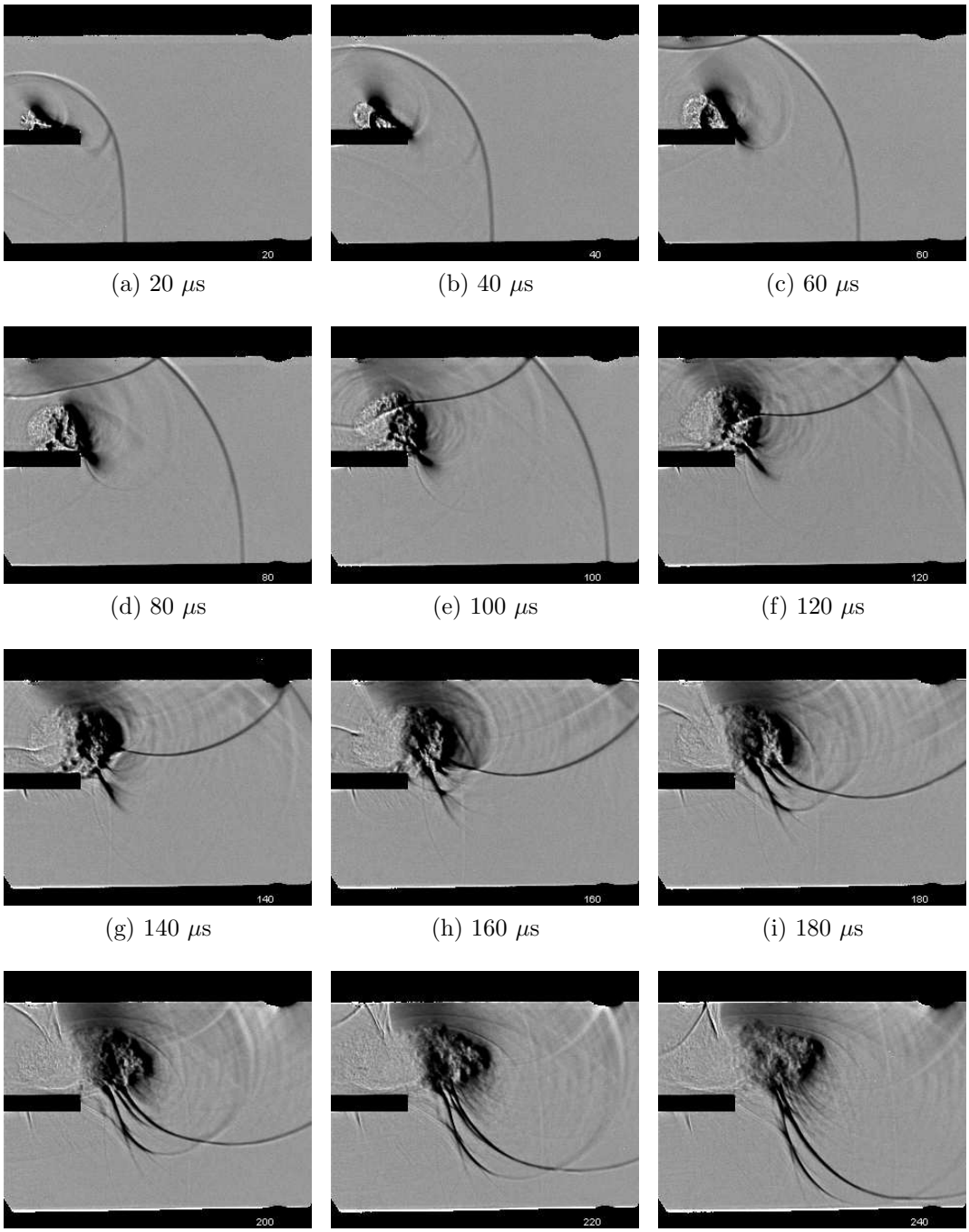

(a) 20 μs (b) 40 μs (c) 60 μs

(d) 80 μs (e) 100 μs (f) 120 μs

(g) 140 μs (h) 160 μs (i) 180 μs

(j) 200 μs (k) 220 μs (l) 240 μs

Figure B.4: Schlieren results of diffraction process around large saw geometry, $\frac{P_4}{P_1} = 12$

B.3 Small Fingers Geometry

B.3.1 P4/P1=4

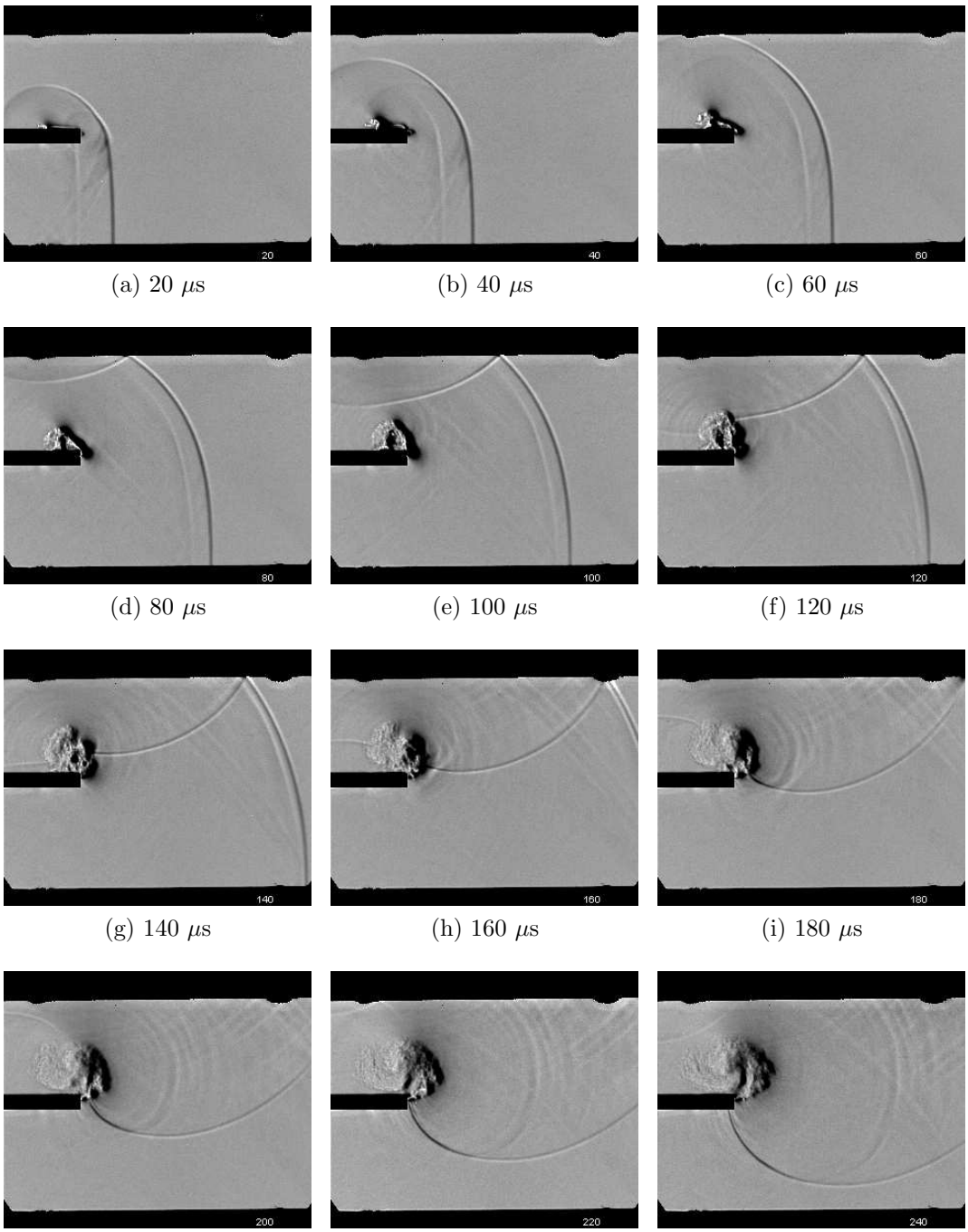

(a) 20 μs (b) 40 μs (c) 60 μs

(d) 80 μs (e) 100 μs (f) 120 μs

(g) 140 μs (h) 160 μs (i) 180 μs

(j) 200 μs (k) 220 μs (l) 240 μs

Figure B.5: Schlieren results of diffraction process around small fingers geometry, $\frac{P_4}{P_1} = 4$

B.3.2 P4/P1=12

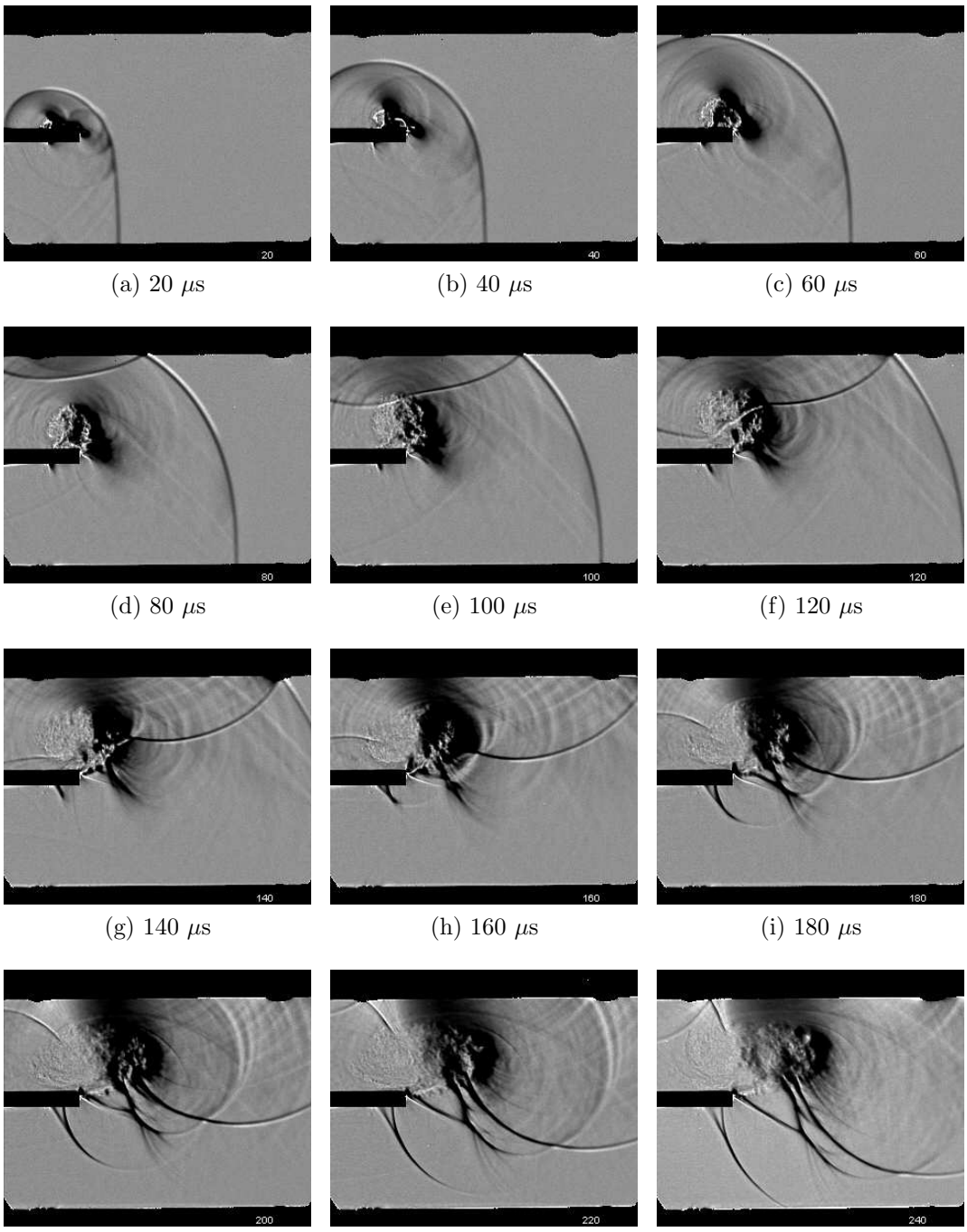

(a) 20 μs (b) 40 μs (c) 60 μs

(d) 80 μs (e) 100 μs (f) 120 μs

(g) 140 μs (h) 160 μs (i) 180 μs

(j) 200 μs (k) 220 μs (l) 240 μs

Figure B.6: Schlieren results of diffraction process around small fingers geometry, $\frac{P_4}{P_1} = 12$

B.4 Large Fingers Geometry

B.4.1 P4/P1=4

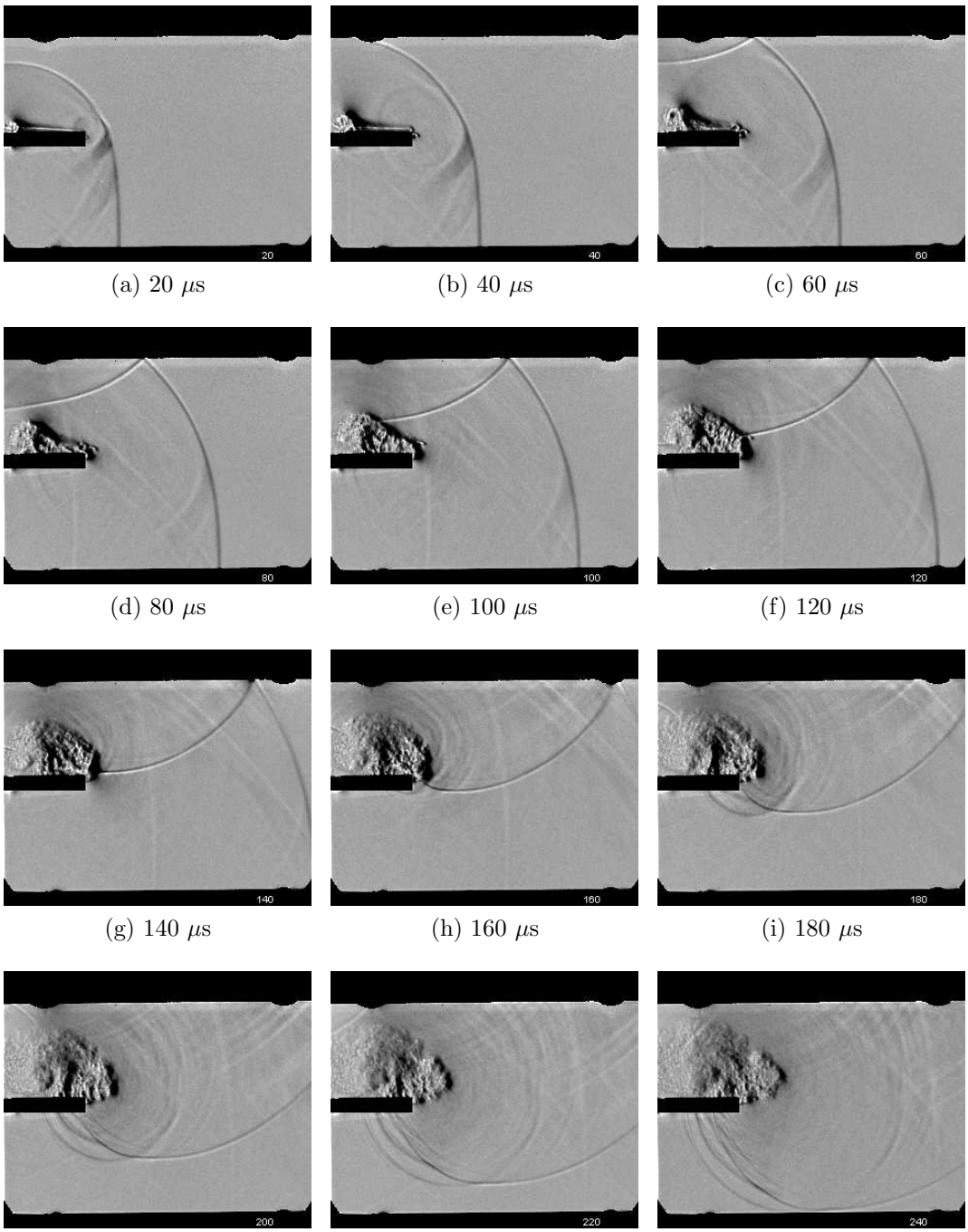

(a) 20 μs (b) 40 μs (c) 60 μs

(d) 80 μs (e) 100 μs (f) 120 μs

(g) 140 μs (h) 160 μs (i) 180 μs

(j) 200 μs (k) 220 μs (l) 240 μs

Figure B.7: Schlieren results of diffraction process around large fingers geometry, $\frac{P_4}{P_1} = 4$

B.4.2 P4/P1=12

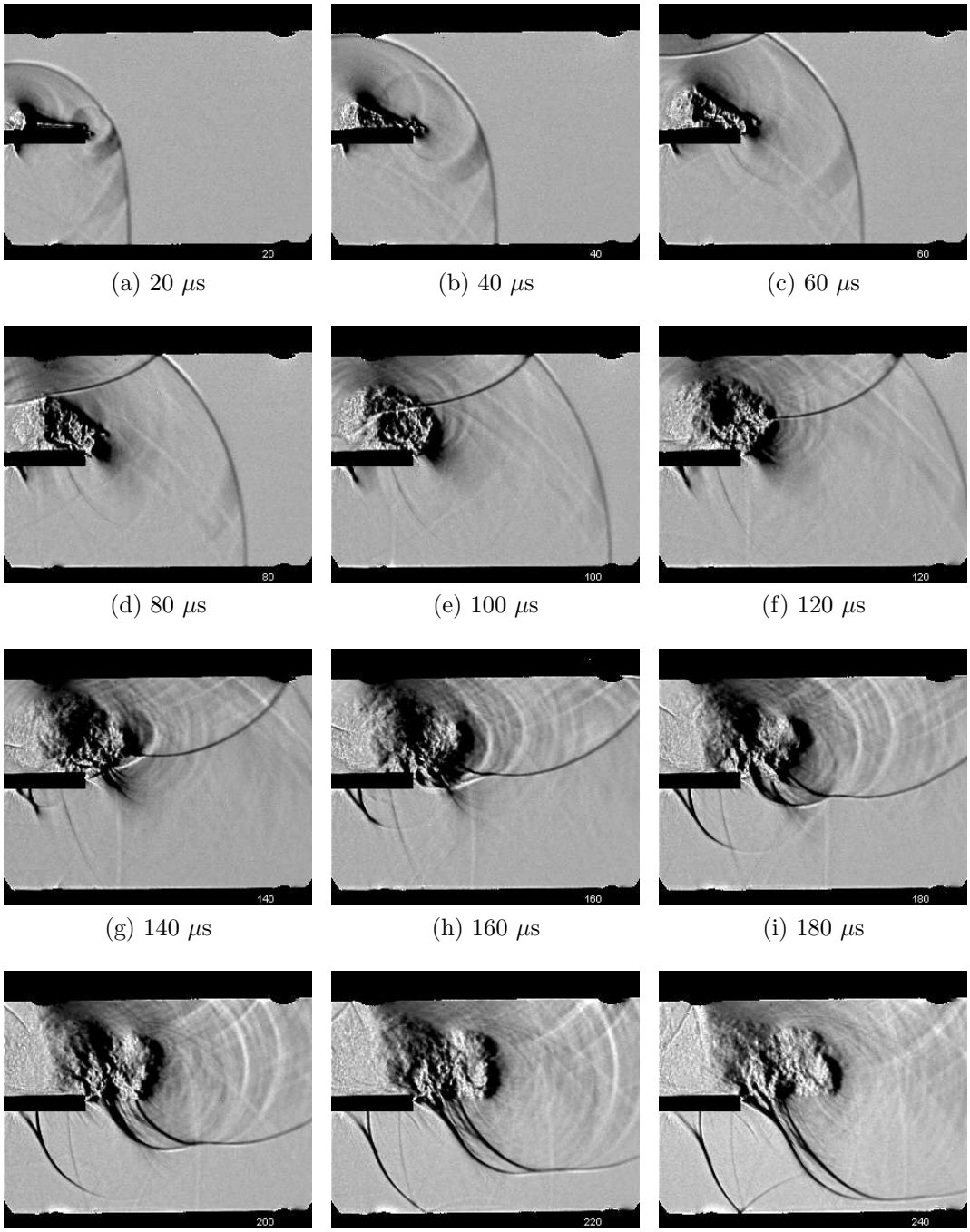

(a) 20 μs (b) 40 μs (c) 60 μs

(d) 80 μs (e) 100 μs (f) 120 μs

(g) 140 μs (h) 160 μs (i) 180 μs

(j) 200 μs (k) 220 μs (l) 240 μs

Figure B.8: Schlieren results of diffraction process around large fingers geometry, $\frac{P_4}{P_1} = 12$

Appendix C

Preliminary Results of Shock Diffraction with Co-Flow

The supersonic nozzle design in Appendix A.1 was continuously fed using the in-house supply of compressed air to give a subsonic or supersonic flow (Mach 1.5). This stream was fed parallel to the shock tube to investigate the effect of the co-flow on the shock wave. Repeatability of flow conditions such as this became a serious issue and would need to be improved upon before subsequent tests. The presence of the co-flow jet entrained flow from the driver section, reducing its pressure, especially for the supersonic case. This made repeatable measurements of the pressure ratio difficult, as the shock tube was not instrumented in such a way. Also, due to the nature of the co-flow jet, it was not possible to perform the image-processing techniques used in the main body of the report. As a result of this, the figures presented here are the raw images captured using the HPV-1.

C.1 Sharp Geometry

C.1.1 P4/P1=4

C.1.2 Subsonic Co-Flow

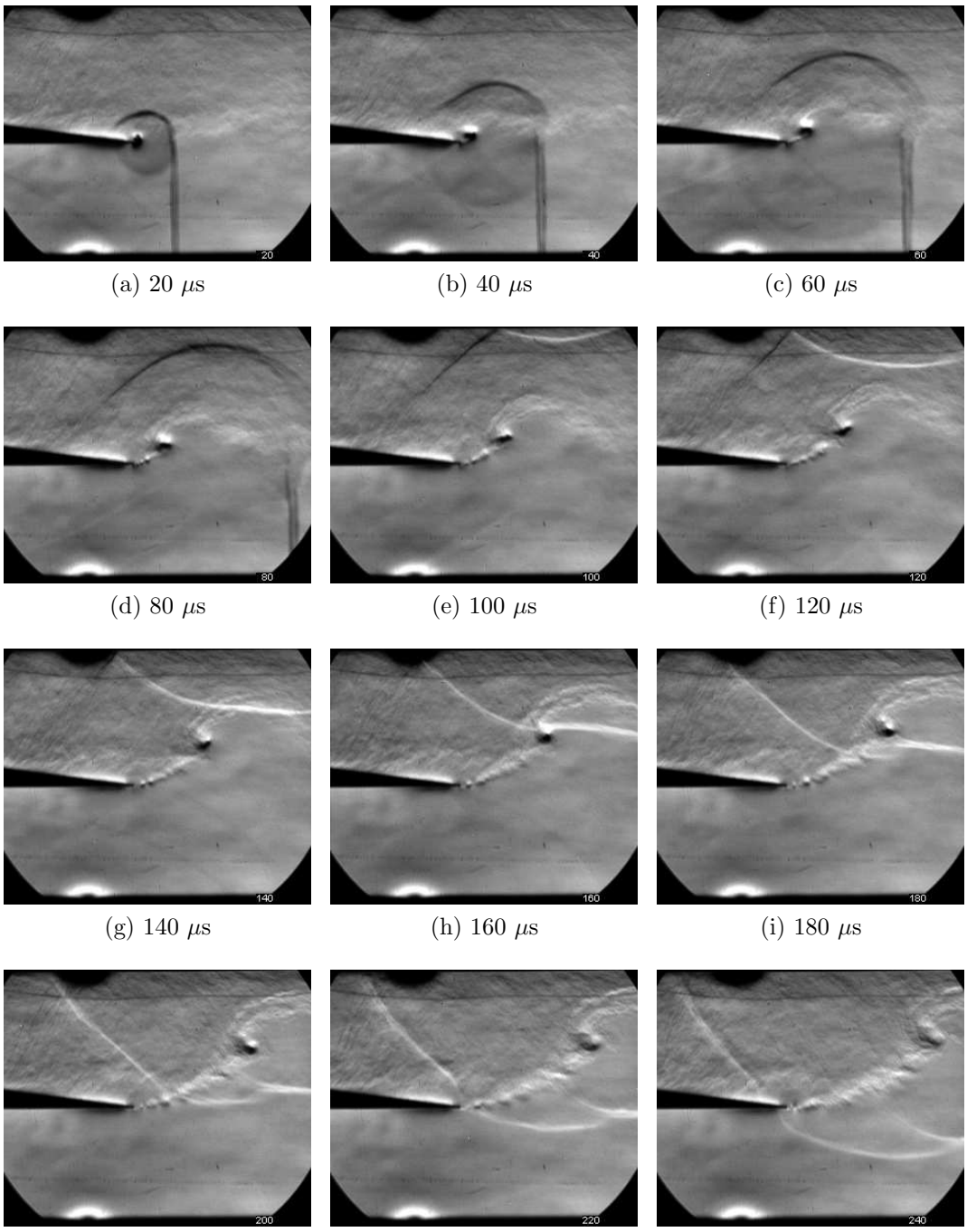

(a) 20 μs (b) 40 μs (c) 60 μs

(d) 80 μs (e) 100 μs (f) 120 μs

(g) 140 μs (h) 160 μs (i) 180 μs

(j) 200 μs (k) 220 μs (l) 240 μs

Figure C.1: Schlieren results of diffraction process around sharp geometry with subsonic co-flow, $\frac{P_4}{P_1} = 4$

C.1.3 Supersonic Co-Flow

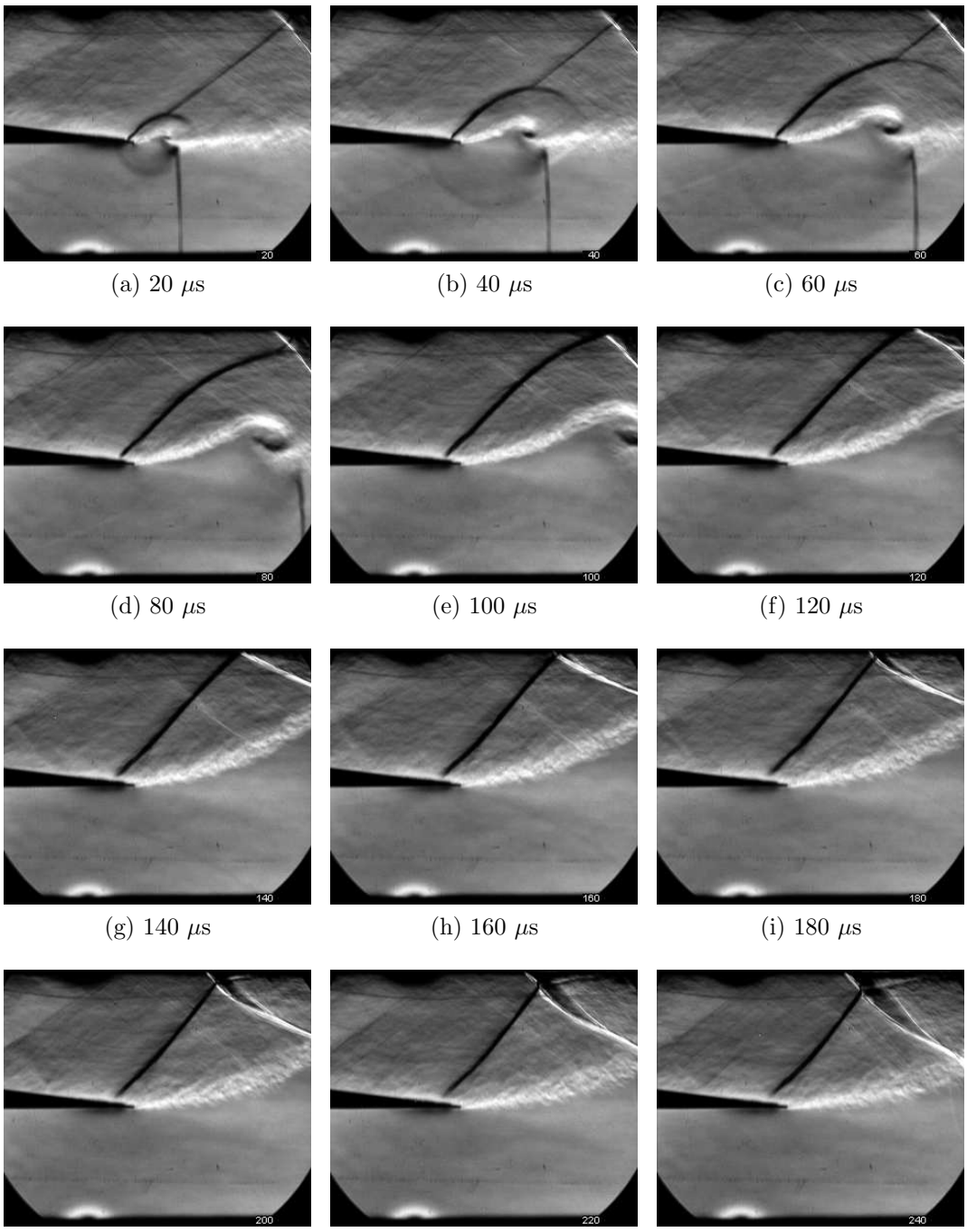

(a) 20 μs (b) 40 μs (c) 60 μs

(d) 80 μs (e) 100 μs (f) 120 μs

(g) 140 μs (h) 160 μs (i) 180 μs

(j) 200 μs (k) 220 μs (l) 240 μs

Figure C.2: Schlieren results of diffraction process around sharp geometry with supersonic co-flow, $\frac{P_4}{P_1} = 4$

C.1.4 P4/P1=12

C.1.5 Subsonic Co-Flow

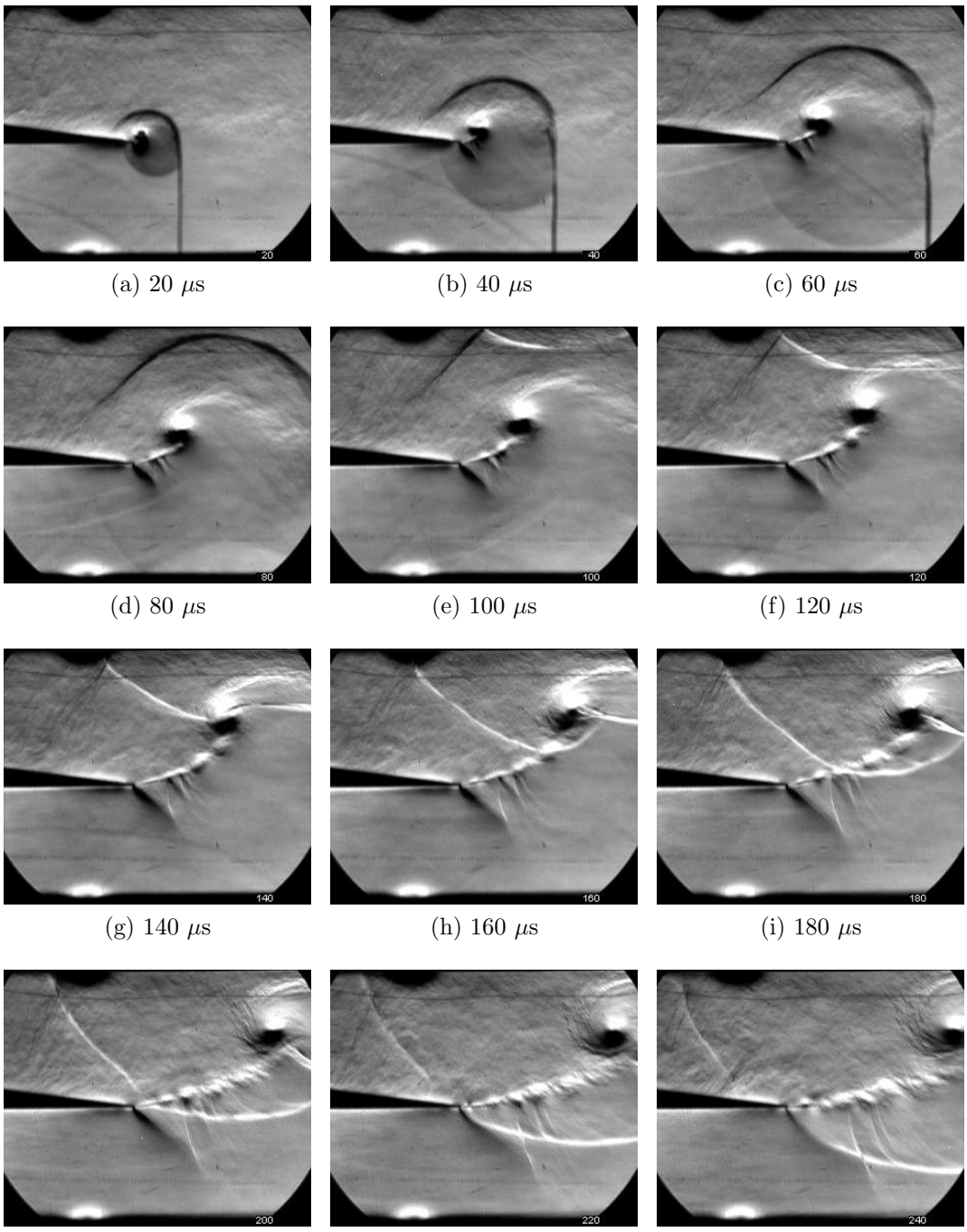

(a) 20 μs (b) 40 μs (c) 60 μs

(d) 80 μs (e) 100 μs (f) 120 μs

(g) 140 μs (h) 160 μs (i) 180 μs

(j) 200 μs (k) 220 μs (l) 240 μs

Figure C.3: Schlieren results of diffraction process around sharp geometry with subsonic co-flow, $\frac{P_4}{P_1} = 12$

C.1.6 Supersonic Co-Flow

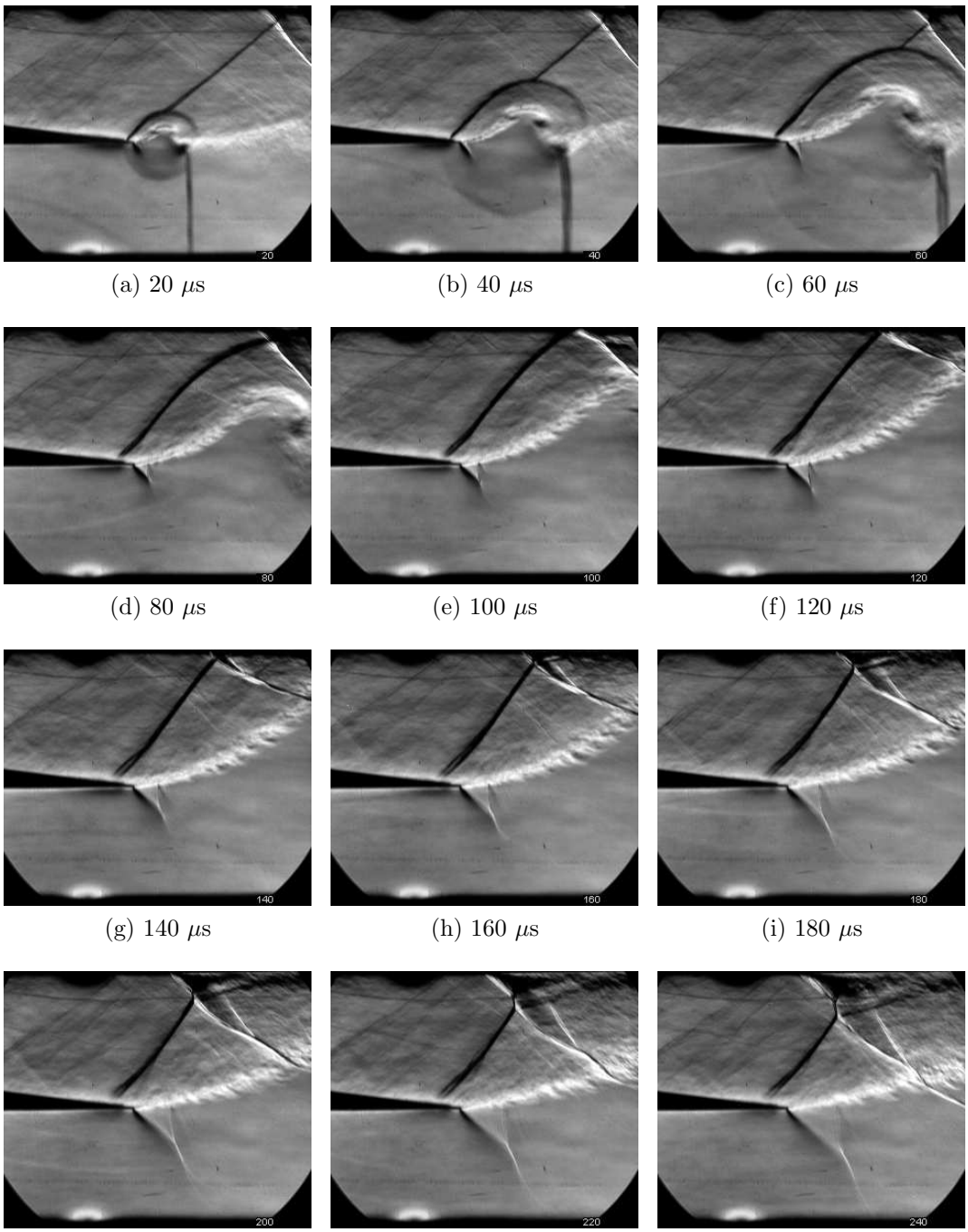

(a) 20 μs (b) 40 μs (c) 60 μs

(d) 80 μs (e) 100 μs (f) 120 μs

(g) 140 μs (h) 160 μs (i) 180 μs

(j) 200 μs (k) 220 μs (l) 240 μs

Figure C.4: Schlieren results of diffraction process around sharp geometry with supersonic co-flow, $\frac{P_4}{P_1} = 12$

C.2 Round Geometry

C.2.1 P4/P1=4

C.2.2 Subsonic Co-Flow

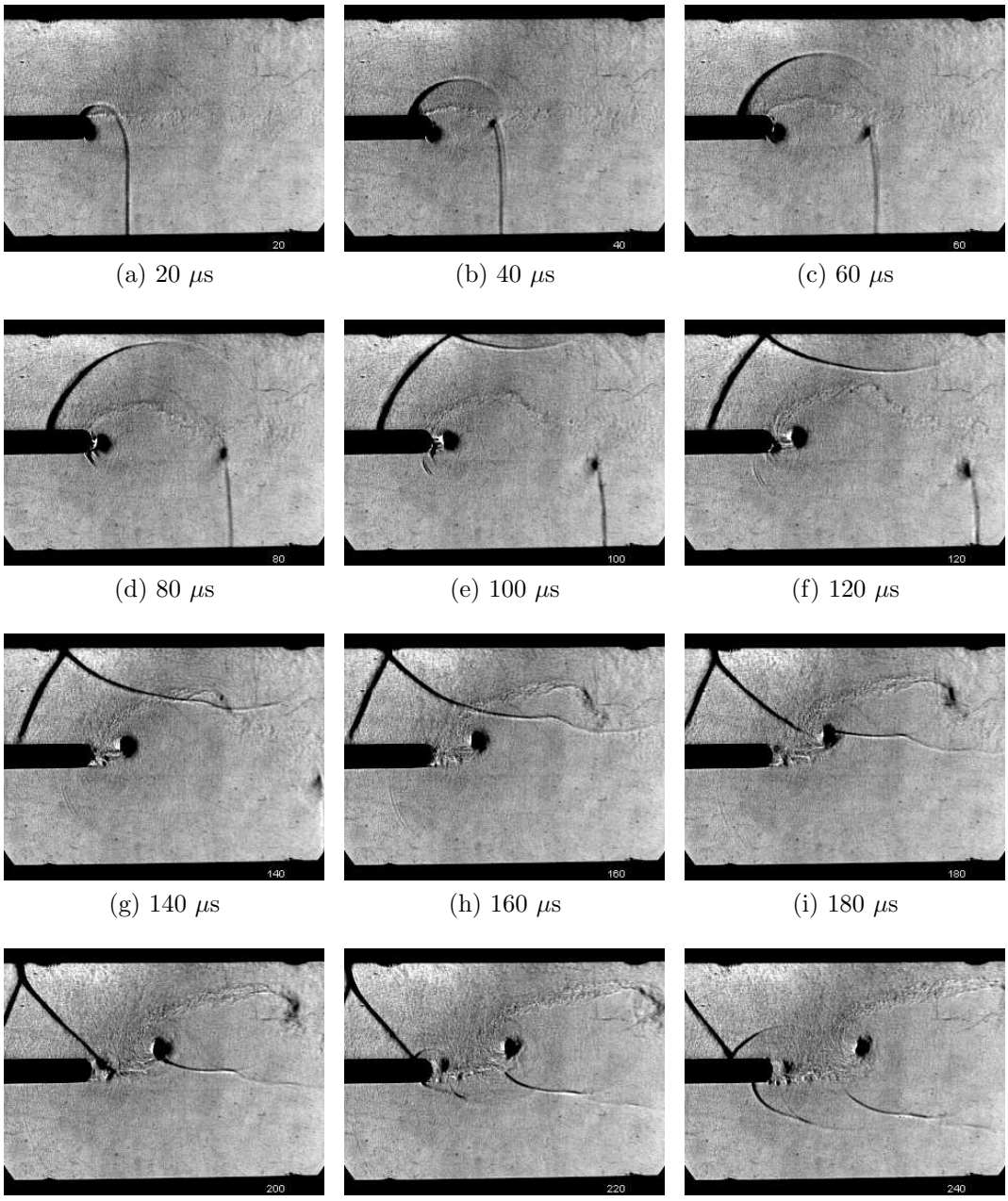

(a) 20 μs (b) 40 μs (c) 60 μs

(d) 80 μs (e) 100 μs (f) 120 μs

(g) 140 μs (h) 160 μs (i) 180 μs

(j) 200 μs (k) 220 μs (l) 240 μs

Figure C.5: Schlieren results of diffraction process around round geometry with subsonic co-flow, $\frac{P_4}{P_1} = 4$

C.2.3 Supersonic Co-Flow

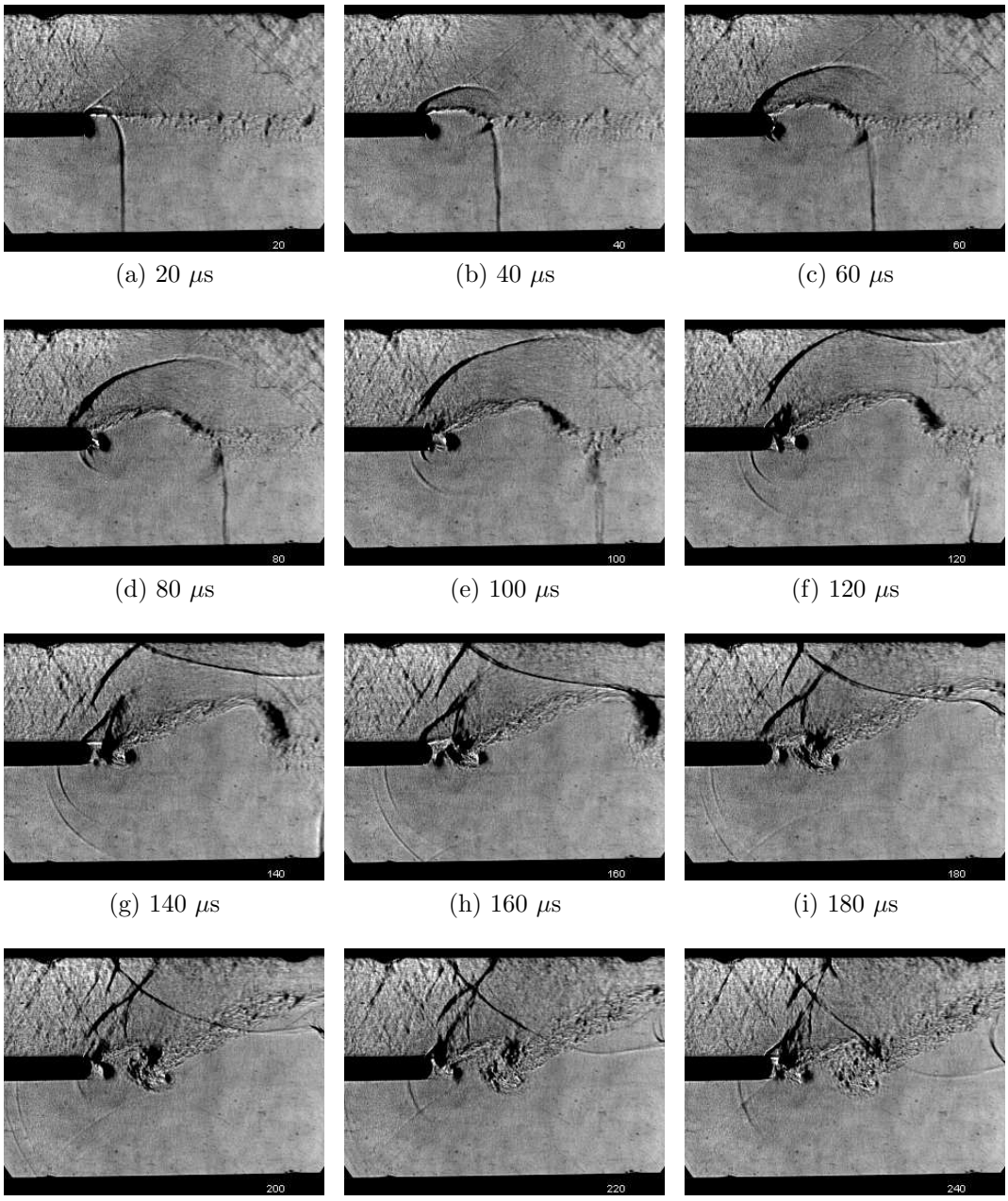

(a) 20 μs (b) 40 μs (c) 60 μs

(d) 80 μs (e) 100 μs (f) 120 μs

(g) 140 μs (h) 160 μs (i) 180 μs

(j) 200 μs (k) 220 μs (l) 240 μs

Figure C.6: Schlieren results of diffraction process around round geometry with supersonic co-flow, $\frac{P_4}{P_1} = 4$

C.2.4 P4/P1=12

C.2.5 Subsonic Co-Flow

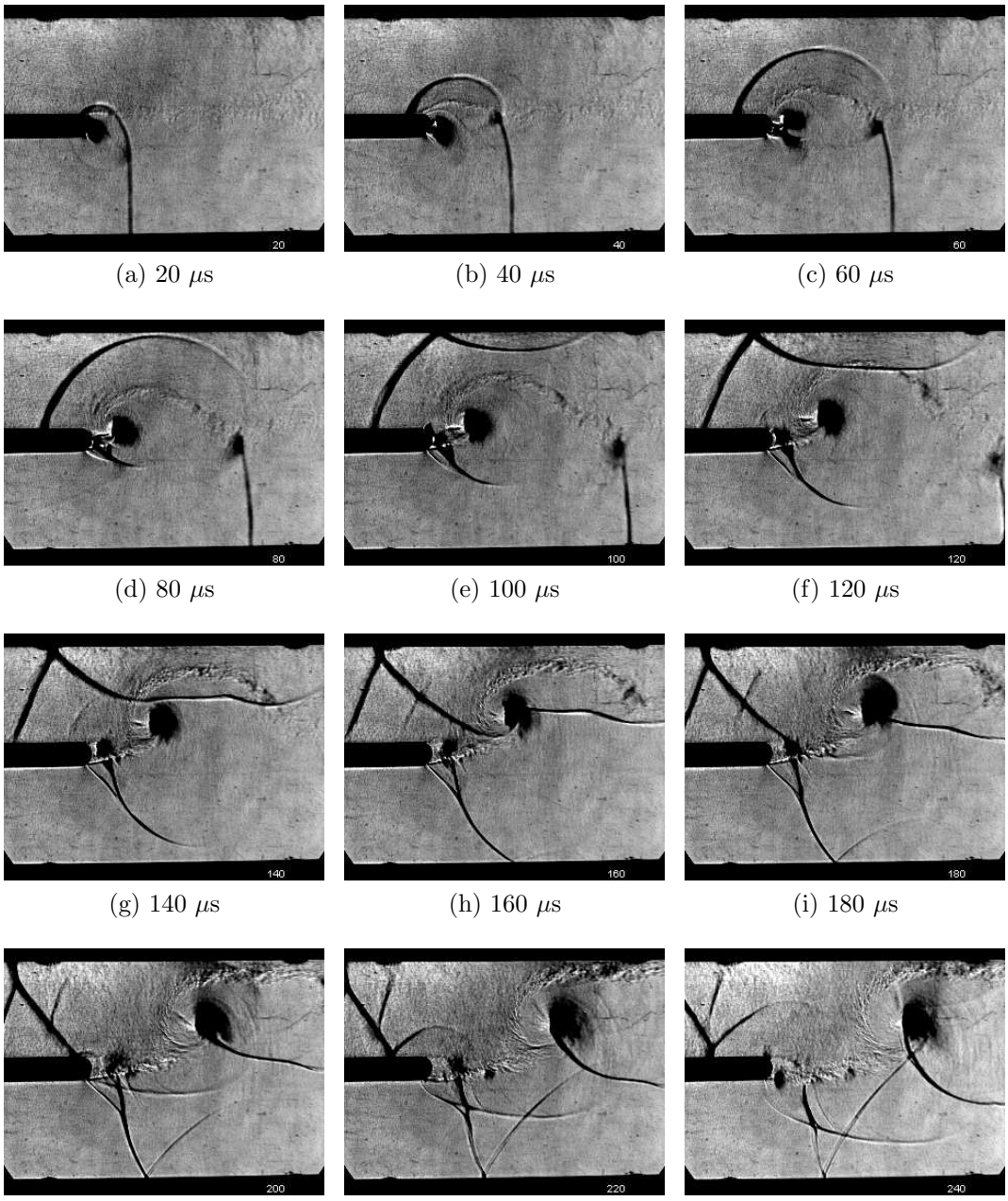

(a) 20 μs (b) 40 μs (c) 60 μs

(d) 80 μs (e) 100 μs (f) 120 μs

(g) 140 μs (h) 160 μs (i) 180 μs

(j) 200 μs (k) 220 μs (l) 240 μs

Figure C.7: Schlieren results of diffraction process around round geometry with subsonic co-flow, $\frac{P_4}{P_1} = 12$

C.2.6 Supersonic Co-Flow

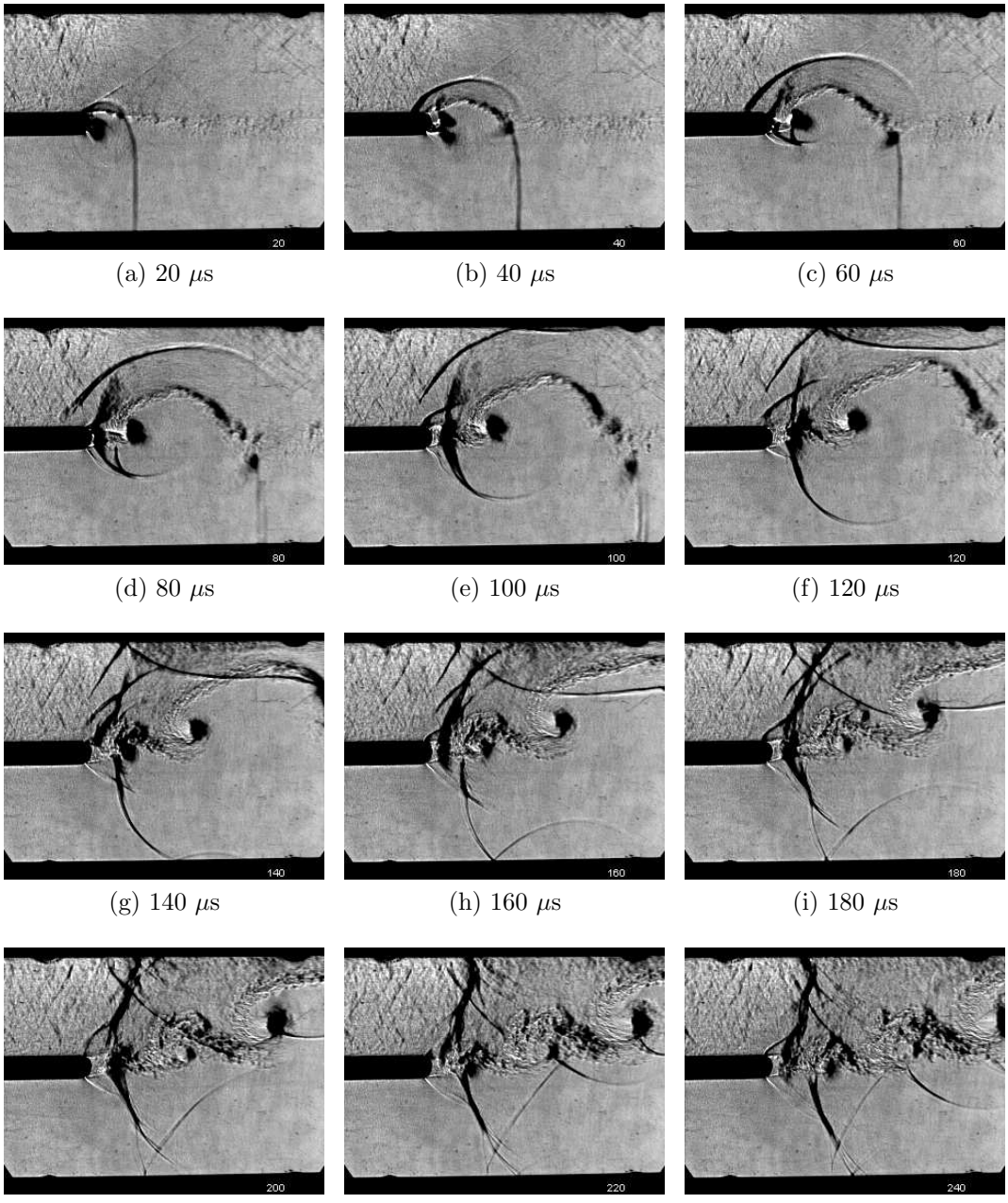

(a) 20 μs (b) 40 μs (c) 60 μs

(d) 80 μs (e) 100 μs (f) 120 μs

(g) 140 μs (h) 160 μs (i) 180 μs

(j) 200 μs (k) 220 μs (l) 240 μs

Figure C.8: Schlieren results of diffraction process around round geometry with supersonic co-flow, $\frac{P_4}{P_1} = 12$